U.S.NRC
United States Nuclear Regulatory Commission
Protecting People and the Environment

NUREG/CR-7254

Seismic Isolation of Nuclear Power Plants Using Sliding Bearings

Office of Nuclear Regulatory Research

AVAILABILITY OF REFERENCE MATERIALS IN NRC PUBLICATIONS

NRC Reference Material

As of November 1999, you may electronically access NUREG-series publications and other NRC records at NRC's Library at www.nrc.gov/reading-rm.html. Publicly released records include, to name a few, NUREG-series publications; *Federal Register* notices; applicant, licensee, and vendor documents and correspondence; NRC correspondence and internal memoranda; bulletins and information notices; inspection and investigative reports; licensee event reports; and Commission papers and their attachments.

NRC publications in the NUREG series, NRC regulations, and Title 10, "Energy," in the *Code of Federal Regulations* may also be purchased from one of these two sources.

1. **The Superintendent of Documents**
   U.S. Government Publishing Office
   Washington, DC 20402-0001
   Internet: bookstore.gpo.gov
   Telephone: (202) 512-1800
   Fax: (202) 512-2104

2. **The National Technical Information Service**
   5301 Shawnee Road
   Alexandria, VA 22312-0002
   www.ntis.gov
   1-800-553-6847 or, locally, (703) 605-6000

A single copy of each NRC draft report for comment is available free, to the extent of supply, upon written request as follows:

Address: **U.S. Nuclear Regulatory Commission**
Office of Administration
Multimedia, Graphics, and Storage & Distribution Branch
Washington, DC 20555-0001
E-mail: distribution.resource@nrc.gov
Facsimile: (301) 415-2289

Some publications in the NUREG series that are posted at NRC's Web site address www.nrc.gov/reading-rm/doc-collections/nuregs are updated periodically and may differ from the last printed version. Although references to material found on a Web site bear the date the material was accessed, the material available on the date cited may subsequently be removed from the site.

Non-NRC Reference Material

Documents available from public and special technical libraries include all open literature items, such as books, journal articles, transactions, *Federal Register* notices, Federal and State legislation, and congressional reports. Such documents as theses, dissertations, foreign reports and translations, and non-NRC conference proceedings may be purchased from their sponsoring organization.

Copies of industry codes and standards used in a substantive manner in the NRC regulatory process are maintained at—

The NRC Technical Library
Two White Flint North
11545 Rockville Pike
Rockville, MD 20852-2738

These standards are available in the library for reference use by the public. Codes and standards are usually copyrighted and may be purchased from the originating organization or, if they are American National Standards, from—

American National Standards Institute
11 West 42nd Street
New York, NY 10036-8002
www.ansi.org
(212) 642-4900

Legally binding regulatory requirements are stated only in laws; NRC regulations; licenses, including technical specifications; or orders, not in NUREG-series publications. The views expressed in contractor prepared publications in this series are not necessarily those of the NRC.

The NUREG series comprises (1) technical and administrative reports and books prepared by the staff (NUREG–XXXX) or agency contractors (NUREG/CR–XXXX), (2) proceedings of conferences (NUREG/CP–XXXX), (3) reports resulting from international agreements (NUREG/IA–XXXX),(4) brochures (NUREG/BR–XXXX), and (5) compilations of legal decisions and orders of the Commission and Atomic and Safety Licensing Boards and of Directors' decisions under Section 2.206 of NRC's regulations (NUREG–0750).

NUREG/CR-7254

U.S.NRC
United States Nuclear Regulatory Commission
Protecting People and the Environment

Seismic Isolation of Nuclear Power Plants Using Sliding Bearings

Manuscript Completed: February 2016
Date Published: May 2019

Prepared by:
M. Kumar[1]
A. Whittaker[2]
M. Constantinou[2]

[1]IIT Gandhinagar, India; formerly graduate student at University at Buffalo, State University of New York
[2]MCEER, University at Buffalo, State University of New York
212 Ketter Hall, Buffalo, NY 14260

Ramón L. Gascot Lozada, NRC Project Manager

Office of Nuclear Regulatory Research

ABSTRACT

Nuclear power plants (NPPs) are designed for earthquake shaking with very long return periods. Seismic isolation is a viable strategy to protect NPP structures from extreme earthquake shaking because it filters a significant fraction of earthquake input energy. This study addresses the seismic isolation of NPP structures using sliding bearings, with a focus on the single concave Friction Pendulum™ (FP) bearing.

Friction at the sliding surface of an FP bearing changes continuously during an earthquake as a function of sliding velocity, axial pressure and temperature at the sliding surface. The temperature at the sliding surface, in turn, is a function of the histories of coefficient of friction, sliding velocity and axial pressure, and the travel path of the slider. A simple model to describe the complex interdependence of the coefficient of friction, axial pressure, sliding velocity and temperature at the sliding surface is proposed, and then *verified* and *validated*.

Seismic hazard for a seismically isolated nuclear power plant is defined in the United States using a uniform hazard response spectrum (UHRS) at mean annual frequencies of exceedance (MAFE) of 10^{-4} and 10^{-5}. A key design parameter is the clearance to the stop (CHS), which is influenced substantially by the definition of the seismic hazard. Four alternate representations of seismic hazard are studied, which incorporate different variabilities and uncertainties. Response-history analyses performed on single FP-bearing isolation systems using ground motions consistent with the four representations at the two shaking levels indicate that the CHS is influenced primarily by whether the observed difference between the two horizontal components of ground motions in a given set is accounted for in the analyses.

The UHRS at the MAFE of 10^{-4} is increased by a design factor (≥ 1) for a conventional (fixed-base) nuclear structure to achieve a target annual frequency of unacceptable performance. Risk-oriented calculations are performed for eight sites across the United States to show that the factor is equal to 1.0 for seismically isolated NPPs, if the risk is dominated by horizontal earthquake shaking.

Response-history analyses using different models of a seismically isolated NPP structure are performed to understand the importance of the choice of friction model, model complexity and vertical ground motion for calculating horizontal displacement response across a wide range of sites and shaking intensities. A friction model for the single concave FP bearing should address heating. The pressure- and velocity-dependencies were not important for the models and sites studied. Isolation-system displacements can be computed using a macro model comprising a single FP bearing.

FOREWORD

As part of their 2008-2011 Seismic Research Program Plan, the Office of Regulatory Research (RES) of the U.S. Nuclear Regulatory Commission initiated an effort to investigate seismic base isolation technology. Base isolation is a technology developed to protect a structure from the damaging effects of earthquake shaking, by essentially decoupling the structure from high frequency, horizontal earthquake shaking. Operating seismically isolated nuclear power plants already exist in France and South Africa. Although base isolation has been effectively used on bridges, commercial buildings and other structures in the United States, there have been no applications on safety-related nuclear facilities in the United States, including nuclear power plants.

The research studied technical bases that would inform design and review guidance for the possible use of seismic isolation technology in nuclear power plants. The focus of the research was new surface-mounted large light water reactor designs but many of its products also are relevant for isolation of structures and components of next generation nuclear power plants. To conduct this research RES sponsored research at the University of Buffalo (UB) and Lawrence Berkeley National Laboratory (LBNL) under a contract to LBNL. This report is a deliverable for that contract that documents the research done on sliding bearings with a focus on the single concave Friction Pendulum™ bearing. A companion report, NUREG/CR-7255, documents the research done on elastomeric bearings, namely on lead-rubber and low-damping rubber bearings.

This research developed numerical models of single concave Friction Pendulum™ bearings, which permit extensive sensitivity analysis of base-isolated nuclear power plants subjected to a wide range of earthquake shaking with varying characteristics and frequency content. The report also documents the results of the sensitivity analyses conducted with those models, that provide data and insights on the performance of the isolator type studied and relate that performance to the design features of the isolator.

The information in this report could help form the basis for regulatory guidance on seismic base isolation, although such work is not planned at present. Specifically, the research focused on characterizing the coefficient of sliding friction at the sliding surface as a function of pressure, velocity and temperature. It then determined the influence of alternate representations of seismic hazard. It further examined the risk associated with the isolation system, and quantified the benefits of different risk-mitigation strategies. The report presents analytical results that inform which representation of an isolated nuclear power plant and which features of the isolator model are needed to compute responses for a wide range of earthquake shaking

The data and results in this report inform the technical basis to ensure readiness of the NRC infrastructure for potential applications that would utilize seismic isolation technologies. A third report, NUREG/CR-7253, “Technical Considerations for Seismic Isolation of Nuclear Facilities,” provides technical considerations, as well as performance and design recommendations addressing the design, construction, and operational needs for SI systems that consider the seismic, risk-informed, performance of structures, systems, and components (SSC). Technical considerations and regulatory challenges identified in that report include performance criteria to address the full scope of seismic demands, methods appropriate for the seismic soil-structure interaction analysis of a seismically isolated plant, defense in depth, reliability of the isolators during the operating life of the plant, and inspection and maintenance procedures.

TABLE OF CONTENTS

LIST OF FIGURES

LIST OF TABLES

EXECUTIVE SUMMARY

Nuclear power plants (NPPs) in the United States are required to be designed and assessed for extreme events, including earthquakes. Severe earthquakes can damage the structures, systems and components (SSCs) of an NPP. A viable strategy to protect these SSCs from extreme earthquake shaking is horizontal base (seismic) isolation. Three types of horizontal seismic isolation bearings are recommended for use in safety-related nuclear facilities in the United States: elastomeric, lead-rubber, and Friction Pendulum™ (FP). This report presents a study on the seismic isolation of NPP structures using single concave FP bearings. The report is divided into three parts, namely, 1) development of a model to describe the evolution of the coefficient of sliding friction at the surface of an FP bearing during earthquake-induced shaking, 2) characterization of seismic hazard and risk associated with the isolated NPPs, and 3) response-history analysis of a seismically isolated NPP subjected to extreme earthquake shaking in the regions of low, moderate and high seismicity.

The coefficient of friction at the sliding surface of an FP bearing changes continuously with the axial pressure on the bearing, velocity at the sliding interface, and temperature at the sliding surface. The axial pressure on the bearing varies due to the vertical component of the ground motion and the response of the isolated superstructure. The velocity of sliding depends on the input ground motions and the properties of the structure and the isolation system, including the coefficient of friction at the sliding surface. The temperature at the sliding surface is a function of histories of axial pressure, sliding velocity, coefficient of friction, and the travel path of the slider relative to the sliding surface. A model to characterize the coefficient of friction at the sliding surface should be able to account for the complex interdependence between the coefficient of friction, axial pressure, sliding velocity and temperature at the sliding surface. Two key assumptions are made to describe the coefficient of friction considering the dependencies of axial pressure, sliding velocity and temperature: 1) coefficient of friction at a small velocity (e.g., 0.001 mm/s) is half that at a high velocity (e.g., 1000 mm/s) irrespective of the axial pressure on the bearing, and 2) temperature at the center of the sliding surface represents the temperature at the sliding surface. These assumptions have been verified to not meaningfully alter isolator horizontal displacements. The influence of the axial pressure, temperature and sliding velocity on the coefficient of friction can be considered independently, as a consequence of the first assumption. The real-time coefficient of friction can be described as a product of a reference coefficient of friction and three factors accounting separately for the effects of axial pressure, temperature and sliding velocity. The model to describe the coefficient of friction is implemented in the Open Source Software for Earthquake Engineering Simulation (OpenSees) bearing element *FPBearingPTV*. The element has been *verified* and *validated* in accordance with ASME guidelines.

The second part of this report deals with the definition of seismic hazard for seismically isolated NPPs. A key design parameter for the isolation system is the clearance to the stop (CHS), which is recommended to be greater than the 99th (90th) percentile displacement for 10,000-year (100,000-year) shaking per the 2019 seismic isolation NUREG/CR. The clearance to the stop is a function of how the seismic hazard is defined. The seismic hazard is typically characterized by uniform hazard response spectrum (UHRS). This definition of seismic hazard can be considerably conservative, particularly at small mean annual frequencies of exceedance (MAFEs) (or long return periods). The second definition of seismic hazard considered in this study is the conditional mean spectrum (CMS), which is based on the UHRS ordinate at a user-defined conditioning period. The CMS does not account for variability in spectral shape given the UHRS ordinate at the conditioning period. Conditional spectra (CS) account for the

variability in the shape of the CMS. A fourth definition of seismic hazard, based on the UHRS, is also considered herein, UHRS-MaxMin, which accounts for the differences between the two orthogonal horizontal components of the ground motion.

Five-percent damped UHRS, CMS and CS with the conditioning periods of 2 s, 3 s and 4 s, and UHRS-MaxMin spectra are developed for the site of Diablo Canyon Nuclear Generating Station (DCNGS) and the return periods of 10,000 and 100,000 years. Friction Pendulum™ bearings with sliding periods of 3 s and 4 s were subjected to the 14 sets of 10,000-year and 100,000-year ground motions. It was observed that 1) the peak isolator displacements of the FP bearings are most significantly affected by the choice of target spectra, 2) the choice of seed motions for the CS-scaled spectra had little influence on isolator displacements, and 3) the 90th percentile 100,000-year isolator displacement response is greater than the 99th percentile 10,000-year displacement for a given choice of target spectrum. At the time of this writing, it is recommended that UHRS be used as target spectra with explicit consideration of the differences between the orthogonal horizontal components of the ground motions (UHRS-MaxMin).

The annual risk associated with the failure of an isolation system in an NPP was determined assuming the requirements (recommendations) for the prototype testing of isolators and umbilical lines per ASCE/SEI 4-16 (seismic isolation NUREG/CR 7253) were satisfied. It was (very) conservatively assumed that the loss of the axial load carrying capacity of a single bearing constituted unacceptable performance of the isolation system. Three strategies to mitigate the seismic risk were considered, namely, 1) testing more bearings to achieve greater confidence in the performance of bearings, 2) testing bearings for a greater displacement and corresponding axial loads, and 3) providing a stop (i.e., restraint on horizontal displacement) at a displacement corresponding to the 90th percentile displacement for beyond design basis shaking (assumed to be 100,000 years for an NPP). Increasing the number of prototype bearings tested and/or testing the bearings to greater displacements than CHS considerably reduces the annual frequency of unacceptable performance. A stop is generally needed to reduce the mean annual frequency of unacceptable performance to less than 10^{-6}.

The third part of the report presents the results of response-history analysis results of NPPs seismically isolated using sliding bearings. Two models of a seismically isolated NPP, one more detailed than the other, were subjected to 10,000-year and 100,000-year shaking at the sites of low, moderate and high seismicity. The coefficient of friction at the sliding surface was defined by five models that considered the dependence of the coefficient of friction on the sliding velocity, axial pressure on the bearing and/or temperature at the sliding surface. The analyses were performed with and without the vertical component of ground motion. The horizontal translational displacement of an isolation system can be reliably estimated using a macro model subjected to the two orthogonal horizontal components of ground motions. Isolation-system displacements should be computed using a friction model that accounts for the temperature dependence of the coefficient of friction; the effects of pressure and velocity dependencies are generally small. In-structure response spectra should be computed using a detailed three dimensional finite element model of the structure subjected to all three components of ground motions. The choice of friction model does not significantly affect floor spectral ordinates, particularly at locations close to the basemat.

A number of journal articles were published since this NUREG/CR was drafted. See Kumar et al. (2017a, 2017b) and Kumar and Whittaker (2017) for information.

ACKNOWLEDGMENTS

Financial support for this research project was provided by the United States Nuclear Regulatory Commission (USNRC) to MCEER via a contract led by Dr. Robert Budnitz at the Lawrence Berkeley National Laboratory (LBNL). The financial support provided by the USNRC and LBNL, and the technical leadership of Dr. Budnitz, is gratefully acknowledged.

A review panel was formed by LBNL to help guide our work and to provide timely feedback on interim deliverables. We sincerely thank members of the panel for their intellectual contributions to the project: Nilesh Chokshi, Antonio Godoy, James Johnson, Annie Kammerer, Robert Kennedy, Don Moore, and Jonathan Stewart.

Robert Roche provided the DYNA model of the sample nuclear power plant studied in this report. Brian Terranova helped with the analysis using the DYNA model. Yin-Nan Huang of the National Taiwan University supplied the ground motions for response-history analysis. We thank Mr. Roche, Mr. Terranova and Dr. Huang for their assistance.

Any opinions, finding and conclusions or recommendations expressed in this publication are those of the authors and do not necessarily reflect the views of MCEER, the University at Buffalo, LBNL or the USNRC.

ABBREVIATIONS AND ACRONYMS

(x,y)	Coordinates of a point in the isolation system
(x_o,y_o)	Coordinates of the center of the isolation system
$(\Delta x_{new},\Delta y_{new})$	X and Y coordinates of the center of a slider after translation and rotation of the isolation system
$(\Delta x_{rot},\Delta y_{rot})$	Change in the X and Y coordinates of a slider due to rotation of the isolation system
$(\Delta x_{trans},\Delta y_{trans})$	Change in the X and Y coordinates of a slider due to translation of the isolation system
$\mu(v)$	Coefficient of friction as a function of sliding velocity
$\mu_{\max}$	High-velocity coefficient of friction
$\mu_{\min}$	Small-velocity coefficient of friction
$\mu_{p=0}$	High-velocity coefficient of friction at zero axial pressure
$\mu_{\max p}$	High-velocity coefficient of friction at a very high axial pressure
$\mu_{p=p_o}$	Coefficient of friction at an axial pressure of p_o
$\mu(T)$	Temperature-dependent coefficient of friction
$\mu(T,t)$	Temperature-dependent coefficient of friction as a function of time
$\mu_{\max T}$	Coefficient of friction at a high temperature
$\mu_{\min T}$	Coefficient of friction at the beginning of the motion at the sliding surface
$\mu_{T=T_o}$	Coefficient of friction measured at T_o
μ	Coefficient of friction
$\mu(p,v)$	Coefficient of friction as a function of axial pressure and sliding velocity
$\mu(p)$	High-velocity coefficient of friction as a function of axial pressure
μ_2 , μ_3 , μ_4	Parameters to define s_{JB} and k_{JB}
a	Parameter to describe the shape of the $\mu(v)$ vs. v relationship

a_h	Heating rate parameter
$a(t)$	Acceleration ordinate at time t
a_e, b_1, b_2, b_3, ϕ	Parameters to define the temperature-dependent coefficient of friction
A_R	Amplification ratio defined as the ratio of spectral accelerations at $0.1H_D$ and H_D
ASB	Auxiliary and shield building
ASME	American Society of Mechanical Engineers
A_r	Area of contact at the sliding surface
a_v	Vertical acceleration
BDB	Beyond design basis
BDBE	Beyond design basis earthquake
CIS	Containment internal structure
CMS	Conditional mean spectrum
CS	Clearance to the stop
CS	Conditional spectra
D	Thermal diffusivity of steel
d	Distance between two adjacent bearings
DBE	Design basis earthquake
DCNGS	Diablo Canyon Nuclear Generating Station
DF	Design factor
DoE	Department of Energy
d_r	Translational displacement of the bearing at the center of the outermost line of bearings of the isolation system
DRS	Design response spectrum

d_t	Translational displacement of the isolation system
E_{CDF}	Expected cumulative distribution function
E_j	Expected count in the bin
F	Horizontal force
f_{AR}	Ratio of the 90th percentile and the median BDB GMRS displacements
f_h	Horizontal loading frequency
F_{Np}	Nominal frequency of unacceptable performance
f_o	External force
FP	Friction Pendulum
f_v	Vertical loading frequency
g	Acceleration due to gravity
GM	Ground motion
GMPE	Ground motion prediction equation
GMRS+	Ground motion response spectrum+
h	Mesh size
H_D	Annual frequency of exceedance of the seismic hazard
HDR	High damping rubber
IEEE	Institute of Electrical and Electronics Engineers
ITER	International Thermonuclear Experimental Reactor
JB	Jarque-Bera test statistic
K	Post-yield stiffness
k	Thermal conductivity of steel

$k(u)$	Lateral stiffness of an FP bearing as a function of lateral displacement
k_1	Lateral stiffness of an FP bearing before sliding begins
k_2	Lateral stiffness of an FP bearing during sliding
K_H	A parameter to characterize the slope of the seismic hazard curve between two MAFEs
k_{JB}	Sample kurtosis
k_p	Factor to account for the effect of axial pressure on the coefficient of friction
k_T	Factor to account for the effect of temperature at the sliding surface on the coefficient of friction
k_v	Factor to account for the effect of sliding velocity on the coefficient of friction
L_1	L_1 norm of the difference between two response histories
$L_{1,n}$	Normalized L_1
L_2	L_2 norm of the difference between two response histories
$L_{2,n}$	Normalized L_2
LDR	Low damping rubber
LR	Lead rubber
LT	Lilliefors test statistic
M	Moment magnitude of an earthquake
m	Multiple of the UHRS at an MAFE of 10^{-4}
MAFE	Mean annual frequency of exceedance
m_s	Mass of the slider of an FP bearing
M_W	Moment due to the vertical force
N	Normal force at the sliding surface
$n_{\max}$	Parameter to define the high-velocity coefficient of friction

$n_{\min}$	Parameter to define the small-velocity coefficient of friction
n_{bins}	Number of bins
n_{cycle}	Number of cycles of loading
N_{data}	Number of data points
NGA	Next Generation Attenuation
n_{JB}	Number of data points in a sample
NPP	Nuclear power plant
N_r	Number of data points
O_{CDF}	Empirical cumulative distribution function
O_j	Observed count in the bin
p	Axial pressure
P	Lateral force
p_r	Axial pressure
p_o	Reference axial pressure
$\hat{p}$	Observed order of accuracy
PEER	Pacific Earthquake Engineering Research
P_F	Frequency of unacceptable performance
$P_{F,isolation}$	Total annual frequency of unacceptable performance of the isolation system
$P_f \mid GM = m$	Annual frequency of unacceptable performance conditioned on m times the UHRS shaking at an MAFE of 10^{-4}
PGA	Peak ground acceleration
PTFE	Polytetrafluoroethylene
PWR	Pressurized Water Reactor

Q	Characteristic strength
q	Heat flux
q_r	Heat flux due to radiation
R	Radius of curvature
r	Source-to-site distance
$r_{contact}$	Radius of the area of contact at the sliding surface of an FP bearing
r_{ij}	i^{th} value of the j^{th} response quantity
r_{orient}	Distance of a bearing from the center of the isolation system
R_P	Ratio of H_D and P_F
S	Shear force on the sliding surface
s_μ	Shear strength of the interface of an FP bearing
s_{o_μ}	Shear strength of the interface of an FP bearing at zero axial pressure
S_a	Spectral acceleration
SA_{H_D}	Spectral acceleration corresponding to a given H_D
SCV	Steel containment vessel
SDC	Seismic design categories
s_{JB}	Sample skewness
SSC	Structure, systems and components
T	Temperature
T_o	Reference temperature
T^*	Conditioning period for the CMS or CS
T_1	Natural period of the bearing before sliding

TFP	Triple Friction Pendulum
$T_{sliding}$	Sliding period
u	Lateral displacement
$\|\dot{u}\|$	Magnitude of velocity of sliding
$\dot{u}$	Horizontal velocity
$\ddot{u}$	Horizontal acceleration
$\bar{u}$	"Exact" solution obtained using the Generalized Richardson Extrapolation Method
$\tilde{u}$	Exact solution of the dynamic equilibrium equation
$u_{exact,i}$	Exact solution at the i^{th} step
$u_{\text{horizontal}}$	Horizontal distance between the sliding surface and the slider
u_h	Numerical solution computed using a mesh size of h
$u_{h,i}$	Numerical solution at the i^{th} step for mesh size of h
$u_{horizontal,t}$	Horizontal displacement of the slider at time t relative to the center of the sliding surface
UHRS	Uniform hazard response spectrum
UHRS-MaxMin	Uniform hazard response spectra with the maximum and minimum components in the two orthogonal horizontal directions
$\dot{u}_x$	Sliding velocity in the X direction
$\dot{u}_y$	Sliding velocity in the Y direction
u_y	Lateral displacement of an FP bearing at which the slope of the lateral force-displacement curve under constant axial force changes
v	Sliding velocity
$\bar{v}$	Average of the sample
VGA	Vertical ground acceleration
v_j	j^{th} data point

v_{relative}	Increase in the height of FP bearing
VRA	Vertical acceleration of the slider relative to the sliding surface
$v_{relative,t}$	Vertical displacement of the slider at time *t* relative to the center of the sliding surface
$\dot{v}_{relative,t}$	Vertical velocity of the slider at time *t* relative to the center of the sliding surface
$\ddot{v}_{relative,t}$	Vertical acceleration of the slider at time *t* relative to the center of the sliding surface
v_{s30}	Shear wave velocity averaged over the upper 30 meters of the soil column
VTA	Vertical total acceleration
W	Axial load on the bearing
w_i	Weight assigned to the i^{th} value of the difference between two response histories
x	Depth below the sliding surface
$x_{\max}$	X coordinate of the centerline of the row of bearings farthest from the centroid of the isolation system
X_p	Standard normal variable corresponding to a probability of exceedance of *p*
$y_{\max}$	Y coordinate of the centerline of the row of bearings farthest from the centroid of the isolation system
α_r	A constant used in the definition of the shear strength at the sliding surface
α	A parameter used for the calculation of *DF*
$\bar{\alpha}$	A multiplier to the logarithmic standard deviation
α_0, α_1, α_2	Constants to define *a*
α_M, α_H	Parameters of the HHT numerical integration method
α_p, β_p	Parameters to define pressure-dependent coefficient of friction
β	Composite standard deviation (Chapter 6)
β_1, β_2	Parameters used to define $\mu(p,v)$
γ, β	Parameters of the Newmark's numerical integration scheme (Chapter 4)

$\gamma_1,\ \gamma_2$	Parameters to define $\mu(T)$
Δ	Lateral deformation
$\delta_1,\ \delta_2,\ \delta_3,\ \delta_4$	Parameters to define the pressure-dependent coefficient of friction
ΔF_x	Incremental force in the X direction
ΔF_y	Incremental force in the Y direction
ΔT	Change in temperature
Δt	Time interval
Δu_x	Displacement increment in the X direction
Δu_y	Displacement increment in the Y direction
Δz	Increase in the height of a bearing
ε_p	Parameter that defines the shape of the $\mu(p)$ vs. p curve
ε	Number of log standard deviations the UHRS ordinate exceeds the median spectral ordinate
ε_h	Discretization error for the mesh size of h
$\varsigma(t)$	Sum of square of acceleration ordinates between time 0 and t
θ	Angle of rotation of a slider (Chapter 4)
θ_m	Value of m corresponding to a 50% probability of unacceptable performance (Chapter 6)
θ_{orient}	Angle between the position vector of a bearing relative to the center of the isolation system and the Y axis
θ_{rot}	Angle of rotation of the isolation system
κ	Ratio of one half the 100,000-year 2 s spectral acceleration at Diablo Canyon to the 100,000-year 2 s spectral acceleration for a site
λ	Weighted average absolute percentage difference
$\lambda_1,\ \lambda_2$	Parameters used to define $\mu_{\min}$
σ_r	Stefen-Boltzman constant

τ	Instant of time
χ^2	χ^2-test statistic
χ_1, χ_2	Parameters that define pressure- and velocity-dependent coefficient of friction

1 INTRODUCTION

1.1 Nuclear Power Plants and Seismic Isolation

In the United States, nuclear power plants (NPPs) are designed for severe internal and external hazards, including earthquakes. Severe earthquakes can challenge new and existing NPPs, with large forces expected in their internal structures, systems and components (SSCs) in design basis shaking. Base isolation is a viable strategy to seismically protect SSCs in NPPs, since it effectively filters a significant fraction of the high frequency horizontal earthquake shaking, and it facilitates standardization of plant designs.

Two impediments to the deployment of base isolation in nuclear power plant structures have been a) a small number of new build NPPs in the United States, and b) a lack of regulatory guidance. The seismic isolation NUREG/CR 7253 (Kammerer *et al.*, 2019) addresses the second impediment by providing recommendations on analysis and design of seismically isolated NPPs and on testing of prototype and production isolators. This NUREG/CR identifies three types of bearings that could be used to seismically isolate an NPP in the United States: low damping rubber (LDR) and lead rubber (LR) elastomeric bearings, and Friction Pendulum™ (FP) sliding bearings.

This NUREG/CR focuses on the seismic isolation of NPPs using single FP bearings, with emphases on isolator behavior, system response and risk calculations. A companion NUREG/CR 7255 (Kumar *et al.*, 2019) addresses elastomeric seismic isolation bearings.

1.2 Objectives of the Report

The key objectives of this report are:

i. Develop and code a model to characterize the coefficient of friction at the sliding surface accounting for changes in the coefficient of friction with sliding velocity, temperature at the sliding surface and axial pressure during the course of earthquake-induced shaking,

ii. Verify and validate the code, following ASME best practice in computational mechanics,

iii. Examine the influence of alternate seismic hazard definitions on the distribution of isolation-system displacements,

iv. Perform risk-based calculations to compute design factors for seismically isolated nuclear power plants, and

v. Understand the influence of modeling choices (e.g., friction model) and loading condition (e.g., static axial pressure, inclusion of vertical ground motion) on the response quantities.

1.3 Organization of the Report

This report is organized into ten chapters and nine appendices. A brief introduction to the seismic isolation of structures is presented in Chapter 2. A model to account for the interdependence of coefficient of friction, sliding velocity, axial pressure and temperature is developed in Chapter 3. The proposed friction model is coded in a new OpenSees (PEER,

2014) element *FPBearingPTV*, which simulates the behavior of a single FP bearing. The assumptions involved in modeling the single FP bearing are discussed, and results on verification and validation of the code are presented in Chapter 4.

Four alternate representations of seismic hazard are discussed in Chapter 5 and ground motions consistent with these representations are developed for different shaking levels. The development of response spectra and the ground motions, and the results of response-history analyses performed on single FP bearing subjected to these ground motions are presented. Risk calculations are performed to determine the design factors for seismically isolated nuclear power plants in Chapter 6.

Chapter 7 presents results of response-history analyses performed with a macro isolator with a range of bearing properties and loading conditions to study the influence of choice of friction model on the horizontal response of a simplified FP isolation system as a function of shaking intensity and bearing parameters (e.g., reference axial pressure, reference coefficient of friction). Chapter 8 presents results of response-history analyses performed with two models of an NPP nuclear island that answer three practical questions, namely, 1) How significantly does the choice of friction model affect horizontal displacement response?, 2) How does the vertical component of ground motion affect horizontal displacement response?, and 3) Can key response quantities be estimated with a macro model of the isolation system?.

The research project is summarized and its important conclusions are presented in Chapter 9. References are listed in Chapter 10.

Appendix A presents the ground motions used for the verification and validation studies. The effect of decoupling the pressure and velocity dependencies of the coefficient of sliding friction is examined in Appendix B.

The vertical accelerations of the slider relative to the sliding surface are estimated in Appendix C for single FP bearing with a range of geometric properties subjected to ground motions scaled to different intensities. Appendix D describes the relative vertical displacement of the sliders in an isolation system composed of single FP bearings subjected to combinations of translational and rotational displacements.

Appendix E presents the seed ground motions that are matched to a number of response spectra in Chapter 5.

Risk calculations for isolation systems designed in accordance with Chapter 12 of ASCE/SEI Standard 4-16 (ASCE, 2017) are presented in Appendix F.

Issues related to amplitude scaling ground motions to represent seismic hazard are discussed in Appendix G. The assumption of lognormality in a number of response quantities of a seismically isolated nuclear structure is confirmed in Appendix H.

2 SEISMIC ISOLATION OF STRUCTURES: AN OVERVIEW

2.1 General

Numerous efforts have been made in the past century to control the response of structures during earthquakes. Recent approaches include the use of 1) mechanisms to change the dynamic properties of a structure to limit the input energy (Robinson, 1982; Zayas *et al.*, 1987), and 2) energy dissipating devices (Aiken *et al.*, 1993; Constantinou and Symans, 1992; Kelly *et al.*, 1972; Pall and Marsh, 1982). Seismic isolation both increases the natural period of a structure to reduce its seismic response and dissipates some of the input energy.

Buildings, bridges and viaducts (e.g., Christopoulos and Filiatrault (2006)), oil platforms (e.g., Fenz *et al.* (2011), Clarke *et al.* (2005)), and nuclear reactors (e.g., Grandis *et al.* (2011)) have been seismically isolated. Records of performance are available for some of the isolated buildings that have experienced significant earthquake shaking.

This chapter presents a brief history of the seismic isolation of buildings. The seismic performance of some isolated buildings is discussed. An overview of the seismic isolation of nuclear structures is presented. The three types of seismic isolation bearings (low damping rubber, lead-rubber and FP bearings) likely to be used in the United States for seismic isolation of nuclear structures are introduced.

2.2 A Review of Seismic Isolation of Building Structures

2.2.1 Early Proposals

Constantinou *et al.* (2007) note that the first seismic isolation system for building structures was proposed by Joules Touaillon in 1870 (US Patent No. 99973). It consisted of two "strong plates" with uniformly located spherical "depressions". Rigid rollers were placed between the two plates at the locations of these depressions. The isolation system is similar to the double concave Friction Pendulum (DCFP) bearing (e.g., Fenz and Constantinou (2006)) with the articulated sliders replaced by rigid rollers. An isolation system with units of two cast-iron plates separated by rigid balls was proposed and implemented by John Milne in 1880s. A handful of ¼ in diameter cast-iron shot was placed between the two cast-iron plates in each unit of the isolation system (Naeim and Kelly, 1999). In 1891, Kawai proposed to put a building on layers of cylindrical logs, which would roll during earthquakes. The layers were to be placed in orthogonal directions on top of each other (Izumi, 1988). More proposals to construct a building on rollers were made by Jacob Bechtold in 1907 (US Patent No. 845046) and by Italian and Portuguese engineers in 1909 (Tassios, 2009).

The first isolation system based on sliding was proposed in 1909 by a British medical doctor, A. Calantarients. He proposed to construct building structures on a "free joint" made up of a layer of sand or talc, which would allow the building to slide in the event of an earthquake (Naeim and Kelly, 1999).

2.2.2 Early Applications

To the knowledge of the author, a seven-story reinforced concrete building in the Crimea is the second building in the world (first was the one designed by John Milne, as discussed in Section 2.2.1) to be isolated using rollers. The isolation system comprised of egg-shaped bearings, which would force the building to rise when subjected to lateral deformation, generating a restoring force (Nazin, 1978).

A building constructed in Tokyo in 1921 responded during 1923 Kanto earthquake as if it was supported on a sliding system. The building foundation rested on a thick layer of good quality soil, below which was there a layer of mud. The building survived the devastating earthquake without much damage, as the layer of mud functioned as a "cushion" to protect the building from seismic waves (Wright, 1977). There have been cases of accidental sliding isolation of buildings, due to poor connection between the superstructure and the foundation. The 1930 Dhubri and 1934 Bihar earthquakes in India (Arya, 1984) and the 1966 Xintai, 1969 Bohai and 1976 Tangshan earthquakes in China (Buckle and Mayes, 1990) provide examples.

A three-story brick and reinforced concrete building constructed in Ashkhabad, Russia in 1959 was likely the first pendulum-suspended building in the world. Columns of this building rested on cradles hanging from the foundation through 1 m long cables (Buckle and Mayes, 1990).

The first building to be isolated using bearings made of natural rubber was a three-story concrete building in Yugoslavia. Completed in 1969, the building rested on large blocks of solid rubber (not reinforced with steel shims like modern elastomeric bearings). The isolation system had comparable values of stiffness in the vertical and horizontal directions (Kelly, 1986).

2.2.3 Modern Applications

Seismic isolation became an attractive alternative for protecting new and existing buildings with the development of technology to perform experiments and numerical simulations. In Japan, the number of seismically isolated buildings was about 75 before 1994. The good performance of isolated buildings in the 1995 Kobe earthquake led to a rapid increase in the use of seismic isolation, with more than 700 buildings isolated in Japan by 2003 (Clark *et al.*, 1999; Kelly, 2004). A similar uptick is taking place in Italy following the 2009 Abruzzo earthquake, which caused significant damage to many conventional buildings and heritage structures (Martelli *et al.*, 2011). Figure 2-1 shows the history of the number of seismically isolated buildings in Japan and Italy.

The modern era in seismic isolation began in 1978 with the isolation of the Clayton Building in New Zealand using lead rubber (LR) bearings (Buckle, 1985; Skinner et al., 1991). Since then, the technology has been used for many new and existing structures, at times to retain the architectural features of a building. Seismic isolation has been preferred over other methods of rehabilitation to preserve historical buildings, with applications including the Oakland, San Francisco and Los Angeles City Halls, the US Court of Appeals building in San Francisco, and the New Zealand Parliament building in Wellington, New Zealand.

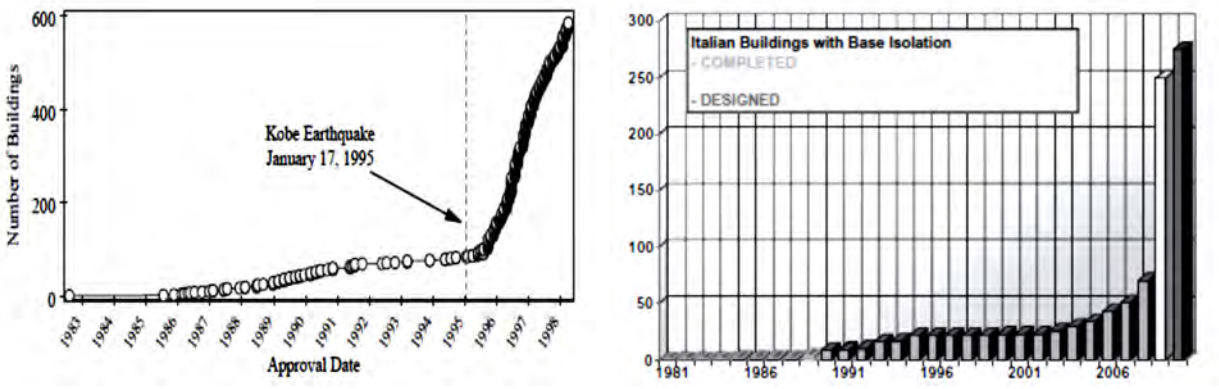

(a) Japan (Clark *et al.*, 1999) (b) Italy (Martelli *et al.*, 2011)

Figure 2-1 Number of Seismically Isolated Buildings

The first isolated building in the United States was the Foothill Communities Law and Justice Center, which was isolated in 1985 using LR bearings. Although the building received significant attention in the engineering community (Kelly, 2004), only seven buildings were isolated in the United States before 1990 and less than 40 were isolated prior to 2000.

2.3 Performance of Seismically Isolated Buildings

Observations of performance of seismically isolated buildings after earthquakes, including the 1994 Northridge earthquake (Clark *et al.*, 1996), 1995 Kobe earthquake (Kelly, 2004) and 2005 Fukuoka earthquake (Morita and Takayama, 2008), have indicated that damage to structural framing systems is minimal. For non-structural components, performance depends on the absolute acceleration or velocity history of the floor on which the component rests (Badillo-Almaraz *et al.*, 2007; Burningham *et al.*, 2007; Filiatrault *et al.*, 2004). Records of acceleration response at different floor levels are available for some isolated buildings that experienced earthquakes. The following sections present discussion on the response of selected isolated buildings in terms of recorded accelerations at different floor levels.

2.3.1 Earthquakes in the USA and Japan During the Late 1980s

Buckle and Mayes (1990) report measured peak accelerations in isolated buildings in the US and Japan during earthquakes in the 1980s, as reproduced in Figure 2-2. The peak roof acceleration recorded in all of the isolated buildings was less than the corresponding peak ground acceleration and was significantly less than the peak roof acceleration recorded in near-by fixed base buildings.

2.3.2 1994 Northridge Earthquake

Clark et al. (1996) reported peak floor accelerations in isolated buildings recorded during 1994 Northridge earthquake. The buildings identified in Figure 2-3, namely, private residence, University of Southern California (USC) Teaching Hospital, Los Angeles Fire Command and

Control Facility (LAFCCF), Rockwell Computer Center Seal Beach, and Foothill Communities Law and Justice Center (FCLJC) were located 21 km, 36 km, 38 km, 66 km and 90 km from the epicenter of the earthquake, respectively. The peak roof acceleration is smaller than the peak ground acceleration (PGA) for the USC Teaching Hospital building only. For the other four structures, the peak roof acceleration was greater than the corresponding PGA due to either

1) impact of the isolated structure on non-structural components placed within the moat, or
2) the small intensity of shaking not triggering the isolation system.

Makris and Deoskar (1996) simulated the response of the private residence, which was close to the epicenter. They concluded that the maximum roof acceleration would have been approximately 1.0 g if the structure was not isolated, significantly greater than the observed acceleration of 0.6 g.

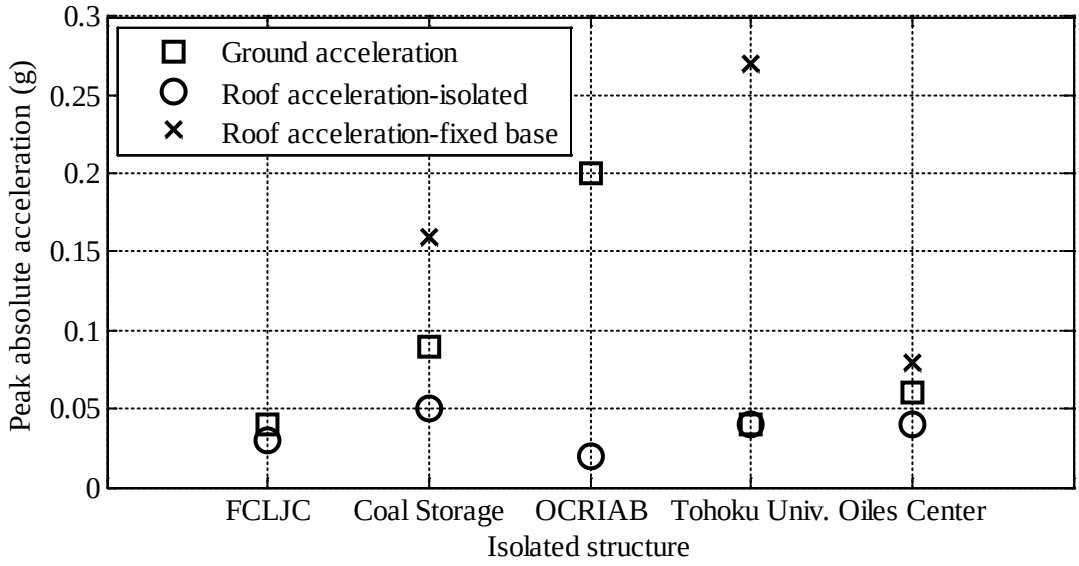

Figure 2-2 Recorded Values of Maximum Absolute Acceleration for Buildings in USA and Japan During Different Earthquakes During the Period 1985-89 (reproduced from Buckle and Mayes (1990))

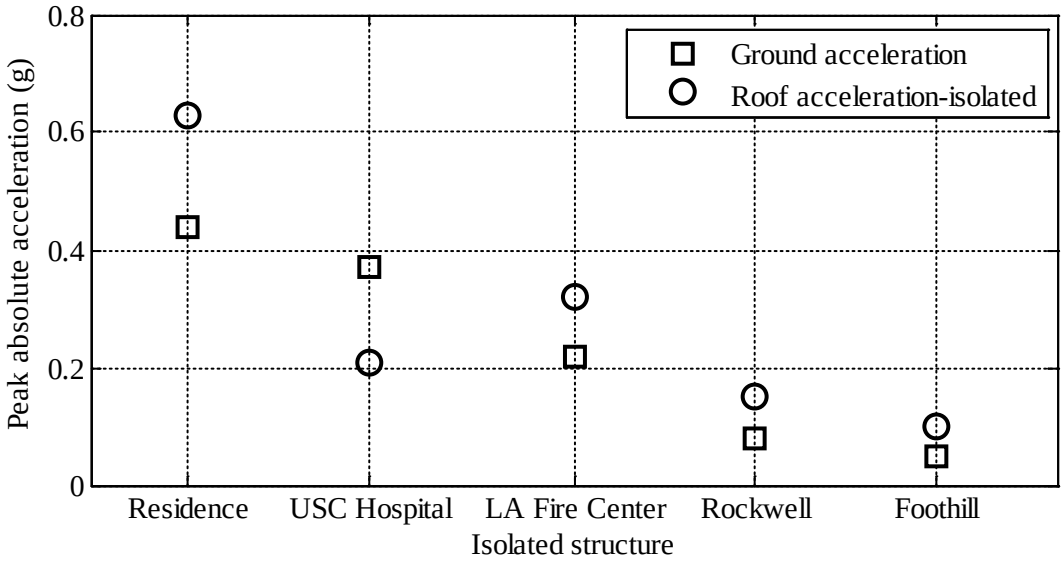

Figure 2-3 Recorded Values of Peak Ground Acceleration and Maximum Roof Acceleration of Isolated Buildings During 1994 Northridge Earthquake (reproduced from Clark *et al.* (1996))

Clark *et al.* (1996) assign the impact at the level of isolation system in the LAFCCF building to the presence of an architectural feature in the seismic gap (moat). A detailed study on the impact was performed by Nagarajaiah and Sun (2001). The acceleration in one horizontal direction was amplified along the height of the structure due to the impact (shown in Figure 2-3). However, in the orthogonal direction, the isolation system was effective because the maximum acceleration at the foundation and roof were 0.18 g and 0.09 g, respectively.

The isolation system of the USC Hospital building performed well as the peak roof acceleration was 0.21 g, about 40% smaller than the peak ground acceleration. The peak acceleration in the lower floors was smaller than 0.13 g (Clark *et al.*, 1996). The amplification of acceleration observed in the FCLJC building was attributed to a small PGA of 0.05 g, which did not trigger the isolation system (Kelly, 2004).

2.3.3 1995 Kobe Earthquake

The rapid increase in the number of seismically isolated buildings in Japan after the 1995 Kobe earthquake (see Section 2.2.3) was attributed in part to the excellent performance of two seismically isolated buildings, Matasumura-Gumi Technical Research Institute and West Japan Postal Saving Computer Center (Kelly, 2004; Nakashima and Chulisp, 2003), during that earthquake. Figure 2-4 presents recorded peak accelerations in these two buildings during the Kobe earthquake, as reported by Kelly (2004). For both buildings, the maximum acceleration recorded at the roof was similar to or less than the PGA in both horizontal directions. The peak vertical acceleration was amplified in both buildings, with the peak roof acceleration being more than 1.6 times the peak vertical ground acceleration. For the Postal Center building, the maximum vertical acceleration at the foundation, first floor and roof were 0.22 g, 0.20 g and 0.38 g, respectively. These values indicate that amplification in vertical acceleration was negligible across the isolation system. The peak roof acceleration could have been high due to the vertical flexibility of the roof framing (e.g., Almazán *et al.* (1998)).

2.3.4 2005 Fukuoka Earthquake

The March 20, 2005 M 7.0 Fukuoka earthquake shook thirteen isolated buildings in the city. Morita and Takayama (2008) reported values of maximum acceleration in two of those buildings (see Figure 2-5). Significant de-amplification of acceleration due to seismic isolation is seen for both buildings in the two horizontal directions.

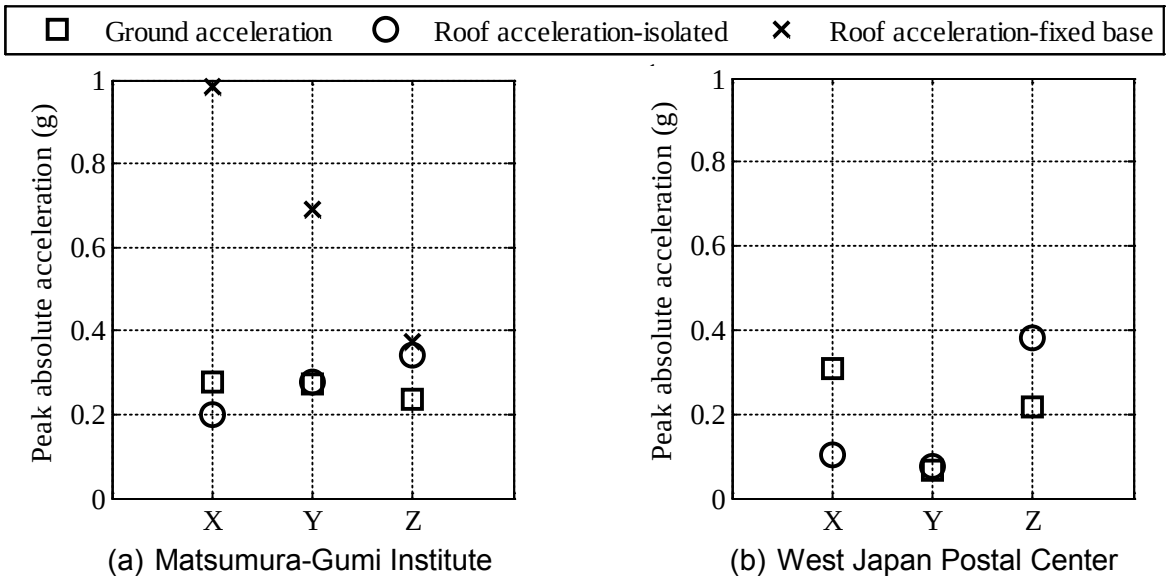

Figure 2-4 Recorded Values of Maximum Acceleration at Ground and Roof of Isolated and Near-By Buildings in Japan During the 1995 Kobe Earthquake (reproduced from Kelly (2004))

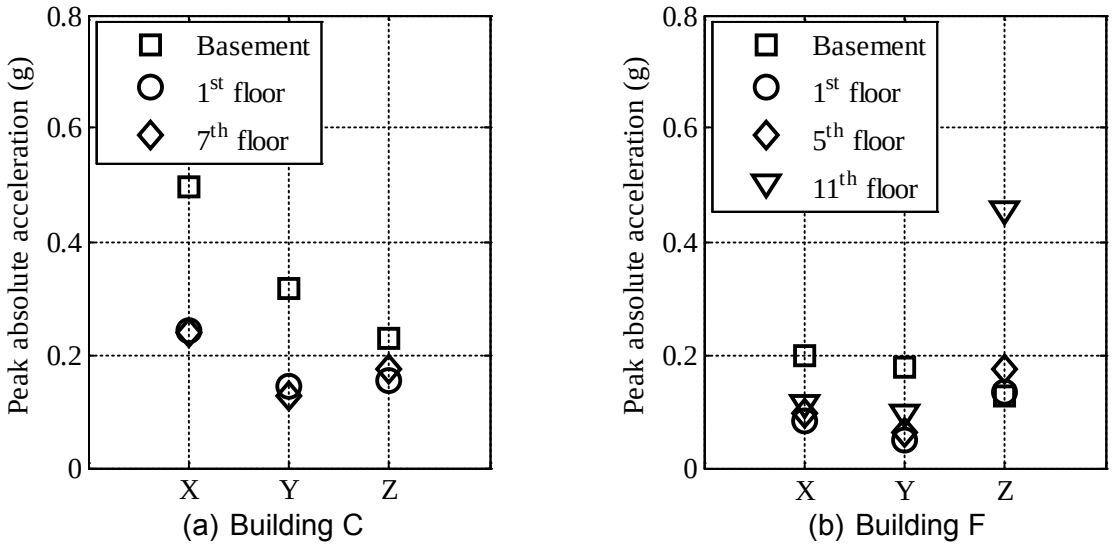

Figure 2-5 Maximum Recorded Acceleration of Two Buildings During the 1995 Fukuoka Earthquake in Japan (reproduced from Morita and Takayama (2008))

Like the Postal Center building (Section 2.3.3), amplification of the vertical motion was very small across the isolation system for the two buildings. For the seven story Building C, the peak roof acceleration (0.18 g) was smaller than the PGA (0.23 g) in the vertical direction. However, for the eleven story Building F, the peak vertical acceleration at the roof was 3.5 times the vertical PGA.

2.4 Seismic Isolation of Safety-Related Nuclear Power Plant Structures

Although there have been more than 10,000 applications of seismic isolation in the world to different types of structures, such as buildings, bridges and offshore oil platforms, only two nuclear power plants had utilized seismically isolated reactors until recently, one in Cruas, France with four Pressurized Water Reactors (PWR) and one in Koeberg, South Africa with two PWRs. Both plants started operating in the early 1980s. The construction of the seismically isolated Jules Horowitz Reactor and International Thermonuclear Experimental Reactor (ITER) in Cadarache, France is in progress (Grandis *et al.*, 2011; Syed *et al.*, 2014).

There are no seismically isolated nuclear structures in the US at present although studies were performed in the late 1980s (e.g., Kelly (1993), Tajirian *et al.* (1990)). Most of the nuclear power plants in the US were licensed in 1970s and 80s, as shown in Figure 2-6. Only four licenses were granted in the 1990s. No license was granted in the 2000s. Two new licenses have been granted recently for nuclear power generation at Vogtle in Georgia and at Summer in South Carolina (USNRC, 2013). More recent studies on the seismic isolation of nuclear structures (Huang *et al.*, 2007; Huang, 2008) have focused on reduction in seismic risk. The first seismic isolation NUREG/CR 7253 (Kammerer *et al.*, 2019) was published in 2019.

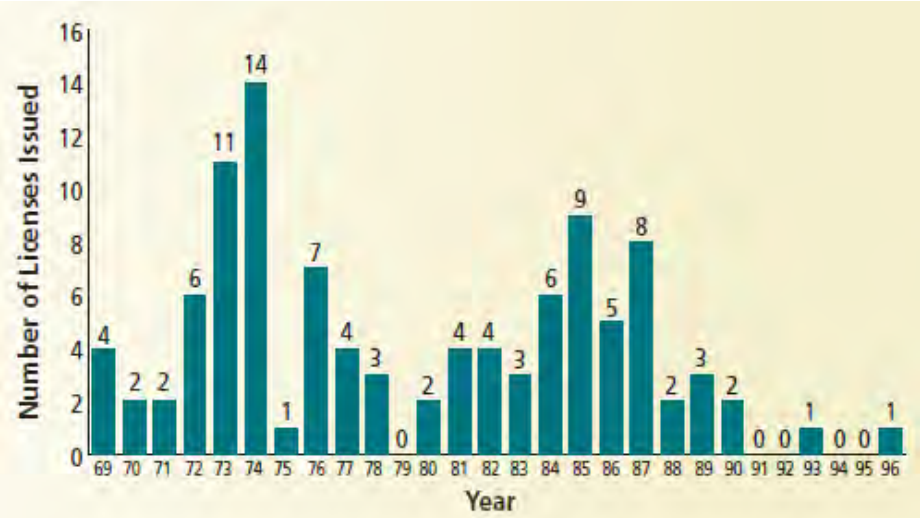

Figure 2-6 Number of Licenses Issued by the United States Nuclear Regulatory Commission to Generate Nuclear Power at Commercial Scale (USNRC, 2012)

2.5 Seismic Isolation Bearings

Three types of seismic isolation bearings are likely to be considered in the US for the seismic isolation of nuclear structures: Low damping rubber (LDR), Lead rubber (LR) and Friction Pendulum™ (FP) bearings (Kammerer et al., 2017). A brief discussion of each of these bearings is presented next.

2.5.1 Low Damping Rubber (LDR) Bearing

Elastomeric bearings are fabricated using alternating layers of rubber and steel shims. Figure 2-7 shows a section through an older elastomeric bearing. Elastomeric bearings can be of three types: low damping rubber (LDR), high damping rubber (HDR) and synthetic rubber. Different elastomers are used in each. The lateral stiffness of a LDR bearing is a function of the shear modulus of rubber, the bonded area, the total thickness of rubber, the axial pressure, the lateral displacement and the ambient temperature (Kumar *et al.*, 2014).

LDR bearings are used often in combination with LR bearings that increase the energy dissipation capacity of an isolation system. Applications of LDR bearings include Salt Lake City and County building, USC University Hospital, Oakland City Hall and the Long Beach Hospital, and the Parliament buildings and National Museum in New Zealand.

2.5.2 Lead Rubber (LR) Bearing

Lead-rubber (LR) bearings are elastomeric bearings with added lead plug (or plugs) to increase energy dissipation capacity (e.g., Robinson (1982)). Figure 2-8 shows the interior construction of a typical LR bearing. The post-yield stiffness of an LR bearing is essentially that of the LDR bearing discussed above. The elastomer is natural rubber. The lead core significantly increases the yield strength and pre-yield stiffness of an LR bearing, which reduces the movement of the superstructure during small earthquakes and under wind loading. The yield strength of the lead core depends on its area, its confinement and on its temperature, which is a function of the loading history. LR bearings were also used in the applications identified in the Section 2.5.1 , together with LDR bearings.

Figure 2-7 Internal Construction of an Elastomeric Bearing (Naeim and Kelly, 1999)

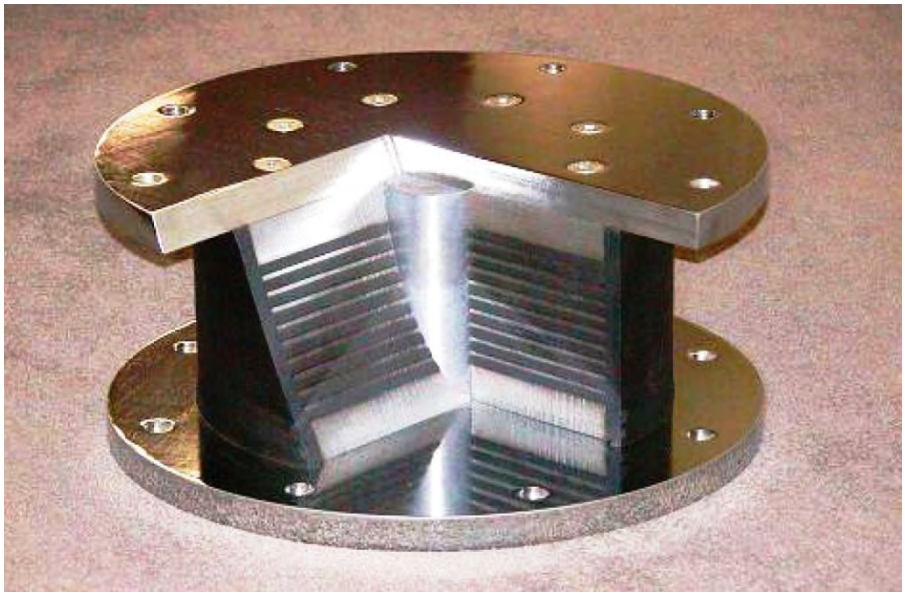

Figure 2-8 Internal Construction of a Lead-Rubber Bearing (Constantinou *et al.*, 2007)

2.5.3 Friction Pendulum™ (FP) Bearing

Figure 2-9 shows a single concave Friction Pendulum™ (FP) bearing comprising a spherical sliding surface of stainless steel, a slider coated with a PTFE-type composite material and a housing plate. The lateral force-displacement relationship of an FP bearing is a function of the coefficient of friction between slider and the sliding surface, the radius of curvature of the sliding surface, the velocity of sliding, the axial load and the temperature at the sliding surface. Chapter 3 presents a model to characterize the lateral force-displacement relationship of FP bearings accounting for those factors that affect the coefficient of friction. Applications of FP bearings include the US Court of Appeals, Hayward City Hall, San Francisco International Airport Terminal, Pasadena City Hall and Benicia-Martinez Bridge, Liquefied Natural Gas Tanks in Greece, and Ataturk International Airport in Turkey.

Figure 2-9 Sliding Plate, Slider and Housing Plate for a Single Friction Pendulum Bearing (EPS, 2011)

3 FRICTION IN SLIDING ISOLATION BEARINGS

3.1 Introduction

The lateral force-displacement behavior of the Friction Pendulum™ (FP) bearing is a function of the coefficient of sliding friction, axial load on the bearing and effective radius of curvature of the sliding surface. The characteristic strength (force at which sliding begins) of the bearing is the product of the coefficient of friction and instantaneous axial load. The coefficient of friction varies during the course of the earthquake with sliding velocity, axial pressure and temperature at the sliding surface. The sliding velocity and axial pressure on the bearing depend on the superstructure response to the earthquake shaking. The temperature on the sliding surface, at a given instant in time, is a function of the histories of the coefficient of friction, sliding velocity and axial pressure, and the travel path of slider on the sliding surface, together with parameters characterizing heat transfer of the materials that form the interface.

A model to simulate the lateral force-displacement behavior of an FP bearing should be able to account for interdependence of the coefficient of sliding friction, the sliding velocity, the temperature at the sliding surface and the instantaneous axial pressure. For nonlinear response-history analysis, the coefficient of sliding friction may have to be updated at every time step depending on the instantaneous values of sliding velocity, temperature at sliding surface and axial pressure. This chapter presents an approach to account for the dependence of the coefficient of friction on these three quantities. Expressions to define the relationship between the coefficient of friction and sliding velocity, axial pressure, and temperature are proposed, based on available experimental data. A suitable assumption is made to decouple the influence of axial pressure and sliding velocity on the coefficient of friction. A method to compute temperature at a point on the sliding surface is described. The temperatures at different points on the sliding surface vary depending on the loading history. A representative value of temperature on the sliding surface is needed to update the coefficient of friction. Two approaches to compute the representative temperature are compared.

3.2 Force-Displacement Behavior

Friction Pendulum™ (FP) bearings are widely used in the United States for seismic isolation of structures. In its single concave configuration, the FP bearing includes a sliding surface of polished stainless steel and an articulated slider coated with PTFE-type composite material. Figure 3-1 is a section through an FP bearing.

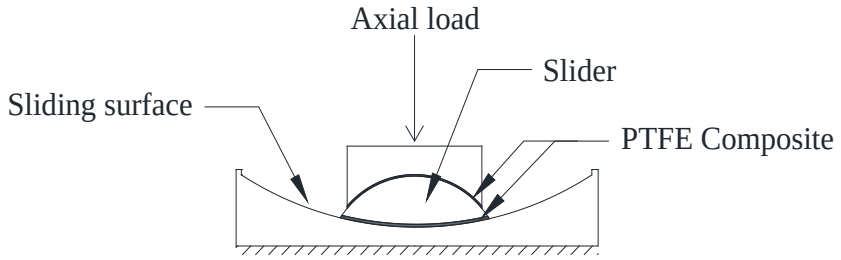

Figure 3-1 Section Through a Single Concave Friction Pendulum™ (FP) Bearing

For fixed values of axial load on the bearing and the coefficient of sliding friction between the sliding surface and the slider, the force-displacement behavior of an FP bearing in a horizontal

direction can be represented by a bilinear curve of Figure 3-2. The curve is characterized by characteristic strength Q, the product of the coefficient of friction and the axial load, and post-yield stiffness K, the ratio of supported axial load to the effective radius of curvature of the bearing. The axial load on a bearing changes continuously during earthquake shaking because of the superstructure response to the vertical and horizontal shaking, leading to continuous changes in Q and K. In addition, the coefficient of sliding friction is a function of the instantaneous values of sliding velocity, axial pressure on the bearing and temperature at the sliding surface, which also change Q. The temperature at the sliding surface at a given instant depends on the histories of sliding velocity, axial pressure and coefficient of friction, and the path traveled by the slider (see Figure 3-3).

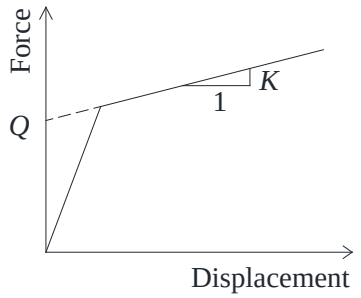

Figure 3-2 Lateral Force-Displacement Relationship of a Single Concave Friction Pendulum™ (FP) Bearing (Zayas *et al.*, 1987)

3.2.1 Dependence of the Coefficient of Friction on the Velocity of Sliding

The relationship between the coefficient of friction and the velocity of sliding at the interface can be described by an exponential function given by Mokha *et al.* (1988):

$$\mu(v) = \mu_{max} - (\mu_{max} - \mu_{min})e^{-av} \quad \textbf{(3-1)}$$

where μ_{min} and μ_{max} are the values of the coefficient of friction at very small and very high velocities of sliding, respectively, a is a parameter describing the shape of the curve, and v is the sliding velocity. The rate parameter a depends on the properties of the PTFE-type composite coating on the slider. For the composite material used in an FP bearing, a is approximately 100 s/m, as noted by Constantinou *et al.* (2007) based on the experimental studies performed by Constantinou *et al.* (1993) and Tsopelas *et al.* (1994a). For this study, a is set equal to 100 s/m, which is the value adopted in past studies (e.g., Fenz and Constantinou (2006), Fenz and Constantinou (2008a)).

It is useful to present the relationship between μ_{min} and μ_{max} as a ratio, since it allows $\mu(v)$ in Equation (3-1) to be expressed as a product of μ_{max} and a factor accounting for the effect of velocity on friction:

$$\mu(v) = \mu_{max} \times \left(1 - \left(1 - \frac{\mu_{min}}{\mu_{max}}\right)e^{-av}\right) \quad \textbf{(3-2)}$$

where all the parameters are defined previously. To simplify the modeling of the velocity dependence of friction for response-history analysis, a fixed value of the ratio of μ_{min} to μ_{max} can be based on experimental observations. Table 3-1 presents the recorded values of μ_{min} and μ_{max} for different PTFE-type composite materials and different values of axial pressure. Material No. 1 was identical to the material used in the FP bearings installed in the retrofit of U.S. Court of Appeals building in San Francisco, California (Constantinou *et al.*, 1993). The ratio of μ_{min} to μ_{max} varies between 0.4 and 1.0. Four of the seven observations reported in Table 3-1 did not exhibit velocity-dependent friction. The ratio of μ_{min} to μ_{max} was 0.39, 0.67 and 0.64 for the remaining three cases. Although the three observations correspond to different materials and different values of axial pressure, it is reasonable to fix the ratio of μ_{min} to μ_{max} at 0.50 and assume it to be applicable for a range of values of axial pressure and for different materials. This value of the ratio was used for each sliding interface in the modeling of Triple Friction Pendulum (TFP) bearings by Fenz and Constantinou (2008a). The expression to define the velocity dependence of the coefficient of friction then simplifies to:

$$\mu(v) = \mu_{max} \times \left(1 - 0.5e^{-av}\right) \quad \textbf{(3-3)}$$

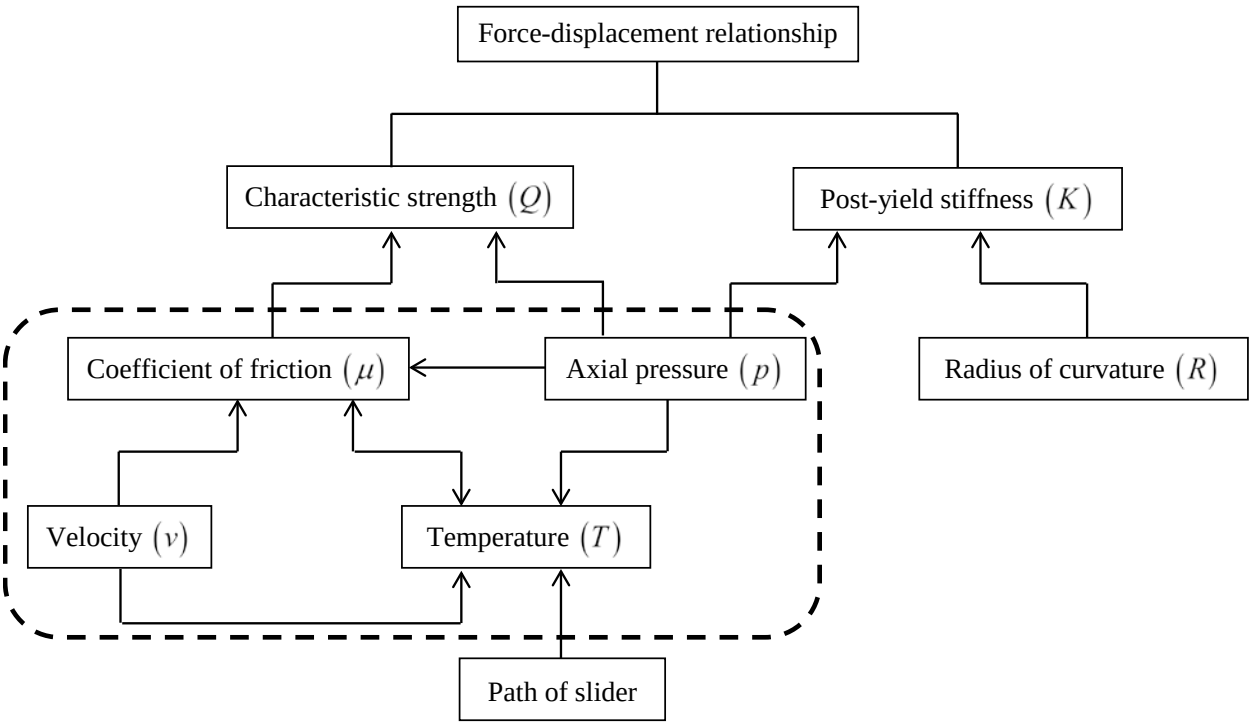

Figure 3-3 Interdependence of Quantities Defining the Force-Displacement Relationship in an FP Bearing

Table 3-1 Observed Values of Low and High Velocity Coefficient of Friction (adapted from Constantinou *et al.* (1993))

Pressure (MPa)	Material	μ_{min}	μ_{max}	μ_{min}/μ_{max}	Comments
17.2	No. 1	0.040	0.104	0.385	
	No. 2	0.115	0.122	0.943	Essentially Coulomb friction
	No. 3	0.090	0.120	0.667	
	No. 4	0.114	0.114	1.000	Essentially Coulomb friction
275.6	No. 1	0.034	0.053	0.642	
	No. 2	0.058	0.058	1.000	Essentially Coulomb friction
	No. 3	0.062	0.062	1.000	Essentially Coulomb friction

3.2.2 Dependence of the Coefficient of Friction on Axial Pressure

Constantinou *et al.* (2007) present a theory for the relationship between the coefficient of friction and axial pressure. The shear strength, s_μ, of the interface of an FP bearing can be considered to vary linearly with axial pressure, p_r, given by the following equation.

$$s_\mu = s_{o_\mu} + \alpha_r p_r \tag{3-4}$$

where s_{o_μ} is shear strength at zero axial pressure, α_r is a constant and other parameters were defined earlier. The friction force F_μ is the product of s_μ and the area of contact A_r. The coefficient of friction μ can be obtained as the ratio of the friction force to the normal force N, as given by the following equation:

$$\mu = \frac{F_\mu}{N} = \frac{s_\mu A_r}{p_r A_r} = \frac{\left(s_{o_\mu} + \alpha_r p_r\right) A_r}{p_r A_r} = \frac{s_{o_\mu}}{p_r} + \alpha_r \tag{3-5}$$

where all the terms were defined earlier. The coefficient of friction decreases asymptotically with increase in axial pressure. This trend is also supported by experimental data, as seen in Figure 3-4, which is adapted from Mokha *et al.* (1996). The figure plots observed values of the coefficient of friction measured at a high velocity against applied axial pressure. The information presented in the figure is based on the experiments performed by Zayas *et al.* (1987), Constantinou *et al.* (1993) and Al-Hussaini *et al.* (1994). Constantinou *et al.* (1993) note that the coefficient of friction at a very small velocity of sliding is not affected by the variation in axial pressure.

The following sections present models proposed in the past to describe pressure dependence of coefficient of friction.

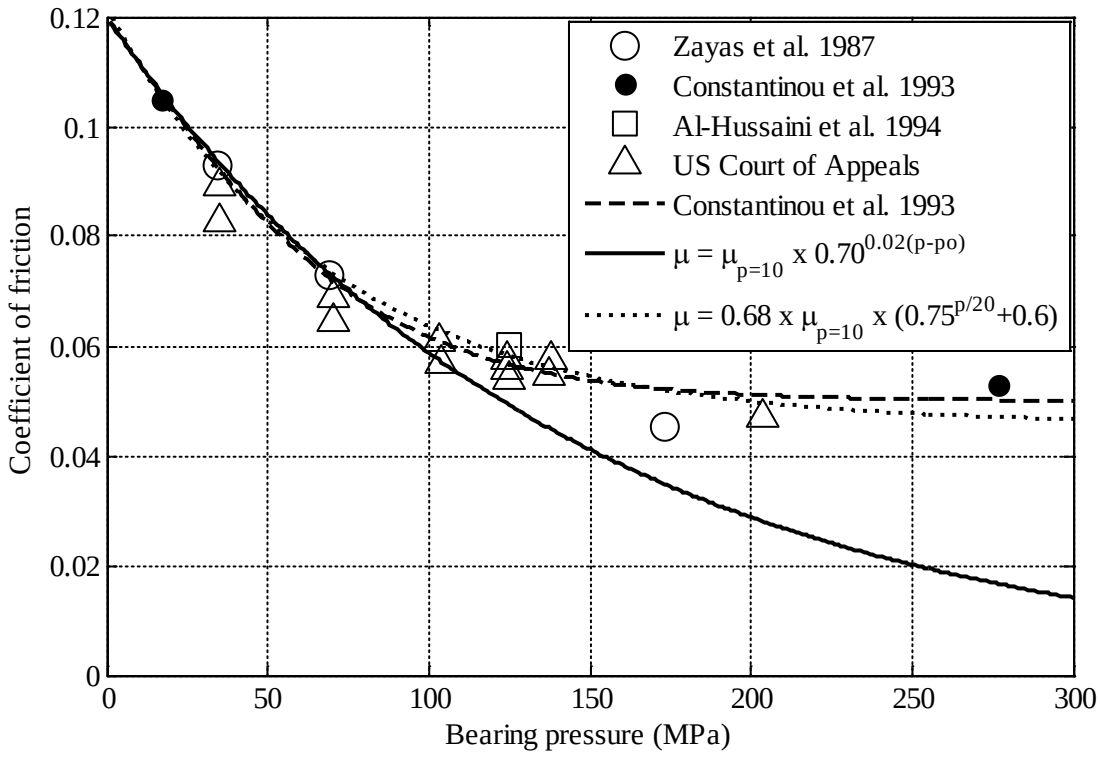

Figure 3-4 Coefficient of Friction Measured at a High Velocity of Sliding Plotted Against Bearing Pressure (adapted from Mokha *et al.* (1996))

3.2.2.1 Past Studies

3.2.2.1.1 Chang et al. (1990)

The variation in the small velocity coefficient of friction with axial pressure is described by Chang *et al.* (1990) using the following expression:

$$\mu_{\min} = \frac{1}{\lambda_1 + \lambda_2 p} \tag{3-6}$$

where λ_1 and λ_2 are determined using experimental data, and p is axial pressure. The coefficient of friction, $\mu(p,v)$, accounting for the coupled effect of sliding velocity and axial pressure is given by

$$\mu(p,v) = \mu_{\min}\left(1+\beta_1\left(\ln\left(1+\beta_2 v\right)\right)\right) \tag{3-7}$$

where $\mu_{\min}$ is defined by Equation (3-6), β_1 and β_2 are obtained from experiments, and v is sliding velocity.

3.2.2.1.2 Tsopelas et al. (1994b)

The relationship between the coefficient of friction at a high velocity of sliding and axial pressure is described using a tangent hyperbolic function as

$$\mu(p) = \mu_{p=0} - \left(\mu_{p=0} - \mu_{\max p}\right)\tanh\left(\varepsilon_p p\right) \quad \textbf{(3-8)}$$

where $\mu_{p=0}$ is the coefficient of friction at zero axial pressure measured at a high velocity of sliding, $\mu_{\max p}$ is the coefficient of friction at very high axial pressure measured at a high velocity of sliding, ε_p is a parameter governing the shape of the curve, and p is the axial pressure on the bearing in MPa. Figure 3-4 plots the relationship given by Equation (3-8) with the values of parameters $\mu_{p=0}$, $\mu_{\max p}$ and ε_p fixed at 0.12, 0.05 and 0.012, respectively. This curve fits quite well to the experimental data presented in Constantinou *et al.* (1993) (see Figure 3-4). This relationship has been incorporated in the computer program 3D-BASIS-ME (Tsopelas *et al.*, 1994b).

Equation (3-8) can be rewritten to allow $\mu(p)$ to be expressed as a product of $\mu_{\max p}$ and a factor accounting for the effect of pressure on the coefficient of friction, as given by the following expression.

$$\mu(p) = \mu_{\max p} \times \left(\frac{\mu_{p=0}}{\mu_{\max p}} - \left(\frac{\mu_{p=0}}{\mu_{\max p}} - 1 \right) \tanh\left(\varepsilon_p p\right) \right) \quad \textbf{(3-9)}$$

where all the terms were defined previously. Values for $\mu_{p=0}$ and $\mu_{\max p}$ for a particular PTFE-type composite material can be determined by experiments.

3.2.2.1.3 Tsai (1997)

An approach similar to Chang *et al.* (1990) has been used by Tsai (1997) to define the pressure and velocity dependence of coefficient of friction:

$$\mu(p,v) = \mu_{\min}\left(1 + \chi_1\left(1 - e^{-\chi_2 v}\right)\right) \quad \textbf{(3-10)}$$

where χ_1 and χ_2 are obtained from experiments and all other parameters were defined previously.

3.2.2.1.4 Dao et al. (2013)

Dao *et al.* (2013) used Equation (3-1) to describe the velocity dependence of the coefficient of friction. The exponent a in the equation is modeled as a function of the instantaneous axial load W :

$$a = \alpha_0 + \alpha_1 W + \alpha_2 W^2 \quad \textbf{(3-11)}$$

where α_0, α_1 and α_2 are constants estimated using experimental data (see panel (a) of Figure 3-5). The variables μ_{max} and μ_{min} are expressed as

$$\mu_{max} = A_{max} W^{n_{max}-1} \quad \textbf{(3-12)}$$

$$\mu_{min} = A_{min} W^{n_{min}-1} \quad \textbf{(3-13)}$$

where A_{max}, A_{min}, n_{max} and n_{min} are estimated using experimental data (see panel (b) of Figure 3-5); n_{max} and n_{min} are positive numbers smaller than 1. This empirical model lacks a physical basis because μ is function of contact pressure and not axial load.

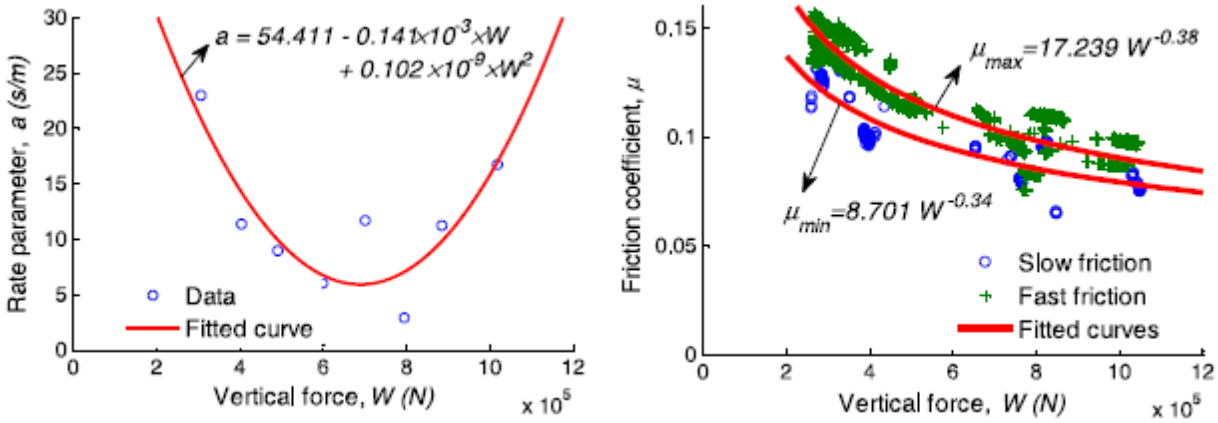

(a) Rate parameter vs. vertical force (b) Coefficient of friction vs. vertical force

Figure 3-5 Modeling Velocity and Pressure Dependence of Coefficient of Friction (Dao *et al.*, 2013)

3.2.2.2 Proposed Model

This study assumes that the coefficient of friction at a very small velocity is half that at a very high velocity of sliding (see Section 3.2.1) for all values of axial pressure. This assumption leads to the velocity dependence of coefficient of friction being defined as the product of the high velocity coefficient of friction and a factor that depends only on the sliding velocity, and not on axial pressure (Equation (3-3)). The assumption does not materially affect the maximum displacement and absolute acceleration responses of an isolated structure, as demonstrated in Appendix B.

The proposed relationship between axial pressure, p, and the coefficient of friction at a high velocity of sliding, $\mu(p)$, is given by

$$\mu(p) = \mu_{p=p_o} \times \alpha_p^{\beta_p(p-p_o)} \quad \textbf{(3-14)}$$

where $\mu_{p=p_o}$ is the coefficient of friction at a reference axial pressure p_o measured at a high velocity of sliding, and α_p and β_p are constants to be determined from experiments. The

constants α_p and β_p determine the shape of the curve. The relationship for the pressure dependence of the coefficient of friction can be readily obtained once α_p, β_p and $\mu_{p=p_o}$ are established. Figure 3-4 presents Equation (3-14) with values of p_o, $\mu_{p=p_o}$, α_p and β_p set equal to 10, 0.11, 0.70 and 0.02, respectively.

Equation (3-14) is applicable only for a range of axial pressure, which is smaller than the range covered by Equation (3-9). For example, $\mu(p) = 0.11 \times 0.7^{0.02(p-10)}$ represents the relationship between the coefficient of friction and axial pressure best if the axial pressure is less than 100 MPa (see Figure 3-4). The parameters of the equation may need to be modified to better fit the experimental data in the desired range of axial pressure.

The target static axial pressure varied between 40 MPa and 110 MPa in the 256 FP bearings used to isolate the U.S. Court of Appeals building (Mokha *et al.*, 1996). The target axial pressure for the 22 FP bearings used in the Benicia-Martinez Bridge was 20 MPa (Zayas *et al.*, 2001). For the 252 Triple Friction Pendulum™ bearings used to isolate the Istanbul Sabiha Gokcen International Airport Terminal Building, the average target axial pressure was 20 MPa on the outer sliding surfaces and 30 MPa on the inner sliding surfaces (Zekioglu *et al.*, 2009). The four FP bearings used in the Arkutun-Dagi oil platform support a total axial load of about 50,000 tons and the average target static axial pressure on the bearings is 50 MPa (Fenz *et al.*, 2011). A total of 69 TFP bearings are planned for New San Bernardino Courthouse. Thirty-two of those bearings have an average target static axial pressure of 10 MPa on the outer sliding surface and 40 MPa on the inner sliding surface. For the remaining 37 bearings, the average axial pressure on the outer and inner sliding surfaces are 20 MPa and 50 MPa, respectively (Sarkisian *et al.*, 2012). This information suggests that FP bearings used in recent applications are subjected to a static axial pressure well below 100 MPa.

Equation (3-14) with appropriate values of the constants satisfactorily fits the experimental data for axial pressure smaller than 100 MPa: $\mu(p) = 0.11 \times 0.7^{0.02(p-10)}$. The assumption that the small velocity coefficient of friction is one half the high velocity coefficient of friction at all levels of axial pressure allows the relationship between the coefficient of friction and the axial pressure to be expressed directly in terms of the coefficient of friction measured at a reference axial pressure multiplied by a factor depending only on axial pressure. The inclusion of additional parameters in Equation (3-14) allows the relationship between the coefficient of friction and axial pressure to be applied for the wide range of values of axial pressure covered in Figure 3-4. A modified expression is:

$$\mu(p) = \delta_1 \times \mu_{p=p_o} \times \left(\delta_2^{\delta_3 p} + \delta_4\right) \qquad \textbf{(3-15)}$$

where δ_1, δ_2, δ_3 and δ_4 are constants (different from Equation (3-14)) determined using experimental data, and the remaining parameters were defined previously. With the values of p_o, $\mu_{p=p_o}$, δ_1, δ_2, δ_3 and δ_4 set equal to 10, 0.11, 0.68, 0.75, 20 and 0.6, respectively, the curve of Equation (3-15) fits well the entire range of experimental observations seen in Figure 3-4.

3.2.3 Dependence of the Coefficient of Friction on Temperature

3.2.3.1 Studies in the Past

Past studies have shown that the coefficient of friction decreases with an increasing number of cycles even if axial pressure and sliding velocity are kept constant, due to the partial melting of the PTFE-type composite coating caused by the increase in temperature at the sliding surface (see Figure 3-6). The decrease in the coefficient of friction has been modeled as a function of the history of the work done on the sliding surface (e.g., Chang *et al.* (1990)) as given by the following expression:

$$\mu(T) = \mu(p,v) \times \left((1-\gamma_1) + \gamma_1 e^{-\gamma_2 \int_0^t \frac{\mu(T,t)-\mu_{\min}(t)}{\mu_{\min}(t)} du} \right) \qquad \textbf{(3-16)}$$

where $\mu(p,v)$ is given by Equation (3-7), γ_1 and γ_2 are determined from experiments, $\mu(T,t)$ is the temperature dependent coefficient of friction at time t and $\mu_{\min}(t)$ is the small velocity coefficient of friction at time t. A similar approach to account for the temperature dependence of friction was adopted by Tsai (1997).

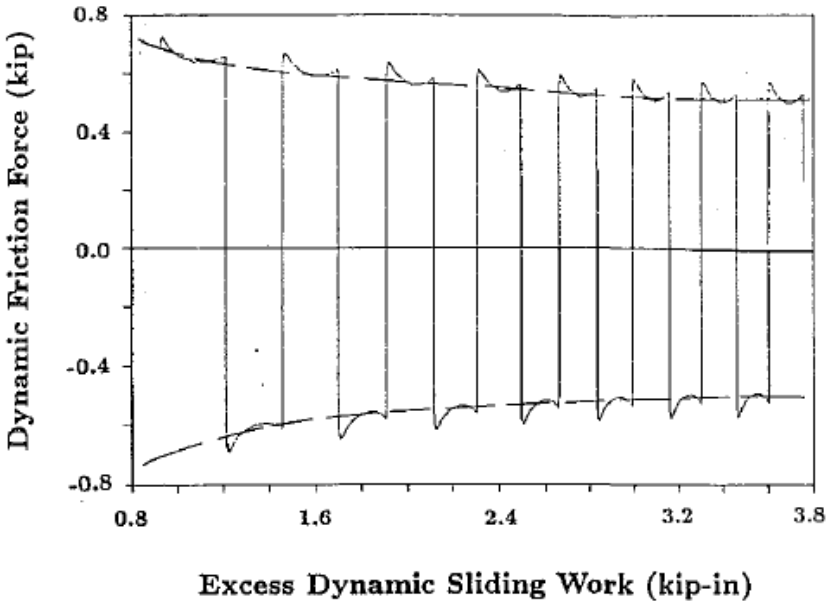

Figure 3-6 Reduction in Friction Force With Number of Cycles (Chang *et al.*, 1990)

The change in the coefficient of sliding friction with an increasing number of cycles (or work done on sliding surface) is reflected in the lateral force-displacement relationship of an FP bearing. Figure 3-7 presents the force-displacement response of an FP bearing when the cyclic displacement was applied at different rates. The coefficient of friction (the ratio of lateral force to normal force at zero displacement) decreases with increases in the number of cycles of loading and the peak velocity.

The sliding at the PTFE-type composite material and steel interface leads to increase in temperature. The change in the coefficient of friction can be expressed as a function of the temperature at the sliding surface. However, the measurement of temperature[1] at the sliding surface is difficult when sliding is taking place (e.g., Wolff (1999), Constantinou *et al.* (1999)). The temperature at a depth below the sliding surface can be measured using a thermocouple, but depending on the properties (e.g., diameter) of the thermocouple, there can be a time lag associated with the measurement of temperature.

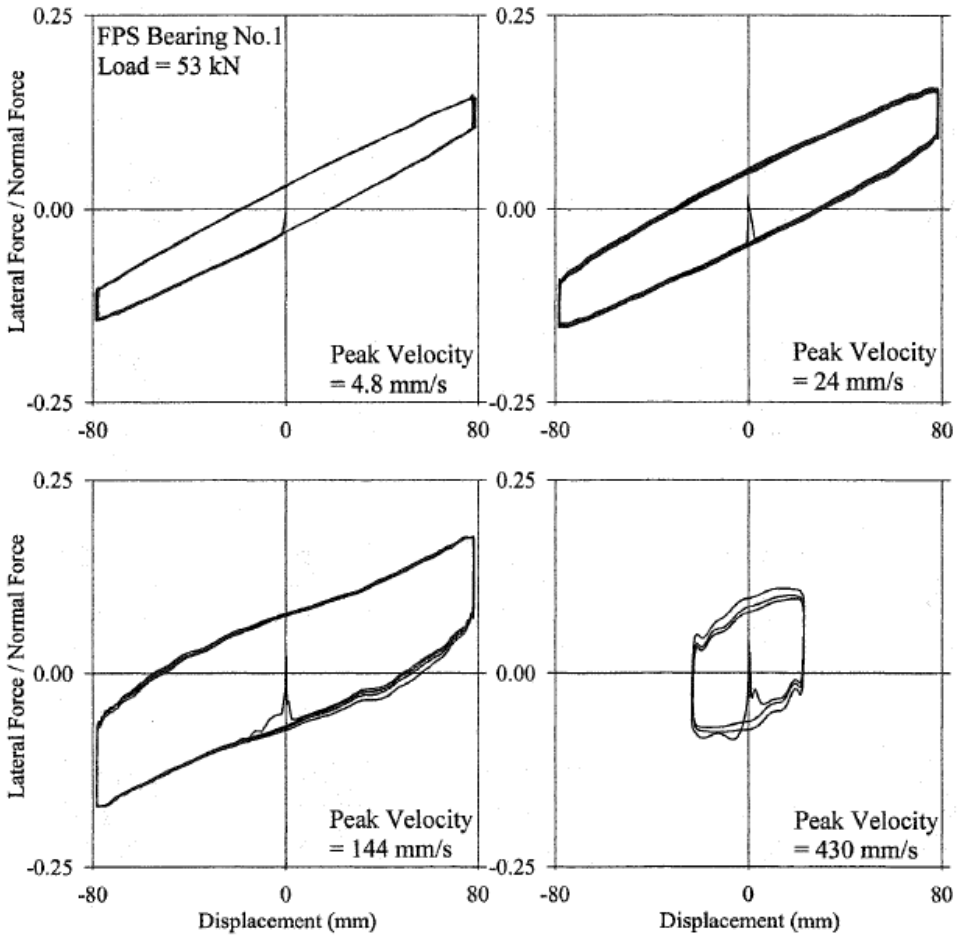

Figure 3-7 Force-Displacement Histories for FP Bearings With Different Magnitudes of Maximum Velocity of Sliding (Wolff, 2003)

An expression to define the temperature dependence of the coefficient of friction has been suggested by Sarlis and Constantinou (2013).

[1] A measurement of temperature at the sliding surface is needed to 1) determine the relationship between the coefficient of friction and temperature (e.g., present study), 2) quantify wear in the liner material (e.g., Drozdov et al. (2007), Drozdov et al. (2010)), and 3) design experiments for seismic qualification of bearings (e.g., Fenz et al. (2011)).

$$\mu(T) = \mu_{\max T} + (\mu_{\min T} - \mu_{\max T}) e^{-a_h T} \quad \textbf{(3-17)}$$

where $\mu_{\min T}$ is the coefficient of friction at the beginning of the motion at the sliding surface, when the temperature is a minimum, $\mu_{\max T}$ is the coefficient of friction at a high temperature $(\approx 1/a_h)$, and a_h is the heating rate parameter.

3.2.3.2 Proposed Relationship

Equation (3-17) describes the decrease in the coefficient of friction from $\mu_{\min T}$ to $\mu_{\max T}$ with increase in temperature from zero to $1/a_h$. If $\mu_{\min T}$ is known at a temperature T_o instead of at zero temperature, then T in the exponent of the equation can be replaced with $(T - T_o)$ to describe the temperature dependence of the coefficient of friction. The shape of the curve described by Equation (3-17) depends on the base e. As will be shown in later chapters, the temperature at the sliding surface affects the response quantities (e.g., peak displacement, peak acceleration) most significantly. It may therefore be necessary to have better control on the rate of decrease in the coefficient of friction with an increase in temperature to best fit available experimental data, which can be achieved by replacing the base e with another number a_e (to be determined from experiments). The resulting equation is

$$\mu(T) = \mu_{\max T} + (\mu_{\min T} - \mu_{\max T}) a_e^{-a_h (T - T_o)} \quad \textbf{(3-18)}$$

where all terms were defined previously. It is desirable to define the coefficient of friction as a product of a reference coefficient of friction and a factor depending only on the temperature at the sliding surface:

$$\mu(T) = \mu_{T=T_o} \times \phi \left(b_1^{T/b_2} + b_3 \right) \quad \textbf{(3-19)}$$

where $\mu_{T=T_o}$ is the high velocity coefficient of friction at a reference temperature T_o, and b_1, b_2 and b_3 are determined from experiments, and ϕ is related to b, c and d as follows

$$\phi = \left(b_1^{T_o/b_2} + b_3 \right)^{-1} \quad \textbf{(3-20)}$$

Constantinou *et al.* (2007) provide information about the change in the coefficient of friction with temperature (see Figure 3-8). A very sharp drop in the coefficient of friction takes place as the temperature at the sliding interface increases from -40˚C to 20˚C. The coefficient decreases further, although not as sharply, as the temperature increases to 50˚C. It is expected that the decrease in the coefficient of sliding friction is smoother at higher temperature and that the coefficient tends to converge to a fixed value at a very high temperature (>250˚C). For the purpose of this study, it was assumed that the ratios of the coefficients of sliding friction with T set equal to -40˚C, 20˚C and 250˚C are 3:2:1 for all values of sliding velocity and axial pressure. The following expression is proposed to define the temperature dependence of friction:

$$\mu(T) = \mu_{T=T_o} \times 0.79 \times \left(0.70^{T/50} + 0.40 \right) \quad \textbf{(3-21)}$$

where $\mu_{T=T_o}$ is the coefficient of friction measured at a reference temperature T_o and $\mu(T)$ is the coefficient of friction at a temperature T measured in °C. T_o is set equal to 20°C. The ratios of the coefficient of friction per Equation (3-21) are 3.0:2.2:1.0, and very close to the target of 3:2:1. The effect of the choice of ratio on maximum displacement response is studied later in the chapter.

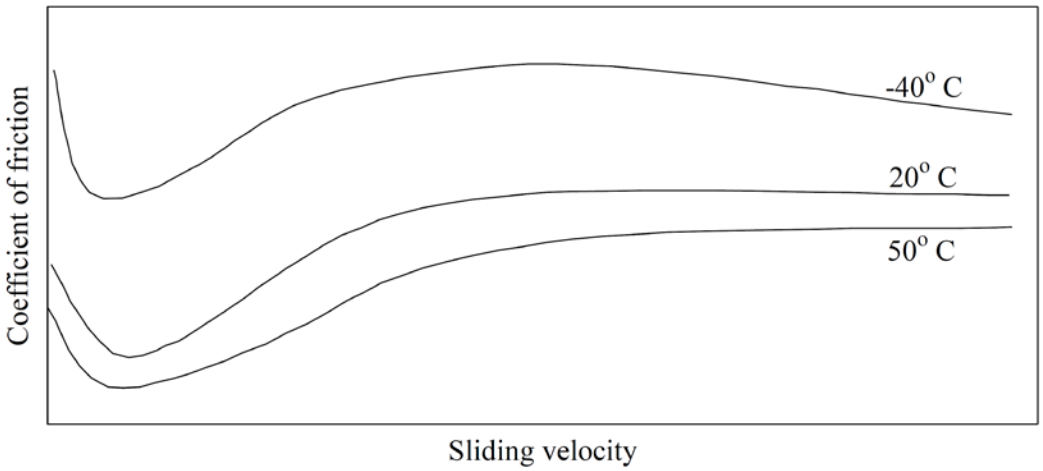

Figure 3-8 Schematic of the Variation in the Coefficient of Friction With Sliding Velocity and Temperature (adapted from Constantinou *et al.* (2007))

3.2.3.3 Method to Compute Temperature

The temperature at a point on the sliding interface depends on the loading path (prior heating of the sliding surface and its decay with time) and the instantaneous heat flux, which in turn is a function of the temperature at the sliding interface. At a given point on the sliding surface, the temperature rise ΔT during the beginning of motion to the time t is calculated using Equation (3-22), which assumes a half space below the contact surface (Constantinou *et al.*, 2007).

$$\Delta T(x,t) = \frac{\sqrt{D}}{k\sqrt{\pi}} \int_0^t q(t-\tau)\, e^{\left(\frac{-x^2}{4D\tau}\right)} \frac{d\tau}{\sqrt{\tau}} \quad \textbf{(3-22)}$$

where x is the depth measured from the sliding surface, D is the thermal diffusivity of steel, k is thermal conductivity of steel and q is heat flux. Based on the information presented in Constantinou *et al.* (2007), D and k are set equal to 4.44×10^{-6} m^2/s and 18 W/(m°C), respectively. The instantaneous heat flux at a monitoring location is the product of the instantaneous values of coefficient of friction, axial pressure and the velocity of sliding, if the monitoring location falls below the slider, and zero otherwise. For the ease of computation, the circular slider is approximated by a square of same area. The temperature at a monitoring location is then calculated as the sum of temperature at the sliding interface at the beginning of the motion and the temperature rise ΔT.

The temperature at a monitoring point increases as the slider passes over it and decreases slowly towards ambient temperature otherwise. Panel (a) of Figure 3-9 shows a schematic of the path of the center of slider as it starts from point 1, travels through points 2, 3 and 4, comes back to point 2 again before heading to point 5. Panel (b) of the figure presents a schematic of the temperature at point 2 as a function of location of the center of slider. There is no change in the temperature as the slider travels from point 1 to point 2. The temperature rises sharply as the slider passes over point 2. The temperature at the point 2 decreases as the slider travels over points 3 and 4, and rises again as the slider passes over it again. The temperature then decreases as the slider moves away towards point 5.

There are two key assumptions involved in the method to compute the temperature at a point on the sliding surface, namely, 1) there is half space below the sliding surface, and 2) radiation losses are insignificant. The significance of the two assumptions in the estimation of the response of sliding isolation systems is examined in the next chapter.

3.2.3.4 Representative Temperature Monitoring Location at the Sliding Surface

The modifications in the properties of the PTFE-type composite coating of the slider due to heating effects, and consequent changes in the coefficient of friction, are a function of the path of the slider on the sliding surface and the temperature at the points on the sliding surface directly below the slider. This section compares the maximum displacement responses of an FP bearing obtained using two approaches to incorporate the temperature dependence of the coefficient of friction defined by Equation (3-21) in a response-history analysis.

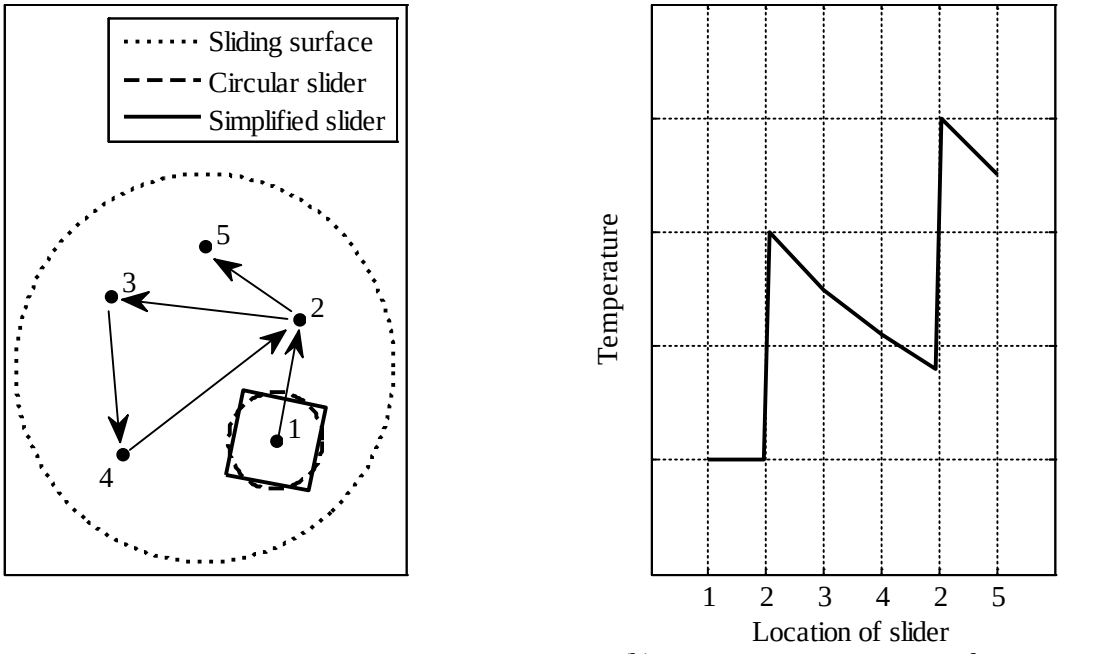

(a) Path of slider (b) Temperature at monitoring location 2

Figure 3-9 Schematic of Rise and Decay in Temperature at a Monitoring Location at the Sliding Surface as the Slider Is Passes Through the Location

In the first approach, temperature is tracked at uniformly distributed monitoring locations (points) on the sliding surface and the average value of the temperature at points directly below the

slider is used for T in Equation (3-21). Panel (a) of Figure 3-10 shows the plan view of an FP bearing with the points distributed in a square pattern. It also shows the path of the center of the slider, when the bearing is subjected to a ground motion. The sides of the equivalent square slider are oriented parallel to the two horizontal axes. For the configuration shown in the panel, the average of the temperature at the two points directly below the slider is used in Equation (3-21) to compute the coefficient of friction, adjusted for heating effects.

Panels (a) and (b) of Figure 3-11 show the path of the center of the slider of an FP bearing with the sliding period of 3 s, the Coulomb-type coefficient of friction 0.06 and static axial pressure of 50 MPa, subjected to ground motions 1 and 30, respectively (details of these ground motions are presented in Appendix A). The radius of the circular slider is 0.2 m. The equivalent square slider is over the center of the sliding surface if the center of the slider is within the dashed circle. It is clear from the two panels that the center of the sliding surface is the most traversed point on the sliding surface. For the second approach to incorporate the temperature dependence of friction in a response-history analysis, the temperature at the center of the sliding surface is used in Equation (3-21), which increases when slider is directly above the center of the bearing and decreases otherwise. The sides of the equivalent square slider are oriented either parallel or perpendicular to the line joining the centers of the slider and the sliding surface, as shown in panel (b) of Figure 3-10. This approach has also been suggested by Constantinou *et al.* (2007).

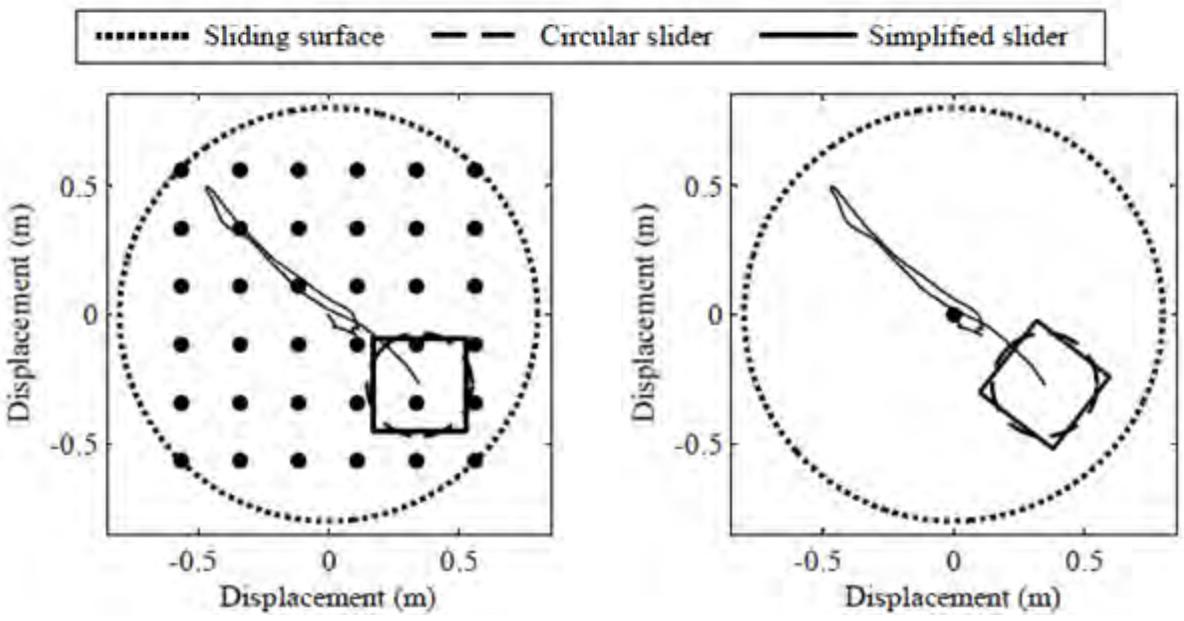

(a) Approach 1 (b) Approach 2

Figure 3-10 Approaches to Incorporate Temperature Dependence of Coefficient of Friction in Response-History Analysis

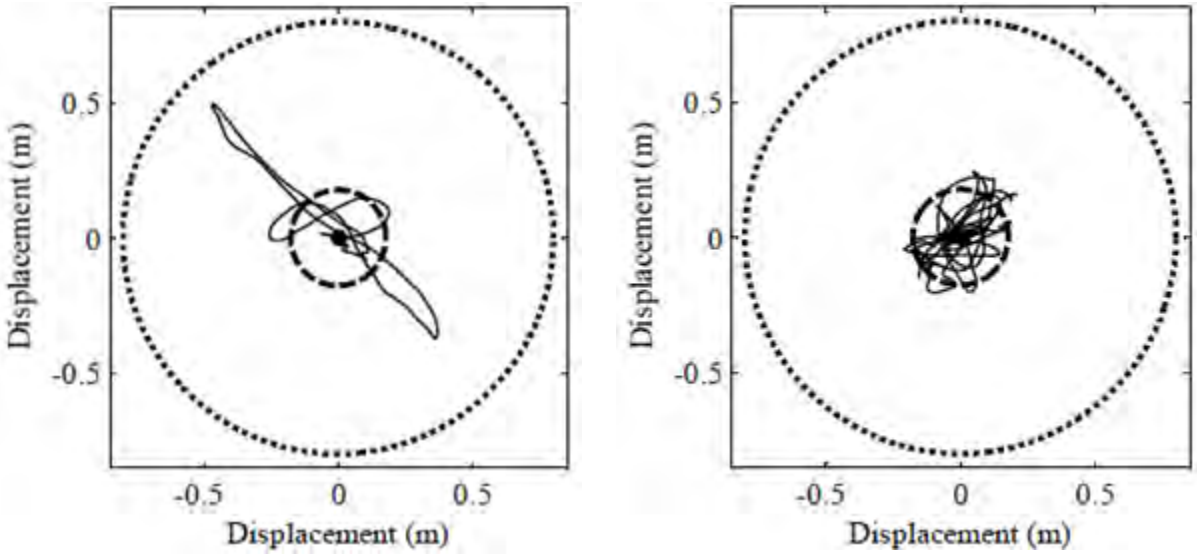

(a) Ground motion 1 (b) Ground motion 30

Figure 3-11 Path of the Center of Slider of an FP Bearing Subjected to the Ground Motions

An FP bearing with sliding period of 3 s, static axial pressure of 50 MPa and the temperature dependence of coefficient of friction defined using the two approaches (Figure 3-10) was subjected to the thirty ground motions (see Appendix A). Two values of spacing between the adjacent points are considered for the first approach: 250 mm and 150 mm. The coefficient of friction at the reference temperature of 20^{o}C is 0.06. Mass proportional damping of 2% of critical was assigned to the system with the proportionality constant updated at every step of the analysis based on the instantaneous eigenvalue of the system.

Figure 3-12 presents the distribution of maximum displacement responses (assuming lognormal distribution) for bearings with the temperature dependent coefficient of friction at the sliding surface defined using the two approaches. The median estimates of maximum displacement obtained using the first approach with spacing of 250 mm and 150 mm differ by less than 2 mm, indicating that the response is not sensitive to the spacing of the points where temperature is computed. The difference in the median responses estimated using the two approaches is 5 mm, whereas 99th percentile response obtained using the first approach is greater by 30 mm compared to that obtained using second approach. Across the thirty ground motions, the minimum, mean and maximum differences in the maximum displacement responses obtained using the two approaches are 0 mm, 20 mm and 80 mm, respectively. It is, therefore, clear that the two approaches approximately yield the same results. Considering its simplicity, the second approach (defining temperature dependence of coefficient of friction based on the temperature at the center of the sliding surface) is adopted in this study.

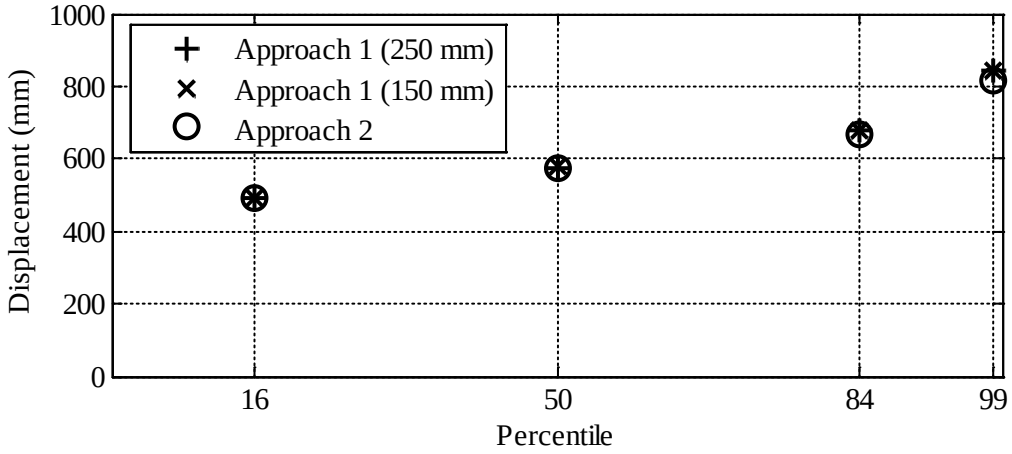

Figure 3-12 Distribution of Maximum Displacement of FP Bearing with the Temperature Dependent Coefficient of Friction Defined Using Different Approaches

3.2.4 Combined Effect of Velocity, Pressure and Temperature on Friction

This section presents the approach to consider the effect of one or more quantities (e.g., pressure and temperature) on the coefficient of friction. The right side of equations (3-3), (3-14) and (3-19) are the product of a reference coefficient of friction multiplied by a factor accounting for velocity, pressure and temperature, respectively. In Equation (3-3), $\mu_{\max}$ is the reference coefficient of friction at a very high velocity of sliding. Similarly, in equations (3-14) and (3-19), $\mu_{p=p_o}$ and $\mu_{T=T_o}$ are the coefficient of friction at a reference axial pressure p_o and a reference temperature T_o, respectively. Based on assumptions and experimental observations mentioned above, the factors accounting for the effect of velocity (k_v), axial pressure (k_p) and temperature (k_T) are given by the following equations.

$$k_v = 1 - 0.5e^{-100v} \quad \textbf{(3-23)}$$

$$k_p = 0.70^{(p-p_o)/50} \quad \textbf{(3-24)}$$

$$k_T = 0.79 \times \left(0.70^{T/50} + 0.40 \right) \quad \textbf{(3-25)}$$

where all the terms are defined previously. Unless stated otherwise, the equations are assumed to be applicable for all PTFE-type composite materials, and the entire range of temperature, axial pressure and velocity of sliding, although the parameters for the equations are obtained based on the experiments performed on bearings with different materials under different loading conditions.

A reference coefficient of friction μ_{ref} is considered, which is defined as the coefficient of friction at a bearing pressure p_o, measured at a high velocity of sliding with the temperature at the sliding surface being T_o (fixed at 20˚C). To consider more than one effect at a time μ_{ref} is

multiplied by appropriate factors. For example, the coefficient of friction accounting for the effect of velocity and temperature is obtained by multiplying μ_{ref} by k_v and k_T. This work has been published in Kumar et al. (2015a).

Based on the equations (3-23), (3-24) and (3-25), panels (a) to (c) of Figure 3-13 show the variation in coefficient of friction with increase in the temperature at the sliding interface for three values of velocity of sliding, 1000 mm/s, 10 mm/s and 0.001 mm/s, with μ_{ref} fixed at 0.09, 0.06 and 0.03, respectively. Panels (d) to (f) of the figure plot the coefficient of friction against axial pressure.

For the temperature at the sliding interface fixed at 200˚C, 50˚C and 20˚C, panels (a) to (c) of Figure 3-14 plot coefficient of friction versus axial pressure, and panels (d) to (f) of the figure show the variation in the coefficient of friction with velocity of sliding at the interface with μ_{ref} set equal to 0.09, 0.06 and 0.03, respectively.

Figure 3-15 shows the plots of coefficient of friction versus temperature at the sliding interface in panels (a) to (c), and the plots of coefficient of friction versus velocity of sliding in panels (d) to (f) for of μ_{ref} set equal to 0.09, 0.06 and 0.03, respectively, for two values of axial pressure: 10 MPa and 50 MPa. The reference coefficients of friction μ_{ref} in Figure 3-13, Figure 3-14 and Figure 3-15 are assumed to be measured at a high velocity of sliding (≈200 mm/s), at a reference axial pressure p_o equal to 10 MPa and at a reference temperature at the sliding interface T_o equal to 20˚C.

3.3 Summary

This chapter focuses on characterization of coefficient of friction at the sliding surface of a Friction Pendulum™ (FP) bearing. The coefficient of friction updates during the course of an earthquake depending on sliding velocity, axial pressure and temperature at the sliding surface. Expressions to define the dependence of coefficient of friction on the three quantities are proposed based on available experimental data. Suitable assumptions are made in order to decouple the expressions. Two methods of tracking temperature at the sliding surface are compared in terms of the impact on the maximum displacement response of a bearing.

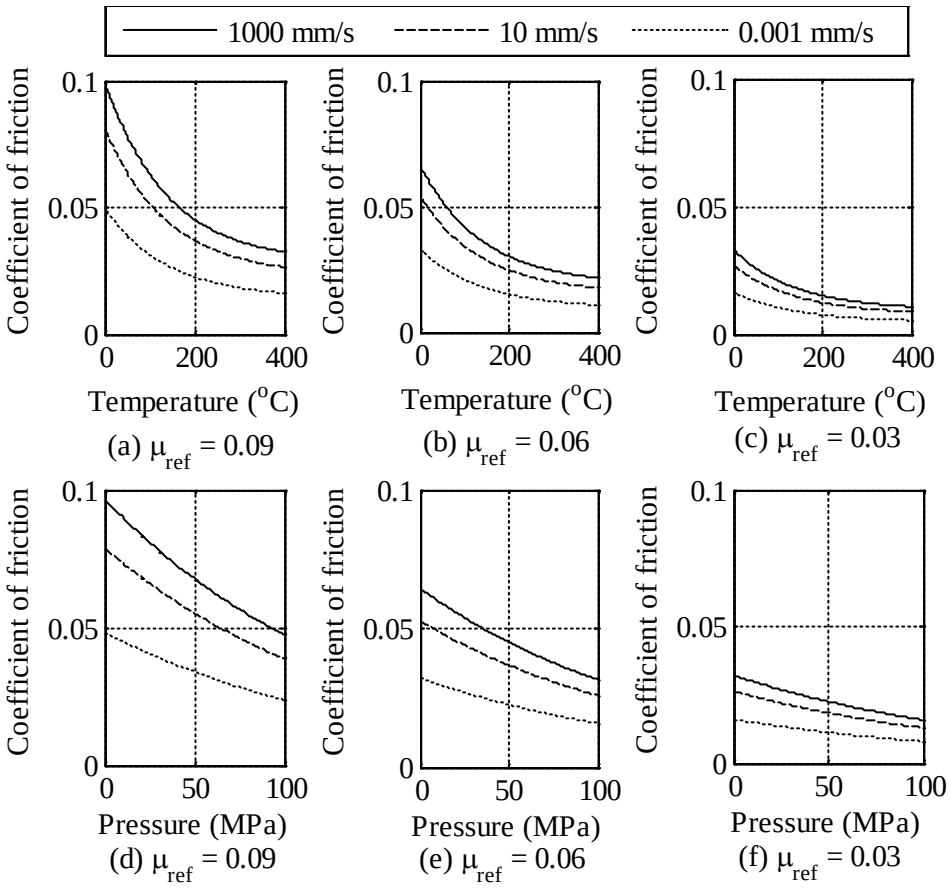

Figure 3-13 Coefficient of Friction Plotted Against Temperature (panels (a)–(c)) and Pressure (panels (d)–(f)) for Three Values of Reference Coefficient of Friction (0.09, 0.06, 0.03) and Three Values of Sliding Velocity (1000 mm/s, 10 mm/s, 0.001 mm/s)

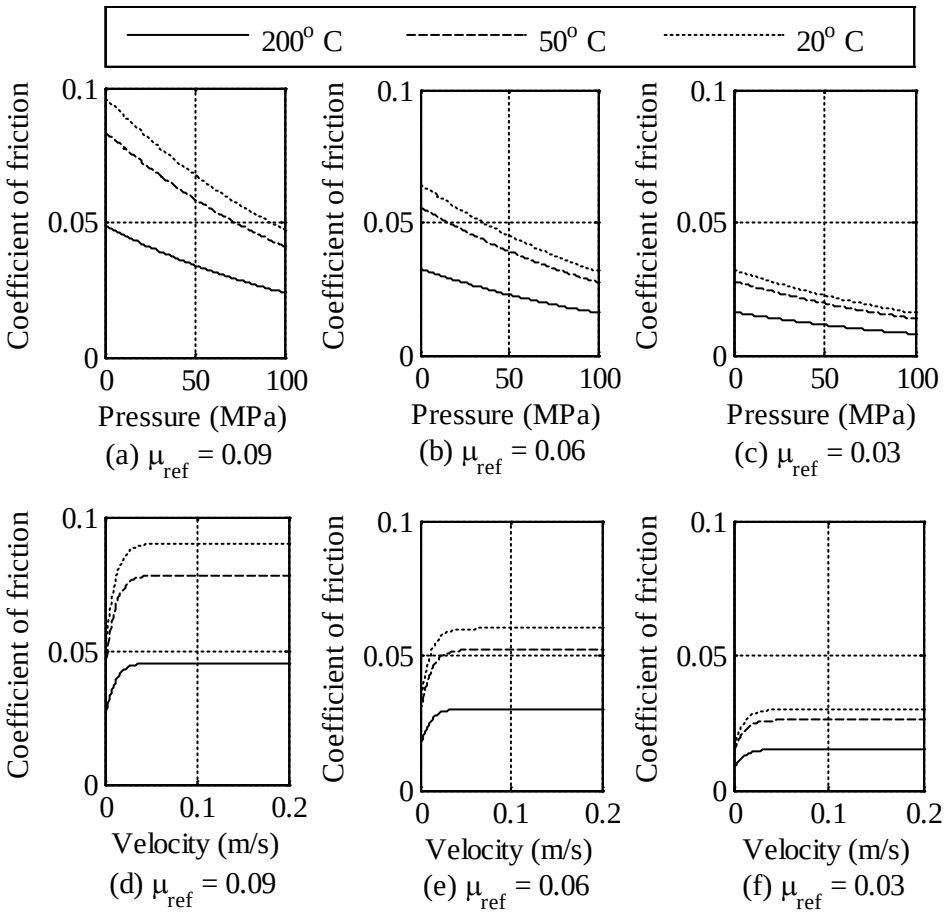

Figure 3-14 Coefficient of Friction Plotted Against Axial Pressure (panels (a)–(c)) and Sliding Velocity (panels (d)–(f)) for Three Values of Reference Coefficient of Friction (0.09, 0.06, 0.03) and Three Values of Temperature at the Sliding Surface (200°C, 50°C, 20°C)

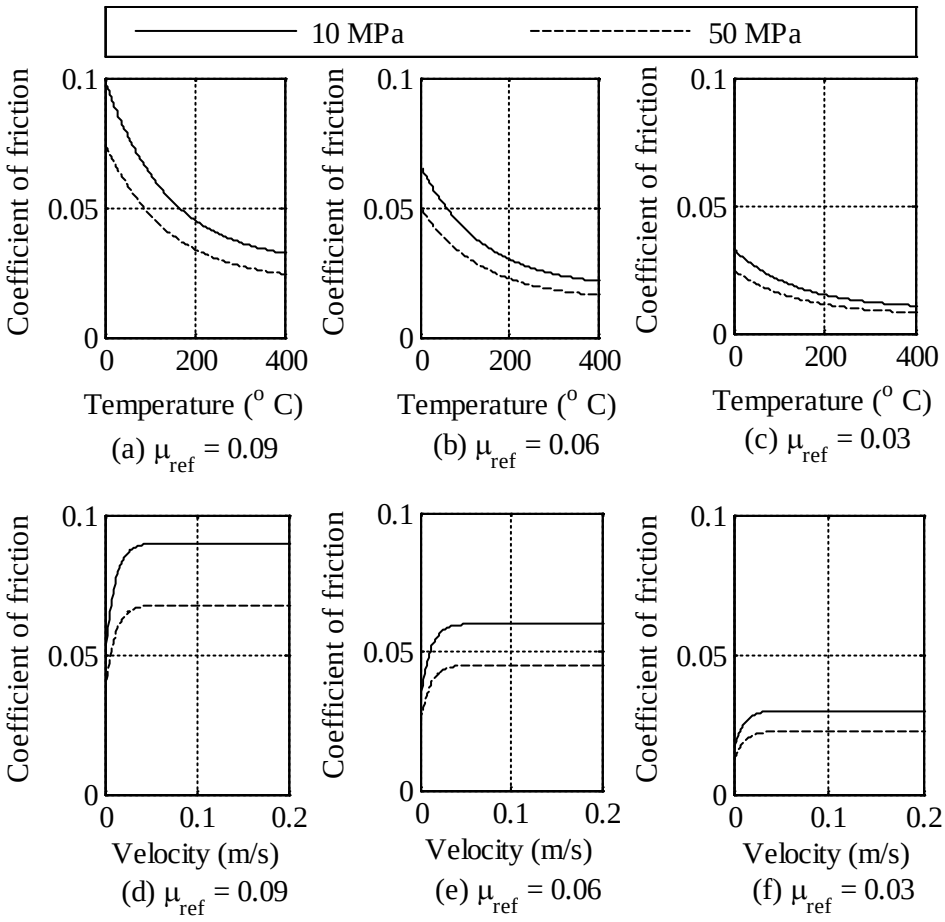

Figure 3-15 Coefficient of Friction Plotted Against Temperature (panels (a)–(c)) and Sliding Velocity (panels (d)–(f)) for Three Values of Reference Coefficient of Friction (0.09, 0.06, 0.03) and Two Values of Axial Pressure (10 MPa, 50 MPa)

4 OPENSEES SLIDING BEARING ELEMENT: VERIFICATION AND VALIDATION

4.1 Introduction

A model to describe friction as a function of axial pressure, temperature at the sliding surface and velocity of sliding was proposed in Chapter 3. This chapter presents the features of the new OpenSees element *FPBearingPTV* that incorporates the friction model. The assumptions in the modeling of the Friction Pendulum™ (FP) bearing are discussed. The element is verified and validated.

4.2 Mathematical Modeling

The FP bearing can displace in six directions, namely, rotate about two horizontal axes, twist about a vertical axis, translate in the vertical direction, and translate in the two horizontal directions. The boundary conditions imposed on the bearing by a foundation and the supported superstructure generally do not allow the bearing to rotate about the two horizontal axes. For torsional motion about the vertical axis to take place, the moment capacity due to friction at the sliding surface or that due to friction between the slider and the housing plate has to be overcome. The slider is considered to be rigid in the vertical direction, but vertical rigid-body motion of the slider accompanies displacement in the horizontal direction.

The translational motion of an FP bearing in the two horizontal directions is a function of the geometrical and material properties (e.g., coefficient of friction at the sliding surface, radius of curvature) and axial load on the bearing. A model to characterize the coefficient of friction at the sliding surface was presented in Chapter 3. For given values of coefficient of friction, axial load and radius of curvature of the sliding surface, the lateral force-displacement of the FP bearing under cyclic loading is described by the curve shown in Figure 4-1(a).

The lateral force-displacement relationship can be mathematically modeled using the theory of plasticity. The motion at the sliding surface is elastic when the resultant external force on the bearing is smaller than that required to overcome friction. Sliding takes place thereafter. The motion on the sliding surface in the elastic and sliding regimes is modeled using the theory of plasticity, which is discussed in detail by Simo and Hughes (1998), Sivaselvan and Reinhorn (2004) and Ray (2013), among others. For a given horizontal displacement increment, the force increment is given by the following expression (Mosqueda *et al.*, 2004):

$$\begin{bmatrix} \Delta F_x \\ \Delta F_y \end{bmatrix} = \frac{W}{R} \begin{bmatrix} \Delta u_x \\ \Delta u_y \end{bmatrix} + \mu W \frac{1}{\|\dot{u}\|} \begin{bmatrix} \dot{u}_x \\ \dot{u}_y \end{bmatrix} \qquad \textbf{(4-1)}$$

where Δu_x and Δu_y are the displacement increments in the two horizontal directions *X* and *Y*, W is the instantaneous axial load on the bearing, R is the radius of curvature of the sliding surface, μ is the coefficient of friction, $\|\dot{u}\|$ is the magnitude of velocity of sliding, $\dot{u}_x$ and $\dot{u}_y$ are the sliding velocities, and ΔF_x and ΔF_y are the incremental forces in the *X* and *Y* directions, respectively.

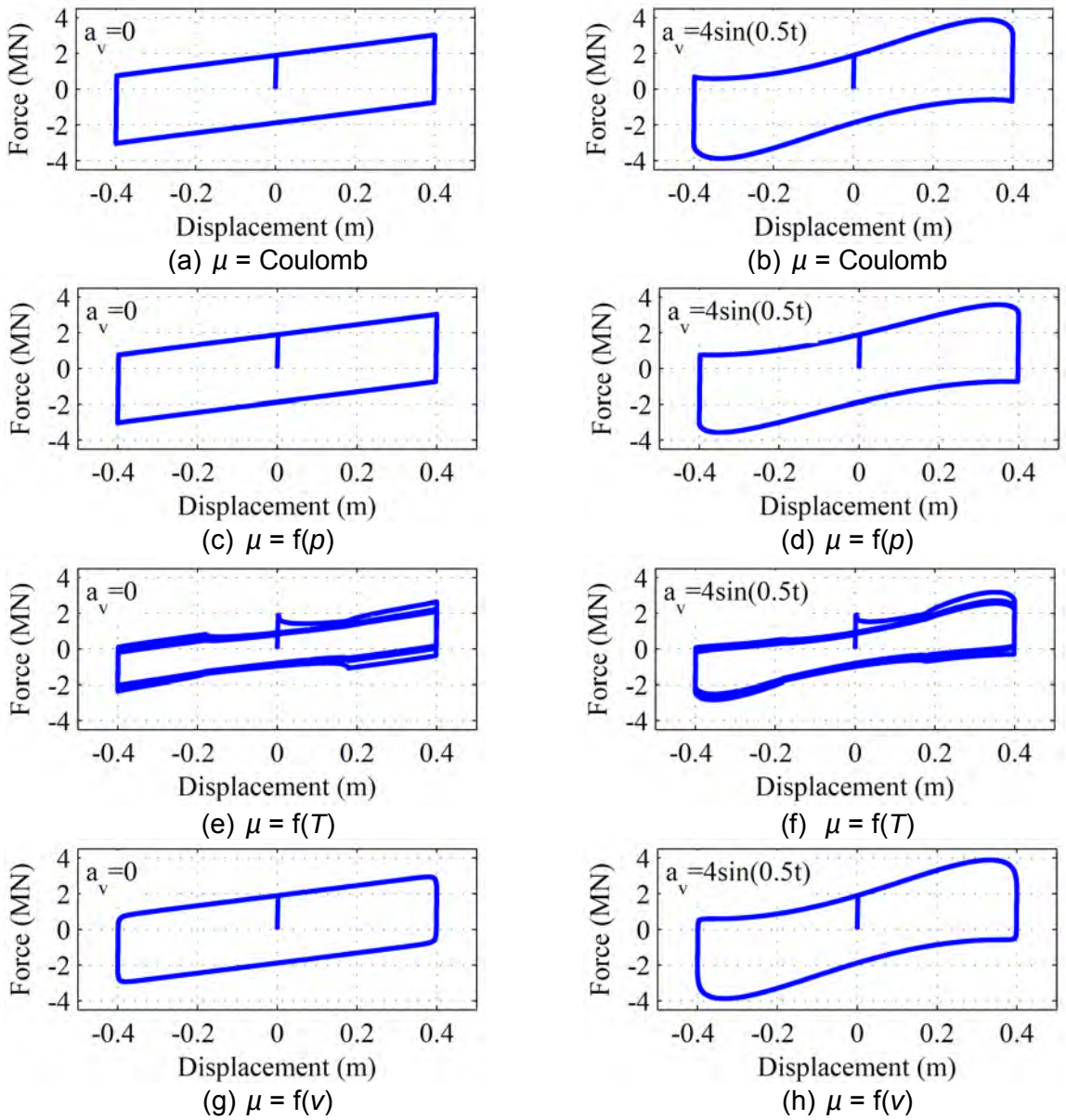

Figure 4-1 Force-Displacement Response of an FP Bearing Subjected to Cyclic Horizontal and Vertical Loading with Different Choices of Friction Model (Coulomb, pressure-dependent, temperature-dependent and velocity-dependent)

4.3 Features of OpenSees Element *FPBearingPTV*

The element *singleFPBearing* is available in the software program OpenSees (PEER, 2014) to model a single Friction Pendulum™ (FP) bearing. It permits the user to choose a friction model with the coefficient of friction defined as a function of sliding velocity, axial pressure or both. There is no friction model available in OpenSees that considers the dependence of the coefficient of friction on temperature at the sliding surface. Suitable modifications were made in the source code of the *singleFPBearing* element to incorporate the dependence of coefficient of

friction on sliding velocity, axial pressure and temperature at the sliding surface, as defined in Chapter 3. The new element is named *FPBearingPTV.* The key features of the new element are discussed below.

Figure 4-1(a) presents the force-displacement response of a bearing with the coefficient of friction defined using a Coulomb model, a sliding period of 3 s, a static axial pressure of 50 MPa, a slider radius of 0.2 m, and a reference coefficient of friction, μ_{ref} of 0.3, subjected to cyclic loading with horizontal displacement described by $u = 0.4\sin(0.25t)$ meters[2].

Figure 4-1(b) presents the force-displacement response of the bearing subjected to a vertical acceleration of $a_v = 4\sin(0.5t)$ m/s^2 in addition to the horizontal cyclic loading of Figure 4-1(a). Figures 4-1(c), 4-1(e) and 4-1(g) present the force-displacement response of the bearing subjected to the horizontal cyclic loading of panel (a), but with the coefficient of friction considered to vary with axial pressure, temperature at the sliding surface and sliding velocity, respectively. Figures 4-1(d), 4-1(f) and 4-1(h) plot the force-displacement response when the bearing is subjected to the horizontal and vertical cyclic loading of panel (b) and the coefficient of friction is pressure-, temperature- and velocity-dependent, respectively.

It is clear from Figure 4-1 that the temperature at the sliding surface affects the coefficient of friction (and the force-displacement history) most significantly (see panels (e) and (f)) during the cyclic loading, for the loadings considered and assumptions made. The coefficient of friction decreases with an increasing number of cycles when the temperature-dependent friction model is considered (compare panel (e) with panels (a), (c) and (g)). It can also be observed from panel (e) that the change in the coefficient of friction is greater (the force-displacement loop is "thinner") when the imposed displacement is smaller than the radius of slider (= 0.2 m), compared to the case for which the displacement is greater than the radius. This is because the temperature at the center of the sliding surface is used to update the coefficient of friction (see Chapter 3). The temperature increases (and the coefficient of friction decreases) when the slider is directly above the center of the bearing and decreases otherwise.

The effect of the velocity dependence of friction can be observed by comparing Figures 4-1(a) and 4-1(g) at the peak displacements (= ±0.4 m). A change in direction of motion takes places at this displacement and the velocity decreases from a positive value to zero to a negative value (or vice-versa). The reduction in the velocity-dependent coefficient of friction associated with the decrease in velocity (as the slider approaches the peak displacement) results in a smoother change in force compared with the Coulomb model.

Figures 4-1(a) and 4-1(c) present the force-displacement histories of the bearing for the Coulomb and pressure-dependent friction models, respectively. The axial pressure is constant for the bearing in the two panels and there is no variation in the coefficient of friction due to change in axial pressure. The force-displacement histories in the two panels are identical. Figures 4-1(b) and 4-1(d) present the force-displacement responses for the Coulomb and the pressure-dependent friction model, respectively, when the time-varying axial load (associated

[2] This combination is selected to demonstrate clearly the influence of sliding velocity and temperature on μ. The chosen values are impractical for a seismic isolation system in a nuclear structure.

with the vertical acceleration) is imposed on the bearing. The influence of changes in axial pressure on the coefficient of sliding friction is seen by comparing the two force-displacement histories (see Figure 4-2).

4.4 Assumptions in Modeling FP Bearings

The assumptions involved in the modeling of FP bearings using the OpenSees element *FPBearingPTV* are discussed in this section.

4.4.1 Normal Force on the Sliding Surface

Figure 4-3(a) shows the forces acting on an FP bearing as the slider rotates through angle θ. Panel (b) of the figure shows the normal force, N, and shear force, S, on the sliding surface. The equilibrium equations in the horizontal and vertical directions on the slider are (e.g., Fenz and Constantinou (2008b)):

$$F - N\sin\theta - S\cos\theta = 0 \qquad \textbf{(4-2)}$$

$$W + S\sin\theta - N\cos\theta = 0 \qquad \textbf{(4-3)}$$

where F is the horizontal force, W is the vertical force, and other parameters were defined previously. Solving the two equations yields the following expression for the horizontal force F.

$$F = \frac{W}{R\cos\theta}u + \frac{S}{\cos\theta} \qquad \textbf{(4-4)}$$

where u is the horizontal displacement, R is the radius of curvature of the sliding surface, and other parameters were defined previously. Variables u, R and θ are related by the following expression.

$$u = R\sin\theta \qquad \textbf{(4-5)}$$

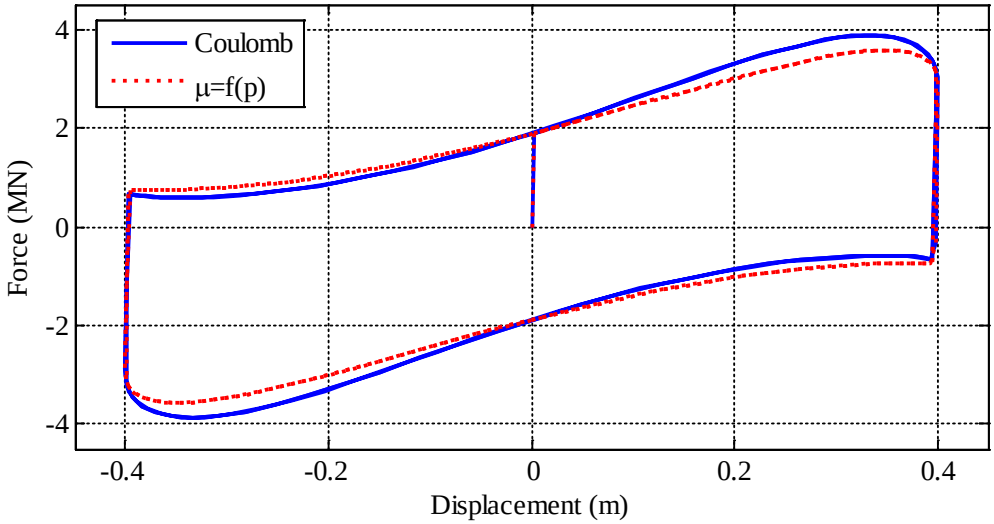

Figure 4-2 Force-Displacement Response of an FP Bearing Subjected to Cyclic Horizontal and Vertical Loading with Friction Described Using Coulomb Model and a Pressure Dependent Friction Model

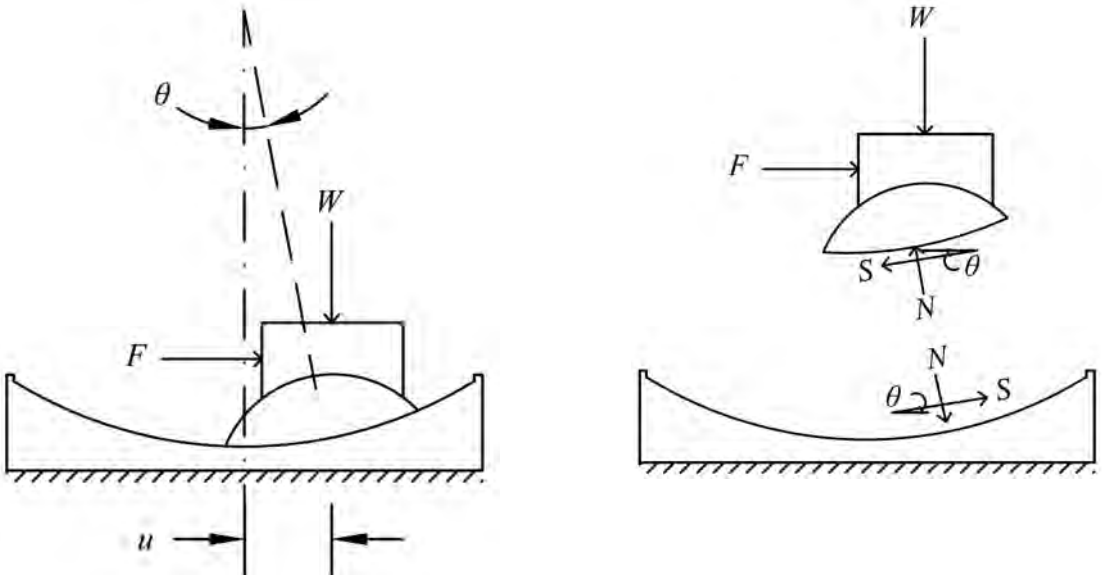

(a) Forces on an FP bearing (b) Forces on the sliding surface

Figure 4-3 Friction Pendulum Bearing in a Deformed Configuration

The shearing force, S, is the product of the coefficient of sliding friction, μ, and the normal force N.

$$S = \mu N \tag{4-6}$$

The normal force, N, is related to the horizontal force, F, and the vertical force, W, as follows:

$$N = F \sin\theta + W \cos\theta \tag{4-7}$$

where all terms were defined previously. Combining (4-4), (4-5), (4-6) and (4-7) yields the following relationship between the normal force, N, and the vertical force, W.

$$N = \frac{W}{\sqrt{1-\left(\frac{u}{R}\right)^2} - \mu\frac{u}{R}} = \frac{W}{\cos\theta - \mu\sin\theta} \qquad \textbf{(4-8)}$$

This expression assumes that the normal pressure on the sliding surface is uniform and the resultant normal force N acts through the center of the contact area at the sliding surface. This, however, is not the case as N shifts from the center of the contact area to balance the horizontal force F, as seen in Figure 4-4, which is adapted from Sarlis and Constantinou (2013). The magnitude of N is a function of forces F and W, and the geometry of the slider. Equation (4-8) does not include the influence of the geometry of the slider.

The ratio of N to W is 1.00, 1.01, 1.03 and 1.07, when u / R is equal to 5%, 10%, 20% and 30%, respectively, per Equation (4-8), with a coefficient of friction at the sliding surface of 0.06. Because $N \approx W$, N is set equal to W for this study, as assumed by Sarlis and Constantinou (2013).

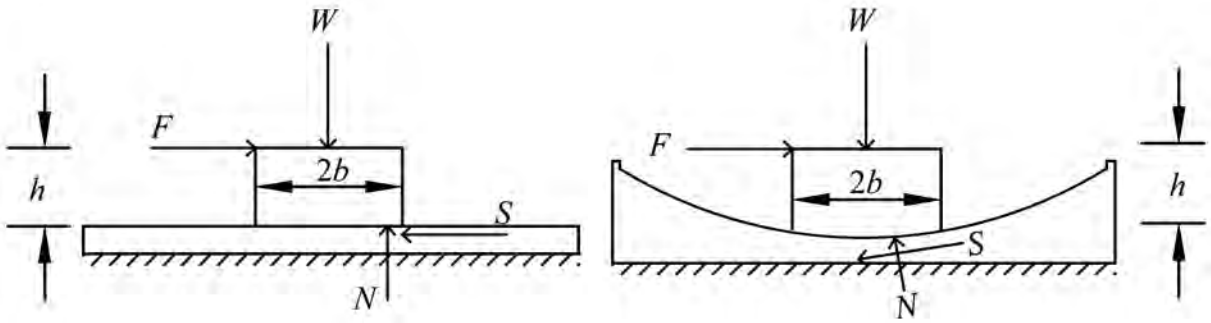

(a) Flat slider (b) FP bearing

Figure 4-4 Resultant Normal Force on Sliding Surfaces (adapted from Sarlis and Constantinou (2013)).

4.4.2 Vertical Acceleration Due to Curvature

The motion of a slider in the horizontal and vertical directions is coupled due to the curvature of the sliding surface. The acceleration of the slider relative to the sliding surface adds to the ground acceleration in the vertical direction, affecting the inertial force and the axial pressure on the bearing, which in turn influences the force-displacement response. Figure 4-5 shows the vertical motion of the slider relative to the sliding surface and that of the ground. In this study, the component of vertical acceleration due to relative motion of the slider on the sliding surface is assumed to be small compared to the vertical component of ground acceleration. See Appendix C for details.

4.4.3 Relative Vertical Displacement in Adjacent Bearings

The slider of an FP bearing rises as it displaces laterally. The increase in height depends on the geometrical properties of the bearing, translation and rotation in the isolation system and

location of the bearing in the isolation system. An isolation system comprising 289 FP bearings spread uniformly over plan dimensions of 96 m $\times$ 96 m (centerline spacing of 6 m) is subjected to combined translations and rotations such that the resultant peak displacement of at least one FP bearing in the system is greater than $0.2R$ (a traditional limit on the maximum displacement in an FP bearing; see Constantinou *et al.* (2011)). A translation of 0.200 m (0.600 m) and/or a rotation of 0.12˚ (0.36˚) is imposed on the isolation system comprising 2 s (4 s) bearings; the rotation corresponds to a displacement of 0.100 m (0.300 m) for the bearing in the outermost row and closest to the center of the isolation system. The maximum increase in height of an FP bearing across all the loading combinations is 0.116 m, and the maximum relative vertical displacement between adjacent bearings is 0.009 m over a distance of 6 m (a gradient of 1/667). This relative displacement is too small to produce significant stresses in an isolated superstructure. See Appendix D for details.

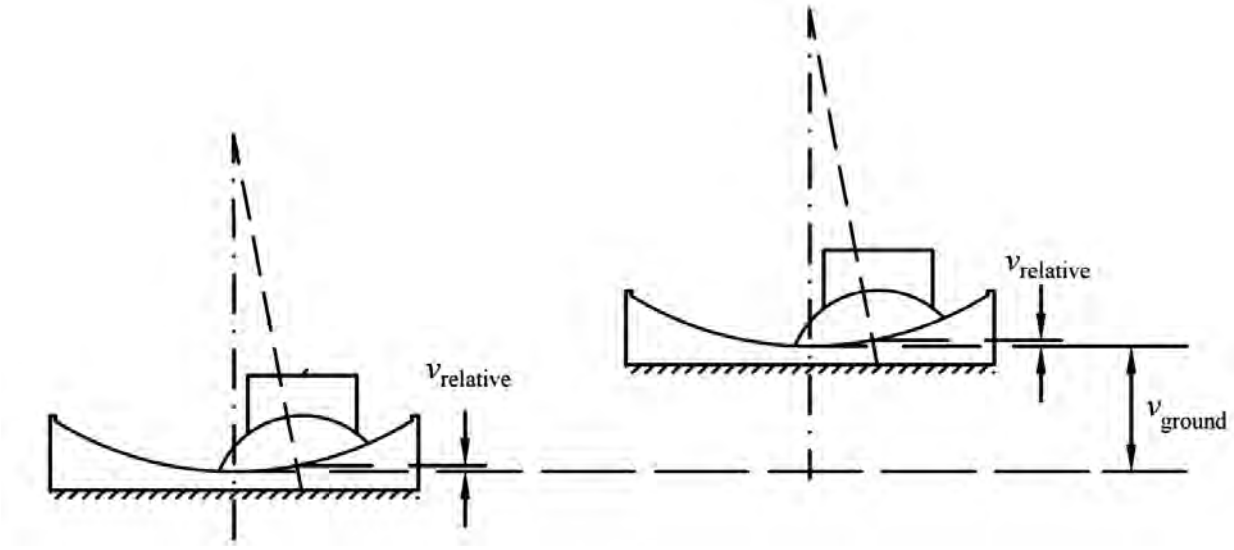

(a) Translation of slider relative to sliding surface, $v_{relative}$

(b) Ground translation, v_{ground}, and $v_{relative}$

Figure 4-5 Vertical Translation of the Slider of an FP Bearing

4.4.4 Moment Due to Horizontal Force Associated with Relative Vertical Displacement

A moment, M_W, due to the vertical force, W, is transferred to the foundation, depending on the horizontal distance, $u_{horizontal}$, between the center of the sliding surface and the line of action of the force (see Figure 4-6):

$$M_W = W u_{horizontal} \quad \textbf{(4-9)}$$

For simplicity, $u_{horizontal}$ is assumed equal to the horizontal displacement of the slider relative to the sliding surface. A moment is transferred to the top of the foundation due to the horizontal force on the slider, F, depending on the vertical distance between the top of the foundation and the line of action of the horizontal force. The component of the moment, M_F, due to the

horizontal force associated with the increase in height of the FP bearing, vrelative, is given by (see Figure 4-6):

$$M_F = Fv_{\text{relative}} = \left(\mu W + \frac{W}{R} u_{\text{horizontal}} \right) v_{\text{relative}} \qquad \textbf{(4-10)}$$

where R is the radius of curvature, μ is the coefficient of friction at the sliding surface and the other parameters were defined previously. Figure 4-6 shows the forces and distances in the horizontal and vertical directions. The distances v_{relative} and $u_{\text{horizontal}}$ are related as follows:

$$v_{\text{relative}} = R - \sqrt{R^2 - u_{\text{horizontal}}^2} \qquad \textbf{(4-11)}$$

where all terms were defined previously. For an FP bearing with the radius of curvature of the sliding surface of R, vertical load of W, coefficient of friction (Coulomb-type) of 0.06 subjected to the horizontal displacement, $u_{\text{horizontal}}$, equal to 10%, 20% and 30% of R, the ratios of moments M_F to M_W are 0.01, 0.03 and 0.06, respectively. Therefore, M_F is considered small and is not included in the moment transferred to the sliding surface.

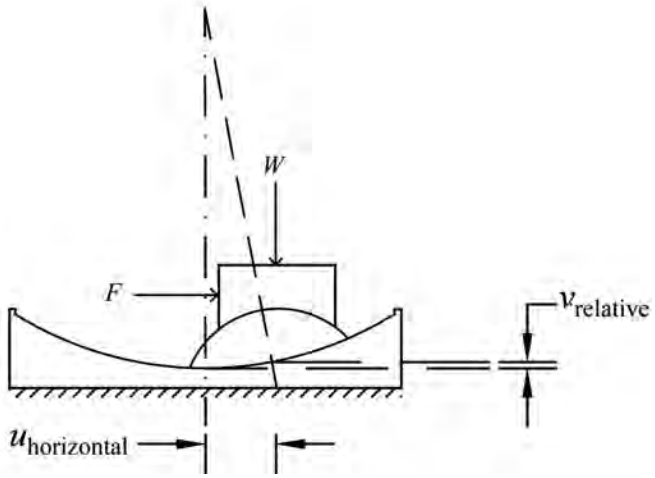

Figure 4-6 Forces and Displacements in an FP Bearing in the Horizontal and Vertical Directions

4.4.5 Impact Following Uplift

During very severe earthquake-induced shaking, there is a possibility of loss of contact between slider, sliding surface and/or housing plate of an FP bearing. The re-engagement of slider with the sliding surface and/or the housing plate following uplift will involve impact, which may produce high axial forces in the bearing. The OpenSees element *FPBearingPTV* does not address this behavior and the axial load is set equal to zero in the event of uplift.

4.4.6 Assumption of Half-Space in Temperature Calculations

The heat generated at the sliding surface has been assumed to be transferred to the sliding surface as if it is a semi-infinite space: 1) the heat generated at the sliding surface is transferred into the stainless steel, and 2) the transfer of heat is perpendicular to the sliding surface. These two assumptions are discussed below.

The slider of an FP bearing is coated with a PTFE-type composite material and the sliding surface is polished stainless steel. The heat generated at the sliding surface is distributed to the composite coating on the slider and the polished stainless steel in a ratio depending on the thermal conductivity and thermal diffusivity of the two materials. At 20ºC, stainless steel has a thermal conductivity (= 16.3 W/(m.ºC)) of about 70 times that of a PTFE-type composite, and the thermal diffusivity of stainless steel (= 4.44×10^{-6} m^2/s) is about 50 times that of the PTFE-type composite (e.g., Constantinou *et al.* (2007)). The fraction of the heat transferred to the PTFE-type composite material is very small and ignored hereafter.

The assumption that heat is transferred in the direction perpendicular to the sliding surface allows for computation of temperature at a point on the sliding surface using a closed form integral. Constantinou *et al.* (2007) estimated (assuming the half-space) that for an FP bearing with the axial pressure of 30.8 MPa, coefficient of friction of 0.05, and a slider radius of 0.250 m, subjected to 10 cycles of displacement-controlled loading with an amplitude of 0.260 m and frequency of 0.6 Hz, the penetration of heat into the sliding surface is 0.030 m (temperature rise at this depth was negligible). This depth is small compared with the size of the heat source (= 0.500 m, the diameter of the slider) and also with the thickness of the sliding surface (> 0.086 m), implying that the assumption of a half-space is valid at the sliding surface.

4.4.7 Radiation Losses

Heat is emitted from a point on the sliding surface through radiation, when the point is exposed to the environment and temperature at the point is greater than the ambient temperature. The heat flux at a point due to radiation, q_r, is given by the Stefan-Boltzmann law (e.g., Incropera and Dewitt (1985)):

$$q_r = \sigma_r \left(T^4 - T_o^4 \right) \qquad \textbf{(4-12)}$$

where σ_r is the Stefan-Boltzmann constant (= 5.67 x 10^{-8} W/(m^{2}K^4)), and T and T_o are temperature at the exposed surface and the ambient temperature, respectively, measured in Kelvin.

Figure 4-7(a) presents the heat flux generated due to friction at the center of the sliding surface of a 3 s FP bearing with a static axial pressure of 50 MPa and a reference coefficient of friction of 0.06, subjected to ground motion 10 (GM10: see Appendix A). Coulomb-type friction is assumed. Mass proportional damping of 2% of critical is assigned to the system with the proportionality constant updated at every time step of the analysis based on the instantaneous fundamental frequency of the system. Figure 4-7(d) plots the heat lost per unit area per unit time (or heat flux) at the center of the sliding surface due to radiation for the bearing, assuming T_o = 20˚C. Figures 4-7(b) and 4-7(c) present the heat flux generated due to friction, and Figures 4-7(e) and 4-7(f) plot the radiation losses at the center of the bearing, when it is subjected to GM20 and GM30, respectively. The range of the heat flux in panels (a) through (c) is 100 times that of panels (d) through (f). It is clear that the radiation losses are very small compared with the heat generated during sliding.

4.5 Verification of OpenSees Element *FPBearingPTV*

The new OpenSees element, *FPBearingPTV*, is verified in this section. Various agencies and professional organizations, such as the US Department of Defense, American Institute of

Aeronautics and Astronautics, and American Society of Mechanical Engineers have adopted definitions of verification and validation; see Oberkampf and Roy (2010). Software is verified to ensure that it provides accurate numerical solutions to a mathematical model, which is often an approximate representation of the conceptual model. Validation ensures that the numerical models and algorithms reasonably recover experimental results. Verification of software often involves comparisons of results obtained using other verified and validated software for select problems. Figure 4-8 shows the process of verification and validation described by the American Society of Mechanical Engineers (ASME, 2006).

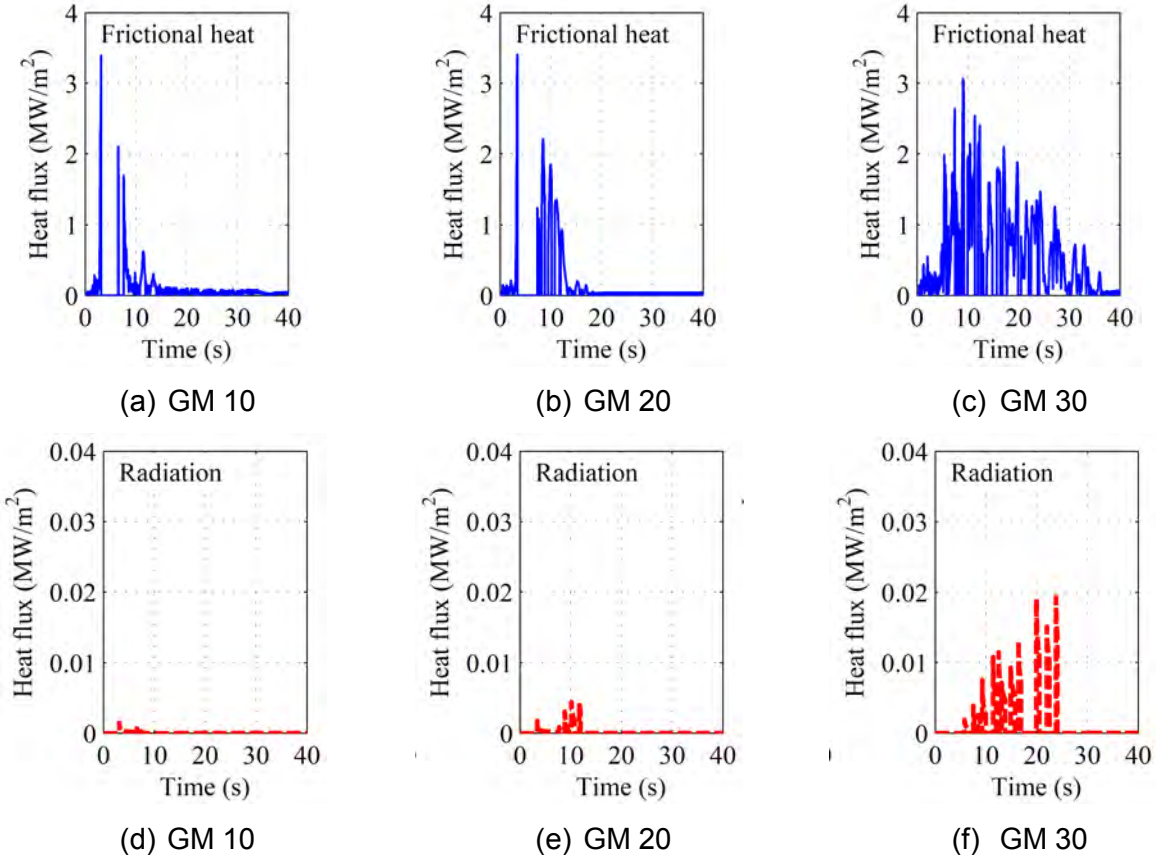

Figure 4-7 Heat Flux Histories Due to Conduction and Radiation at the Center of the Sliding Surface of an FP Bearing

The procedure suggested by Oberkampf and Roy (2010) is generally followed for the verification of the new OpenSees element. A similar approach has been used for the verification of new OpenSees elements for elastomeric and lead-rubber bearings (Kumar *et al.*, 2014). Validation of *FPBearingPTV* element is based on available experimental data.

Suitable metrics are needed to quantify the differences between the response histories obtained using two software programs (verification) or from software and an experiment (validation). The norms L_1 and L_2 are commonly used to quantify the differences (e.g., Sarin *et al.* (2010), Oberkampf and Roy (2010)). The two norms can characterize the magnitude of the differences between the two response histories.

$$L_1 = \frac{1}{N_r}\sum_{i=1}^{N_r}\left|r_{i,1} - r_{i,2}\right| \qquad \textbf{(4-13)}$$

$$L_2 = \left(\frac{1}{N_r}\sum_{i=1}^{N_r}\left(\left|r_{i,1} - r_{i,2}\right|\right)^2\right)^{1/2} \qquad \textbf{(4-14)}$$

where N_r is the number of data points, and r_{i1} and r_{i2} are the values of response quantities at the i^{th} step obtained from either the software programs, or from the software and the experimental studies. The metrics are normalized (e.g., Oberkampf and Barone (2006)) to quantify the differences between a response quantity (e.g., force history, displacement history) obtained from two processes, independent of the magnitude of the response quantity.

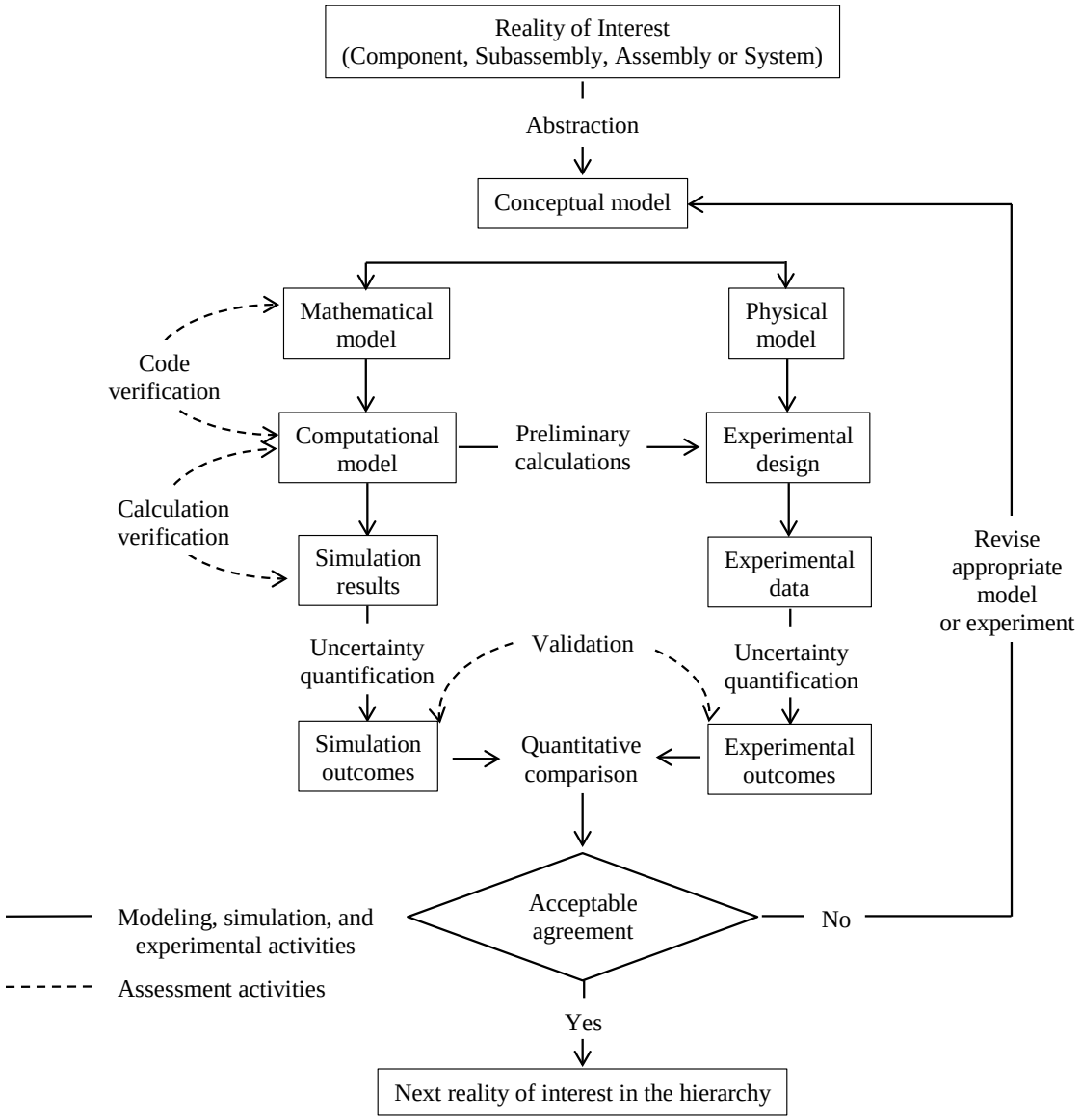

Figure 4-8 Verification and Validation Process (reproduced from ASME (2006))

$$L_{1,n} = \frac{1}{N_r}\sum_{i=1}^{N_r}\left|\frac{r_{i,1}-r_{i,2}}{r_{i,1}}\right|\times 100 \qquad \textbf{(4-15)}$$

$$L_{2,n} = \left(\frac{1}{N_r}\sum_{i=1}^{N_r}\left(\left|\frac{r_{i,1}-r_{i,2}}{r_{i,1}}\right|\right)^2\right)^{1/2} \qquad \textbf{(4-16)}$$

where $L_{1,n}$ and $L_{2,n}$ are the normalized estimates of the differences in the two response histories, and other parameters were defined previously.

The normalized metrics (e.g., (4-15)) can be high due to small *base* values, as noted by Schwer (2007) and Kat and Els (2012). For example, suppose at the 10th step of an analysis that the lateral force responses, $r_{10,1}$ and $r_{10,2}$, obtained from two programs are 2000 kN and 2100 kN, respectively, and at the 20th step of analysis the responses, $r_{20,1}$ and $r_{20,2}$, are 10 kN and 110 kN, respectively. The difference in force at the 10th and 20th steps are both 100 kN, whereas the percentage differences at the two steps are 5% and 1000%, respectively. The normalized percentage difference for the response histories incorporates the percentage differences of 5% and 1000% with equal weight (= $1/N_r$), if computed using (4-15). A better representation of accuracy can be achieved by assigning a weight, w_i, based on the amplitude of the response at an analysis step, which reduces the contribution of small to inconsequential values to the percentage difference:

$$w_i = \frac{|r_{i1}|}{\sum_{i=1}^{N_r}|r_{i1}|} \qquad \textbf{(4-17)}$$

The resulting metric, weighted average absolute percentage difference, λ, is expressed as:

$$\lambda = \sum_{i=1}^{N_r} w_i\left|\frac{r_{i1}-r_{i2}}{r_{i1}}\right|\times 100 \qquad \textbf{(4-18)}$$

Another expression for λ is obtained by substituting (4-17) into (4-18):

$$\lambda = \sum_{i=1}^{N_r}\left|\frac{r_{i1}-r_{i2}}{\sum_{i=1}^{N_r}|r_{i1}|}\right|\times 100 = \frac{\sum_{i=1}^{N_r}|r_{i1}-r_{i2}|}{\sum_{i=1}^{N_r}|r_{i1}|}\times 100 \qquad \textbf{(4-19)}$$

The differences between two response histories may be great if there is a phase difference between the two histories, even when the amplitudes of the peaks compare well. Metrics have been proposed to quantify the differences due to magnitude and phase differences separately (e.g., Schwer (2007), Kat and Els (2012)). However, the relatively simple metrics given by (4-13), (4-15) and (4-19) are used here. The metric given by (4-19) is less sensitive to the phase difference between the response histories than (4-15); the former metric assigns a smaller

weight for smaller base values[3], whereas the later metric adds the differences with equal weight. In addition to these three metrics, relative differences between peaks of the histories are compared. The differences between the peaks of two histories do not depend on the phase difference between the histories.

4.5.1 Code Verification

Code verification is performed to ensure that the software produces correct results by examining for algorithmic and coding mistakes. In the following sections, three tests, namely, symmetry test, code-to-code comparison and order-of-accuracy test, are performed on an FP bearing modeled using the OpenSees element *FPBearingPTV*.

4.5.1.1 Symmetry Test

A schematic of the symmetry test is presented in Figure 4-9. Panel (a) shows the global coordinate system. Panel (b) of the figure presents the undeformed configuration of the element between two nodes. Node 1 is assigned fixed boundary conditions. Figure 4-9(c) shows a horizontal load applied to Node 2, which results in a deformation Δ. The element along with the boundary conditions is then inverted in Figure 4-9(d). The horizontal force of Figure 4-9(c) on the element in Figure 4-9(d) should produce a displacement equal to that in Figure 4-9(c).

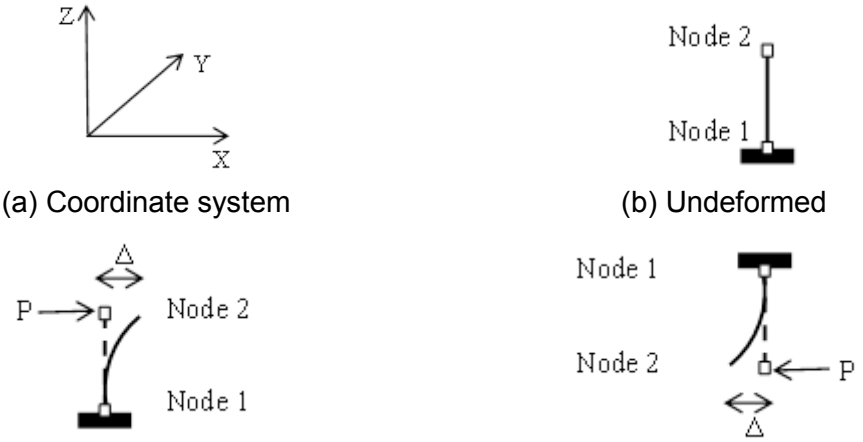

(a) Coordinate system (b) Undeformed

(c) Deformed (Case 1) (d) Inverted and deformed (Case 2)

Figure 4-9 The Symmetry Test (e.g., Oberkampf and Roy (2010)).

To perform the symmetry test on the *FPBearingPTV* element, two cases are considered. For Case 1, the slider is atop the sliding surface, the sliding surface is fixed to the ground, and a cyclic displacement history is applied to the slider (Figure 4-9(c)). The bearing is inverted for Case 2; the sliding surface is atop the slider. The sliding surface is assigned fixed boundary conditions and the cyclic displacement history of Case 1 is applied to the slider (Figure 4-9(d)) but in the opposite direction. The resulting force and moment histories on the slider and sliding surface are then compared.

[3] A phase difference may lead to a great estimate of percentage difference between two histories with maximum contributions from differences at small base values.

An FP bearing with the sliding period of 3 s, static axial pressure of 50 MPa and the reference coefficient of friction of 0.3 is subjected to a cyclic displacement history $u = 0.4\sin(0.25t)$, in units of meters and seconds. The friction at the sliding surface is Coulomb-type. The radius of the slider is 0.2 m. The displacement history is applied at Node 2 in the positive and negative X directions for Case 1 and Case 2, respectively (see Figure 4-9). The maximum expected lateral force (moment) is 3009 kN (2513 kN-m); the computed value is 3029 kN (2514 kN-m). Figure 4-10(a) shows the external force histories at Node 1 (sliding surface) in the positive X direction for Case 1 and Case 2. The force histories are equal in magnitude, but opposite in sign. Figure 4-10(b) presents the force histories at Node 2 (slider). Figures 4-10(c) and 4-10(d) present the forces in the positive Z direction at Node 1 and Node 2, respectively, for the two cases. The forces are equal in magnitude but opposite in sign. Figure 4-10(e) plots the moment history at Node 1 (sliding surface) for the two cases and Figure 4-10(f) plots the history at Node 2 (slider), which is zero as the slider is considered articulated and does not allow moment transfer.

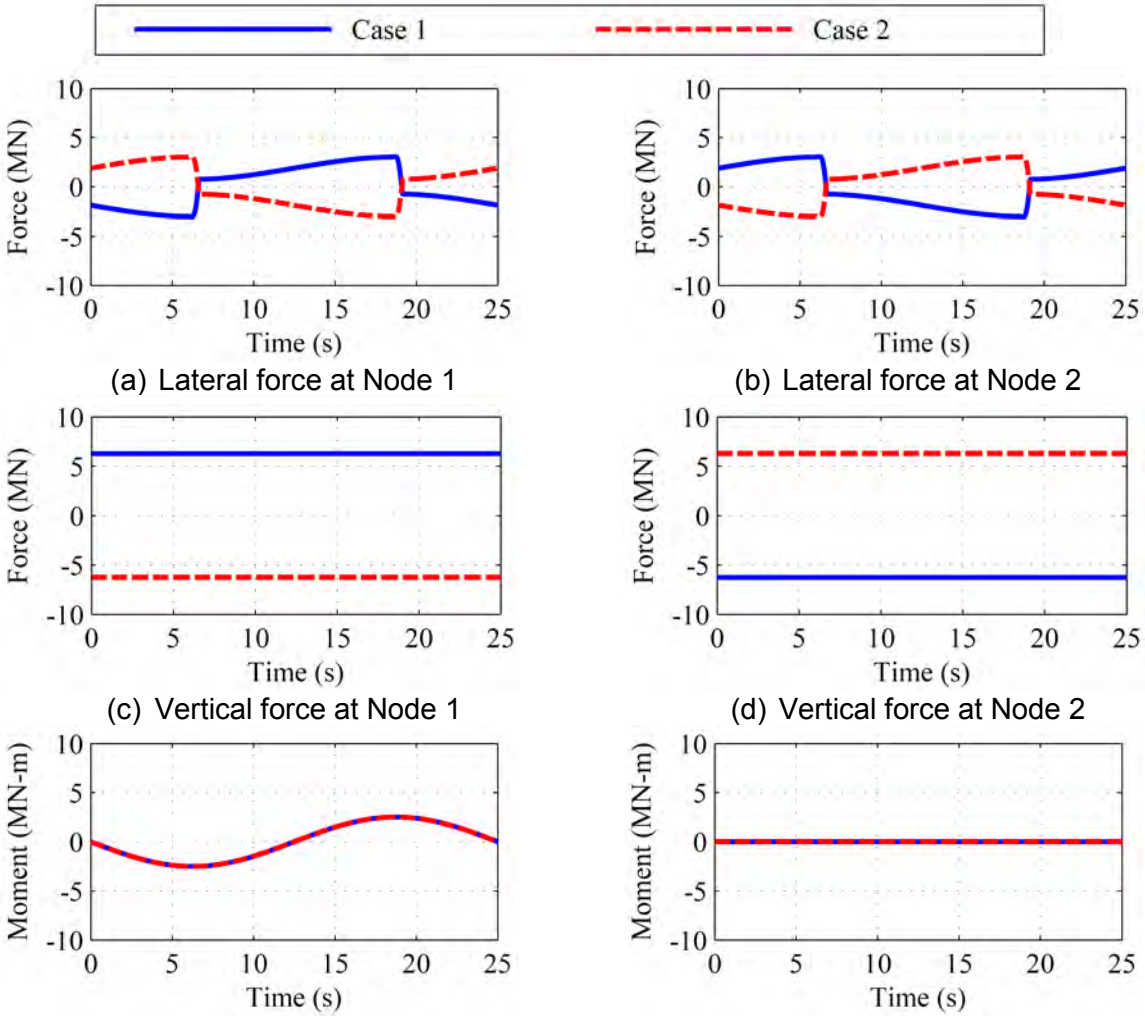

Figure 4-10 History of Forces and Moments at Sliding Surface (Node 1) and Slider (Node 2) for Case 1 and Case 2 of Figure 4-9

4.5.1.2 Code-to-Code Comparison

This exercise compares response quantities obtained from the analysis of an identical model using different software. The verification of the new OpenSees element *FPBearingPTV* is performed in two steps. In the first step, a single FP bearing with friction at the sliding surface described by the Coulomb model is subjected to a set of horizontal and vertical ground motions and the force-displacement responses are compared with those obtained from the analyses performed using ABAQUS (Dassault, 2013) and SAP2000 (CSI, 2013).

In the second step, an FP bearing with a flat sliding surface is subjected to displacement histories with different amplitudes and frequencies, and implementation of the pressure-, temperature- and velocity-dependent friction models are verified. The history of total force at the sliding surface in the horizontal direction and of temperature at selected points on the sliding surface obtained using the ABAQUS and OpenSees models are compared.

4.5.1.2.1 Code Verification

The base codes used to verify the new OpenSees element are SAP (CSI, 2013) and ABAQUS (Dassault, 2013). The program SAP is widely used to perform analysis of fixed-base and seismically isolated buildings, bridges and other structures, including seismically isolated nuclear structures (e.g., Huang *et al.* 2007, 2013). To the knowledge of the author, SAP has not been formally verified. ABAQUS is a finite element program that provides numerical solutions to a wide range of problems, including structural and thermo-mechanical. The components of the software (e.g., elements, materials) have been verified against analytical solutions. Details on verification are provided at http://abaqus.software.polimi.it/v6.14/books/ver/default.htm. ABAQUS has been used for many studies related to the nuclear industry (e.g., Kadak (2000), Inagaki *et al.* (2004), Cizelj and Simonovski (2011)).

4.5.1.2.2 Comparison of Response-History Analysis Results

A single FP bearing with a static axial pressure of 50 MPa, a coefficient of friction of 0.06, and friction at the sliding surface described using the Coulomb model is subjected to GM1 of Appendix A. No damping is assigned to the system. The yield displacement is 0.001 m. The analysis is performed using the *FPBearingPTV* element in OpenSees and the *Friction Isolator* link element in SAP2000. The link element in SAP2000 has been used to simulate the results from a shake table test performed on a seven story steel building isolated using FP bearings, as reported in the documentation of the software. Figure 4-11 shows the displacement (panels (a) and (b)) and force (panels (c) and (d)) histories of the slider in the two horizontal directions obtained using SAP2000 and OpenSees.

The maximum difference in the peak displacements at a given time instant are 0.003 m and 0.002 m in the two horizontal directions, which are tiny compared with the corresponding maximum displacements of 0.480 m and 0.510 m. The value of λ (Equation (4-19)) for the displacement response histories obtained using SAP and OpenSees are 0.6% and 0.3% in the X and Y directions, respectively. The peak difference in force at a given time instant is 110 kN in both horizontal directions, compared with the maximum forces of 2300 kN and 2400 kN, respectively. The value of λ for the lateral force histories obtained using SAP and OpenSees are 0.7% and 0.8% in the X and Y directions, respectively.

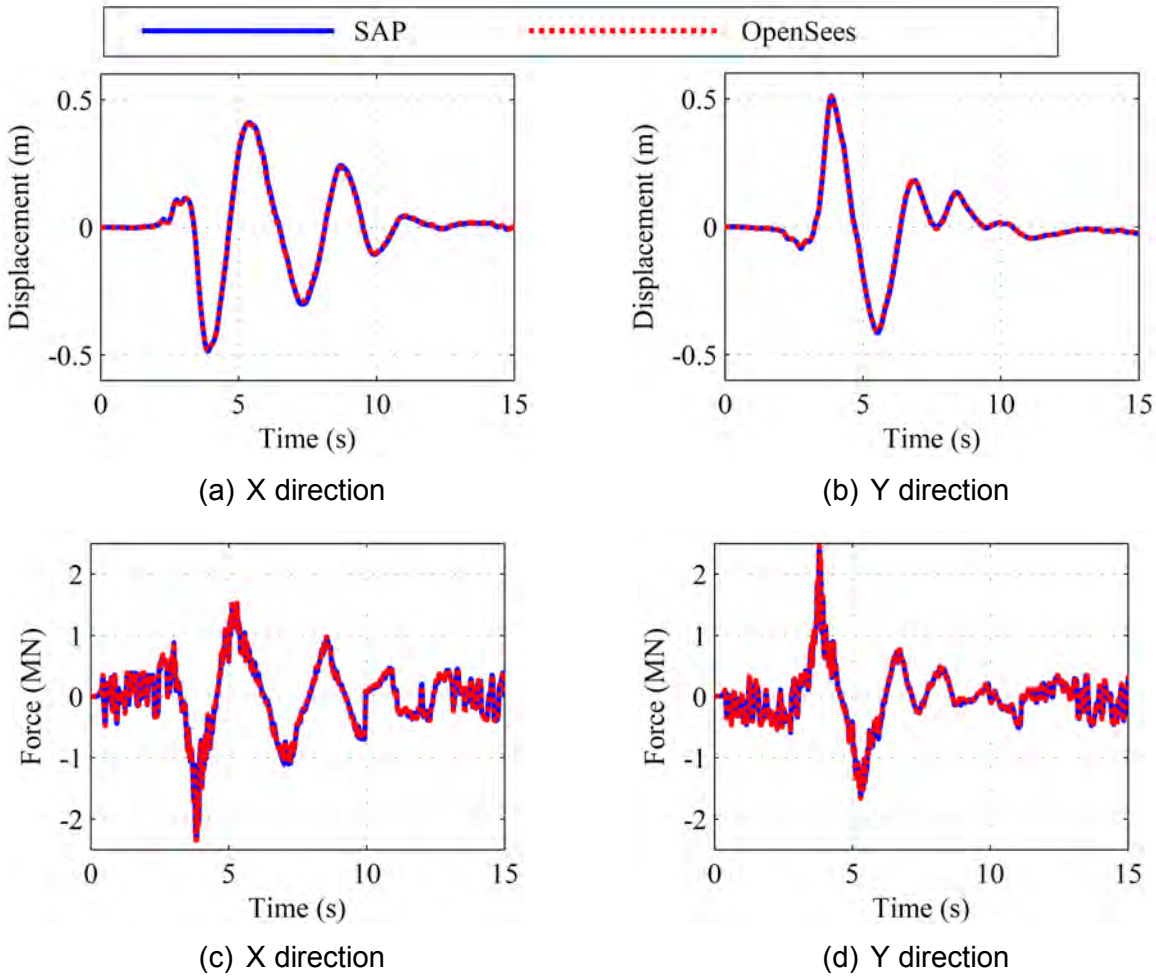

Figure 4-11 Force-Displacement Histories of an FP Bearing Subjected to GM1 Obtained Using SAP2000 and OpenSees

4.5.1.2.3 Verification of the Implementation of the Friction Model

The second step of code verification verifies the implementation of the axial pressure, temperature and sliding velocity dependent friction models in the OpenSees element *FPBearingPTV.* A flat slider is used for this purpose. The flat surface is realized in OpenSees by assigning a very high value of radius of curvature for a single FP bearing. The slider is square with side dimensions of 0.060 m. The eight analysis cases of Table 4-1 are considered. In addition to a static pressure of 50 MPa, a sinusoidal pressure history with the amplitude of 50 MPa and the loading frequency of 1 Hz is applied to the slider in the vertical direction. Figure 4-12(a) presents the axial pressure history on the slider. The slider is subjected to two displacement histories, one with small amplitude and high frequency (cases 1–4 in Table 4-1) and the other with high amplitude and low frequency (cases 5–8 in Table 4-1). The peak velocities associated with the two displacement histories are 0.075 m/s and 0.190 m/s, respectively. Figure 4-12(b) presents the horizontal displacement histories imposed on the slider. The assumption of an infinite half space made for the temperature calculation at the center of the sliding surface (see Chapter 3) is realized when the amplitude of motion is small (cases 1–4 in Table 4-1).

It was established in Chapter 3 that the temperature at the center of the sliding surface is representative of the temperature at the sliding surface when the bearing is subjected to earthquake ground motion, and can be used to update the temperature-dependent coefficient of sliding friction during a response-history analysis. For this set of analyses, the reference coefficient of friction at the sliding surface, measured at a high velocity of sliding, at the temperature of 20°C and at a static axial pressure of 50 MPa, is set equal to 0.3[4]. Four friction models, namely, Coulomb (cases 1 and 5), velocity dependent (cases 2 and 6), axial pressure dependent (cases 3 and 7) and temperature dependent (cases 4 and 8) are considered.

The results obtained from the displacement-controlled analyses performed using OpenSees are compared with those obtained using ABAQUS. Figure 4-13 shows the meshed model of the flat slider in ABAQUS. The eight-node C3D8T coupled temperature-displacement brick elements are assigned to the mesh. The sliding plate is 0.240 m long, 0.120 m wide and 0.030 m thick. The slider's dimensions are $0.060 \times 0.060 \times 0.010$ m. Master and slave surfaces are selected by the user for a surface-to-surface contact problem in ABAQUS. Finer meshes are recommended for the slave surface than the master surface. For the present study, the mesh sizes for the sliding plate (slave) and slider (master) are 0.005 m and 0.006 m, respectively. The slider and the sliding plate are assumed to be steel with thermal conductivity and specific heat of 18 W/(m°C) and 516.44 J/(kg°C), respectively. Mass density, Young's modulus and Poisson's ratio considered for steel are 7,850 kg/m^3, 210 GPa and 0.3, respectively. The heat generated during sliding is assigned to the sliding plate. The initial temperature of the slider and the sliding surface is 20°C. The sliding plate is assigned fixed boundaries and the slider is free to translate.

Figure 4-14 shows the temperature at the surface of the flat slider at the end of 10 seconds of motion $u = 0.006\sin(4\pi t)$ (Case 1 of Table 4-1). The maximum temperature at the surface is 300°C. The corresponding temperature profile at a section perpendicular to the sliding surface is shown in Figure 4-15. The maximum depth of heat penetration into the plate below at 10 s is less than 0.015 m (half its total thickness). Figure 4-16 presents the temperature profile at the sliding surface when a displacement history $u = 0.06\sin(\pi t)$ is imposed on the slider (Case 5 of Table 4-1). The maximum temperature at the sliding surface is about 400°C. The maximum depth of heat penetration into the plate below is less than 0.015 m, as seen in Figure 4-17.

Figure 4-18(a) plots the lateral force at the surface of the flat slider obtained using ABAQUS and OpenSees, when the coefficient of friction at the sliding surface is defined using Coulomb model and the slider is subjected to a displacement history $u = 0.006\sin(4\pi t)$ (Case 1 of Table 4-1). The lateral force histories compare well; the difference in the amplitudes of the peaks is 1% and λ for the ABAQUS and OpenSees force histories for the 10 s of motion is 7% (see Table 4-2). The maximum percentage difference between the force histories occurs when the direction of motion changes, as seen in Figure 4-19: time interval between 2 s and 2.5 s from Figure 4-18. The differences for all eight cases are listed in Table 4-2.

[4] The dimensions of the slider and the sliding plate, and peak displacement were selected so that the 1) computational time for analyses was not great, and 2) temperature rise at the external surfaces of the sliding plate (except the sliding surface) was zero at the end of analysis. The size of the slider selected for this study (0.060 m square) is small compared with that commonly used in practice.

Table 4-1 Analysis Cases to Verify the Implementation of Friction Model in the OpenSees Element FPBearingPTV

Case	p_o (MPa)[1]	u_o (mm)[2]	f_h (Hz)[2]	f_v (Hz)[1]	Friction model	Notation
1	50	6	2	1	Coulomb	$\mu = \text{Coulomb}$
2	50	6	2	1	Velocity dependent	$\mu = f(v)$[3]
3	50	6	2	1	Pressure dependent	$\mu = f(p)$[1]
4	50	6	2	1	Temperature dependent	$\mu = f(T)$[4]
5	50	60	0.5	1	Coulomb	$\mu = \text{Coulomb}$
6	50	60	0.5	1	Velocity dependent	$\mu = f(v)$
7	50	60	0.5	1	Pressure dependent	$\mu = f(p)$
8	50	60	0.5	1	Temperature dependent	$\mu = f(T)$

[1]Vertical loading history: $p = p_o\left(1+\sin\left(2\pi f_v t\right)\right)$; t : time; p: axial pressure; f_v: vertical loading frequency

[2]Horizontal displacement history: $u = u_o \sin\left(2\pi f_h t\right)$; u : displacement; f_h : horizontal displacement frequency

[3]v : sliding velocity

[4]T : temperature at the sliding surface

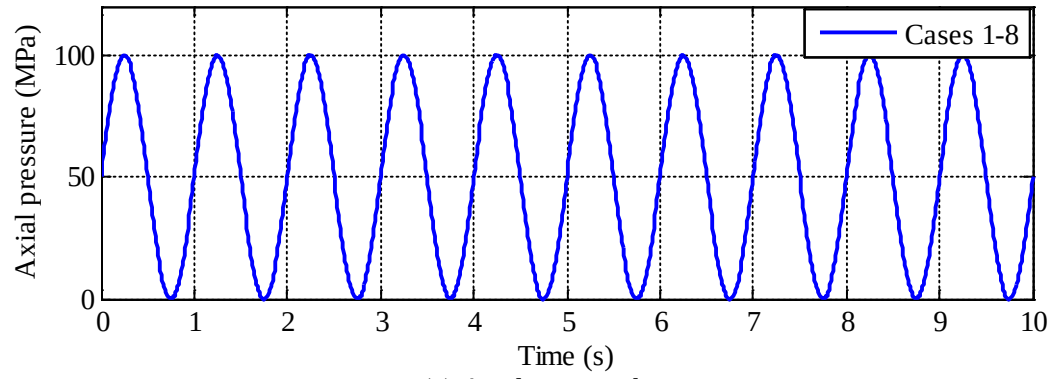

(a) Axial pressure history

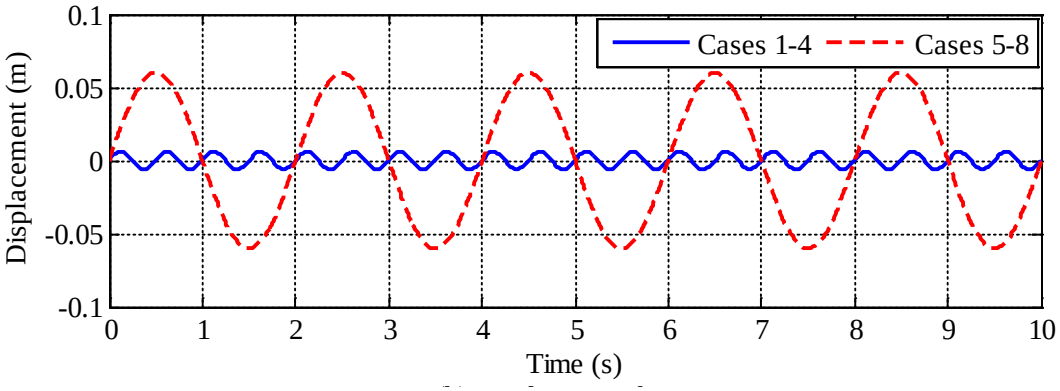

(b) Displacement history

Figure 4-12 Axial Pressure and Displacement Histories Applied on the Slider of the Flat Slider

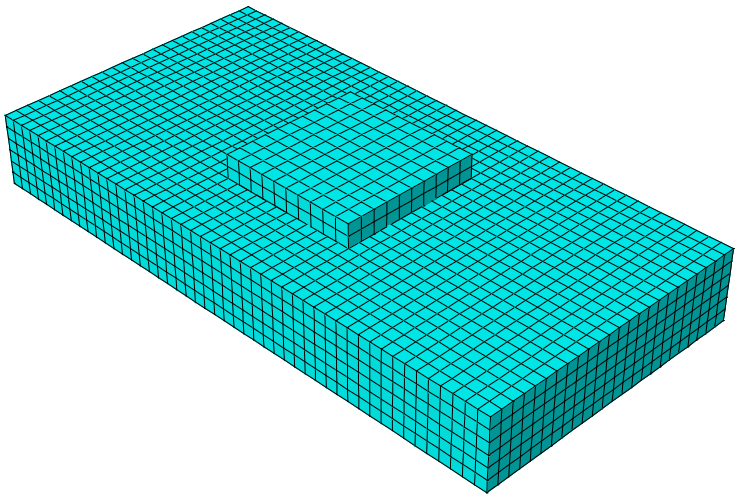

Figure 4-13 The Model of Flat Slider Bearing in ABAQUS

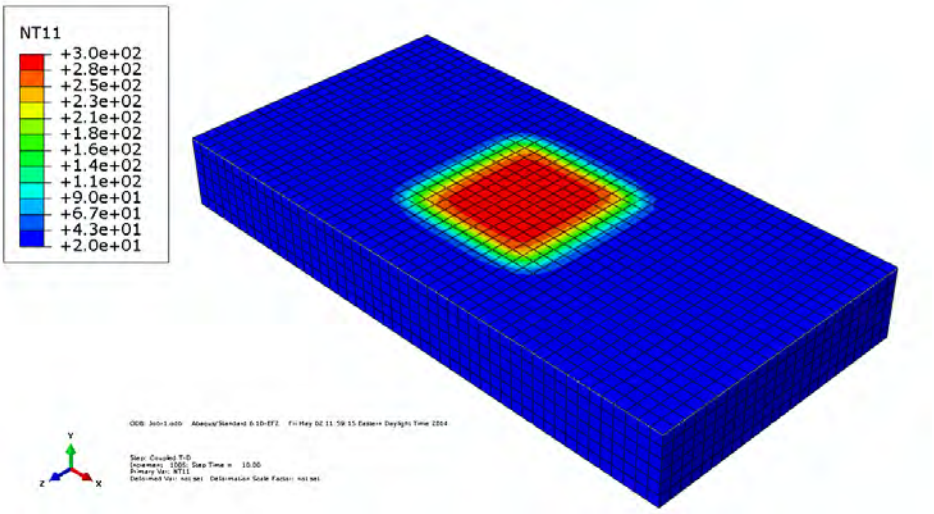

Figure 4-14 **Temperature (°C) Distribution at the Sliding Surface with Friction Defined Using Coulomb Model, Horizontal Displacement History of $u = 0.006\sin(4\pi t)$, Case 1 of Table 4-1**

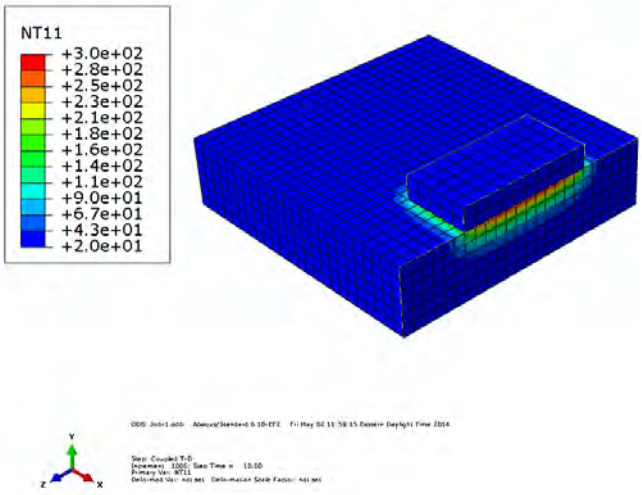

Figure 4-15 **Temperature (°C) Distribution at a Section Perpendicular to the Sliding Surface with Friction Defined Using Coulomb Model, Horizontal Displacement History of $u = 0.006\sin(4\pi t)$, Case 1 of Table 4-1**

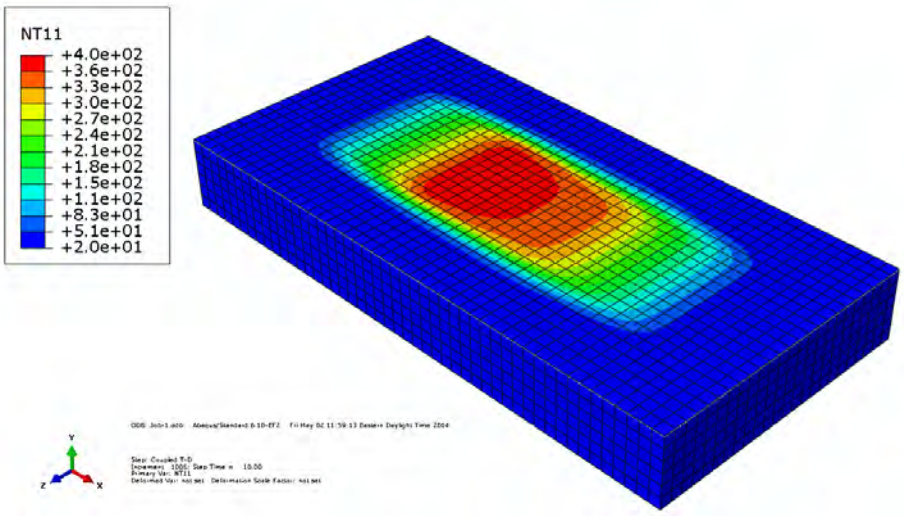

Figure 4-16 Temperature (oC) Distribution at the Sliding Surface with Friction Defined Using Coulomb Model, Horizontal Displacement History of u = 0.06sin(πt) Case 5 of Table 4-1

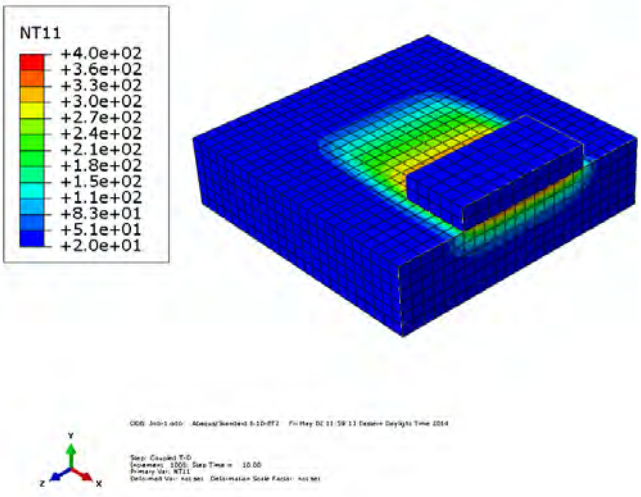

Figure 4-17 Temperature (oC) Distribution at a Section Perpendicular to the Sliding Surface with Friction Defined Using Coulomb Model, Horizontal Displacement History of u = 0.06sin(πt) Case 5 of Table 4-1

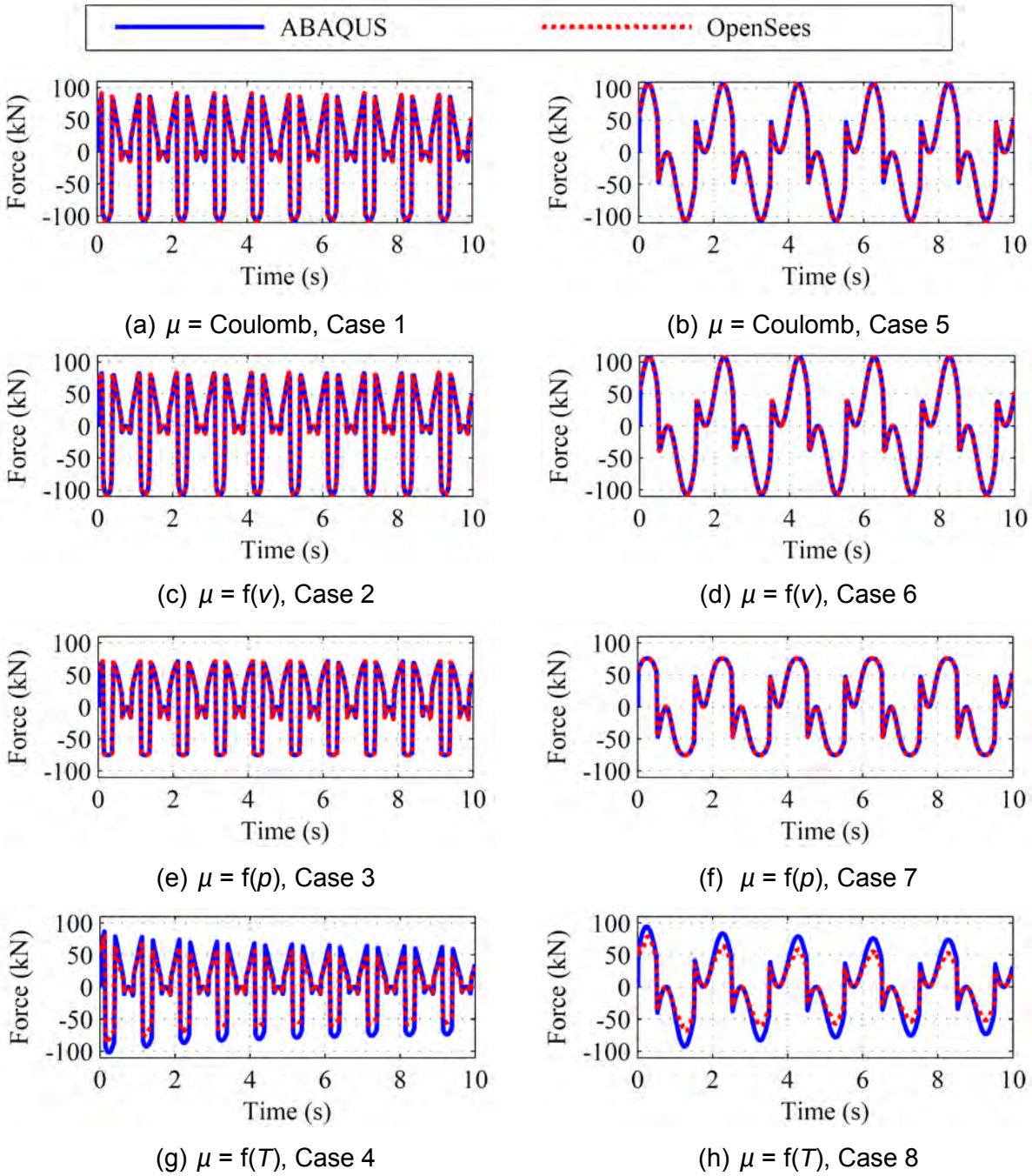

(a) μ = Coulomb, Case 1

(b) μ = Coulomb, Case 5

(c) μ = f(v), Case 2

(d) μ = f(v), Case 6

(e) μ = f(p), Case 3

(f) μ = f(p), Case 7

(g) μ = f(T), Case 4

(h) μ = f(T), Case 8

Figure 4-18 Lateral Force Histories for the Eight Cases Listed in Table 4-1

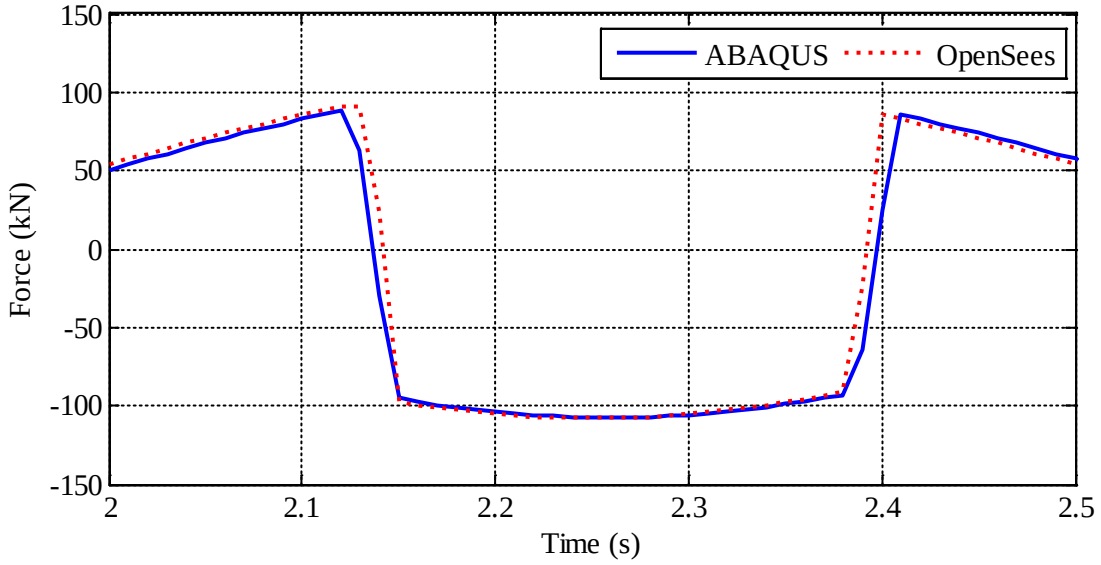

Figure 4-19 Lateral Force Histories for Case 1 of Table 4-1

Table 4-2 Differences Between Force and Temperature Histories Obtained Using ABAQUS and OpenSees

Case	Friction model	Force		Temperature	
		% difference between peaks	% difference, λ	% difference between peaks	% difference, λ
1	$\mu =$ Coulomb	1	7	10	9
2	$\mu = f(v)$	1	7	10	9
3	$\mu = f(p)$	0	8	7	9
4	$\mu = f(T)$	14	24	11	14
5	$\mu =$ Coulomb	0	5	25	12
6	$\mu = f(v)$	0	5	25	12
7	$\mu = f(p)$	0	4	25	12
8	$\mu = f(T)$	17	26	4	20

The peak forces computed using ABAQUS and OpenSees differ by less than 1% when the friction model does not include heating effects and λ for these six cases ranges between 4% and 8% (panels (a) through (f) of Figure 4-18; also see Table 4-2). The differences are greater for panels (g) and (h), which present force histories for the cases when the coefficient of friction varies with temperature at the sliding surface. The difference in the peak values and the value of λ for these two panels are 15% and 25%, respectively (see Table 4-2). The differences in these force histories are great because the temperature at the sliding surface is calculated differently in the two software, which in turn affects the coefficient of friction and the lateral force. In the OpenSees element *FPBearingPTV*, the temperature at the center of the 0.240 $\times$ 0.120 m plate below the slider is considered to be representative of the temperature at the interface.

In ABAQUS, the coefficient of friction at a point of contact on the sliding surface is computed using the temperature at the contact point. Further, the OpenSees element assumes an infinite half space below (heat flows vertically downward) to compute temperature, whereas the ABAQUS solution considers that the heat imparted into the sliding plate flows in all directions.

Figure 4-20(a) plots the temperature histories at the center of the sliding surface for Case 1 of Table 4-1 obtained using ABAQUS and OpenSees. The difference between the peaks of the two histories is 10% (see Table 4-2). The difference for Figure 4-20(b) is 25%, which presents results for Case 5 of Table 4-1. The peaks computed using OpenSees are greater than those computed using ABAQUS for both the panels because of the infinite half space conditions assumed in the OpenSees temperature calculations. The percentage difference is greater in Figure 4-20(b) as the conditions at the center of the sliding surface are substantially different from an infinite half space during the relatively large amplitude motion (see Figure 4-21 for the schematic). Figure 4-21(a) shows the entire sliding surface receiving heat from an external source (e.g., frictional heating); panel (b) shows the heat source (slider) symmetrically located with respect to the center of sliding surface, and panels (c) and (d) show the configuration of the slider in which the center of the slider is away from the center of sliding surface. The configuration of Figure 4-21(a) most closely produces the conditions of an infinite half space. The assumption of a half space leads to a small overestimation in the temperature at the center of the sliding surface for the configuration of panel (b), but substantial overestimations for the configurations of panels (c) and (d).

Friction at the sliding surface was described using the Coulomb model for Figures 4-20(a) and 4-20(b). Figures 4-20(c) and 4-20(d) plot the temperature histories for the velocity-dependent friction model, and Figures 4-20(e) and 4-20(f) plot the histories for the pressure-dependent friction model. The temperature histories in panels Figures 4-20(c) and 4-20(e) are similar to that in Figure 4-20(a). The differences in the peak amplitudes obtained using ABAQUS and OpenSees are between 7% and 10% for the three panels. The parameter λ for each of the three panels is 9%. The difference between the peak amplitudes and λ are 25% and 12%, respectively, for each of Figures 4-20(b), 4-20(d) and 4-20(f) (see Table 4-2).

Figures 4-20(g) and 4-20(h) present results for the case where friction is temperature-dependent. The peak amplitudes obtained using the two programs differ by 11% and 4%, and λ is 14% and 20%, for the two panels, respectively. The values of λ for these two panels are greater than for the other six panels. Moreover, the ABAQUS-predicted temperature is greater than that obtained using OpenSees for most of the history for these two panels, unlike the other six panels. This is expected since the temperature histories computed using OpenSees are greater compared to ABAQUS when the friction models do not include heating effects (Figures 4-20(a) through 4-20(f)) and a temperature-dependent friction model would result in smaller values of the coefficient of friction, heat generated at the sliding surface and temperature rise.

The results presented in this section are summarized as follows. The OpenSees element *FPBearingPTV* produces accurate estimates of lateral force histories (peaks computed within 1% error) when the friction model does not include heating effects. The error can be as great as 15% when heating effects are considered in the friction model. The element computes the peak temperature at the center of sliding surface with an error of about 10% (25%) when amplitude of displacement loading is small (large).

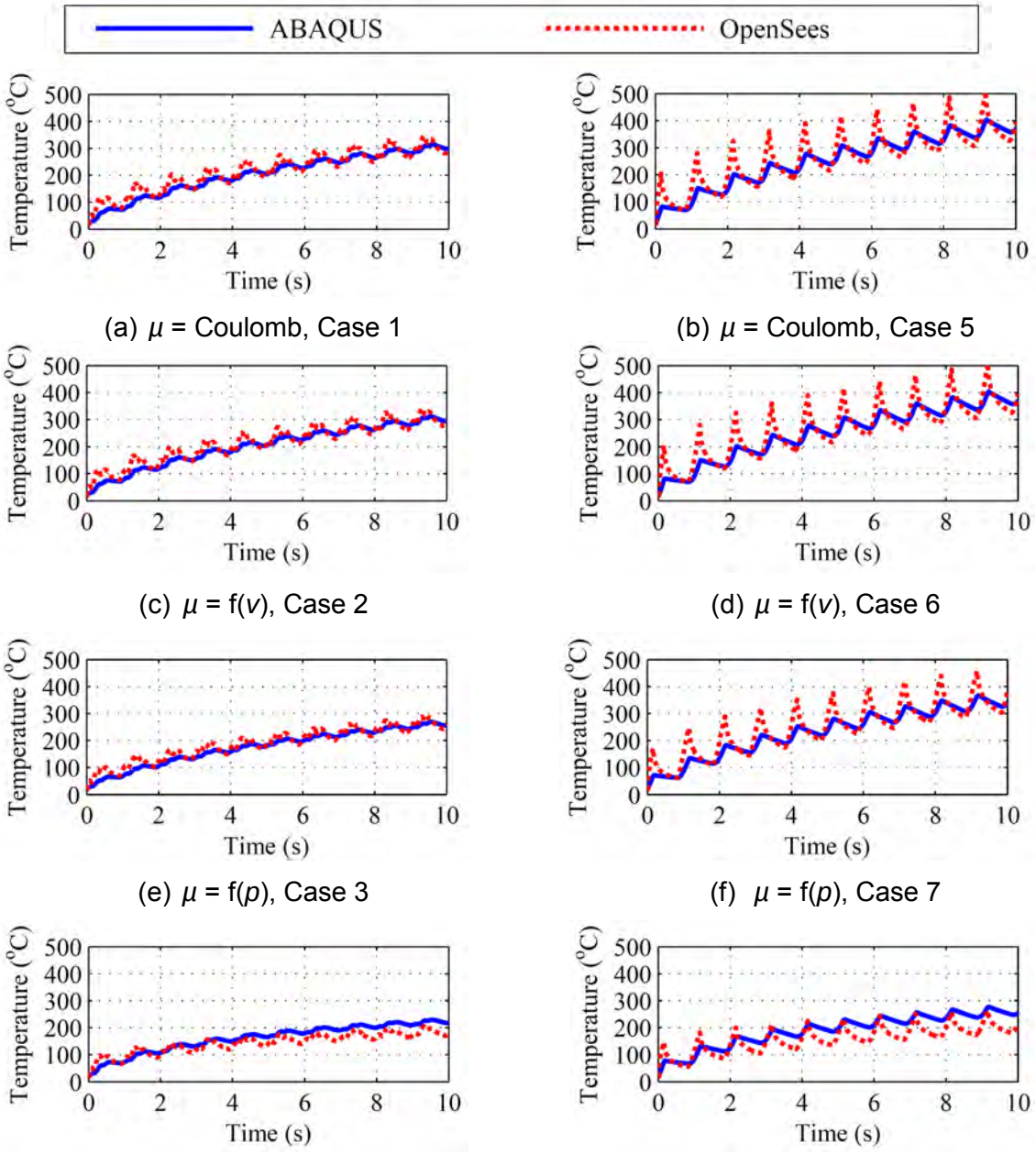

Figure 4-20 Temperature Histories at the Sliding Surface of the Flat Slider for the Eight Cases Listed in Table 4-1

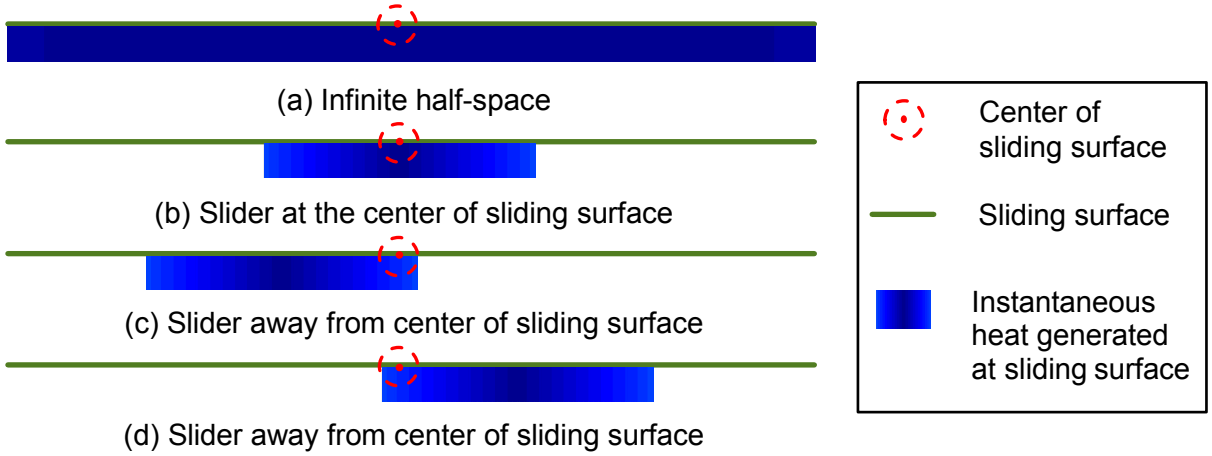

Figure 4-21 Location of Heat Source (slider) Relative to the Center of the Sliding Surface at Different Time Instants

4.5.1.3 Order-of-Accuracy Test

A discretized solution to a differential equation converges to the exact solution (or becomes accurate) as the discretization step in time and/or space is reduced. The order of accuracy refers to the rate at which the numerical solution converges to the exact solution. The rate can be estimated using theoretical and empirical methods and are called *formal order of accuracy* and *observed order of accuracy*, respectively. Oberkampf and Roy (2010) discuss formal and observed orders of accuracy. The approaches to compute the formal and observed orders of accuracy of the numerical solution to the mathematical model of the FP bearing (Equation (4-1)) are presented in this section.

The lateral force-displacement relationship of an FP bearing can be described using a bilinear relationship, if it is subjected to a monotonic loading. Figure 4-22(a) presents the lateral force-displacement relationship of an FP bearing. Before sliding, the lateral stiffness, k_1, is:

$$k_1 = \frac{\mu W}{u_y} \tag{4-20}$$

where μ the coefficient of friction defined using the Coulomb model, W is the axial load on the bearing, and u_y is the displacement at which the slope of the curve changes. The stiffness of the second segment of the force-displacement relationship, k_2, is given by the ratio of axial load, W, to the radius of curvature of the sliding surface, R:

$$k_2 = \frac{W}{R} \tag{4-21}$$

where all terms were defined previously.

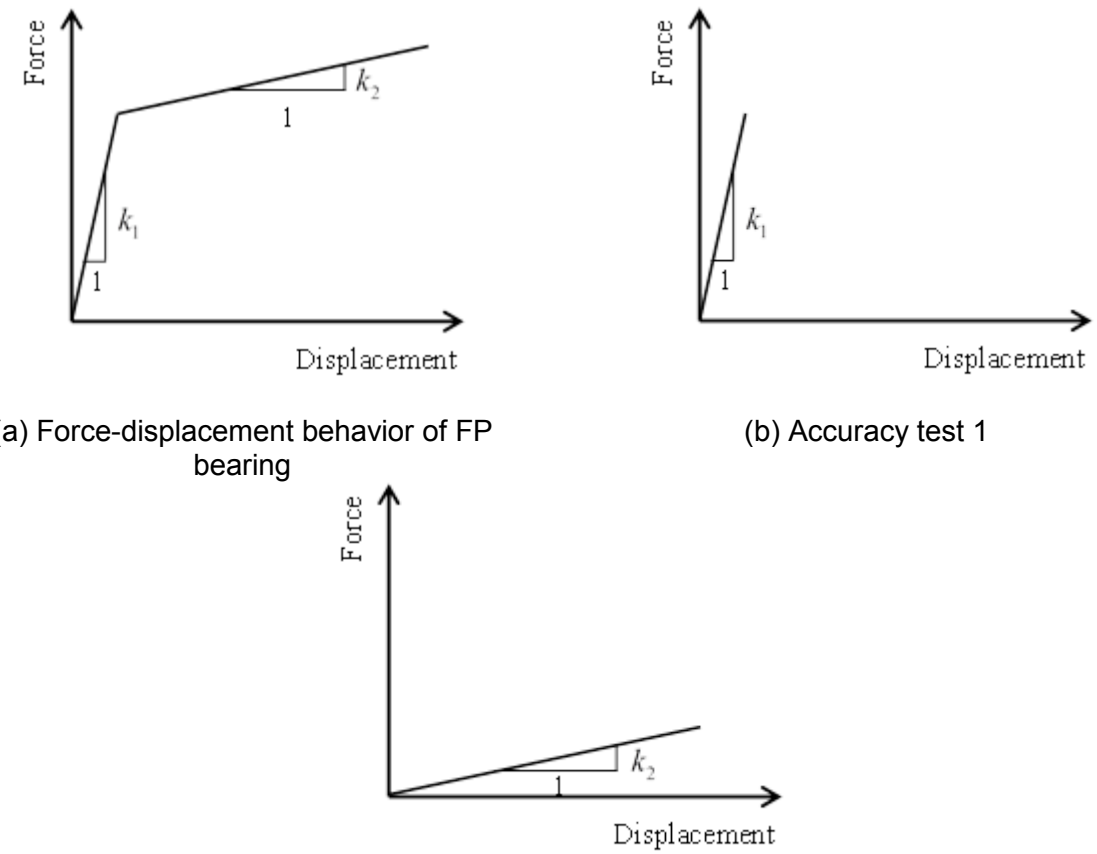

(a) Force-displacement behavior of FP bearing

(b) Accuracy test 1

(c) Accuracy test 2

Figure 4-22 Schematic of Order of Accuracy Tests

The undamped equation of motion of the slider of the FP bearing is given by the following equation.

$$m_s\ddot{u} + k(u)u = f_o \tag{4-22}$$

where m_s is the mass associated with the slider, u is the lateral displacement, $\ddot{u}$ is the acceleration, $k(u)$ is the instantaneous stiffness, which can be either k_1 or k_2, and f_o is the external force. For convenience, the order of accuracy test is performed in two steps. In the first step, a sinusoidal acceleration history with high frequency but small amplitude is applied to the slider so that the maximum displacement of the slider is less than u_y (Figure 4-22(b)). In the second step, the FP bearing is subjected to another sinusoidal history with small frequency and high amplitude (Figure 4-22(c)). The coefficient of friction is set equal to an extremely small value in this case to realize the linear system with an stiffness of k_2. The discretized form of (4-22) is

$$m_s \frac{u_{i+1} - 2u_i + u_{i-1}}{(\Delta t)^2} + k(u)u_i - f_{oi} = 0 \tag{4-23}$$

where u_i is the displacement of slider relative to the sliding surface and f_{oi} is the external force acting on the slider in the i^{th} time step, Δt is the length of time step, and other variables were defined previously. The Taylor series expansion of u_{i+1} and u_{i-1} relative to u_i are given below.

$$u_{i+1} = u_i + \left.\frac{\partial u}{\partial t}\right|_i \Delta t + \left.\frac{\partial^2 u}{\partial t^2}\right|_i \frac{(\Delta t)^2}{2!} + \left.\frac{\partial^3 u}{\partial t^3}\right|_i \frac{(\Delta t)^3}{3!} + \left.\frac{\partial^4 u}{\partial t^4}\right|_i \frac{(\Delta t)^4}{4!} + O\left(\Delta t^5\right) \tag{4-24}$$

$$u_{i-1} = u_i - \left.\frac{\partial u}{\partial t}\right|_i \Delta t + \left.\frac{\partial^2 u}{\partial t^2}\right|_i \frac{(\Delta t)^2}{2!} - \left.\frac{\partial^3 u}{\partial t^3}\right|_i \frac{(\Delta t)^3}{3!} + \left.\frac{\partial^4 u}{\partial t^4}\right|_i \frac{(\Delta t)^4}{4!} + O\left(\Delta t^5\right) \tag{4-25}$$

where $\left.\frac{\partial^n u}{\partial t^n}\right|_i$ is n^{th} derivative of u with respect to t at i^{th} time step, and all other terms were defined previously. Combining equations (4-23), (4-24) and (4-25) yields

$$m_s \frac{u_{i+1} - 2u_i + u_{i-1}}{(\Delta t)^2} + ku_i - f_{oi} = m\frac{\partial^2 u}{\partial t^2} + ku - f_o\Big|_i + \underbrace{m\left.\frac{\partial^4 u}{\partial t^4}.\frac{(\Delta t)^2}{12}\right|_i + \ldots}_{\text{Truncation error}} \tag{4-26}$$

where all the terms were defined previously. The formal order of accuracy of the numerical scheme is 2, the highest power of Δt in the truncation error.

The *observed order of accuracy* is the actual order of accuracy computed for a series of finite elements meshes and is defined as (Oberkampf and Roy, 2010):

$$\hat{p} = \frac{\ln\left(\frac{\varepsilon_{2h}}{\varepsilon_h}\right)}{\ln(2)} \tag{4-27}$$

where $\hat{p}$ is the observed order of accuracy and ε_h is the discretization error when the mesh size is h; ε_h is computed as

$$\varepsilon_h = \frac{1}{N_{data}} \sum_{i=1}^{N_{data}} \left| u_{exact,i} - u_{h,i} \right| \tag{4-28}$$

where N_{data} is the number of data points, $u_{exact,i}$ is the exact solution at the i^{th} step, $u_{h,i}$ is the numerical solution when mesh size is h at the i^{th} step and $|\,.\,|$ denotes an absolute value.

The sliding surface of an FP bearing with a sliding period of 3 s, static axial pressure of 50 MPa, and a Coulomb-type coefficient of friction of 0.3 is subjected to an acceleration history $\ddot{u}_g = \sin(8\pi t)$ m/s^2 and *observed order of accuracy* is computed for the elastic range (see Figure 4-22b). The radius of the slider is 0.200 m. The yield displacement (the displacement at the transition between the two slopes in Figure 4-22(a)) is set equal to 0.001 m. The

acceleration history is chosen such that the maximum relative displacement response of the bearing (= 0.0006 m) is smaller than the yield displacement (= 0.001 m). The 0.5 s long input acceleration history is defined at 0.01 s intervals. Numerical solutions are computed (in double precision; 16 significant digits) using OpenSees with analysis steps set equal to 0.01 s, 0.005 s, 0.0025 s, 0.00125 s, 0.000625 s and 0.0003125 s. The numerical solutions obtained using the Generalized Richardson Extrapolation method are considered as the exact solutions (e.g., Roy *et al.* (2003)):

$$\bar{u} = u_h + \frac{u_h - u_{2h}}{3} \tag{4-29}$$

where $\bar{u}$ is the "exact" solution, h is the analysis time step (= 0.00005 s), and u_h is the numerical solution corresponding to an analysis step h. Table 4-3 presents the *observed order of accuracy* (given by (4-27)) for different analysis step sizes, which approaches 2 as the step size is reduced, which is also the formal order of accuracy for the numerical scheme. Figure 4-23 plots the numerically obtained displacement histories for the different analysis steps. Figure 4-24 presents the corresponding force-displacement histories.

Table 4-3 Order of Accuracy for the Analysis Scheme Used in the OpenSees Element FPBearingPTV

Regime	Analysis step size (s)		Observed order of accuracy (Equation (4-27))	Formal order of accuracy
	Δt_2	Δt_1		
Elastic	0.01	0.005	1.976	2
	0.005	0.0025	1.999	
	0.0025	0.00125	1.999	
	0.00125	0.000625	2.000	
	0.000625	0.0003125	2.000	
Plastic	0.01	0.005	2.000	
	0.005	0.0025	2.000	
	0.0025	0.00125	2.000	
	0.00125	0.000625	2.000	
	0.000625	0.0003125	2.000	

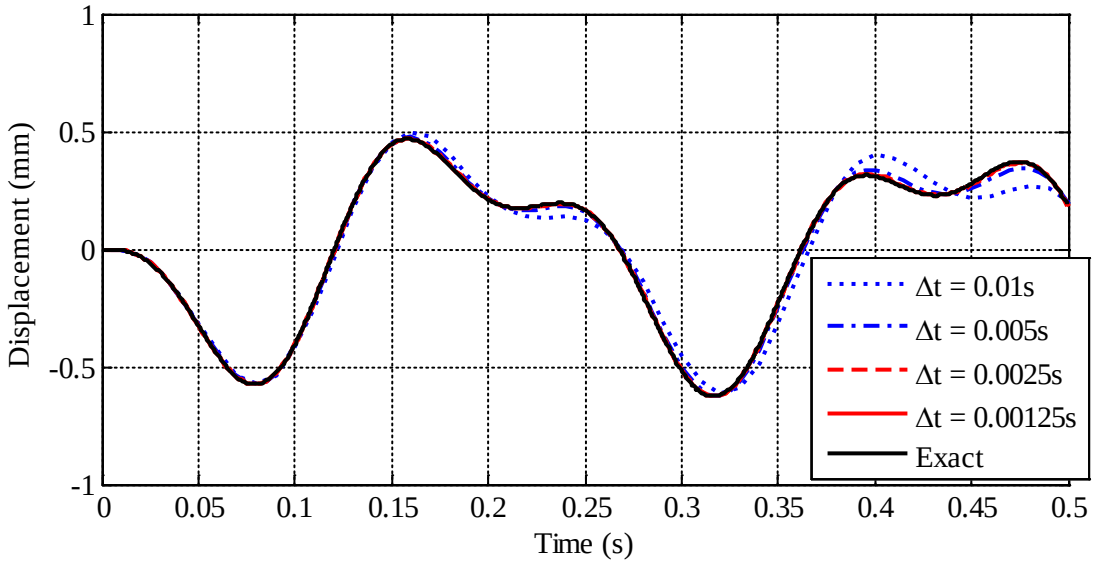

Figure 4-23 Relative Displacement Histories in the Elastic Range (Figure 4-22(b))

The same 3 s FP bearing with 50 MPa static axial pressure but now with a Coulomb-type coefficient of friction of 0.00000001 is subjected to an acceleration history $\ddot{u}_g = \sin(\pi t)$ m/s^2 and *observed order of accuracy* is computed (in double precision; 16 significant digits) for the plastic range (Figure 4-22(c)). The yield displacement of the bearing is set equal to 0.0000000001 m. No external damping is provided. The exact solution is obtained using the method used for elastic range. Figure 4-25 presents the displacement histories for different analysis steps. Figure 4-26 plots the force-displacement histories. The *observed order of accuracy* is equal to the formal order of accuracy (= 2) for all time steps (see Table 4-3).

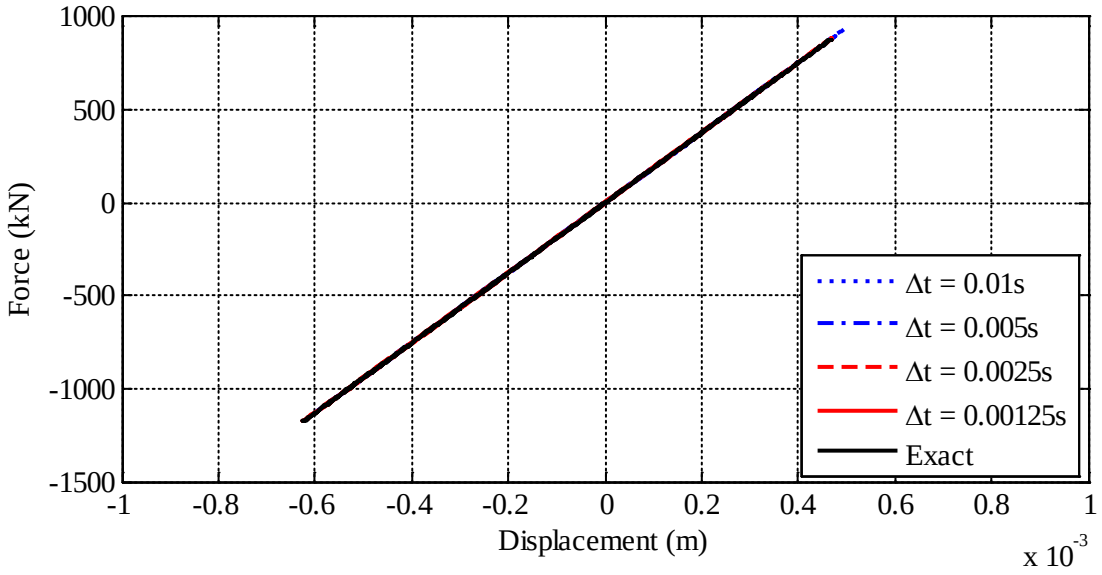

Figure 4-24 Force-Displacement Histories in the Elastic Range (Figure 4-22(b))

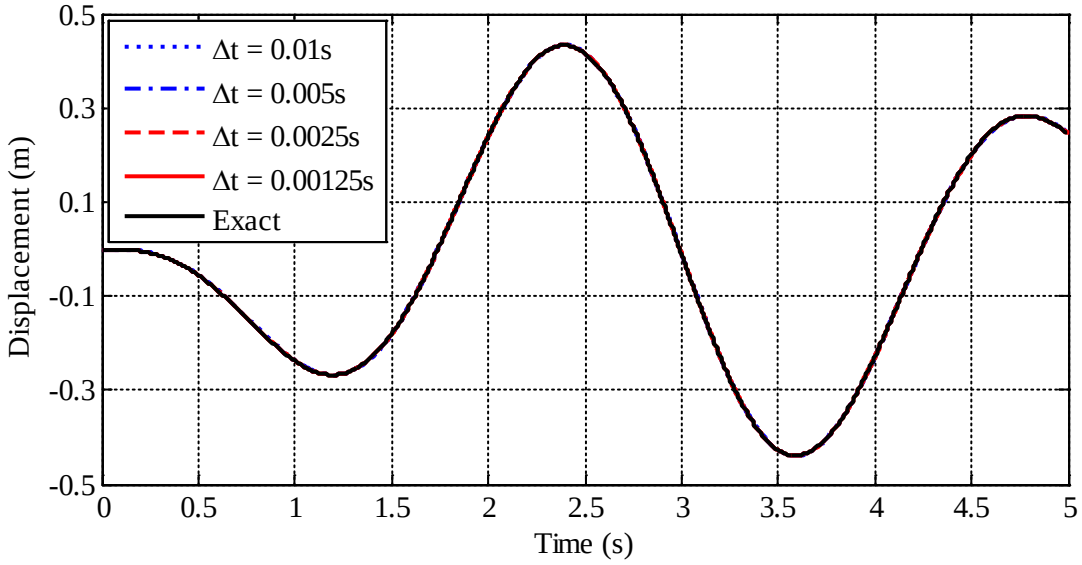

Figure 4-25 Relative Displacement Histories in the Inelastic Range (Figure 4-22(c))

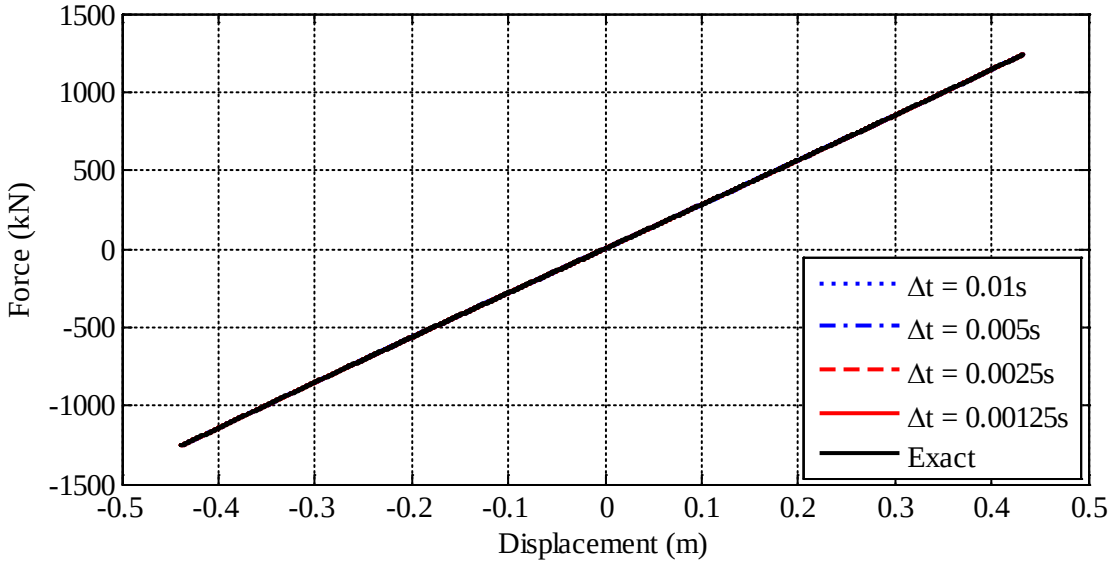

Figure 4-26 Force-Displacement Histories in the Inelastic Range (Figure 4-22(c))

4.5.2 Solution Verification

A numerical solution can have four sources of error, namely, 1) round-off error, 2) statistical sampling error, 3) iterative error, and 4) discretization error. Round-off errors arise due to low precision (small number of significant digits) in computations. Such errors may be significant for an ill-conditioned system. Round-off errors are small compared to the discretization errors. This is demonstrated by comparing the errors in numerical solutions (Equation (4-28)) reported in Figure 4-25, when computations are performed with single and double precision (Table 4-4). For a given analysis time step, the choice of precision has negligible influence on the error. The error, however, decreases by 75% with a reduction in analysis time step by 50%. Statistical

sampling errors are not relevant for this study since deterministic equations are solved. Iterative error is the difference in the numerical and exact solutions due to the tolerance set for an acceptable numerical solution. This error can be controlled by setting a sufficiently small tolerance. Discretization is usually the largest source of error in a numerical solution and is the focus of this study.

Table 4-4 Discretization Errors for Computations Performed in Single and Double Precisions

	Precision	Analysis time step		
		0.01 s	0.005 s	0.0025 s
Error (m) (Equation (4-28))	Single	0.00005269	0.00001316	0.00000328
	Double	0.00005268	0.00001317	0.00000329

4.5.2.1 Discretization Error

The discretization error is defined as the difference between the exact solution and the numerical solution computed using a mesh size h:

$$\varepsilon_h = u_h - \tilde{u} \tag{4-30}$$

where u_h is the numerical solution computed using a mesh size h, $\tilde{u}$ is the exact solution and other parameters were defined previously. The new OpenSees element *FPBearingPTV* does not involve discretization in space, so h in the above equation refers to the analysis time step. Discretization error is computed in this section for an FP bearing with the force-displacement behavior shown in Figure 4-22(a). The exact solution is estimated using the Generalized Richardson Extrapolation method (e.g., Oberkampf and Roy (2010)) discussed below.

The expression for discretization error in a $\bar{p}^{th}$-order accurate numerical scheme is

$$\varepsilon_h = u_h - \tilde{u} = g_{\bar{p}} h^{\bar{p}} + g_{\bar{p}+1} h^{\bar{p}+1} + g_{\bar{p}+2} h^{\bar{p}+2} + \ldots \tag{4-31}$$

where g_i are constants and other parameters were defined previously. For two grid spacings h and rh $(r > 1)$, the numerical solutions can be written as

$$\begin{aligned} u_h &= \tilde{u} + g_{\bar{p}} h^{\bar{p}} + g_{\bar{p}+1} h^{\bar{p}+1} + O\left(h^{\bar{p}+2}\right) \\ u_{rh} &= \tilde{u} + g_{\bar{p}} (rh)^{\bar{p}} + g_{\bar{p}+1} (rh)^{\bar{p}+1} + O\left(h^{\bar{p}+2}\right) \end{aligned} \tag{4-32}$$

where all terms were defined previously. Equation (4-32) is simplified to

$$\tilde{u} = u_h + \frac{u_h - u_{rh}}{r^{\bar{p}} - 1} + g_{\bar{p}+1} h^{\bar{p}+1} \frac{r^{\bar{p}} (r-1)}{r^{\bar{p}} - 1} + O\left(h^{\bar{p}+2}\right) = \bar{u} + O\left(h^{\bar{p}+1}\right) \tag{4-33}$$

where $\bar{u}$ is the Generalized Richardson Extrapolation estimate of the exact solution given by

$$\bar{u} = u_h + \frac{u_h - u_{rh}}{r^{\bar{p}} - 1} \qquad \textbf{(4-34)}$$

where all the terms were defined previously. The order of accuracy, $\bar{p}$, is not known for the differential equation representing the force-displacement relationship of an FP bearing (Figure 4-22(a)). However, $\bar{p}$ is 2 when the two segments of the force-displacement curve are considered separately (see Section 4.5.1.3). For r equal to 2 (e.g., Roy *et al.* (2003)) and $\bar{p}$ equal to 2, (4-34) reduces to

$$\bar{u} = u_h + \frac{u_h - u_{2h}}{3} \qquad \textbf{(4-35)}$$

and is used to estimate the exact solution and the discretization error. Equation (4-35) is identical to (4-29).

An FP bearing with a sliding period of 3 s, static axial pressure of 50 MPa and a Coulomb-type coefficient of sliding friction of 0.06 is subjected to a sinusoidal ground acceleration history $\ddot{u}_g = \sin(\pi t)$ m/s^2. The acceleration history is specified at intervals of 0.01 s. The response-history analyses are performed at the time-steps of 0.01 s, 0.005 s, 0.0025 s and 0.00125 s. The input ground acceleration at an analysis step (e.g., 0.005 s) is obtained from the ground acceleration history (specified at 0.01 s) using linear interpolation. The yield displacement of the bearing is 0.001 m. No damping is assigned to the system. Figure 4-27 presents the displacement histories of the slider for different time steps. Figure 4-28 plots the computed force histories. Figure 4-29 presents the force-displacement loops. The differences between the histories and loops computed using different time steps are negligible. The average absolute errors (given by (4-28)) in displacement are 0.000014 m, 0.000007 m and 0.000001 m for time steps of 0.01 s, 0.005 s and 0.0025 s, respectively; the maximum displacement is 0.130 m. The average absolute errors in the computed lateral force histories are 80 N, 30 N and 5 N, respectively, for the three time steps; the maximum force is 740,000 N.

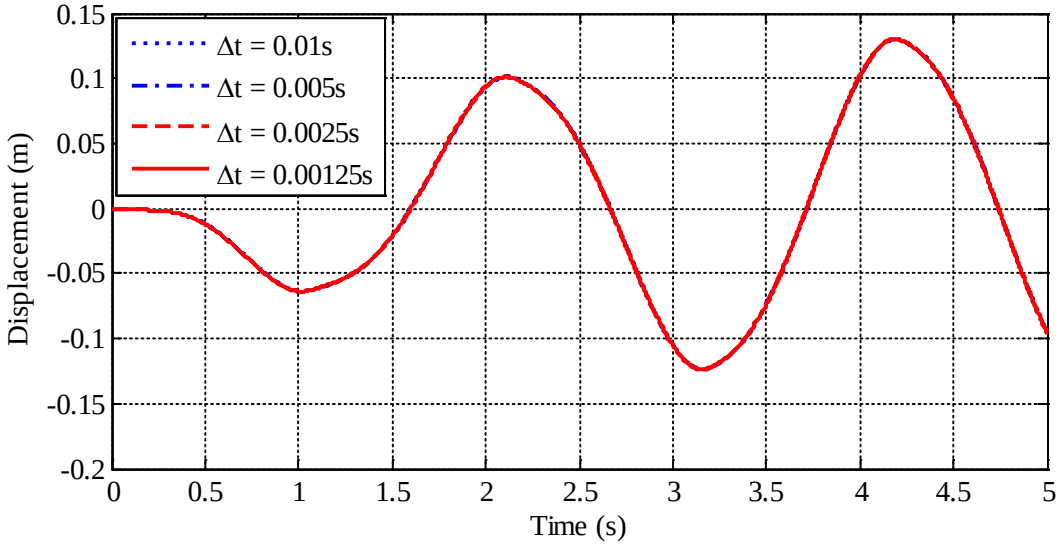

Figure 4-27 Displacement Histories Calculated Using Different Time Steps

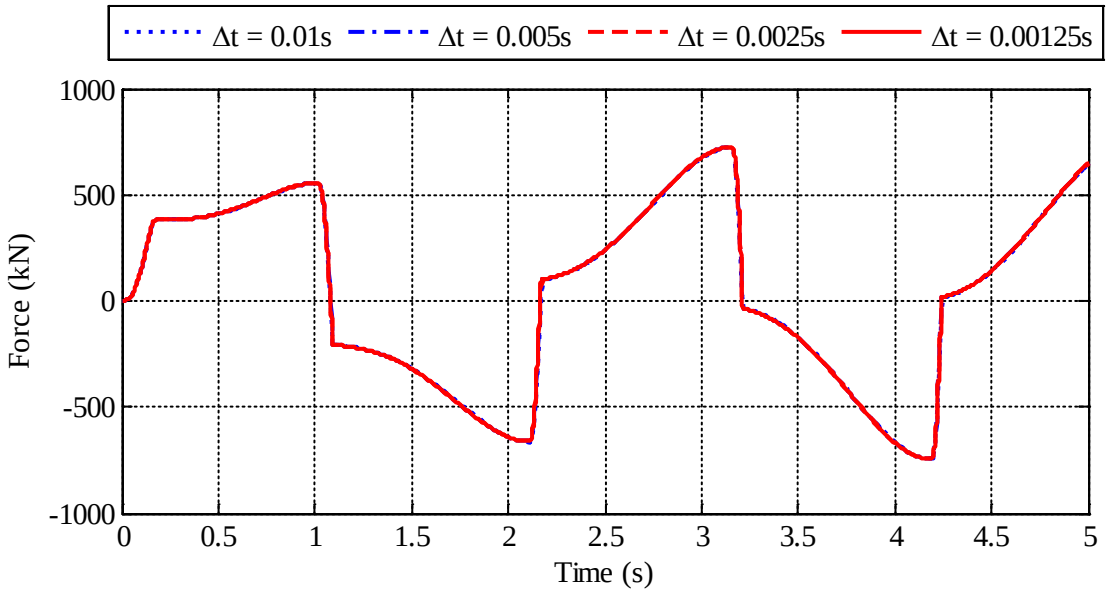

Figure 4-28 Lateral Force Histories Calculated Using Different Time Steps

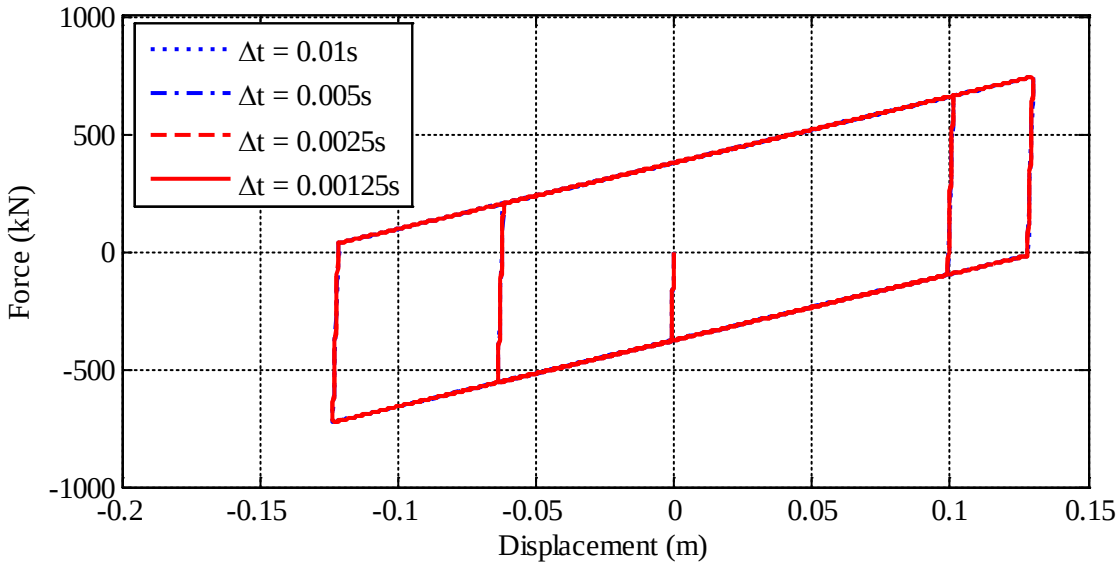

Figure 4-29 Force-Displacement Relationships Calculated Using Different Time Steps

4.5.2.2 Influence of Integration Scheme

The numerical solution approaches the exact solution as the analysis time step is reduced (see Section 4.5.1.3). These numerical integrations were performed using the Constant Average Acceleration method (Bathe, 1996). Responses calculated using different numerical integration schemes, namely, Linear Acceleration, Hilber-Hughes-Taylor (HHT) and Generalized-α, are compared below.

The following equations represent a family of numerical integration methods known as Newmark's method (e.g., Chopra (2007)):

$$\begin{aligned} \dot{u}_{i+1} &= \dot{u}_i + \left((1-\gamma)\Delta t\right)\ddot{u}_i + \left(\gamma\Delta t\right)\ddot{u}_{i+1} \\ u_{i+1} &= u_i + \left(\Delta t\right)\dot{u}_i + \left(\left(0.5-\beta\right)\left(\Delta t\right)^2\right)\ddot{u}_i + \left(\beta\left(\Delta t\right)^2\right)\ddot{u}_{i+1} \end{aligned} \quad \textbf{(4-36)}$$

where u_i is the displacement response at the i^{th} time-step, an overdot represents the derivative with respect to time, γ and β are parameters that define the variation of acceleration over a time step, and other parameters were defined previously. Newmark's method is known as the Constant Average Acceleration method for γ of 1/2 and β of 1/4, and the Linear Acceleration method for γ of 1/2 and β of 1/6. Equations (4-36) and (4-37) are used to compute the response quantities u_{i+1}, $\dot{u}_{i+1}$ and $\ddot{u}_{i+1}$.

$$m_s\ddot{u}_{i+1} + ku_{i+1} = f_{o,i+1} \quad \textbf{(4-37)}$$

where all parameters were defined previously.

The HHT method (Hilber *et al.*, 1977) uses Newmark's scheme (Equation (4-36)) with a change in the equilibrium equation (Equation (4-37)) as follows.

$$m_s\ddot{u}_{i+1} + \left(1+\alpha_H\right)ku_{i+1} - \alpha_H ku_i = f_{o,i+1} \quad \textbf{(4-38)}$$

where α_H is a new parameter introduced in the HHT method. For Newmark's methods, α_H is 0.

Like the HHT method, the Generalized-α method (Chung and Hulbert, 1993) uses Newmark's scheme to compute the displacement and velocity (Equation (4-36)) but introduces a new parameter, α_M, in the equilibrium equation.

$$\left[\left(1+\alpha_M\right)m_s\ddot{u}_{i+1} - \alpha_M m\ddot{u}_i\right] + \left(1+\alpha_H\right)ku_{i+1} - \alpha_H ku_i = f_{o,i+1} \quad \textbf{(4-39)}$$

An FP bearing with a sliding period of 3 s, static axial pressure of 50 MPa and a Coulomb-type coefficient of friction of 0.06 is subjected to a ground acceleration history $\ddot{u}_g = \sin\left(\pi t\right)$ m/s^2. No additional damping is assigned to the system. The acceleration history is specified at 0.01 s intervals and the response-history analyses are performed at time steps of 0.005 s. The analyses are performed for the five sets of the parameters α_H, α_M, γ and β listed in Table 4-5. Figure 4-30 plots the lateral displacement histories for the five sets. The differences are negligible with peak displacements ranging between 0.130 m and 0.133 m.

Table 4-5 Parameters for Numerical Schemes Used in Analyses

Numerical scheme	Analysis case	γ	β	α_H	α_M
Newmark's Method	Case 1	0.5	0.25	0	0
Newmark's Method	Case 2	0.5	0.166	0	0
HHT Method	Case 3	0.8	0.4225	0.3	0
HHT Method	Case 4	0.6	0.3025	0.1	0
Generalized-α Method	Case 5	0.5	0.25	0.2	0.2

4.5.3 Concluding Remarks on Verification Studies

The new OpenSees element *FPBearingPTV* is verified because 1) the element produces correct results when used in an inverted configuration, 2) pressure, velocity and temperature dependencies of the coefficient of friction are coded correctly, 3) the rates of convergence of the numerical solutions for the elastic and inelastic regimes (separately examined) are equal to the respective theoretical rates, and 4) the errors in the numerical solutions are negligible compared to the magnitudes of the quantities of interest.

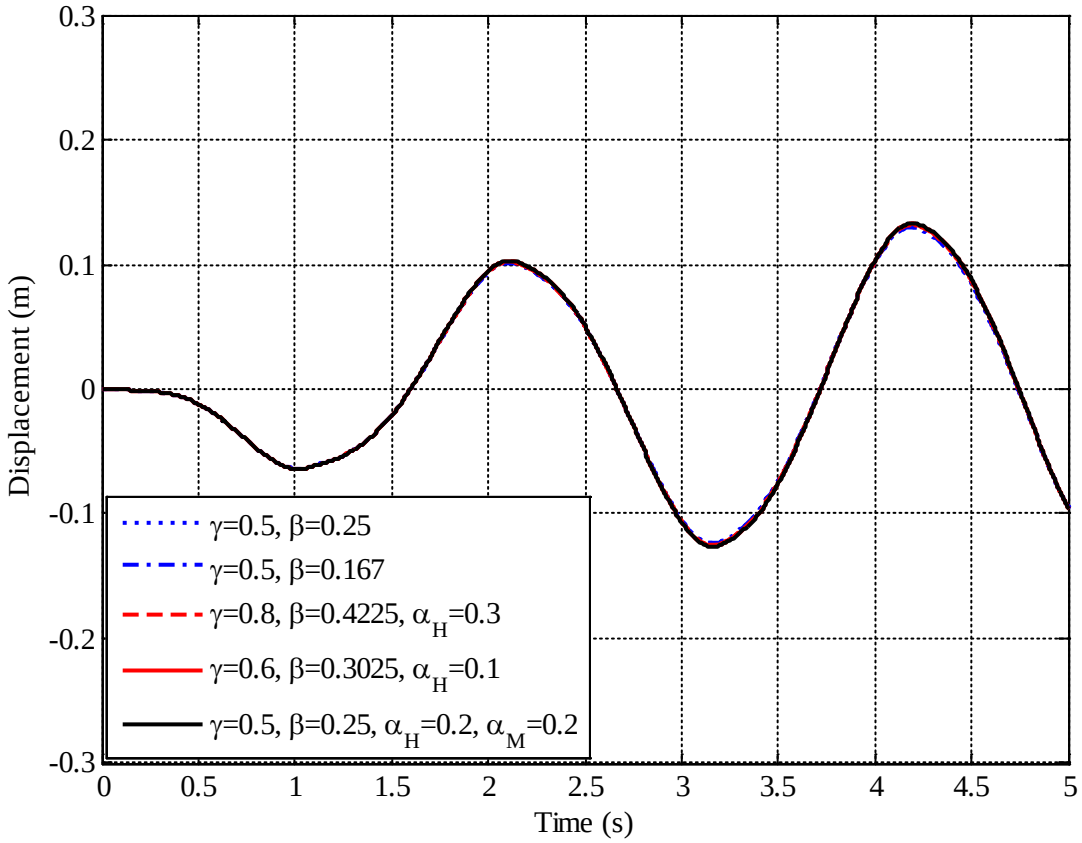

Figure 4-30 Lateral Displacement Histories for the Five Sets of Analysis Parameters Listed in Table 4-5

4.6 Validation of OpenSees Element *FPBearingPTV*

Validation of a software program is performed to determine if it is capable of simulating experimental observations (Oberkampf and Roy, 2010). The OpenSees element *FPBearingPTV* incorporates the model presented in Chapter 3 to account for the dependencies of the coefficient of sliding friction on axial pressure, sliding velocity and temperature at the sliding interface. Validation of the element requires that the experimentally recorded responses of FP bearings with known geometrical and material properties (e.g., reference coefficient of friction measured at a given static pressure, temperature of 20°C and a high sliding velocity) are captured by the *FPBearingPTV* element.

Experimental data are used to validate the element (see Table 4-6), which investigate force-displacement response and/or temperature below the sliding surfaces of FP bearings with

different geometrical and material properties, and different levels of axial pressure, subjected to cycles of displacement-controlled loading. Many of the figures that follow present data reported by others; these data were digitized from the original documents.

The axial pressure was reportedly held constant for each experiment considered in this study (but there is no way to confirm this). Validation of the model for the pressure dependence of friction under cyclic loading is therefore not possible using available data. However, and as shown in later chapters of this report, consideration of the pressure dependence of friction is not important for the accurate estimation of key response quantities in isolated structures, including peak isolator displacements and floor spectral ordinates.

The velocity dependence of the coefficient of friction is not validated herein because it matters only when the sliding velocity is small (during low intensity ground motions), which is of no practical importance. The small-velocity experiments are simulated[5] using μ_{ref} equal to the maximum coefficient of friction during the experiment[6] rather than using the definition adopted in Chapter 3.

Temperature is expected to be the most important factor that influences the coefficient of friction at the sliding surface during an earthquake. There are two ways to validate *FPBearingPTV* for temperature dependence of friction: 1) compare the computed temperature at the sliding surface with experimentally recorded temperature (e.g., experiment 5 in Table 4-6), and 2) indirectly by comparison of computed and experimentally recorded lateral force and/or force-displacement histories (e.g., experiment 12 in Table 4-6).

It is extremely difficult to measure a temperature history at a sliding surface, while sliding is taking place, for the reasons described in Wolff (1999). However, most experiments on FP bearings report lateral force-displacement histories.

The reference coefficients of friction (along with the values of axial pressure, temperature and sliding velocity, at which the coefficient of friction was measured) were not reported for any of the experiments considered in this study. Rather, these have been estimated from available information (e.g., recorded force-displacement response) for the simulations discussed below. In addition to the estimated value of the reference coefficient of friction, the reported values for axial pressure, loading history, radius of curvature of bearings, and the radius of slider are used to develop the model. The coefficient of friction is considered to vary with axial pressure, temperature on the sliding surface, and sliding velocity, as described in Chapter 3, for the simulations of the following sections unless noted otherwise. The force-displacement histories[7] and/or temperature histories below the center of sliding surface simulated using the *FPBearingPTV* element are compared with the experimentally recorded responses for the 16 experiments of Table 4-6.

---

[5] Experimentally recorded temperature below the sliding surface has been used to validate the theory to compute temperature at the sliding surface. Some of these experiments were performed at small velocities.

[6] The relationship between velocity and coefficient of friction for liner materials may be different from that assumed in this study. Numerical simulations with reference coefficient of friction corresponding to a high velocity of sliding will not capture recorded responses during small-velocity tests. These experimental responses are captured best using a reference coefficient of friction equal to the maximum coefficient of friction recorded during the experiment.

[7] The force-displacement histories are compared in terms of 1) energy dissipated during different cycles, and 2) coefficients of friction at zero horizontal displacement.

Table 4-6 List of Experiments Used to Validate the OpenSees Element *FPBearingPTV*

Experiment Number	Paper/report	Bearing properties			Loading		
		R[1] (m)	μ[2]	$r_{contact}$[3] (m)	Axial Pressure (MPa)	u[4] (m)	n_{cycle}[5]
1	CERF (1998)	2.2	0.12	0.14	10.9	$0.15\sin(\pi t)$	3
2			0.09	0.14	10.9	$0.076\sin(4\pi t)$	2.5
3			0.09	0.14	36.3	$0.11\sin(4\pi t)$	2.5
4			0.13	0.20	25.7	$0.31\sin(\pi t)$	2
5	Wolff (1999), Constantinou *et al.* (1999)	∞[7]	0.10	0.0475	13.8	$0.025\cos(0.5\pi t)$	1
6			0.12	0.0475	13.8	$0.025\cos(\pi t)$	2
7			0.13	0.0475	13.8	$0.025\cos(2\pi t)$	2
8			0.13	0.0475	13.8	$0.025\cos(4\pi t)$	3
9			0.13	0.0475	12	$0.096\cos(0.26\pi t)$	2
10			0.15	0.0475	12	$0.096\cos(0.52\pi t)$	2
11			0.14	0.0475	12	$0.096\cos(1.06\pi t)$	3
12	Constantinou *et al.* (2007)	3.96	0.05	0.26	30.8	0.25 m amplitude, 0.6 Hz frequency	10[6]
13	Lomiento *et al.* (2013)	2.5	0.08	0.26	15	$0.2\sin(0.002\pi t)$	1
14			0.06	0.26	30	$0.2\sin(0.002\pi t)$	1
15			0.11	0.26	15	$0.2\sin(0.16\pi t)$	2
16			0.075	0.26	30	$0.2\sin(0.16\pi t)$	2

[1]Radius of curvature of sliding surface
[2]Back calculated reference coefficient of friction
[3]Radius of contact area
[4]Lateral displacement history of the slider
[5]Number of simulated force-displacement cycles
[6]First three and last cycle simulated
[7]Flat slider

4.6.1 CERF (1998)

FP bearings with a sliding period of 3 s (radius of curvature of 2.23 m) were subjected to different levels of axial load and horizontal displacement histories. The radius of the contact area at the sliding surface for the first three experiments was 0.140 m, and was 0.200 m for the fourth experiment. The static axial pressure on the bearing ranged between 11 MPa (experiments 1 and 2) and 36 MPa (experiment 3). The peak velocities for the experiments were between 0.470 m/s (experiment 1) and 1.380 m/s (experiment 3).

Figure 4-31(a) plots the experimentally recorded and simulated (using the *FPBearingPTV* element in OpenSees) force-displacement histories for experiment number 1 of Table 4-6. The properties of the bearing, and the imposed static and displacement-controlled loading history used in the numerical simulation are listed in the table: μ_{ref} = 0.12, p_o = 10.9 MPa,

R = 2.23 m, slider radius = 0.14 m, $u = 0.15\sin(\pi t)$ in meters. The sudden drop in the force at the beginning of experiment is attributed to the chosen cyclic loading history. Subjecting a bearing to a sinusoidal displacement history with an initial displacement of zero (a sine function) requires the initial velocity (a cosine function) to increase quickly, generating inertial effects at the beginning of the experiment that distorts the force-displacement relationship. The reduction in the coefficient of friction is evident from the change in the level of shearing force at a given displacement with an increasing number of cycles.

The experimentally recorded and numerically simulated force-displacement histories are compared using a) energy dissipated in each cycle, and b) the coefficient of friction at zero lateral displacement. Figure 4-31(b) plots the first experimentally recorded and numerically simulated cycles considered for the energy calculation, which begin and end at +0.135 m, namely, a displacement cycle +0.135 m → +0.150 m → -0.150 m → +0.135 m[8]. The beginning and end of the cycle are identified in the figure. The energy dissipated during this cycle is 40 kN-m. Figure 4-31(c) presents the energy dissipated in the first three cycles computed from the digitized force-displacement curve from the experiment and from the numerical simulation. The *experimental*[9] and *numerical*[1] values differ by between 1% and 8% for the three cycles. The difference in the total energy dissipated in the three cycles is 3%.

Figure 4-31(d) plots the coefficient of friction at zero displacement for experiment 1. The coefficient decreased from 0.1 to 0.08 between the end of the first half cycle and the end of the third cycle. The maximum difference between the *experimental* and *numerical* values is 5%.

The maximum and minimum values of energy dissipated in a cycle during the experiment, and the coefficients of friction at zero displacement obtained from the experimental data are listed in Table 4-7. The table also presents the percentage difference between the total energy dissipated and the coefficient of friction at zero displacement in the experiments and in the numerical simulations.

[8] The cycle is considered to begin at displacement equal to +0.135 m instead of the beginning of the experiment (0.000 m) so that the aforementioned inertial effects are not included in the energy calculations.

[9] Herein, an *experimental* value is that calculated using data from the experiment and a *numerical* value is that calculated from the simulations using *FPBearingPTV*.

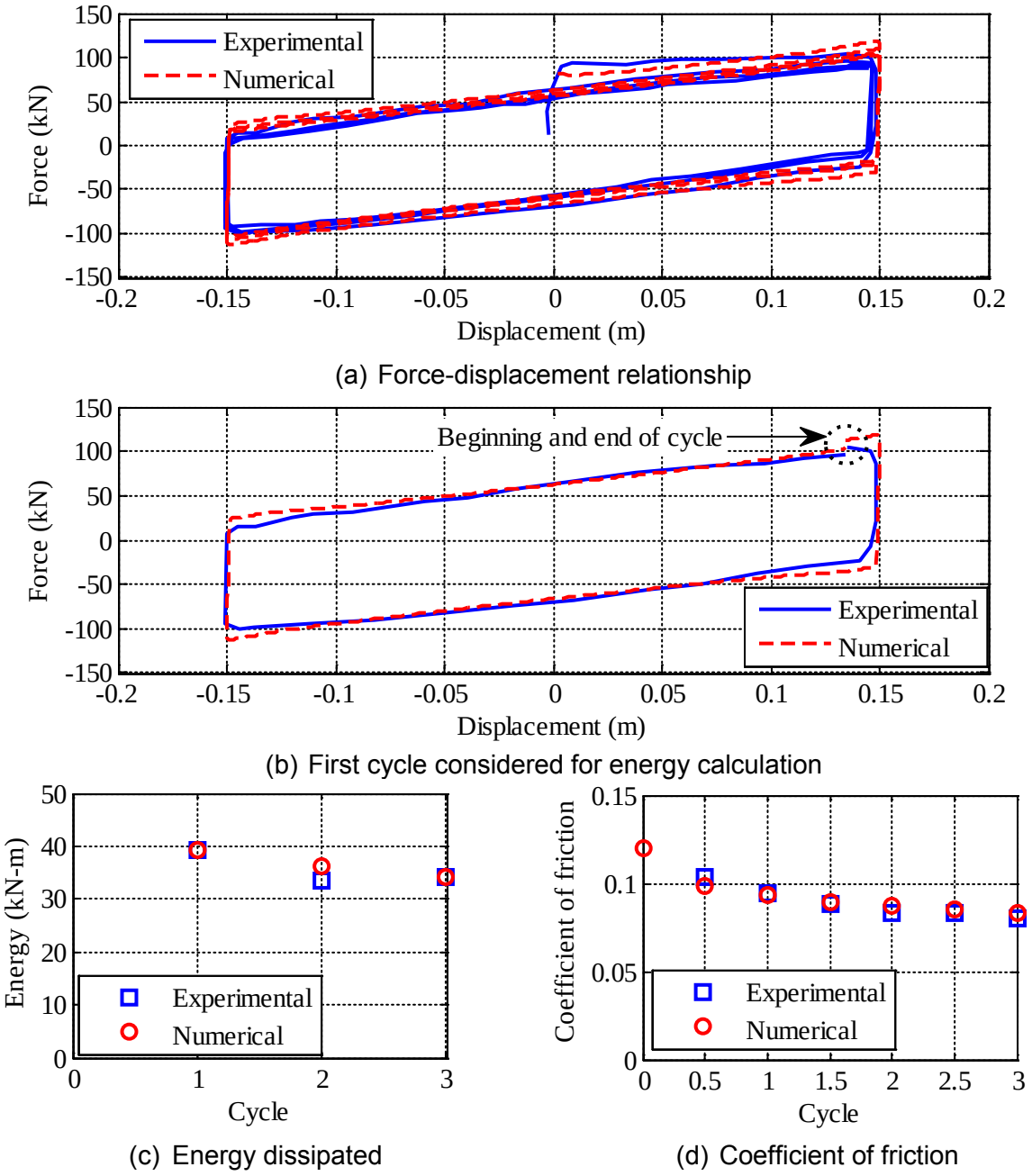

Figure 4-31 Experimentally Recorded and Numerically Simulated Force-Displacement Relationships for Experiment Number 1 of Table 4-6

The force-displacement histories, energy dissipated per cycle and coefficient of friction at zero displacement for experiments 2, 3 and 4 of Table 4-6 are presented in Figures 4-32, 4-33 and 4-34, respectively, together with *numerical* responses. Table 4-6 lists the parameters used to perfom these numerical simulations. The energy dissipated in a cycle for these experiments is computed as described previously in the section (e.g., Figure 4-31(b)). Results are summarized in Table 4-7. The difference in the total energy dissipated in the experiments and the numerical simulations ranges between 2% and 14% for the four tests. The maximum differences in the coefficients of friction at zero displacement range between 5% and 17%.

4.6.2 Wolff (1999), Constantinou et al. (1999)

Experiments 5 to 11 in Table 4-6 are reported in Wolff (1999) and Constantinou *et al.* (1999). Two sets of experimental data are available: 1) normalized force-displacement histories, and 2) temperature histories at a point 0.0015 m below the center of the sliding surface. The radius of the contact area for the bearings in the experiments was 0.0475 m. The static axial pressure (displacement amplitude) was 13.8 MPa (0.025 m) for experiments 5 through 8, and 12 MPa (0.096 m) for experiments 9, 10 and 11. The properties of the bearings and the loading parameters used in the numerical simulations of the experiments are listed in Table 4-6.

Table 4-7 Energy Dissipated and Coefficient of Friction at Zero Displacement in Different Cycles of Loading for the Experiments of Table 4-6

Exp. No	Figure	Number of cycles	Energy dissipated per cycle (kN-m)			Coefficient of friction		
			Max[1]	Min[1]	% difference between total energies[2]	Max[1]	Min[1]	Maximum % difference
1	Figure 4-31	3	40	34	3	0.10	0.08	5
2	Figure 4-32	2.5	22	18	2	0.08	0.06	10
3	Figure 4-33	2.5	60	50	14	0.06	0.04	14
4	Figure 4-34	2	310	220	7	0.09	0.06	17
5	Figure 4-35	1	1	1	1	0.10	0.10	4
6	Figure 4-36	2	1	1	3	0.12	0.10	4
7	Figure 4-37	2	1	1	3	0.13	0.11	6
8	Figure 4-38	3	1	1	5	0.13	0.10	9
9	Figure 4-39	2	4	4	9	0.13	0.12	5
10	Figure 4-40	2	4	4	11	0.14	0.13	3
11	Figure 4-41	3	4	3	6	0.14	0.11	8
12	Figure 4-45	3	280	210	14	0.04	0.02	19
13	Figure 4-47	1	210	210	5	0.08	0.08	4
14	Figure 4-48	1	320	320	4	0.06	0.06	6
15	Figure 4-49	2	260	210	1	0.11	0.07	19
16	Figure 4-50	2	330	250	3	0.08	0.04	23

[1]Obtained from experiment

[2]Total energy dissipated in completed cycles (e.g., 2 cycles if 2.5 cycles are simulated)

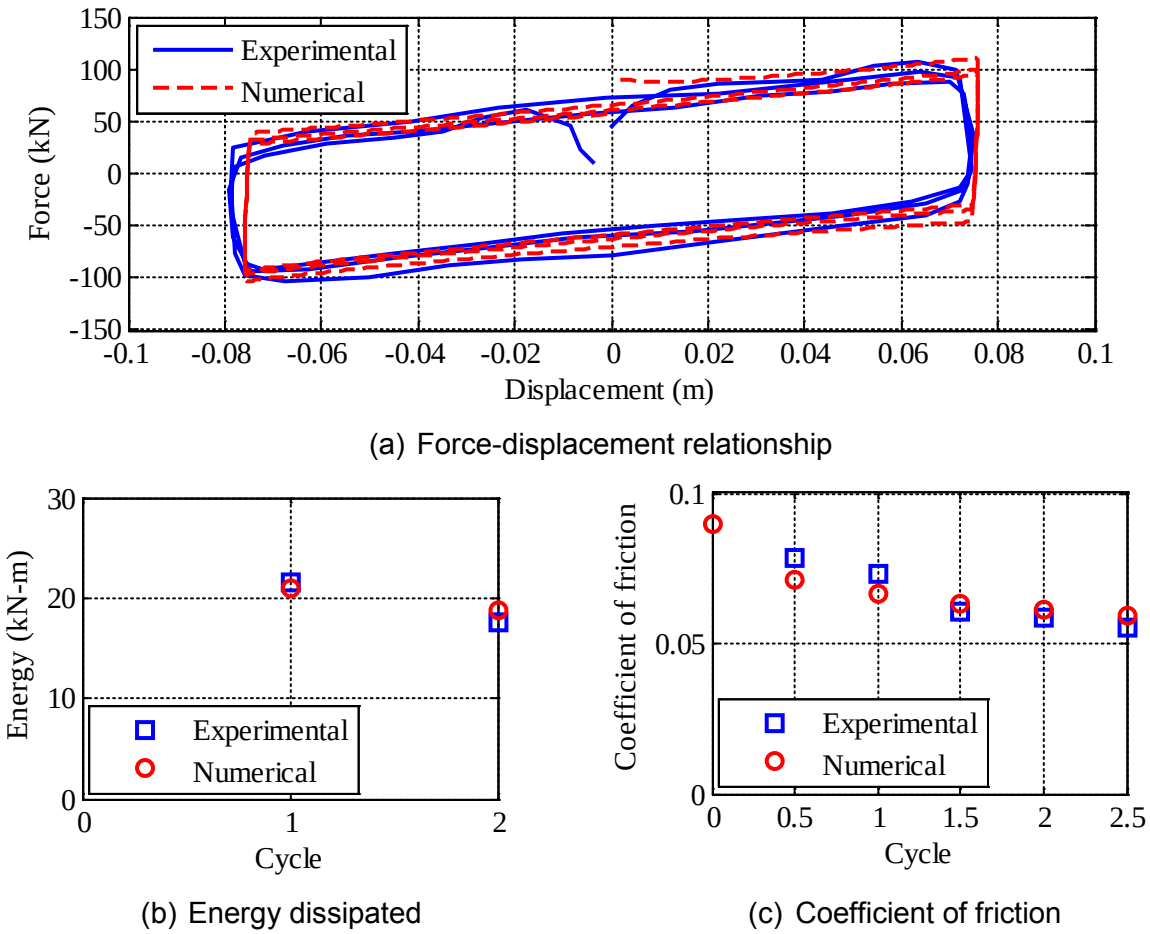

Figure 4-32 Experimentally Recorded and Numerically Simulated Force-Displacement Relationships for Experiment Number 2 of Table 4-6

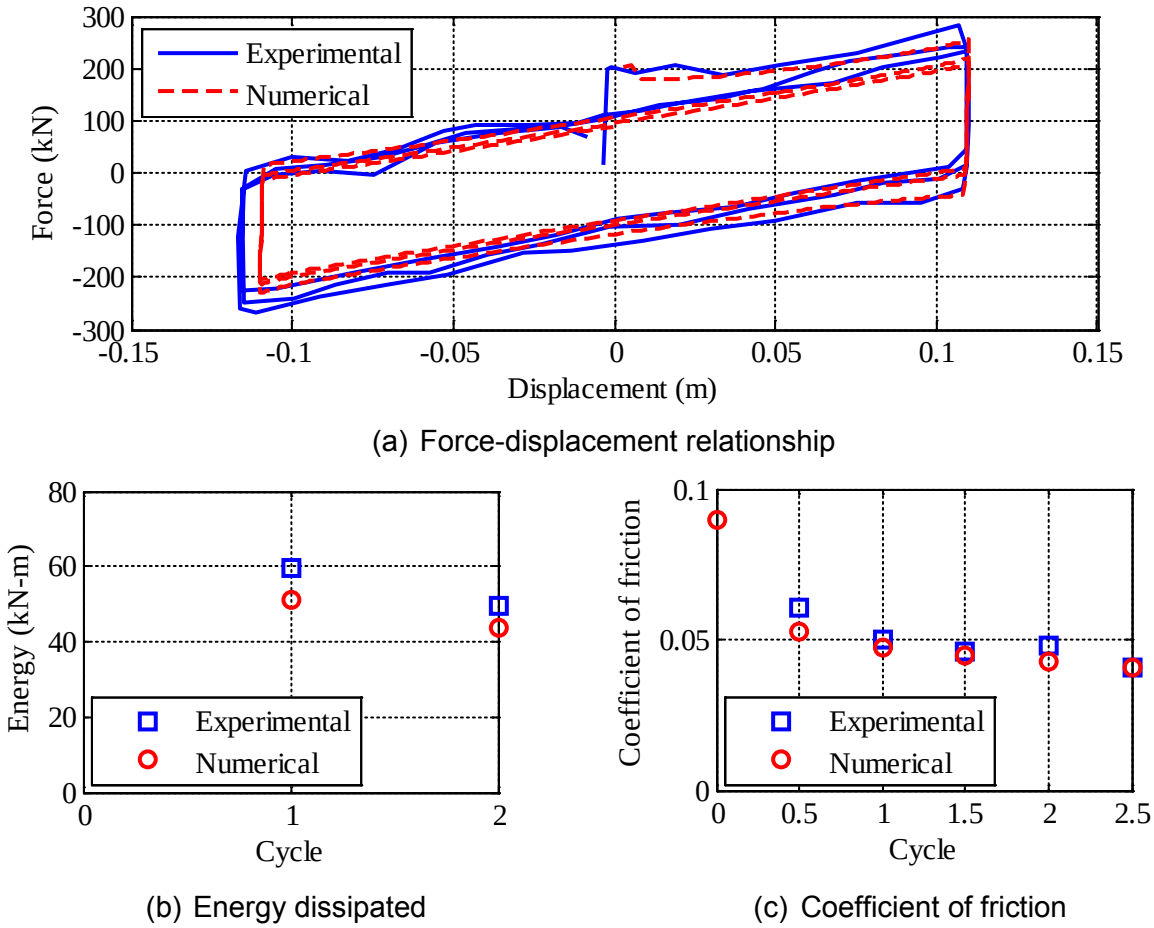

Figure 4-33 Experimentally Recorded and Numerically Simulated Force-Displacement Relationships for Experiment Number 3 of Table 4-6

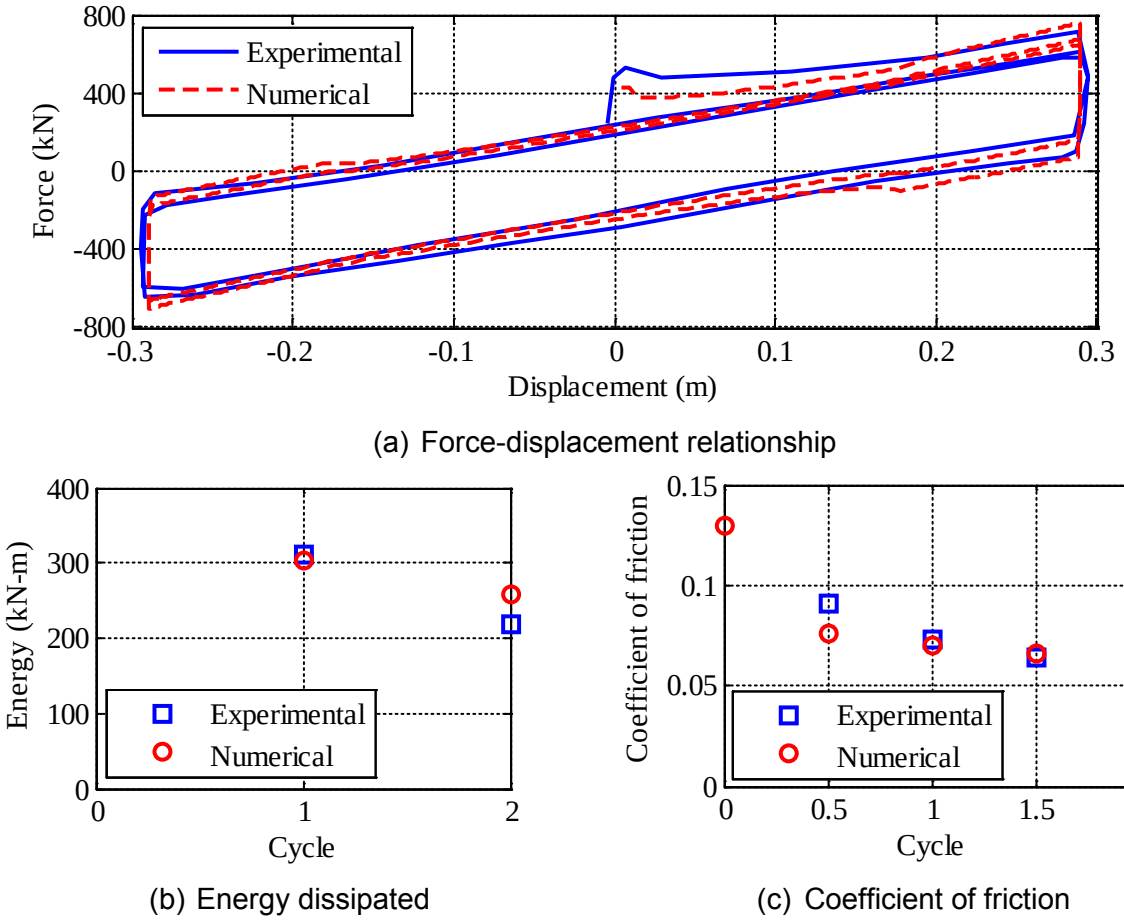

Figure 4-34 Experimentally Recorded and Numerically Simulated Force-Displacement Relationships for Experiment Number 4 of Table 4-6

4.6.2.1 Force-Displacement Response

Figure 4-35(a) presents the recorded and numerically simulated force-displacement relationships for experiment 5 of Table 4-6: p_o = 13.8 MPa, radius of curvature = ∞ (flat slider), slider radius = 0.0475 m, $u = 0.025\sin(0.5\pi t)$ in meters. The peak velocity for this experiment was 0.00625 m/s (small-velocity test; see Chapter 3 and Section 4.6). The value of μ_{ref} is set equal to 0.10 for the simulation, which is the maximum coefficient of friction recorded during the experiment. Figures 4-35(b) and 4-35(c) present the energy dissipated per cycle and the coefficient of friction at zero displacement, respectively. The energy dissipated in the cycle obtained from the experiment and the numerical simulation differs by 1%. The coefficients of friction at zero displacement differ by less than 4%.

Figures 4-36, 4-37 and 4-38 present the force-displacement responses for experiments 6, 7 and 8 of Table 4-6, respectively. The geometry of the FP bearing, axial pressure and amplitude of motion in the three experiments are the same as those for experiment 5, but the loading frequencies are 0.5 Hz, 1 Hz and 2 Hz, respectively. The other parameters used for the simulations are listed in Table 4-6. Results for the four experiments are summarized in Table 4-7. The total energy dissipated in the experiments and the numerical simulations differ by less

than 5%, and the maximum differences between the *experimental* and *numerical* values of the coefficient of friction at zero displacement range between 4% and 9%.

Experiments 9, 10 and 11 were performed by subjecting sliders to a static pressure of 12 MPa, and displacement history with an amplitude of 0.096 m and frequencies of 0.13 Hz, 0.26 Hz and 0.53 Hz, respectively. Table 4-6 lists the values of the parameters used for the simulations. Figures 4-39, 4-40 and 4-41 present the experimental and numerical force-displacement relationships for the three experiments, respectively. Results are summarized in Table 4-7. The total energy dissipated during the experiments differ from the numerically simulated values by between 6% to 11%, and the *experimental* and *numerical* values of the coefficient of friction at zero displacement differ by less than 8% for the three tests.

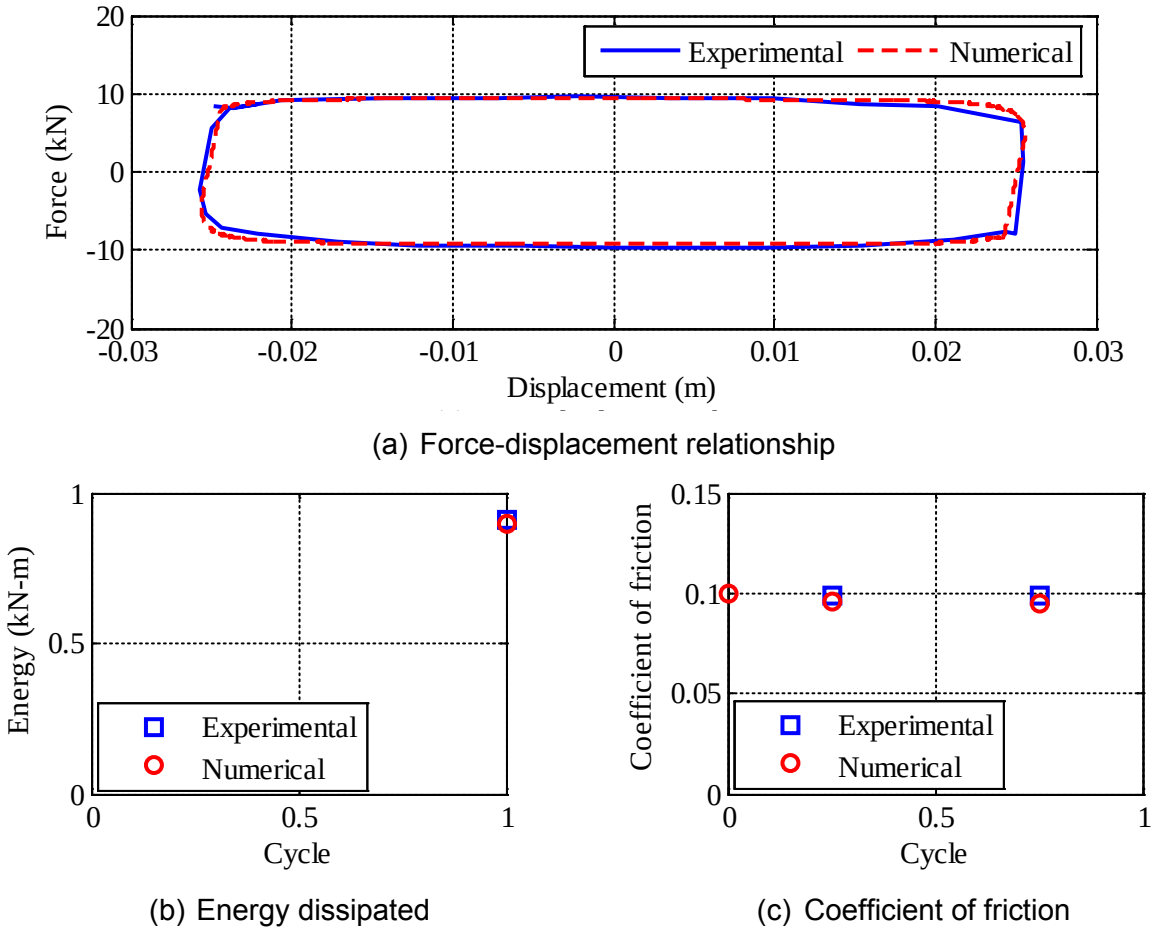

(a) Force-displacement relationship

(b) Energy dissipated

(c) Coefficient of friction

Figure 4-35 Experimentally Recorded and Numerically Simulated Force-Displacement Relationships for Experiment Number 5 of Table 4-6

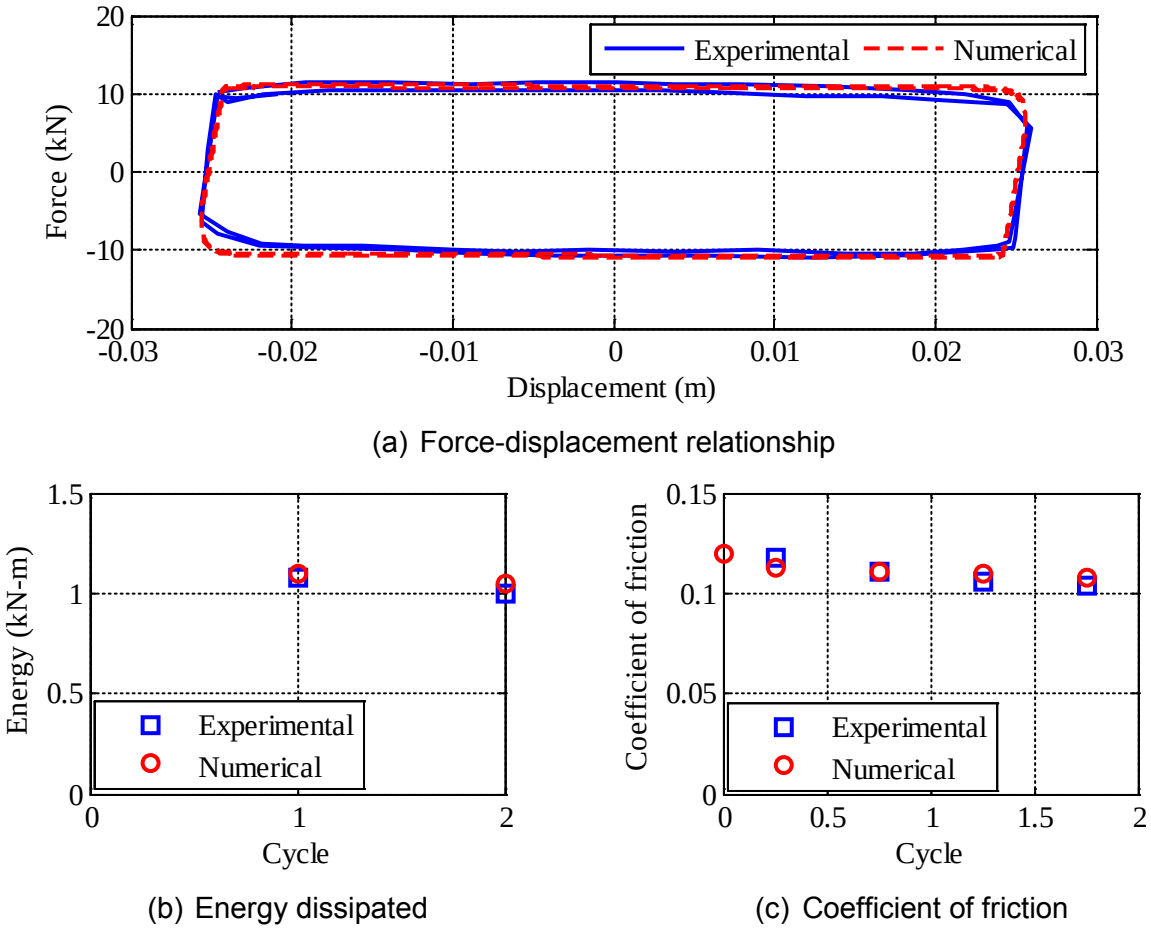

Figure 4-36 Experimentally Recorded and Numerically Simulated Force-Displacement Relationships for Experiment Number 6 of Table 4-6

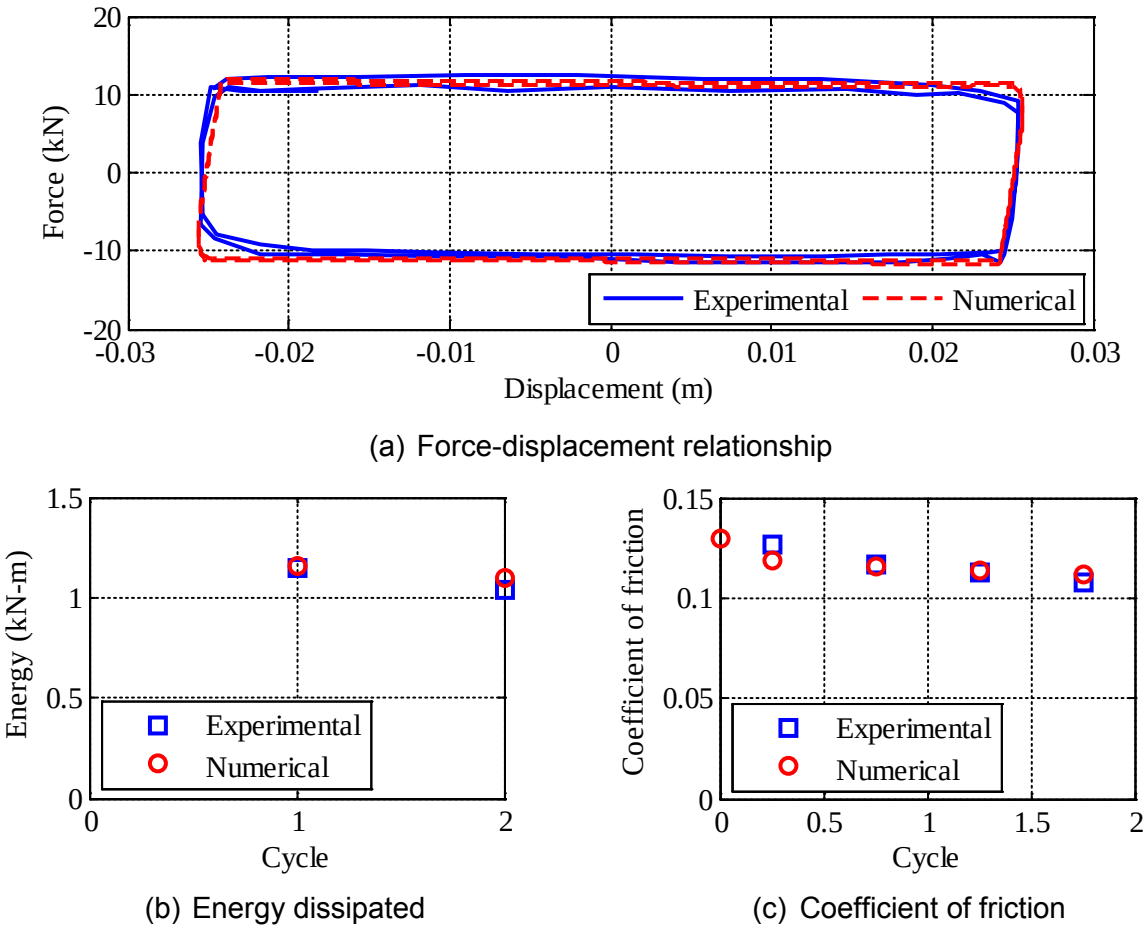

(a) Force-displacement relationship

(b) Energy dissipated

(c) Coefficient of friction

Figure 4-37 Experimentally Recorded and Numerically Simulated Force-Displacement Relationships for Experiment Number 7 of Table 4-6

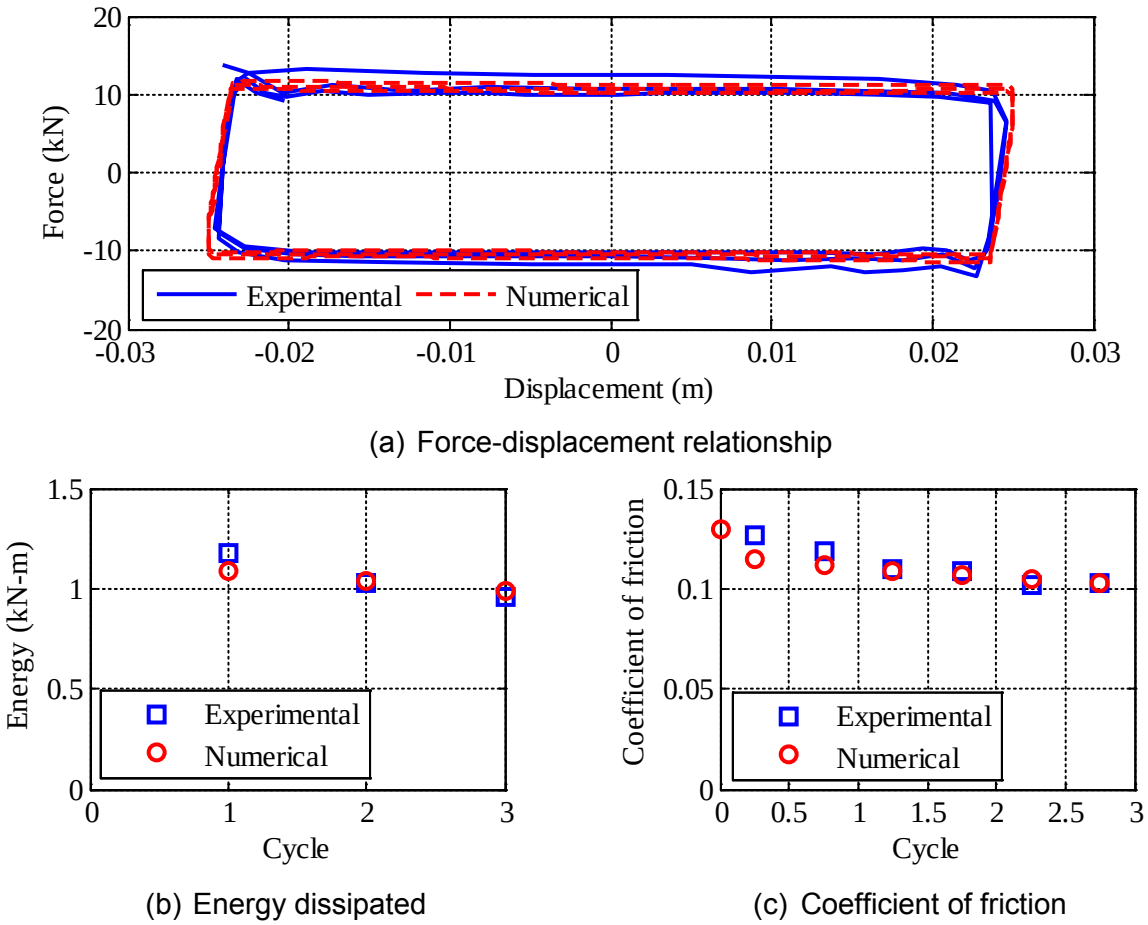

(a) Force-displacement relationship

(b) Energy dissipated

(c) Coefficient of friction

Figure 4-38 Experimentally Recorded and Numerically Simulated Force-Displacement Relationships for Experiment Number 8 of Table 4-6

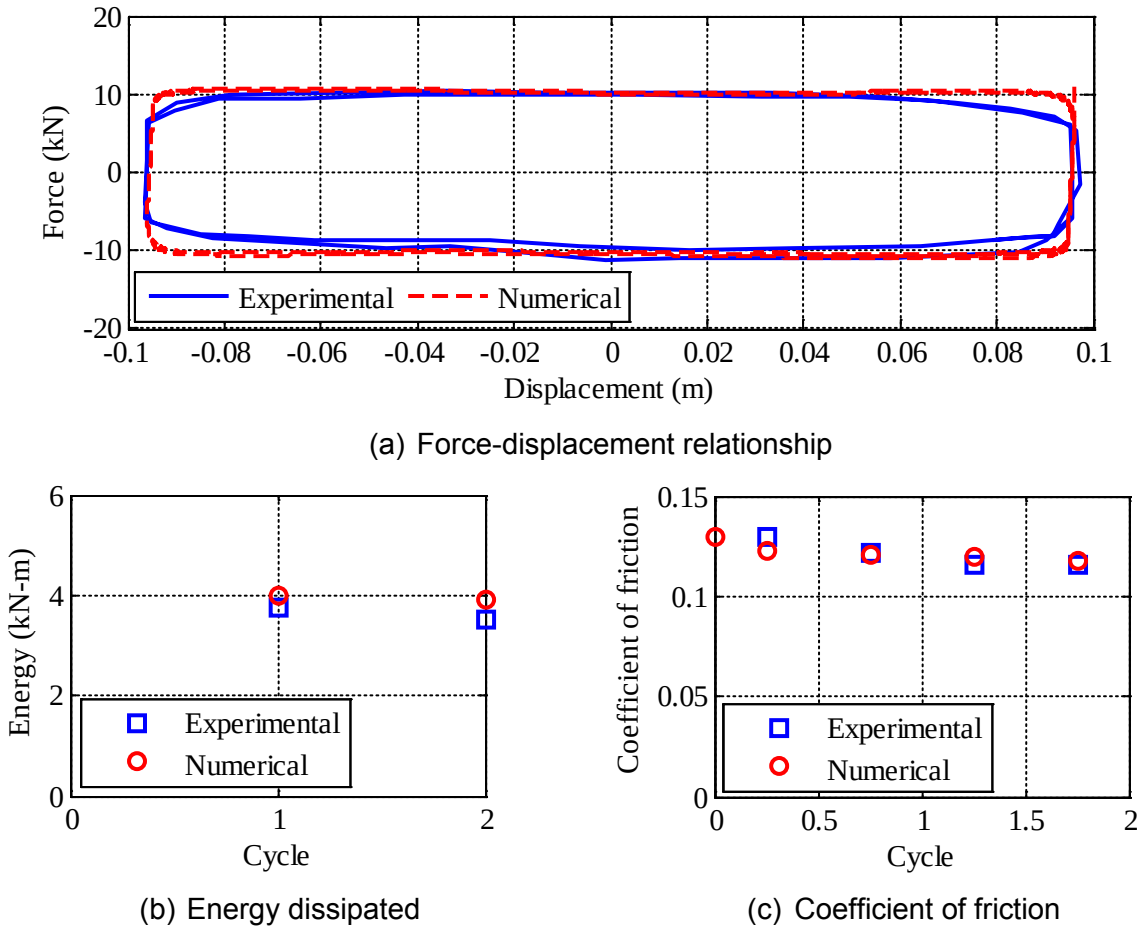

(a) Force-displacement relationship

(b) Energy dissipated

(c) Coefficient of friction

Figure 4-39 Experimentally Recorded and Numerically Simulated Force-Displacement Relationships for Experiment Number 9 of Table 4-6

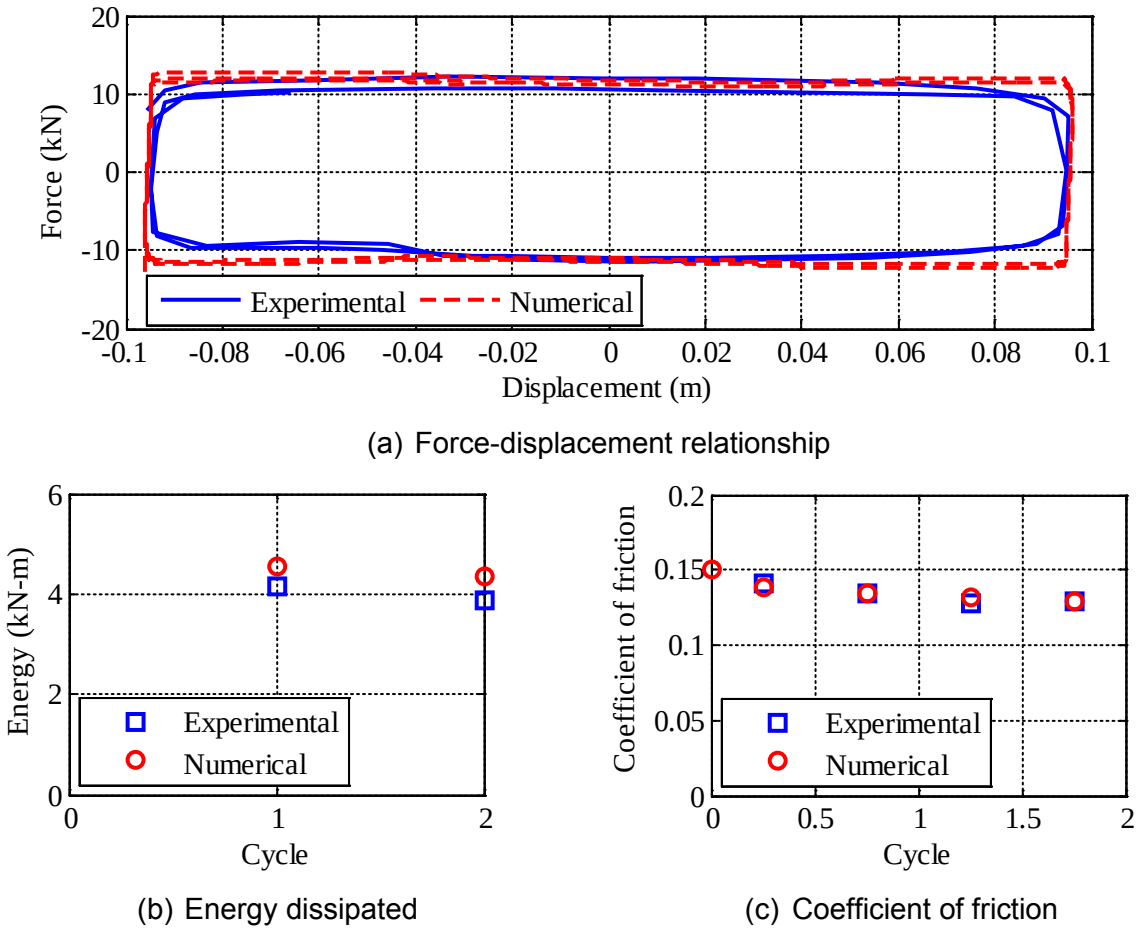

(a) Force-displacement relationship

(b) Energy dissipated

(c) Coefficient of friction

Figure 4-40 Experimentally Recorded and Numerically Simulated Force-Displacement Relationships for Experiment Number 10 of Table 4-6

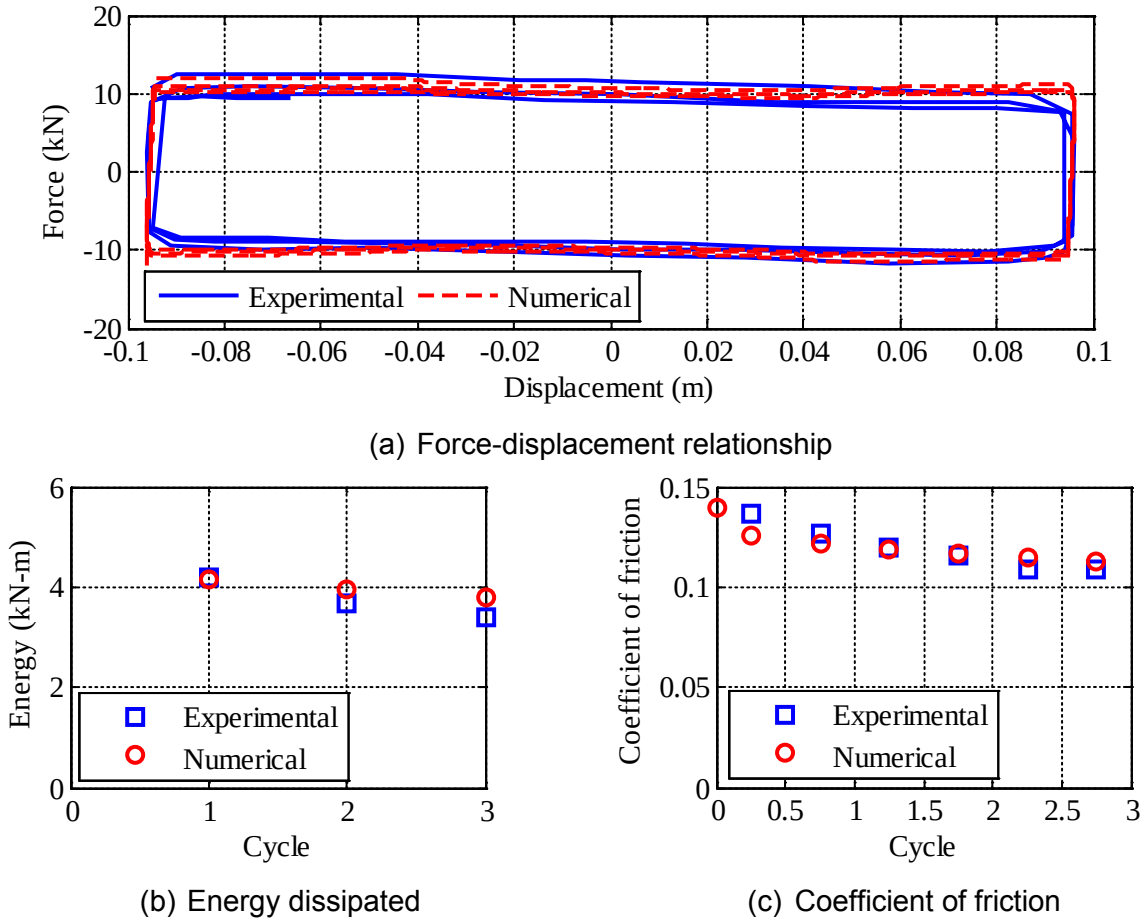

(a) Force-displacement relationship

(b) Energy dissipated

(c) Coefficient of friction

Figure 4-41 Experimentally Recorded and Numerically Simulated Force-Displacement Relationships for Experiment Number 11 of Table 4-6

4.6.2.2 Temperature at the Sliding Surface

The temperature histories at a point below the center of the sliding surface for experiments 5 through 11 of Table 4-6 are compared with numerical predictions in support of the validation exercise. Details on the bearings and loading parameters used in the simulations are provided in Table 4-6. The OpenSees element *FPBearingPTV* computes temperature at the center of the sliding surface using (3-22) with depth below sliding surface set equal to zero. The temperature histories below the sliding surface are computed using (3-22) and compared with the experimental results.

Figure 4-42(a) presents the experimentally recorded and computed histories of temperature at a point 0.0015 m below the center of the sliding surface of the flat slider subjected to a static axial pressure of 13.8 MPa, and a lateral displacement history with an amplitude of 0.025 m and a frequency of 0.25 Hz (experiment 5 of Table 4-6). The radius of the contact area is 0.0475 m. Panels (b), (c) and (d) of the figure present histories for loading frequencies of 0.5 Hz, 1 Hz and 2 Hz, respectively (experiments 6, 7 and 8). The computed history matches the recorded history well when the frequency of loading is small. The differences between the two histories increase with loading frequency, which is attributed to the time lag with which the thermocouple records temperature (see Chapter 3).

Figure 4-43(a) presents temperature histories at a point 0.0015 m below the center of the sliding surface. The axial pressure on the bearing was 12 MPa. A sinusoidal displacement history with amplitude of 0.096 m and a frequency of 0.13 Hz was imposed on the slider (experiment 9 of Table 4-6). Figures 4-43(b) and 4-43(c) present results for a loading frequency of 0.26 Hz and 0.53 Hz, respectively (experiments 10 and 11). The temperature rises as the slider passes over the center of the sliding surface and decreases otherwise. The computed histories match the experimentally recorded histories well, especially for the lower loading frequencies: 0.13 Hz and 0.26 Hz.

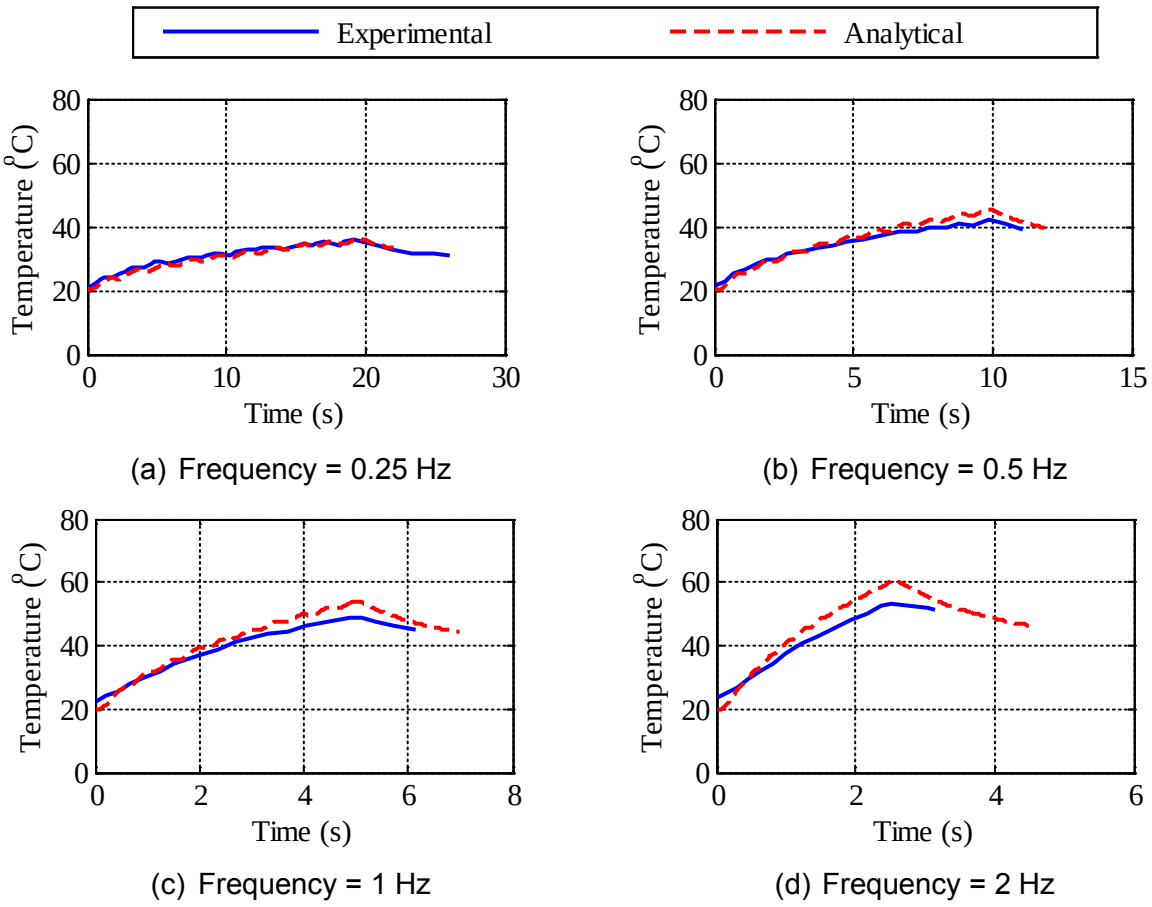

Figure 4-42 Histories of Temperature at a Point 1.5 Mm Below the Center of a Flat Slider with Static Axial Pressure of 13.8 MPa Subjected to a Lateral Displacement Loading with an Amplitude of 25 mm (experiments 5, 6, 7 and 8 of Table 4-6)

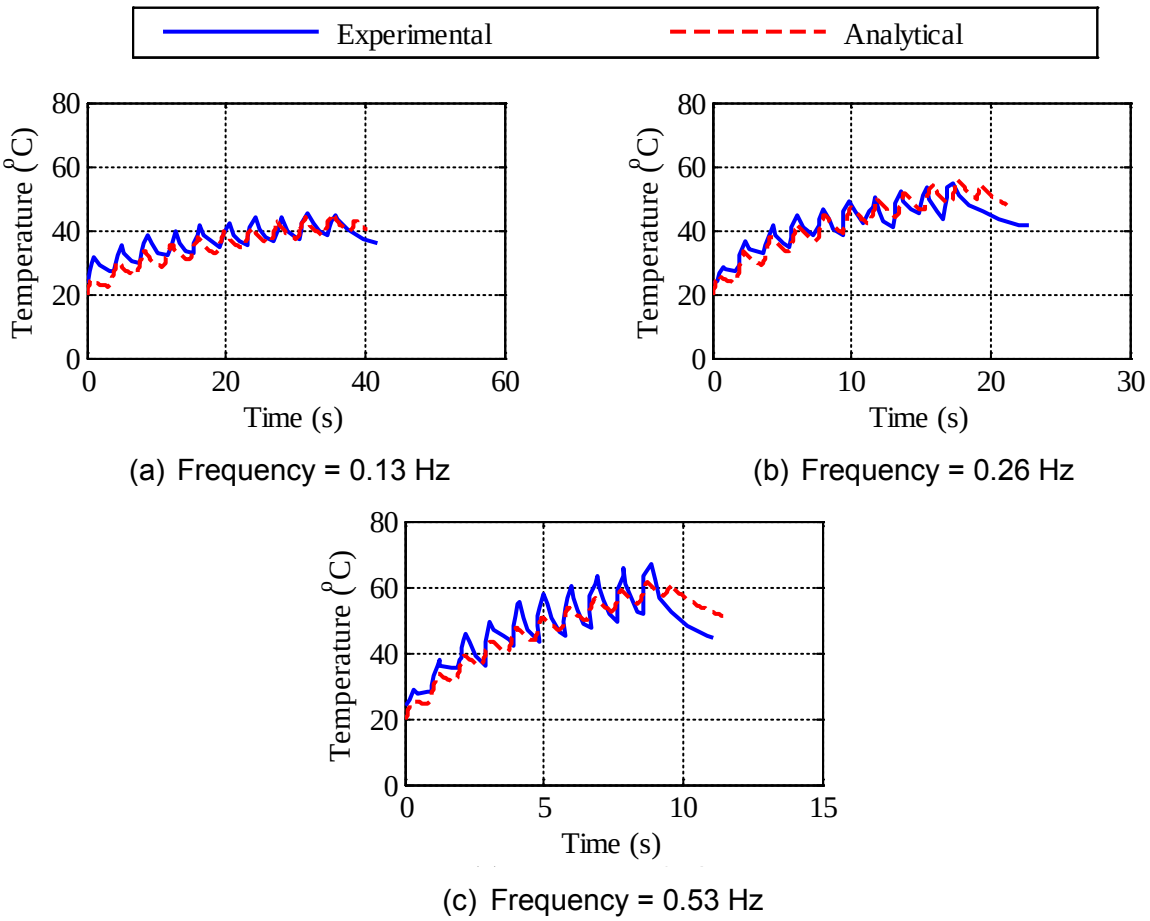

Figure 4-43 Histories of Temperature at a Point 1.5 mm Below the Center of a Flat Slider with Static Axial Pressure of 12 MPa Subjected to a Lateral Displacement Loading with Amplitude of 96 mm (experiments 9, 10 and 11 of Table 4-6)

4.6.3 Constantinou *et al.* (2007)

Constantinou *et al.* (2007) report the results of tests performed on an FP bearing with a radius of curvature of 3.96 m, a static axial pressure of 30.8 MPa and the displacement history plotted in Figure 4-44 (experiment 12 of Table 4-6). Figure 4-45(a) presents the first three force-displacement cycles obtained from the experiment and the numerical simulation. The parameters used in the numerical simulation are listed in Table 4-6. Panels (b) and (c) of the figure present the energy dissipated in the first three cycles and the coefficients of friction at zero displacement. The total energy dissipated in the experiment and in the numerical simulation differs by 14%. The differences between the coefficients of friction at zero displacement are 4%, 19%, 4%, 15%, 11% and 4% (see Table 4-7). There appears to be a bias in the experimentally recorded force-displacement loops (the coefficient of friction increased instead of decreasing from the end of 0.25 (1.25, 2.25) cycle to the end of 0.75 (1.75, 2.75) cycle; see Figure 4-45(c)), which led to significant differences between the experimental and numerical values of the coefficients of friction.

The FP bearing was subjected to 10 loading cycles of which three are reproduced in Figure 4-45. It was not possible to digitize the experimentally recorded force-displacement histories between the fourth and ninth cycles. The experimentally recorded and numerically simulated force-displacement histories for the 10th cycle are presented in Figure 4-46. The energy dissipated in the experiment in the 10th cycle is 142 kN-m; the numerically simulated value is 147 kN-m. The experimentally recorded and numerically simulated values of the coefficient of friction are both approximately 0.02 in the 10th cycle. The temperature at the center of sliding surface at the end of 10 cycles of loading is estimated to be 262°C and the coefficient of friction decreased by about 50% during the experiment[10].

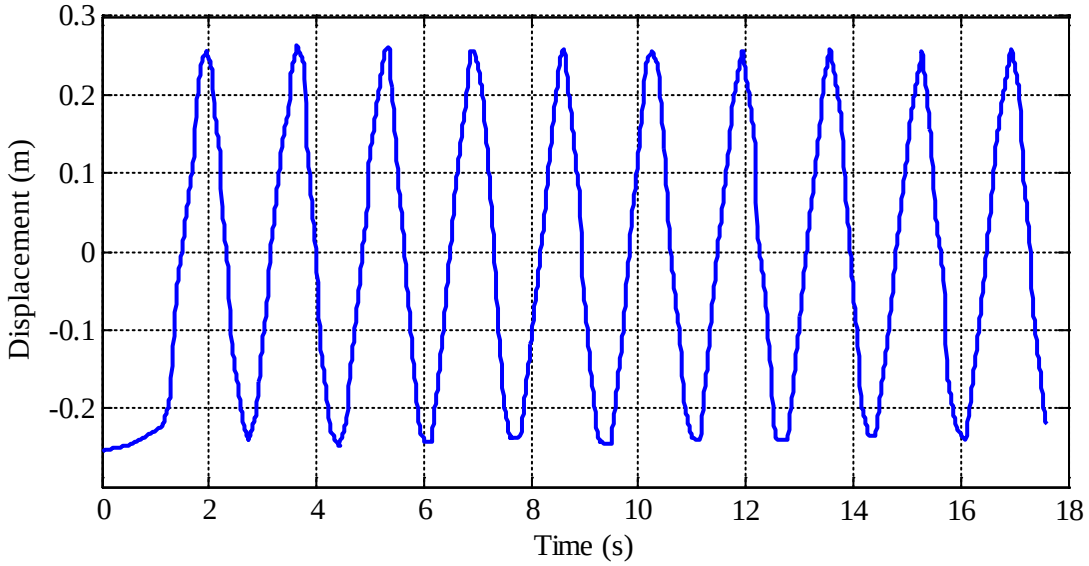

Figure 4-44 FP Bearing Displacement History from Experiment 12 of Table 4-6 (adapted from Constantinou et al. (2007))

[10] The temperature-dependent friction model proposed in Chapter 3 assumes the ratio of $\mu(T)$ at $T = 20°C$ and 250°C is 2:1.

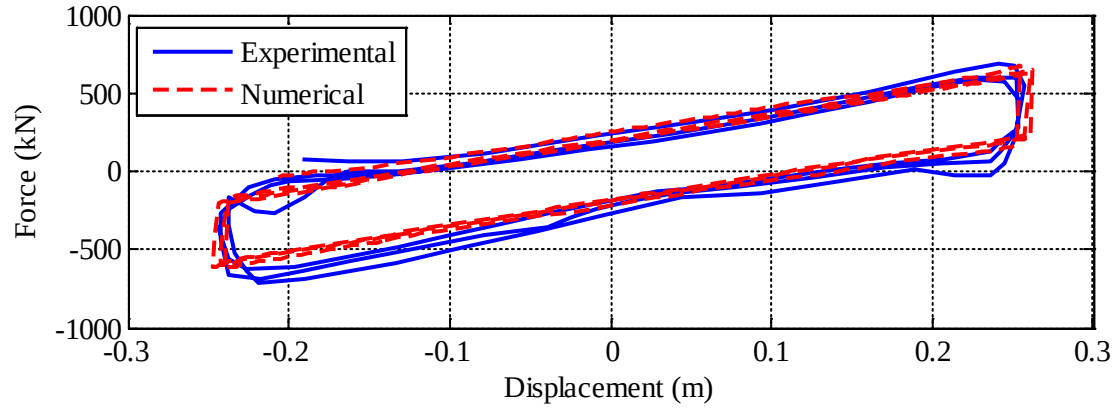

(a) Force-displacement relationship

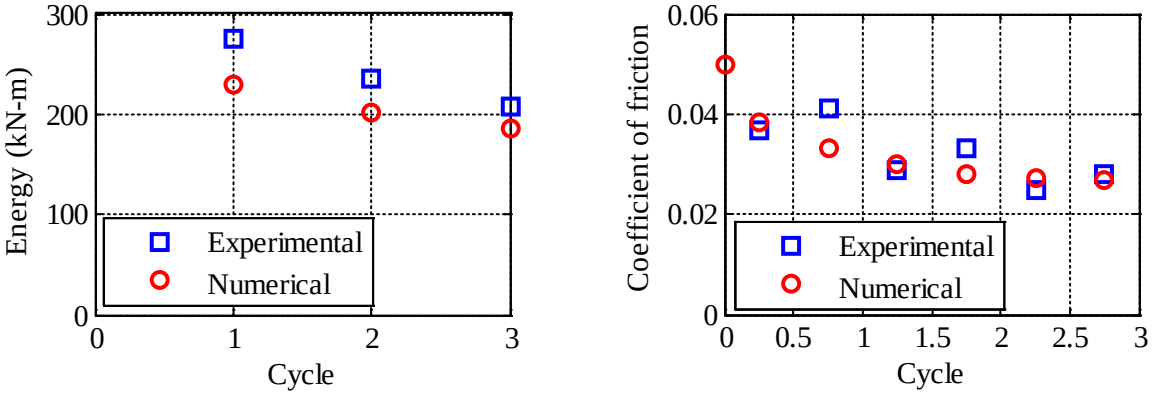

(b) Energy dissipated

(c) Coefficient of friction

Figure 4-45 First Three Cycles of Experimentally Recorded and Numerically Simulated Force-Displacement Relationships for Experiment Number 12 of Table 4-6

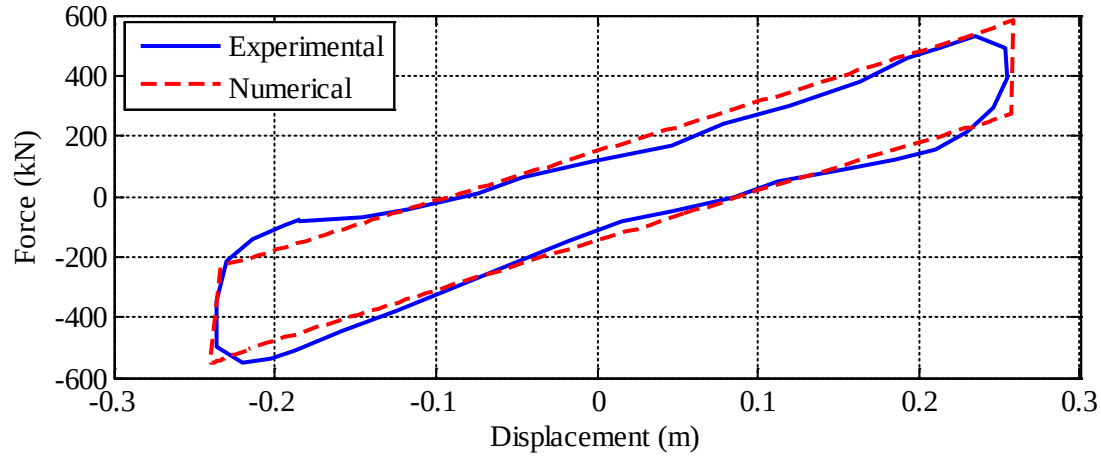

Figure 4-46 Tenth Cycle of Experimentally Recorded and Numerically Simulated Force-Displacement Relationships for Experiment Number 12 of Table 4-6

4.6.4 Lomiento *et al.* (2013)

Lomiento *et al.* (2013) performed experiments on an FP bearing with a radius of curvature of 2.5 m at two loading frequencies (0.001 and 0.08 Hz) and two axial pressures (15 and 30 MPa). The parameters used for the numerical simulations are listed in Table 4-6. Figure 4-47(a) presents the force-displacement relationships of the FP bearing with 15 MPa static axial pressure subjected to a displacement history with amplitude of 0.200 m and frequency of 0.001 Hz (experiment 13 of Table 4-6). Figures 4-47(b) and 4-47(c) present the energy dissipated and coefficients of friction at zero displacement. Figures 4-48, 4-49 and 4-50 present results for experiments 14, 15 and 16, respectively. Experiments 13 and 14 are small-velocity tests; experiments 15 and 16 are high-velocity tests. The energy dissipated in the experiments and calculated from the numerical simulations differs by less than 5%. The difference between the *experimental* and *numerical* values of the coefficient of friction at zero displacement ranges between 4% and 23% (see Table 4-7).

4.6.5 Concluding Remarks on Validation

Experimental data are used to validate the new OpenSees element *FPBearingPTV*. Two responses are considered: force-displacement relationships, and recorded temperature below the sliding surface. Challenges with these validation studies include: 1) key parameters including the coefficient of friction (along with reference pressure and reference temperature) and material properties of the liner were not reported for any experiment, and 2) the axial pressure was kept (approximately) constant during the experiments, which did not allow the model to be validated for the pressure dependence of the coefficient of friction under cyclic loading.

The new OpenSees element reasonably simulates 1) the experimentally recorded force-displacement relationships when the coefficient of sliding friction does not change considerably during the experiment (e.g., in small-velocity tests), 2) the reduction in the coefficient of friction associated with the increase in temperature at the sliding surface due to frictional heating for a range of loading conditions and mechanical properties, and 3) the recorded temperature history below the sliding surface[11], especially when the amplitude and frequency of the displacement-controlled loading are small.

[11] The model for the temperature dependence of friction coded in the *FPBearingPTV* element is used to compute the temperature below the sliding surface.

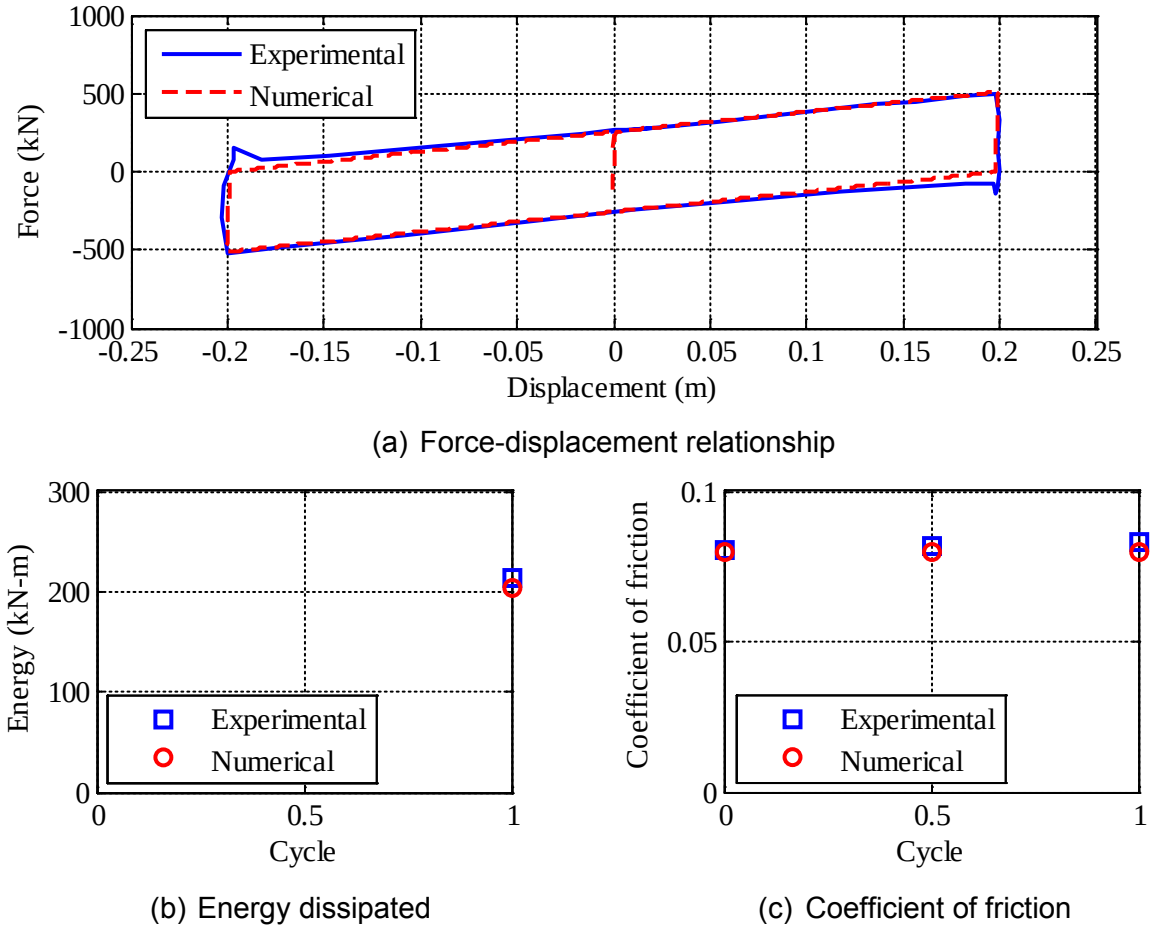

Figure 4-47 Experimentally Recorded and Numerically Simulated Force-Displacement Relationships for Experiment Number 13 of Table 4-6

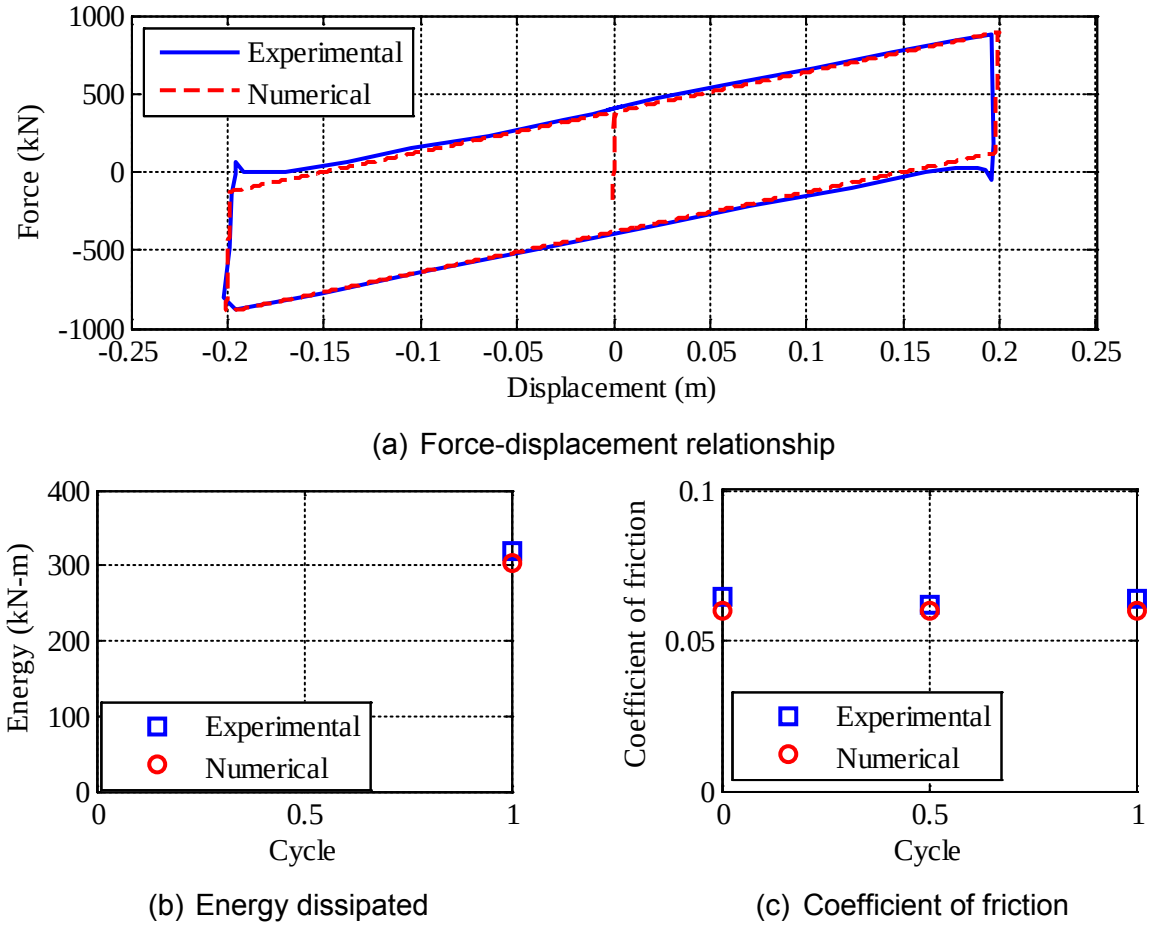

Figure 4-48 Experimentally Recorded and Numerically Simulated Force-Displacement Relationships for Experiment Number 14 of Table 4-6

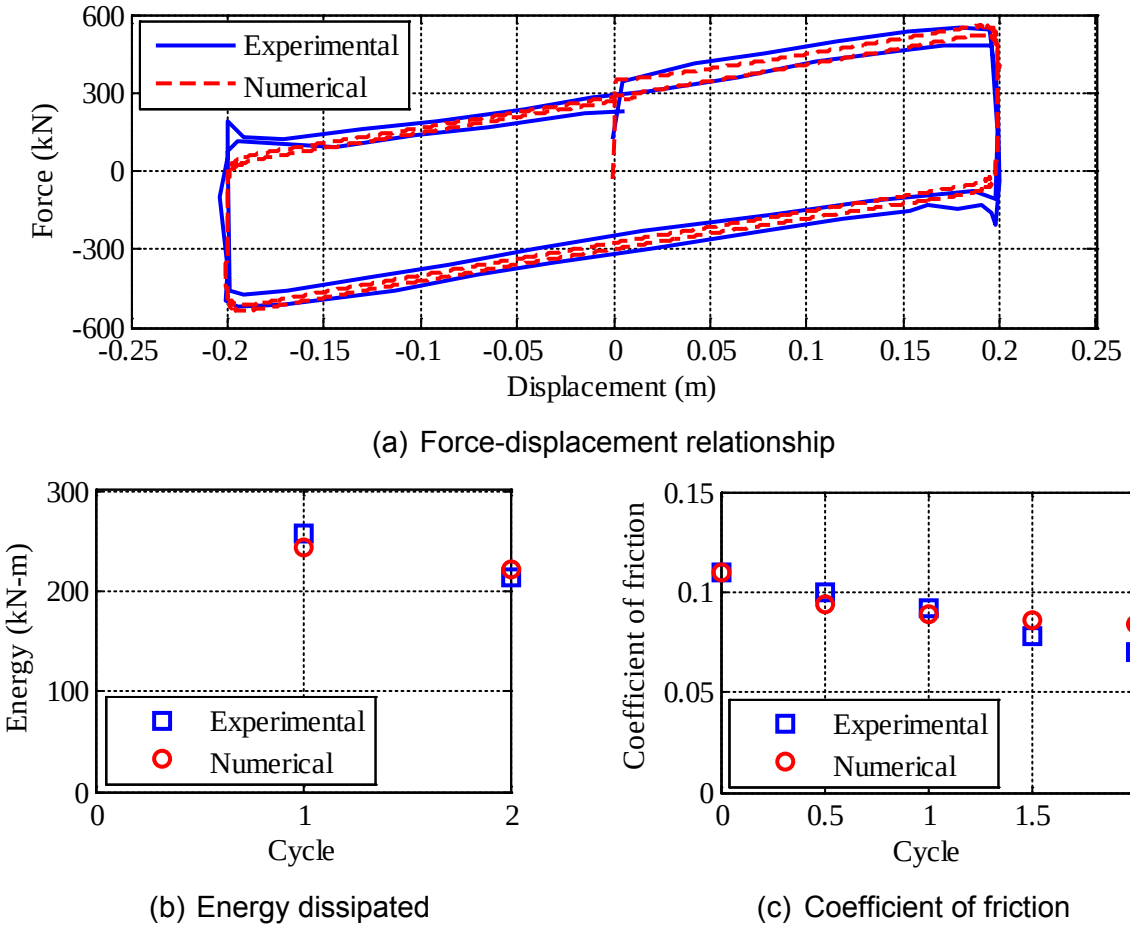

Figure 4-49 Experimentally Recorded and Numerically Simulated Force-Displacement Relationships for Experiment Number 15 of Table 4-6

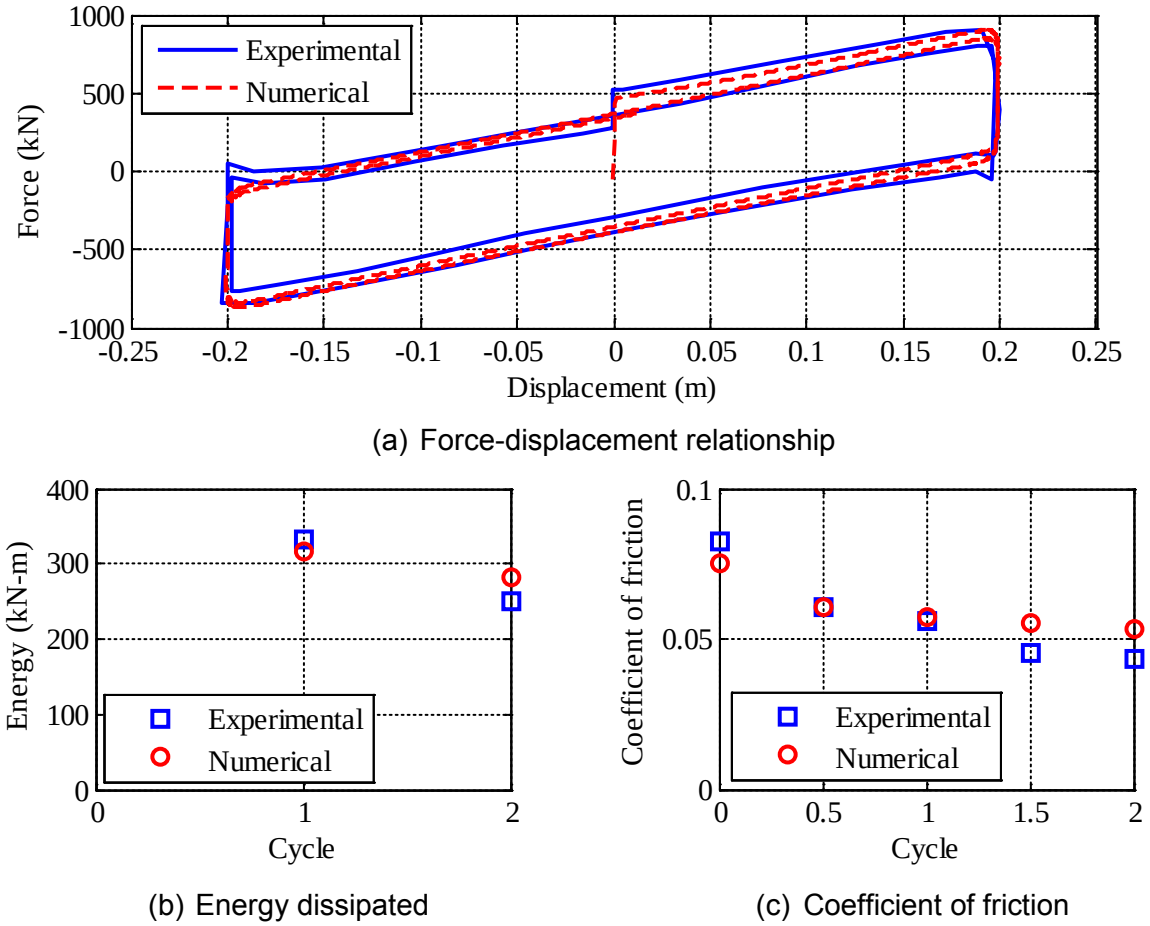

Figure 4-50 Experimentally Recorded and Numerically Simulated Force-Displacement Relationships for Experiment Number 16 of Table 4-6

5 ALTERNATE REPRESENTATIONS OF SEISMIC HAZARD FOR SEISMICALLY ISOLATED NUCLEAR STRUCTURES

5.1 Introduction

Two levels of seismic hazard will be considered for the design of seismically isolated nuclear structures: ground motion response spectrum+ (GMRS+) and beyond design basis (BDB) GMRS, at the mean annual frequencies of exceedance (MAFE) of 10^{-4} and 10^{-5}, respectively (see Kammerer *et al*. (2017)). Distributions of responses of the seismically isolated nuclear structure are computed for each hazard level, which are then used to determine values of design parameters (e.g., clear distance between the isolated superstructure and the stop). These distributions are significantly influenced by the definition of the seismic hazard.

Three basic representations of seismic hazard are investigated in this chapter: uniform hazard response spectrum (UHRS), conditional mean spectrum (CMS), and conditional spectra (CS). The UHRS is the traditional measure of seismic hazard in the nuclear industry. The CMS, which was proposed relatively recently, is based on the UHRS, but has a spectral shape consistent with that of recorded ground motions. The CS account for the variability in the ordinates of CMS at periods other than the conditioning period. Given a representation of the hazard (UHRS, CMS or CS), the spectra in the two orthogonal horizontal directions are the same. A fourth characterization of seismic hazard is also considered, constructed using the UHRS, but recognizing that the amplitude of one horizontal component is different from its perpendicular component: UHRS-MaxMin (e.g., Huang *et al.* (2009)). The uncertainties included in these four hazard descriptions are discussed in Section 5.2.

The four representations of seismic hazard are compared in terms of distributions of spectral displacement and the peak displacement response of single FP bearings, as introduced in Section 5.3. Sets of ground motions consistent with the UHRS, UHRS-MaxMin, CMS and CS, with MAFEs of 10^{-4} and 10^{-5}, for the site of the Diablo Canyon Nuclear Generating Station in California are developed in Sections 5.4 and 5.5, respectively. The distributions of displacement demand on Friction Pendulum™ (FP) bearings with different geometrical and material properties, subjected to the ground motions consistent with the four representations of ground motion, are computed and analyzed in Section 5.6. Recommendations for design practice are proposed in Section 5.7.

5.2 Uncertainty and Variability in Alternate Representations of Seismic Hazard

5.2.1 Introduction

The uncertainties and variabilities in UHRS, UHRS-MaxMin, CMS and CS are discussed in the following sections.

5.2.2 Uniform Hazard Response Spectrum (UHRS)

The seismic hazard at a site is typically described using a UHRS (see McGuire (2004) for details). The spectral ordinate at each period in the UHRS has the same probability of exceedance (e.g., 2%) in a specified time interval (e.g., 50 years). The probability of exceedance is also described in terms of an annual frequency of exceedance. For example, a probability of exceedance of 2% in 50 years is equivalent to an annual frequency of exceedance

of approximately 4×10^{-4}. The UHRS accounts for the aleatory[12] uncertainties in magnitude and location (source characteristics) of a possible earthquake, and in the intensity measure (IM[13]) given the magnitude, location and other source properties. Different models (e.g., ground motion prediction equations[14, 15]) are used to quantify the source characteristics and IMs, because of uncertainties in the understanding of earthquake processes (e.g., type of faults, wave propagation characteristics). Such uncertainties are epistemic, which may be reduced as more data becomes available. These model uncertainties are generally accounted for using logic trees, each branch of which represents a model (e.g., a ground motion prediction equation) that is assigned a weight, based typically on engineering judgment. Finally, and period-by-period, the weighted spectral ordinates are added to construct the UHRS at a user-specified mean annual frequency of exceedance (MAFE).

Uniform hazard response spectra with MAFEs of 10^{-4} and 10^{-5} are considered here for the design of seismically isolated nuclear power plants (see Kammerer et al. (2017)). Figure 5-1 shows the UHRS[16] (solid line) for the site of the Diablo Canyon Nuclear Generating Station in Southern California corresponding to the hazard with 2% probability of exceedance in 200 years (an MAFE of 1.01×10^{-4} or a return period of 9,900 years), obtained from http://geohazards.usgs.gov/deaggint/2008/ on June 15, 2014, for the shear wave velocity in the upper 30 m of the soil column of 760 m/s: the boundary between Site Classes B and C per ASCE 7-10 (ASCE, 2010). Data for an MAFE of 1.00×10^{-4} is not available at the USGS website. Other data from this website are used to develop consistent UHRS and CMS.

The hazard corresponding to MAFEs of 1.00×10^{-4} and 1.01×10^{-4} are not significantly different as evident by comparing the spectral acceleration ordinates at Diablo Canyon and seven other sites[17] of nuclear facilities across the United States and four periods (see Table 5-1). The ordinates were obtained using a different USGS application available at http://geohazards.usgs.gov/hazardtool/application.php, accessed on December 30, 2014. The spectral accelerations at these two hazard levels are computed assuming a linear variation in spectral acceleration with MAFE in the logarithmic space. There is a less than 1% difference between the spectral accelerations at these two hazard levels for the eight sites and four periods. Therefore, for the purpose of the discussion that follows, the seismic hazard at a 2% probability of exceedance in 200 years (MAFE of 1.01×10^{-4}, return period of 9,900 years) is considered identical to the seismic hazard at an MAFE of 10^{-4}.

A UHRS can be disaggregated by magnitude, site-to-source distance, and epsilon, where the latter is the number, positive or negative, of log standard deviations the UHRS ordinate exceeds

---

[12] Uncertainties associated with a random process that cannot be reduced by collection of additional data.

[13] Typically spectral acceleration.

[14] The ground motion prediction equation for a spectral acceleration in a horizontal direction (e.g., Campbell and Bozorgnia (2008)) is obtained from regression analysis performed on the geometric mean of the spectral accelerations in two orthogonal horizontal directions. The prediction equation for vertical spectral acceleration is obtained either by regression analysis on measured vertical spectral acceleration or by using ratios of vertical to horizontal spectral acceleration (e.g., Gülerce and Abrahamson (2011)).

[15] The geometric mean of the spectral accelerations in two horizontal directions depends on the orientation of the recording device. The recorded motions in the two directions can be rotated through all possible angles and a median value can be used in the derivation of a ground motion prediction equation (e.g., Boore et al. (2006), Beyer and Bommer (2006)).

[16] The USGS website provides CMS for a user-specified conditioning period. The UHRS ordinate at the conditioning period T^* is equal to the CMS ordinate.

[17] The seismic hazard at these sites is studied in Chapter 6.

the median spectral ordinate calculated using a given ground motion prediction equation. Figures 5-2 and 5-3 present the hazard disaggregation of the UHRS of Figure 5-1 at periods of 0.5 s and 3 s, respectively. The (M, r, ε) combinations (modal) at these two periods are (7.0, 6.8 km, 1.2) and (7.4, 5.7 km, 1.0), respectively.

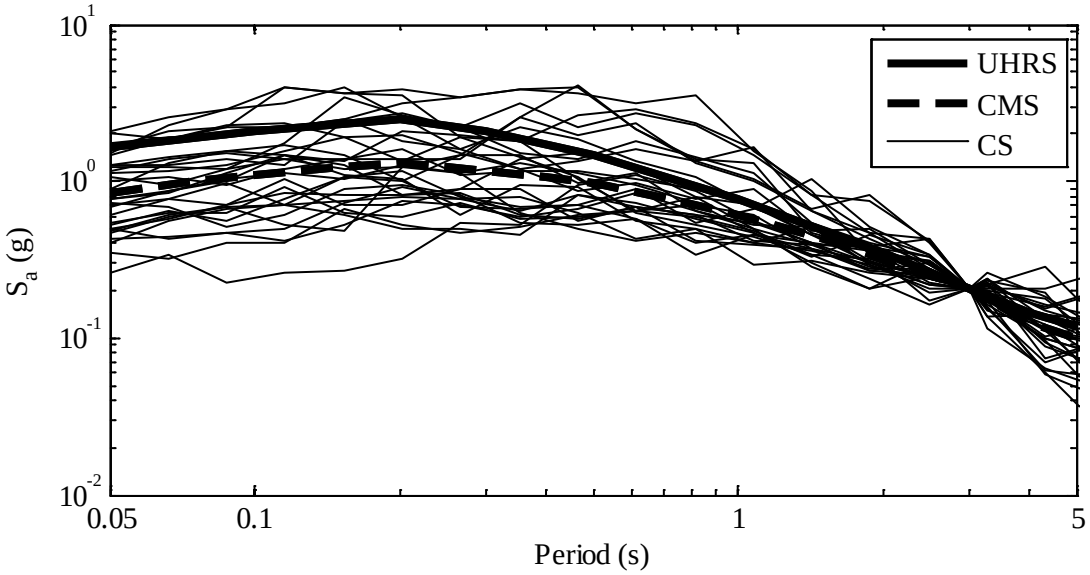

Figure 5-1 Examples of a Uniform Hazard Response Spectrum (UHRS), and a Conditional Mean Spectrum (CMS) and Conditional Spectra (CS) with a Conditioning Period of 3 s

Table 5-1 Ratios of Spectral Ordinates Corresponding to MAFE of 1.00×10^{-4} and 1.01×10^{-4}

Period (s)	Site							
	Diablo Canyon	North Anna	Summer	Vogtle	Oak Ridge	Hanford	Idaho	Los Alamos
0.1	1.003	1.006	1.005	1.005	1.005	1.004	1.004	1.005
0.2	1.003	1.006	1.005	1.004	1.006	1.004	1.003	1.006
1	1.003	1.006	1.004	1.004	1.005	1.004	1.003	1.006
2	1.004	1.005	1.004	1.004	1.005	1.004	1.004	1.006

5.2.3 Uniform Hazard Response Spectrum with Maximum and Minimum Components (UHRS-MaxMin)

The response spectra corresponding to the two orthogonal horizontal components of recorded ground motion are consistently different from each other (e.g., Boore *et al.* (2006), Beyer and Bommer (2006)). Ground motions spectrally matched to the UHRS cannot address the difference between orthogonal components. A uniform hazard response spectrum with *maximum* and *minimum* components (UHRS-MaxMin) accounts for the variability in the ratio of spectral accelerations in the two orthogonal horizontal directions, in addition to the uncertainties considered in the development of UHRS. The UHRS-MaxMin response spectra can be derived by amplitude scaling the UHRS, up and down, by a set of factors (e.g., Huang *et al.* (2009)).

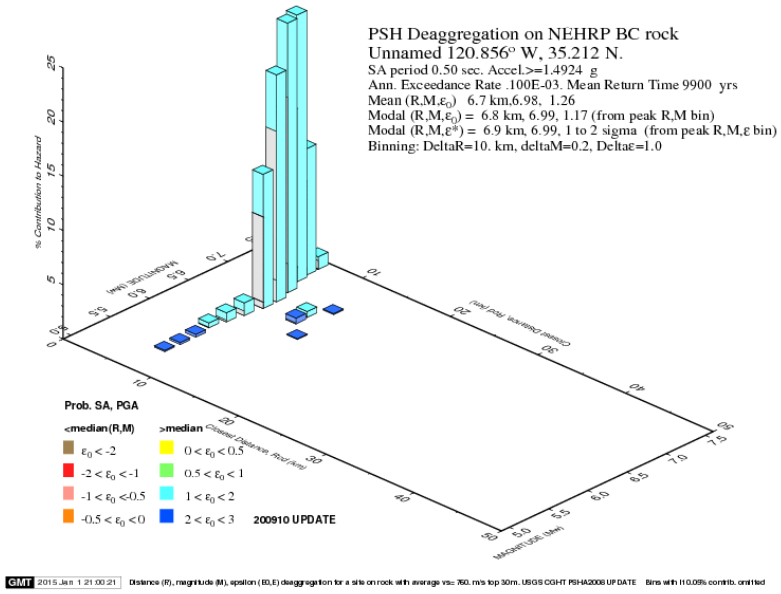

Figure 5-2 Disaggregation of 10,000-Year Seismic Hazard at 0.5 s Period for the Diablo Canyon Site

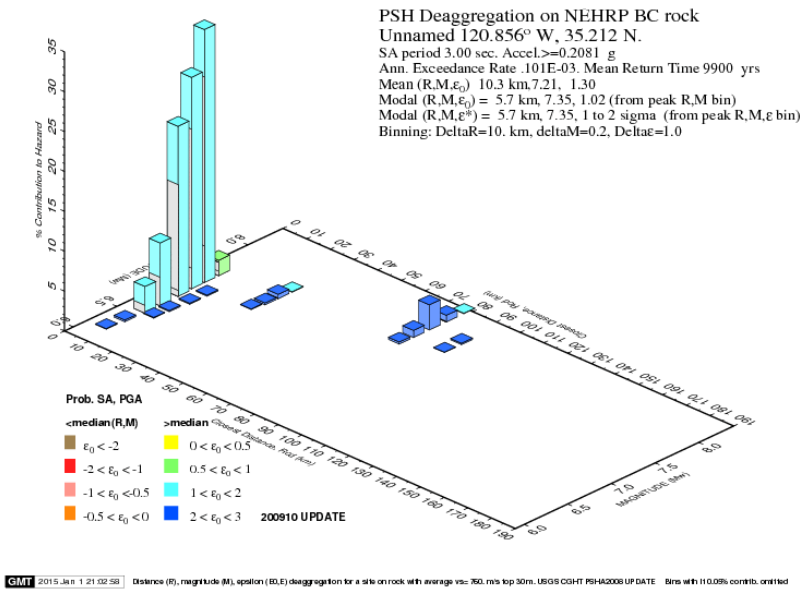

Figure 5-3 Disaggregation of 10,000-Year Seismic Hazard at 3 s Period for the Diablo Canyon Site

5.2.4 Conditional Mean Spectrum (CMS)

Baker and Cornell (2006) developed the conditional mean spectrum, also described by some as a scenario spectrum, to better describe the ground motion spectrum associated with a combination of magnitude, distance, and epsilon. The CMS is derived from a UHRS using a conditioning period and correlations between spectral accelerations at different periods, where

the correlation coefficients are based on equations derived from recorded ground motion data. The conditioning period is commonly set equal to the first mode translational period (e.g., see NIST (2011)). At this period, the ordinate of the CMS is set equal to that of the UHRS. The choice of conditioning period may not be clear if the structure is irregular or has different first mode translational periods in the two orthogonal horizontal directions (e.g., FEMA (2012)), but that is not an issue with seismically isolated structures. The ordinates of the CMS of Figure 5-1 (dashed line) are similar to those of the UHRS in the vicinity of the conditioning period (3 s), which is an expected outcome for large epsilon motions.

5.2.5 Conditional Spectra (CS)

Conditional spectra (CS) address the randomness in the CMS ordinates given the spectral ordinate at the conditioning period (e.g., Jayaram *et al.* (2011), NIST (2011)). Figure 5-1 presents 30 CS with conditioning period of 3 s, representing the seismic hazard at the Diablo Canyon site with an MAFE of 10^{-4}. The spectral ordinates of the UHRS, CMS and CS are equal at 3 s. The mean of the conditional spectral ordinates at a given period is equal to the CMS ordinate at that period.

5.3 Seismic Hazards, Spectral Displacements and Isolator Displacements

The seismic isolation NUREG/CR 7253"Technical considerations for seismic isolation of nuclear facilities" (Kammerer *et al*., 2019) requires that the probability of unacceptable performance of a seismically isolated nuclear structure be less than 1% and 10% under seismic hazard represented by GMRS+ and BDB GMRS, respectively. Impact of the isolated structure on the surrounding stop is considered unacceptable performance. Estimates of the 99th and 90th percentile peak isolation-system displacements for the two levels of earthquake shaking, respectively, are needed to determine the minimum clear distance between the isolated structure and the stop. The distributions of the peak displacements are a function of the chosen representation of the GMRS and BDB GMRS. Alternate representations are presented and investigated in the following sections.

Four representations of the seismic hazard are considered. The first three are 1) uniform hazard response spectrum (UHRS), 2) conditional mean spectrum (CMS), and 3) conditional spectra (CS). Traditional practice in the nuclear industry ASCE, (2005) defines seismic input using a UHRS. Each of the three spectra is a geometric mean spectrum: a composite of the ordinates along two orthogonal horizontal axes, which are assumed to be identical. A fourth representation of ground shaking is considered, also based on the UHRS, for which the ordinates of the spectra along one horizontal axis are consistently different from those on the perpendicular axis: the Max-Min spectra developed by Huang et al. (2009) that were used to underpin the isolation provisions in Chapter 12 of ASCE 4-16 ASCE, (2017).

The following sections investigate the 10,000-year and 100,000-year UHRS, UHRS-MaxMin, CMS and CS for the site of the Diablo Canyon Nuclear Generating Station. Distributions of spectral displacements for the four representations are compared for the two return periods. Ground motions consistent with these response spectra are developed. Distributions of peak displacement response of single FP bearings with a range of geometrical and material properties subjected to the ground motions consistent with different representations of seismic hazard are studied.

5.4 10,000-Year Spectra, Ground Motions, Spectral Displacements and Isolator Displacements

5.4.1 UHRS, UHRS-MaxMin, CMS and CS

Figure 5-1 presents the 5% damped UHRS, and CMS and CS with a conditioning period of 3 s for the site of the Diablo Canyon Nuclear Generating Station (latitude = 35.21162 N, longitude = 120.85562 W) at a 2% probability of exceedance in 200 years (return period = 9900 years, MAFE = 1.01×10^{-4})[18] assuming an average shear wave velocity in the upper 30 m of the soil column of 760 m/s. Conditional mean spectra are obtained from the USGS website http://geohazards.usgs.gov/deaggint/2008/, accessed on June 15, 2014, using the GMPE of Campbell and Bozorgnia (2008). A consistent UHRS is obtained from CMS with different conditioning periods, noting that the UHRS ordinate at a period T^* is equal to the CMS ordinate at T^*, where T^* is the conditioning period. Conditional spectra are calculated using software available at http://web.stanford.edu/~bakerjw/gm_selection.html, accessed on June 15, 2014. This software uses the Campbell and Bozorgnia (2008) GMPE[19] to generate a set of CS. The (M, r, ε) triple at a period of 3 seconds is (6.71, 5.5 km, 1.92), using the Campbell and Bozorgnia (2008) GMPE. The CMS from the USGS website and the covariance matrix obtained using the software of the Baker Research Group are used to generate the 30 conditional spectra of Figure 5-1.

A set of 30 ground motions is spectrally matched to the UHRS using RSPMatch (Hancock *et al.*, 2006). The horizontal components of the UHRS-scaled ground motions are then amplitude scaled by a set of factors (e.g., f_1 for the GM1 component in the X direction and $1/f_1$ for the GM1 component in the Y direction) to recognize that the response spectrum of one horizontal component of the recorded ground motion is different from that in the orthogonal horizontal direction. The derivation of the factors are described in Huang *et al.* (2009) and the factors are listed in Table 5-2. These ground motions are designated as either "UHRS-MaxMin-scaled" or "MaxMin-scaled", and the corresponding response spectra are designated as either "UHRS-MaxMin" or "MaxMin".

Ten thousand year return period UHRS, and CMS and 30 CS corresponding to conditioning periods of 2, 3 and 4 seconds are generated for the Diablo Canyon site. Figure 5-4(a) presents 5% damped UHRS, and CMS and CS in the horizontal direction corresponding to a conditioning period, T^*, of 2 s for the Diablo Canyon site and an MAFE of 10^{-4} (or return period of 10,000 years). Figures 5-4(b) and 5-4(c) present similar information for T^* of 3 s and 4 s, respectively. Response spectra in the vertical direction are generated using vertical-to-horizontal (V-H) ratios Gülerce and Abrahamson,(2011) and a (magnitude, distance) pair of (7, 5 km). Figure 5-5 presents the V-H ratios for a rock site and the source-to-site distance of 5 km. Figure 5-5(a) presents the ratios from Gülerce and Abrahamson (2011) for a range of magnitudes. Figure 5-5(b) presents the ratios used in this study to obtain vertical UHRS, CMS and CS.

---

[18] The spectral accelerations with 2% exceedance probability in 200 years (MAFE of 1.01×10^{-4}) are assumed to be identical to those corresponding to an MAFE of 1.00×10^{-4} (see Section 5.2.2).

[19] The only GMPE coded into the software.

Table 5-2 List of Factors Used to Amplitude Scale the Ground Motions Spectrally Matched to the UHRS

GM	Direction		GM	Direction	
	X	Y		X	Y
1	1.21	0.83	16	1.49	0.67
2	1.26	0.79	17	1.24	0.81
3	1.09	0.92	18	1.40	0.71
4	1.17	0.85	19	1.56	0.64
5	1.71	0.58	20	1.61	0.62
6	1.32	0.76	21	1.44	0.69
7	1.42	0.70	22	1.28	0.78
8	1.25	0.80	23	1.38	0.72
9	1.22	0.82	24	1.31	0.76
10	1.52	0.66	25	1.46	0.68
11	0.99	1.01	26	1.05	0.95
12	1.11	0.90	27	1.37	0.73
13	1.34	0.75	28	1.35	0.74
14	1.14	0.88	29	1.29	0.78
15	1.19	0.84	30	1.16	0.86

5.4.2 Ground Motions Spectrally Matched to UHRS

The set of 30 ground motions listed in Table E-1 are scaled to match the UHRS of Figure 5-4 in the period range of 0.5 s to 4 s, where the choice of period range is based on the following analysis.

The lateral force-displacement relationship for an FP bearing with a Coulomb-type coefficient of friction under constant axial load can be described by a bilinear relationship. The natural period before sliding, T_1, is given by:

$$T_1 = 2\pi\sqrt{\frac{u_y}{\mu g}} \qquad \textbf{(5-40)}$$

where u_y is the lateral displacement at which sliding begins and μ is the coefficient of friction.

The yield displacement u_y can be taken as 0.001 m and a representative coefficient of friction is 0.06 (0.1). The corresponding T_1 is 0.25 s (0.2 s), suggesting initially that the lower bound on the range should be 0.25 s. The sliding periods of the FP bearings considered in this study are no greater than 4 s, with effective periods, based on secant stiffness, of much less than 4 s if the displacement is small. The period range[20] for spectral matching of 0.5 s to 4 s (and not 0.2 s to 4 s) is a compromise associated with the significant computational expense of decreasing the lower bound on the range from 0.5 s to 0.2 s. The influence of the value of yield displacement on peak displacement is examined later in this chapter.

[20] Spectrally matching a ground motion component to a randomly generated conditional spectrum (discussed later) can be computationally expensive if the period range is broad. Accordingly, the seed ground motions are spectrally matched over a period range that will significantly influence peak isolation-system displacement, namely, 0.5 s to 4 s.

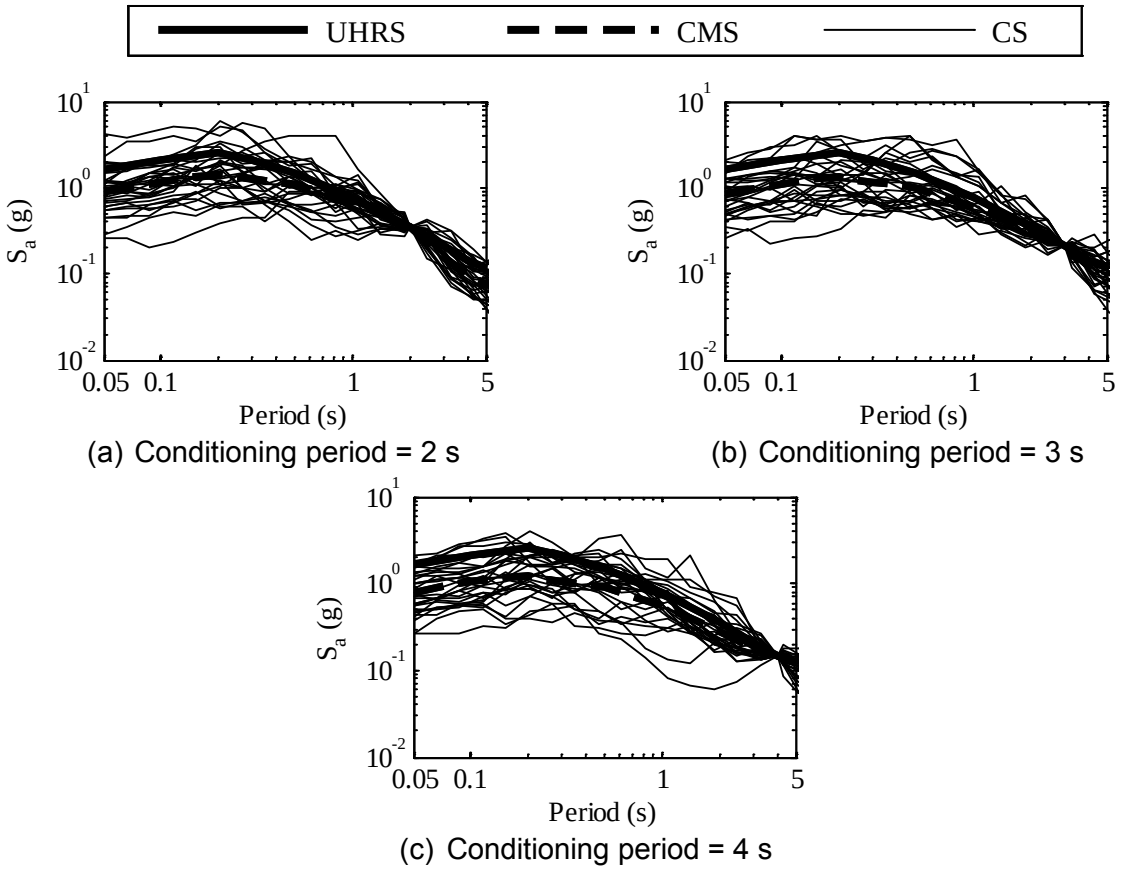

Figure 5-4 Target Uniform Hazard Spectrum (UHRS), and Conditional Mean Spectrum (CMS) and Conditional Spectra (CS) with Conditioning Periods of 2 s, 3 s and 4 s for the Diablo Canyon Site Corresponding to a Return Period of 10,000 Years

For the UHRS, the target spectra in the two orthogonal horizontal directions are identical. The (horizontal) UHRS of Figure 5-4 is multiplied by the V-H ratios of Figure 5-5(b) to obtain the target spectrum in the vertical direction. Figure 5-6(a) presents the response spectra of the 30 seed ground motions of Table E-1 spectrally matched to the UHRS in X direction. The UHRS is plotted in the panel. Figures 5-6(b) and 5-6(c) present identical information in the Y and Z directions, respectively. The spectra of the matched motions are virtually identical to the target spectra.

5.4.3 Ground Motions Consistent with UHRS-MaxMin

The response spectra of the scaled ground motions of Section 5.4.2 are identical in the two horizontal directions. The ground motions consistent with UHRS-MaxMin spectra are developed by amplitude scaling, up or down, the two horizontal components of the spectrally matched ground motions of Section 5.4.2. The scaling factors are listed in Table 5-2. The vertical component of UHRS-MaxMin-scaled motions is identical to that for the UHRS-scaled motions. Figure 5-7 presents the response spectra of the ground motions consistent with UHRS-MaxMin.

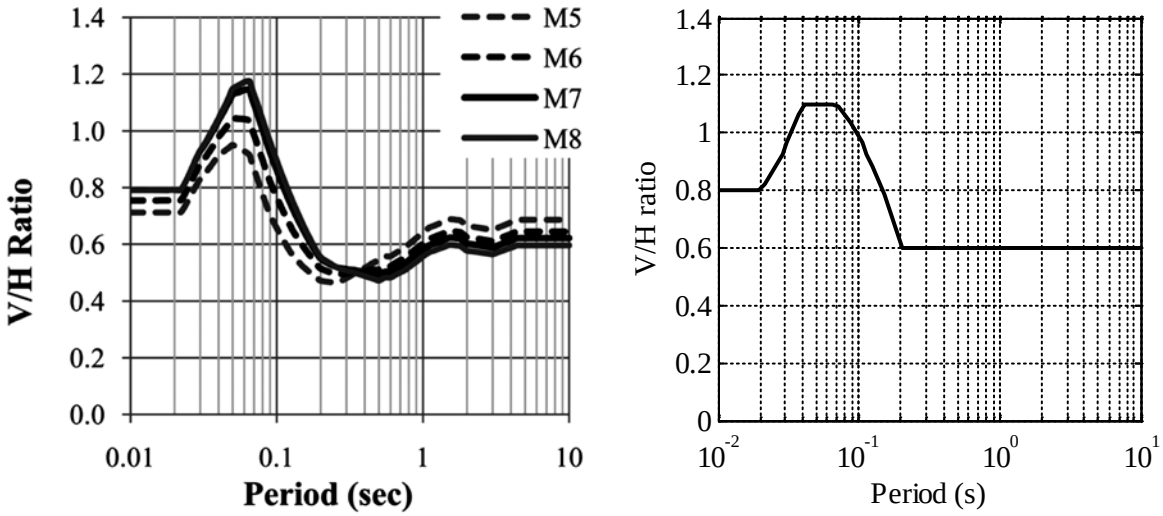

(a) Gülerce and Abrahamson (2011) (b) Assumed V/H ratio

Figure 5-5 Median Ratio of Vertical to Horizontal Spectral Response on a Rock Site with a Source-to-Site Distance of 5 km

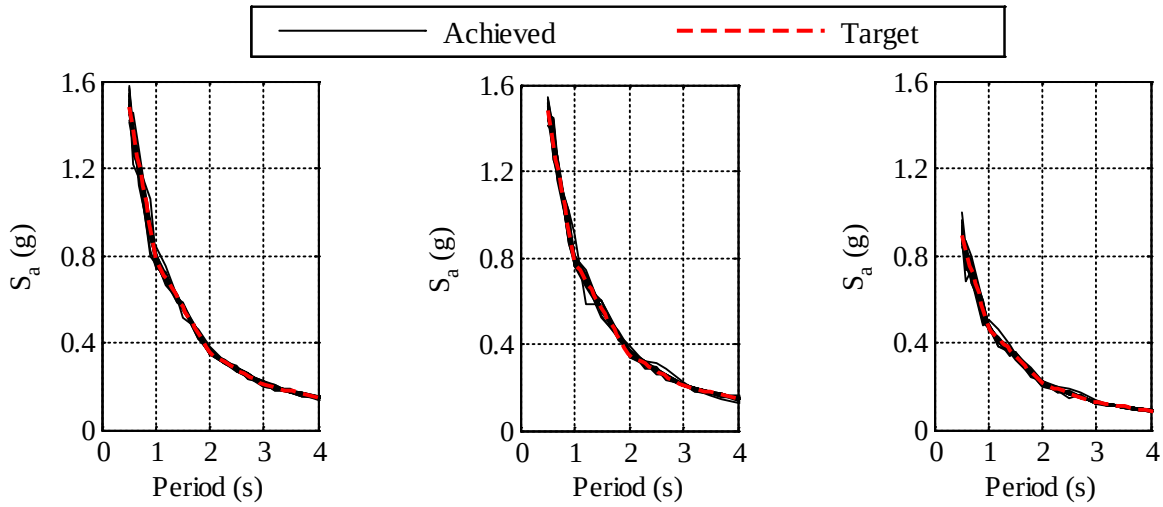

(a) X direction (b) Y direction (c) Z direction

Figure 5-6 Response Spectra of 30 Seed Ground Motions Spectrally Matched to the 10,000 Year Uniform Hazard Spectra for the Diablo Canyon Site

5.4.4 Ground Motions Spectrally Matched to CMS

Conditional mean spectra with conditioning periods of 2 s, 3 s and 4 s are used to represent 10,000-year seismic hazard at the Diablo Canyon site. The three CMS are plotted in Figure 5-4. The 30 seed motions of Table E-2 are spectrally matched to the three CMS, in the vertical and two horizontal directions, in the period range of 0.5 s to 4 s. The CMS in the vertical direction are obtained by multiplying the (horizontal) CMS of Figure 5-4 by the V/H of Figure 5-5(b). Figures 5-8(a), 5-8(b) and 5-8(c) present the target conditional mean spectrum with a conditioning period of 2 s and the response spectra of the 30 spectrally matched motions in the

X, Y and Z directions, respectively. The other panels in the figure present identical information for conditioning periods of 3 s and 4 s. The spectra of the matched motions are virtually identical to the target spectra.

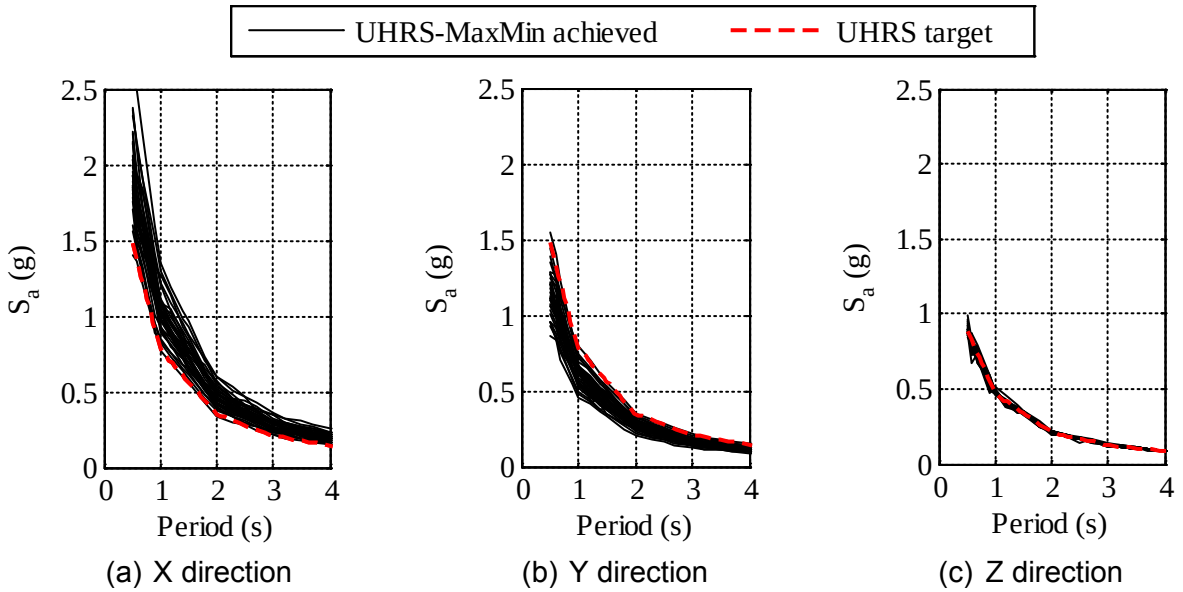

Figure 5-7 Response Spectra of 30 Ground Motions Consistent with the 10,000-Year UHRS MaxMin for the Diablo Canyon Site

5.4.5 Ground Motions Spectrally Matched to CS

A set of 30 conditional spectra is generated for each of the three conditioning periods: 2 s, 3 s and 4 s (see Figure 5-4): CS Set 1, CS Set 2 and CS Set 3. Three sets of 30 seed ground motions are used: GM Set 1, GM Set 2 and GM Set 3. Details on the seed motions are presented in Appendix E. The 30 ground motion records of GM Set 1 are matched to the 30 conditional spectra of CS Set 1 (each record scaled to one conditional spectrum). Similarly, the ground motions of GM Set 2 and GM Set 3 are matched to the spectra of CS Set 1. The three sets of seed ground motions are also matched to the other two sets of conditional spectra, CS Set 2 and CS Set 3. The end product of this exercise is three sets of ground motions matched to each of the three sets of conditional spectra.

Figure 5-9(a) presents the 12th of the 30 conditional spectra in the horizontal direction corresponding to T^* = 2 s (Figure 5-4(a)) and a return period of 10,000 years. The 5% damped response spectra of a horizontal component (say X) of the 12th ground motion record from GM Set 1 (NGA number 3269), GM Set 2 (NGA Number 1488) and GM Set 3 (NGA Number 2897) spectrally matched to the 12th conditional spectrum are also plotted in the figure. The ground motions are listed in Tables E-3, E-4 and E-5, respectively. Figures 5-9(b) and 5-9(c) present identical information in the Y (horizontal) and Z (vertical) directions, respectively. Figures 5-9(d), 5-9(e) and 5-9(f) present information for T^* = 3 s (Figure 5-4(b)), in the X, Y and Z directions, respectively. Figures 5-9(g), 5-9(h) and 5-9(i) present data for a conditioning period of 4 s. The target and computed spectra compare well in each of the nine panels.

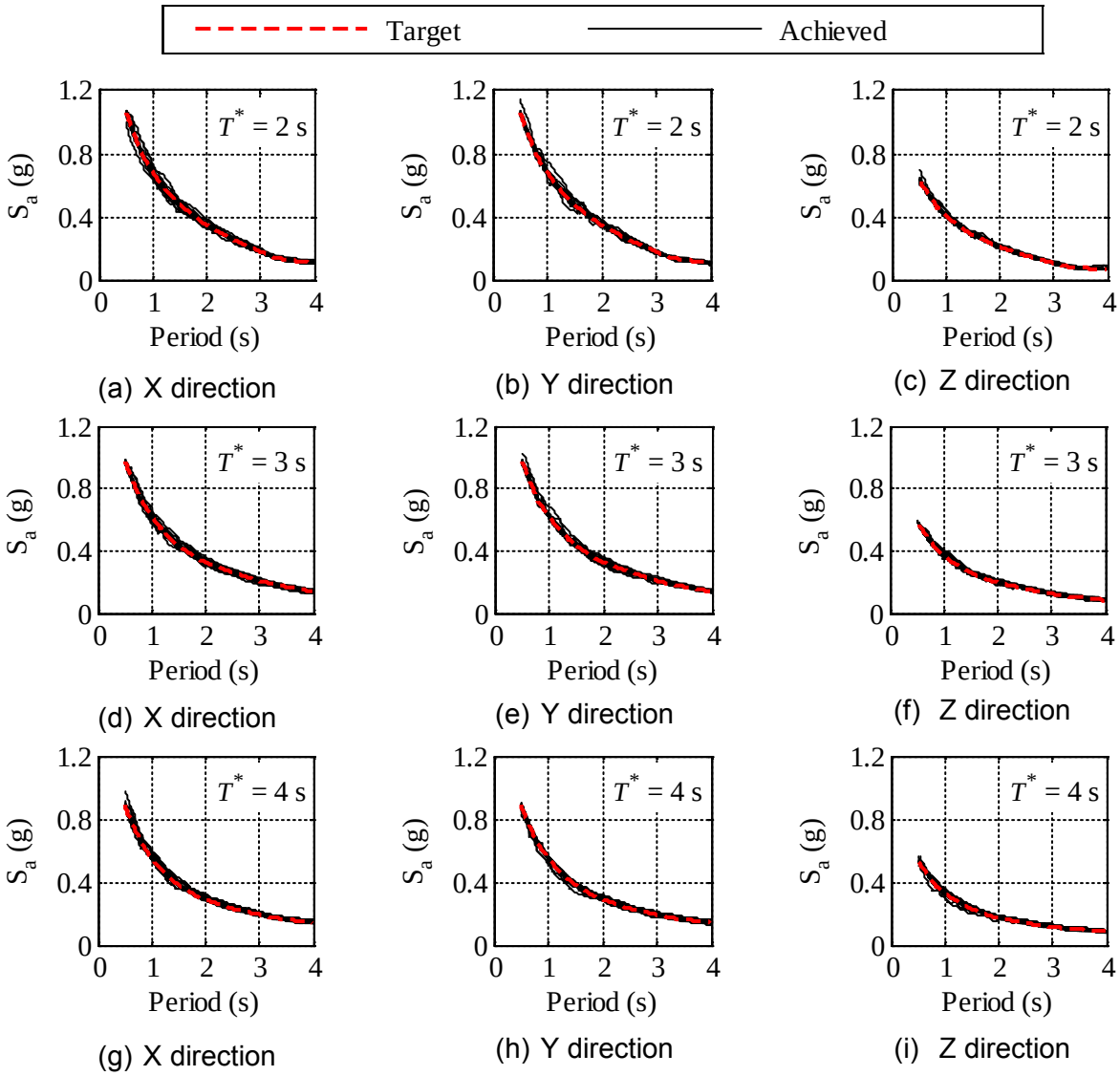

Figure 5-8 Response Spectra of 30 Seed Ground Motions Spectrally Matched to the 10,000-Year Conditional Mean Spectra for the Diablo Canyon Site

Figure 5-10(a) presents the percentage difference between the 30 target spectra of Figure 5-4(a) and the 30 spectrally matched ground motions using GM Set 1 (Table E-3). Results are presented for the two horizontal and vertical directions, and five natural periods: 0.5 s, 1 s, 2 s, 3 s and 4 s. Figure 5-10(d) and 5-10(g) present information for conditioning periods of 3 s and 4s. The remaining panels in Figure 5-10 present identical information for the other GM sets and all three conditioning periods.

There are 15 curves plotted in Figure 5-10(a) (3 directions $\times$ 5 natural periods). The percentage difference averaged across all the 30 ground motions is less than 0.6% for periods less than 3 s in the two horizontal and vertical directions. The maximum absolute difference ranges between 2% and 9% for periods less than 3 s. The averaged percentage error is less than 4.5% for a period of 4 s; the maximum absolute difference is 30%. The spectral ordinates are often very small (e.g., 0.03 g) at 4 s (see Figure 5-4) and a difference of even 0.01 g

between the target and computed spectra results in a high percentage difference. Figure 5-10 presents the percentage differences for all the 810 combinations (3 conditioning periods × 3 GM Sets × 30 ground motions × 3 directions). Across all combinations, the maximum absolute difference between the target and computed spectra is less than 15% for periods less than 3 s and less than 35% for the 4 s period.

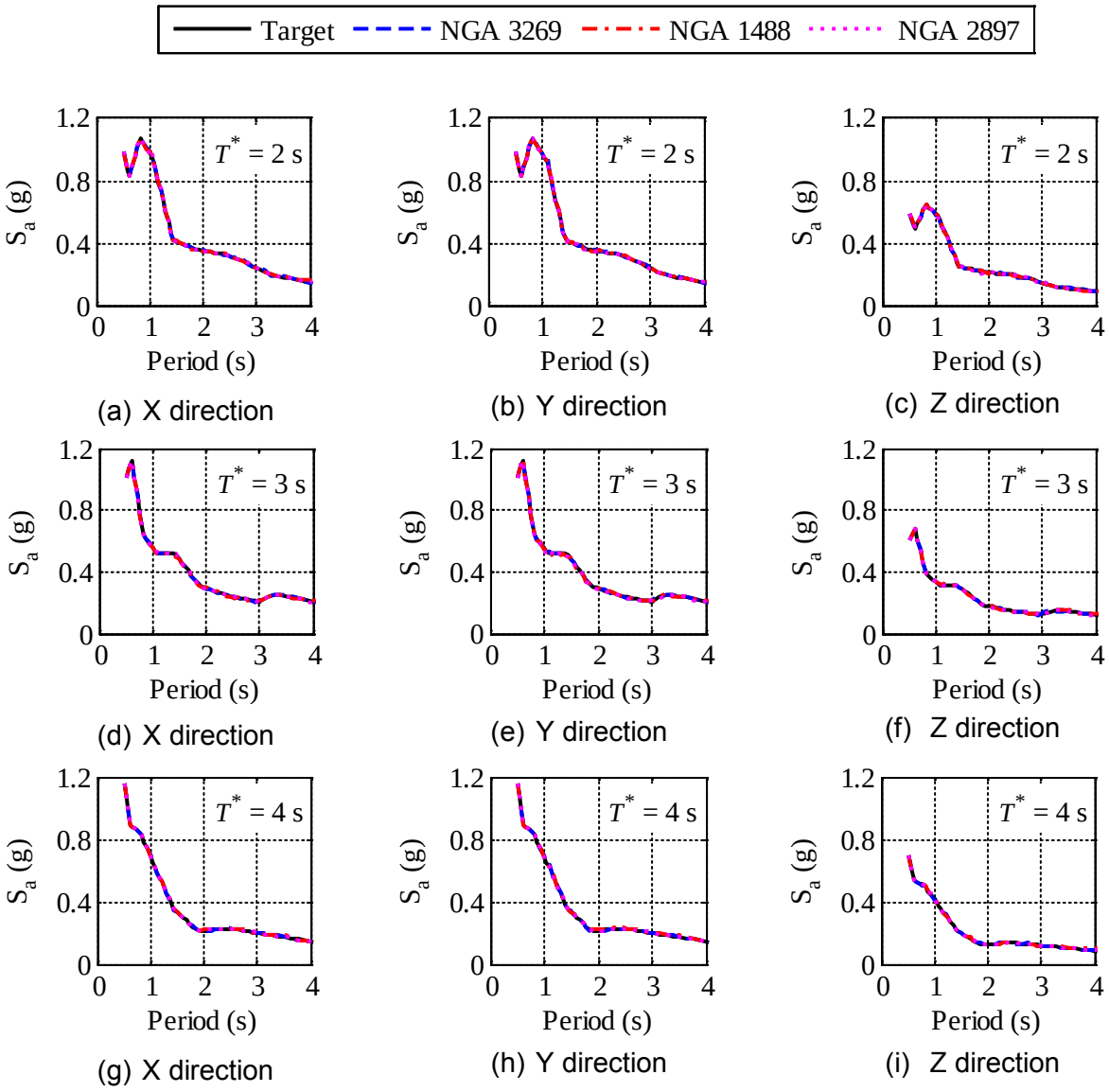

Figure 5-9 Target Conditional Spectrum Number 12 and Response Spectra of Ground Motion Record Number 12 from the Three Sets (NGA numbers 3269, 1488 and 2897 from GM Sets 1, 2 and 3, respectively, of Appendix E) Spectrally Matched to the Corresponding Target Conditional Spectrum

Figure 5-11(a) presents the mean of the 30 target conditional spectra for the conditioning period of 2 s (Figure 5-4(a)) and the mean of the computed spectra of the X component of the 30 ground motions for each of the three spectrally matched GM Sets (Tables E-3, E-4 and E-5).

Figure 5-11(b) presents the standard deviation in the target and computed spectra, noting that the value is zero at the conditioning period of 2 s. The remaining panels in the figure present the corresponding information for conditioning periods of 3 s and 4 s. The mean and standard deviation of the spectral ordinates of the scaled motions compare very well with the target values.

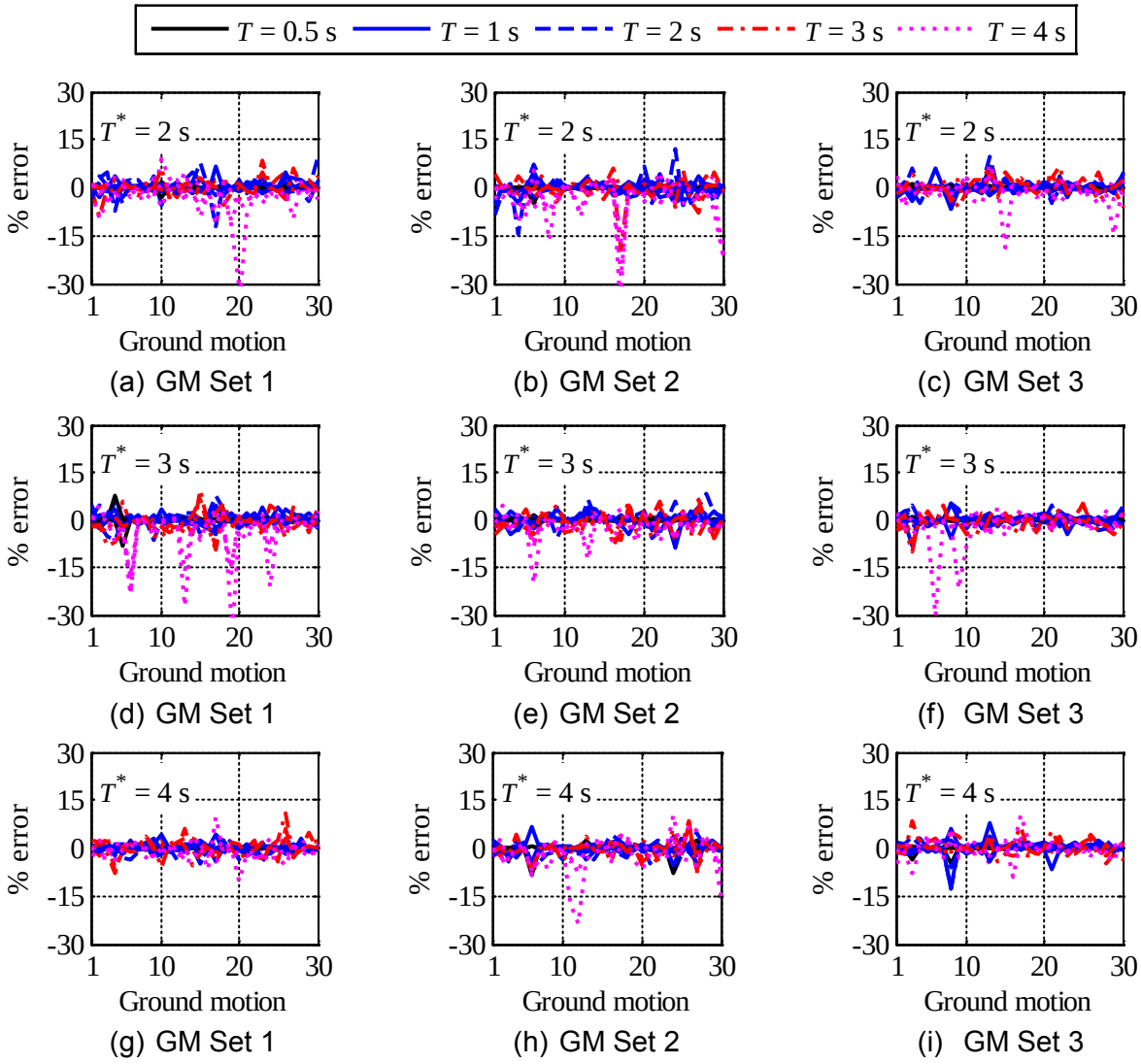

Figure 5-10 Percentage Difference Between the Target and Computed 5%-Damped Acceleration Response Spectra for Three Conditioning Periods, Three Sets of 30 Ground Motions, Two Horizontal and One Vertical Directions, and Five Values of Natural Period

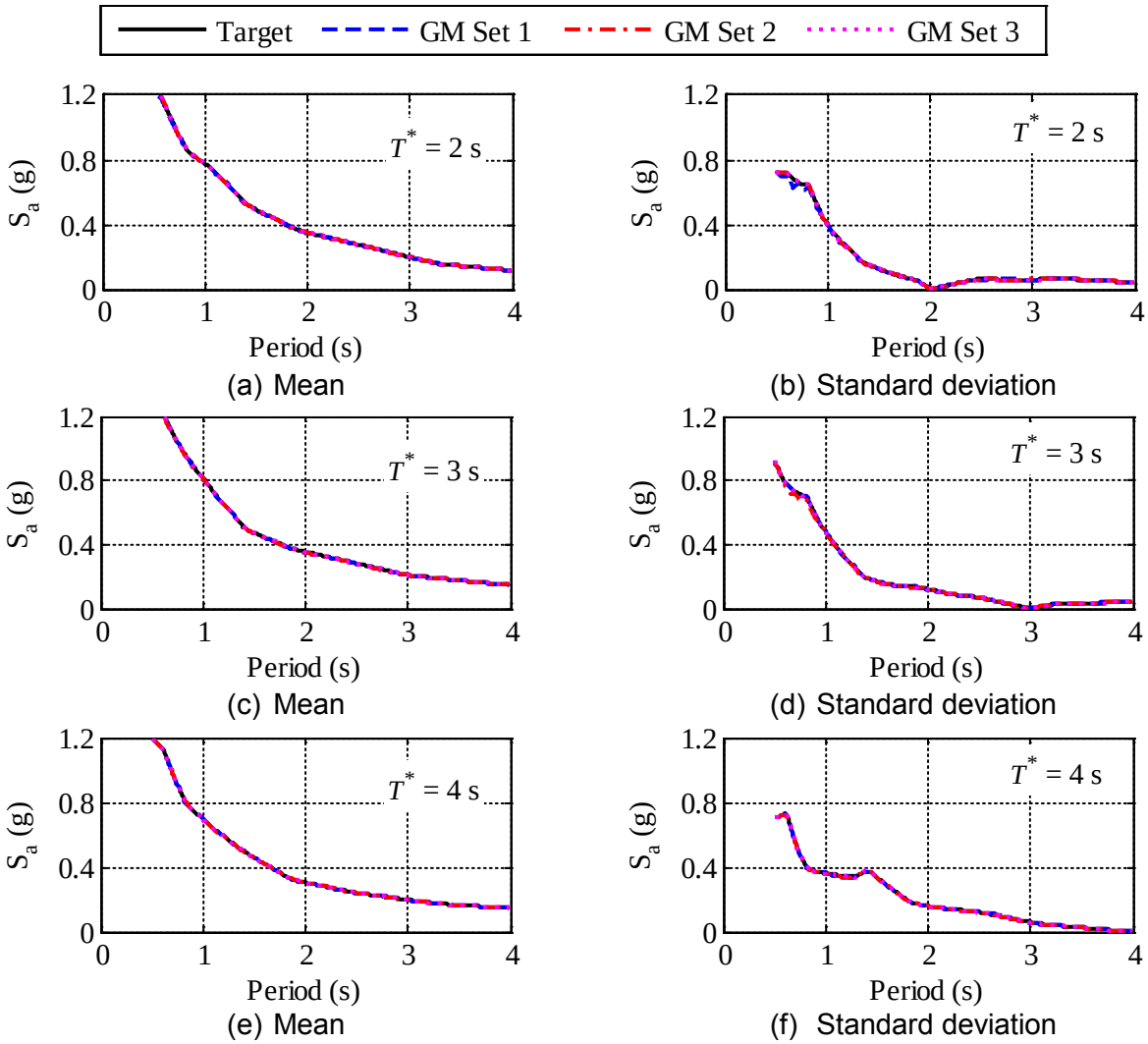

Figure 5-11 Mean and Standard Deviation of Target Conditional Spectra and Spectra of Spectrally Matched Motions in the X Direction

5.4.6 Spectral Displacements

The four preceding subsections present sets of 10,000-year ground motions spectrally matched to the UHRS (1), UHRS-MaxMin (1), CMS with three conditioning periods (3), and CS with three conditioning periods (9). All 14 sets of 30 spectrally matched ground motions could represent the 10,000-year return period seismic hazard at Diablo Canyon.

Figure 5-12 (Figure 5-13) presents the distributions of spectral displacement of the 14 sets of 30 ground motions at different periods in the X (Y) direction. The Max (Min) component of the MaxMin set is aligned in the horizontal X (Y) direction (see Table 5-2). The spectral displacements for a set of scaled ground motions are assumed to distribute lognormally at a given period.

Figure 5-12(a) presents the distributions of spectral displacement in the X direction at a period of 1.5 s for the ground motions spectrally matched to the 1) UHRS, 2) UHRS-MaxMin, 3) CMS with T^* = 2 s, and 4) CS with T^* = 2 s. The UHRS- (CMS-) scaled ground motions produce a

median spectral displacement of 0.31 m (0.27 m) and differ from the corresponding 99th percentile spectral displacement by only 0.02 m (0.02 m). The UHRS-MaxMin-scaled ground motions produce a median (99th percentile) spectral displacement of 0.41 m (0.55 m). The spectral displacements of the three sets of 30 CS-scaled ground motions distribute in similar manner to one another since the ground motions are scaled to the same set of CS. The median (99th percentile) spectral displacements for each of the three sets of CS scaled ground motions is 0.26 m (0.49 m).

Figure 5-12(b) presents the distributions of spectral displacement at a period of 2 s with T^* = 2 s. There is little difference in the distribution of the spectral displacements for the UHRS-, CMS- and CS-scaled ground motions, which is an expected result given the scaling procedures employed. A similar observation is made for Figures 5-12(g) and 5-12(l), distributions of spectral displacement at periods of 3 s and 4 s, respectively, and T is equal to T^*. The distributions of spectral displacements corresponding to the UHRS-MaxMin scaled motions in these three panels are similar to that in Figure 5-12(a).

For those cases where $T_{sliding} \neq T^*$ (panels other than (b), (g) and (l)), the trends are similar to Figure 5-12(a), namely, 1) the spectral displacements of the UHRS-scaled motions are greater than those of the CMS-scaled motions, 2) the distributions of spectral displacement of the three sets of CS-scaled motions are similar, 3) the spectral displacements of the UHRS-scaled ground motions exceed those of the CS-scaled ground motions until approximately the 65th percentile, 4) the 84+th spectral displacements of the CS-scaled motions are significantly greater than those of the UHRS- and CMS-scaled motions, and 5) the spectral displacements for the ground motions consistent with UHRS-MaxMin exceed those for the other three spectra at percentiles below 90 and ordinates for the CS-scaled motions exceed those for UHRS-MaxMin-scaled motions at percentiles greater than 90 in some cases.

The distributions of spectral displacement reported in Figure 5-13 (Y direction) are identical to those in Figure 5-12 (X direction), except for the UHRS-MaxMin-scaled ground motions because they were amplitude scaled with reciprocal (and smaller in almost all cases) factors (see Table 5-2).

All 14 sets of ground motions (consistent with UHRS, UHRS-MaxMin, CMS or CS) considered in this section reasonably represent the 10,000-year earthquake hazard at the Diablo Canyon site. There are significant differences in the spectral displacements at a given period for the 14 sets of ground motions. The subsequent section examines the influence of hazard representation on the displacement response of simple isolation systems with FP bearings.

5.4.7 Response of FP Bearings

The distributions of peak displacement of FP bearings with a range of geometrical properties, subjected to the sets of 10,000-year return period ground motions introduced previously, are presented and compared in this section.

The seed ground motions of Appendix E are scaled over a period range of 0.5 s to 4 s (see Sections 5.4.2 through 5.4.5). Consequently, there is limited *control* on the peak ground acceleration (PGA) of the scaled ground motions in the three orthogonal directions. If the ground motions had been scaled in the period range that included much short periods (e.g., 0.01 s), the vertical PGA of the UHRS-scaled motions would have been the product of the horizontal PGA (= 0.95 g) and V-H ratio at a short period (= 0.8, Figure 5-5(b)), namely, about

0.8 g. However, the PGA of the UHRS-scaled motions in the vertical direction ranged between 0.3 g to 2.9 g. Loss of contact between the slider and the sliding surface (uplift) takes place when the vertical ground acceleration exceeds 1 g because the superstructure is assumed rigid in the vertical direction. The lateral stiffness of the FP bearings is zero when the supported weight is zero (i.e., uplift). The calculation of the peak displacement of an FP bearing may be incorrect if two conditions are met, namely, 1) the vertical ground motions are not scaled appropriately in the short period range, and 2) the vertical PGA of the ground motion is much larger than the greater of the target vertical PGA and 1.0 g.

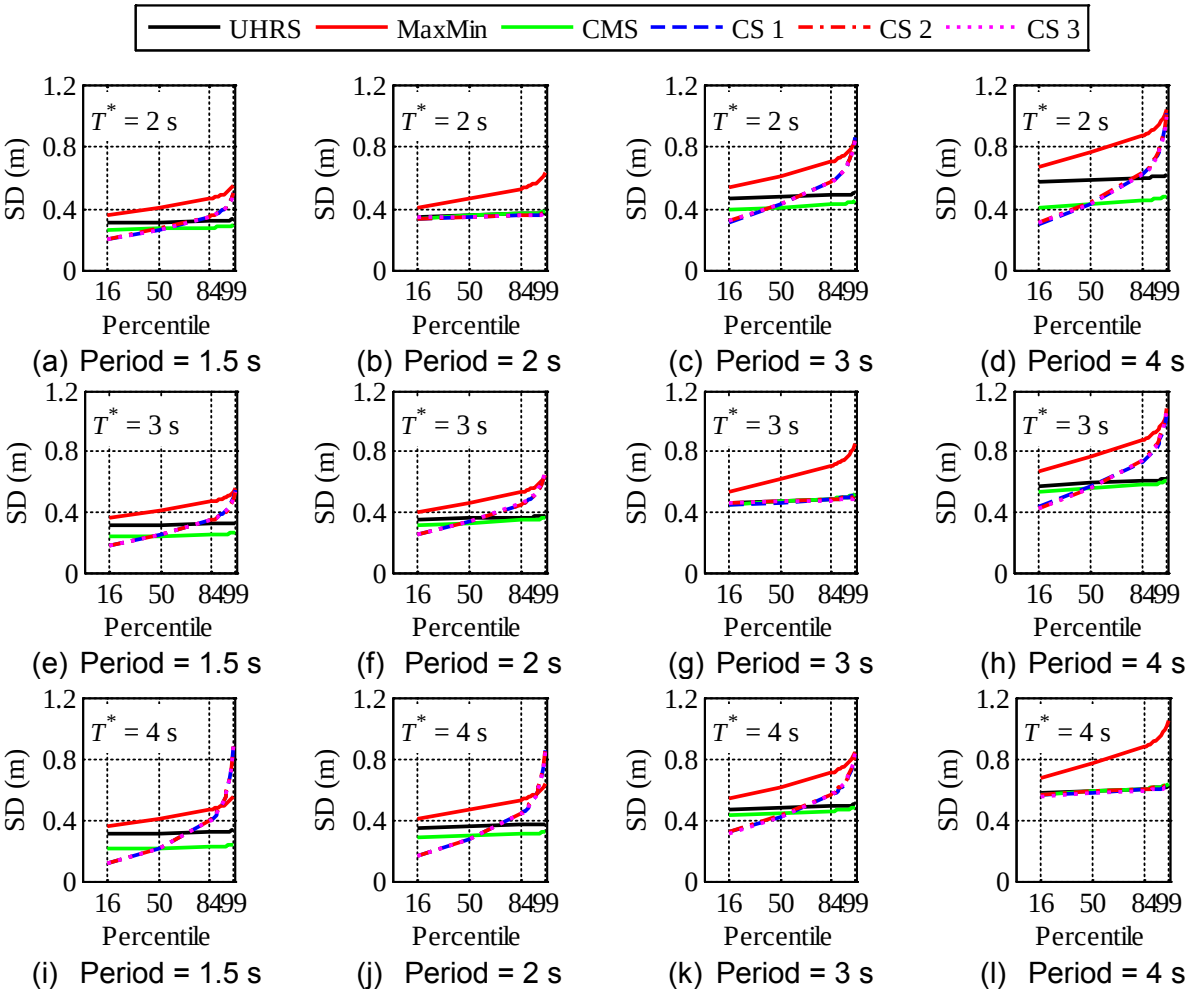

Figure 5-12 Distributions of Spectral Displacement (SD) for the UHRS-, UHRS-MaxMin-, CMS-, and CS-Scaled Ground Motions in the X Direction at Periods of 1.5 s, 2 s, 3 s and 4 s, and Conditioning Periods, T^*, of 2 s, 3 s, and 4 s for the CMS and CS

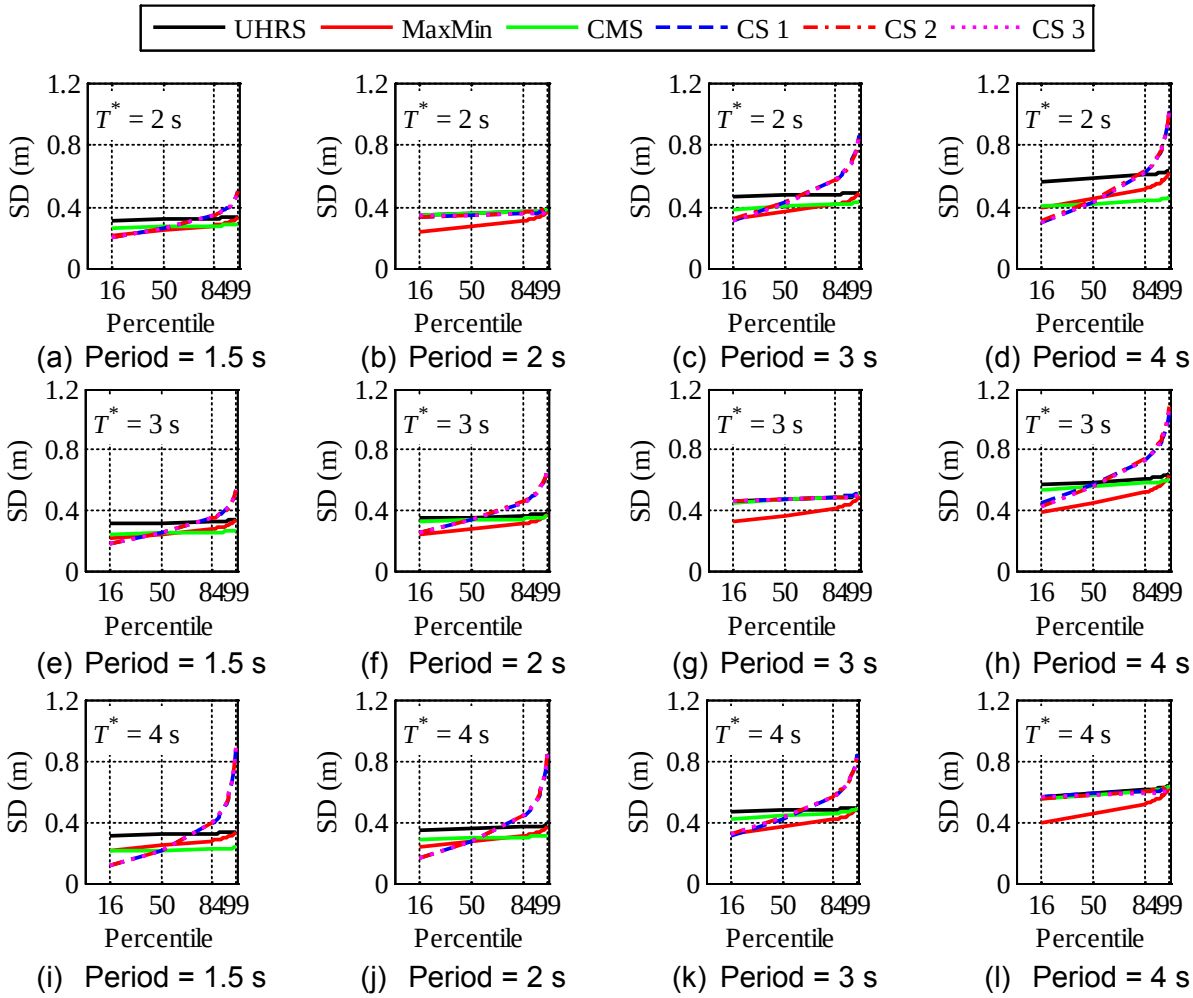

Figure 5-13 Distributions of Spectral Displacement (SD) for the UHRS-, UHRS-MaxMin-, CMS-, and CS-Scaled Ground Motions in the Y Direction at Periods of 1.5 s, 2 s, 3 s and 4 s, and Conditioning Periods, T^*, of 2 s, 3 s, and 4 s for the CMS and CS

To understand the importance of the vertical component of the ground motion on peak horizontal displacement response, an FP bearing with a sliding period of 3 s, a Coulomb-type coefficient of friction of 0.1 and a static axial pressure of 50 MPa is analyzed[21]. The vertical PGA for 23 of the 30 ground motions spectrally matched to the UHRS is less than 1.0 g. Two sets of response-history analyses are performed for these 23 motions: 1) considering the vertical component, and 2) ignoring the vertical component. Mass proportional damping of 2% is assigned to the system with the proportionality coefficient computed using the sliding period of the bearing. The distributions of peak horizontal displacement for the two cases are presented in Figure 5-14. The displacement responses are assumed to distribute lognormally. The distributions match closely. The peak horizontal displacement is not considerably affected by the vertical component of ground motion, provided there is no loss of contact at the sliding

[21] Single FP bearings with these properties are also studied in the latter sections of the chapter. The choice of properties is considerably limited by the excessive displacement demand on the bearings subjected to the ground motions representing 100,000-year seismic hazard.

surface, as observed in experiments by Mosqueda *et al.* (2004). The vertical component of ground motion is thus ignored for the response-history analyses performed in the remainder of this chapter.

The spectral matching exercise was performed over a period range of 0.5 s to 4 s, because increasing the lower bound from 0.2 s to 0.5 s (corresponding to u_y equal to 0.006 m and a coefficient of friction of 0.1) would not significantly affect peak displacement responses in the isolation systems. Figure 5-15 presents the distribution of peak horizontal displacement responses of the FP bearing of Figure 5-14 subjected to the 23 ground motions, including vertical components, with u_y set equal to 0.001 m and 0.006 m. The differences in the peak displacements are tiny and support the decision to set the lower bound on the period for spectral matching to 0.5 s.

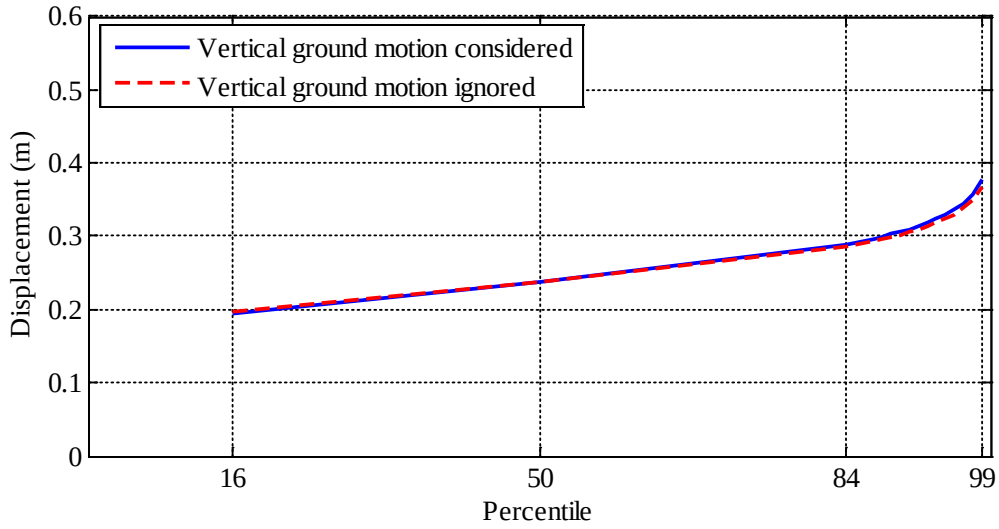

Figure 5-14 Distributions of Peak Horizontal Displacement of an FP Bearing Subjected to 23 Ground Motions

A series of analyses are performed to study the response of isolated structures subjected to the ground motions consistent with the four alternate representations of seismic hazard (see Sections 5.4.2 through 5.4.5). Friction Pendulum bearings with sliding periods, T_{sliding}, of 3 s and 4 s, with a Coulomb-type coefficient of friction of 0.1[22, 23], and static axial pressure of 50 MPa are subjected to 1) a set of 30 ground motions spectrally matched to the UHRS, 2) the 30 UHRS-scaled motions amplitude scaled to be consistent with UHRS-MaxMin, 3) a set of 30 seed ground motions spectrally matched to the CMS of Figure 5-4 with the conditioning periods, T^*, of 2 s, 3 s and 4 s, and 4) three sets of 30 ground motions spectrally matched to the three sets of CS of Figure 5-4. Mass proportional damping of 2% is assigned to the system, with the proportionality coefficient based on the sliding period of the bearing. The peak horizontal

[22] The ground motions considered in this section and in the following section impose significant displacement demand on the FP bearings, which dictates the choice of properties of FP bearings: sliding period of 3 s and 4 s, and coefficient of friction of 0.1.

[23] The 3 s (4 s) FP isolator has a radius of curvature, *R*, of 2.3 m (4 m). For the coefficient of friction of 0.1, the effective period of the isolator is 1.7 s (2.3 s), 2.1 s (2.8 s) and 2.5 s (3.3 s), respectively, at the displacement of 0.05*R*, 0.1*R* and 0.2*R*.

displacements are assumed to distribute lognormally. Figure 5-16 presents the distributions of peak horizontal displacements of the FP bearings subjected to the seven sets of 30 ground motions.

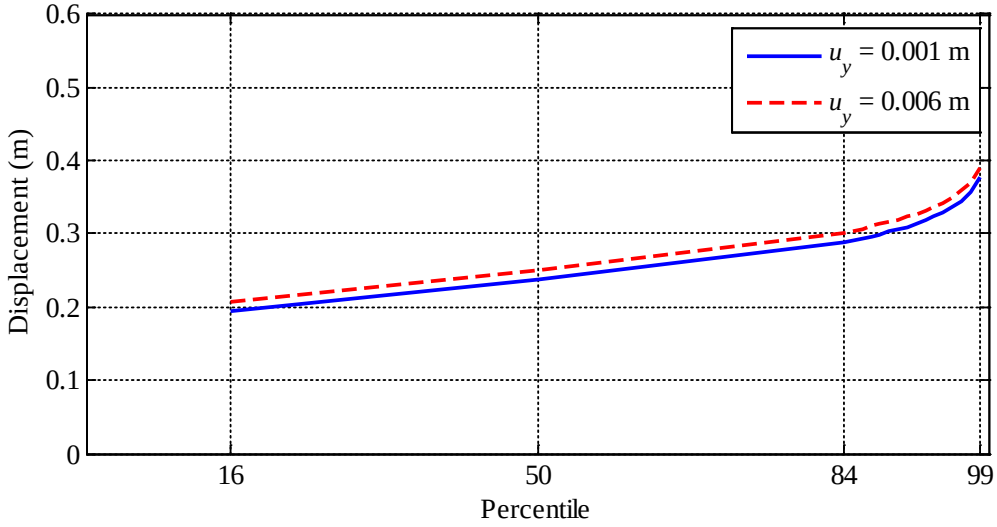

Figure 5-15 Distribution of Displacement Demand for 23 Ground Motions with Yield Displacement Set Equal to 0.001 m and 0.006 m

Figure 5-16(a) presents the distributions of peak displacement of the 3 s FP bearing subjected to the ground motions consistent with UHRS, UHRS-MaxMin, and CS and CMS with T^* of 2 s (Figure 5-4(a)). The peak displacements for the UHRS-scaled motions are greater than the CMS- and CS- scaled motions at percentiles smaller than 80; the displacements for the CMS- and CS-scaled motions are comparable up to 80th percentile. The displacements for the UHRS-MaxMin-scaled motions are greater than those for the other three representations of seismic hazard, at percentiles less than 95. The CS-displacements are greatest at 95+ percentiles. The ratios of displacements for UHRS-MaxMin- (CMS-, CS[24]-) to UHRS-scaled motions are 1.26 (0.73, 0.72), 1.34 (0.85, 1.15) and 1.42 (0.95, 1.67) at 50th, 90th and 99th percentiles, respectively. The observations for the 4 s bearing (Figure 5-16(b)) are similar to those for the 3 s bearing.

Data for conditioning periods of 3 s and 4 s are presented in Figures 5-16(c) through 5-16(f). The general trends are the same as those noted above for a conditioning period of 2 s. The 95+th percentile peak displacements are greatest for the CS-scaled motions. The ratios[25] of peak displacements for the UHRS-MaxMin- (CMS-, CS-) to UHRS-scaled motions are 1.26

[24] The greatest of the three values (one for each of the three sets of CS-scaled motions) is used.

[25] Greater among those for bearings with sliding periods of 3 s and 4 s.

(0.75, 0.79), 1.34 (0.87, 1.25) and 1.42 (0.98[26], 1.83) at the 50th, 90th and 99th percentiles, respectively, for a conditioning period of 3 s, and 1.26 (0.63, 0.62), 1.34 (0.77, 1.44) and 1.42 (0.91, 2.89), respectively, for a conditioning period of 4 s.

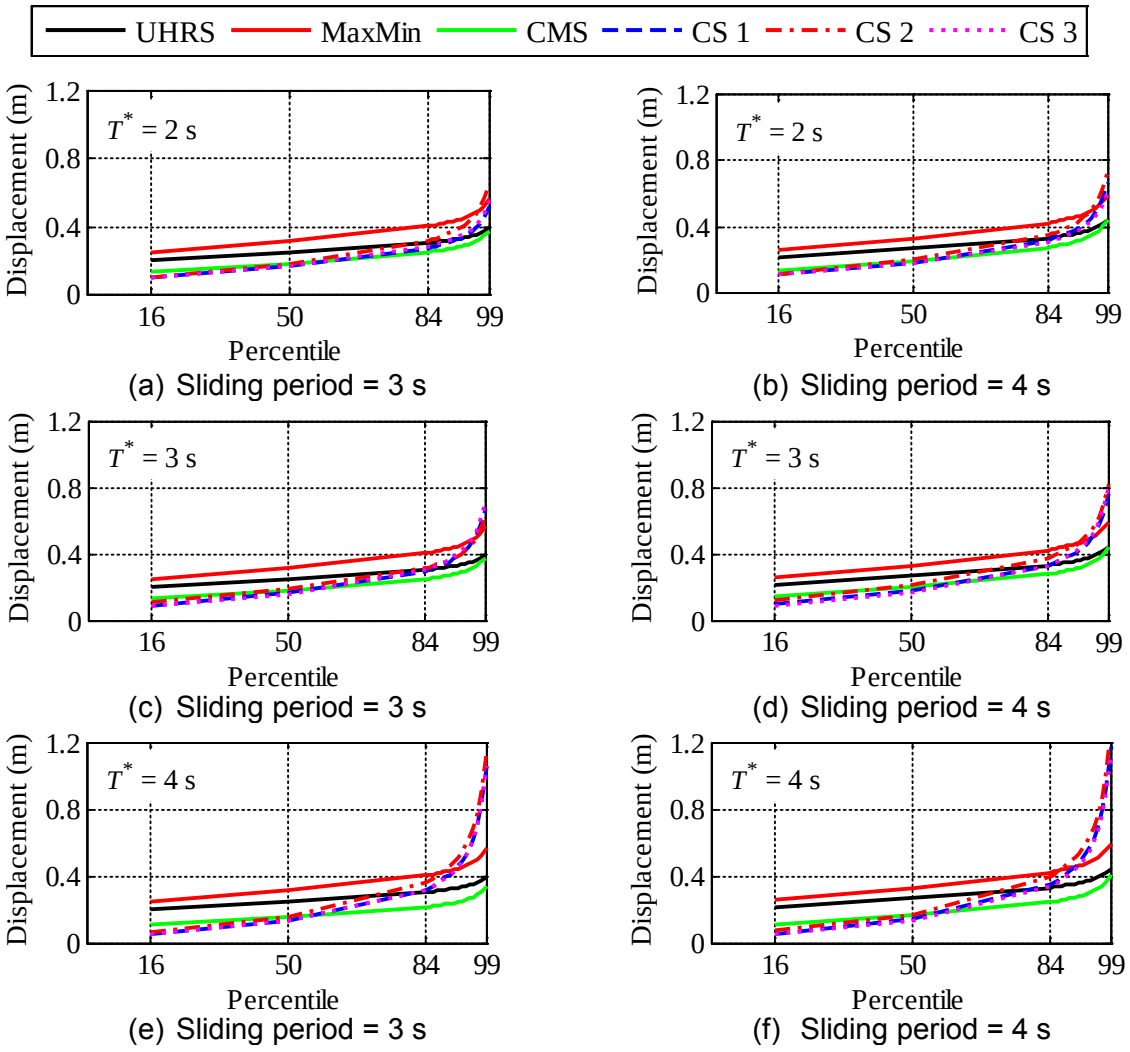

Figure 5-16 Distributions of Maximum Displacement of FP Bearings with a Coulomb-Type Coefficient of Friction of 0.1 and a Static Axial Pressure of 50 MPa Subjected to Ground Motions Consistent with Different Representations of 10,000-Year Shaking at the Diablo Canyon Site

[26] The 99th percentile displacements for the CMS-scaled motions differ by less than 2% from those for the UHRS-scaled motions, even though the CMS ordinates are considerably smaller than the UHRS ordinates at periods other than the conditioning period (see Figures 5-12 and 5-13). This is explained by the higher dispersion in the CMS-displacements. For example, the peak displacements of an FP bearing with a sliding period of 3 s and coefficient of friction of 0.1 subjected to the 30 UHRS-scaled motions range between 0.16 m and 0.36 m, with a median of 0.25 m. The displacements range between 0.087 m and 0.32 m, with a median of 0.18 m, for the bearing subjected to the 30 CMS-scaled motions with conditioning period of 3 s. Although the median CMS displacement is smaller than the median UHRS displacement, the greater dispersion (standard deviation of 0.059 m vs. 0.050 m) increases the 99th percentile displacement, computed assuming a lognormal distribution, to within 2% of the UHRS value.

Different representations of the 10,000-year seismic hazard at the site of the Diablo Canyon Nuclear Generating Station have been investigated: the traditional UHRS; a variant of the UHRS to account for differences in the two horizontal components of ground motions: UHRS-MaxMin; and the CMS and CS. Isolation-system displacements for the UHRS-MaxMin-scaled ground motions are greater than those for the other three representations at percentiles less than about 90. The displacements for the CMS- and CS- scaled motions are comparable at percentiles smaller than 80, especially for conditioning periods of 2 s and 3 s. The UHRS isolation-system displacements are greater than the CMS- and CS-displacements at percentiles smaller than 70, which is an expected result for nonlinear isolators such as the FP (and lead-rubber) bearings. The ratio of the displacements for CMS- or CS-scaled motions to the UHRS-scaled motions at a given percentile is a function of the conditioning period and the isolator sliding period.

5.5 100,000-Year Spectra, Ground Motions, Spectral Displacements and Isolator Displacements

5.5.1 UHRS, UHRS-MaxMin, CMS and CS

Figure 5-17 presents the UHRS for the Diablo Canyon site for return periods of 10,000 and 100,000 years and Site Class B per ASCE 7-10. The ratios of the spectral ordinates at the two return periods are plotted in Figure 5-18. The ratios are between 2.0 to 2.2 over a period range of 0.5 s to 4 s. The 100,000-year UHRS is reasonably well calculated by multiplying the 10,000-year UHRS by 2.1. The UHRS-MaxMin spectra consistent with the 100,000-year hazard are also obtained by amplitude scaling the 10,000-year UHRS-MaxMin spectra[27] by a factor of 2.1.

Figures 5-19(a), 5-19(b) and 5-19(c) present the magnitude, source-to-site distance and ε, respectively, for a range of return periods and natural structural periods, corresponding to the Campbell and Bozorgnia (2008) GMPE (data obtained from http://geohazards.usgs.gov/deaggint/2008/, June 15, 2014). The magnitude, distance and ε each trend to constant values at longer return periods. For a period of 2 s, the magnitude corresponding to 75-year return period is 6.19, which increases to 6.66 for a 10,000-year return period and to 6.72 for 20,000-year return period. The corresponding values for source-to-site distance are 34.7 km, 5.7 km and 4.8 km, respectively, and for ε are 0.63, 1.88 and 2.02. Only ε changes appreciably at the longer return periods. Assuming that the magnitude and distance for a 100,000-year return period are equal to those for a 20,000-year return period (the greatest return period for which USGS data are available), the values of ε for 100,000-year hazard at periods of 2 s, 3 s and 4 s are 2.85, 2.91 and 2.84, respectively, which are considerably greater than the values of 2.02, 2.08 and 2.08, respectively, for a return period of 10,000 years.

Conditional mean spectra with a conditioning period of 3 s are plotted in Figure 5-20 for return periods of 10,000 and 20,000 years for Diablo Canyon. Also plotted in the figure is the 10,000-year CMS increased by a factor of 1.26. The spectral ordinate of the scaled 10,000-year CMS is equal to that for the 20,000-year CMS at the conditioning period, and is greater than that for the 20,000-year CMS at other periods. The shape of the CMS at a given conditioning period

[27] The distributions of amplitude scaling factors in the two directions are assumed identical for the two return periods.

is a function of the hazard level and the shape of a CMS can be expected to be sharper at the conditioning period at greater hazard levels: an attribute of positive epsilon motions identified by Baker and Cornell (2006).

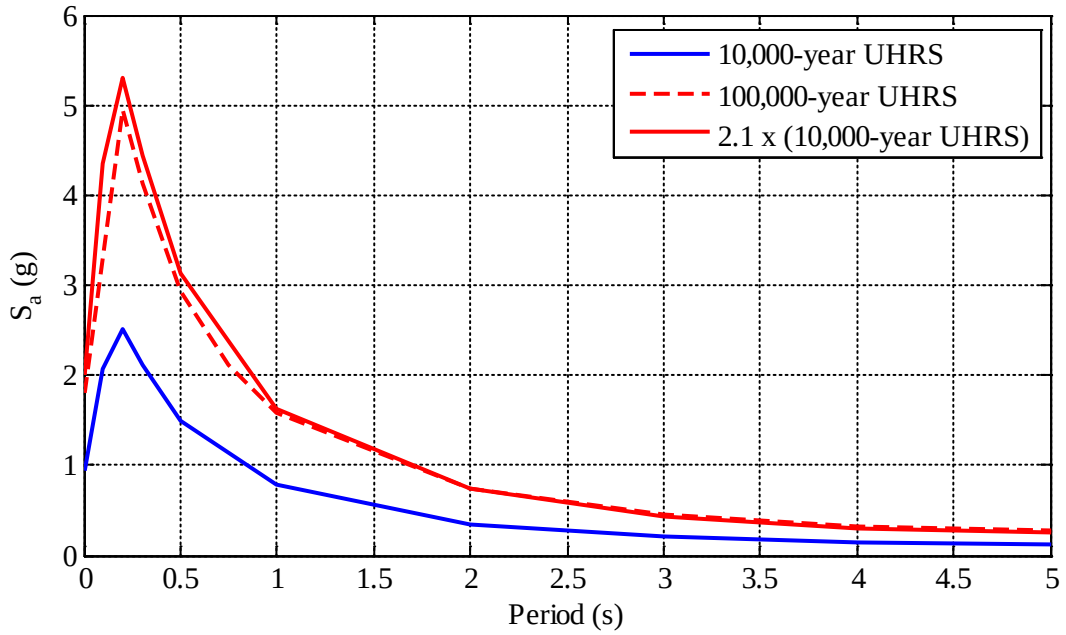

Figure 5-17 10,000- and 100,000-Year Return Period UHRS for Diablo Canyon Site

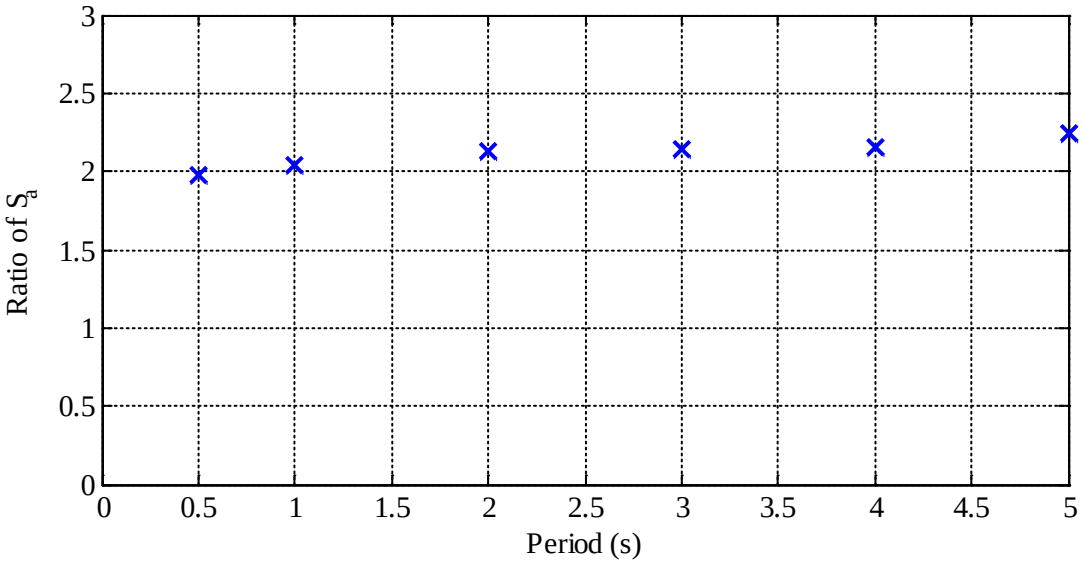

Figure 5-18 Ratio of Spectral Ordinates of the UHRS at 100,000 Years to 10,000 Years at the Diablo Canyon Site

The USGS website does not provide CMS for a return period of 100,000 years. In this study, 100,000-year CMS are obtained by amplitude scaling the corresponding 10,000-year CMS by 2.1 (see Section 5.5.1), which is a conservative representation of the seismic hazard (see for example Figure 5-20) for periods other than the conditioning period.

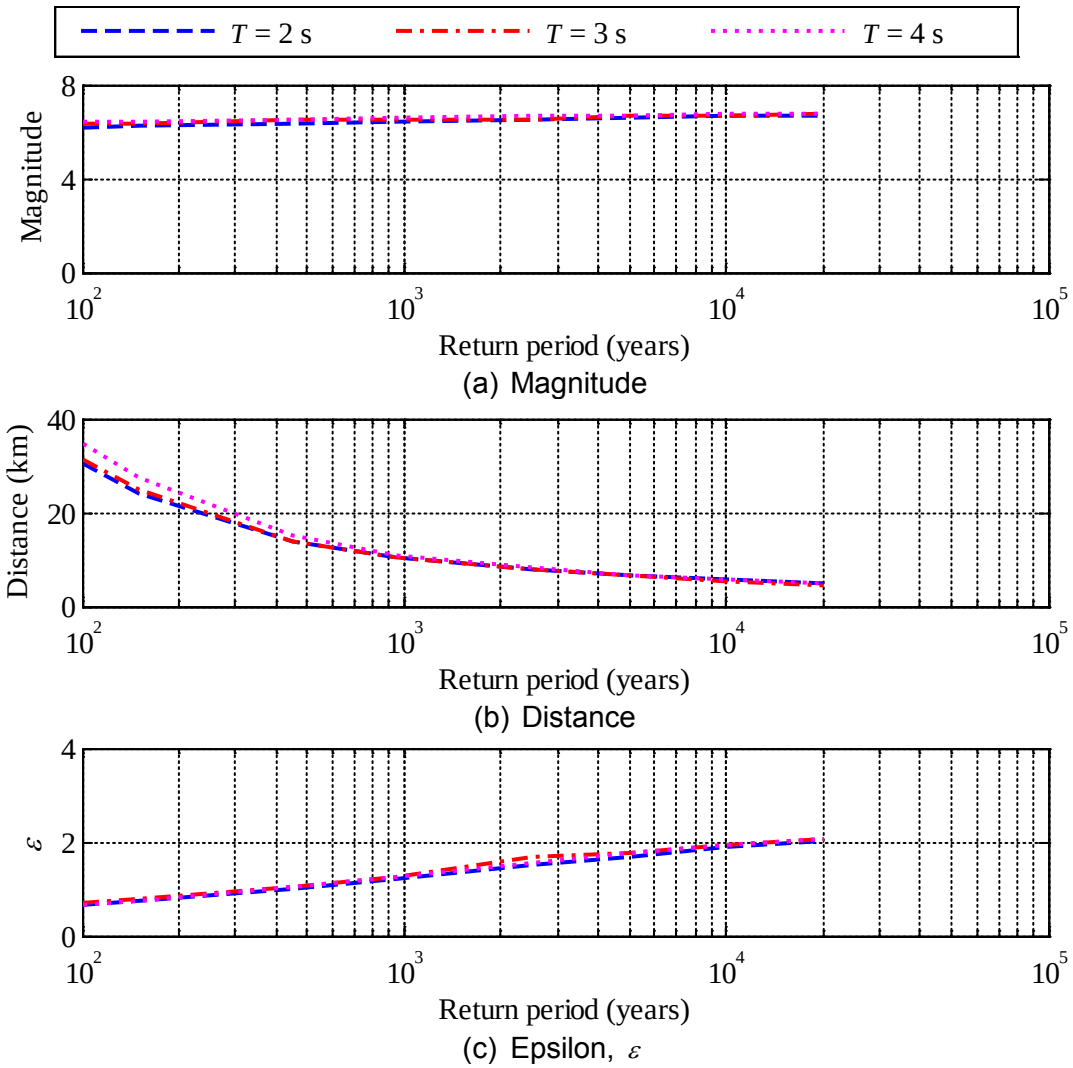

Figure 5-19 Combinations of Magnitude, Source-to-Site Distance, and ε for the Diablo Canyon Site

As noted previously, the CS account for the variability in the CMS ordinates at periods other than the conditioning period. The variability is a function of the parameters of the earthquake (M and R) and the correlations between ε at different periods (see for example Jayaram *et al.* (2011), Baker and Jayaram (2008)). The correlation coefficient between ε at two periods is a function only of the two periods and not of the values of ε at the two periods. Therefore, the distributions of the CS ordinates at periods other than the conditioning period are controlled by M and R but not ε. Since the disaggregated M and R are not considerably different for the 10,000-year and 100,000-year return periods (see Figure 5-19), the distributions of the CS ordinates at different periods are expected to be comparable at the two hazard levels.

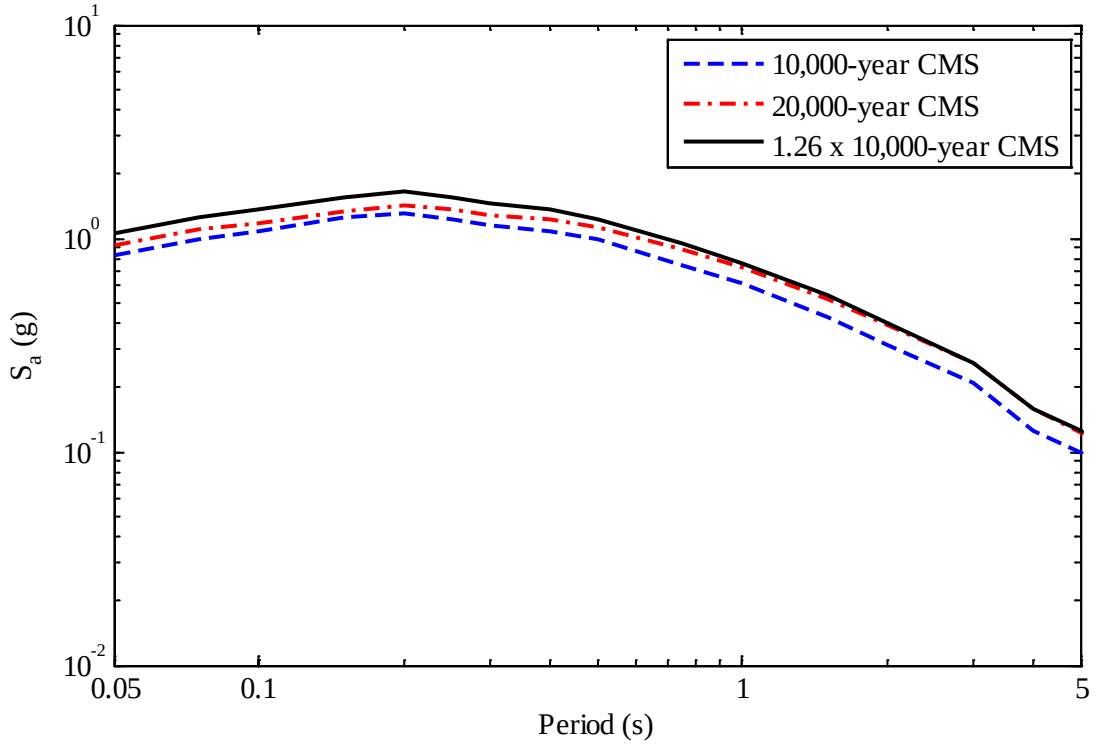

Figure 5-20 Conditional Mean Spectra a Conditioning Period of 3 s for Seismic Hazards with the Return Periods of 10,000 and 20,000 Years

The information necessary to generate 100,000-year CS are not available on the USGS website and they are obtained instead by amplitude scaling the corresponding 10,000-year CS. Noting that the shape of the CMS becomes sharper at the conditioning period as the return period is increased, and thus an increased ε given constant values of M and R, the CS obtained by amplitude scaling are likely conservative for the 100,000-year return period. Accordingly, the 100,000-year CS are obtained by amplitude scaling the corresponding 10,000-year CS by a factor of 2.1.

5.5.2 Ground Motions

The 100,000-year UHRS (UHRS-MaxMin) ground motions are obtained by amplitude scaling the 10,000-year UHRS (UHRS-MaxMin) ground motions by a factor of 2.1. The ground motions consistent with the 100,000-year CMS (CS) for the conditioning periods of 2 s, 3 s and 4 s are obtained by amplitude scaling the corresponding 10,000-year CMS (CS) ground motions by a factor of 2.1.

5.5.3 Spectral Displacements

Since the 100,000-year UHRS, UHRS-MaxMin, CMS and CS are developed by amplitude scaling the corresponding 10,000-year response spectra, the spectral displacements for the 100,000-year ground motions are obtained by amplitude scaling the spectral displacements for the 10,000-year ground motions (Figures 5-12 and 5-13) by 2.1.

5.5.4 Response of FP Bearings

Figure 5-16 presented the distributions of peak horizontal displacement of FP bearings with sliding periods of 3 s and 4 s, a Coulomb-type coefficient of friction of 0.1, and a static axial pressure of 50 MPa, subjected to ground motions representing a return period of 10,000 years. Figure 5-21 presents the corresponding distributions for a return period of 100,000 years. The general trends in the distributions of the peak displacements are similar. These distributions are studied further in the following section.

5.6 Response of FP Bearings to 10,000- and 100,000-Year Ground Motions

The 50th, 90th and 99th percentile displacements from Figure 5-16 (10,000-year hazard) and Figure 5-21 (100,000-year hazard) are compared in Figures 5-22 and 5-23 for the 3 s and 4 s FP bearings, respectively.

Figure 5-22(a) presents the median responses of an FP bearing with a sliding period of 3 s subjected to ground motions consistent with 10,000-year UHRS, UHRS-MaxMin, CMS and CS. The median responses are greatest for the UHRS-MaxMin-scaled motions followed by the UHRS-scaled motions. The responses for CMS- and CS-scaled motions are comparable. The median responses for the 100,000-year ground motions presented in Figure 5-22(b) follow a similar trend to the responses for the 10,000-year ground motions. Figures 5-22(c) and 5-22(d) present the 90th percentile responses for 10,000-year and 100,000-year ground motions, respectively. The UHRS-MaxMin responses exceed those for the UHRS-scaled, and CMS- and CS-scaled motions with conditioning periods of 2 s and 3 s. The responses for the CS-scaled motions with a conditioning period of 4 s are either similar or greater than those for the UHRS-MaxMin motions. Figure 5-22(e) presents the 99th percentile responses for the 10,000-year ground motions. The responses for CS-scaled motions are considerably greater than those for the UHRS-MaxMin-scaled motions, especially for the conditioning period of 4 s[28]. The responses for UHRS-scaled motions are virtually identical to those for the CMS-scaled motions. Figure 5-23 presents the companion results for the 4 s FP bearing. The general trends in the two figures are similar.

The 90th percentile peak displacements corresponding to a return period of 100,000 years are greater than the 99th percentile peak displacements corresponding to a return period of 10,000 years, regardless of the choice of target spectra (UHRS, UHRS-MaxMin, CMS or CS). Therefore, the 90th percentile displacement for the 100,000-year earthquake shaking will determine the clear distance between the isolated superstructure and surrounding stop. At percentiles less than 90, the responses for UHRS-MaxMin motions are greater than those for the other three representations of seismic hazard. The 90th percentile peak displacements for the 100,000-year (and 10,000-year) earthquake shaking calculated using UHRS-MaxMin-scaled ground motions exceed those for the UHRS-scaled motions by a factor of between 1.2 and 1.4. The 90th percentile responses for the CMS-scaled (CS-scaled) motions, with conditioning periods of 2 s and 3 s, differ from those for the UHRS-scaled motions by between 2% and 16% (0% and 26%), at the two hazard levels.

[28] The choice of conditioning period of 4 s for the sliding period of 3 s would be poor because the effective period of the isolation system will always be less than 3 s.

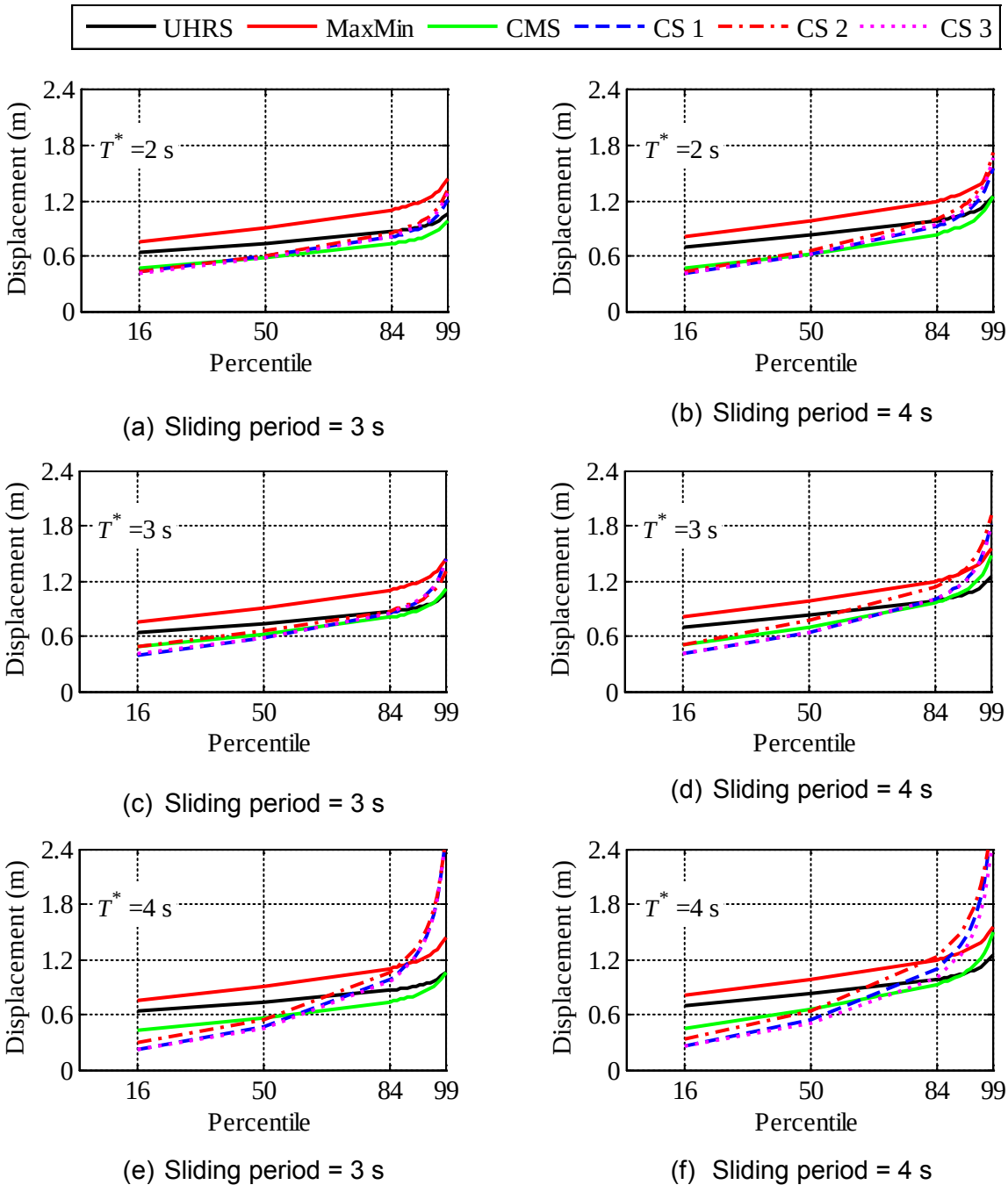

Figure 5-21 Distributions of Maximum Displacement of FP Bearings with a Coulomb-Type Coefficient of Friction of 0.1 and a Static Axial Pressure of 50 MPa Subjected to Ground Motions Consistent with Different Representations of 100,000-Year Shaking at the Diablo Canyon Site

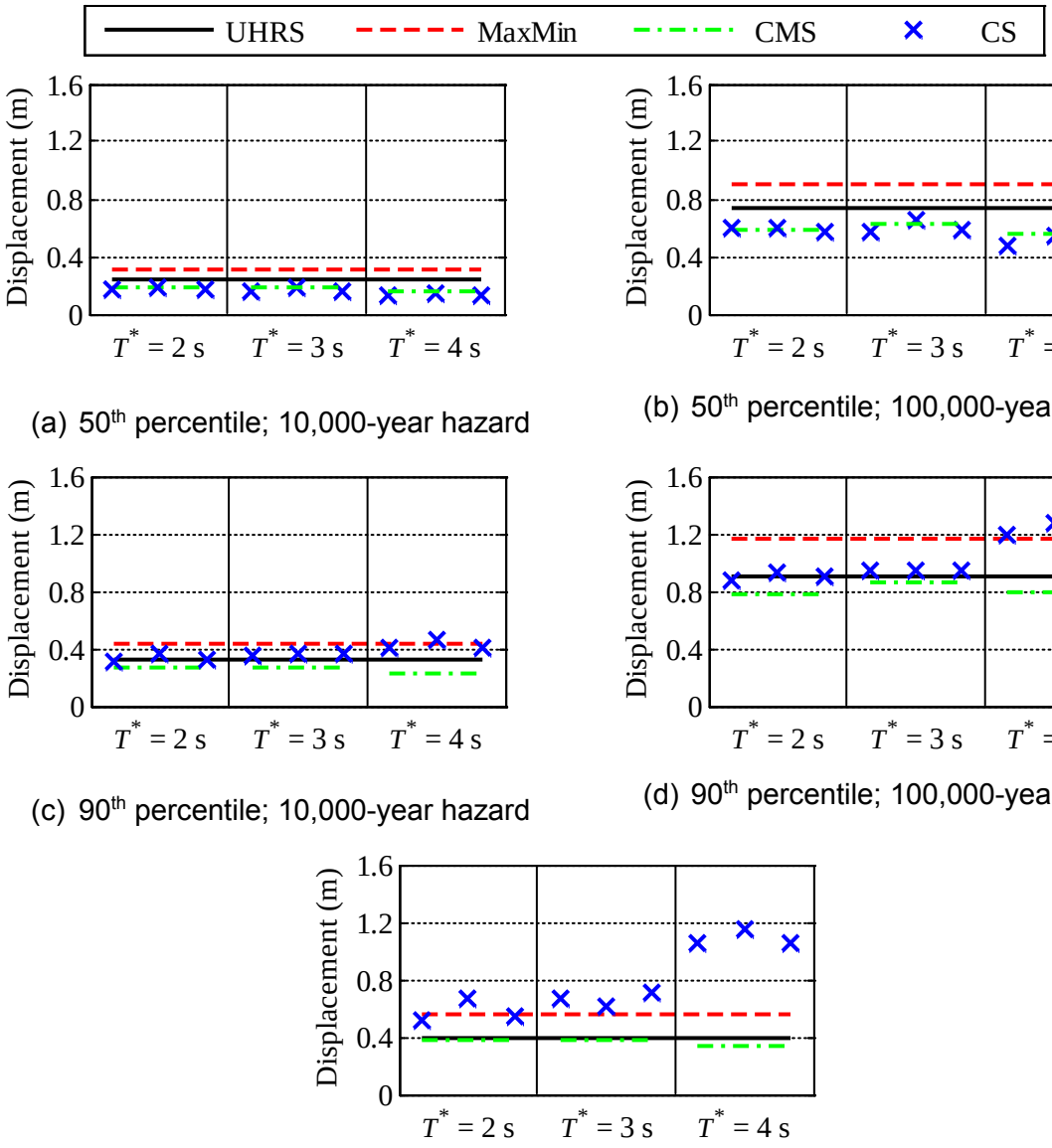

(a) 50th percentile; 10,000-year hazard

(b) 50th percentile; 100,000-year hazard

(c) 90th percentile; 10,000-year hazard

(d) 90th percentile; 100,000-year hazard

(e) 99th percentile; 10,000-year hazard

Figure 5-22 Median, 90th and 99th Percentile Peak Displacement Responses of an FP Bearing with a Sliding Period of 3 s Subjected to 10,000-Year and 100,000-Year UHRS-, UHRS-MaxMin-, CMS- and CS-Scaled Ground Motions

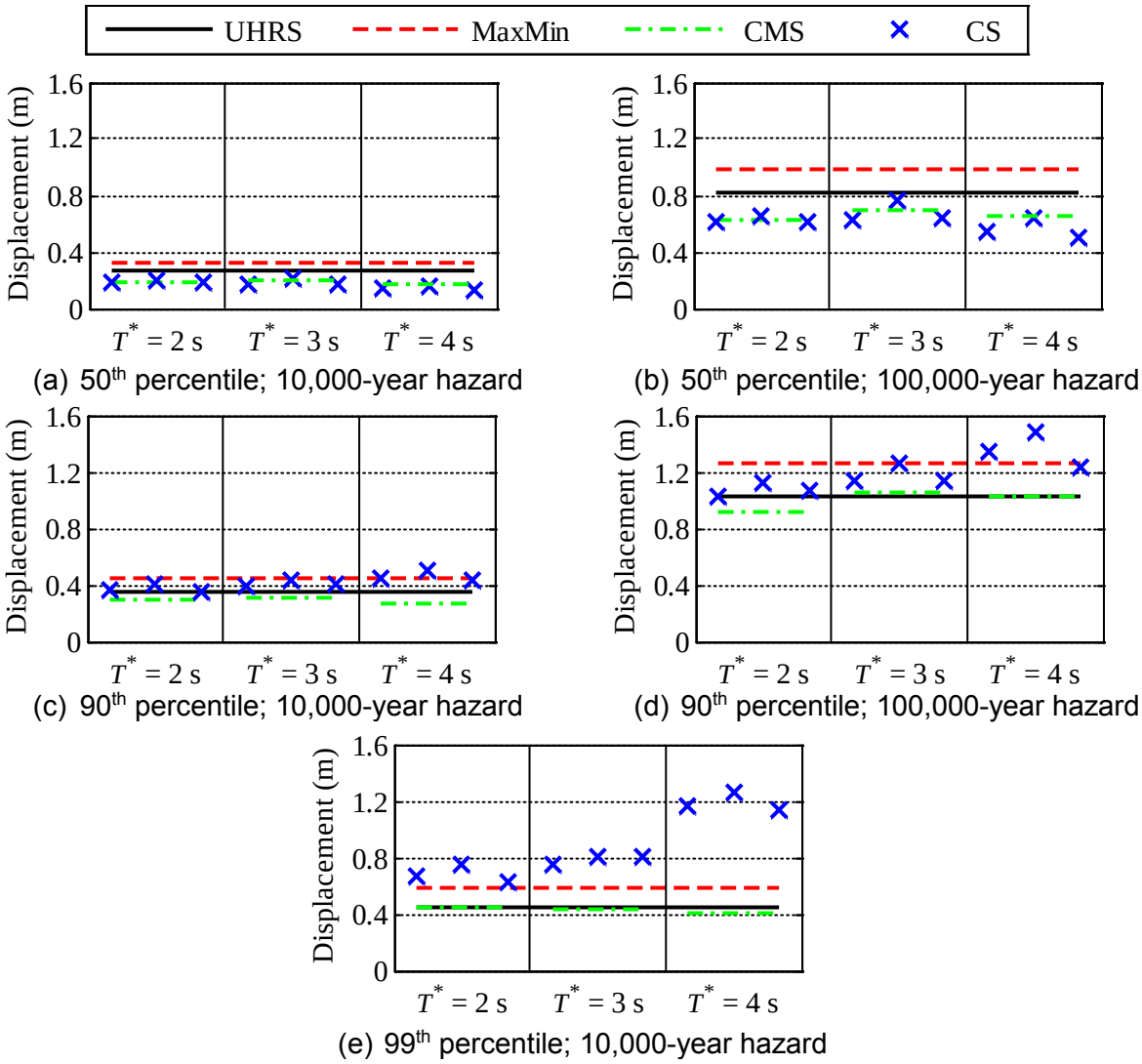

Figure 5-23 Median, 90th and 99th Percentile Peak Displacement Responses of an FP Bearing with a Sliding Period of 4 s Subjected to 10,000-Year and 100,000-Year UHRS-, UHRS-MaxMin-, CMS- and CS-Scaled Ground Motions

Figures 5-22 and 5-23 present the response of FP bearings with sliding periods of 3 s and 4 s, static axial pressure of 50 MPa, and a Coulomb-type coefficient of friction of 0.1, subjected to the sets of ground motions consistent with the four representations of 10,000-year and 100,000-year earthquake shaking. To determine if the conclusions drawn from these results are broadly applicable, single FP bearings with a sliding period of 3 s, reference coefficients of friction of 0.06 and 0.1, static axial pressures of 10 MPa and 50 MPa, and friction at the sliding surface described using both the Coulomb model and the *p-T-v* model, are subjected to all of the ground motions of Sections 5.4 and 5.5, except for the CS-scaled motions with a conditioning period of 4 s (the displacements of the FP bearings subjected to the 100,000-year CS-scaled motions with a conditioning period of 4 s exceed, for some ground motions, the radius of curvature of the bearing, leading to numerical problems). The 50th, 90th and 99th percentiles peak displacements are presented in Figures 5-24 through 5-31. The observations made on the results presented in Figures 5-22 and 5-23 for the 3 s and 4 s FP bearings are also

applicable to the 3 s FP bearings, irrespective of the axial pressure on the bearing, the choice of friction model, and/or to hazard level. These observations are summarized below:

i. The peak horizontal displacement responses of FP bearings are most significantly influenced by the choice of target spectra: UHRS, UHRS-MaxMin, CMS or CS.
ii. Three sets of 30 ground motions were matched to each CS set. The choice of seed ground motions was found to have an insignificant effect on the response, compared with the choice of the target spectra.
iii. The median peak horizontal displacements are greatest for the UHRS-MaxMin-scaled ground motions followed by UHRS-scaled motions. The median responses to the CMS- and CS-scaled motions are similar.
iv. At the 90th percentile, the peak horizontal displacements for
    a. the CMS-scaled motions with conditioning periods of 2 s and 3 s differ by between 2% and 16% from those for the UHRS-scaled motions, and
    b. the UHRS-MaxMin-scaled motions are greater than those for other three representations of seismic hazard.
v. At the 99th percentile, the peak horizontal displacement for 10,000-year shaking for
    a. the CMS-displacements differ from those for the UHRS-displacements by up to 9%.
    b. the UHRS-MaxMin motions are substantially greater than those for the UHRS- or CMS-scaled motions.
vi. The 90th percentile peak horizontal displacement for 100,000-year shaking is greater than the 99th percentile peak horizontal displacement for 10,000-year shaking, for a given choice of target spectrum.
vii. The 90th percentile peak horizontal displacements for the UHRS-MaxMin-scaled motions are approximately 1.3 times those for the UHRS-scaled motions for both 10,000- and 100,000-year shaking.
viii. The 90th percentile peak displacement of an FP bearing with friction defined using the *p-T-v* model subjected to the UHRS-MaxMin-motions is greater than that of an FP bearing with friction defined using the Coulomb model subjected to the UHRS-motions by a factor of between 1.4 and 1.7 (1.3 and 1.5) for 10,000-year (100,000-year) shaking, for all combinations of static axial pressure and reference coefficient of friction. The factor increases with increases in static axial pressure from 10 MPa to 50 MPa and reference coefficient of friction from 0.06 to 0.1.

5.7 Conclusions

The following conclusions are drawn from the results of the response-history analyses performed on single FP bearings with a range of properties subjected to ground motions consistent with return periods of 10,000 years and 100,000 years at the site of Diablo Canyon Nuclear Generating Station:

i. The UHRS should be used as the target spectrum with explicit consideration of the differences between the orthogonal horizontal components of the ground motions: UHRS-MaxMin ground motions.

ii. An important design parameter for a seismic isolation system is the clearance to the stop, which is required to be greater than the 99th (90th) percentile peak displacement for 10,000-year (100,000-year) shaking. The 90th percentile peak displacement for the 100,000-year shaking is consistently greater than the 99th percentile peak displacement

for the 10,000-year shaking. A smaller set of ground motions (e.g., 30) can be used to compute a 90th percentile displacement than would be needed to compute a 99th percentile displacement.

iii. The 90th percentile peak displacement of an FP bearing with friction described using *p-T-v* model subjected to 100,000-year UHRS-MaxMin motions can be estimated by multiplying the median displacement of an FP bearing with friction described by the Coulomb model, subjected to the 10,000-year UHRS motions, by a factor of between 3.4 and 4.3, that depends on the static axial pressure and the reference coefficient of friction.

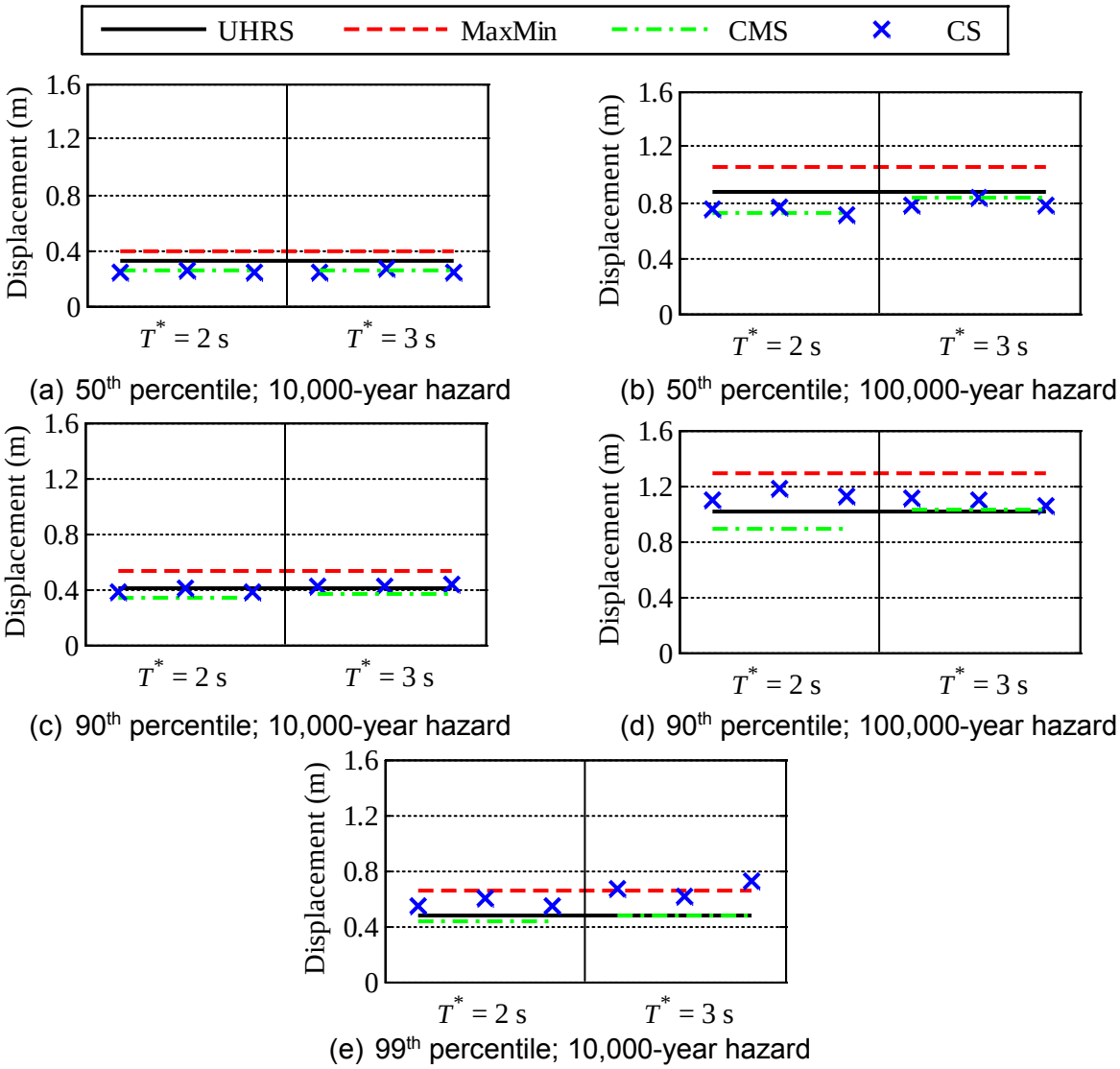

(a) 50th percentile; 10,000-year hazard

(b) 50th percentile; 100,000-year hazard

(c) 90th percentile; 10,000-year hazard

(d) 90th percentile; 100,000-year hazard

(e) 99th percentile; 10,000-year hazard

Figure 5-24 Median, 90th and 99th Percentile Peak Displacement Responses of an FP Bearing with a Sliding Period of 3 s, Static Axial Pressure of 10 MPa, Reference Coefficient of Friction of 0.06, and Coulomb Friction Model, Subjected to 10,000-Year and 100,000-Year UHRS-, UHRS-MaxMin-, CMS- and CS-Scaled Ground Motions

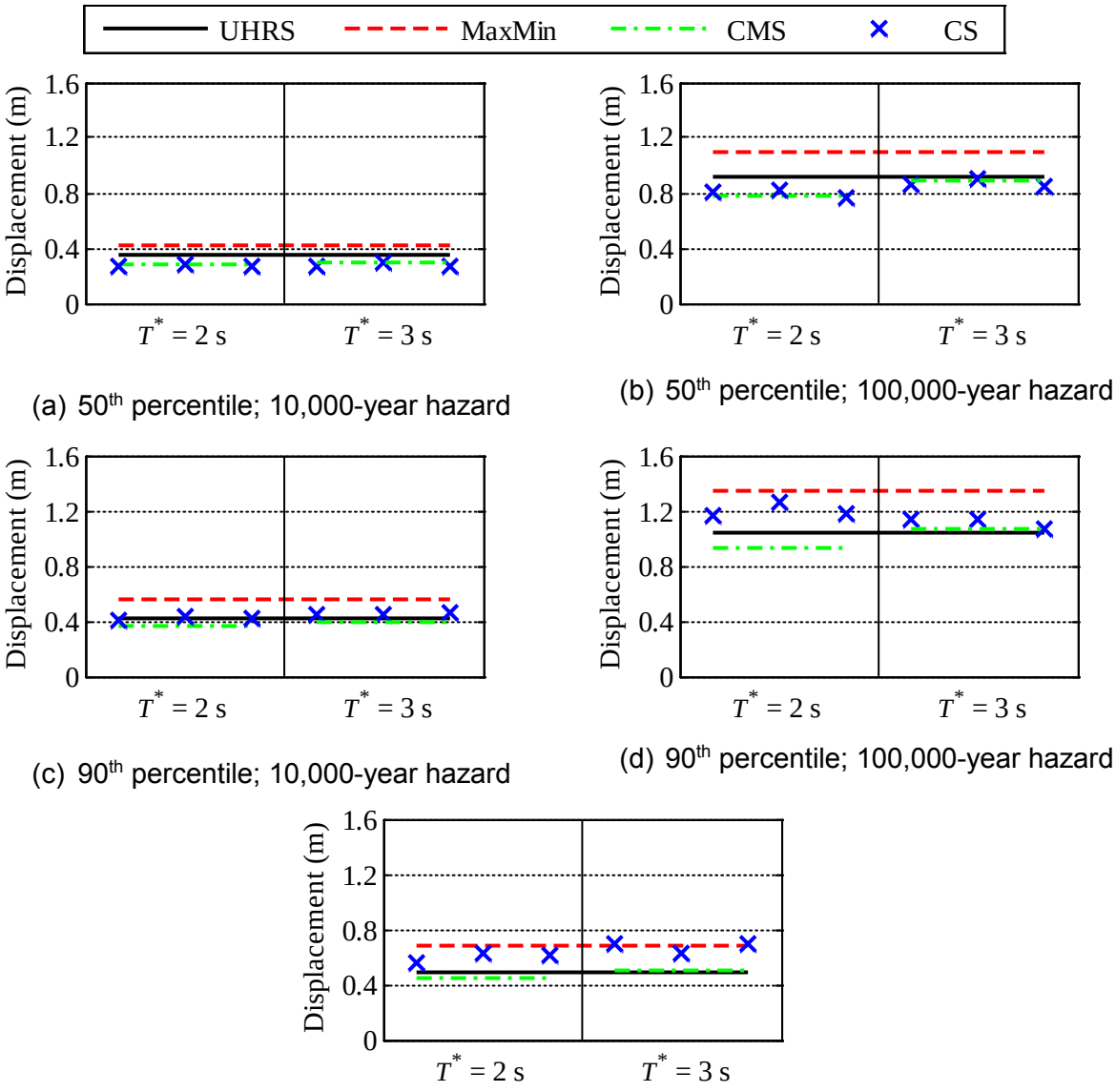

(a) 50th percentile; 10,000-year hazard

(b) 50th percentile; 100,000-year hazard

(c) 90th percentile; 10,000-year hazard

(d) 90th percentile; 100,000-year hazard

(e) 99th percentile; 10,000-year hazard

Figure 5-25 Median, 90th and 99th Percentile Peak Displacement Responses of an FP Bearing with a Sliding Period of 3 s, Static Axial Pressure of 10 MPa, Reference Coefficient of Friction of 0.06, and *p-T-v* Friction Model, Subjected to 10,000-Year and 100,000-Year UHRS-, UHRS-MaxMin-, CMS- and CS-Scaled Ground Motions

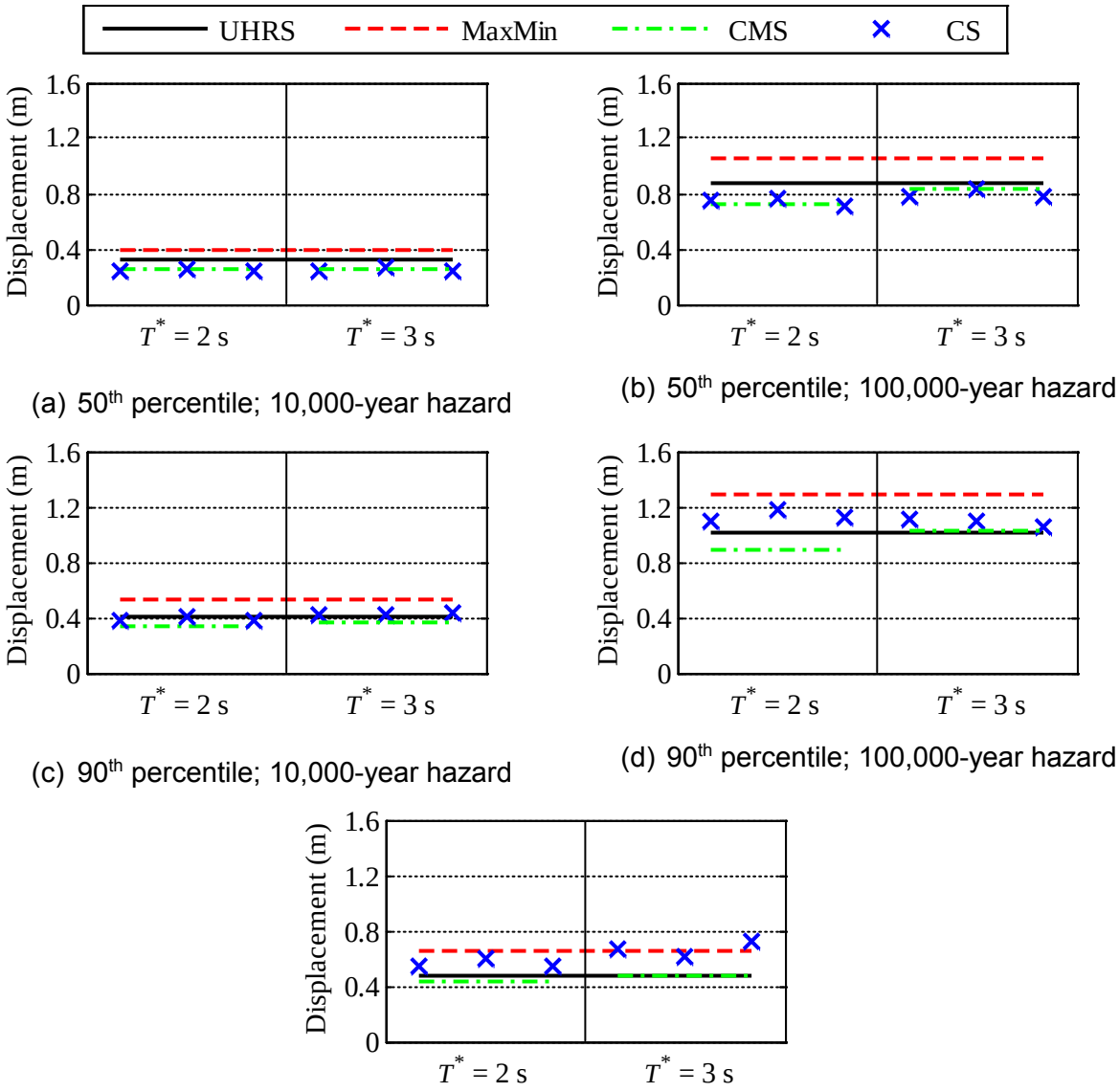

(a) 50th percentile; 10,000-year hazard

(b) 50th percentile; 100,000-year hazard

(c) 90th percentile; 10,000-year hazard

(d) 90th percentile; 100,000-year hazard

(e) 99th percentile; 10,000-year hazard

Figure 5-26 Median, 90th and 99th Percentile Peak Displacement Responses of an FP Bearing with a Sliding Period of 3 s, Static Axial Pressure of 50 MPa, Reference Coefficient of Friction of 0.06, and Coulomb Friction Model, Subjected to 10,000-Year and 100,000-Year UHRS-, UHRS-MaxMin-, CMS- and CS-Scaled Ground Motions

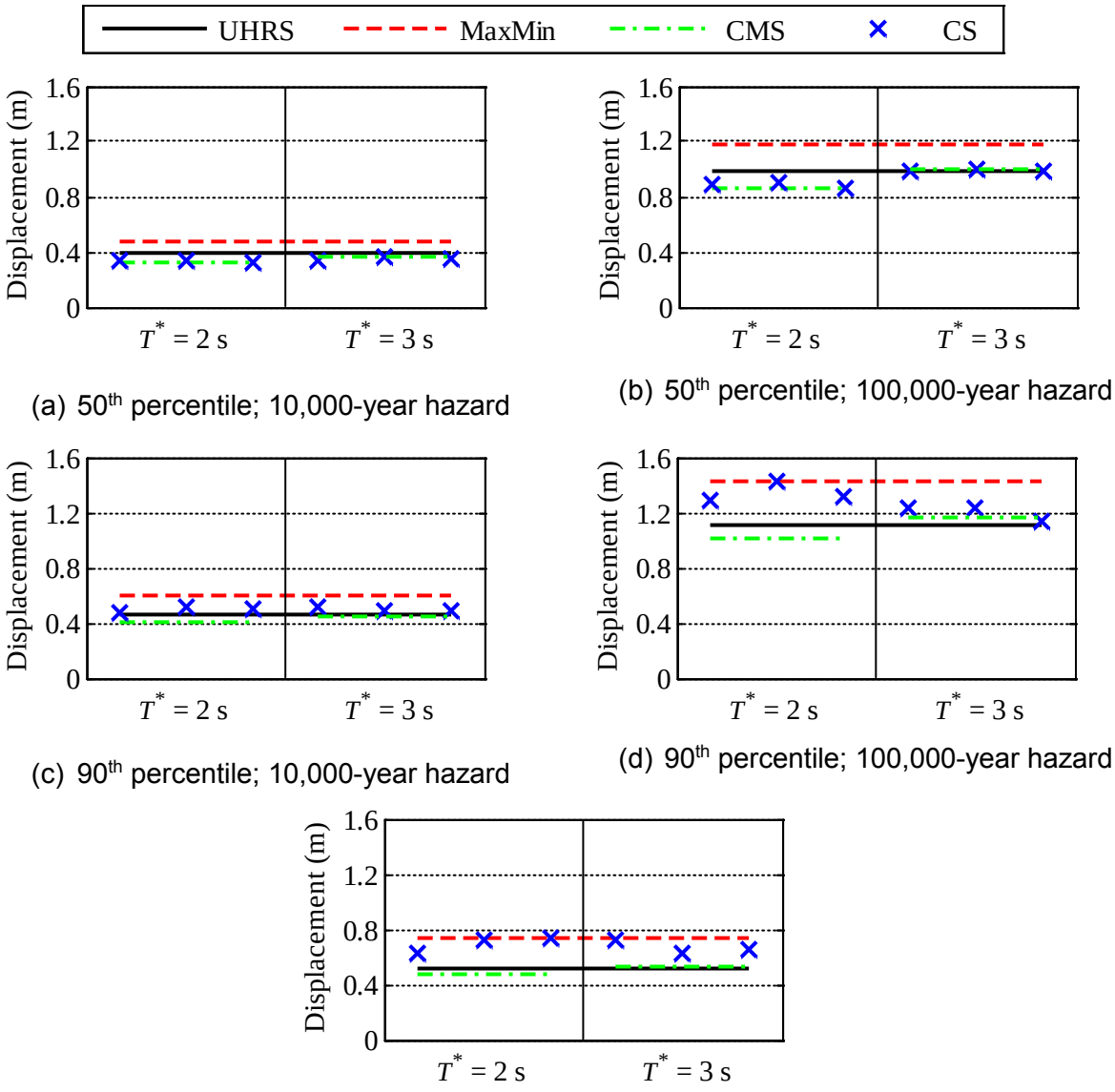

(a) 50th percentile; 10,000-year hazard

(b) 50th percentile; 100,000-year hazard

(c) 90th percentile; 10,000-year hazard

(d) 90th percentile; 100,000-year hazard

(e) 99th percentile; 10,000-year hazard

Figure 5-27 Median, 90th and 99th Percentile Peak Displacement Responses of an FP Bearing with a Sliding Period of 3 s, Static Axial Pressure of 50 MPa, Reference Coefficient of Friction of 0.06, and *p-T-v* Friction Model, Subjected to 10,000-Year and 100,000-Year UHRS-, UHRS-MaxMin-, CMS- and CS-Scaled Ground Motions

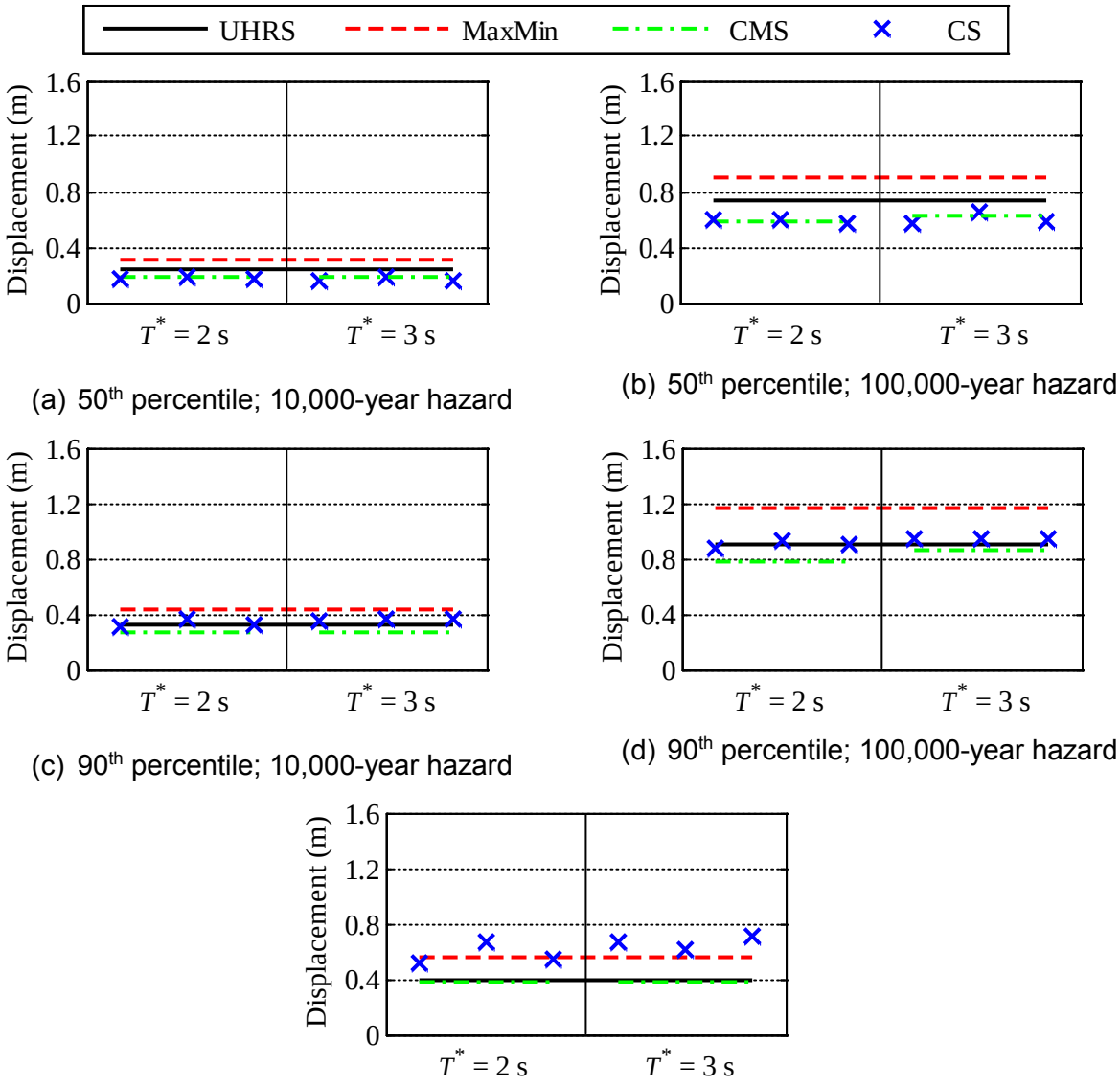

(a) 50th percentile; 10,000-year hazard

(b) 50th percentile; 100,000-year hazard

(c) 90th percentile; 10,000-year hazard

(d) 90th percentile; 100,000-year hazard

(e) 99th percentile; 10,000-year hazard

Figure 5-28 Median, 90th and 99th Percentile Peak Displacement Responses of an FP Bearing with a Sliding Period of 3 s, Static Axial Pressure of 10 MPa, Reference Coefficient of Friction of 0.1, and Coulomb Friction Model, Subjected to 10,000-Year and 100,000-Year UHRS-, UHRS-MaxMin-, CMS- and CS-Scaled Ground Motions

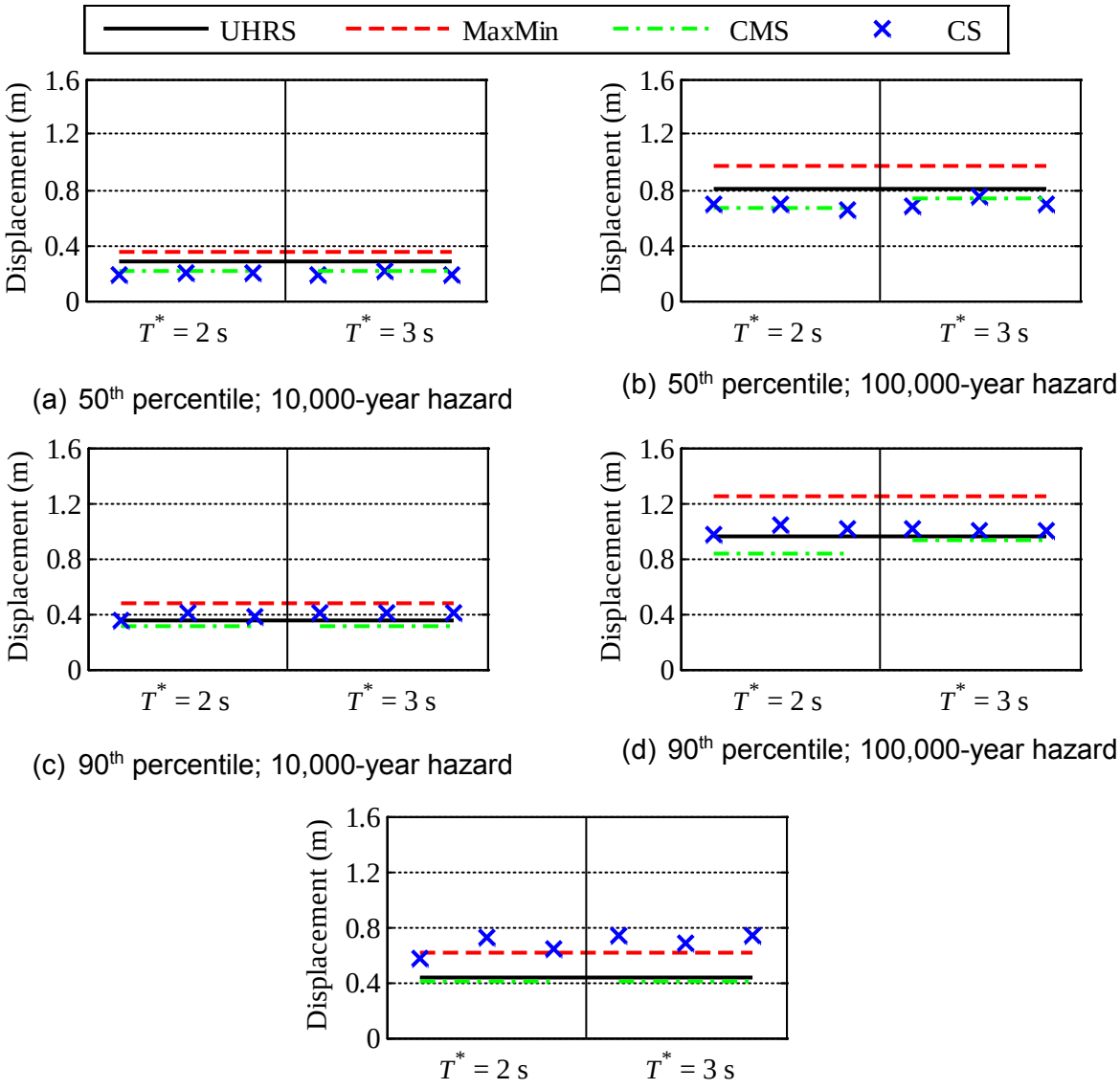

Figure 5-29 Median, 90th and 99th Percentile Peak Displacement Responses of an FP Bearing with a Sliding Period of 3 s, Static Axial Pressure of 10 MPa, Reference Coefficient of Friction of 0.1, and *p-T-v* Friction Model, Subjected to 10,000-Year and 100,000-Year UHRS-, UHRS-MaxMin-, CMS- and CS-Scaled Ground Motions

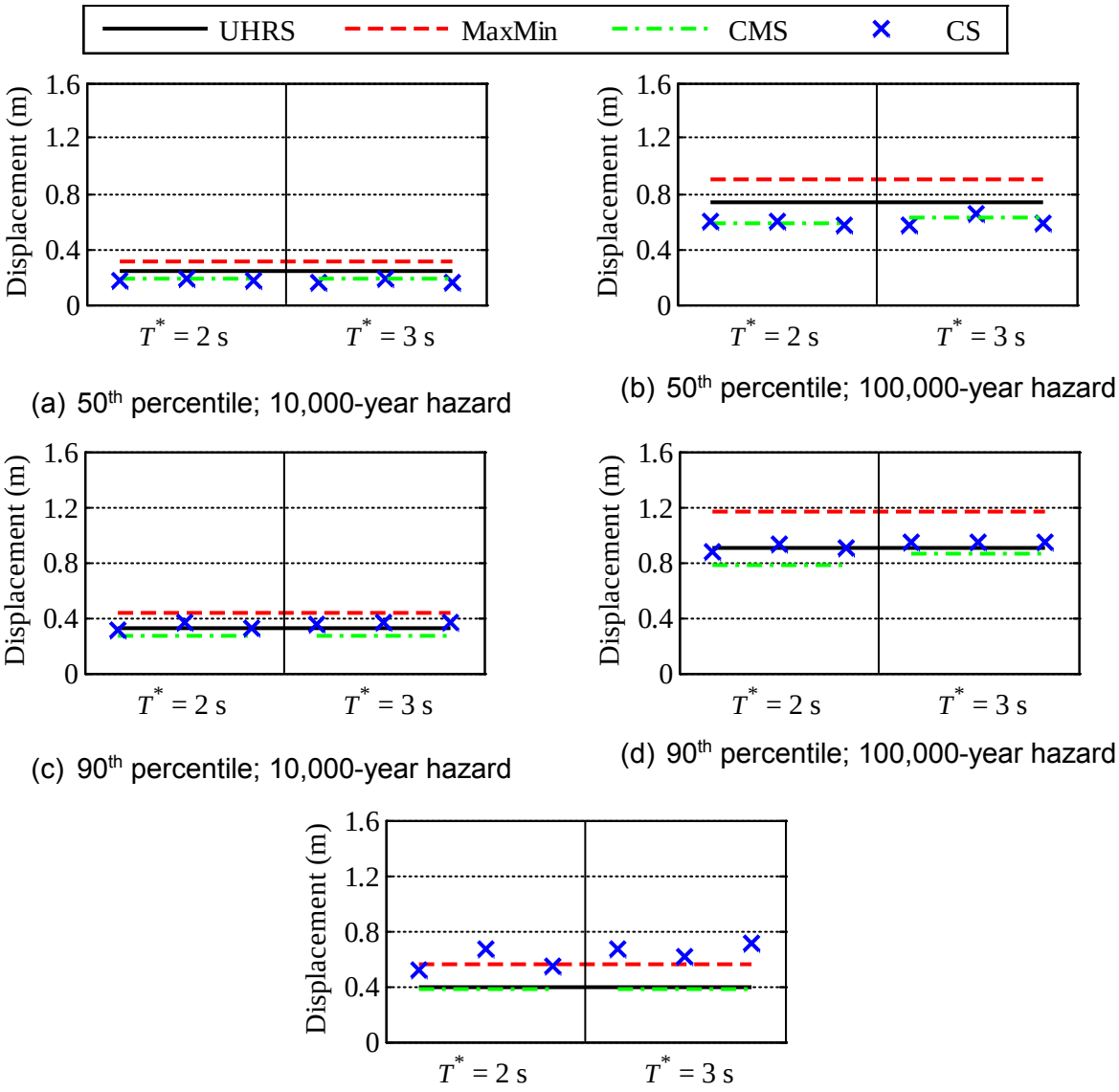

Figure 5-30 Median, 90th and 99th Percentile Peak Displacement Responses of an FP Bearing with a Sliding Period of 3 s, Static Axial Pressure of 50 MPa, Reference Coefficient of Friction of 0.1, and Coulomb Friction Model, Subjected to 10,000-Year and 100,000-Year UHRS-, UHRS-MaxMin-, CMS- and CS-Scaled Ground Motions

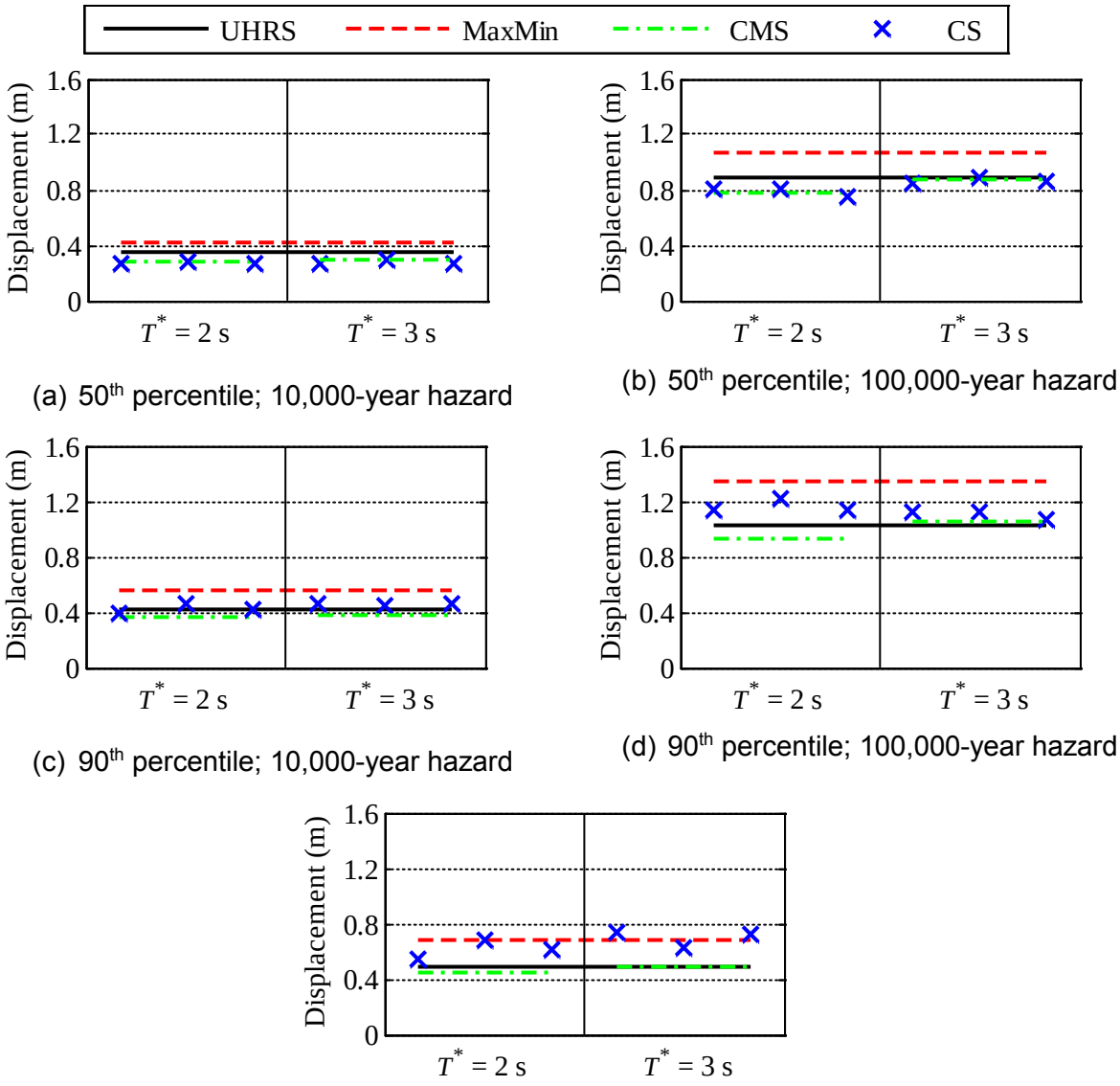

Figure 5-31 Median, 90th and 99th Percentile Peak Displacement Responses of an FP Bearing with a Sliding Period of 3 s, Static Axial Pressure of 50 MPa, Reference Coefficient of Friction of 0.1, and *p-T-v* Friction Model, Subjected to 10,000-Year and 100,000-Year UHRS-, UHRS-MaxMin-, CMS- and CS-Scaled Ground Motions

6 SEISMIC HAZARD DEFINITIONS FOR NUCLEAR POWER PLANTS

6.1 Introduction

The seismic design of a conventional (or fixed-base) nuclear structure is performed using a graded approach outlined in ASCE 43-05 (ASCE, 2005) entitled "Seismic design criteria for structures, systems, and components and nuclear facilities". Five seismic design categories (SDCs) and four limit states are identified. The target annual frequencies of unacceptable performance are smaller for higher SDCs. The four limit states, A through D, refer to large, moderate and limited permanent deformations, and essentially elastic behavior, respectively. Seismic design categories 3, 4 and 5 are addressed in ASCE 43-05. A nuclear structure, system or component is assigned an SDC according to ANSI/ANS 2.26 (ANS, 2010). Nuclear power plants are assigned to SDC 5.

The seismic hazard for the analysis and design of *conventional* (or fixed-base) nuclear structures is defined as the product of a uniform hazard response spectrum (UHRS) at a SDC-based mean annual frequency of exceedance (MAFE) and a design factor (e.g., RG 1.208 (USNRC, 2007a), ASCE (2005)). Two levels of seismic hazard will be considered for the analysis and design of seismically *isolated* nuclear structures: 1) a design basis earthquake per ASCE 43-05 and ASCE 4-16 (ASCE, 2017) and a ground motion response spectrum (GMRS) per RG 1.208, and 2) a beyond design basis earthquake per ASCE 4 and a beyond design basis GMRS per Kammerer et al. (2019). The hazard definitions and performance goals for conventional and isolated nuclear power plants are studied in this chapter, with the objective of determining design factors for seismically isolated nuclear power plants. Design factors for other isolated safety-related nuclear structures are not calculated.

Seismic hazard curves for eight sites of nuclear facilities in the United States are presented in Section 6.2. The definitions of seismic hazard and performance goals for conventional and seismically isolated nuclear power plants are discussed in Sections 6.3 and 6.4, respectively. Seismic hazard definitions for conventional and seismically isolated nuclear power plants are compared in Section 6.5. The total annual frequencies of unacceptable performance for the isolated superstructure, individual isolators and umbilical lines are estimated in Section 6.6 for a seismically isolated nuclear power plant at each of the eight sites. Companion risk calculations for Department of Energy-regulated isolated nuclear structures are presented in Appendix F. Design factors are determined in Section 6.7.

6.2 Seismic Hazard at the Site of Nuclear Facilities in the United States

Figure 6-1 presents seismic hazard curves (spectral acceleration versus MAFE) at eight sites of nuclear facilities across the United States (see Figure 6-2) for four periods: 0.1 s, 0.2 s, 1 s and 2 s and 5% damping. The data are downloaded from the USGS website: http://geohazards.usgs.gov/hazardtool/application.php (accessed on December 30, 2014) and are associated with a shear wave velocity in the upper 30 m of the soil column of 760 m/s. For each of the eight sites and four periods of Figure 6-1, the spectral accelerations at MAFE of 10^{-3}, 4×10^{-4} and 10^{-4} are computed assuming a linear variation of spectral acceleration with MAFE in logarithmic space between adjacent data points. A similar assumption of linearity in the logarithmic space for a 10-fold change in MAFE is made in ASCE (2005). For the remainder of this chapter, spectral acceleration at a given MAFE (or MAFE for a given spectral acceleration) is computed assuming linearity between two adjacent data points of the seismic hazard curve in the logarithmic space, unless noted otherwise.

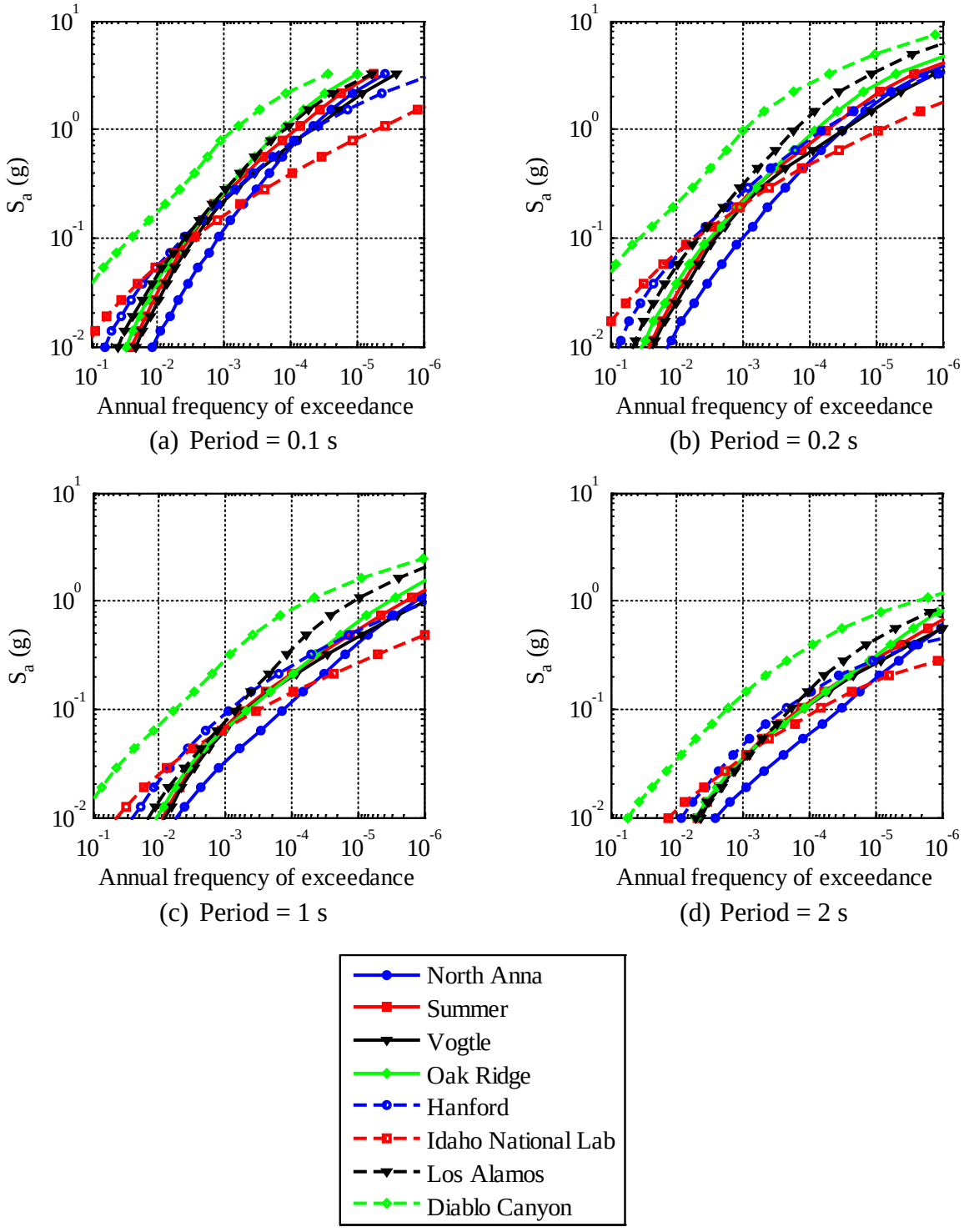

Figure 6-1 Seismic Hazard Curves for Eight Sites of Nuclear Facilities in the United States and 5% Damping

The spectral accelerations at MAFE of 10^{-3}, 4×10^{-4} and 10^{-4} are used to normalize the data of Figure 6-1 to a spectral acceleration of 1.0 g at the three MAFE, and the normalized curves are plotted in Figures 6-3, 6-4[29] and 6-5[30], respectively.

6.3 Conventional Nuclear Power Plants

6.3.1 Seismic Hazard Definition

The seismic hazard for the analysis and design of conventional (or fixed-base) nuclear structures is defined in ASCE 43-05 (ASCE, 2005). This risk-oriented definition of hazard was first implemented in the United States Department of Energy guideline "Natural phenomena hazards design and evaluation criteria for Department of Energy facilities" (USDOE, 1994). The design response spectrum, DRS, is obtained by multiplying the ordinates of the UHRS by a design factor, DF:

$$DRS = DF \times \text{UHRS} \qquad \textbf{(6-1)}$$

and it represents design basis earthquake shaking.

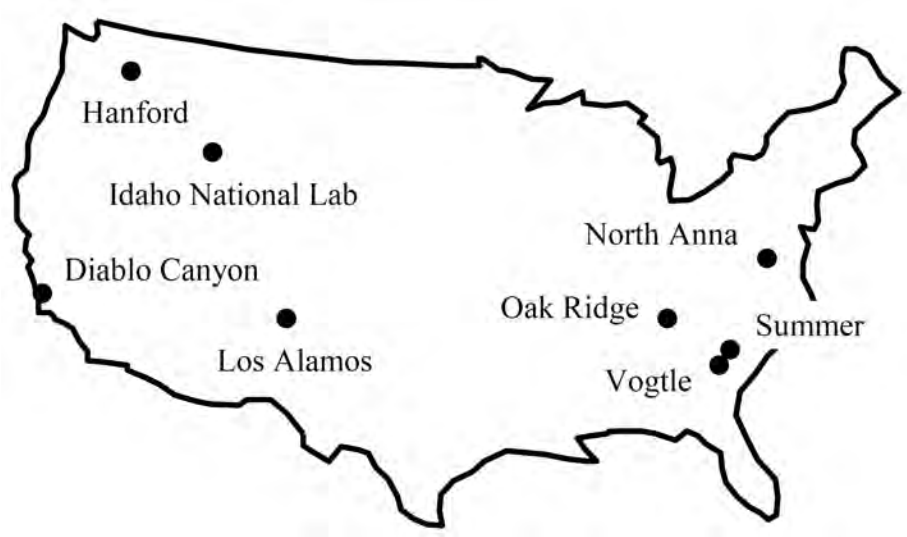

Figure 6-2 Locations of Eight Nuclear Facilities in the United States

[29] The figure is similar to Figure C1-1 of ASCE 43-05.

[30] The figure is similar to Figure C2-1 of ASCE 43-05, with horizontal and vertical axes switched.

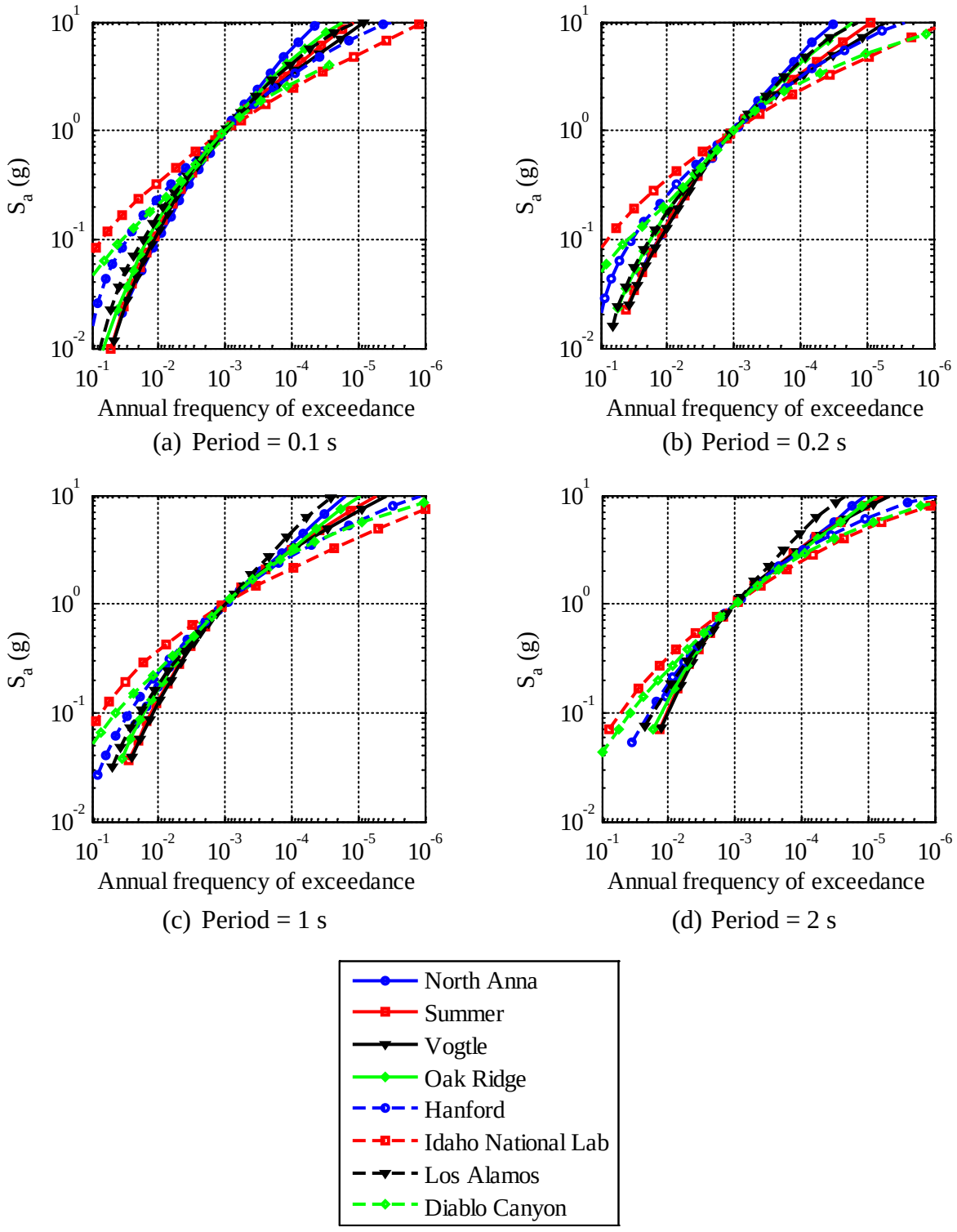

Figure 6-3 Seismic Hazard Curves Normalized by the Spectral Ordinate at an Annual Frequency of Exceedance of 10^{-3}

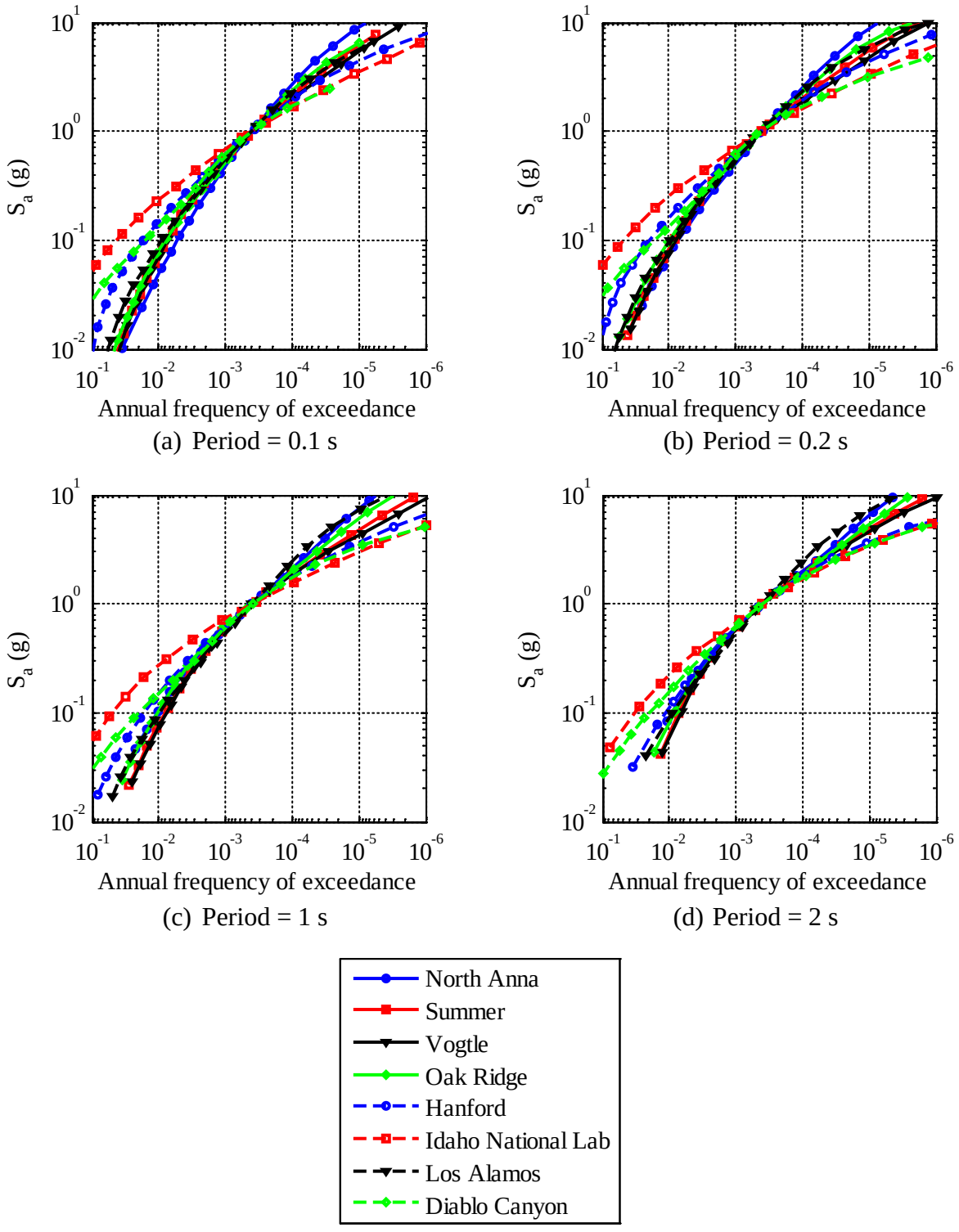

Figure 6-4 Seismic Hazard Curves Normalized by the Spectral Ordinate at an Annual Frequency of Exceedance of 4×10^{-4}

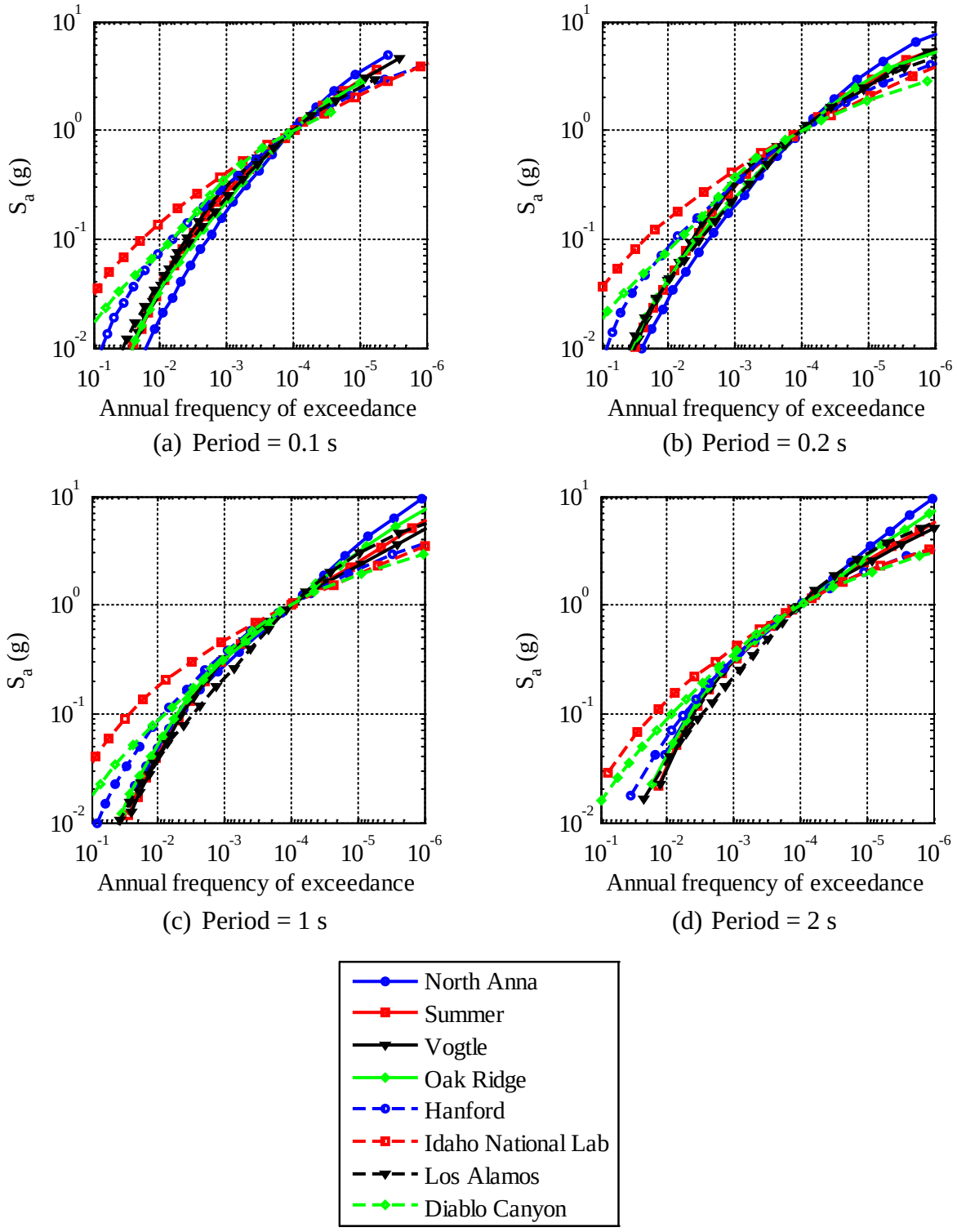

Figure 6-5 Seismic Hazard Curves Normalized by the Spectral Ordinate at an Annual Frequency of Exceedance of 10^{-4}

For a non-isolated nuclear structure, the UHRS is increased by DF to achieve the target R_P (e.g., 10) for a given H_D (e.g., 10^{-4}). ASCE 43-05 provides an expression to compute DF, namely,

$$DF = \max\left(1.0,\ 0.6\left(A_R\right)^{\alpha}\right) \tag{6-2}$$

where α is 0.4 (0.8, 0.8) for SDC 3 (4, 5), and A_R is

$$A_R = \frac{SA_{0.1H_D}}{SA_{H_D}} \tag{6-3}$$

where $SA_{0.1H_D}$ and SA_{H_D} are 5% damped spectral accelerations corresponding to annual frequencies of exceedance of $0.1H_D$ and H_D, respectively.

Figures 6-3, 6-4 and 6-5 show that the values of A_R depend strongly on the site and the value of MAFE considered. North Anna is an Eastern US site; Hanford is a Western US site. For a period of 0.1 s and MAFE of 10^{-2} (10^{-3}, 10^{-4}), A_R for these two sites are 9.8 (5.6, 3.4) and 4.2 (3.2, 2.3), respectively. The values of A_R for all eight sites are listed in Table 6-1. Focusing on an MAFE of 10^{-4}, which is the basis for the design of nuclear power plants (NPPs) in the United States, it is clear that A_R is greater in the Eastern and Central United States than in the Western United States, irrespective of period. For conventional (fixed-base) nuclear facilities, the data at periods of 0.1 s and 0.2 s are relevant for calculating the design factor. For isolated nuclear facilities, the data at periods of 1 s and 2 s must also be considered.

Table 6-1 Values of A_R for Sites of Nuclear Facilities in the United States

Period (s)	H_D	Site							
		North Anna	Summer	Vogtle	Oak Ridge	Hanford	Idaho	Los Alamos	Diablo Canyon
0.1	10^{-2}	9.8	8.2	8.3	6.7	4.2	2.9	6.0	4.7
	10^{-3}	5.6	3.6	3.3	4.5	3.2	2.4	4.2	2.7
	10^{-4}	3.4	2.9	2.8	2.8	2.3	2.1	2.5	-[1]
0.2	10^{-2}	7.2	7.3	7.6	5.5	3.9	2.8	5.7	4.7
	10^{-3}	5.0	3.3	3.1	4.1	3.1	2.3	4.3	2.7
	10^{-4}	3.4	2.8	2.5	2.9	2.3	2.0	2.6	1.9
1	10^{-2}	5.5	7.7	8.1	5.9	4.2	2.7	5.5	4.0
	10^{-3}	3.6	3.2	3.1	3.2	2.7	2.1	4.6	2.9
	10^{-4}	3.5	2.5	2.3	3.1	2.1	1.9	2.9	1.9
2	10^{-2}	6.5	9.3	9.8	7.6	5.5	3.1	5.8	4.0
	10^{-3}	3.3	3.3	3.2	3.1	3.0	2.5	4.6	2.8
	10^{-4}	3.2	2.5	2.4	2.8	2.0	2.0	2.9	2.0

[1] Information not available at the USGS website.

6.3.2 Performance Objectives

The design of non-isolated, safety-related nuclear structures follows a graded approach. Five seismic design categories (SDCs 1 through 5) and four limit states (A, B, C and D) are considered, as introduced previously.

The target frequencies of unacceptable performance, P_F, for the three SDCs (3, 4 and 5) are 10^{-4}, 4×10^{-5} and 10^{-5} for shaking with mean annual exceedance frequencies, H_D, of 4×10^{-4}, 4×10^{-4} and 10^{-4}, respectively. A probability ratio, R_P, is defined as the ratio of the H_D and P_F:

$$R_P = \frac{H_D}{P_F} \tag{6-4}$$

For SDC 5, which is appropriate for nuclear power plants, H_D, P_F and R_P are 10^{-4}, 10^{-5} and 10, respectively.

The design factor is derived considering uncertainties in seismic demand and deterministic component capacity and expected component inelastic energy dissipation to achieve a target R_P. It is given by (e.g., USDOE (1994), ASCE (2005)):

$$DF = \frac{1}{F_{Np}}\left(R_P e^{-\left(X_P K_H \beta - \frac{1}{2}(K_H\beta)^2 \right)} \right)^{1/K_H} \tag{6-5}$$

where F_{Np} is the nominal frequency of unacceptable performance, K_H is a parameter to characterize the slope of the seismic hazard curve between two MAFEs[31] (wherein the slope is linear in the log-log space), β is a composite standard deviation associated with the mean seismic fragility curve, X_p is the standard normal variable corresponding to a failure probability, and other parameters were defined previously. The value of β typically ranges between 0.3 and 0.6 for nuclear structures and components (see Section 2.2.1.2 of the commentary to ASCE 43-05). The parameter K_H in (6-6) and A_R in (6-3) are related by (ASCE, 2005)

$$K_H = \frac{1}{\log(A_R)} \tag{6-6}$$

where all parameters were defined previously. The DF given by (6-6) is approximated using (6-2), which is derived from a regression analysis between DF and A_R for different values of R_P and β (e.g., USDOE (1994)).

The target performance goals specified in ASCE 43-05 can also be achieved if it is demonstrated that 1) the probability of unacceptable performance under the seismic hazard

[31] A ten-fold ratio is considered (e.g., between MAFEs of 10^{-4} and 10^{-5}).

DRS is less than 1%, and 2) the probability of unacceptable performance under 1.5 times *DRS* is less than 10%. It is shown in the commentary to the ASCE 43-05 that the target performance goals for the three SDCs (3, 4 and 5) are reasonably achieved if the above two criteria are satisfied and *DF* is given by (6-2).

6.4 Seismically Isolated Nuclear Power Plants

6.4.1 Seismic Hazard Definition

The seismic isolation NUREG /CR 7253 (Kammerer *et al*., 2019) identifies two levels of seismic hazard for design, namely, a ground motion response spectrum+ (GMRS+) and a beyond design basis (BDB) GMRS. The GMRS is calculated per Regulatory Guide RG 1.208 USNRC, (2007a), "A performance-based approach to define the site-specific earthquake ground motion". This Regulatory Guide is based on ASCE 43-05 ASCE, (2005), which was drafted for conventional (fixed-base) nuclear structures. The GMRS is the product of the UHRS with an MAFE of 10^{-4} (SDC 5) and *DF* , and is similar to the *DRS* for conventional nuclear structures. The GMRS+ is the envelope of the GMRS and a regulator-specific minimum response spectrum (e.g., an appropriate spectral shape anchored to a peak ground acceleration of 0.1 g). The BDB GMRS envelopes a uniform hazard response spectrum with an MAFE of 10^{-5} and a spectrum with ordinates 167% of the GMRS+.

6.4.2 Performance Objectives

The following performance goals are identified in Kammerer *et al*. (2019) for the isolated superstructure, individual isolators and umbilical lines: 1) the probability of the isolated superstructure striking the surrounding stop should be less than 1% for GMRS+ shaking, 2) the probability of the isolated superstructure striking the stop should be less than 10% for BDB GMRS shaking, 3) the probability of loss of axial load capacity of the isolators at a displacement equal to the clearance to the stop (CS) should be less than 10%, and 4) there should be a less than 10% probability of loss for function for safety-related umbilical lines at a displacement equal to the CS. These performance objectives are satisfied by providing the CS equal to or greater than the 90th percentile displacement under BDB GMRS shaking[32], and designing/testing the bearings and umbilical lines to perform with 90% confidence at a displacement equal to the CS. The performance objectives are summarized in Table 6-2. The annual frequencies of unacceptable performance for the isolated superstructure, individual isolators and the umbilical lines are estimated in the following section, assuming the objectives of Table 6-2 are achieved.

6.5 Spectral Demands for Conventional and Isolated Nuclear Power Plants

This section compares the definitions of seismic hazard for conventional and seismically isolated nuclear power plant structures, namely, 1) UHRS[33] at MAFE of 10^{-4}, 2) $1.67 \times$ UHRS at MAFE of 10^{-4}, 3) UHRS at MAFE of 10^{-5}, and 4) $DF \times$ UHRS at MAFE of 10^{-4}, for the eight sites of Figure 6-2 and 5% damping. Spectral acceleration at an MAFE is computed assuming a linear variation of spectral acceleration with MAFE between two adjacent

[32] It is shown in Chapter 5 that the clearance to the stop is controlled by the 90th percentile BDB GMRS displacement.

[33] It is demonstrated later in this chapter that the design factors can be set equal to 1.0 for seismically isolated nuclear power plants.

data points on the seismic hazard curve in the logarithmic space (see Section 6.2). The first three hazard definitions are relevant for seismically isolated nuclear power plants and the fourth, given by (6-2), forms the design basis for conventional (non-isolated) nuclear power plants. The design factor, DF, is computed for SDC 5, which is appropriate for nuclear power plant structures, per (6-3) and is used to calculate the DRS for a conventional (non-isolated) nuclear power plant. Figure 6-6(a) presents the 5%-damped spectral acceleration ordinates for the four hazard levels, for the North Anna site, at periods of 1 s and 2 s: periods relevant for isolated nuclear structures. The ordinates at 1 s (2 s) are 0.12 g (0.06 g), 0.19 g (0.09 g), 0.19 g (0.09 g) and 0.41 g (0.19 g) for the UHRS at MAFE of 10^{-4}, $DF \times$UHRS at MAFE of 10^{-4}, $1.67 \times$UHRS at MAFE of 10^{-4}, and UHRS at MAFE of 10^{-5}, respectively. Figures 6-6(b) through 6-6(h) present the ordinates for the other seven sites. The ordinates for $1.67 \times$UHRS at MAFE of 10^{-4} are a) greater than those of the DRS for conventional nuclear structures, namely, $DF \times$UHRS at MAFE of 10^{-4}, and b) always smaller than those of the UHRS at MAFE of 10^{-5}. The spectral accelerations presented in Figure 6-6 are tabulated in Table 6-3 and the return periods corresponding to the spectral accelerations are listed in Table 6-4.

Table 6-2 Performance and Design Expectations for Seismically Isolated Nuclear Power Plant Structures[1] (adapted from Kammerer et al. (2019))

	Isolation system		Superstructure design and performance	Umbilical line design and performance	Moat or stop design and performance
Ground motion levels	**Isolator unit and system design and performance criteria**	**Approach to demonstrating acceptable performance of an isolator unit**			
GMRS+[2] Envelope of RG 1.208 GMRS and the minimum foundation input motion[3]	No long-term change in mechanical properties. Extremely high confidence of the isolation system surviving without damage when subjected to the mean displacement of the isolator system under the GMRS+ loading.	Perform production testing on each isolator for the mean system displacement under the GMRS+ loading and corresponding axial force.	Superstructure design and performance to conform to NUREG-0800 for GMRS+ loading.	Umbilical line design and performance to conform to NUREG-0800 for GMRS+ loading.	Moat gap sized such that there is less than 1% probability of the superstructure impacting the moat or stop for GMRS+ loading.
BDBE GMRS[4] Envelope of the UHRS at a MAFE of 1×10^{-5} and 167% of the GMRS+ per ISG 20	90% confidence of each isolator and the isolation system surviving without loss of gravity-load capacity at the mean displacement under BDBE GMRS loading.	Perform prototype testing on a sufficient number of isolators at the CS[5] displacement and the corresponding axial force to demonstrate acceptable performance with 90% confidence. Limited isolator unit damage is acceptable but load-carrying capacity must be maintained.	Less than a 10% probability of the superstructure contacting the moat or stop under BDBE GMRS loading.	Greater than 90% confidence that each type of safety-related umbilical line, together with its connections, shall remain functional for the CS displacement. Performance may be demonstrated by testing, analysis or a combination of both.[6]	Moat gap sized such that there is less than a 10% probability of the superstructure impacting the moat or stop for BDB GMRS loading. Stop designed to survive impact forces associated with isolation system displacement to 95th percentile BDBE isolation system displacement.[7] Limited damage to the moat or stop is acceptable but the moat/stop should perform its function.

1. Analysis and design of safety-related components and systems shall conform to NUREG-0800.
2. 10CFR50 Appendix S requires the use of an appropriate free-field spectrum (often the RG 1.60 spectral shape) with a peak ground acceleration of no less than 0.10g at the foundation level.
3. The analysis can be performed once using a composite spectrum or twice using the GMRS and the minimum spectrum separately.
4. The analysis can be performed once using a composite spectrum or twice using the 1×10^{-5} MAFE UHRS and the 167%GMRS+ separately.
5. CS=Clearance to the Stop
6. Seismic Category 2 SSCs whose failure could impact the functionality of umbilical lines shall also remain functional for the CS displacement.
7. Impact velocity calculated at the displacement equal to the CS assuming cyclic response of the isolation system for motions associated with the 95th percentile (or greater) BDB GMRS displacement.

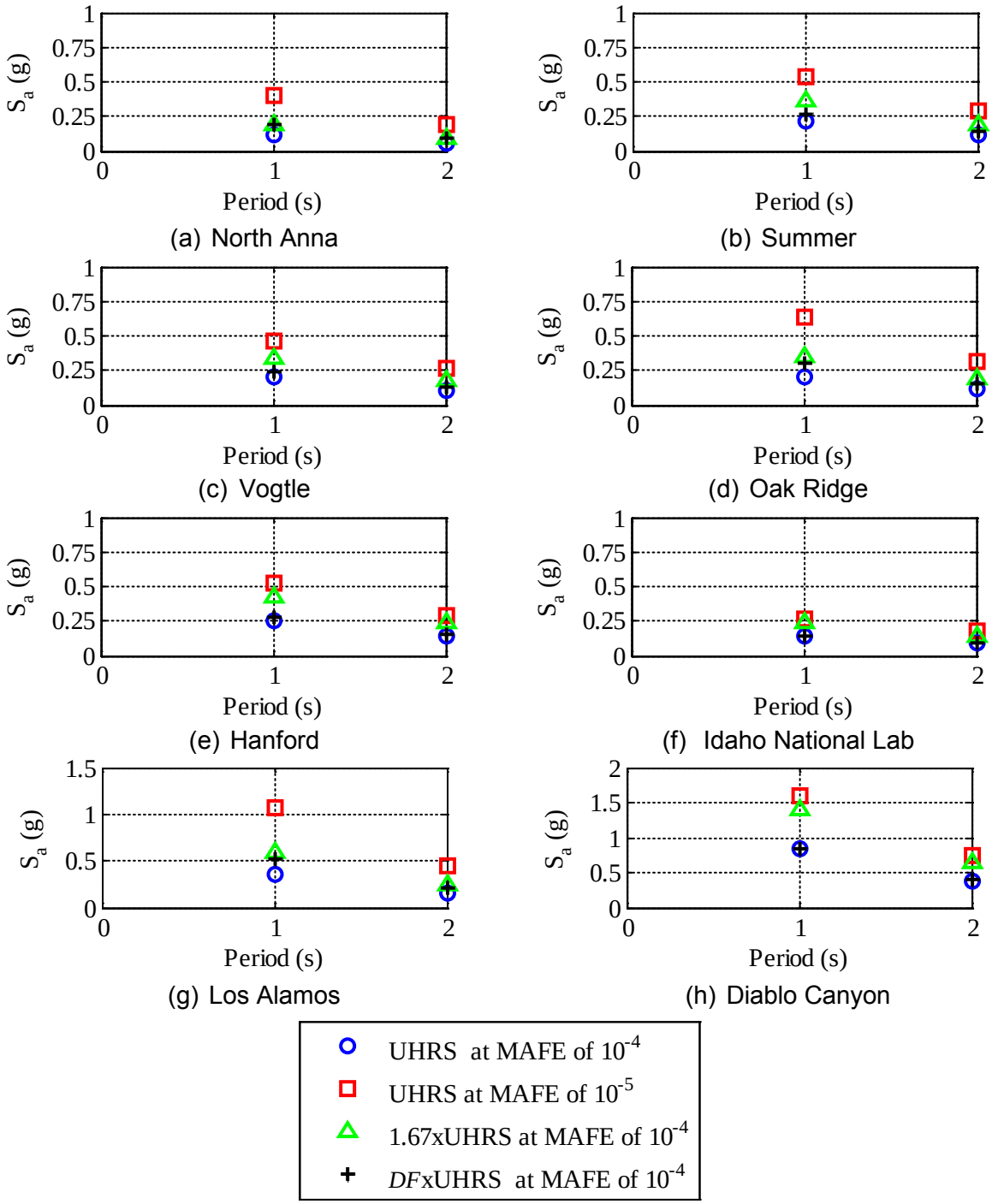

Figure 6-6 Spectral Ordinates Corresponding to Different Definitions of Seismic Hazard at Eight Sites of Nuclear Facilities; 5% Damping

Table 6-3 Five Percent Damped Spectral Ordinates (in g) at 1 s and 2 s for Seismic Hazards Defined for Conventional and Seismically Isolated Nuclear Power Plants at Eight Sites of Nuclear Facilities (also see Figure 6-6)

Period (s)	Hazard definition	Site							
		North Anna	Summer	Vogtle	Oak Ridge	Hanford	Idaho	Los Alamos	Diablo Canyon
1	UHRS1[1]	0.12	0.22	0.20	0.21	0.25	0.14	0.36	0.83
	UHRS2[2]	0.41	0.54	0.47	0.64	0.53	0.27	1.06	1.59
	1.67×UHRS1	0.19	0.36	0.34	0.35	0.42	0.23	0.60	1.39
	DF×UHRS1	0.19	0.27	0.24	0.31	0.27	0.14	0.51	0.84
2	UHRS1	0.06	0.12	0.11	0.11	0.14	0.09	0.15	0.38
	UHRS2	0.19	0.29	0.26	0.31	0.29	0.18	0.44	0.75
	1.67×UHRS1	0.10	0.19	0.18	0.19	0.24	0.15	0.25	0.64
	DF×UHRS1	0.09	0.15	0.13	0.15	0.15	0.09	0.21	0.39

[1]UHRS with an MAFE of 10^{-4}
[2]UHRS with an MAFE of 10^{-5}

Table 6-4 Return Periods Corresponding to the 5% Damped Spectral Accelerations at 1 s and 2 s Reported in Table 6-3 (in 1000s of years)

Period (s)	Hazard definition	Site							
		North Anna	Summer	Vogtle	Oak Ridge	Hanford	Idaho	Los Alamos	Diablo Canyon
1	UHRS1[1]	10	10	10	10	10	10	10	10
	UHRS2[2]	100	100	100	100	100	100	100	100
	1.67×UHRS1	25	35	39	28	46	61	26	59
	DF×UHRS1	24	17	15	21	13	10	19	10
2	UHRS1	10	10	10	10	10	10	10	10
	UHRS2	100	100	100	100	100	100	100	100
	1.67×UHRS1	28	34	36	31	48	48	26	54
	DF×UHRS1	24	17	16	20	12	12	19	11

[1]UHRS with an MAFE of 10^{-4}
[2]UHRS with an MAFE of 10^{-5}

6.6 Annual Frequency of Unacceptable Performance of Isolated Nuclear Power Plants

6.6.1 Hazard Definition

The seismic hazard is defined, for the purpose of estimating the annual frequency of unacceptable performance, as multiples, m, of the UHRS at MAFE of 10^{-4}, taken as the average of the spectral acceleration ordinates at 1 s and 2 s[34, 35] reported in Figure 6-1. This definition does not include the design factor recommended by RG 1.208 and ASCE 43-05 at the

[34] The periods of 1 s and 2 s are relevant for seismically isolated structures, as noted previously.

[35] The amplification ratios for 1 s and 2 s and at MAFE of 10-4 differ by less than 10% for the eight sites of Table 6-1.

MAFE of 10^{-4} (see Section 6.3.1) for the reason shown later. The seismic hazard curves considered for the nuclear facilities at the eight sites of Figure 6-2 are plotted in Figure 6-7.

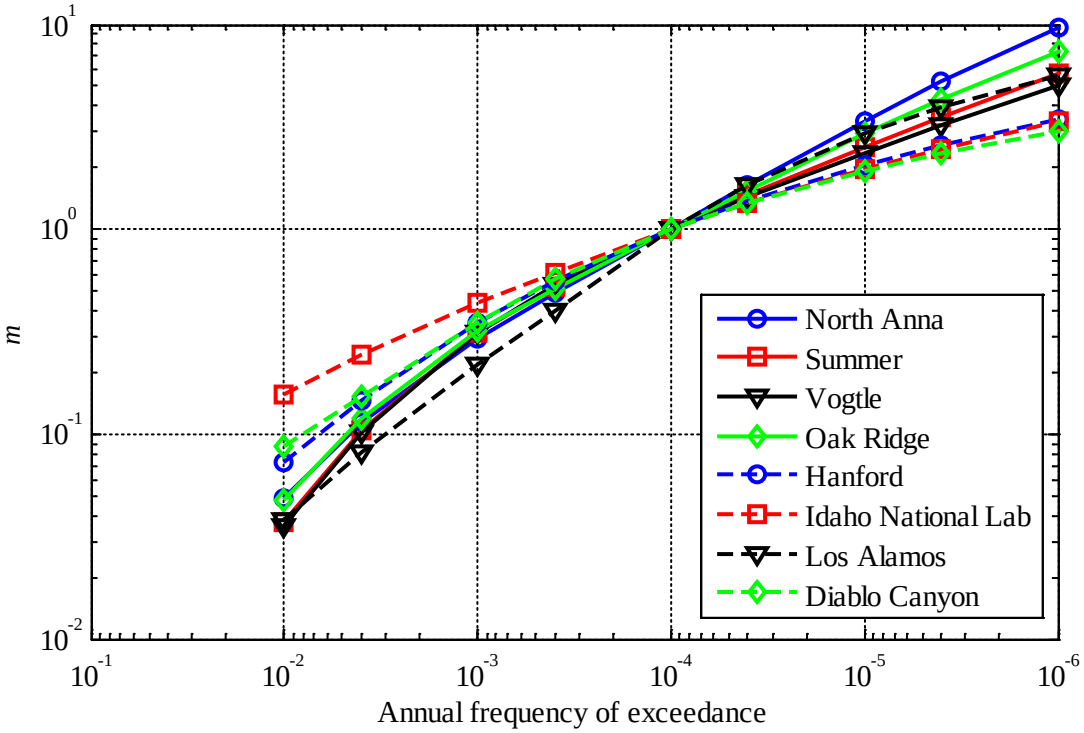

Figure 6-7 Annual Frequency of Exceedance of Multiples, *m*, of UHRS with MAFE of 10^{-4}

6.6.2 Annual Frequency of Unacceptable Performance of the Isolated Superstructure

The superstructure of a seismically isolated nuclear power plant will include structural components that will be designed in accordance with materials standards such as ACI 349 (ACI, 2013a), ACI 359 (ACI, 2013b) and AISC N690 (AISC, 2012) and safety-critical mechanical and electrical systems and components designed in accordance with standards prepared by the American Society of Mechanical Engineers (ASME) and the Institute of Electrical and Electronics Engineers (IEEE). These structural, mechanical and electrical components must be designed, per materials standards, for the forces, displacements and accelerations associated with GMRS+ shaking per Table 6-2, as a minimum.

Seismic isolation of certified plant designs has been proposed as a viable strategy to expand the use of nuclear power plants, where some of these certified designs have been seismically qualified for horizontal design basis shaking that is represented by a USNRC RG 1.60 (USAEC (1973), USNRC (2014)) spectrum anchored to peak ground acceleration of 0.3 g. For this spectrum and peak acceleration, and assuming that the period of the fixed-base superstructure is in the range of 0.1 to 0.3 seconds, the horizontal spectral response at 5% damping will be no less than 0.75 g, which would form the design basis for the structural components. The mechanical and electrical safety-related systems and components would be typically designed, per ASME and IEEE standards, for floor spectral demands much in excess of 1.0 g. If the annual frequency of unacceptable performance of structures, systems and components in a (fixed-base) certified plant design meets the requirements of USNRC, there will exist a

considerable margin if the certified plant is seismically isolated. Noting that the focus to date has been on response to horizontal shaking, the response to vertical shaking will be no better and no worse if the superstructure is isolated using either sliding or elastomeric bearings. In summary, the isolation of a certified plant design will reduce the annual frequency of unacceptable performance of the superstructure below the value permitted by the USNRC.

Huang *et al.* (2010) showed that the seismic robustness of structures, systems and components (SSCs) in nuclear power plants could be substantially reduced if the plant was seismically isolated. The associated reduction in cost of the structures, systems and components could substantially offset (or eliminate) the costs associated with the seismic isolators, pedestals, foundation and associated excavation (if the plant is embedded). If this reduction in demand is incorporated in design, the nuclear steam supply system vendor would have to demonstrate, through plant-level systems analysis, that the resultant SSC designs met USNRC-required performance goals.

Herein, it is assumed that the annual frequency of unacceptable performance of the isolated superstructure, system and components is less than that of the corresponding fixed-base nuclear power plant.

One recommendation of the seismic isolation NUREG/CR 7253 is that there be a less than 10% probability of the superstructure impacting the moat or stop under BDB GMRS shaking. This deterministic objective is met by setting the clearance to the stop, along each horizontal axis of the plant, to be no less than the 90th percentile displacement calculated for BDB GMRS shaking along that axis. Analysis of the isolated superstructure for impact loadings associated with collision with the stop is not required if this clearance to the stop is provided.

6.6.3 Annual Frequency of Unacceptable Performance of the Isolation System

In the seismic domain, the isolation system represents a singleton: failure of the isolation system could correspond to unacceptable performance of the nuclear plant in terms of core damage or large release of radiation. It is not possible to generically relate the failure of individual isolators to the failure of an isolation system. The failure of one isolator in a system of four could trigger system failure. The failure of one isolator in a system of 250 would be inconsequential. Herein, and very conservatively, the failure of one isolator is assumed to represent the failure of the isolation system.

To compute the annual frequency of unacceptable performance of an isolator unit, an isolator-unit fragility function must be convolved over an appropriate seismic hazard curve. The hazard curves assumed here for the eight sites of Figure 6-2 are based on the averaged values, site by site, for periods of 1.0 and 2.0 seconds. The fragility function for an isolator unit is defined by a median, θ_m, and log standard deviation, β, as follows

$$\theta_m - X_p \beta = \log(m) \qquad \textbf{(6-7)}$$

where X_p corresponds to a probability of exceedance of p for a normally distributed data set, and other parameters were defined previously. If tight quality control on isolator production is maintained, the variability in the properties of isolator units of a given size will be small. Three values of β are considered here, namely, 0.01, 0.02 and 0.05. If a stop is constructed, the probability of isolator failure at calculated displacements equal to or greater than the clearance to the stop (CS) is equal to that at the stop. Two calculations of the annual frequency of isolator

failure are performed below, one assuming that no stop is present and one assuming the stop is installed at the 90th percentile BDB GMRS displacement.

As noted in Section 6.4.2 , isolators are *prototype* tested to ensure that they can sustain the 90th percentile BDB GMRS displacement and the co-existing axial force with 90+% confidence. Practically, this requires all of the prototype isolators to resist this combination of displacement and axial force unless very large numbers of prototypes are to be tested (to achieve the 90+% confidence). Likely a small number of *prototype* isolators will be tested to greater displacements and forces to demonstrate compliance. Assume that the displacement capacity of the isolation system is equal to the 90th percentile displacement for BDB GMRS shaking, which is approximately equal to the median displacement for 110% BDB GMRS[36] shaking, as shown in Chapter 7. Based on this assumption, and values of 90% (1 isolator in 10 fails), 95% (1 isolator in 20 fails) and 99% (1 isolator in 100 fails) confidence, (6-7) is rewritten as:

$$\theta_m - \alpha\beta = \log\left(f_{AR} \times A_R\right) \qquad \textbf{(6-8)}$$

where α is 1.28, 1.64, and 2.33, respectively, and f_{AR} is 1.1. The fragility curves for isolators tested with 90% confidence at median displacement for 110% BDB GMRS shaking (or 90th percentile displacement for BDB GMRS shaking) are shown in Figure 6-8. The fragility curves for 95% and 99% confidence at median displacement for 110% BDB GMRS shaking are shown in Figures 6-10 and 6-11, respectively. Figure 6-12 presents fragility curves for 90% confidence at median displacement for 125% BDB GMRS shaking $\left(f_{AR} = 1.25\right)$.

The total annual frequency of unacceptable performance of the isolation system, $P_{F,\text{isolation}}$, is given by (e.g., ASCE (2005)):

$$P_{F,\text{isolation}} = -\int_0^\infty \frac{d}{dm} H_D \times \left(P_f \mid GM = m\right) dm \qquad \textbf{(6-9)}$$

where $\left(P_f \mid GM = m\right)$ is the annual frequency of unacceptable performance conditioned on m times UHRS shaking at an MAFE of 10^{-4}, and other parameters were defined previously. Table 6-5 presents a sample calculation of $P_{F,\text{isolation}}$ for the site of Diablo Canyon, and β , α and f_{AR} set equal to 0.01, 1.28 and 1.1, respectively (i.e., 90% confidence on bearings tested at median displacement for 110% BDB GMRS shaking). The hazard and fragility curves for Diablo Canyon, plotted in Figures 6-7 and 6-8(a), respectively, are used to generate Table 6-5. This data can be used to disaggregate the risk, as presented in Figure 6-9(a). Table 6-6 presents the same calculation as Table 6-5, but for the site of North Anna; corresponding disaggregation of risk is presented in Figure 6-9(b). The disaggregated risk peaks at m of 2.2 and 3.9 for the two sites, respectively, which correspond to 1.14 and 1.16 times the BDB GMRS shaking at Diablo Canyon and North Anna, respectively. Shifting the peaks to greater values of m would reduce total risk, because the disaggregated risk for a given range of m would correspond to a

[36] These calculations are performed in Chapter 7 for three sites, namely, Diablo Canyon, Vogtle and North Anna, to cover the range of A_R at H_D of 10^{-4} for 1 s and 2 s and the eight sites of Figure 6-2 (see Table 6-1). One hundred and ten percent is appropriate for Diablo Canyon and conservative (low) for the other eight sites.

smaller H_D. This shift can be achieved by either testing the bearings with a greater confidence or testing them for greater displacements and axial forces (i.e., greater shaking intensity).

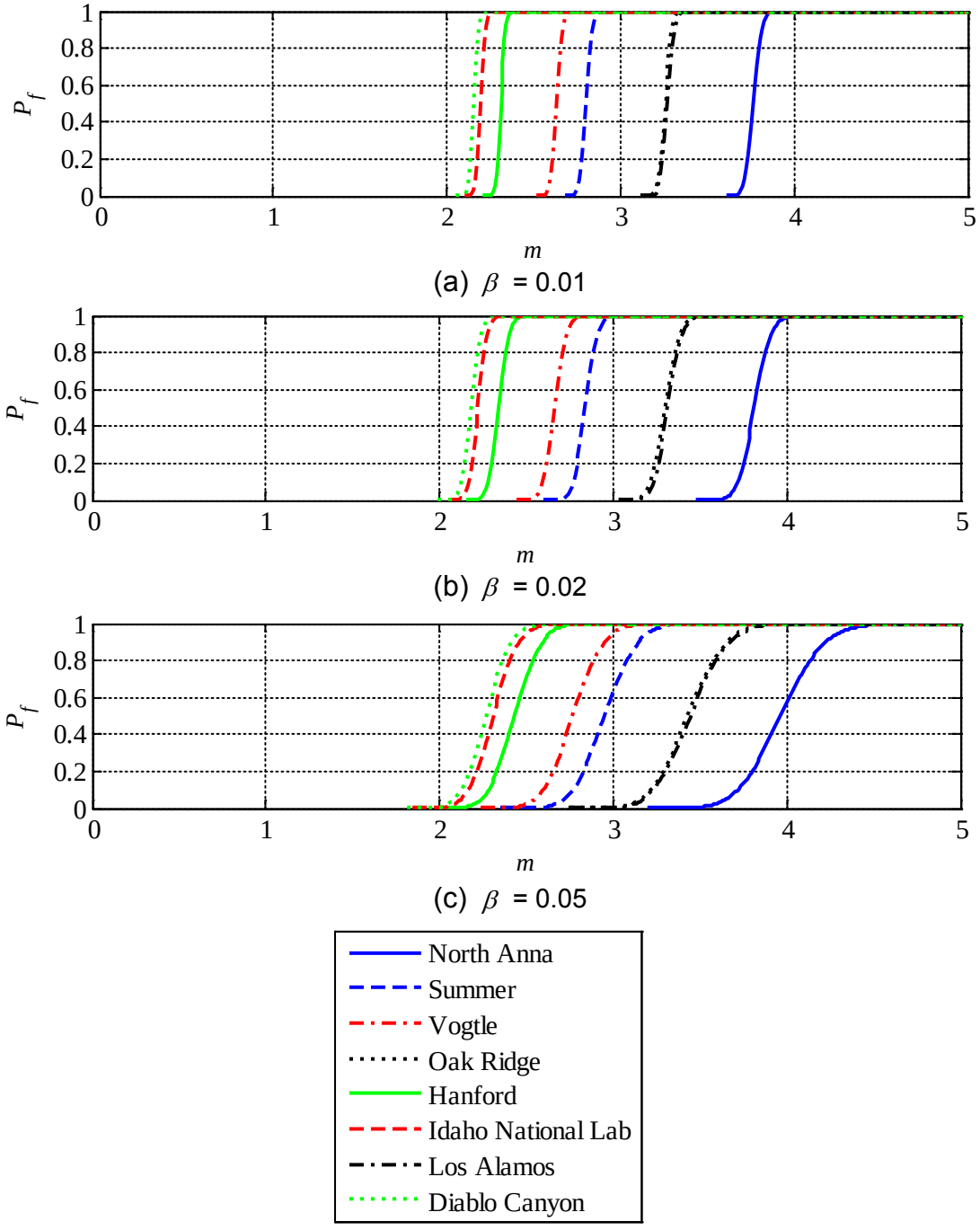

Figure 6-8 Probability of Unacceptable Performance, P_f, of Individual Isolator Units for 90% Confidence at the Median Displacement for 110% BDB GMRS Shaking Plotted Against Multiples, *m*, of UHRS Shaking with MAFE of 10^{-4}, Without a Stop

Table 6-5 Example Calculation of Total Annual Frequency of Unacceptable Performance of Individual Isolator Units at Diablo Canyon for β = 0.01, f_{AR} = 1.1 and α = 1.28 (90% confidence)

1	2	3	4	5	6	7	8
m_1	m_2	$m_3 = (m_1 + m_2)/2$	$P_f(m_3)$ [1]	$H_D(m_1)$	$H_D(m_2)$	ΔH_D (Col 5 – 6)	$P_f(m_3) \times \Delta H_D$
0.500	1.000	0.750	0	5.2×10^{-4}	1.0×10^{-4}	4.2×10^{-4}	0
1.000	1.500	1.250	0	1.0×10^{-4}	2.7×10^{-5}	7.3×10^{-5}	0
1.500	2.067	3.567	0	7.3×10^{-5}	7.2×10^{-5}	1.0×10^{-6}	0
2.067	2.087	2.077	1.4×10^{-4}	7.2×10^{-6}	6.8×10^{-6}	3.3×10^{-7}	4.7×10^{-11}
2.087	2.107	2.097	3.7×10^{-3}	6.8×10^{-6}	6.5×10^{-6}	3.1×10^{-7}	1.2×10^{-9}
2.107	2.147	2.127	0.1	6.5×10^{-6}	6.0×10^{-6}	5.8×10^{-7}	6.1×10^{-8}
2.147	2.187	2.167	0.73	6.0×10^{-6}	5.4×10^{-6}	5.2×10^{-7}	3.8×10^{-7}
2.187	2.207	2.197	0.98	5.4×10^{-6}	5.2×10^{-6}	2.4×10^{-7}	2.3×10^{-7}
2.207	2.227	2.217	1.0	5.2×10^{-6}	5.0×10^{-6}	2.3×10^{-7}	2.3×10^{-7}
2.227	2.247	2.237	1.0	5.0×10^{-6}	4.8×10^{-6}	2.2×10^{-7}	2.2×10^{-7}
2.247	2.500	3.768	1.0	4.8×10^{-6}	2.7×10^{-6}	2.1×10^{-6}	2.1×10^{-6}
2.500	3.000	2.750	1.0	2.7×10^{-6}	1.0×10^{-6}	1.7×10^{-6}	1.7×10^{-6}
3.000	4.000	3.500	1.0	1.0×10^{-6}	1.3×10^{-7}	8.7×10^{-6}	8.7×10^{-7}
4.000	5.000	4.500	1.0	1.3×10^{-7}	1.8×10^{-8}	1.1×10^{-7}	1.1×10^{-7}
5.000	5.288	5.144	1.0	1.8×10^{-8}	1.0×10^{-8}	8×10^{-9}	8×10^{-9}
					$P_{F,\text{isolation}} = \sum P_f(m_3) \times \Delta H_D = 5.9\times10^{-6}$		

[1] $P_f(m_3) = (P_f \mid GM = m_3)$

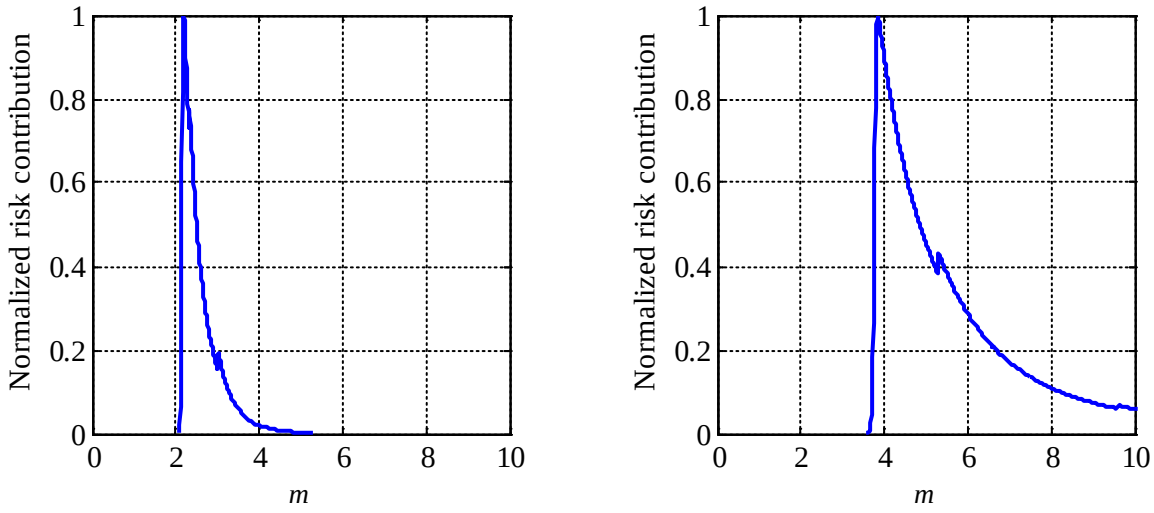

(a) Diablo Canyon (b) North Anna

Figure 6-9 Disaggregation of Risk for Individual Isolators

Table 6-6 Example Calculation of Total Annual Frequency of Unacceptable Performance of Individual Isolator Units at North Anna for β = 0.01, f_{AR} = 1.1 and α = 1.28 (90% confidence)

1	2	3	4	5	6	7	8
m_1	m_2	$m_3 = (m_1 + m_2)/2$	$P_f(m_3)$ [1]	$H_D(m_1)$	$H_D(m_2)$	ΔH_D (Col 5 – 6)	$P_f(m_3) \times \Delta H_D$
0.500	1.000	0.750	0	3.8×10^{-4}	9.9×10^{-5}	2.8×10^{-4}	0
1.000	2.000	1.500	0	9.9×10^{-5}	2.7×10^{-5}	7.2×10^{-5}	0
2.000	3.000	2.500	0	2.7×10^{-5}	1.3×10^{-5}	1.4×10^{-5}	0
3.000	3.601	3.301	0	1.3×10^{-5}	8.8×10^{-6}	4.2×10^{-6}	0
3.601	3.641	3.621	5.4×10^{-5}	8.8×10^{-6}	8.6×10^{-6}	2.0×10^{-7}	1.1×10^{-11}
3.641	3.681	3.661	2.8×10^{-3}	8.6×10^{-6}	8.4×10^{-6}	1.9×10^{-7}	5.2×10^{-10}
3.681	3.721	3.701	4.6×10^{-2}	8.4×10^{-6}	8.2×10^{-6}	1.8×10^{-7}	8.4×10^{-9}
3.721	3.761	3.741	2.7×10^{-1}	8.2×10^{-6}	8.0×10^{-6}	1.8×10^{-7}	4.8×10^{-8}
3.761	3.801	3.781	6.7×10^{-1}	8.0×10^{-6}	7.9×10^{-6}	1.7×10^{-7}	1.2×10^{-7}
3.801	3.841	3.821	9.3×10^{-1}	7.9×10^{-6}	7.7×10^{-6}	1.7×10^{-7}	1.6×10^{-7}
3.841	3.881	3.861	9.9×10^{-1}	7.7×10^{-6}	7.5×10^{-6}	1.6×10^{-7}	1.6×10^{-7}
3.881	3.921	3.901	1	7.5×10^{-6}	7.4×10^{-6}	1.6×10^{-7}	1.6×10^{-7}
3.921	3.961	3.941	1	7.4×10^{-6}	7.2×10^{-6}	1.5×10^{-7}	1.5×10^{-7}
3.961	4.001	3.981	1	7.2×10^{-6}	7.1×10^{-6}	1.5×10^{-7}	1.5×10^{-7}
4.001	5	4.5005	1	7.1×10^{-6}	4.5×10^{-6}	2.6×10^{-6}	2.6×10^{-6}
5	10	7.5	1	4.5×10^{-6}	9.0×10^{-7}	3.6×10^{-6}	3.6×10^{-6}
10	20	15	1	9.0×10^{-7}	1.3×10^{-7}	7.7×10^{-7}	7.7×10^{-7}
20	40	30	1	1.3×10^{-7}	1.2×10^{-7}	1.2×10^{-7}	1.2×10^{-7}
					$P_{F,\text{isolation}} = \sum P_f(m_3) \times \Delta H_D = 8.0\times10^{-6}$		

[1] $P_f(m_3) = (P_f \mid GM = m_3)$

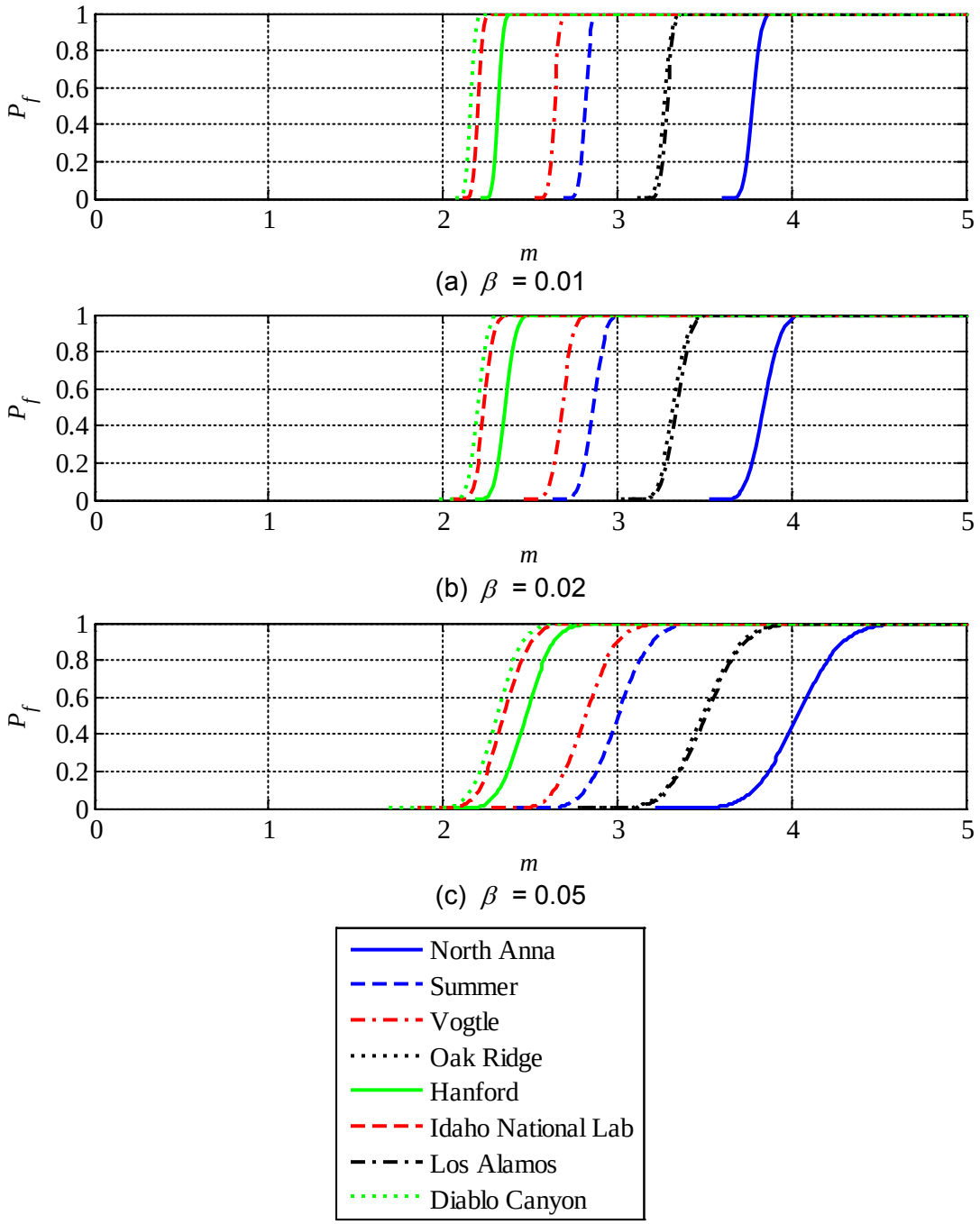

Figure 6-10 Probability of Unacceptable Performance, P_f, of Individual Isolator Units for 95% Confidence at the Median Displacement for 110% BDB GMRS Shaking Plotted Against Multiples, *m*, of UHRS Shaking with MAFE of 10^{-4}, Without a Stop

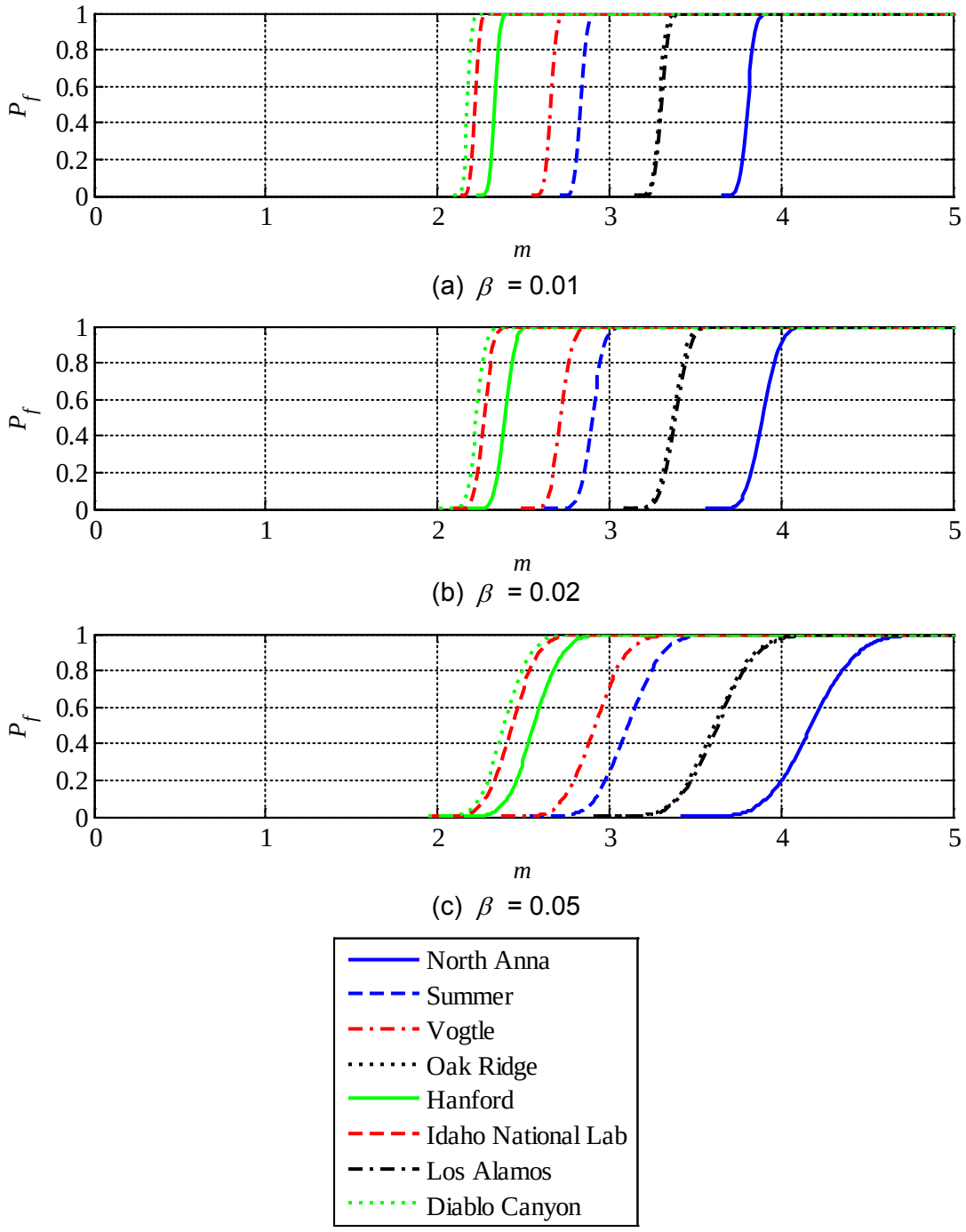

Figure 6-11 Probability of Unacceptable Performance, P_f, of Individual Isolator Units for 99% Confidence at the Median Displacement for 110% BDB GMRS Shaking Plotted Against Multiples, *m*, of UHRS Shaking with MAFE of 10^{-4}, Without a Stop

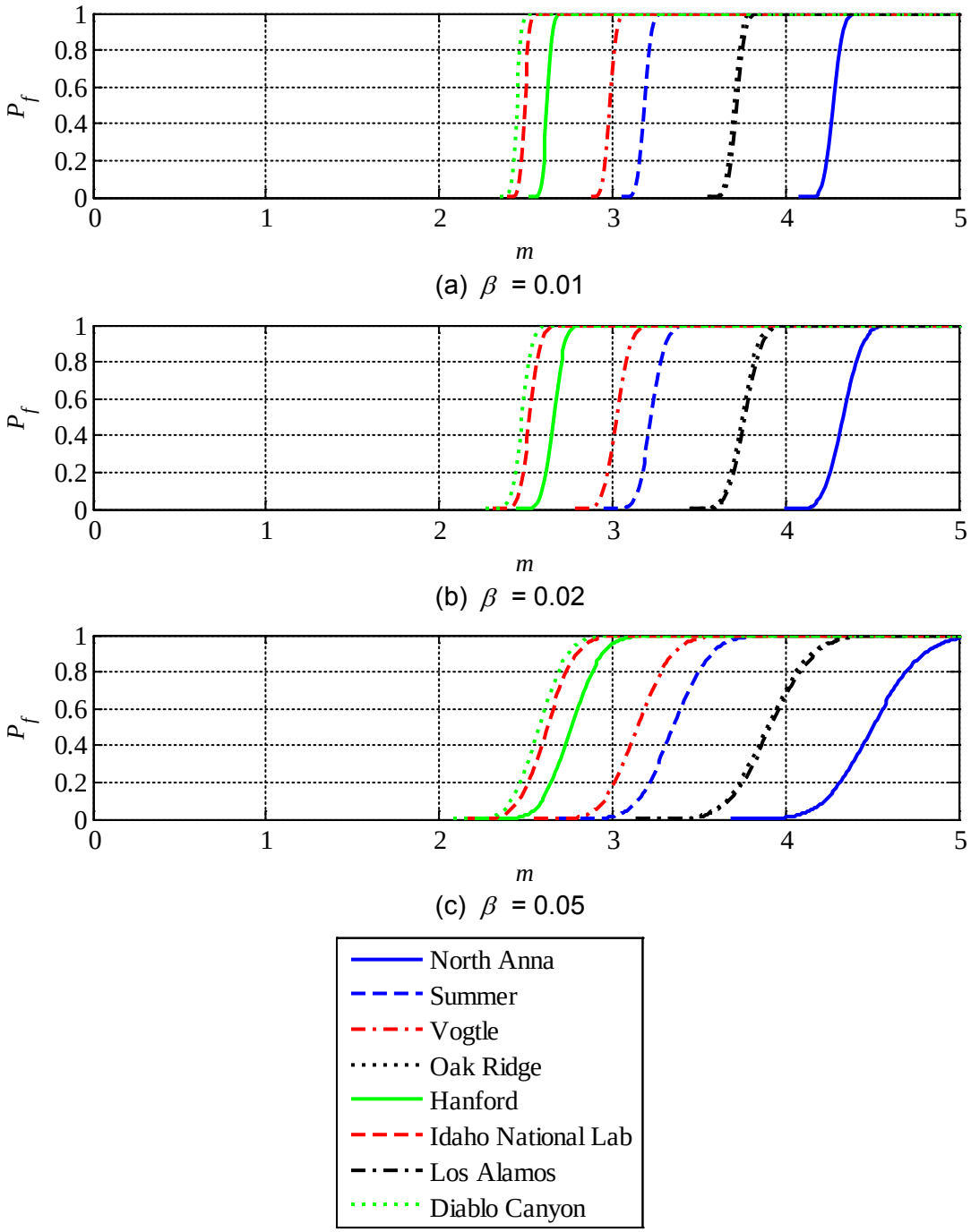

Figure 6-12 Probability of Unacceptable Performance, P_f, of Individual Isolator Units for 90% Confidence at the Median Displacement for 125% BDB GMRS Shaking Plotted Against Multiples, *m*, of UHRS Shaking with MAFE of 10^{-4}, Without a Stop

The annual frequencies of exceedance for the eight sites of Figure 6-2 are presented in Tables 6-7, 6-8, 6-9 and 6-10 corresponding to the fragility curves of Figures 6-8, 6-10, 6-11 and 6-12, respectively. The frequencies are less than 10^{-5} for all combinations of site and β.

Expectedly, the annual frequency of unacceptable performance of the isolation system decreases if the bearings are tested with a greater confidence at a given displacement.

Table 6-7 Annual Frequency of Unacceptable Performance ($\times 10^{-6}$) of Individual Isolator Units Tested with 90% Confidence at the Median Displacement for 110% BDB GMRS Shaking, Without a Stop

	Site							
	North Anna	Summer	Vogtle	Oak Ridge	Hanford	Idaho	Los Alamos	Diablo Canyon
$\beta = 0.01$	8.0	7.5	7.2	7.8	6.5	6.5	7.1	5.9
$\beta = 0.02$	7.8	7.2	7.0	7.5	6.2	6.2	6.9	5.5
$\beta = 0.05$	7.3	6.6	6.3	6.9	5.3	5.4	6.2	4.7

Table 6-8 Annual Frequency of Unacceptable Performance ($\times 10^{-6}$) Of Individual Isolator Units Tested with 95% Confidence at the Median Displacement for 110% BDB GMRS Shaking, Without a Stop

	Site							
	North Anna	Summer	Vogtle	Oak Ridge	Hanford	Idaho	Los Alamos	Diablo Canyon
$\beta = 0.01$	8.0	7.4	7.2	7.7	6.4	6.4	7.1	5.8
$\beta = 0.02$	7.7	7.1	6.8	7.4	6.0	6.0	6.7	5.4
$\beta = 0.05$	7.0	6.3	5.9	6.6	5.0	5.0	5.8	4.3

Table 6-9 Annual Frequency of Unacceptable Performance ($\times 10^{-6}$) of Individual Isolator Units Tested with 99% Confidence at the Median Displacement for 110% BDB GMRS Shaking, Without a Stop

	Site							
	North Anna	Summer	Vogtle	Oak Ridge	Hanford	Idaho	Los Alamos	Diablo Canyon
$\beta = 0.01$	7.9	7.3	7.0	7.6	6.2	6.2	6.9	5.6
$\beta = 0.02$	7.5	6.8	6.6	7.2	5.6	5.7	6.4	5.0
$\beta = 0.05$	6.5	5.7	5.3	6.1	4.3	4.3	5.2	3.6

Table 6-10 Annual Frequency of Unacceptable Performance ($\times 10^{-6}$) of Individual Isolator Units Tested with 90% Confidence at the Median Displacement for 125% BDB GMRS Shaking, Without a Stop

	Site							
	North Anna	Summer	Vogtle	Oak Ridge	Hanford	Idaho	Los Alamos	Diablo Canyon
$\beta = 0.01$	6.2	5.3	4.9	5.7	3.8	3.8	4.8	3.1
$\beta = 0.02$	6.0	5.1	4.7	5.6	3.6	3.6	4.6	2.9
$\beta = 0.05$	5.6	4.7	4.3	5.1	3.1	3.1	4.1	2.4

Importantly, the annual frequency of unacceptable performance for the isolation system will be much smaller than the values presented in Tables 6-7, 6-8, 6-9 and 6-10, because 1) failure of a small fraction of the isolators in an isolation system will not compromise the performance of the isolation system, and 2) the displacement and force demands on the isolators will not be fully correlated. (The prototype isolators will be tested by type, for maximum and not average axial forces and displacements.)

Consider Tables 6-7 and 6-10 and the sites of Los Alamos and Diablo Canyon. Increasing the displacement for prototype isolator testing from median displacement for 110% BDB GMRS shaking to median displacement for 125% BDB GMRS shaking reduces the annual frequency of unacceptable performance by 30% to 50%. The percentage reduction is smaller for North Anna because a significant fraction of the risk accrues at large values of m (see Figure 6-9). The disaggregated risk for m between 4 and 5 is 2.6×10^{-6} for North Anna (see Table 6-6) and 1.1×10^{-7} for Diablo Canyon (see Table 6-5): a difference by a factor of more than 20.

The peak isolator displacement will vary as a function of isolation system (period, coefficient of friction) and site. To enable a comparison of horizontal displacement demands at the eight sites, consider that 100,000-year spectral demands at a period of 2 s and 5% damping presented in Table 6-3. The spectral displacement at six of the eight sites of Figure 6-2, namely, North Anna, Summer, Vogtle, Oak Ridge, Hanford and Idaho are less than one half that at Diablo Canyon. Increasing the displacement capacity of the isolation system and testing the isolator units at one half of the 90th percentile displacement for BDB GMRS shaking at Diablo Canyon will reduce the risk of unacceptable performance but may not increase the cost of the isolation system. The corresponding isolator fragility curve can be derived approximately by increasing the factor f_{AR} in (6-9) by the ratio, κ, of one half the 100,000-year 2 s spectral acceleration for Diablo Canyon to the 100,000-year 2 s spectral acceleration at the site. The ratio κ ranges between 1.2 and 2.1 for the six sites. The fragility functions are shown in Figure 6-13 for β = 0.01, 0.02, and 0.05. The annual frequencies of unacceptable performance for the isolator units tested at a displacement (and corresponding axial force) equal to half the 90th percentile displacement for BDB GMRS shaking at Diablo Canyon are listed in Table 6-11. These frequencies are smaller than those reported in Table 6-7 by a factor of between 2 and 35.

The above calculations were performed assuming no stop was present. If a stop is constructed at the 90th percentile BDB GMRS displacement, the fragility curves presented in the Figures 6-8, 6-10, 6-11 and 6-12 will be truncated as shown in Figures 6-14, 6-15, 6-16 and 6-17, respectively. The corresponding annual frequencies of unacceptable performance of individual isolator units are listed in Tables 6-12, 6-13, 6-14 and 6-15, respectively. These frequencies are smaller than 10^{-6} for all combinations of site and β, and decrease substantially with greater confidence in an isolator's performance.

Providing a stop (and thus the displacement capacity of FP bearing) at the six sites of Figure 6-13 equal to one half that required at Diablo Canyon would reduce the annual frequency of unacceptable performance. The fragility curves corresponding to $f_{AR} = 1.1\kappa$ are plotted in Figure 6-18 and the annual frequencies of unacceptable performance are listed in Table 6-16. These frequencies are smaller than those of Table 6-12 by a factor of between 2 and 40.

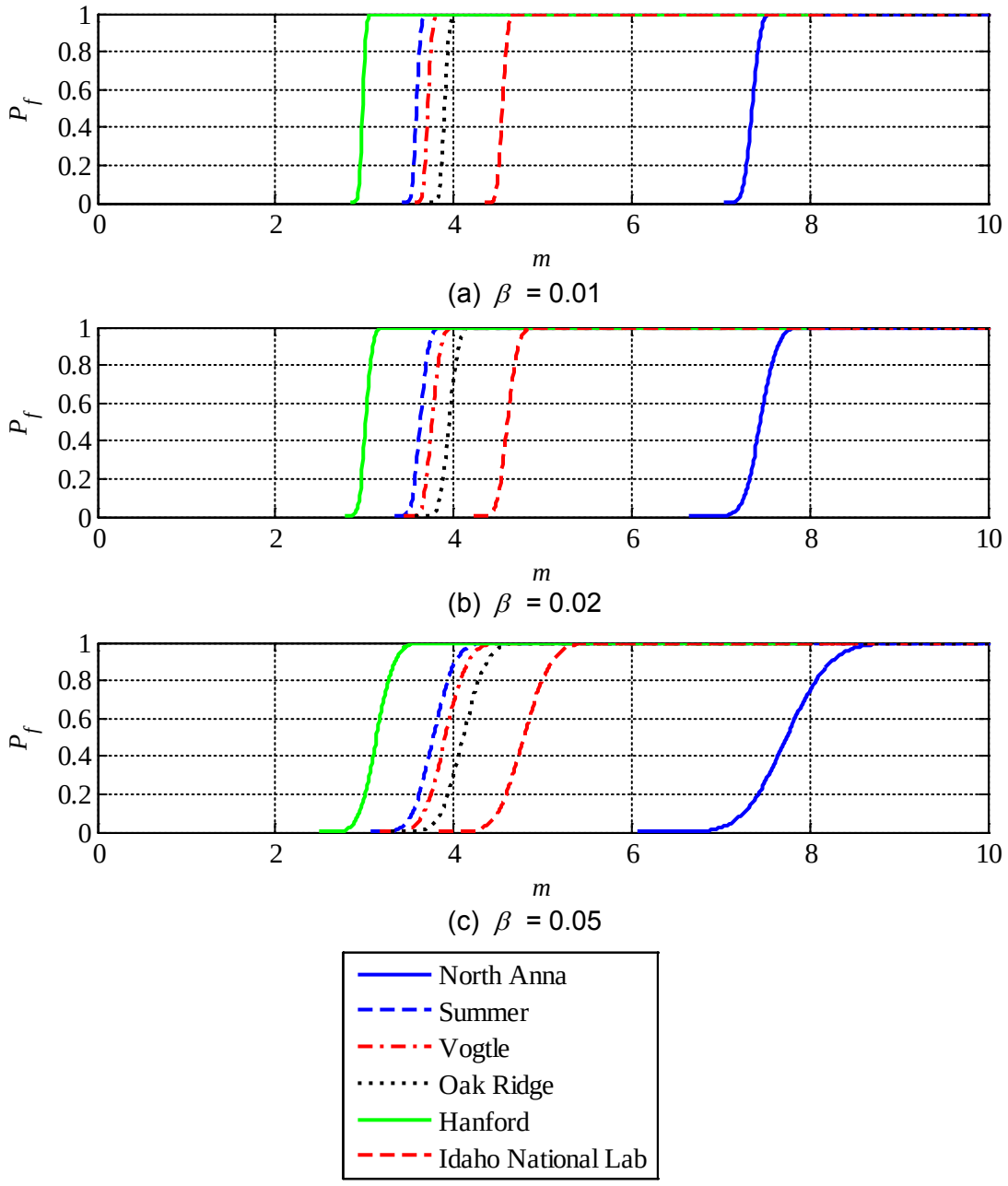

Figure 6-13 Probability of Unacceptable Performance, P_f, of the Individual Isolator Units Tested with 90% Confidence at One Half of the 90th Percentile Displacement for BDB GMRS Shaking for Diablo Canyon ($f_{AR} = 1.1\kappa$) Plotted Against Multiples, *m*, of UHRS Shaking with MAFE of 10^{-4}, Without a Stop

Table 6-11 Annual Frequency of Unacceptable Performance ($\times 10^{-6}$) of Individual Isolator Units Tested with 90% Confidence at One Half of the 90th Percentile Displacement for BDB GMRS Shaking for Diablo Canyon, Without a Stop

	Site					
	North Anna	Summer	Vogtle	Oak Ridge	Hanford	Idaho
$\beta = 0.01$	1.9	3.8	2.5	5.1	2.1	0.2
$\beta = 0.02$	1.8	3.7	2.4	4.9	2.0	0.2
$\beta = 0.05$	1.7	3.4	2.2	4.5	1.7	0.2

6.6.4 Annual Frequency of Unacceptable Performance of the Safety-Related Umbilical Lines

The safety-related umbilical lines are designed per NUREG-0800 (USNRC, 2007b) at GMRS+ shaking and the *prototypes* are tested for a 90+% confidence at a displacement equal to the CS (or 90th percentile displacement for BDB GMRS shaking), as noted in Section 6.4.2 . The seismic isolation NUREG/CR 7253 recommends that all prototype safety-related umbilical lines be tested to demonstrate a 90+% confidence. Testing a smaller number of *prototype* umbilical lines may be sufficient if the variability in the behavior of umbilical lines is small and a confidence of greater than 90% is established at a displacement equal to the CS.

The annual frequency of unacceptable performance of safety-related umbilical lines is calculated using an approach similar to that for the isolation system presented in Section 6.6.3. Failure of each safety-related umbilical line is very conservatively assumed to result in core melt and release of radiation, because mitigating measures are ignored, noting they will vary as a function of plant design. The fragility curves of the umbilical lines tested with different confidence and shaking level combinations are considered identical to those plotted in Figures 6-8 through 6-12 for individual isolator units, if a stop is not present, and Figures 6-14 through 6-17, if a stop is present. The resulting annual frequencies of unacceptable performance are less than 10^{-5} and 10^{-6} if a stop is absent and present, respectively (see Tables 6-7 through 6-15).

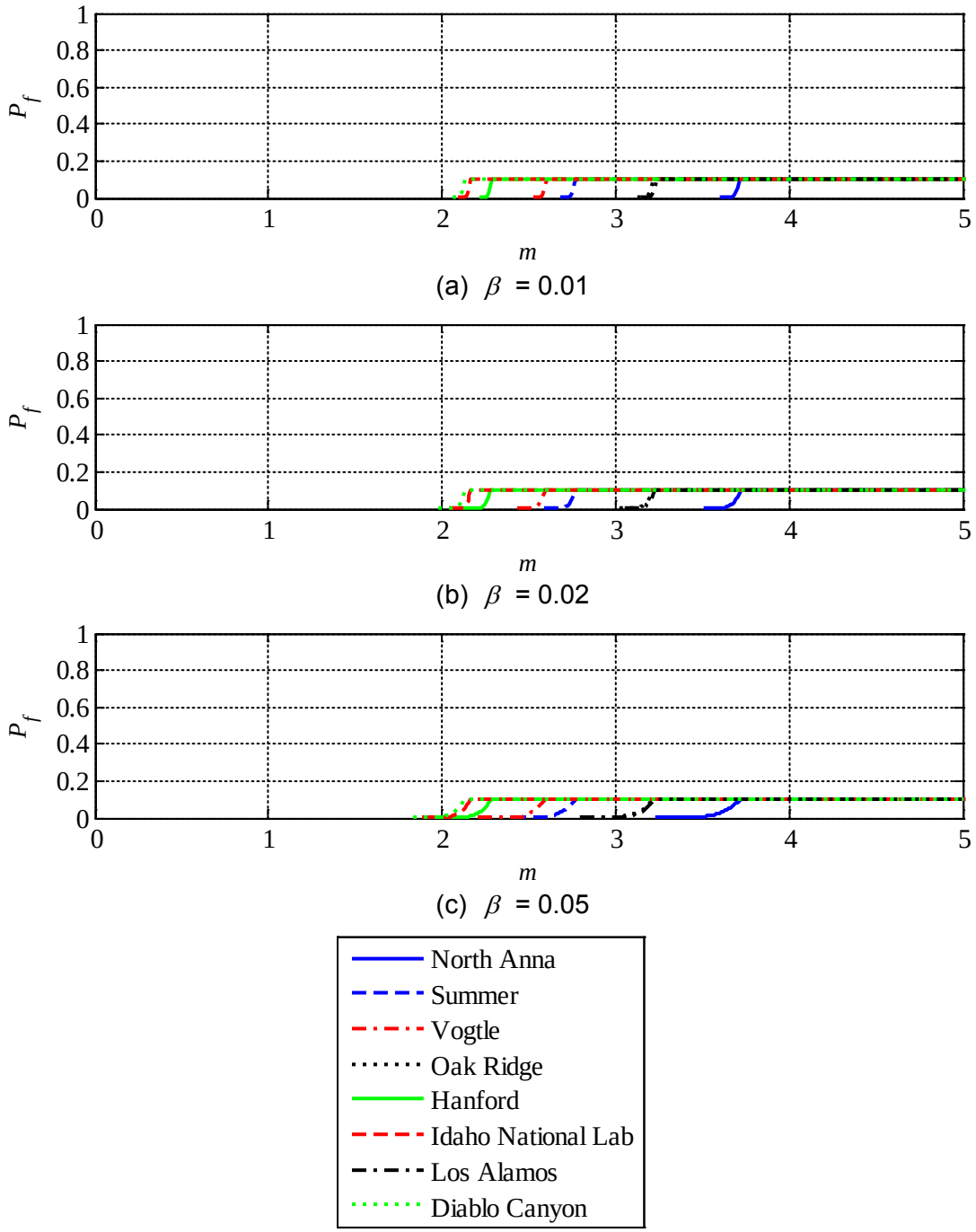

Figure 6-14 Probability of Unacceptable Performance, P_f, of Individual Isolator Units for 90% Confidence at the Median Displacement for 110% BDB GMRS Shaking Plotted Against Multiples, *m*, of UHRS Shaking with MAFE of 10^{-4}, with a Stop at the 90th Percentile Displacement for BDB GMRS Shaking

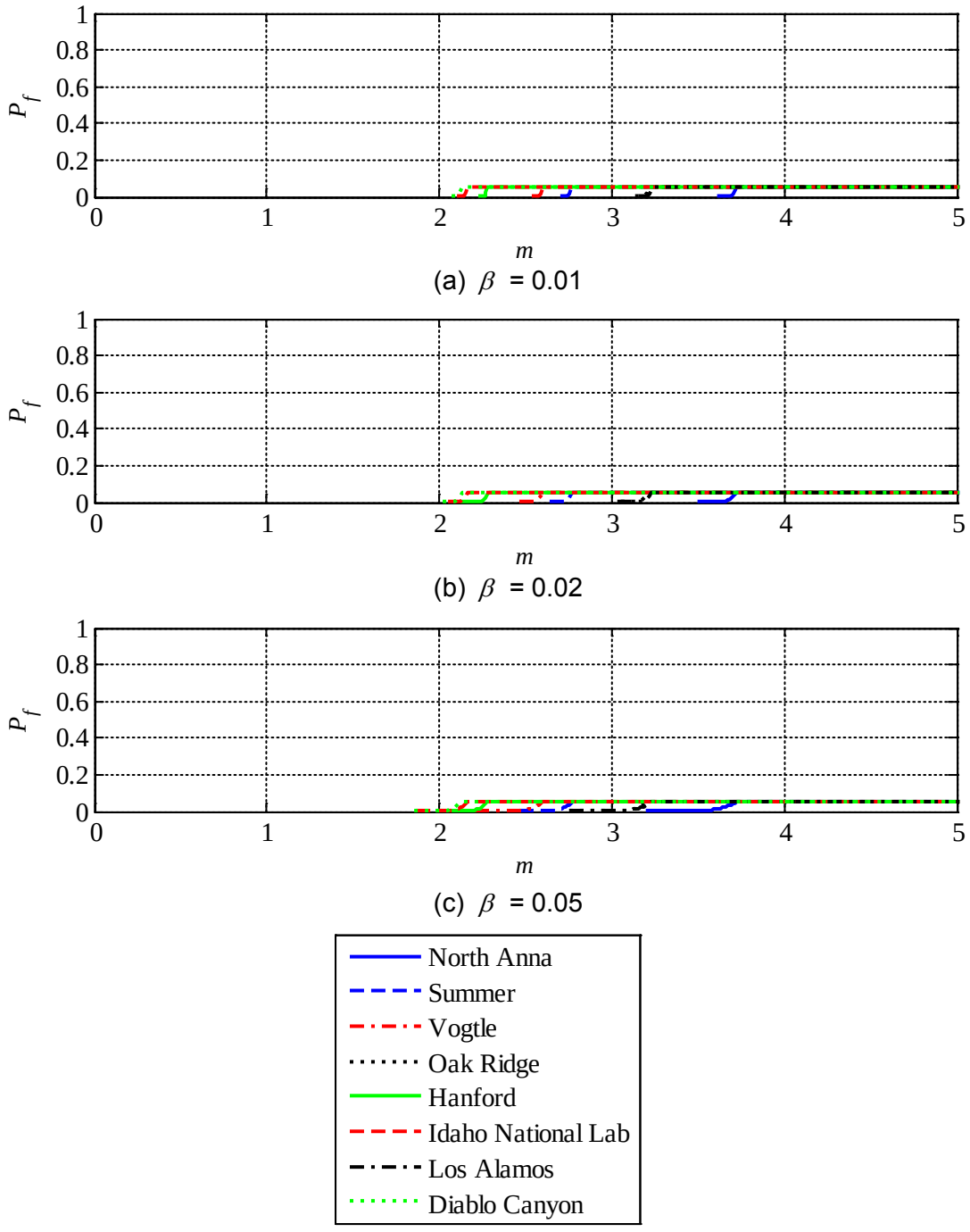

Figure 6-15 Probability of Unacceptable Performance, P_f, of Individual Isolator Units for 95% Confidence at the Median Displacement for 110% BDB GMRS Shaking Plotted Against Multiples, *m*, of UHRS Shaking with MAFE of 10^{-4}, with a Stop at the 90th Percentile Displacement for BDB GMRS Shaking

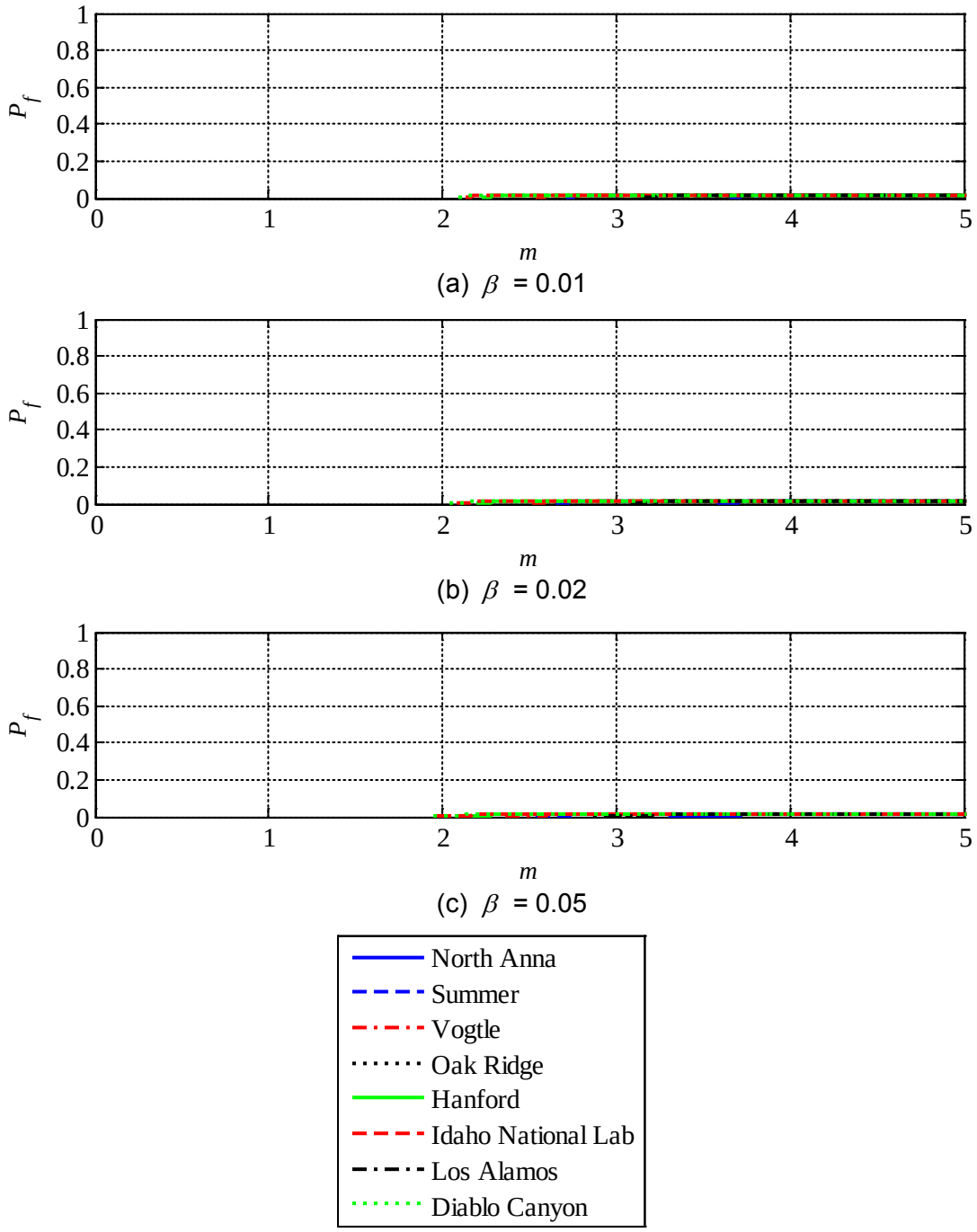

Figure 6-16 Probability of Unacceptable Performance, P_f, of Individual Isolator Units for 99% Confidence at the Median Displacement for 110% BDB GMRS Shaking Plotted Against Multiples, m, of UHRS Shaking with MAFE of 10^{-4}, with a Stop at the 90th Percentile Displacement for BDB GMRS Shaking

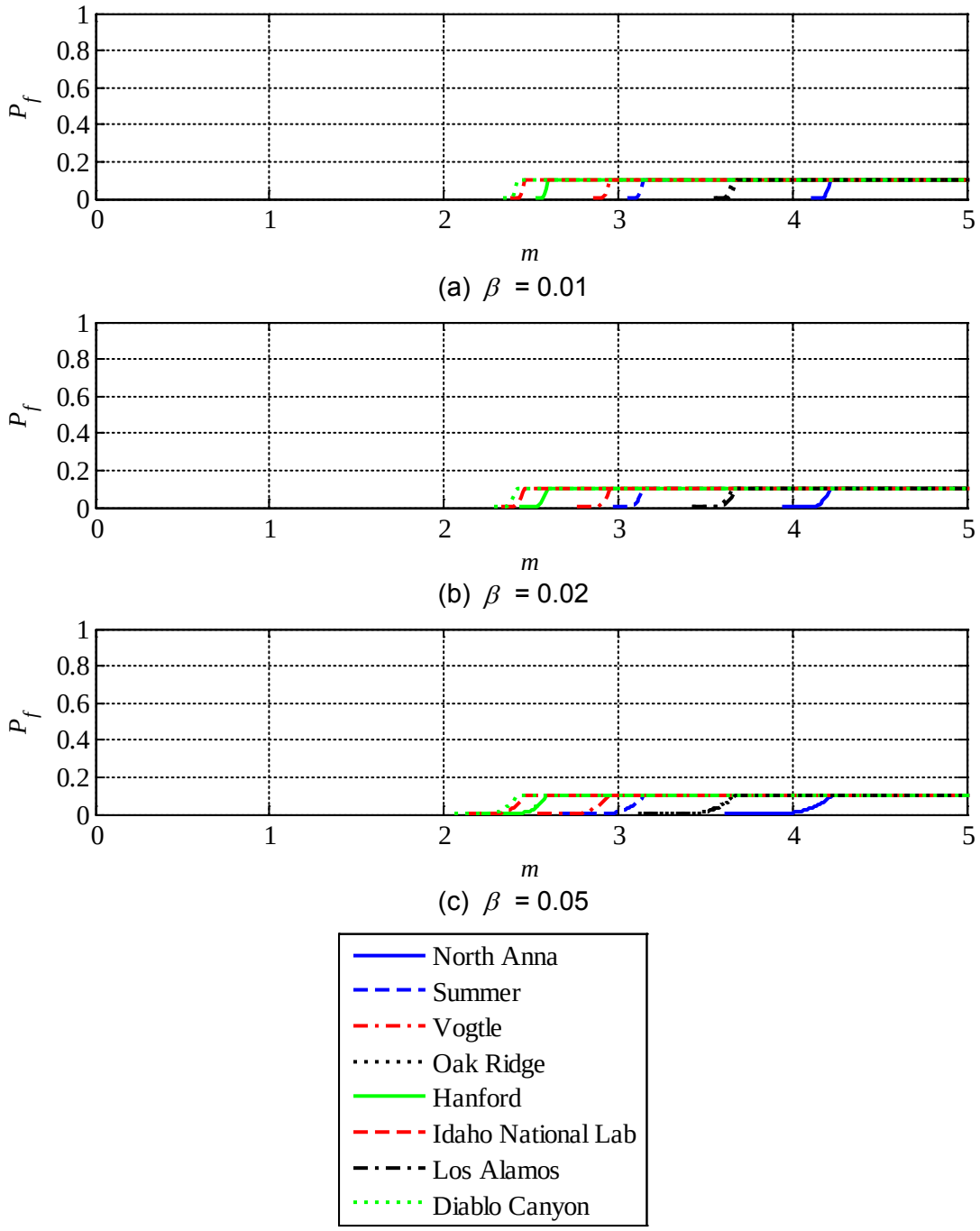

Figure 6-17 Probability of Unacceptable Performance, P_f, of Individual Isolator Units for 90% Confidence at the Median Displacement for 125% BDB GMRS Shaking Plotted Against Multiples, *m*, of UHRS Shaking with MAFE of 10^{-4}, with a Stop at the 90th Percentile Displacement for BDB GMRS Shaking

Table 6-12 Annual Frequency of Unacceptable Performance ($\times 10^{-6}$) of Individual Isolator Units Tested with 90% Confidence at the Median Displacement for 110% BDB GMRS Shaking, with a Stop at the 90th Percentile Displacement for BDB GMRS Shaking

	Site							
	North Anna	Summer	Vogtle	Oak Ridge	Hanford	Idaho	Los Alamos	Diablo Canyon
$\beta = 0.01$	0.8	0.8	0.8	0.8	0.7	0.7	0.8	0.6
$\beta = 0.02$	0.8	0.8	0.8	0.8	0.7	0.7	0.8	0.7
$\beta = 0.05$	0.9	0.8	0.8	0.8	0.8	0.8	0.8	0.7

Table 6-13 Annual Frequency of Unacceptable Performance ($\times 10^{-6}$) of Individual Isolator Units Tested with 95% Confidence at the Median Displacement for 110% BDB GMRS Shaking, with a Stop at the 90th Percentile Displacement for BDB GMRS Shaking

	Site							
	North Anna	Summer	Vogtle	Oak Ridge	Hanford	Idaho	Los Alamos	Diablo Canyon
$\beta = 0.01$	0.4	0.4	0.4	0.4	0.3	0.3	0.4	0.3
$\beta = 0.02$	0.4	0.4	0.4	0.4	0.4	0.4	0.4	0.3
$\beta = 0.05$	0.4	0.4	0.4	0.4	0.4	0.4	0.4	0.3

Table 6-14 Annual Frequency of Unacceptable Performance ($\times 10^{-6}$) of Individual Isolator Units Tested with 99% Confidence at the Median Displacement for 110% BDB GMRS Shaking, with a Stop at the 90th Percentile Displacement for BDB GMRS Shaking

	Site							
	North Anna	Summer	Vogtle	Oak Ridge	Hanford	Idaho	Los Alamos	Diablo Canyon
$\beta = 0.01$	0.08	0.08	0.08	0.08	0.07	0.07	0.08	0.06
$\beta = 0.02$	0.08	0.08	0.08	0.08	0.07	0.07	0.08	0.07
$\beta = 0.05$	0.09	0.08	0.08	0.08	0.07	0.07	0.08	0.07

Table 6-15 Annual Frequency of Unacceptable Performance ($\times 10^{-6}$) of Individual Isolator Units Tested with 90% Confidence at the Median Displacement for 125% BDB GMRS Shaking, with a Stop at the 90th Percentile Displacement for BDB GMRS Shaking

	Site							
	North Anna	Summer	Vogtle	Oak Ridge	Hanford	Idaho	Los Alamos	Diablo Canyon
$\beta = 0.01$	0.6	0.6	0.5	0.6	0.4	0.4	0.5	0.3
$\beta = 0.02$	0.6	0.6	0.5	0.6	0.4	0.4	0.5	0.3
$\beta = 0.05$	0.7	0.6	0.5	0.6	0.4	0.4	0.5	0.4

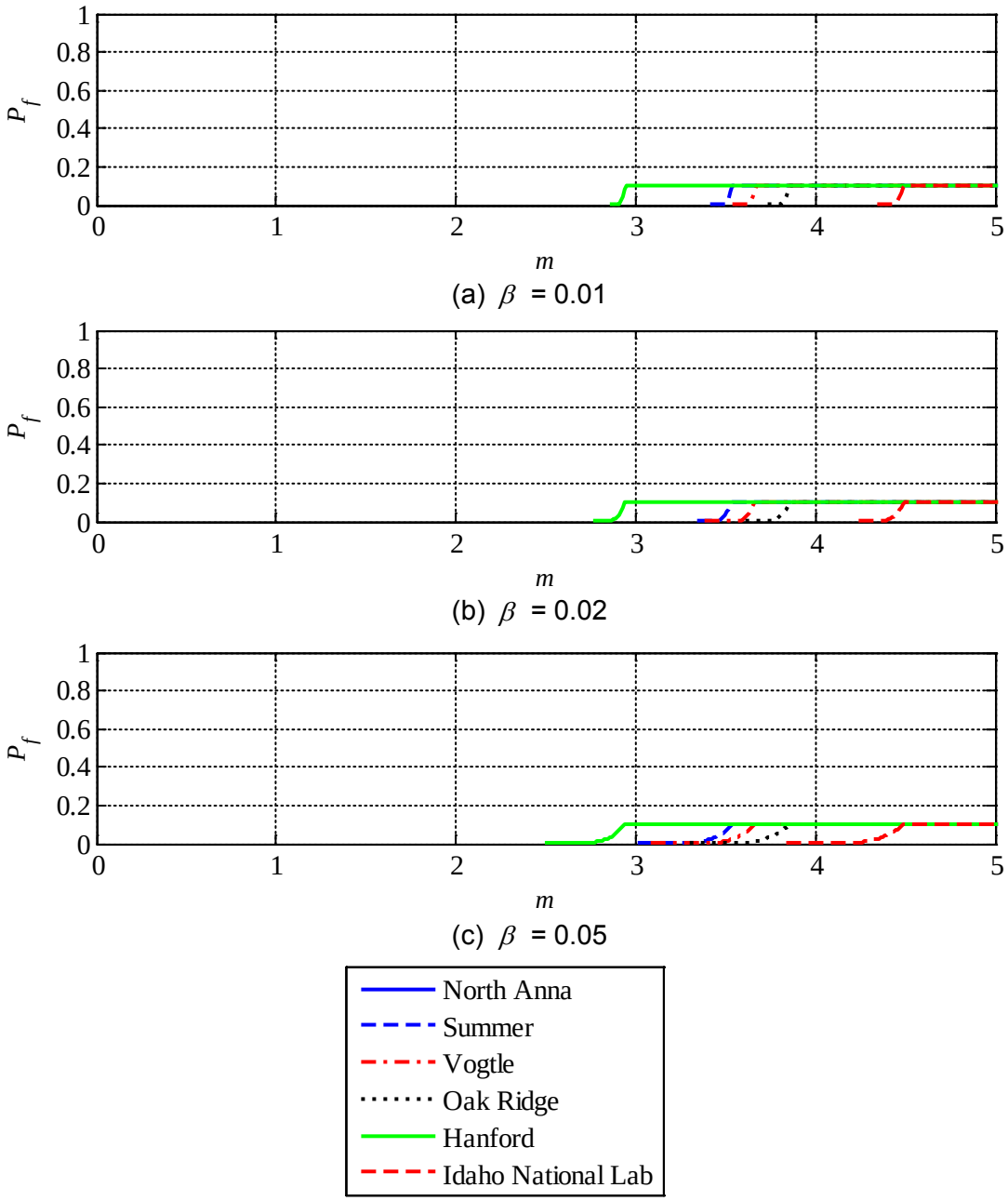

Figure 6-18 Probability of Unacceptable Performance, P_f, of Individual Isolator Units Tested with 90% Confidence for the Median Displacement for 110% κ BDB GMRS Shaking Plotted Against Multiples, *m*, of UHRS Shaking with MAFE of 10-4, with a Stop at the Median Displacement for 110% κ BDB GMRS Shaking

Table 6-16 Annual Frequency of Unacceptable Performance ($\times 10^{-6}$) of Individual Isolator Units Tested with 90% Confidence at the Median Displacement for 110%κ BDB GMRS Shaking, with a Stop at the Median Displacement for 110%κ BDB GMRS Shaking

	Site					
	North Anna	Summer	Vogtle	Oak Ridge	Hanford	Idaho
$\beta = 0.01$	0.19	0.40	0.27	0.53	0.23	0.02
$\beta = 0.02$	0.20	0.41	0.27	0.54	0.23	0.02
$\beta = 0.05$	0.20	0.43	0.28	0.55	0.25	0.02

6.7 Design Factor for Seismically Isolated Nuclear Power Plants

The target annual frequency of unacceptable performance for a structure, system or component in a conventional (fixed base) nuclear power plant (SDC 5 per ASCE 43-05) is 10^{-5}. This goal is achieved by using materials standards such as ACI 349 and seismic demands consistent with a ground motion response spectrum calculated as the product of a UHRS at an annual frequency of exceedance of 10^{-4} and a design factor, *DF*, which is 1.0 or greater.

The calculations presented in Section 6.6 were based on a GMRS calculated using a UHRS at an annual frequency of exceedance of 10^{-4} and *DF* equal to 1.0, and an BDB GMRS that is defined, for the sites considered here, by a UHRS at an annual frequency of exceedance of 10^{-5}. These calculations show that the annual frequency of unacceptable performance is less than 10^{-5} if no stop is provided and less than 10^{-6} if a stop is installed at the 90th percentile BDB GMRS displacement, confirming that *DF* can be set equal to 1.0 for seismically isolated nuclear power plants.

The derivation of the design factor in ASCE 43-05 focuses on the effects of horizontal earthquake shaking. The vertical elements in the gravity and lateral load resisting systems in a nuclear power plant such as AP1000 (Schulz, 2006) are walls and not columns, for which failure due to excessive vertical loading is extremely unlikely because design axial stresses are very low. A much greater seismic margin is expected in the vertical direction than the horizontal direction. Since the vertical seismic demands in an isolated nuclear power plant should be no greater than those in a conventional (fixed base) nuclear power plant, there is no need to increase the vertical UHRS by a design factor to compute the GMRS. Seismically isolated nuclear structures with columns providing much of the vertical load resistance (regardless of cause) should be evaluated for shaking in excess of design basis to ensure their annual frequency of unacceptable performance is less than 10^{-5}.

7 SEISMIC ISOLATION OF NUCLEAR STRUCTURES USING FRICTION PENDULUM™ BEARINGS

7.1 Introduction

This chapter presents the results of response-history analyses of rigid nuclear power plant structures seismically isolated using Friction Pendulum™ (FP) bearings. A single FP bearing is considered appropriate to represent the isolated superstructure, with the mass of the superstructure attached to the slider of the bearing and the sliding surface fixed to the ground. Bearings are subjected to ground motions consistent with 10,000-year and 100,000-year seismic hazard at two sites: 1) Diablo Canyon, CA, a site of high seismicity, and 2) Vogtle, GA, a site of moderate seismicity. A set of 30 ground motions are spectrally matched to the 10,000-year uniform hazard response spectrum (UHRS) for the Diablo Canyon site. Sets of ground motions consistent with 100,000-year hazard for Diablo Canyon, and 10,000-year and 100,000-year hazards for Vogtle are obtained by amplitude scaling the spectrally matched motions. The 10,000-year ground motions for Diablo Canyon are also amplitude scaled by 1.5 and 1.67 to represent the minimum hazard level for the site of Diablo Canyon for which the probability of unacceptable performance of isolated nuclear structures, systems and components must be less than 10% per the provisions of ASCE 43-05 (2005) and Kammerer et al. (2019), respectively.

Single FP bearings with a range of geometrical and material properties are subjected to the ground motions at the two hazard levels for the two sites with a goal of answering the following questions:

i. What is the influence of the choice for model for the variation in the coefficient of friction at the sliding surface (e.g., Coulomb model, pressure-dependent) on key response quantities (e.g., isolation system displacement, floor spectra)?

ii. Is the influence of the choice of friction model, if any, a function of shaking intensity and/or bearing parameters (e.g., static axial pressure, reference coefficient of friction)?

iii. How does the response of a single FP bearing change with shaking intensity and/or change in bearing parameters?

iv. Is the clearance to the stop determined by the 90^{th} percentile peak displacement for 100,000-year shaking or the 99^{th} percentile peak displacement for the 10,000-year shaking?

v. Is the median displacement for 1.1 times 100,000-year shaking less than or equal to the 90^{th} percentile displacement for 100,000-year shaking?

Ground motions consistent with 10,000-year and 100,000-year earthquake shaking are developed in Sections 7.2 and 7.3 for the sites of Diablo Canyon and Vogtle, respectively. Modeling of isolators and analysis are discussed in Section 7.4. Key results are presented in Section 7.5.

7.2 Diablo Canyon: 10,000-Year and 100,000-Year Earthquake Shaking

Figure 7-1 presents the UHRS for the Diablo Canyon site and a return period of 10,000 years, obtained from the USGS website http://geohazards.usgs.gov/hazardtool/application.php (accessed on July 15, 2014). The set of 30 seeds motions listed in Table 7-1 are spectrally matched to the UHRS in the two horizontal directions. The target spectrum in the vertical direction is obtained by multiplying the UHRS of Figure 7-1 with the ratio of vertical to horizontal spectra of Figure 5-5. The period range considered for spectral matching is 0.01 s to 5 s. The response spectra of the scaled motions are plotted with the target spectra in Figure 7-2.

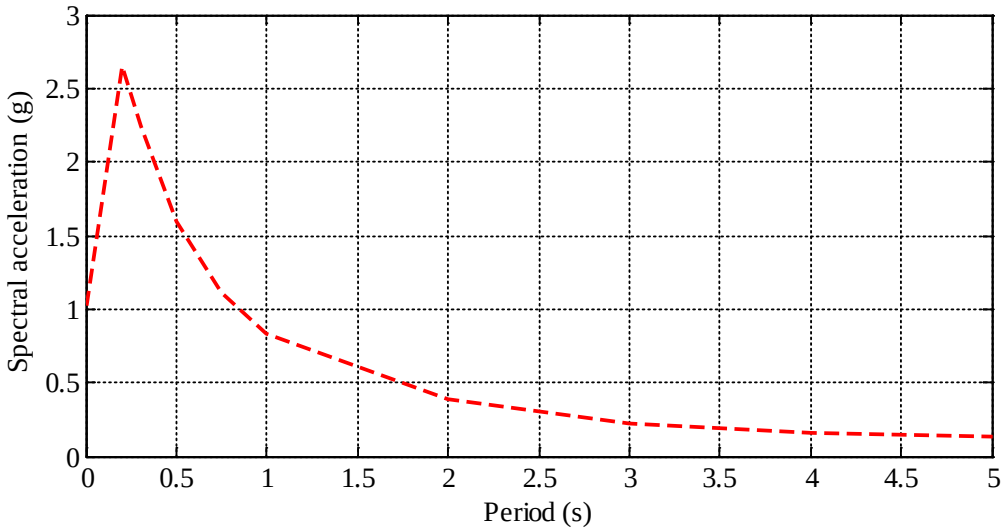

Figure 7-1 10,000 Year Return Period UHRS for the Diablo Canyon Site

The 100,000-year UHRS for horizontal shaking is also obtained from the USGS website. The ratios of the 100,000-year to 10,000-year spectral ordinates at selected natural periods are plotted in Figure 7-3. The ratios range between 1.8 and 1.9 for period less than 1 s and between 1.9 and 2.1 at longer periods. The 10,000-year ground motions for Diablo Canyon (see Figure 7-2) amplitude scaled by a factor of 2.0[37] are considered to represent 100,000-year shaking at the site. A discussion on appropriateness of amplitude scaling the ground motions consistent with a shaking level at a site to represent the seismic hazard at a different shaking level is presented in Appendix G.

7.3 Vogtle: 10,000-Year and 100,000-Year Earthquake Shaking

The 10,000-year and 100,000-year UHRS for the site of the Vogtle nuclear power plant (latitude: 33.1433 N, longitude: 81.7606 W) are obtained from the USGS website identified previously. The two spectra are plotted in Figure 7-4 for Site Class B per ASCE 7-10 (ASCE (2010)), namely, V_{s30} equal to 760 m/s.

[37] The 10,000-year CMS, UHRS and CS are consistent with each other in Chapter 5. These ordinates are obtained from CMS data available at the USGS website. Conditional mean spectrum data are not available for 100,000-year shaking, which is obtained directly from the hazard curves from the USGS assuming a linear relationship between frequency and an intensity measure (e.g., PGA) in the log space. Uniform hazard response spectrum data are available at both return periods from the USGS website.

The ground motions of Figure 7-2 are amplitude scaled to represent 10,000-year and 100,000-year shaking at the Vogtle site. The ratio of 10,000-year UHRS ordinates for Vogtle to Diablo Canyon ranges between 0.2 and 0.3 for periods between 0.01 s and 2 s (see Figure 7-5). Similarly, the ratio of the spectral ordinates of the Vogtle 100,000-year UHRS to the Diablo Canyon 10,000-year UHRS ranges between 0.5 and 0.9 at periods less than 1 s, and between 0.5 and 0.7 at longer periods. The ground motions of Figure 7-2, amplitude scaled by the

factors of 0.25 and 0.6, are assumed to approximately represent 10,000-year and 100,000-year earthquake shaking, respectively, at the site of the Vogtle nuclear power plant (see also Appendix G).

Table 7-1 Seed Motions

Sl No	NGA Number	Event	Year	Magnitude	Epicentral Distance (km)
1	72	San Fernando	1971	6.6	24
2	77	San Fernando	1971	6.6	12
3	80	San Fernando	1971	6.6	39
4	180	Imperial Valley	1979	6.5	28
5	284	Irpinia	1980	6.9	33
6	285	Irpinia	1980	6.9	23
7	68	San Fernando	1971	6.6	40
8	292	Irpinia	1980	6.9	30
9	763	Loma Prieta	1989	6.9	29
10	179	Imperial Valley	1979	6.5	27
11	161	Imperial Valley	1979	6.5	43
12	810	Loma Prieta	1989	6.9	16
13	184	Imperial Valley	1979	6.5	27
14	957	Northridge	1994	6.7	64
15	1107	Kobe	1995	6.9	24
16	994	Northridge	1994	6.7	25
17	1011	Northridge	1994	6.7	19
18	1012	Northridge	1994	6.7	14
19	1021	Northridge	1994	6.7	50
20	1050	Northridge	1994	6.7	20
21	1051	Northridge	1994	6.7	20
22	1078	Northridge	1994	6.7	15
23	1091	Northridge	1994	6.7	38
24	1528	Chi-Chi	1999	7.6	45
25	159	Imperial Valley	1979	6.5	3
26	879	Landers	1992	7.3	44
27	754	Loma Prieta	1989	6.9	31
28	802	Loma Prieta	1989	6.9	27
29	1633	Manjil	1990	7.4	40
30	1144	Gulf of Aqaba	1995	7.2	93

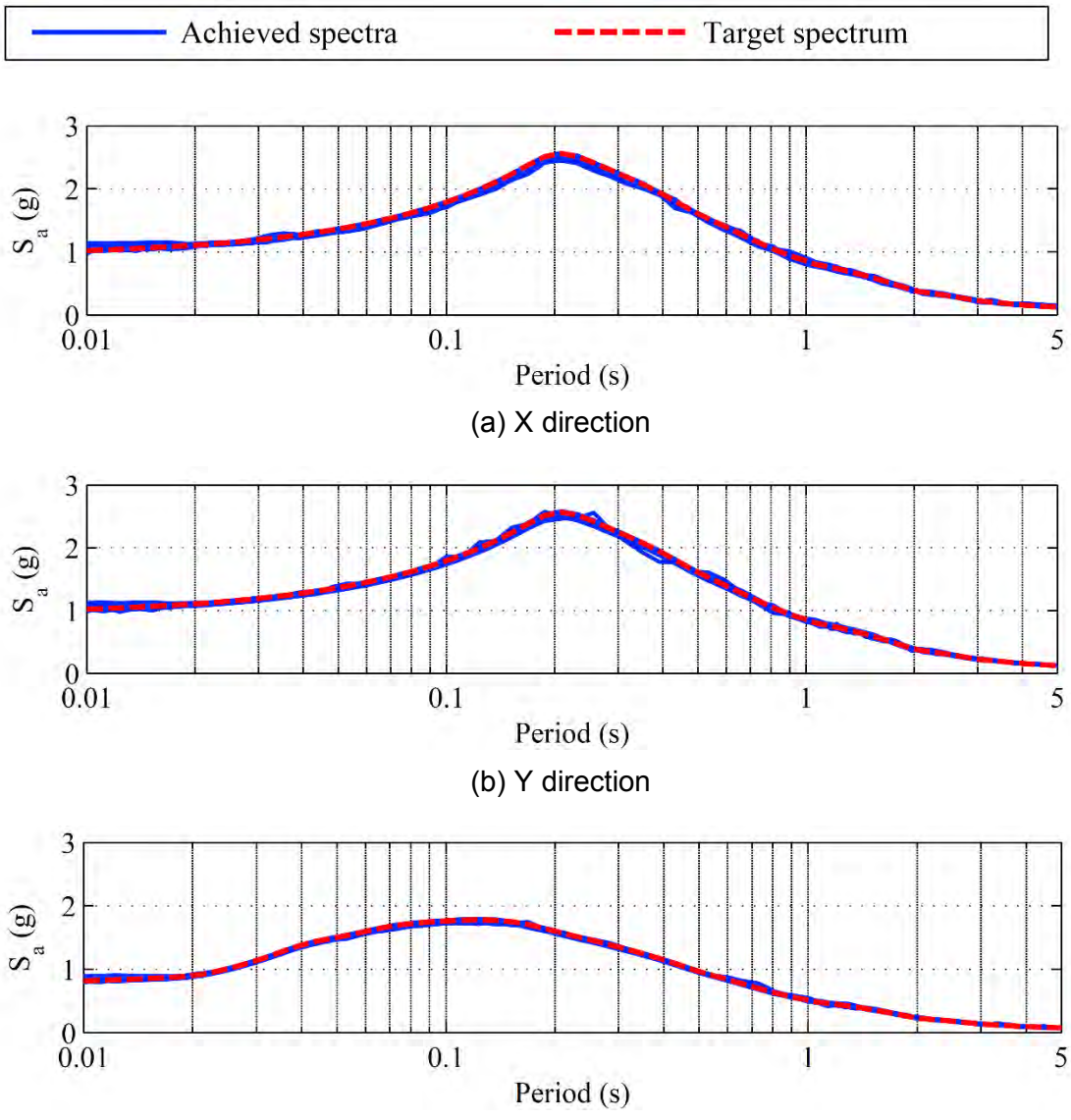

(a) X direction

(b) Y direction

(c) Z direction

Figure 7-2 Response Spectra of the Ground Motions Spectrally Matched to the 10,000 Year Return Period UHRS for the Diablo Canyon Site

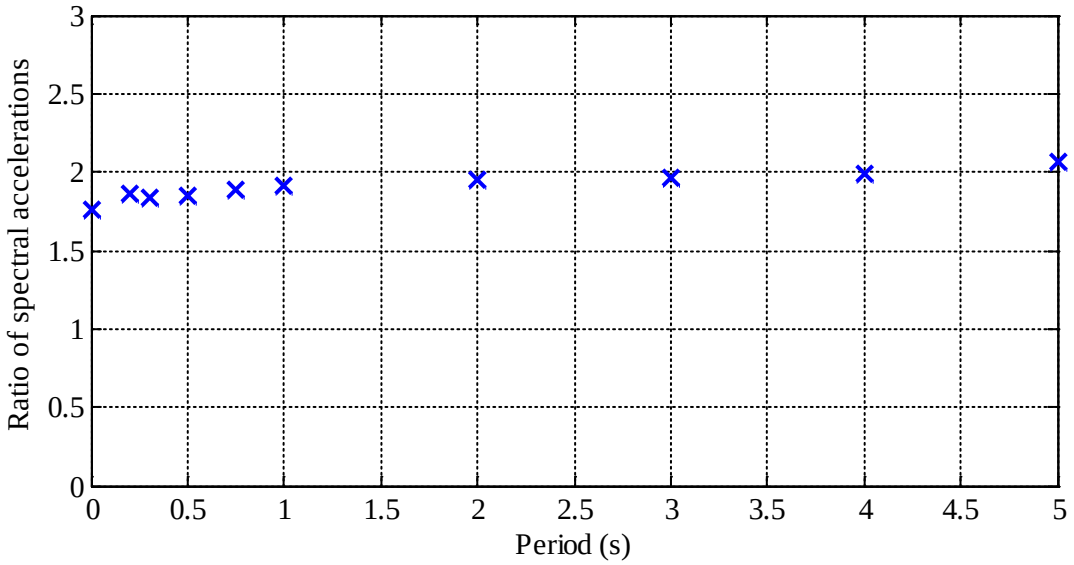

Figure 7-3 Ratio of UHRS Spectral Ordinates for 100,000 Years to 10,000 Years at the Diablo Canyon Site

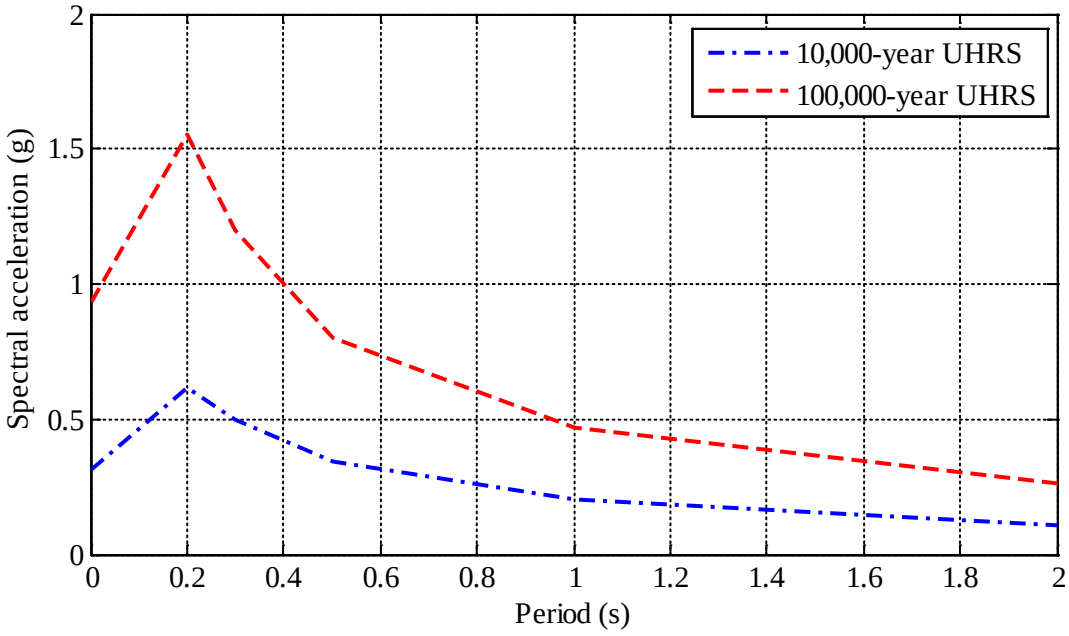

Figure 7-4 10,000-Year and 100,000-Year Return Period Uniform Hazard Spectra for the Site of the Vogtle Nuclear Power Plant (V_{s30} = 760 m/s)

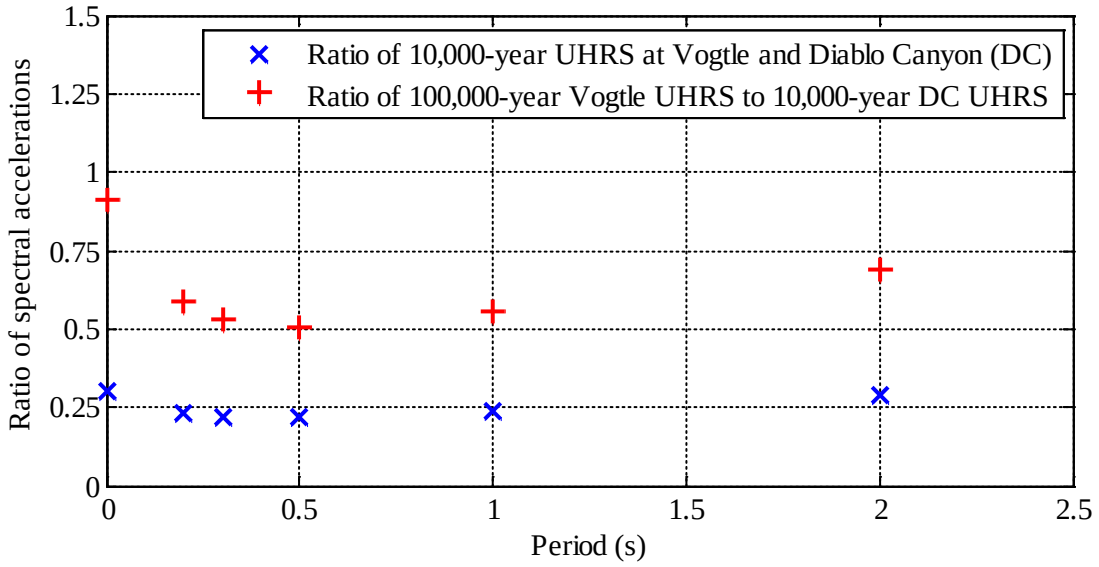

Figure 7-5 Ratios of Spectral Accelerations of 10,000-Year and 100,000-Year UHRS for the Vogtle Site to Spectral Accelerations of 10,000-Year UHRS for the Diablo Canyon Site

7.4 Isolator Modeling and Analysis

7.4.1 Properties of Friction Pendulum™ Bearings

Four values of sliding period (1.5 s, 2 s, 3 s and 4 s) are considered herein. The coefficient of friction, $\mu(p,T,v)$, adjusted for the effects of instantaneous values of axial pressure on the bearing, p, temperature at the sliding surface, T, and sliding velocity, v, is given by

$$\mu(p,T,v) = \mu_{ref} \times (k_p k_T k_v) \quad \textbf{(7-1)}$$

where μ_{ref} is the reference coefficient of friction, and k_p, k_T and k_v are factors (see Chapter 3) to account for the effects of pressure, temperature and velocity, respectively, and all other parameters were defined previously. Three values of μ_{ref} are considered: 0.03, 0.06 and 0.09. The factor k_p is defined for a reference axial pressure, p_o. Two values of p_o are considered: 10 MPa and 50 MPa. Five models to characterize coefficient of friction at the sliding surface that consider the influences of pressure, temperature and velocity are listed in Table 7-2.

Table 7-2 Friction Models That Consider Pressure, Temperature and Velocity Effects

	Friction model	Notation
Model 1	Coulomb	$\mu = \text{Coulomb}$
Model 2	Pressure dependent	$\mu = f(p)$
Model 3	Temperature dependent	$\mu = f(T)$
Model 4	Velocity dependent	$\mu = f(v)$
Model 5	Pressure, temperature and velocity dependent	$\mu = f(p,T,v)$

7.4.2 Input Ground Motions

Thirty sets of ground motions spectrally matched to the 10,000-year UHRS for Diablo Canyon, with six amplitude scaling factors, namely, 0.25, 0.6, 1.0, 1.5, 1.67 and 2.0, are used for analysis. The purpose of each scale factor is described in Table 7-3.

7.4.3 Modeling

A single FP bearing is modeled in OpenSees using the verified and validated OpenSees element *FPBearingPTV* (see Chapter 4). The mass corresponding to the static axial pressure on the bearing is assigned to the slider of the bearing in the two horizontal and vertical directions. The sliding surface is a fixed boundary. The rotational degrees of freedom about the two horizontal axes of the slider are restrained, and the slider is free to translate in the two horizontal directions. Assumptions on the modeling of FP bearings are discussed in Chapter 4. Mass proportional damping of 2% of critical, with the proportionality constant based on the sliding period of the FP bearing, is assigned to the system.

Table 7-3 Amplitude Scaling Factors to Represent Seismic Hazard at Different Sites

Amplitude scaling factor	Shaking intensity	Remarks
0.25	25%	10,000-year hazard at Vogtle
0.6	60%	100,000-year hazard at Vogtle
1.0	100%	10,000-year hazard at Diablo Canyon
1.5	150%	Minimum hazard level for Diablo Canyon at which target probability of unacceptable performance is less than 10% per ASCE (2005)
1.67	167%	Minimum hazard level for Diablo Canyon at which target probability of unacceptable performance is less than 10% per Kammerer et al. (2019)
2.0	200%	100,000-year hazard at Diablo Canyon

7.4.4 Vertical Component of Ground Motions

The instantaneous axial load on an FP bearing subjected to a set of three-component ground motion is a function of the static weight and the vertical component of ground motion. The instantaneous axial load is zero and loss of contact at the sliding surface takes place when the vertical ground acceleration exceeds the acceleration due to gravity. The lateral strength and stiffness of the single FP bearing are zero following the loss of contact. The vertical components of the ground motions are ignored in this chapter for amplitude scaling factors (see Table 7-3) greater than or equal to 1.5 because contact for the single isolator "system" is lost. The effects of ignoring the vertical component of ground motion on response are examined in Chapter 8.

7.4.5 Analysis Cases

FP bearings with four values of sliding period, three values of μ_{ref}, two values of reference axial pressure and friction at the sliding surface defined by five friction models are subjected to thirty sets of ground motions scaled to six intensities: a total of 21,600 (= $4 \times 3 \times 2 \times 5 \times 30 \times 6$) response-history analyses. The bearings experienced displacement demand greater than the corresponding radius of curvature for some combinations of geometrical, material properties, and intensity levels, leading to numerical problems. These combinations are ignored and are listed in Table 7-4 (a total of 4,200 response-history analyses). Select results from the remaining 17,400 response-history analyses are presented in the following sections.

Table 7-4 Combinations of Amplitude Scaling Factor, Sliding Period and Reference Coefficient of Friction Not Considered

Amplitude scaling factor	Sliding period	μ_{ref}
1.0	1.5 s	0.03
1.5	1.5 s	0.03, 0.06, 0.09
1.67	1.5 s	0.03, 0.06, 0.09
1.67	2 s	0.03
2.0	1.5 s, 2 s	0.03, 0.06, 0.09

7.5 Results

7.5.1 Coefficient of Friction

The change in the coefficient of friction over the duration of strong shaking is studied in this section. The duration of strong shaking for a component of the ground motion record is estimated using the approach suggested by Trifunac and Brady (1975). The history of cumulative sum of square of acceleration ordinates is computed

$$\zeta(t) = \int_{t=0}^{t} a(t)^2 \, dt \qquad \textbf{(7-2)}$$

where $\zeta(t)$ is the sum of square of the acceleration ordinates between time 0 and t, and $a(t)$ is the acceleration ordinate at time t. The duration of strong shaking for an acceleration history is defined by the difference in time between $\zeta(t)$ equal to 5% and 95% of its maximum value, and for a three-component ground motion is taken as the greater of the values computed for the two horizontal directions. Figure 7-6 presents the beginning and end of strong shaking for the 30 ground motions. The duration of strong shaking ranges between 6.6 s for ground motion (GM) number 18 to 30.9 s for GM29.

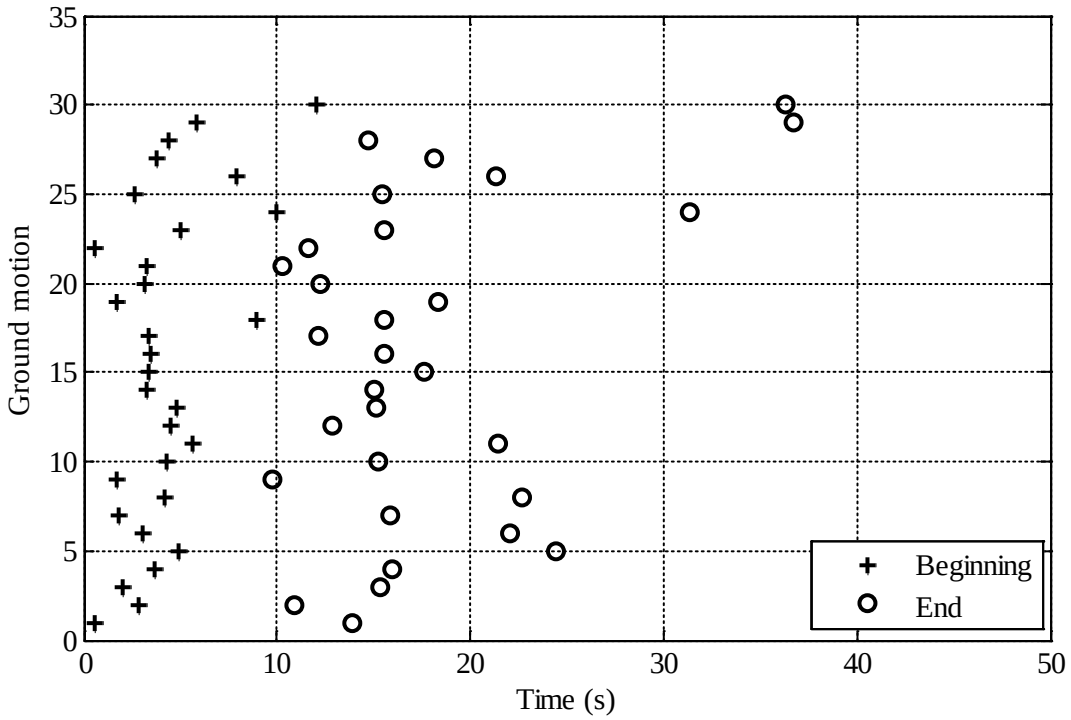

Figure 7-6 Duration of Strong Shaking for the Ground Motions

Figure 7-7(a) presents the histories of the coefficient of friction at the sliding surface of the FP bearing with a sliding period of 3 s, μ_{ref} of 0.06 and a static axial pressure of 50 MPa subjected to GM29 with amplitude scaling factor of 1.0. The histories are presented for two friction models: $\mu = f(p,T,v)$ and $\mu = \text{Coulomb}$. Also shown in the panel are the beginning and end of

strong shaking for the ground motion. The duration of strong shaking is denoted by T_{ss} in the figure. The value of μ at the start of shaking is 0.03 $\left(=\mu_{\min}=\mu_{\max}/2\right)$ because the velocity is small. The coefficient of friction ranges between 0.02 and 0.05 over the duration of strong shaking, with an average of 0.03 for the $\mu=f\left(p,T,v\right)$ model. The coefficient is 0.06 for the Coulomb model.

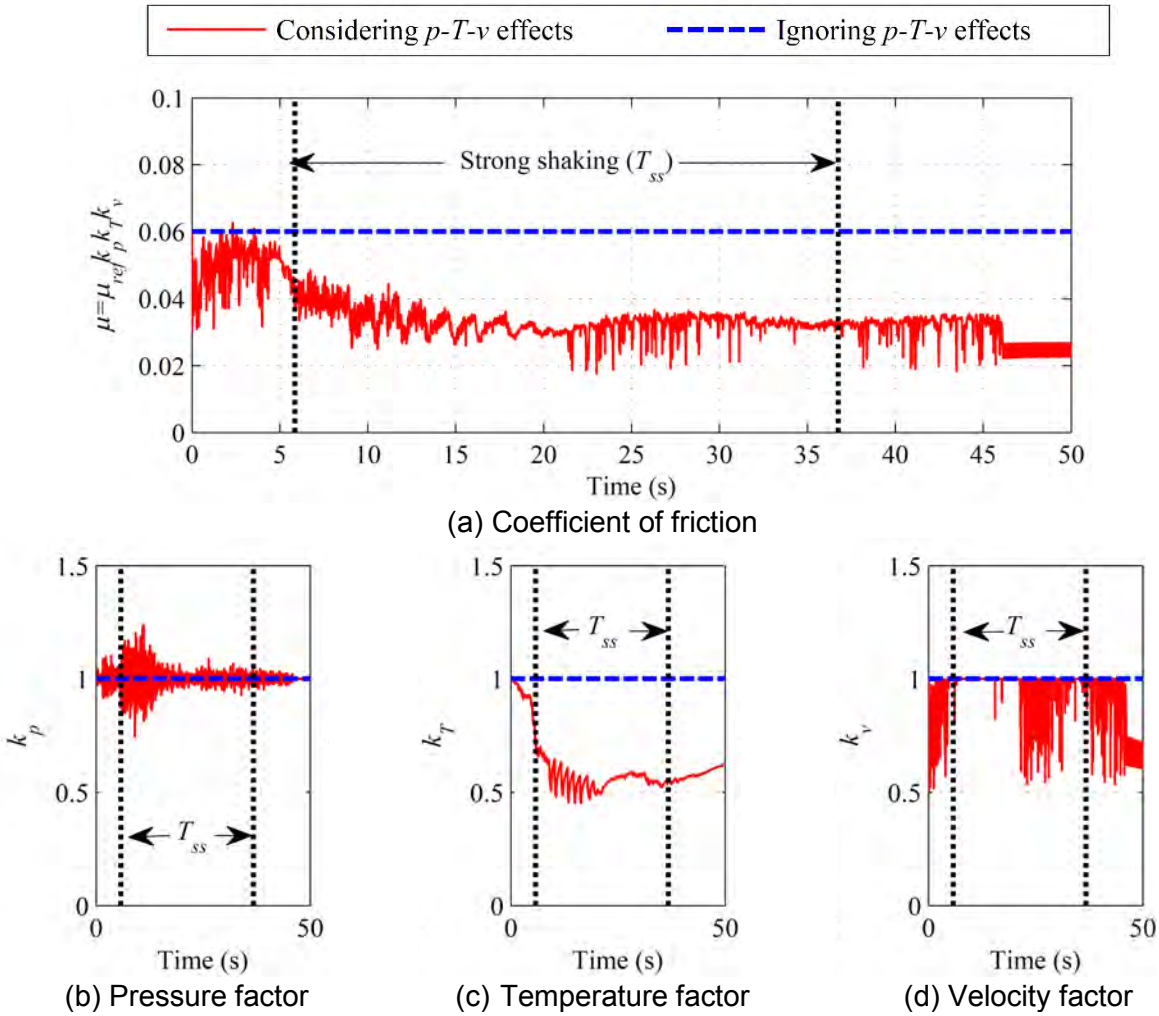

(a) Coefficient of friction

(b) Pressure factor

(c) Temperature factor

(d) Velocity factor

Figure 7-7 Histories of Coefficient of Friction, and Factors Accounting for the Influences of Axial Pressure, Temperature and Velocity for the 3 s FP Bearing with a Reference Coefficient of Friction of 0.06 Subjected to GM29

High frequency changes in the pressure factor, k_p, observed in Figure 7-7(b) are due to the vertical component of ground motion. The factor k_p varies between 0.7 and 1.2, with an average of 1.0. Figure 7-7(c) presents the history of the temperature factor, k_T, which varies between 0.5 and 0.7, with an average of 0.6 over the duration of strong shaking. The velocity factor, k_v, varies between 0.5 and 1.0, with an average of about 1.0 during the strong shaking (Figure 7-7(d)).

Figure 7-8(a) presents the coefficient of friction at the sliding surface averaged over the duration of strong shaking for the FP bearing with a sliding period of 2 s, p_o of 10 MPa and μ_{ref} of 0.06, for each of the 30 ground motions with an amplitude scaling factor of 1.0. The averaged coefficients are reported for each of the five friction models of Table 7-2.

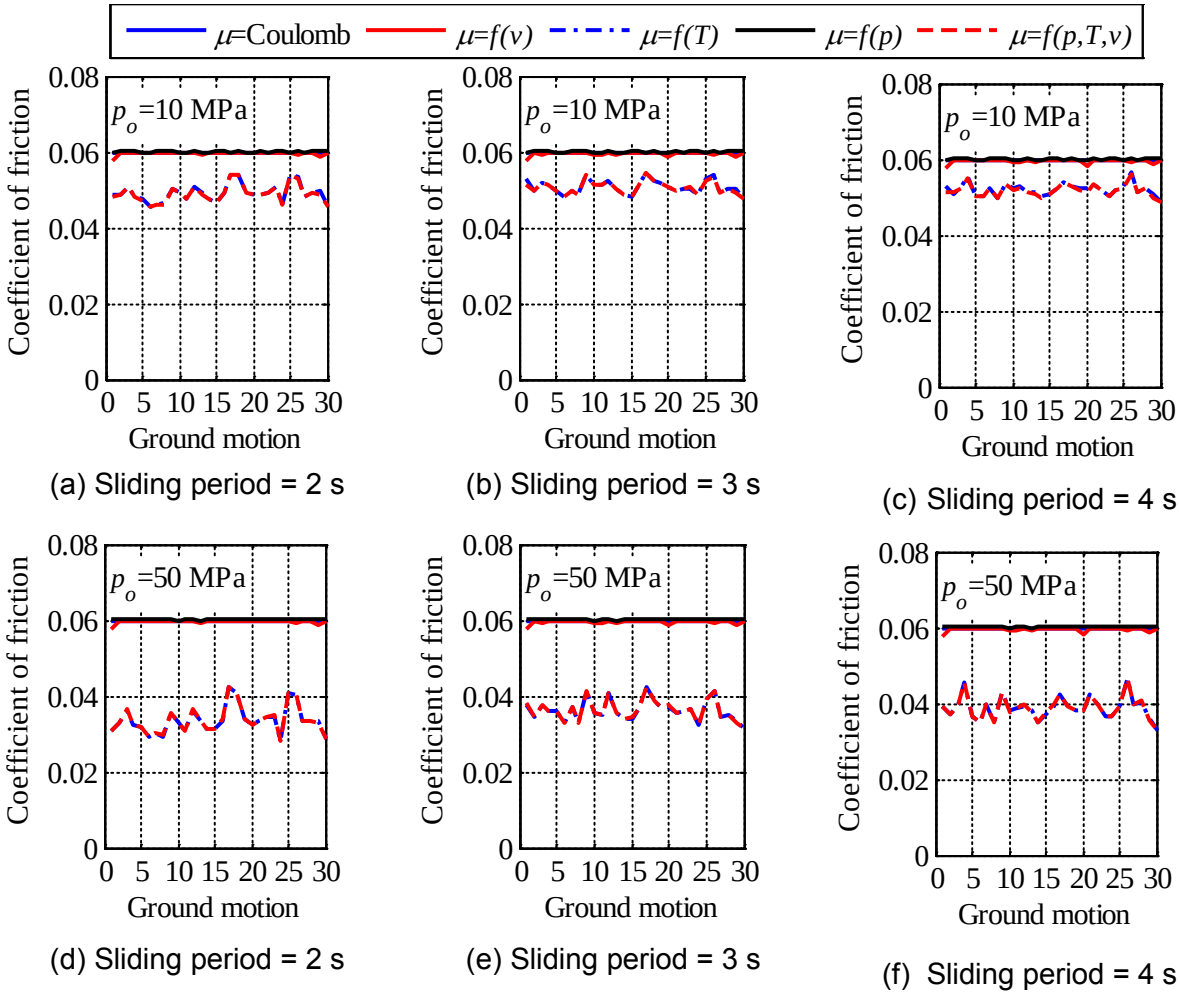

Figure 7-8 Coefficient of Friction Averaged over the Duration of Strong Shaking for Bearings with Different Geometrical Properties and Static Axial Load; μ_{ref} = 0.06, Amplitude Scale Factor = 1.0

The results of Figure 7-8(a) can be grouped into two bins, depending on whether the friction model includes heating effects. The average coefficients of friction are 0.06 when friction is defined using the Coulomb model, pressure-dependent model or velocity-dependent model, and range between 0.046 and 0.054 when the friction is defined using the temperature-dependent model or the model that considers all the three dependencies. Across the 30 ground motions, the average coefficient of friction over the duration of shaking is 0.049 (0.06) when heating effects are considered (ignored). In the remainder of this chapter, "average-30 coefficient of friction" is the average value of the coeffcient of friction over the duration of strong shaking for the 30 ground motions, unless noted otherwise.

Figures 7-8(b) and 7-8(c) present the average coefficient of friction over the duration of strong shaking for the bearings with sliding periods of 3 s and 4 s, respectively, for each ground motion set. The average coefficients of friction are 0.06 when heating effects are ignored, and 0.051 and 0.052 for the two panels, respectively, when the effects are considered. Figures 7-8(d), 7-8(e) and 7-8(f) present results for the 2 s, 3 s and 4 s FP bearings, respectively, with p_o of 50 MPa. Heating effects are more prominent for these three panels as the higher static axial pressure leads to greater heat generation at the sliding surface, greater increase in temperature, and a larger reduction in the coefficient of friction. The average-30 coefficient of friction is 0.034, 0.036 and 0.039, respectively, for the three panels when the heating effects are included in the friction model.

The results presented in Figure 7-8 suggest that the average coefficient of friction for a given ground motion is most heavily influenced by 1) whether the friction model includes heating effects, and 2) the static axial pressure on the bearing. The coefficient is 15% (35-40%) smaller when the friction model includes heating effects and p_o is 10 MPa (50 MPa). The change in the average-30 coefficient of friction due to heating with sliding period is small, with the least effect at a sliding period of 4 s.

Figure 7-9 presents the average-30 coefficients of friction for the FP bearing with a sliding period of 3 s, μ_{ref} of 0.03, 0.06 and 0.09, and p_o of 10 MPa and 50 MPa subjected to the ground motions scaled by the six factors of Table 7-3. The velocity and temperature dependencies of friction influence the average-30 coefficient of friction for an amplitude scale factor of 0.25: the minimum average-30 coefficient of friction computed using all five friction models is 9% (12%, 13%) smaller than μ_{ref} for p_o of 10 MPa and μ_{ref} of 0.03 (0.06, 0.09), as seen in Figure 7-9(a) (7-9(c), 7-9(e)). The difference is 17% (22%, 26%) for p_o of 50 MPa (see Figure 7-9(b) (7-9(d), 7-9(f))). The average-30 coefficient of friction is influenced primarily by whether heating effects are included in the friction model for amplitude scale factors of 0.6 or greater; velocity effects are negligible for these scale factors (≥0.6). Average-30 coefficient of friction are smaller for a higher μ_{ref} and/or p_o. The average-30 coefficient of friction increases at greater shaking intensities, which appears to be counter intuitive. However, at the greater intensities of shaking, the slider traverses a much greater distance, spending less time over the center of the bearing, where the temperature is computed. Although more energy is dissipated at the higher intensities of shaking, it is distributed over a much greater area of the sliding surface.

Figure 7-10 presents the average-30 coefficient of friction as a function of shaking intensity up to 60% for FP bearings with a sliding period of 1.5 s, where an intensity of 100% corresponds to design basis shaking at Diablo Canyon. Figure 7-11 presents the results for a 2 s bearing for factors up to 1.0[38]. Figure 7-12 presents results for a 4 s FP bearing subjected to the ground motions with scaling factors of 0.25, 0.60, 1.00, 1.50, 1.67 and 2.00. From Figures 7-9 through 7-12, it can be observed that

[38] Higher intensities for the 1.5 s and 2.0 s bearings give rise to displacements greater than 0.5*R*, which are impractical for FP isolators.

i. The influence of the choice of friction model is small when the shaking intensity and p_o are small: 25% and 10 MPa, respectively. In this case, the effect of heating on the average-30 coefficient of friction is less than 10% (on average), regardless of the sliding period and μ_{ref} .

ii. The average-30 coefficient of friction computed using a temperature-dependent friction model is smaller than the corresponding μ_{ref} by approximately 10% (15%, 20%) for μ_{ref} of 0.03 (0.06, 0.09), p_o of 10 MPa and shaking intensity of 60% and greater.

iii. At p_o of 50 MPa and a shaking intensity of 25% ($\geq$60%), the average-30 coefficient of friction, adjusted for heating effects, is smaller than μ_{ref} by approximately 15% (30%), 20% (40%) and 25% (45%) for μ_{ref} of 0.03, 0.06 and 0.09, respectively.

iv. The difference between the average-30 coefficient of friction computed using a temperature-dependent friction model and μ_{ref} increases as shaking intensity increases from 25% to 60% or 100% due to greater sliding velocities resulting in more heat generation and a higher reduction in the coefficient of friction. At even greater intensities (>100%), the difference between the average-30 coefficient of friction and μ_{ref} tends to decrease, which is attributed to the distribution of the heat generated on the sliding surface in a relatively large area.

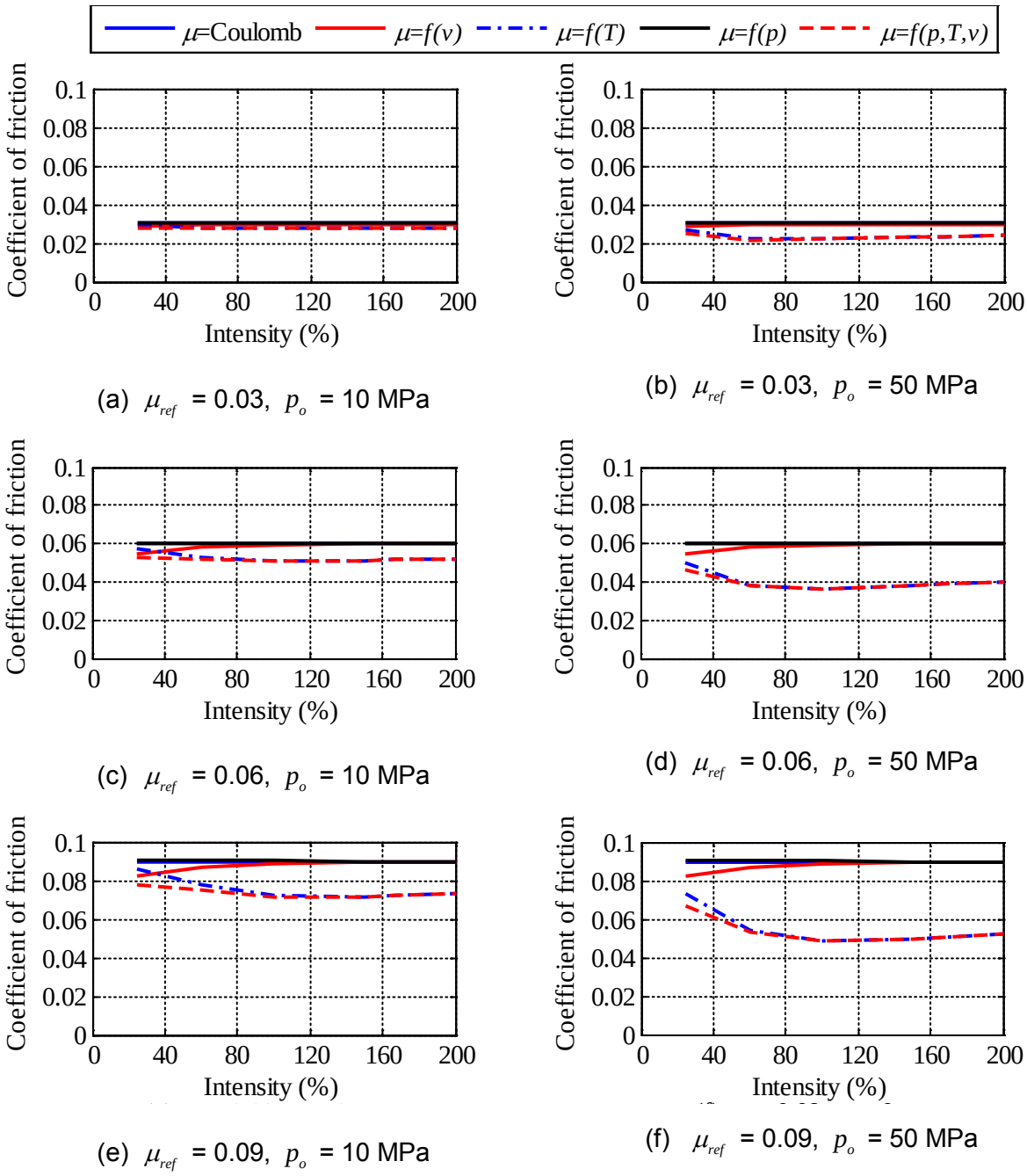

Figure 7-9 Coefficient of Friction in the Duration of Strong Shaking Averaged over 30 Ground Motions as a Function of Shaking Intensity for an FP Bearing with a Sliding Period of 3 s

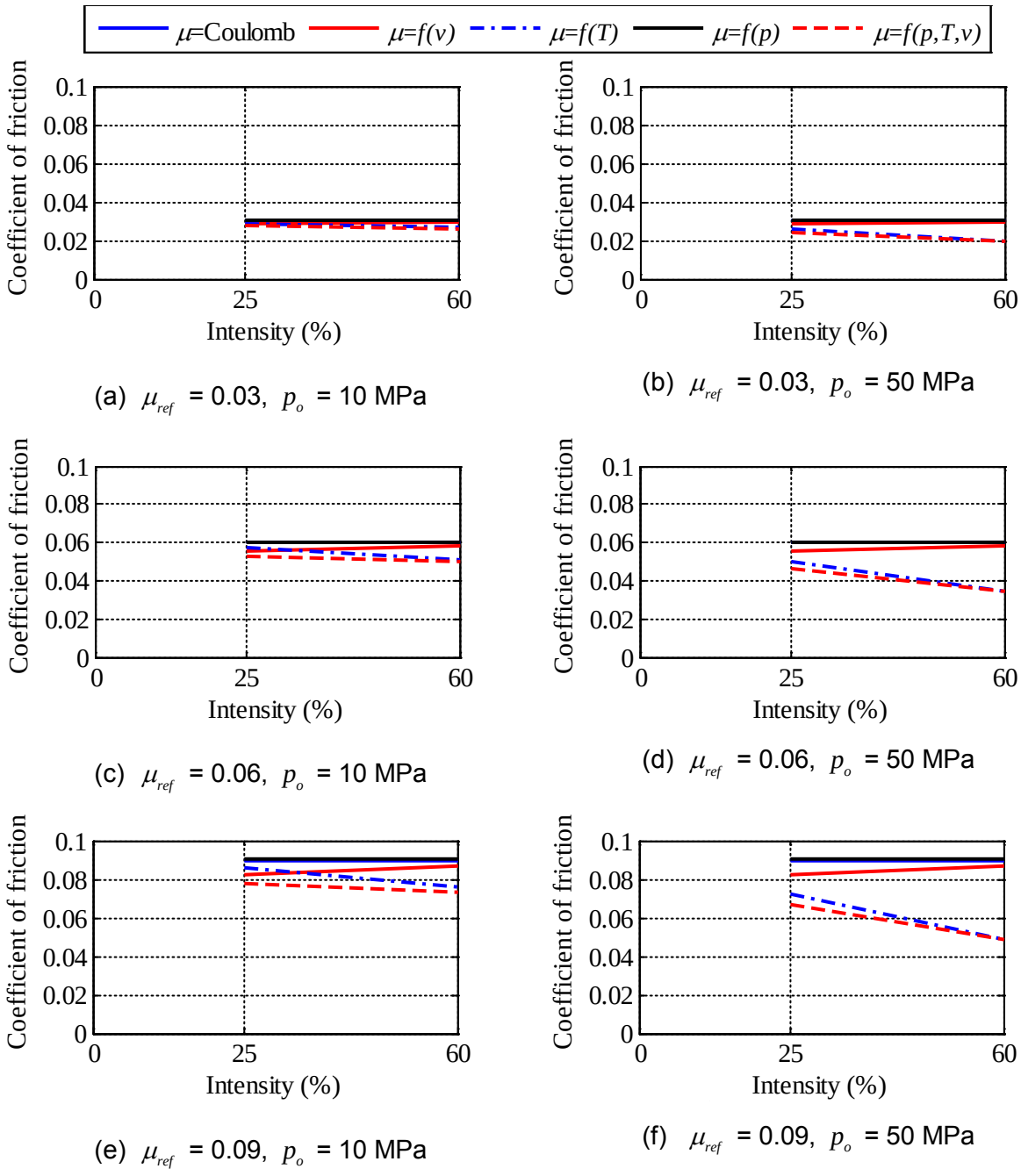

Figure 7-10 Coefficient of Friction in the Duration of Strong Shaking Averaged over 30 Ground Motions as a Function of Shaking Intensity for an FP Bearing with a Sliding Period of 1.5 s

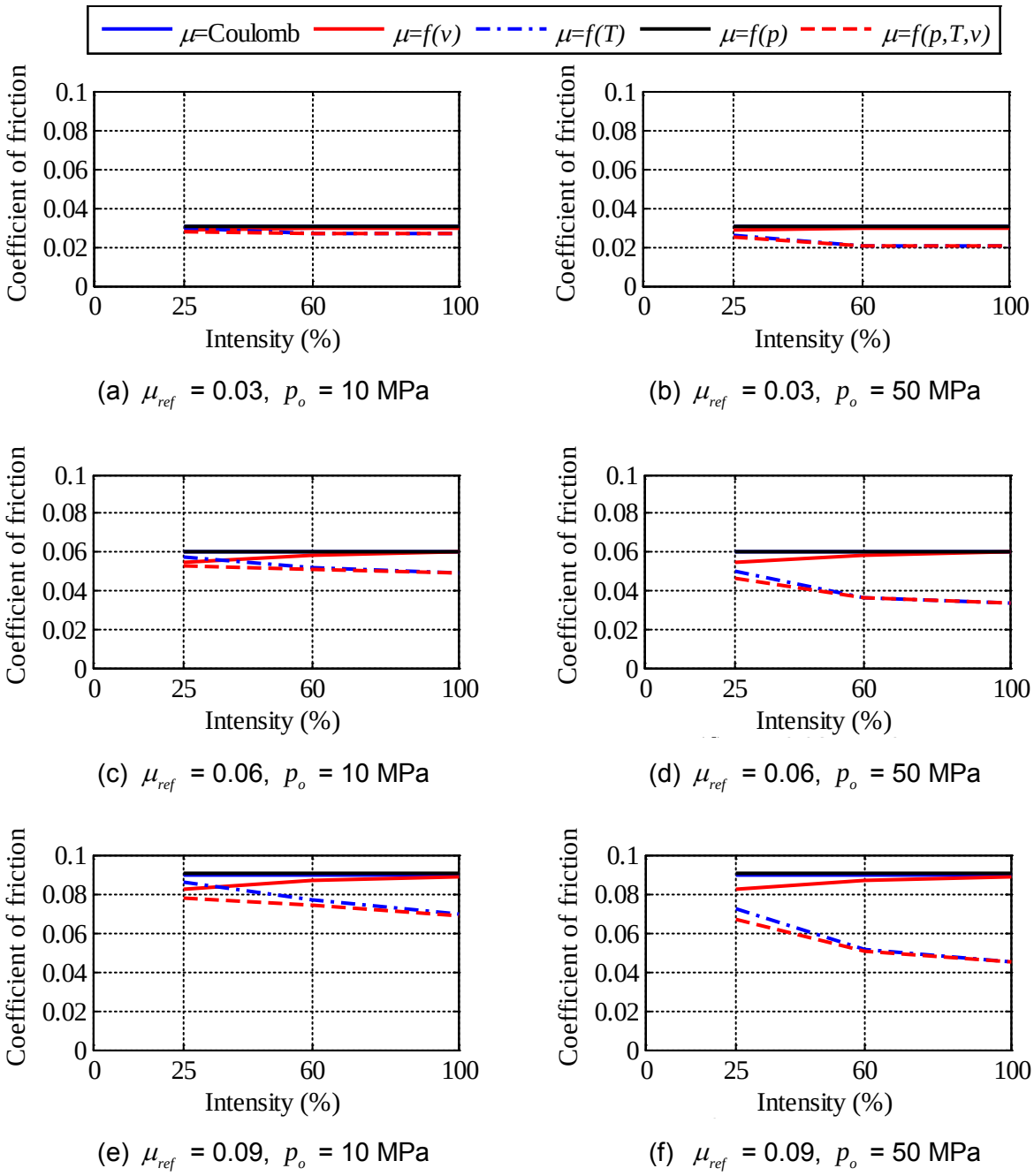

(a) μ_{ref} = 0.03, p_o = 10 MPa

(b) μ_{ref} = 0.03, p_o = 50 MPa

(c) μ_{ref} = 0.06, p_o = 10 MPa

(d) μ_{ref} = 0.06, p_o = 50 MPa

(e) μ_{ref} = 0.09, p_o = 10 MPa

(f) μ_{ref} = 0.09, p_o = 50 MPa

Figure 7-11 Coefficient of Friction in the Duration of Strong Shaking Averaged over 30 Ground Motions as a Function of Shaking Intensity for an FP Bearing with a Sliding Period of 2 s

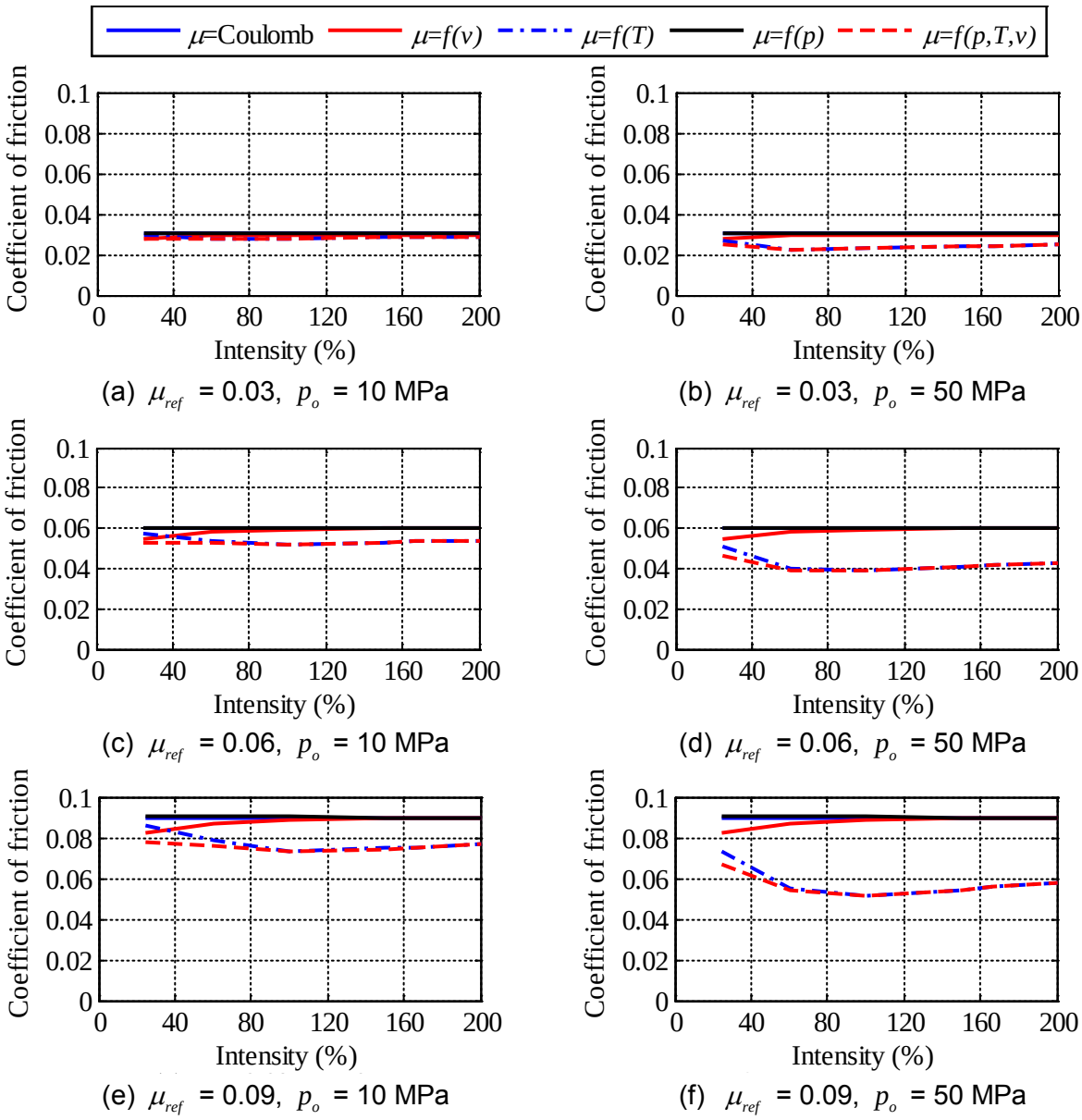

Figure 7-12 Coefficient of Friction in the Duration of Strong Shaking Averaged over 30 Ground Motions as a Function of Shaking Intensity for an FP Bearing with a Sliding Period of 4 s

7.5.2 Force-Displacement Response

Figure 7-13(a) presents the force-displacement response in a horizontal direction (say X) of the single FP bearing with a sliding period of 3 s, μ_{ref} of 0.06, friction at the sliding surface defined using the Coulomb model, and p_o of 10 MPa, subjected to GM30 with the amplitude scaling factor of 1.0. Figure 7-13(c) presents the response when friction is described using $\mu = f\left(p,T,v\right)$ model. The reduction in the coefficient of friction is evident by comparing the shearing forces in panels (a) and (c). The maximum displacements in the two panels are 0.27 m and 0.30 m, respectively. Panels (b) and (d) present the force-displacement response

for p_o of 50 MPa, and friction at the sliding surface described by the Coulomb model and $\mu = f(p,T,v)$ model, respectively. The peak displacements in these two panels are 0.27 m and 0.39 m, respectively. There is a greater reduction in the coefficient of friction at the higher static axial pressure.

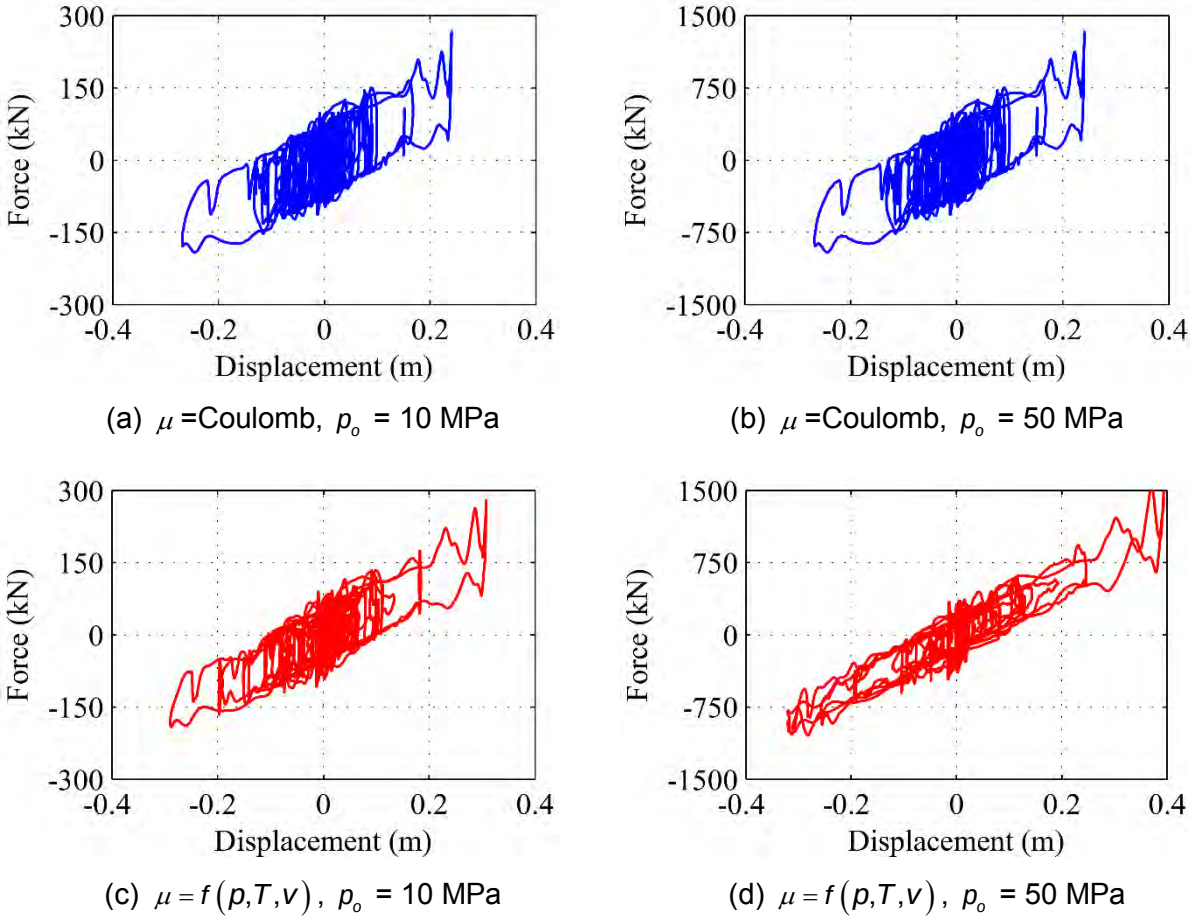

(a) μ =Coulomb, p_o = 10 MPa

(b) μ =Coulomb, p_o = 50 MPa

(c) $\mu = f(p,T,v)$, p_o = 10 MPa

(d) $\mu = f(p,T,v)$, p_o = 50 MPa

Figure 7-13 Force-Displacement Histories of an FP Bearing in X Direction with a Sliding Period of 3 s and μ_{ref} of 0.06, Subjected to GM30 at 100% Shaking Intensity

7.5.3 Displacement Demand

Figure 7-14(a) presents the 16th, 50th, 84th and 99th percentiles of peak displacements of the FP bearing with a sliding period of 3 s, a μ_{ref} of 0.03 with the coefficient of friction defined using the five models of Table 7-2, and a p_o of 10 MPa subjected to the 30 ground motions amplitude scaled by 1.0. The 30 values of peak displacements are assumed to distribute lognormally; the assumption is verified in Appendix H. The distribution is virtually unaffected by the choice of friction model. Figures 7-14(b) and 7-14(c) present the distributions of peak displacements for μ_{ref} of 0.06 and 0.09, respectively. The median (99th percentile) peak displacements for the five friction models differ from each other by approximately 10% (5%).

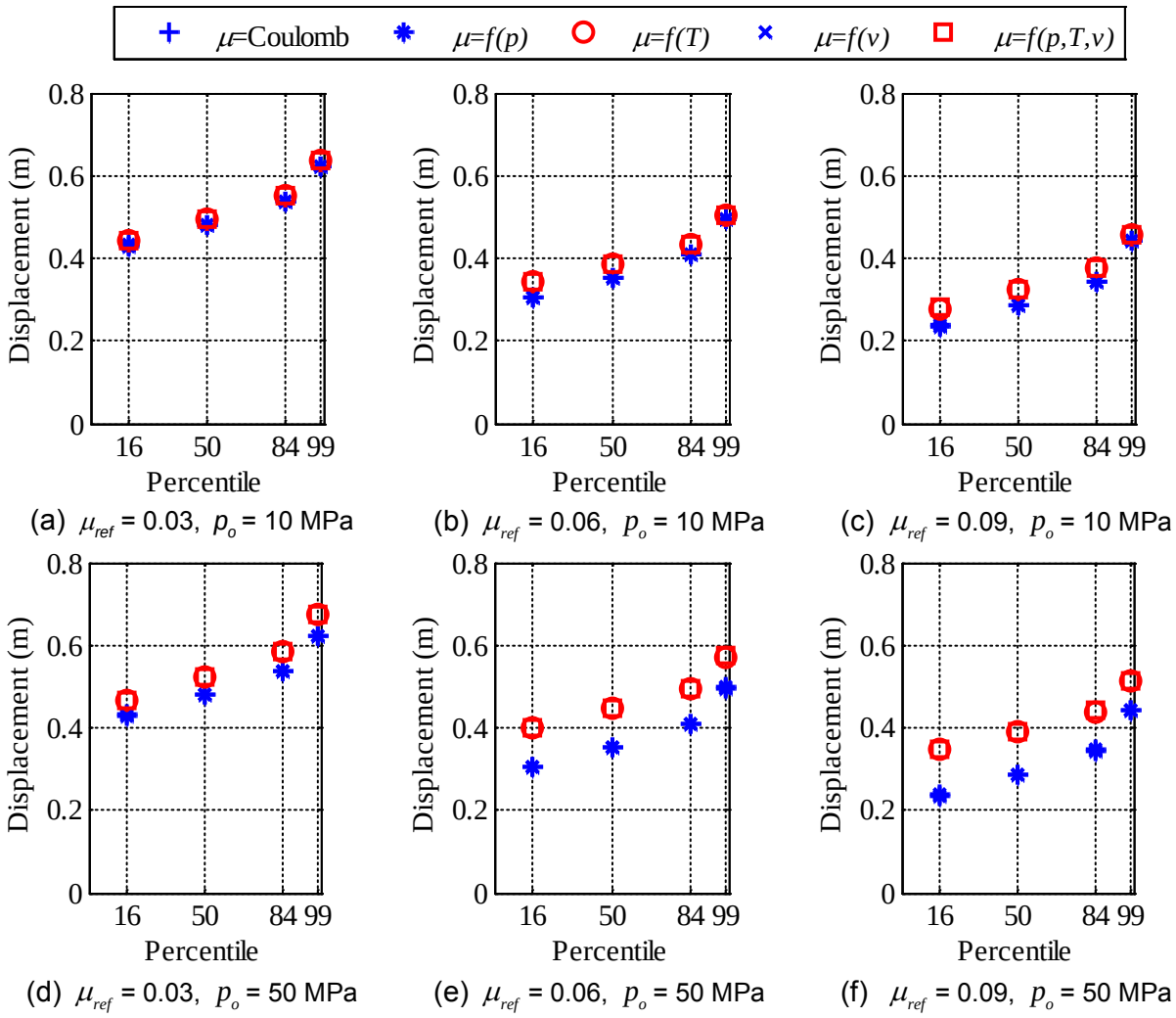

Figure 7-14 Distribution of Peak Displacements of FP Bearing with a Sliding Period of 3 s, Subjected to the 30 Ground Motions Amplitude Scaled by 1.0

Figures 7-14(d), 7-14(e) and 7-14(f) present the distributions for of 50 MPa and μ_{ref} of 0.03, 0.06 and 0.09, respectively. The distributions are significantly influenced by heating effects. The median (99th percentile) displacement estimates are greater by about 10% (10%), 25% (15%) and 40% (15%), respectively, for the three panels if the effects of heating are included in the friction model.

Figure 7-15 presents the 50th percentile (or median) peak displacements of the 3 s FP bearing subjected to ground motions scaled using the six factors of Table 7-3. Median displacements for p_o of 10 MPa and μ_{ref} of 0.03 are plotted against shaking intensity in Figure 7-15(a). The displacements are not influenced by the choice of friction model. Figures 7-15(c) and 7-15(e) present results for μ_{ref} of 0.06 and 0.09, respectively. The median displacements are greater by less than 10% (15%) when the friction model addresses heating, for μ_{ref} of 0.06 (0.09). The percentage difference is greatest for shaking intensities of 60% or 100% for the reason given previously.

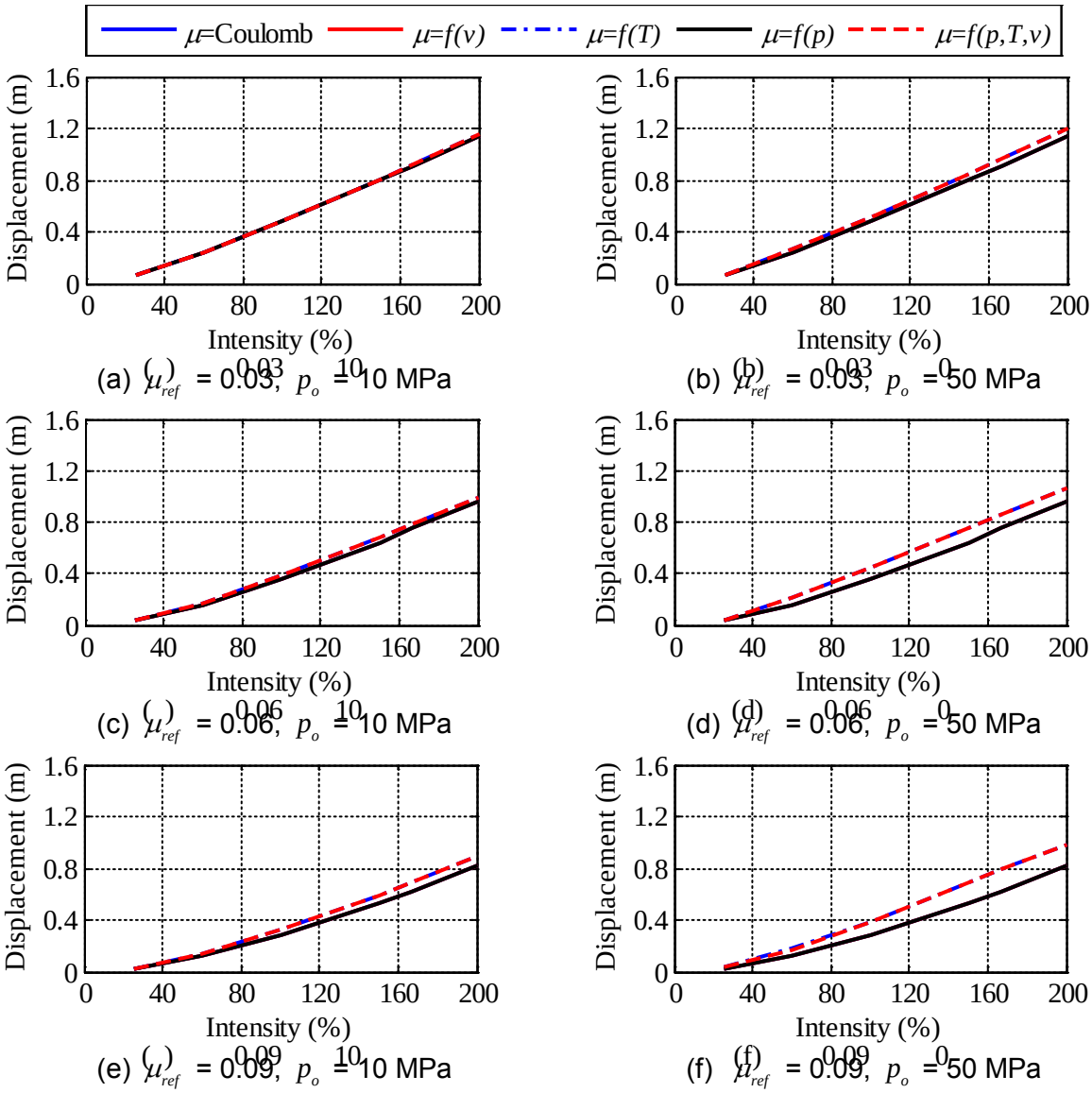

Figure 7-15 Median Displacement Demand on an FP Bearing with a Sliding Period of 3 s Subjected to the 30 Ground Motions Amplitude Scaled to Different Intensities

Figure 7-15(b) presents results for the bearing and ground motions of Figure 7-15(a) but for p_o of 50 MPa. The median peak displacements obtained using the temperature-dependent friction models are greater than those obtained using the Coulomb model by between 5% to 15%. Figure 7-15(d) presents results for μ_{ref} of 0.06. The maximum percentage difference is approximately 30%, at the shaking intensity of 60%, which decreases to 15% (10%) at the shaking intensity of 25% (200%). Figure 7-15(f) presents results for μ_{ref} of 0.09. The peak percentage difference is 40% at a shaking intensity of 60%. The difference decreases to 10% (20%) at a shaking intensity of 25% (200%). Figure 7-16 presents the 90th percentile peak

displacements of the FP bearing with a sliding period of 3 s. At p_o of 10 MPa (50 MPa), the displacements obtained using a friction model that accounts for heating effects are greater by less than 2% (10%), 5% (20%) and 10% (25%) for μ_{ref} of 0.03, 0.06 and 0.09, respectively, for different intensities.

Figure 7-17 (Figure 7-18) presents the median (90th percentile) peak displacement demand on an FP bearing with sliding period of 1.5 s subjected to ground motions with shaking intensities of 25% and 60%. Figure 7-19 (Figure 7-20) presents the median (90th percentile) peak displacements of the 2 s FP bearing subjected to the 30 ground motions with shaking intensities of 25%, 60% and 100%. Figure 7-21 (Figure 7-22) presents the median (90th percentile) peak displacements of the 4 s FP bearings subjected to ground motions scaled to intensities of 25%, 60%, 100%, 150%, 167% and 200%. From Figures 7-14 through 7-22, it can be observed that

i. The influence of the choice of friction model on peak displacement is negligible at a shaking intensity of 25%, irrespective of sliding period, p_o and μ_{ref}.

ii. At shaking intensities of 60% or greater, the choice of friction model does not affect the peak displacements materially at p_o = 10 MPa. The influence of the choice of friction model increases slightly with an increase in μ_{ref}.

iii. Heating effects significantly influence the peak displacement at p_o = 50 MPa. Peak displacements are very sensitive to the choice of μ_{ref}. At shaking intensities of 60+%, the median peak displacement estimated using a temperature-dependent friction model can be 15%, 30% and 45% greater than that estimated using a Coulomb model for μ_{ref} of 0.03, 0.06 and 0.09, respectively. The percentage differences are comparatively insensitive to the sliding period.

iv. The 90th percentile displacements are less influenced by the choice of friction model than the median estimates, in a relative sense.

v. Peak displacements are most influenced by the choice of friction model at a shaking intensity of 60% and/or 100%, because the travel path increases significantly at intensities greater than 100%.

7.5.3.1 Clear Distance Between an Isolated Nuclear Structure and Its Stop

The forthcoming Nuclear Regulatory guideline for seismically isolated nuclear power plants requires the clear distance between the isolated superstructure and the stop to no less than the 99th (90th) percentile peak displacement for 10,000 (100,000)-year earthquake shaking, calculated along each axis of the structure. Two sites are considered herein, Vogtle and Diablo Canyon, to establish which hazard level controls the required clearance. The set of 30 ground motions for 10,000-year shaking at Diablo Canyon are amplitude scaled by 0.25 (0.60) to characterize 10,000 (100,000)-year shaking at Vogtle (see Section 7.3 and Appendix G). Similarly, the ground motions are scaled by 1.0 (2.0) to represent 10,000 (100,000)-year shaking at Diablo Canyon (see Section 7.2 and Appendix G).

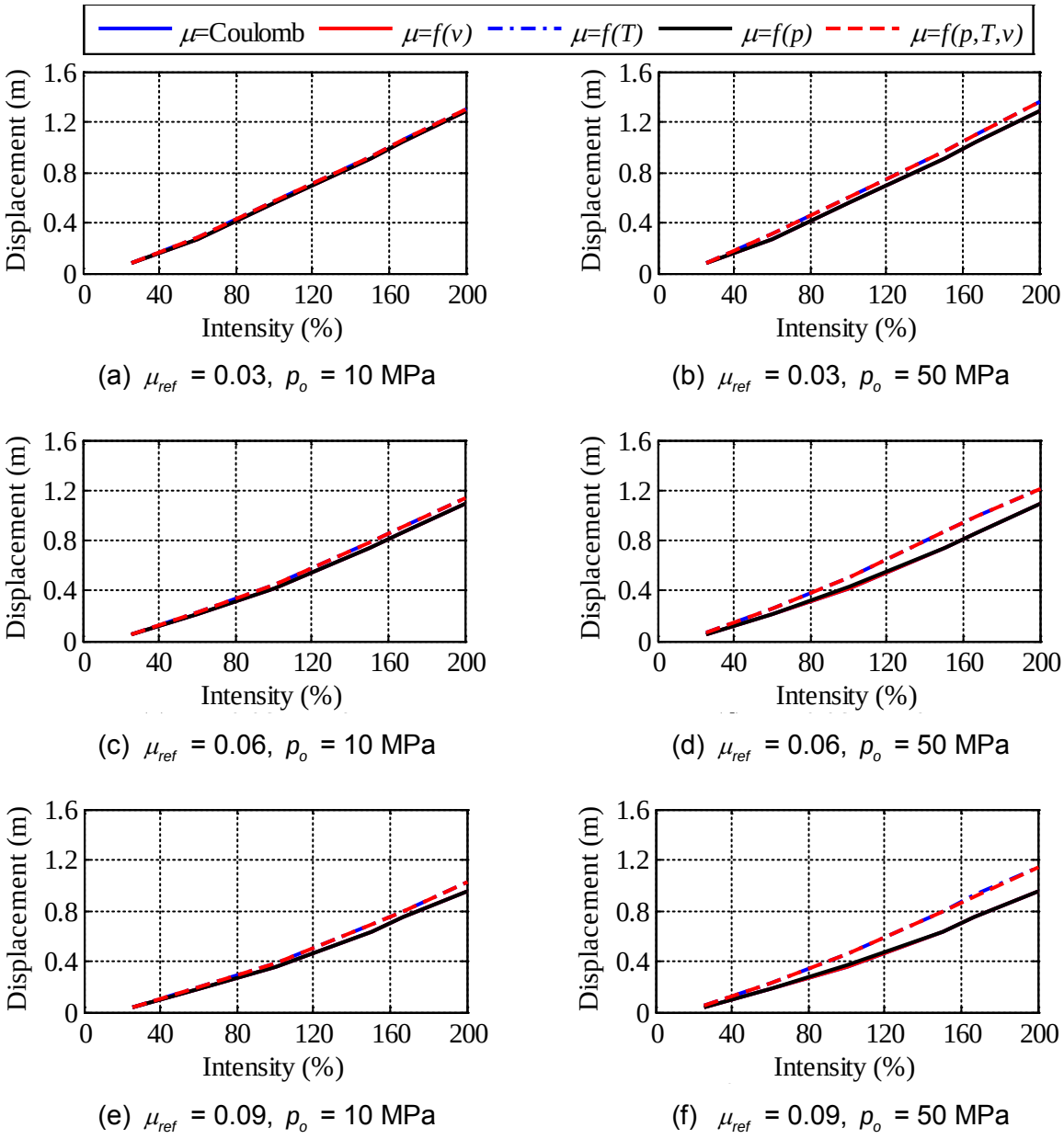

Figure 7-16 90th Percentile Displacement Demand on an FP Bearing with a Sliding Period of 3 s Subjected to the 30 Ground Motions Amplitude Scaled to Different Intensities

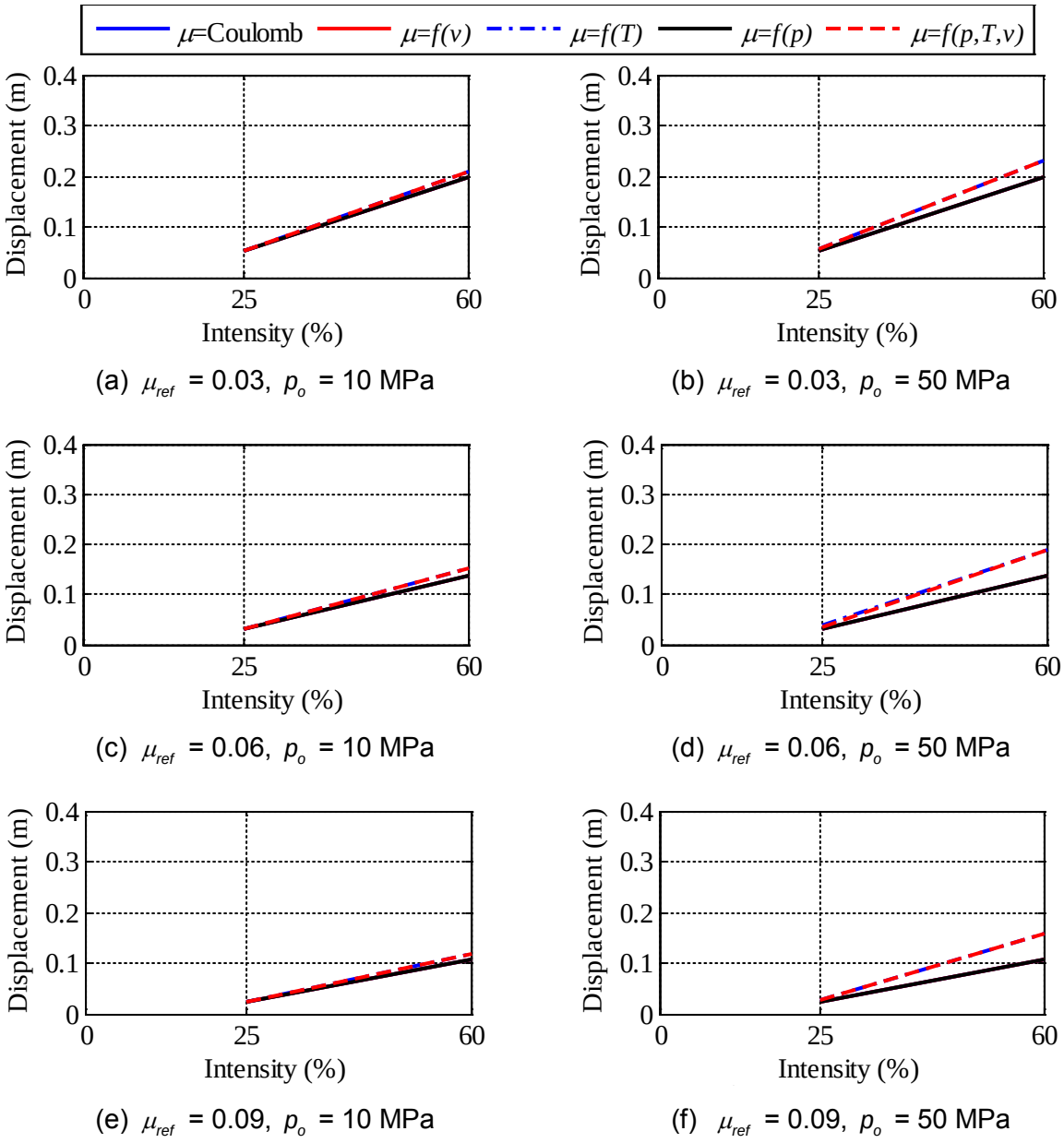

Figure 7-17 Median Displacement Demand on an FP Bearing with a Sliding Period of 1.5 s Subjected to the 30 Ground Motions Amplitude Scaled to Different Intensities

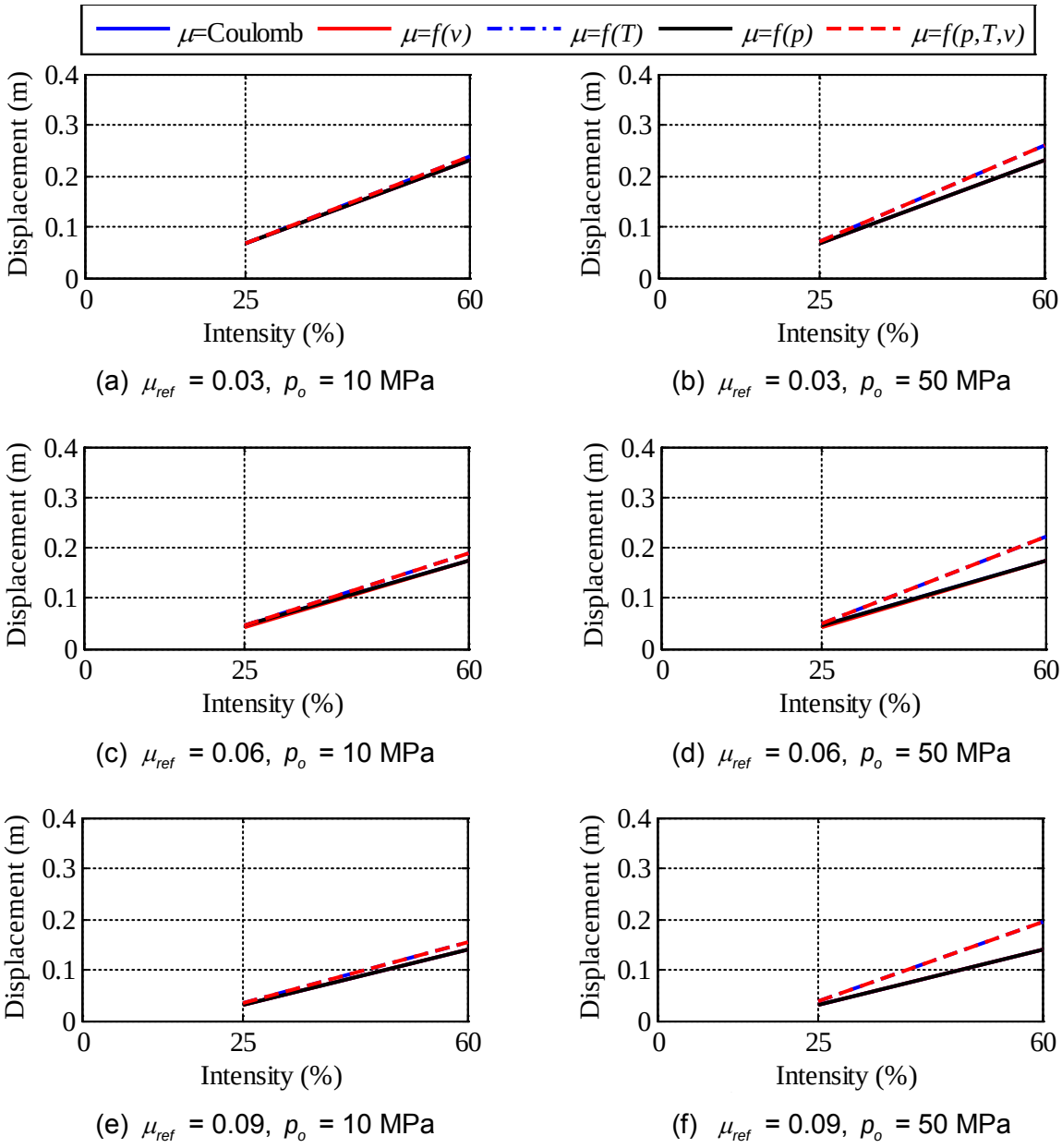

Figure 7-18 90th Percentile Displacement Demand on an FP Bearing with a Sliding Period of 1.5 s Subjected to the 30 Ground Motions Amplitude Scaled to Different Intensities

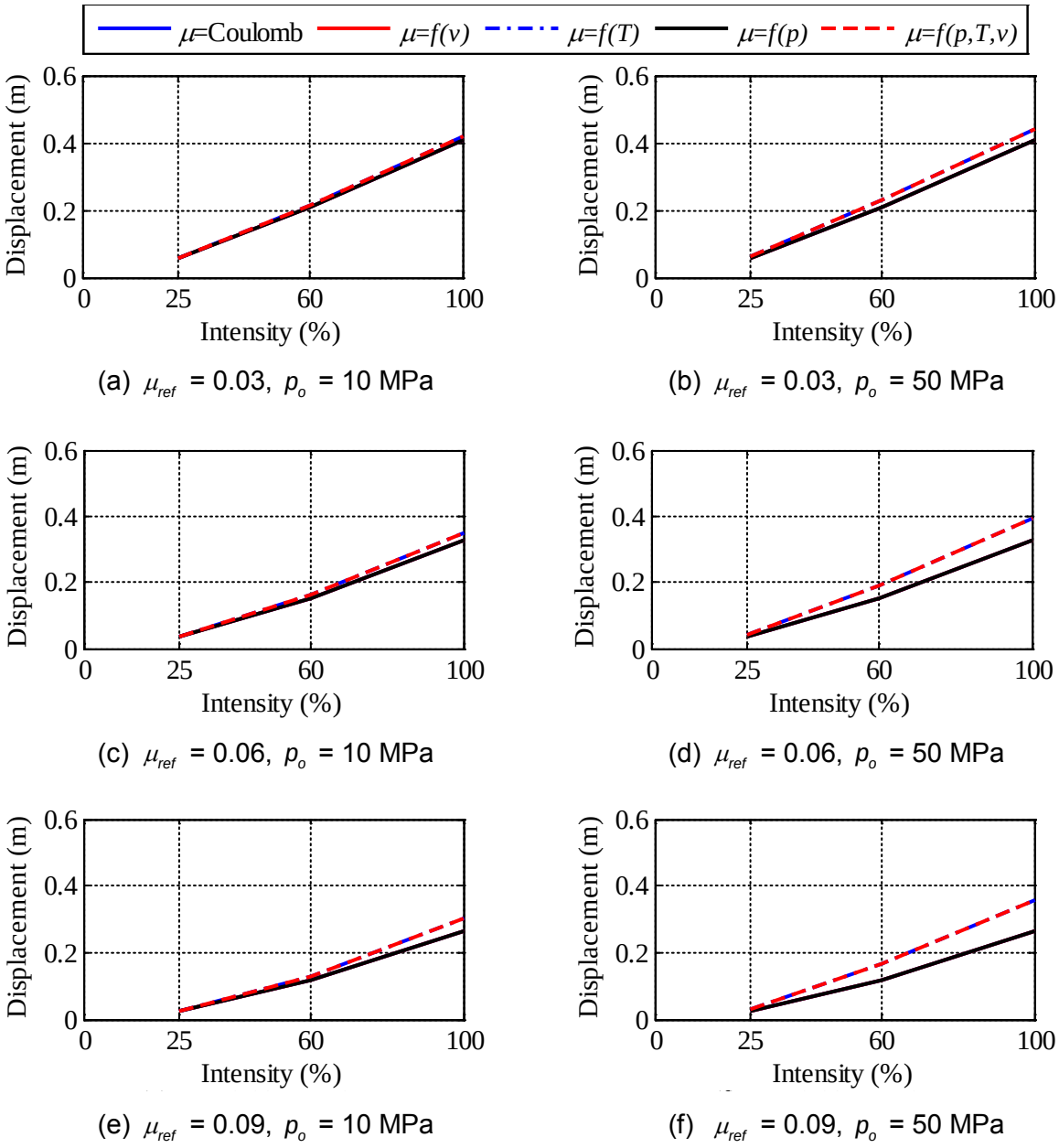

Figure 7-19 Median Displacement Demand on an FP Bearing with a Sliding Period of 2 s Subjected to the 30 Ground Motions Amplitude Scaled to Different Intensities

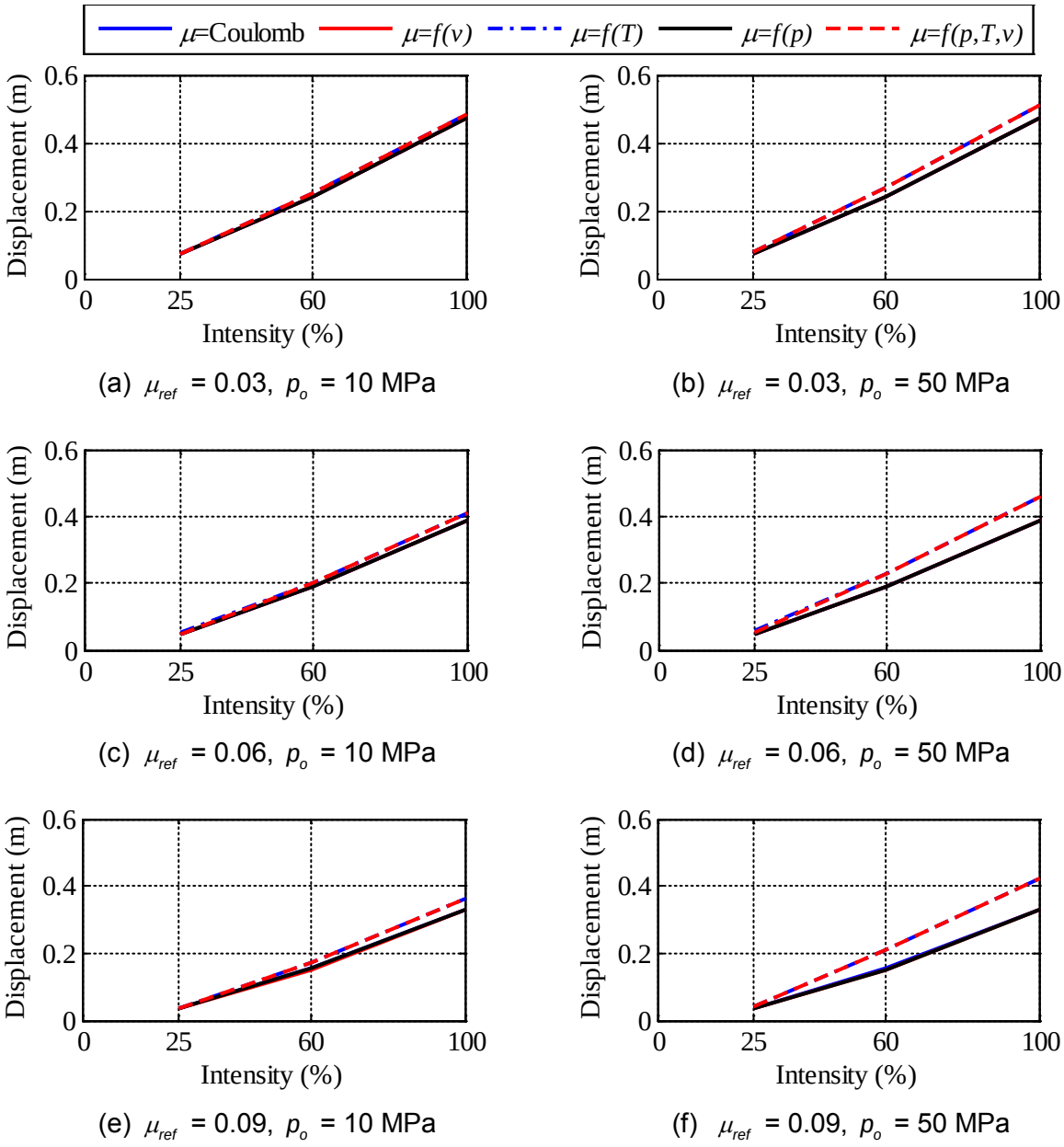

Figure 7-20 90th Percentile Displacement Demand on an FP Bearing with a Sliding Period of 2 s Subjected to the 30 Ground Motions Amplitude Scaled to Different Intensities

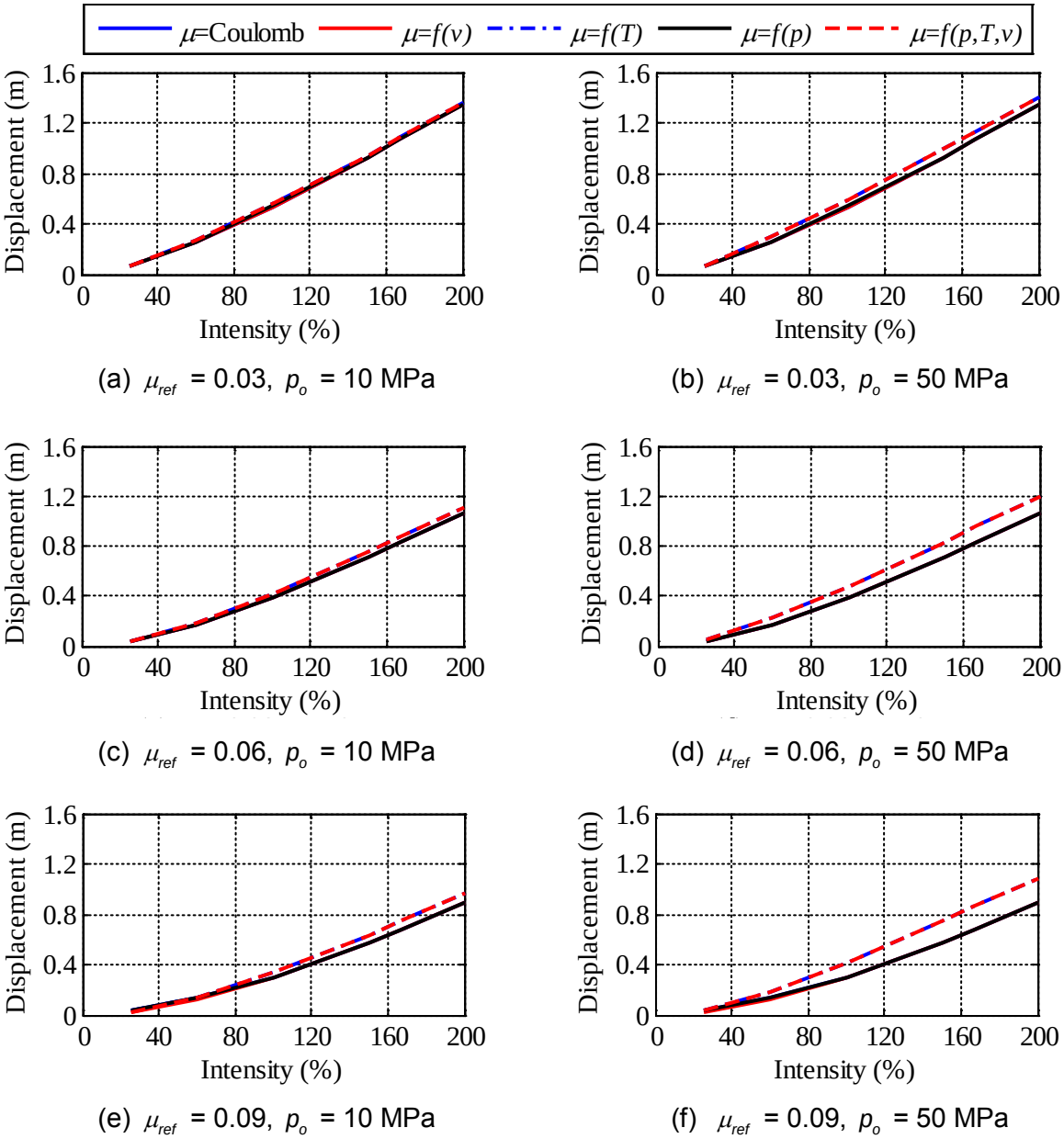

Figure 7-21 Median Displacement Demand on an FP Bearing with a Sliding Period of 4 s Subjected to the 30 Ground Motions Amplitude Scaled to Different Intensities

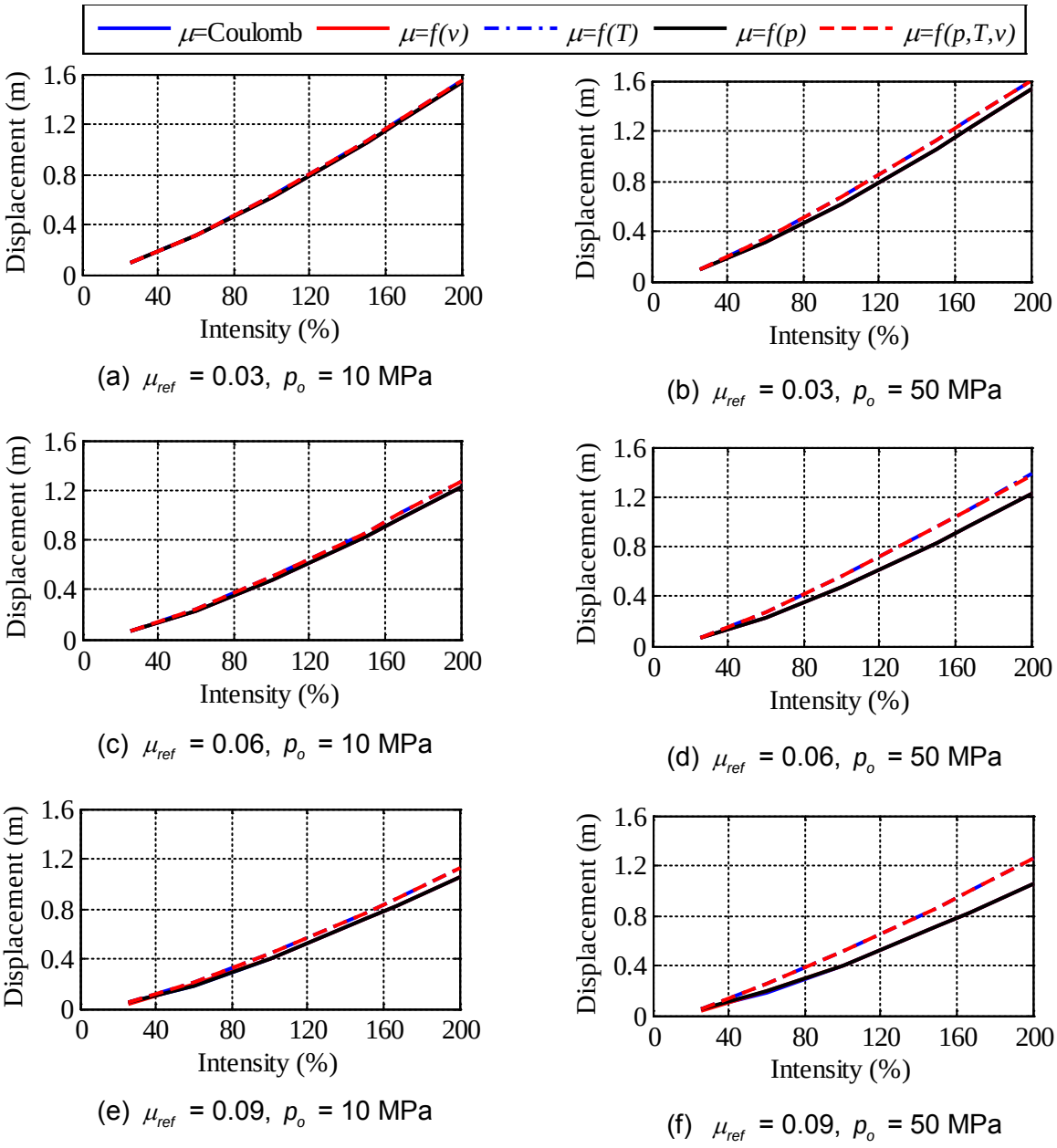

Figure 7-22 90th Percentile Displacement Demand on an FP Bearing with a Sliding Period of 4 s Subjected to the 30 Ground Motions Amplitude Scaled to Different Intensities

7.5.3.1.1 Vogtle

Figure 7-23 presents the 99th (90th) percentile peak displacements for FP bearings with sliding periods, $T_{sliding}$, of 1.5 s, 2 s, 3 s and 4 s, p_o of 10 MPa and 50 MPa, and μ_{ref} of 0.03, 0.06 and 0.09, subjected to the 30 ground motions scaled by 0.25 (0.60). The 90th percentile peak displacements for the 100,000-year shaking are greater than the 99th percentile peak

displacements for the 10,000-year shaking for all combinations of $T_{sliding}$, p_o, μ_{ref} and choice of friction model. In this figure, DBE (BDBE) denotes results for 10,000 (100,000)-year earthquake shaking.

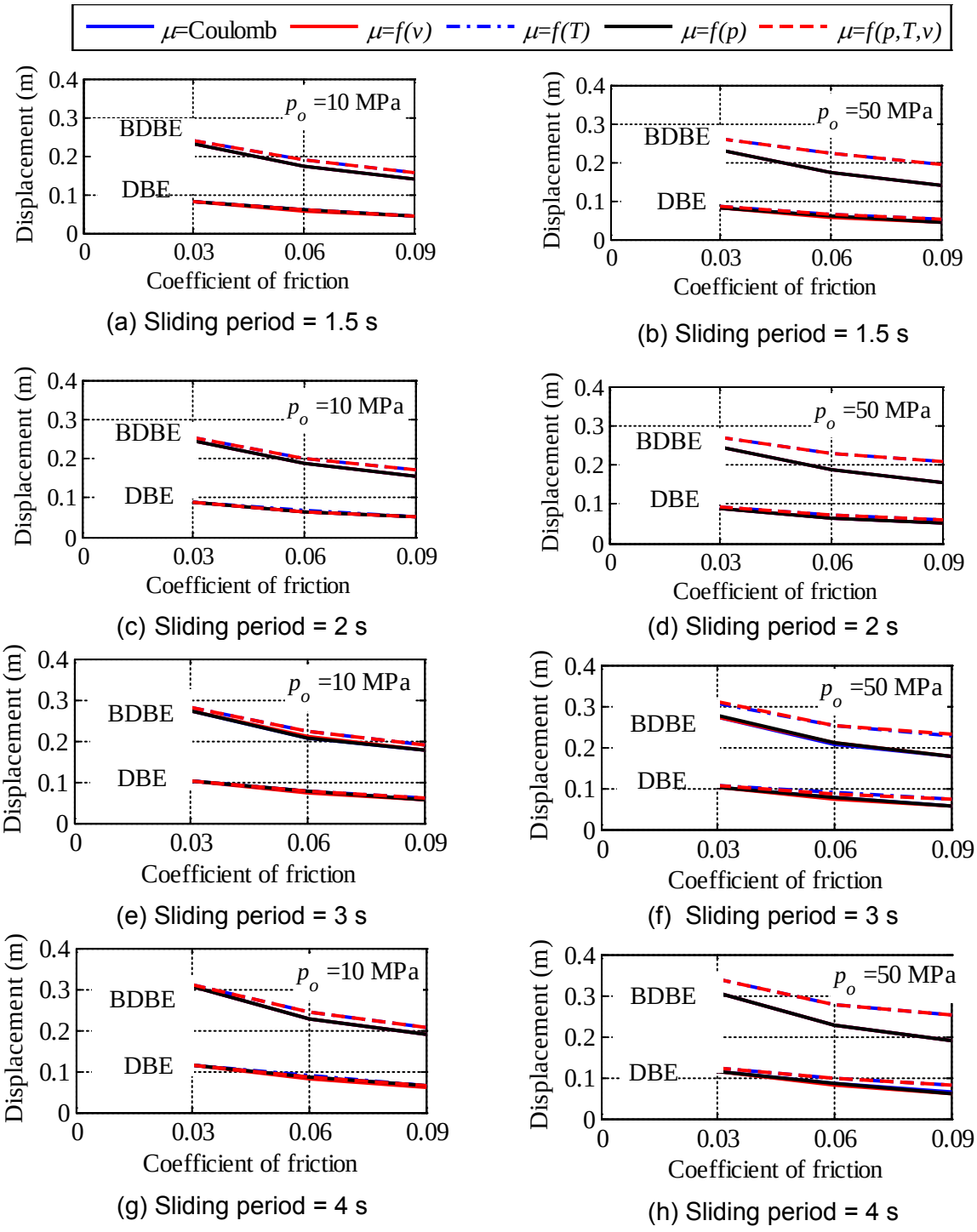

(a) Sliding period = 1.5 s

(b) Sliding period = 1.5 s

(c) Sliding period = 2 s

(d) Sliding period = 2 s

(e) Sliding period = 3 s

(f) Sliding period = 3 s

(g) Sliding period = 4 s

(h) Sliding period = 4 s

Figure 7-23 99th Percentile Displacement for DBE Shaking and 90th Percentile Displacement for BDBE Shaking at Vogtle

7.5.3.1.2 Diablo Canyon

Figure 7-24 presents 99th (90th) percentile displacements for FP bearings with $T_{sliding}$ of 3 s and 4 s, p_o of 10 MPa and 50 MPa, and μ_{ref} of 0.03, 0.06 and 0.09, subjected to ground motions at 100% (200%) shaking. The 90th percentile displacement for 100,000-year shaking is greater than the 99th percentile displacement for 10,000-year shaking. Similar to Figure 7-23, DBE (BDBE) represents 10,000 (100,000)-year shaking in Figure 7-24.

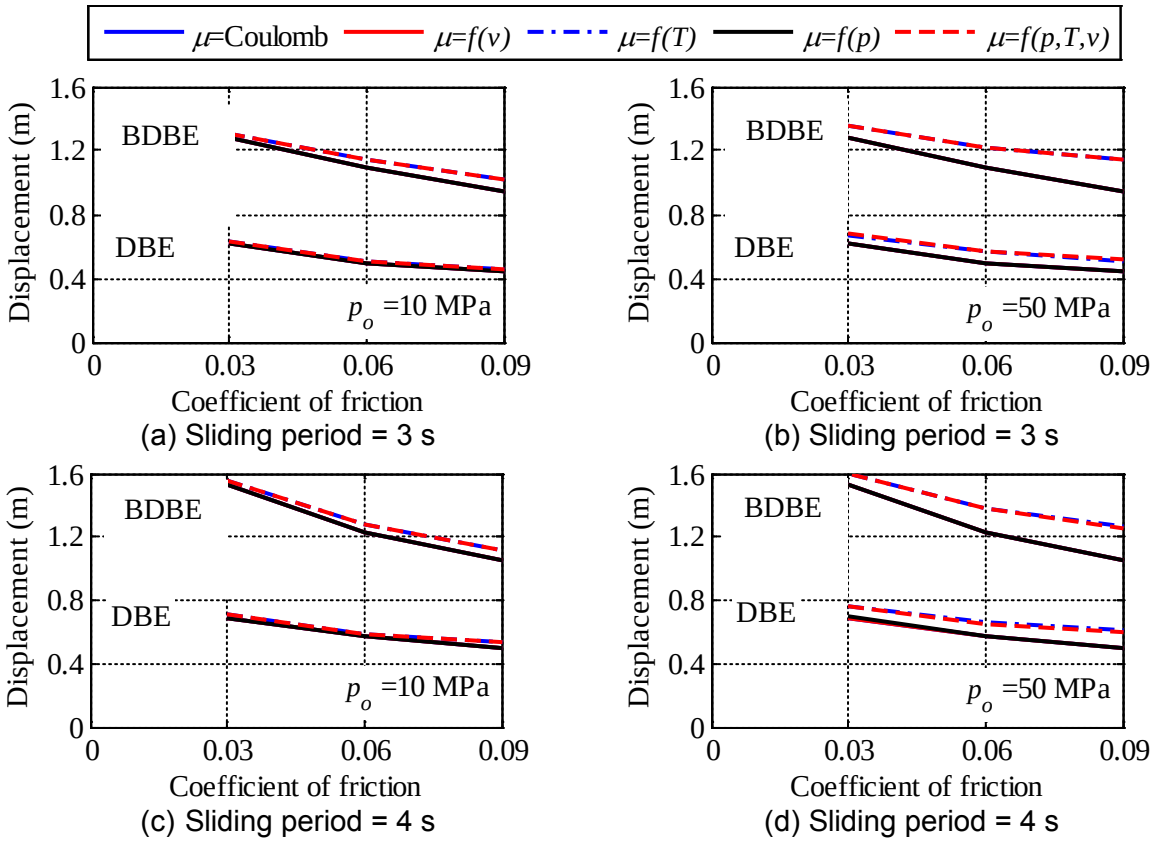

Figure 7-24 99th Percentile Displacement for DBE Shaking and 90th Percentile Displacement for BDBE Shaking at Diablo Canyon

7.5.3.1.3 Clearance to the Stop

The results presented in Figures 7-23 and 7-24 make it clear that the clearance to the stop is dictated by the 90th percentile displacement for 100,000-year earthquake shaking.

7.5.3.2 Relationships Between Median and 90th Percentile Displacements and Hazard Levels

Fragility curves were developed for individual isolators and safety-related umbilical lines in Chapter 6, which assumed that the clearance to the stop (90th percentile displacement for 100,000-year shaking) is greater than or equal to the median displacement for 1.1 times 100,000-year shaking. The assumption is verified below for three sites spanning the range of seismic hazard considered herein (see Table 6-3): Diablo Canyon, Vogtle and North Anna.

Spectrally matched ground motions consistent with 10,000-year shaking were developed for Diablo Canyon in Section 7.2. These ground motions were amplitude scaled to represent 100,000-year shaking at Diablo Canyon (×2), and 10,000-year (×0.25) and 100,000-year (×0.60) shaking at Vogtle; see Sections 7.2 and 7.3. Ground motions for 100,000-year shaking at North Anna are generated by amplitude scaling the 10,000-year Diablo Canyon motions by 0.50, which is the average of the ratios of the 1 s and 2 s spectral ordinates for 100,000-year shaking at North Anna to those for 10,000-year shaking at Diablo Canyon; see Table 6-3.

Single FP bearings with sliding periods of 3 s and 4 s, μ_{ref} of 0.06 and 0.09, p_o of 50 MPa and friction at the sliding surface described using Coulomb model and $\mu = f(p,T,v)$ model subjected to the ground motions with shaking intensities of 25%, 50%, 75%, 100%, 125%, 150%, 175%, 200%, 225%, 250%, 275% and 300%. The median displacements are plotted against shaking intensity in Figures 7-25 and 7-26 for the bearings with friction at the sliding surface described using the Coulomb and $\mu = f(p,T,v)$ models, respectively.

The intensity at which the median displacement is equal to the 90th percentile displacement for 100,000-year shaking ranges between 1.10 and 1.13 times the 100,000-year shaking for Diablo Canyon, 1.13 and 1.24 for Vogtle, and 1.16 and 1.25 for North Anna, across all combinations of sliding period, μ_{ref} and definitions of friction model considered in Figures 7-25 and 7-26. Therefore, it is conservative (overestimating risk) to assume that the median displacement for 1.1 times 100,000-year shaking is equal to the 90th percentile displacement for 100,000-year shaking for the purpose of developing fragility curves for individual isolator units or umbilical lines.

7.5.4 Temperature at the Sliding Surface

The temperature at the center of the sliding surface is considered appropriate to characterize heating effects (see Chapter 3). It is a function of the histories of axial pressure on the bearing, sliding velocity and coefficient of friction, in addition to the path of the slider relative to the sliding surface. This section reports temperature at the center of the sliding surface of FP bearings with different geometrical and material properties subjected to ground motions with a range of shaking intensities.

Figure 7-27 presents the percentiles of the temperature (assumed lognormal distribution; see Appendix H) at the center of the sliding surface of an FP bearing with a sliding period of 3 s, μ_{ref} of 0.03, 0.06 and 0.09, and p_o of 10 MPa and 50 MPa, subjected to the ground motions amplitude scaled by 1.0. The influence of choice of friction model is small on the temperature estimates at p_o of 10 MPa (Figures 7-27(a) through 7-27(c)). Results for p_o of 50 MPa are presented in Figures 7-27(d), 7-27(e) and 7-27(f) for μ_{ref} of 0.03, 0.06 and 0.09, respectively: the inclusion of heating effects influences the response significantly. The median peak temperatures for p_o of 50 MPa and μ_{ref} of 0.03, 0.06 and 0.09 are 210˚C, 350˚C and 480˚C, respectively, when the friction model ignores heating effects, and 150˚C, 220˚C and 280˚C, respectively, when it does. The 99th percentile peak temperatures for the three panels are 300˚C, 550˚C and 740˚C[39], respectively, when the heating effects are ignored and 200˚C, 290˚C and 380˚C, respectively, otherwise.

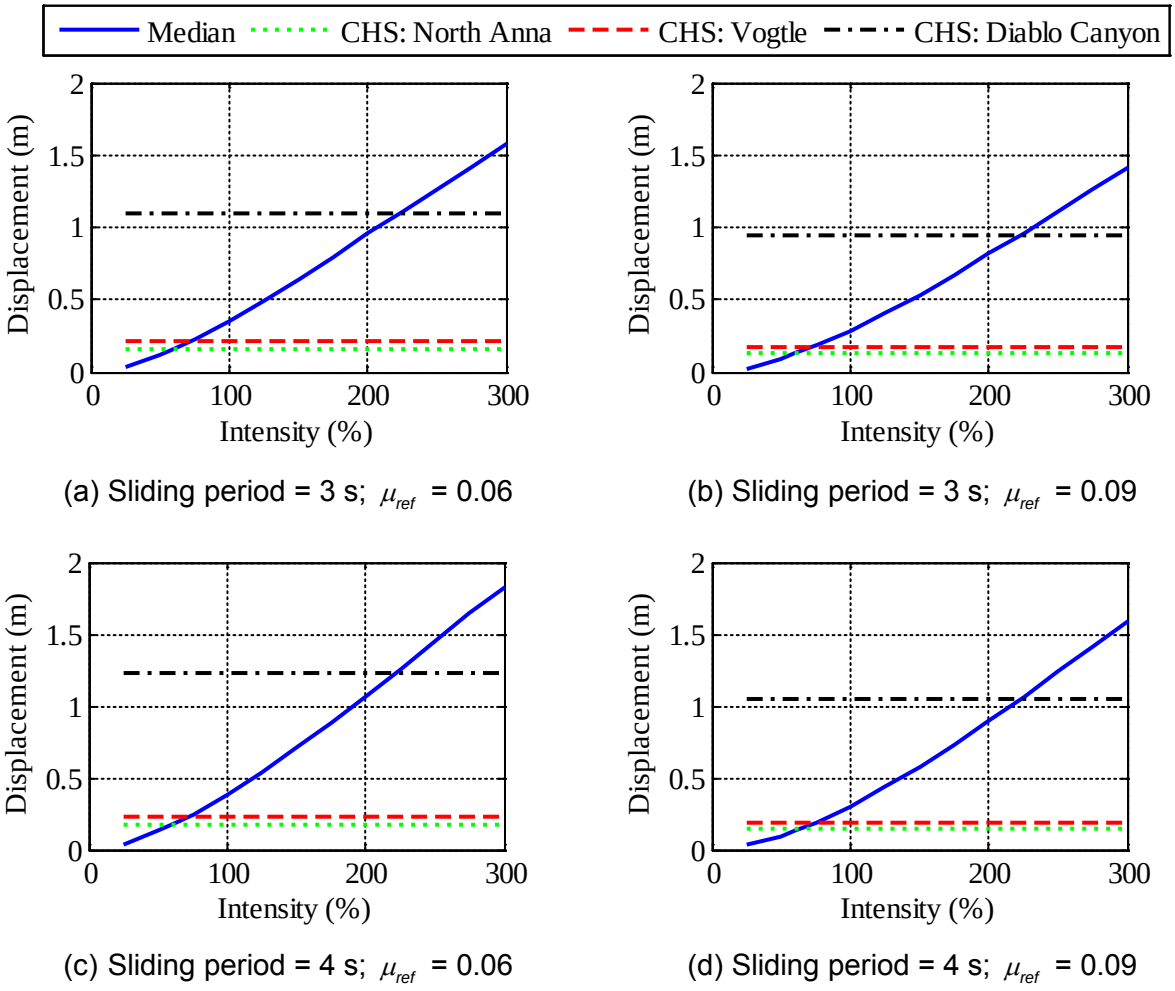

Figure 7-25 Median Displacement Plotted Against Intensity of Shaking for a Single FP Bearing with Friction at the Sliding Surface Described Using the Coulomb Model; Clearance to the Stop (CS) Corresponds to the 90th Percentile Displacement for 100,000-Year Shaking

Figure 7-28 (Figure 7-29) presents the median (90th percentile) peak temperatures at the sliding surface of a 3 s FP bearing subjected to the set of 30 ground motions amplitude scaled by 0.25, 0.6, 1.0, 1.5, 1.67 and 2.0. The influence of the friction model is negligible at shaking intensity of 25%, irrespective of p_o and μ_{ref}. At p_o of 10 MPa (panels (a), (c) and (e)), the peak temperature is not sensitive to the choice of friction model. The median (90th percentile) peak temperature can be greater by 70˚C (210˚C), 180˚C (250˚C) and 300˚C (400˚C) if the friction model ignores heating effects for μ_{ref} of 0.03, 0.06 and 0.09, respectively, at p_o of 50 MPa and

[39] There are no data available to characterize the performance of the FP composite at 740˚C.

a shaking intensity of 100% and greater. The peak temperature at the center of the sliding surface, and consequently the difference in the peak temperatures obtained using the two friction models, trends to a constant value at intensities greater than 100% because the slider traverses a path farther away from the center of the sliding surface during much of the strong shaking.

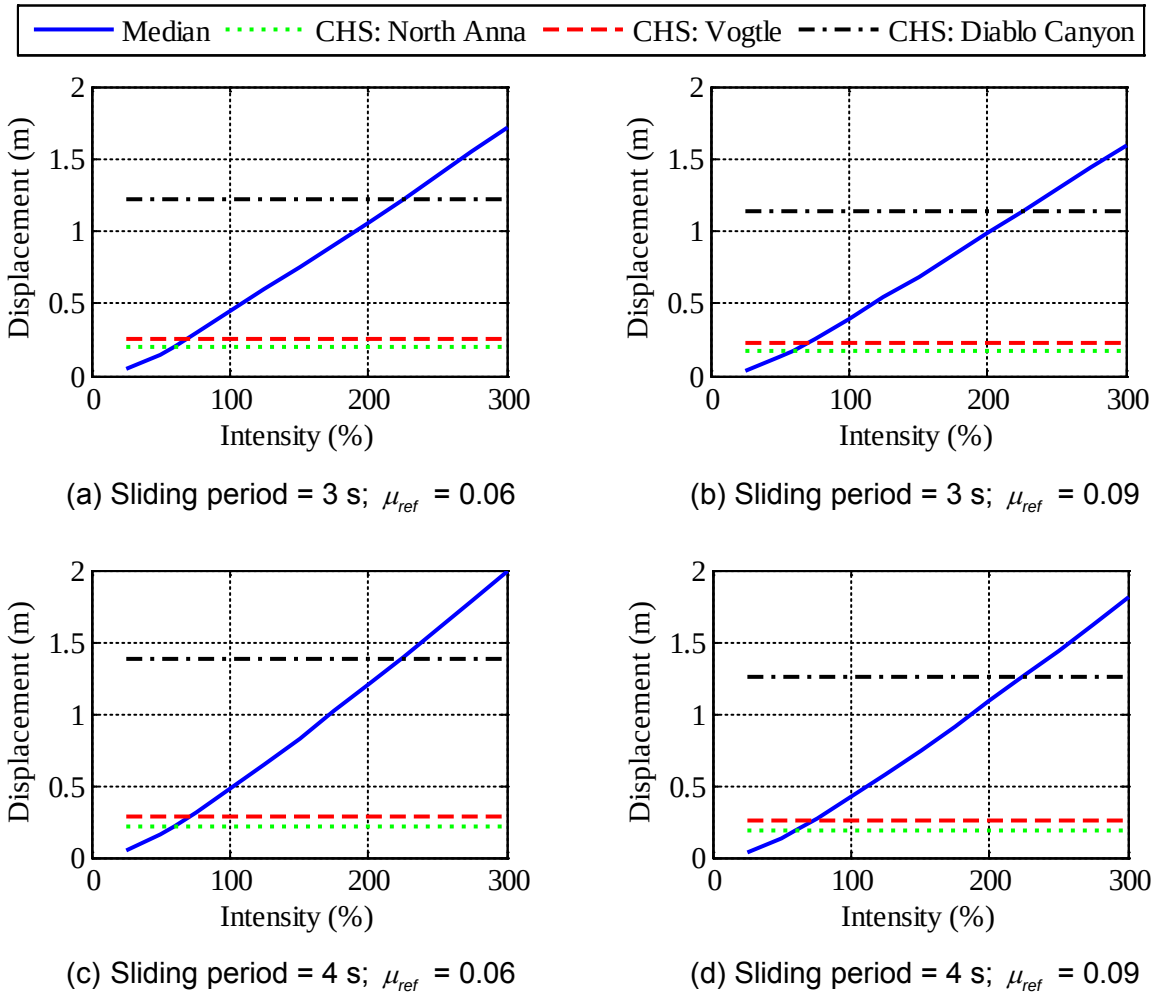

(a) Sliding period = 3 s; μ_{ref} = 0.06

(b) Sliding period = 3 s; μ_{ref} = 0.09

(c) Sliding period = 4 s; μ_{ref} = 0.06

(d) Sliding period = 4 s; μ_{ref} = 0.09

Figure 7-26 Median Displacement Plotted Against Intensity of Shaking for a Single FP Bearing with Friction at the Sliding Surface Described Using the *p-T-v* Model; Clearance to the Stop (CS) Corresponds to the 90th Percentile Displacement at 100,000-Year Shaking

The median (90th percentile) peak temperatures at the center of the sliding surface of FP bearings with sliding periods of 1.5 s, 2 s and 4 s, subjected to ground motions with different amplitude scaling factors, are presented in Figures 7-30 (7-31), 7-32 (7-33) and 7-34 (7-35), respectively. The results for all of the cases considered in this section can be summarized as follows:

i. The peak temperatures are smaller when the friction model includes the temperature dependence of the coefficient of friction, because the coefficient of friction decreases with increase in temperature, leading to smaller heat generation and temperature rise.

ii. The velocity and axial pressure dependences of the coefficient of friction do not influence the peak temperature.

iii. The choice of friction model is not important for low amplitude shaking (shaking intensity of 25%) and small contact pressure (p_o = 10 MPa here).

iv. The importance of the choice of friction model increases with μ_{ref}.

v. The estimates of median and 90th percentile peak responses are most significantly affected by whether the friction model includes temperature dependence of friction, when shaking intensity is greater than or equal to 100%, p_o is 50 MPa and μ_{ref} is 0.09. The difference in the median (90th percentile) peak temperature due to choice of friction model can be as great as 300ºC (400ºC).

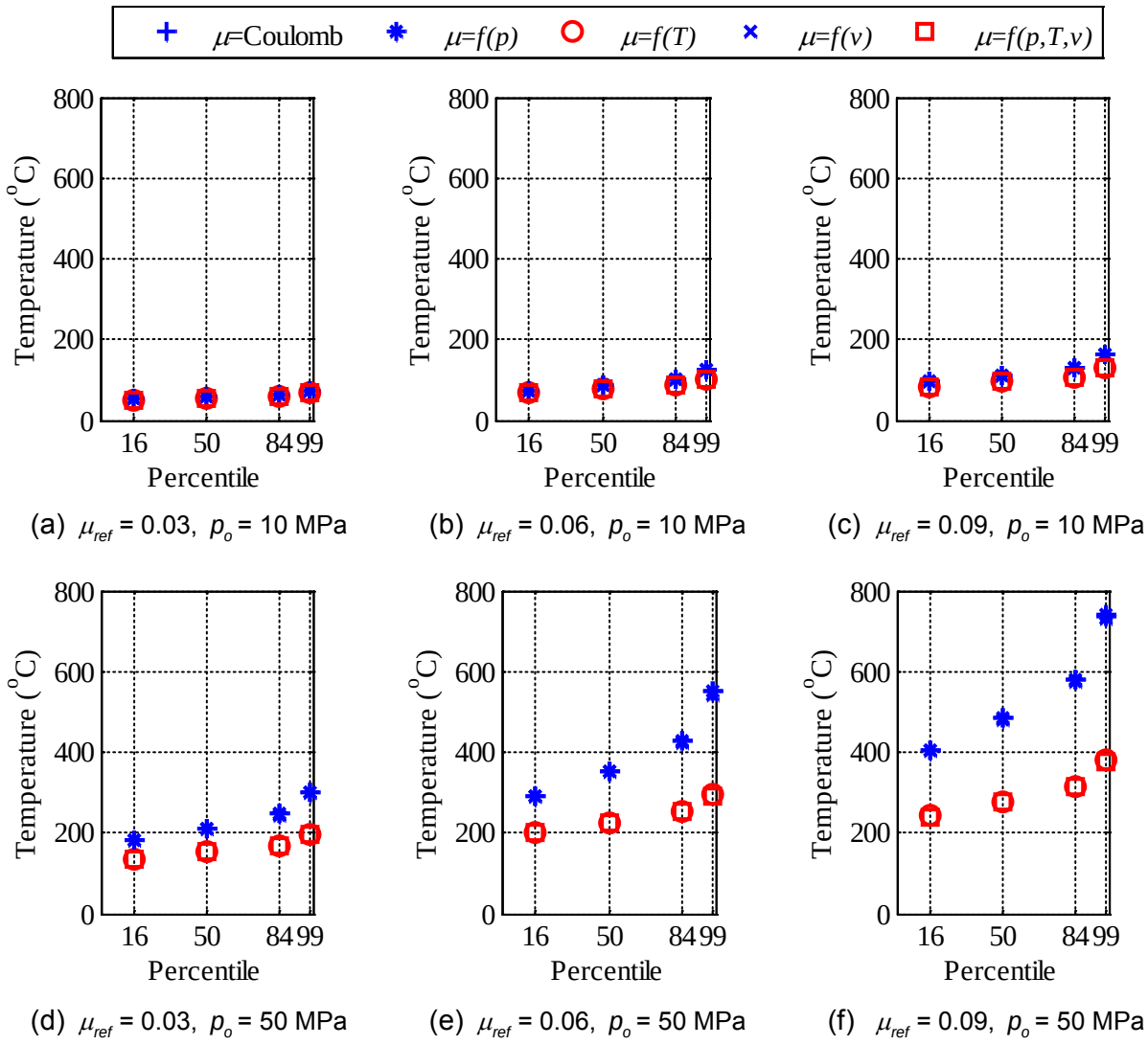

Figure 7-27 Distribution of Peak Temperature at the Center of the Sliding Surface of the FP Bearing with Sliding Period of 3 s Subjected to the 30 Ground Motions with an Amplitude Scale Factor of 1.0

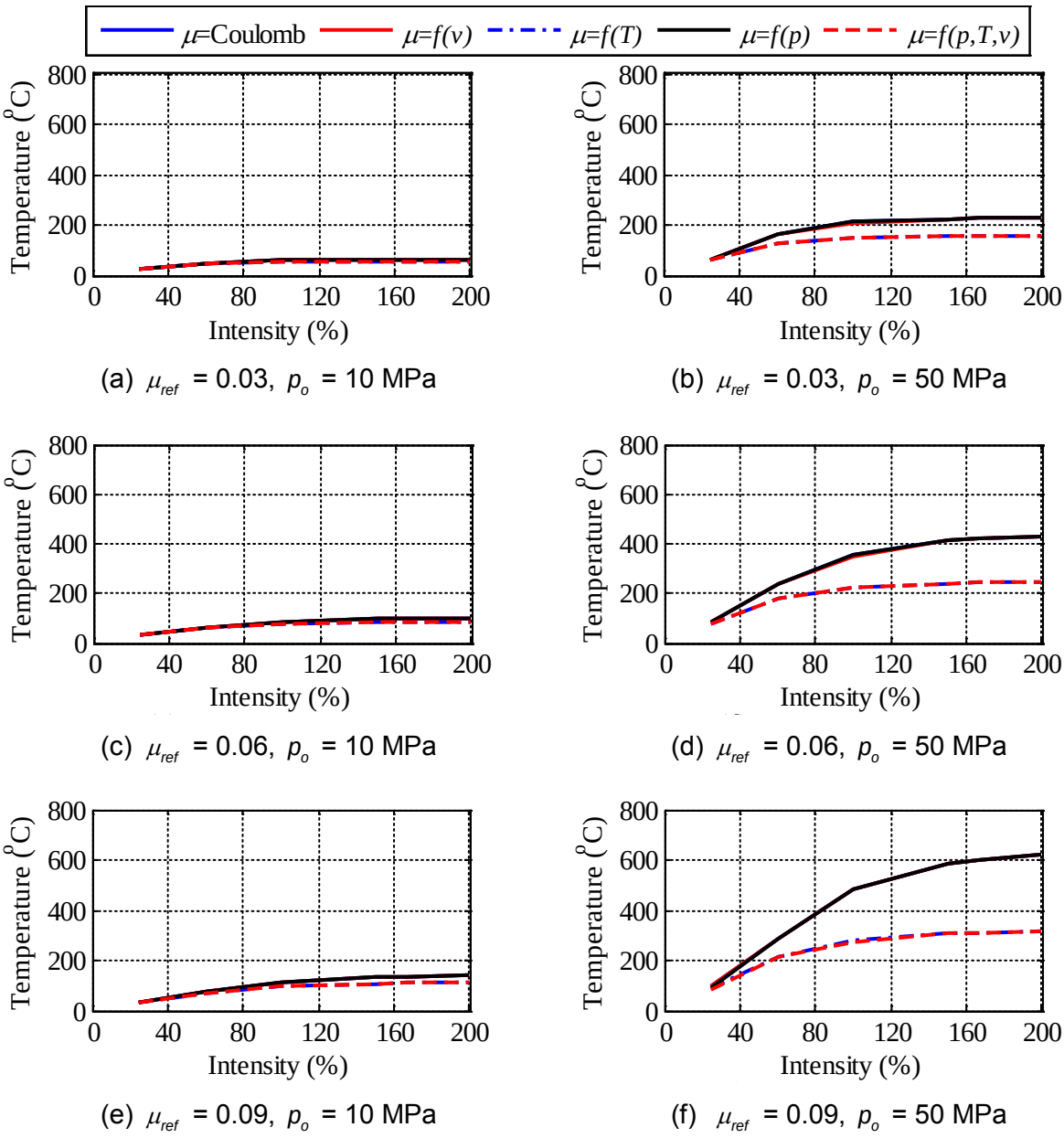

Figure 7-28 Distribution of Peak Temperature at the Center of the Sliding Surface of the FP Bearing with Sliding Period of 3 s Subjected to the 30 Ground Motions with an Amplitude Scale Factor of 1.0

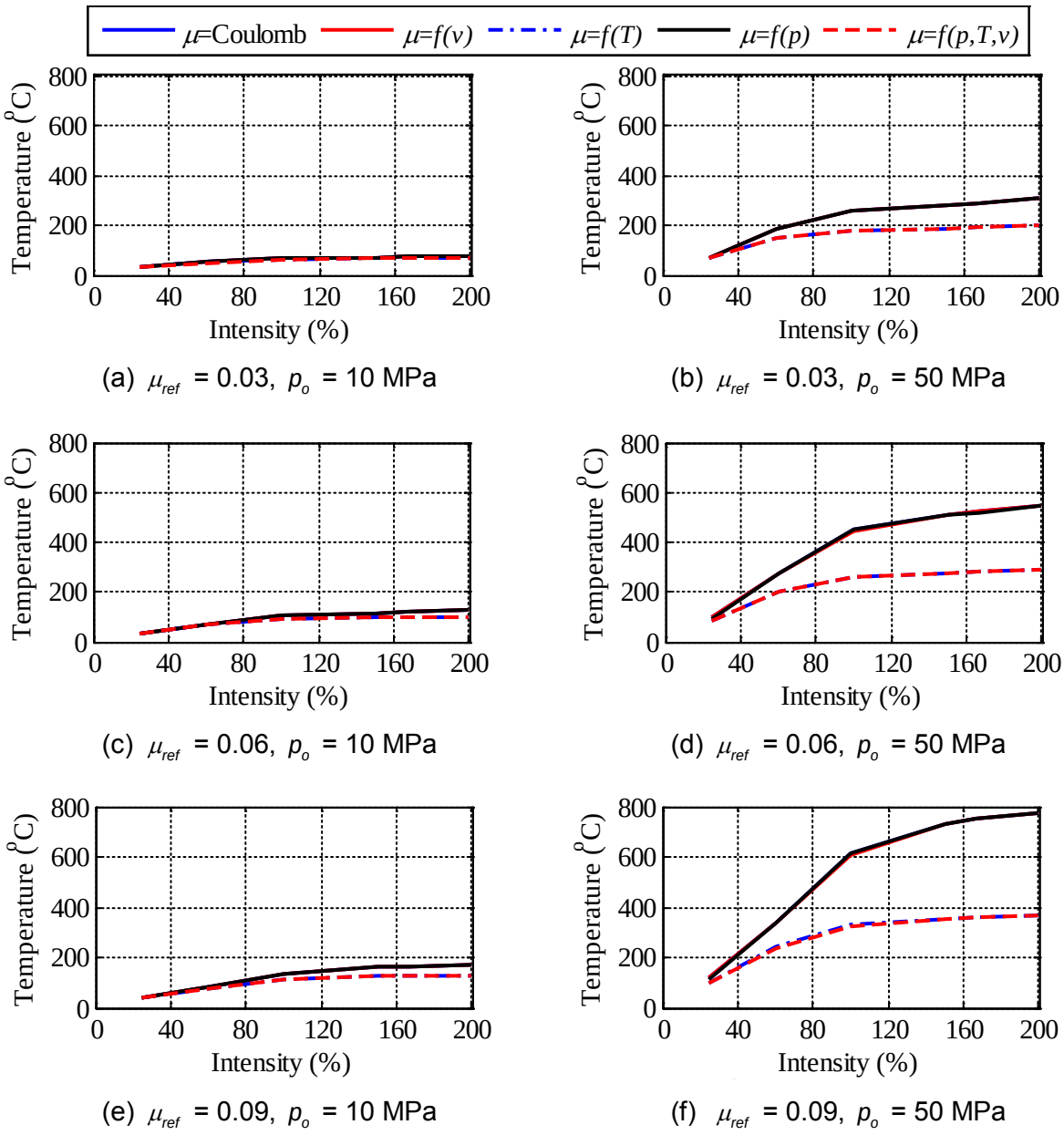

Figure 7-29 90th Percentile Peak Temperature at the Center of the Sliding Surface of the FP Bearing with a Sliding Period of 3 s Subjected to the 30 Ground Motions Amplitude Scaled to Different Intensities

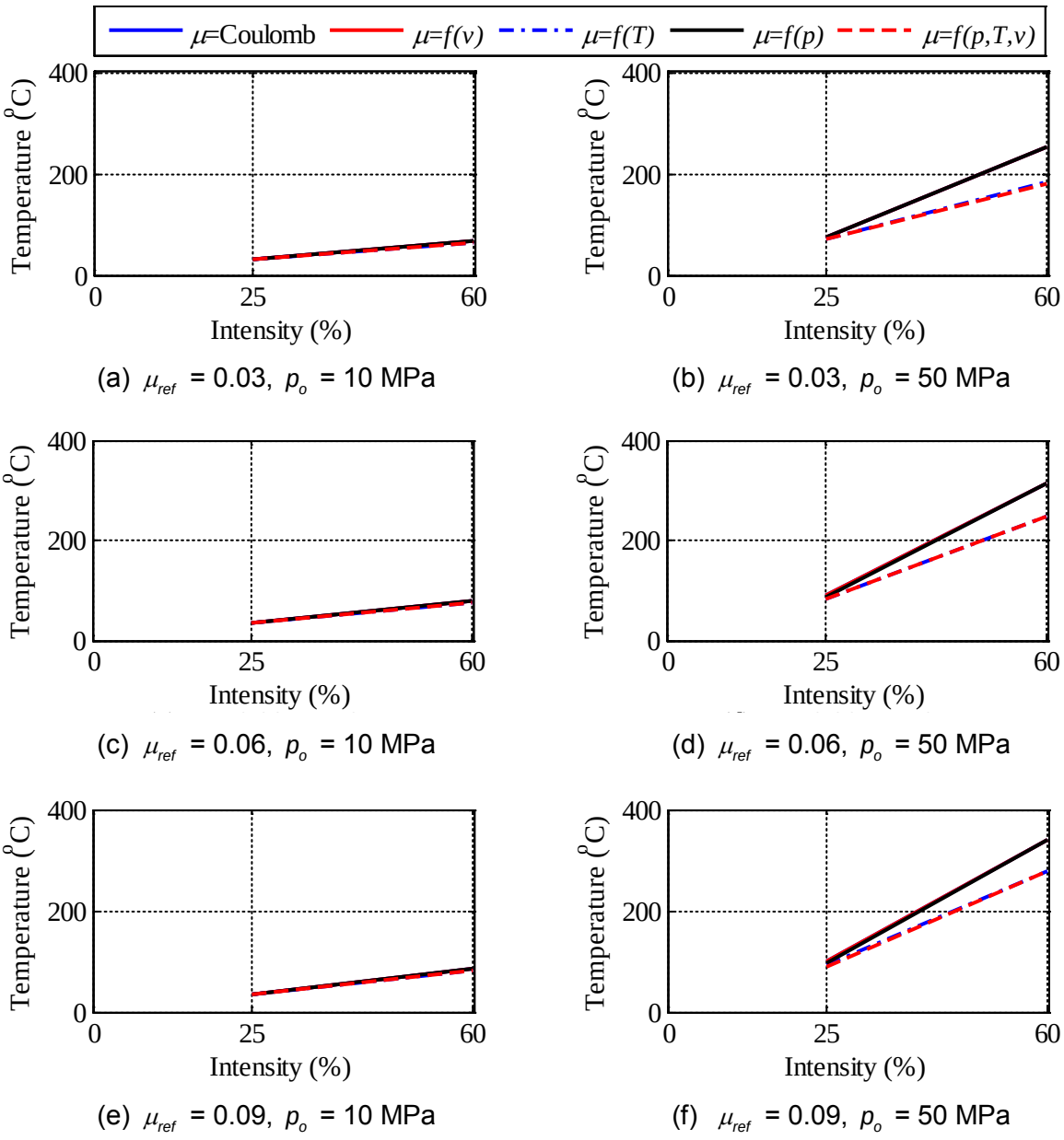

Figure 7-30 Median Peak Temperature at the Center of the Sliding Surface of the FP Bearing with a Sliding Period of 1.5 s Subjected to the 30 Ground Motions Amplitude Scaled to Different Intensities

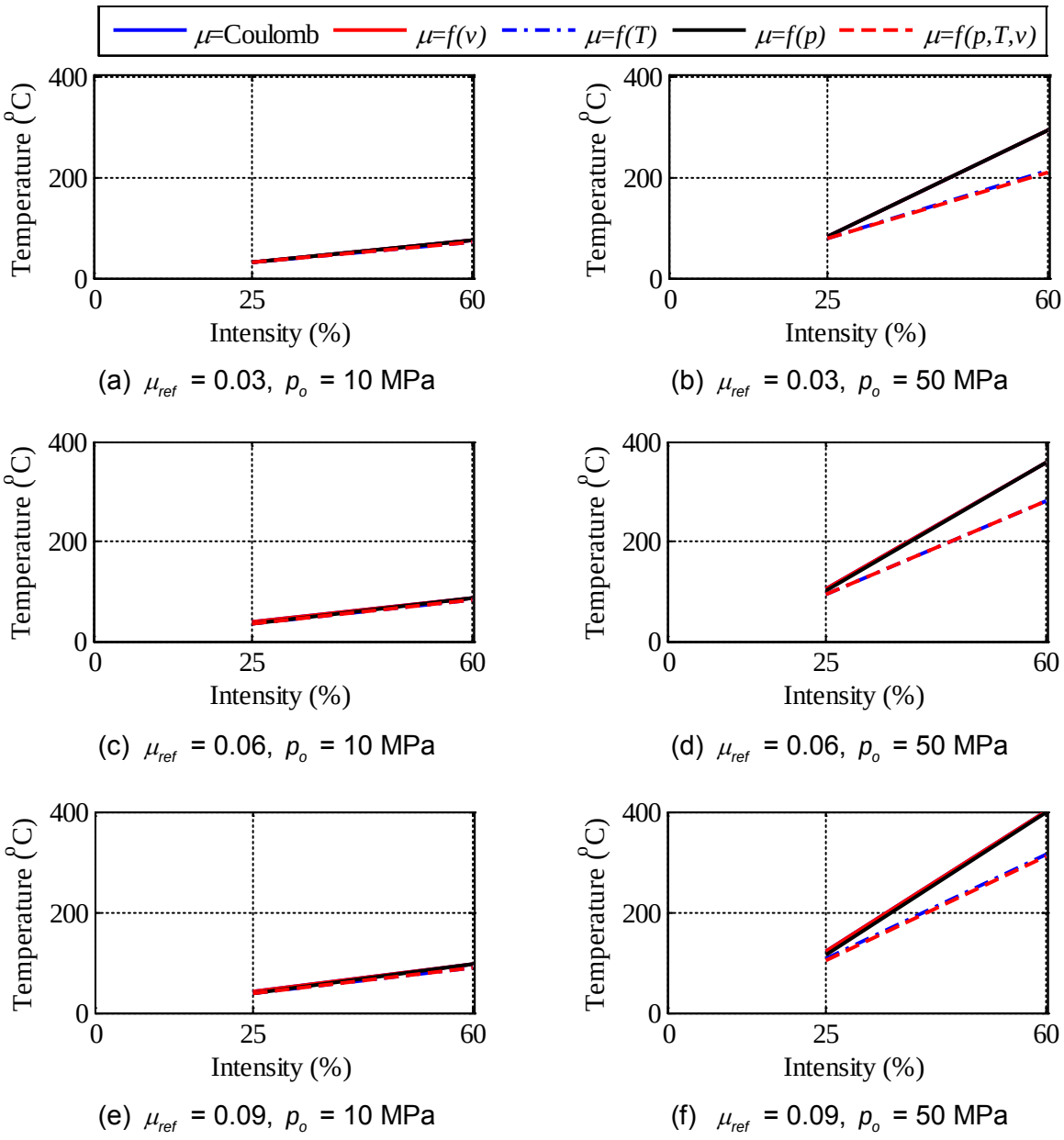

Figure 7-31 90th Percentile Peak Temperature at the Center of the Sliding Surface of the FP Bearing with a Sliding Period of 1.5 s Subjected to the 30 Ground Motions Amplitude Scaled to Different Intensities

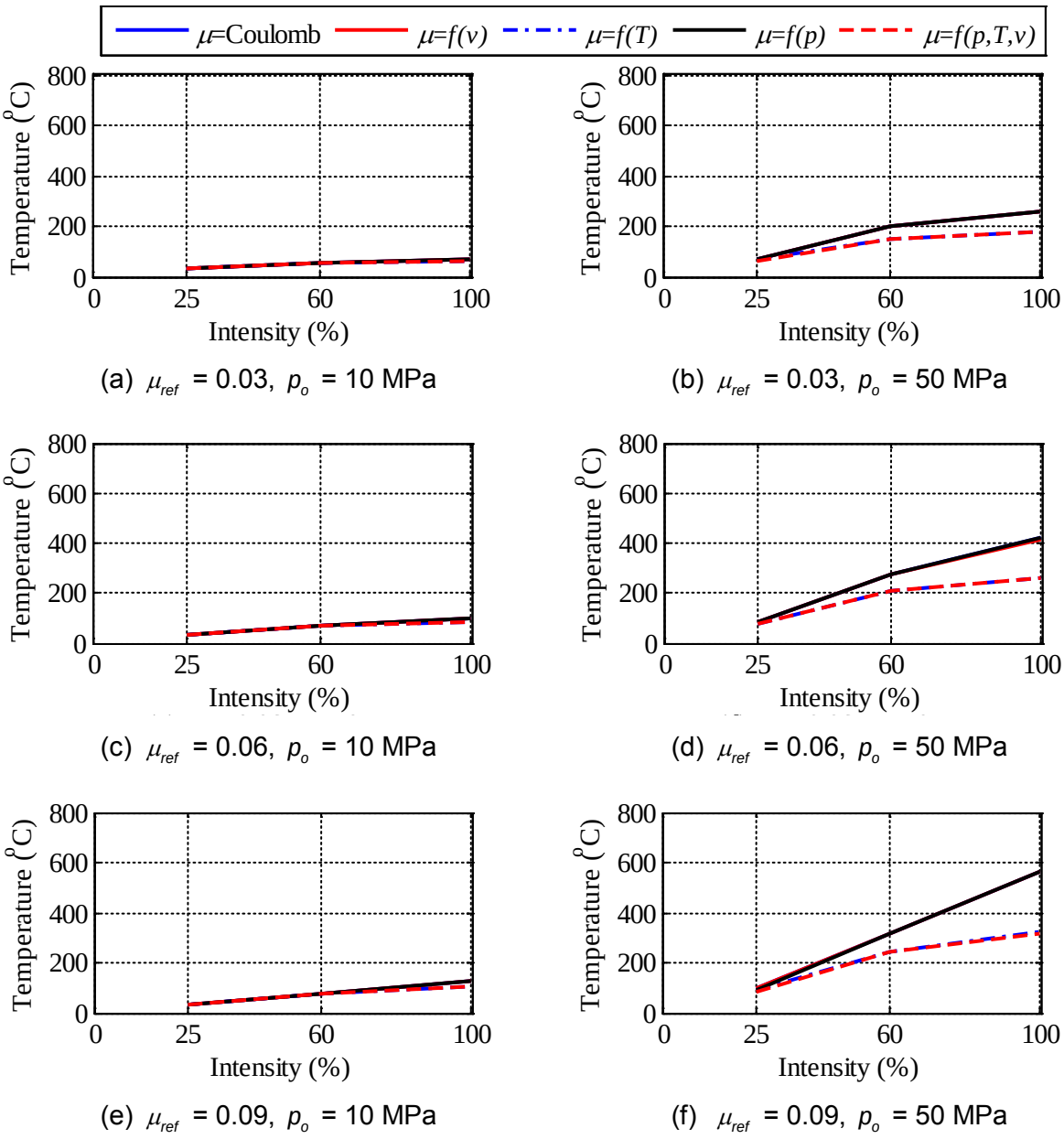

(a) μ_{ref} = 0.03, p_o = 10 MPa

(b) μ_{ref} = 0.03, p_o = 50 MPa

(c) μ_{ref} = 0.06, p_o = 10 MPa

(d) μ_{ref} = 0.06, p_o = 50 MPa

(e) μ_{ref} = 0.09, p_o = 10 MPa

(f) μ_{ref} = 0.09, p_o = 50 MPa

Figure 7-32 Median Peak Temperature at the Center of the Sliding Surface of the FP Bearing with a Sliding Period of 2 s Subjected to the 30 Ground Motions Amplitude Scaled to Different Intensities

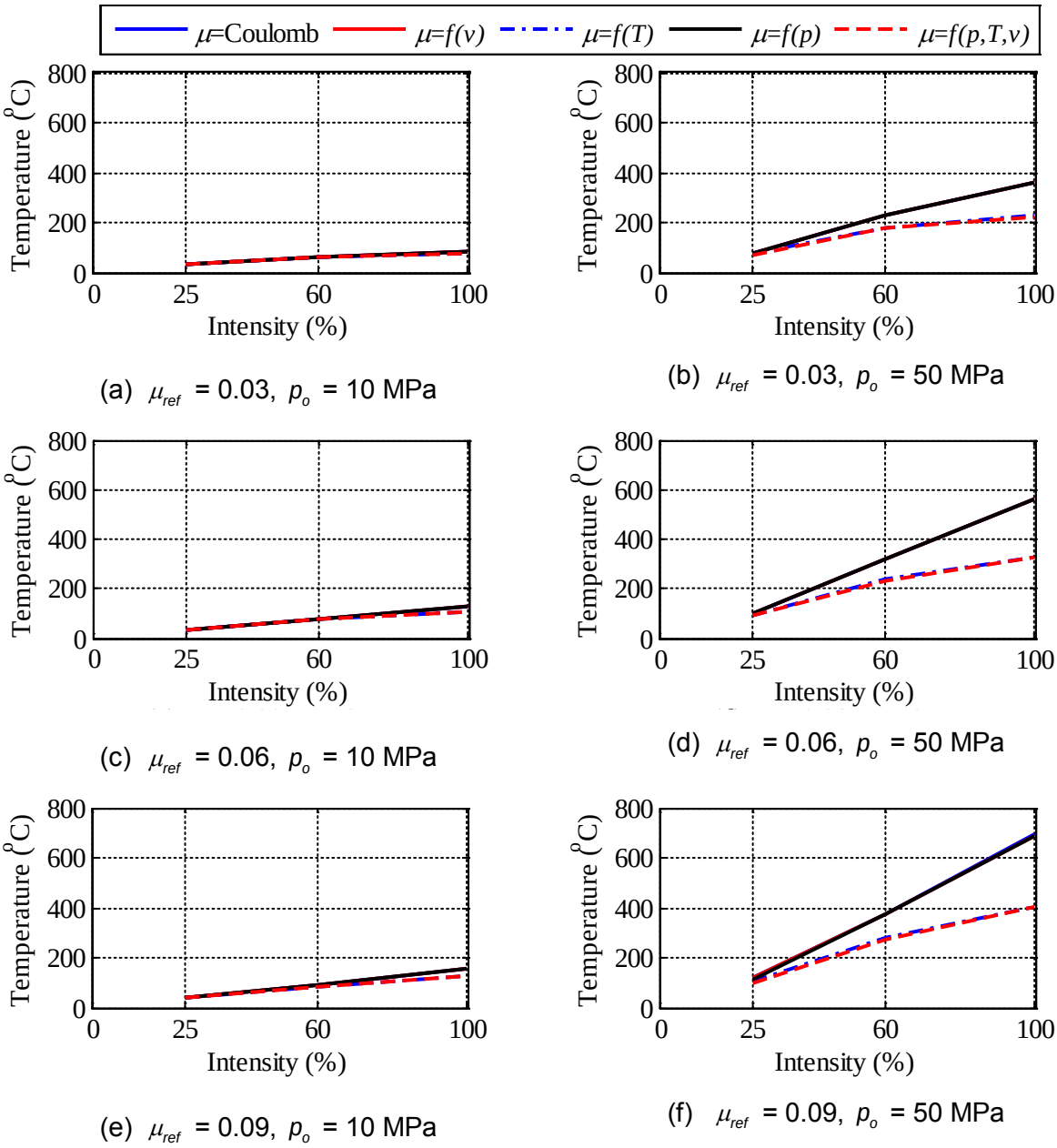

Figure 7-33 90th Percentile Peak Temperature at the Center of the Sliding Surface of the FP Bearing with a Sliding Period of 2 s Subjected to the 30 Ground Motions Amplitude Scaled to Different Intensities

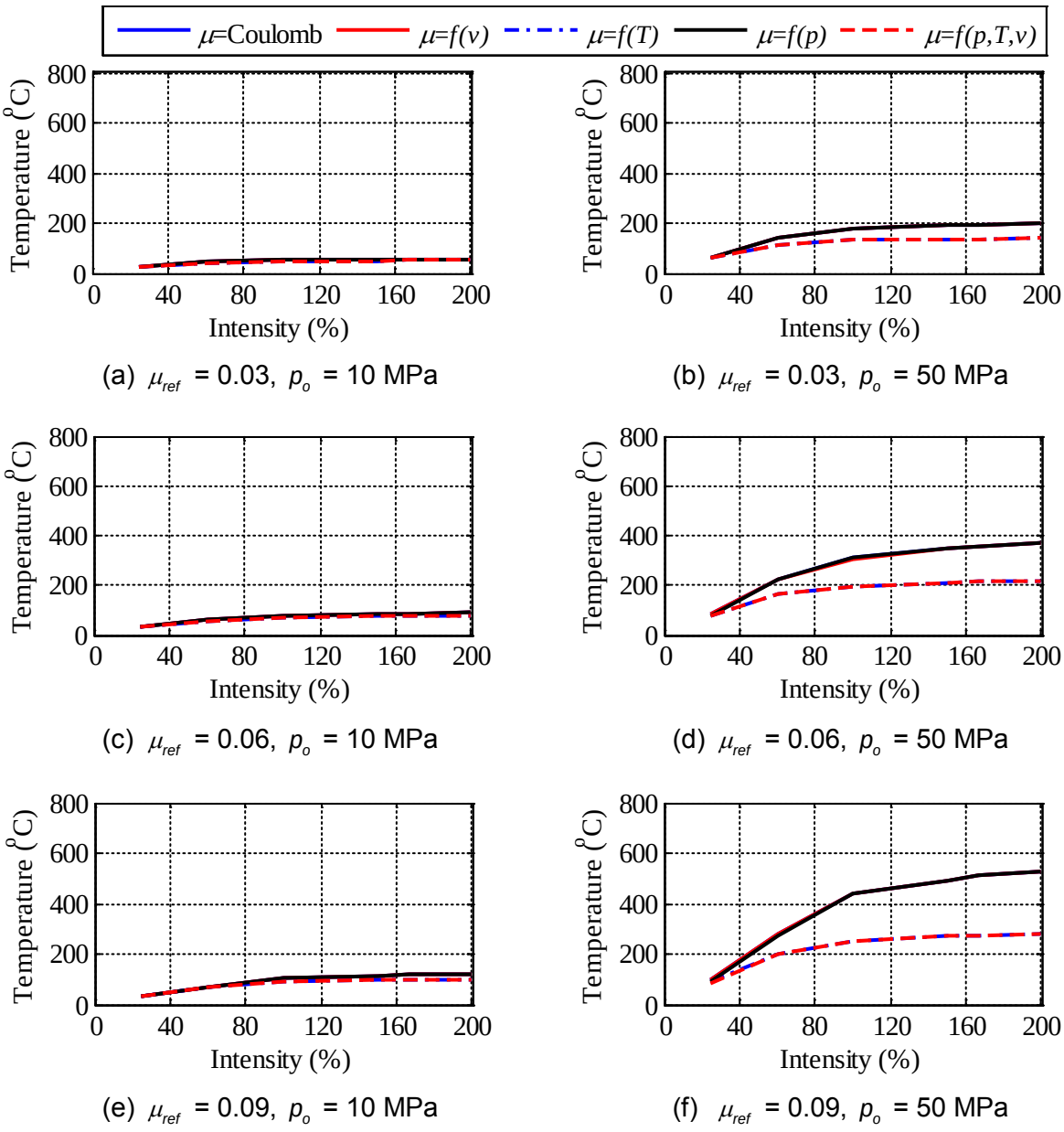

Figure 7-34 Median Peak Temperature at the Center of the Sliding Surface of the FP Bearing with a Sliding Period of 4 s Subjected to the 30 Ground Motions Amplitude Scaled to Different Intensities

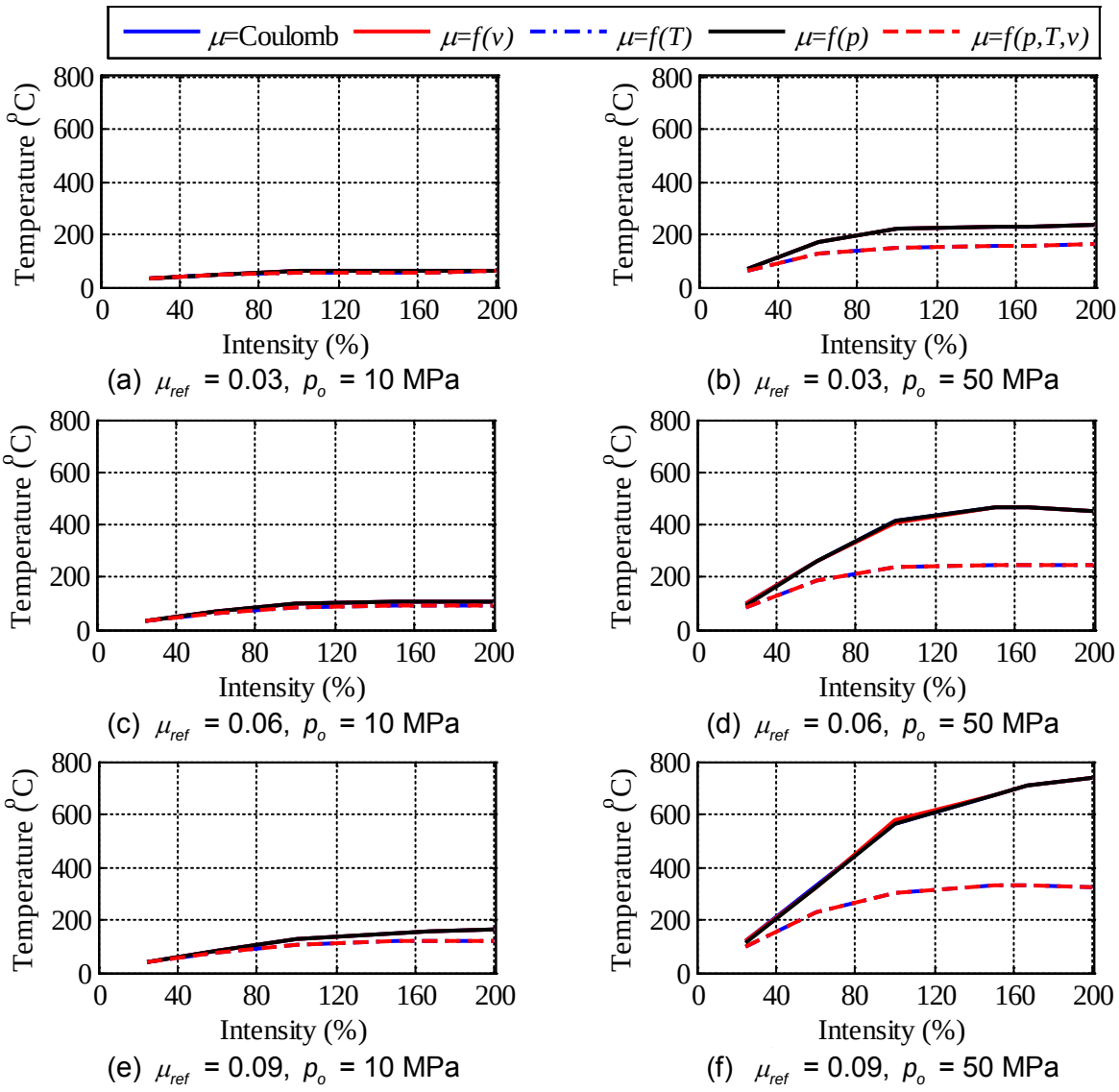

Figure 7-35 90th Percentile Peak Temperature at the Center of the Sliding Surface of the FP Bearing with a Sliding Period of 4 s Subjected to the 30 Ground Motions Amplitude Scaled to Different Intensities

7.5.5 Floor Response Spectra

Figure 7-36(a) (7-36(b)) presents the 50th and 99th percentile response spectra in a horizontal direction (say X) corresponding to the absolute acceleration of the slider of the FP bearing with a sliding period of 3 s, μ_{ref} of 0.03 and p_o of 10 MPa (50 MPa) subjected to the 30 ground motions amplitude scaled by 1.0. The 30 values of response spectral ordinates (one for each set of ground motions) are assumed to distribute lognormally; see Appendix H. The influence of the choice of friction model is negligible for μ_{ref} of 0.03.

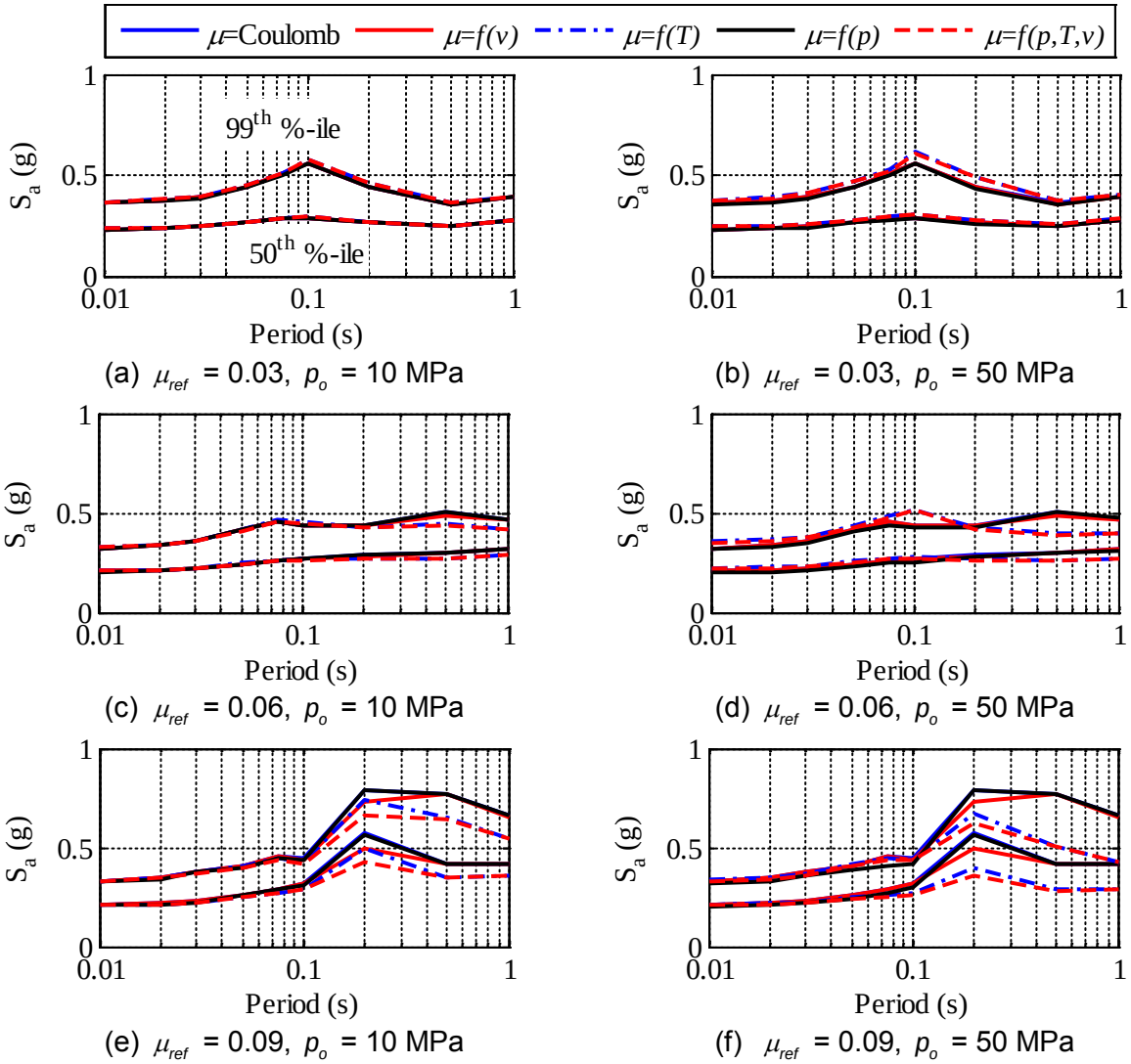

Figure 7-36 Five Percent Damped Response Spectra in X Direction Corresponding to the Absolute Acceleration of the Slider of the FP Bearing with Sliding Period of 3 s Subjected to the 30 Ground Motions with Amplitude Scaling Factor of 1.0

Figures 7-36(c) and 7-36(d) present results for μ_{ref} of 0.06. The spectral ordinates vary by up to ±20% for different choices of friction model, relative to those computed using Coulomb model, at periods longer than 0.07 s, noting that only heating affects the ordinates.

Figures 7-36(e) and 7-36(f) present results for μ_{ref} of 0.09. The floor spectral ordinates are not affected by the choice of friction model at periods shorter than 0.07 s, irrespective of p_o and μ_{ref}. The friction model affects the spectral ordinates at periods longer than 0.1 s. Consideration of heating can reduce the spectral demand by 0.1 g (0.2 g) or 20% (35%) for p_o of 10 MPa (50 MPa), at the higher percentiles. Consideration of the dependence of friction on pressure and velocity has no meaningful effect on spectral response.

Figure 7-37 presents the 5%-damped 50th and 90th percentile peak floor spectral accelerations in a horizontal direction (say X) at 0.01 s, 0.1 s and 0.5 s corresponding to the absolute acceleration of the slider of the 3 s FP bearing with p_o of 10 MPa and 50 MPa, and μ_{ref} of 0.06, subjected to the 30 ground motions amplitude scaled by the six factors of Table 7-3. Figure 7-37(a) presents spectral ordinates at 0.01 s for p_o of 10 MPa. The spectral ordinates are not influenced by the choice of friction model. The significance of the friction model is seen at p_o of 50 MPa (Figure 7-37(b)), although the effect is small. Figures 7-37(c) and 7-37(d) present spectral accelerations at 0.1 s for p_o of 10 MPa and 50 MPa, respectively; spectral ordinates at 0.5 s are presented in Figures 7-37(e) and 7-37(f). Figure 7-38 presents companion results to Figure 7-37 in the orthogonal horizontal direction (say Y). The magnitude of ordinates and influences of the choice of friction model on floor spectral ordinates are comparable to those with Figure 7-37.

Panels (b), (d) and (f) of Figure 7-37 (and Figure 7-38) present the spectral ordinates for p_o of 50 MPa at periods 0.01 s, 0.1 s and 0.5 s, respectively. The spectral acceleration at a very short period (e.g., 0.01 s) is equal to the peak floor acceleration, which is approximately the ratio of the peak lateral force to the mass associated with the slider. It is seen in panels (b) of the two figures that the 0.01 s ordinates for different friction models are comparable, implying that the peak lateral force in the bearing is not influenced by the choice of friction model. The observations for spectral acceleration at 0.1 s (see panel (d)) are similar to those at 0.01 s. The ordinates at 0.5 s are sensitive to whether the friction model includes heating effects, especially at intensities smaller than 100%. The period of 0.5 s can be seen as a *transition* period between the pre-sliding regime (0.3 s) and the sliding regime (3 s). The trends seen in Figures 7-37(f) and 7-38(f) are consistent with prior observations regarding the intensity of shaking (0.6 or 1.0) for which the heating effects are greatest.

Figures 7-39 through 7-44 present floor spectral ordinates in the two horizontal directions corresponding to the absolute acceleration of slider of the 1.5 s FP bearing with μ_{ref} of 0.03, 0.06 and 0.09, p_o of 10 MPa and 50 MPa, subjected to the ground motions with amplitude scale factors of 0.25 and 0.60. Figures 7-45 through 7-50 present the spectral ordinates for the 2 s bearing with amplitude scale factors of 0.25, 0.60 and 1.00[40], Figures 7-51 through 7-60 present results for 3 s and 4 s bearings.

Figure 7-61 (7-62) presents the median (90th percentile) peak floor spectral ordinates at 0.01 s, 0.1 s and 0.5 s periods corresponding to the absolute acceleration in the X direction of the slider of the 3 s FP bearing with p_o of 50 MPa as a function of μ_{ref} at different levels of shaking intensity. In terms of floor spectra, the key observations from Figures 7-37 through 7-62 are:

i. The choice of friction model is unimportant at μ_{ref} = 0.03.

ii. The choice of friction model is unimportant for p_o = 10 MPa, and shorter periods (i.e., 0.01 s and 0.1 s).

[40] Higher scale factors are not considered because the displacement demands on the bearing are considerably greater than 0.5*R*, which is impractical for FP bearings.

iii. The differences in the spectral ordinates relative to those computed using the Coulomb model due to choice of friction model are less than 0.1 g (or 15%) at 0.01 s (and 0.1 s) for p_o of 50 MPa.

iv. For amplitude scale factors of 1.5 and smaller, the spectral ordinates at 0.5 s computed using a friction model that considers heating are smaller than those computed using a Coulomb (no heating) model: up to 35% smaller for p_o of 50 MPa and μ_{ref} of 0.09.

v. The velocity and pressure dependencies of the coefficient of friction do not materially influence floor spectra.

vi. The spectral acceleration ordinates at a short period (e.g., 0.01 s), which is also the peak floor acceleration, do not change considerably with increase in μ_{ref} .

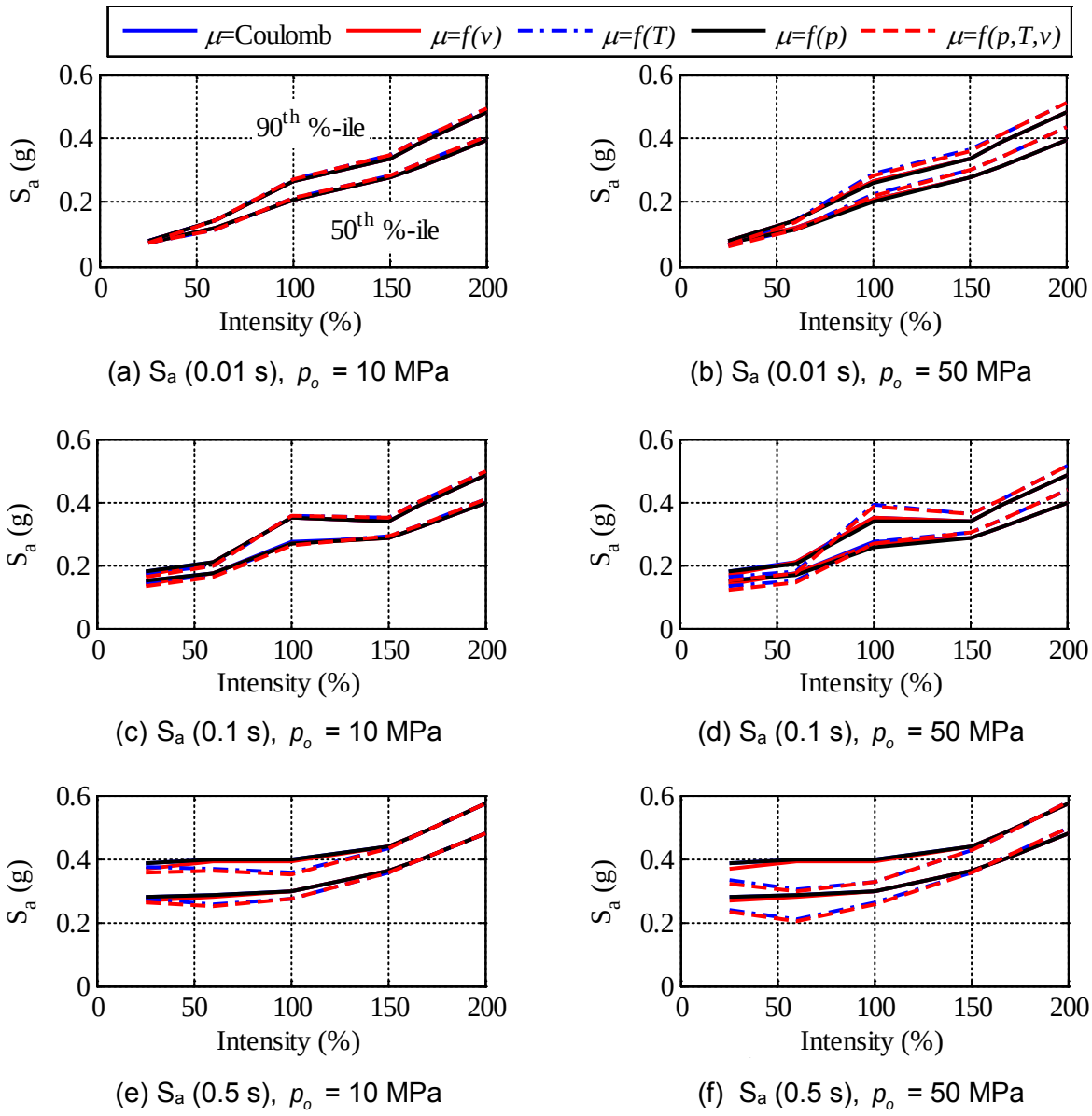

Figure 7-37 Five Percent Damped 50th and 90th Percentile Peak Floor Spectral Ordinates at Periods of 0.01 s, 0.1 s and 0.5 s, Corresponding to the Absolute Acceleration Response of the Slider in the X Direction of an FP Bearing with a Sliding Period of 3 s, Reference Axial Pressures of 10 MPa and 50 MPa, and Reference Coefficient of Friction of 0.06, Subjected to the 30 Ground Motions Amplitude Scaled to Different Intensities

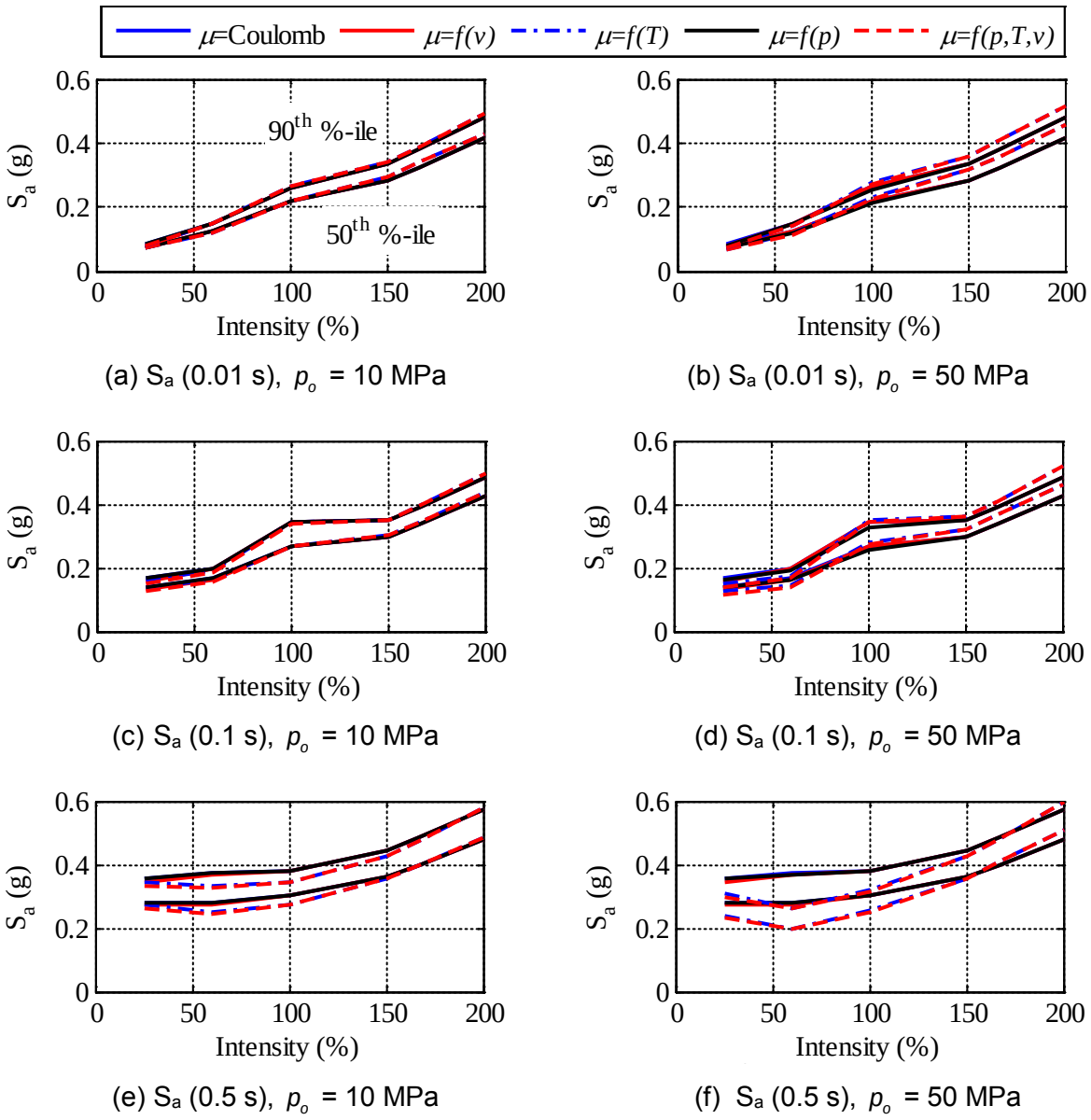

Figure 7-38 Five Percent Damped 50th and 90th Percentile Peak Floor Spectral Ordinates at Periods of 0.01 s, 0.1 s and 0.5 s, Corresponding to the Absolute Acceleration Response of the Slider in the Y Direction of an FP Bearing with a Sliding Period of 3 s, Reference Axial Pressures of 10 MPa and 50 MPa, and Reference Coefficient of Friction of 0.06, Subjected to the 30 Ground Motions Amplitude Scaled to Different Intensities

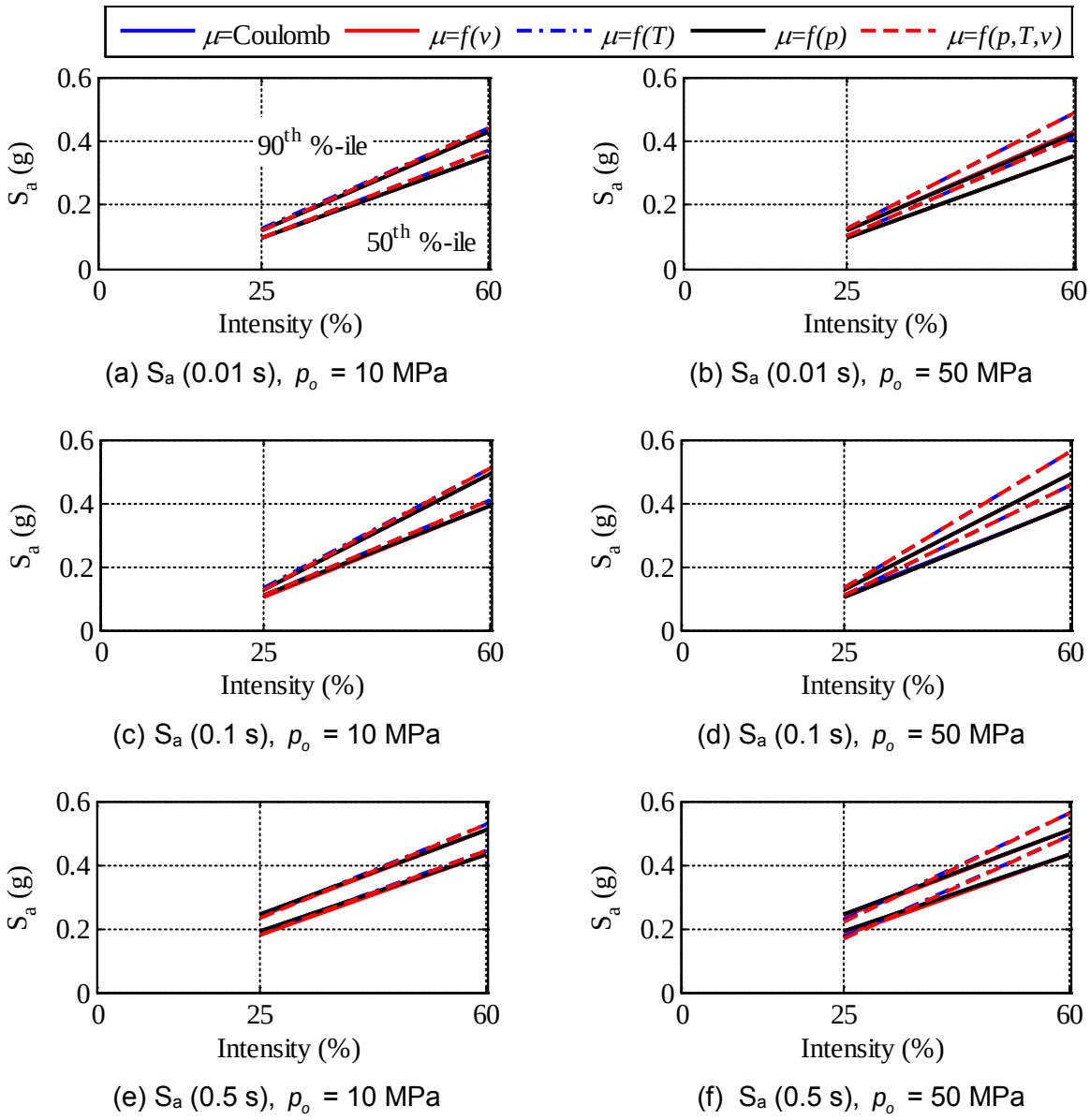

Figure 7-39 Five Percent Damped 50th and 90th Percentile Peak Floor Spectral Ordinates at Periods of 0.01 s, 0.1 s and 0.5 s, Corresponding to the Absolute Acceleration Response of the Slider in the X Direction of an FP Bearing with a Sliding Period of 1.5 s, Reference Axial Pressures of 10 MPa and 50 MPa, and Reference Coefficient of Friction of 0.03, Subjected to the 30 Ground Motions Amplitude Scaled to Different Intensities

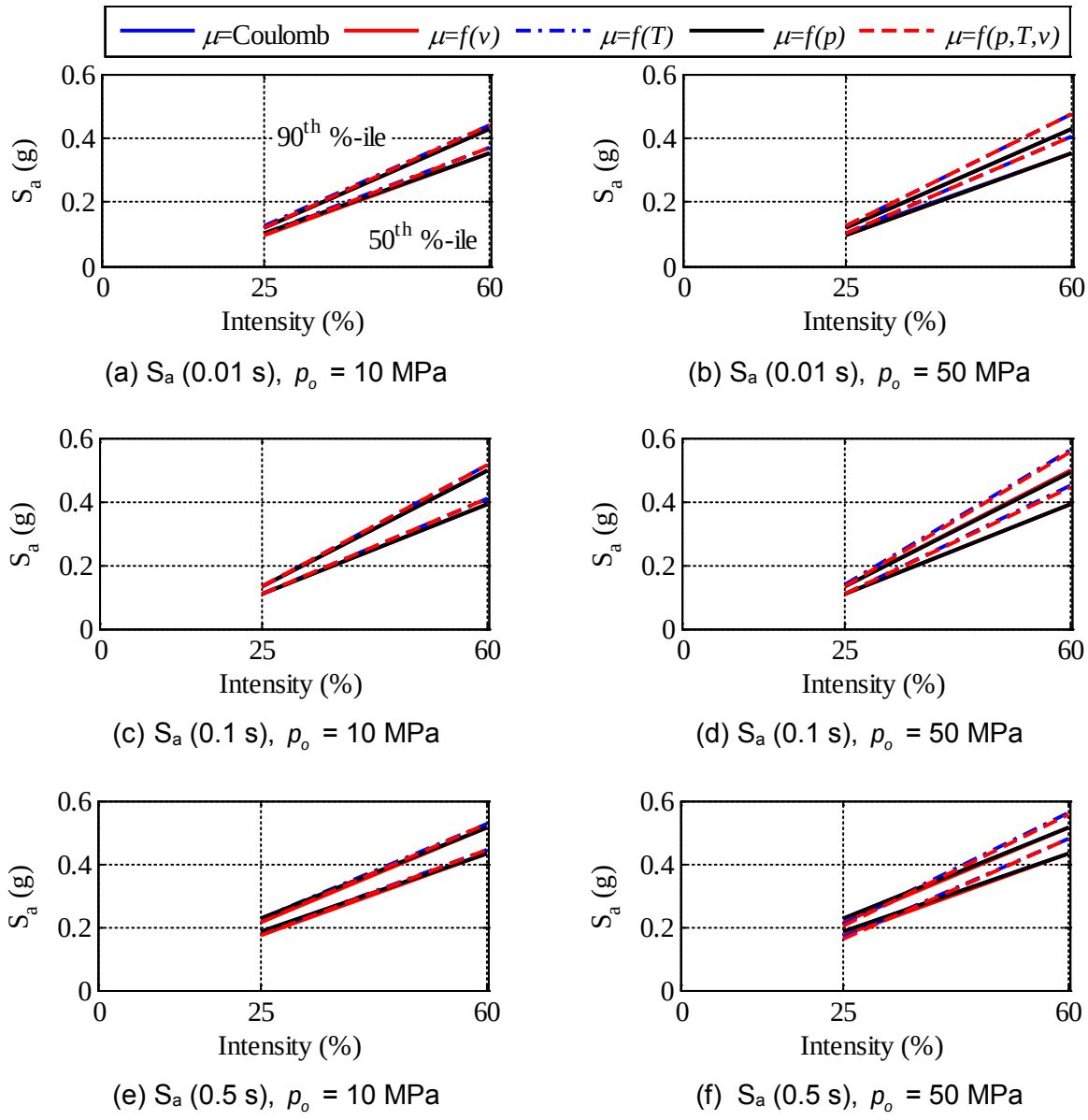

Figure 7-40 Five Percent Damped 50th and 90th Percentile Peak Floor Spectral Ordinates at Periods of 0.01 s, 0.1 s and 0.5 s, Corresponding to the Absolute Acceleration Response of the Slider in the Y Direction of an FP Bearing with a Sliding Period of 1.5 s, Reference Axial Pressures of 10 MPa and 50 MPa, and Reference Coefficient of Friction of 0.03, Subjected to the 30 Ground Motions Amplitude Scaled to Different Intensities

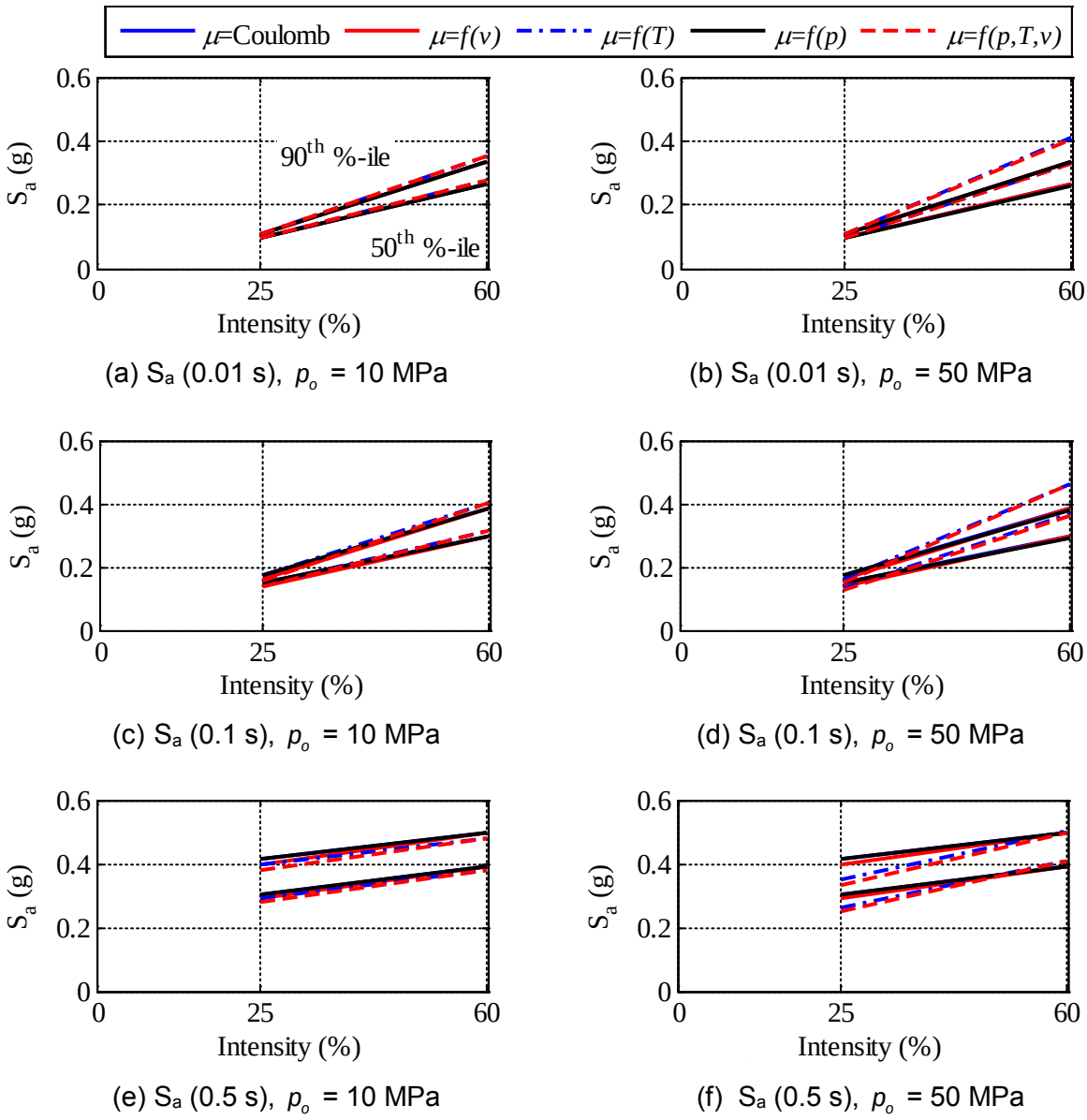

Figure 7-41 Five Percent Damped 50th and 90th Percentile Peak Floor Spectral Ordinates at Periods of 0.01 s, 0.1 s and 0.5 s, Corresponding to the Absolute Acceleration Response of the Slider in the X Direction of an FP Bearing with a Sliding Period of 1.5 s, Reference Axial Pressures of 10 MPa and 50 MPa, and Reference Coefficient of Friction of 0.06, Subjected to the 30 Ground Motions Amplitude Scaled to Different Intensities

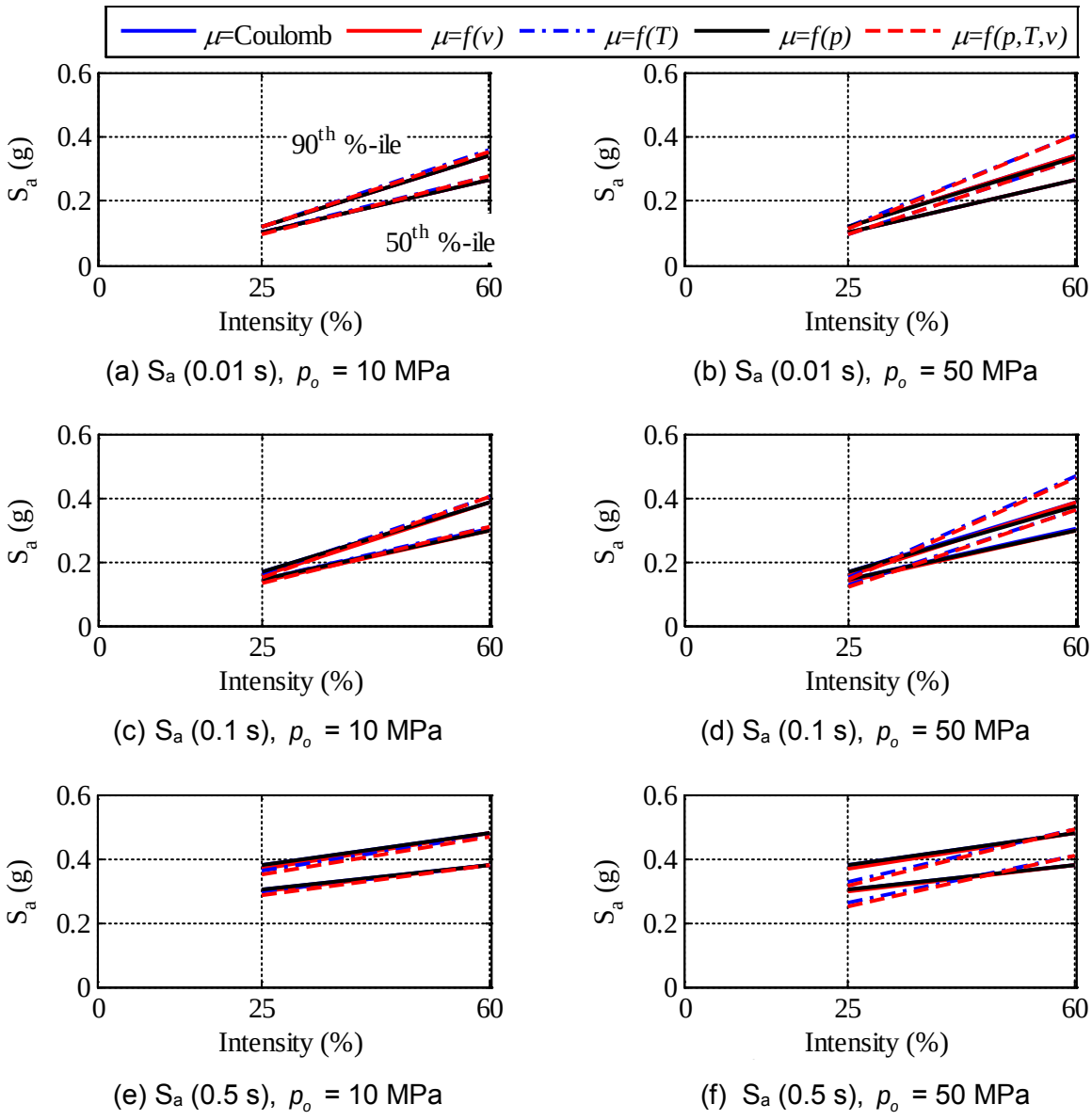

Figure 7-42 Five Percent Damped 50th and 90th Percentile Peak Floor Spectral Ordinates at Periods of 0.01 s, 0.1 s and 0.5 s, Corresponding to the Absolute Acceleration Response of the Slider in the Y Direction of an FP Bearing with a Sliding Period of 1.5 s, Reference Axial Pressures of 10 MPa and 50 MPa, and Reference Coefficient of Friction of 0.06, Subjected to the 30 Ground Motions Amplitude Scaled to Different Intensities

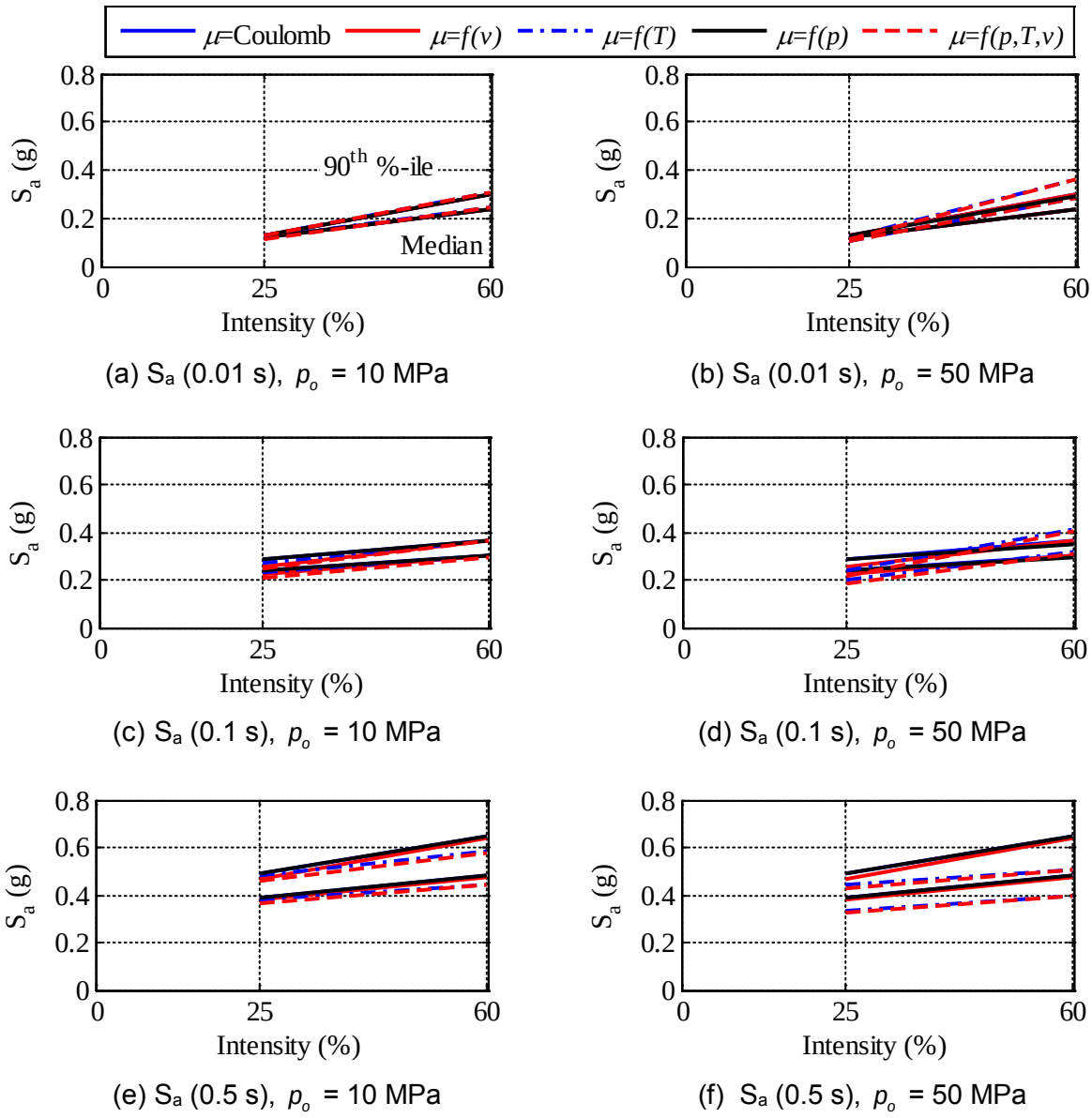

(a) S_a (0.01 s), p_o = 10 MPa

(b) S_a (0.01 s), p_o = 50 MPa

(c) S_a (0.1 s), p_o = 10 MPa

(d) S_a (0.1 s), p_o = 50 MPa

(e) S_a (0.5 s), p_o = 10 MPa

(f) S_a (0.5 s), p_o = 50 MPa

Figure 7-43 Five Percent Damped 50th and 90 th Percentile Peak Floor Spectral Ordinates at Periods of 0.01 s, 0.1 s and 0.5 s, Corresponding to the Absolute Acceleration Response of the Slider in the X Direction of an FP Bearing with a Sliding Period of 1.5 s, Reference Axial Pressures of 10 MPa and 50 MPa, and Reference Coefficient of Friction of 0.09, Subjected to the 30 Ground Motions Amplitude Scaled to Different Intensities

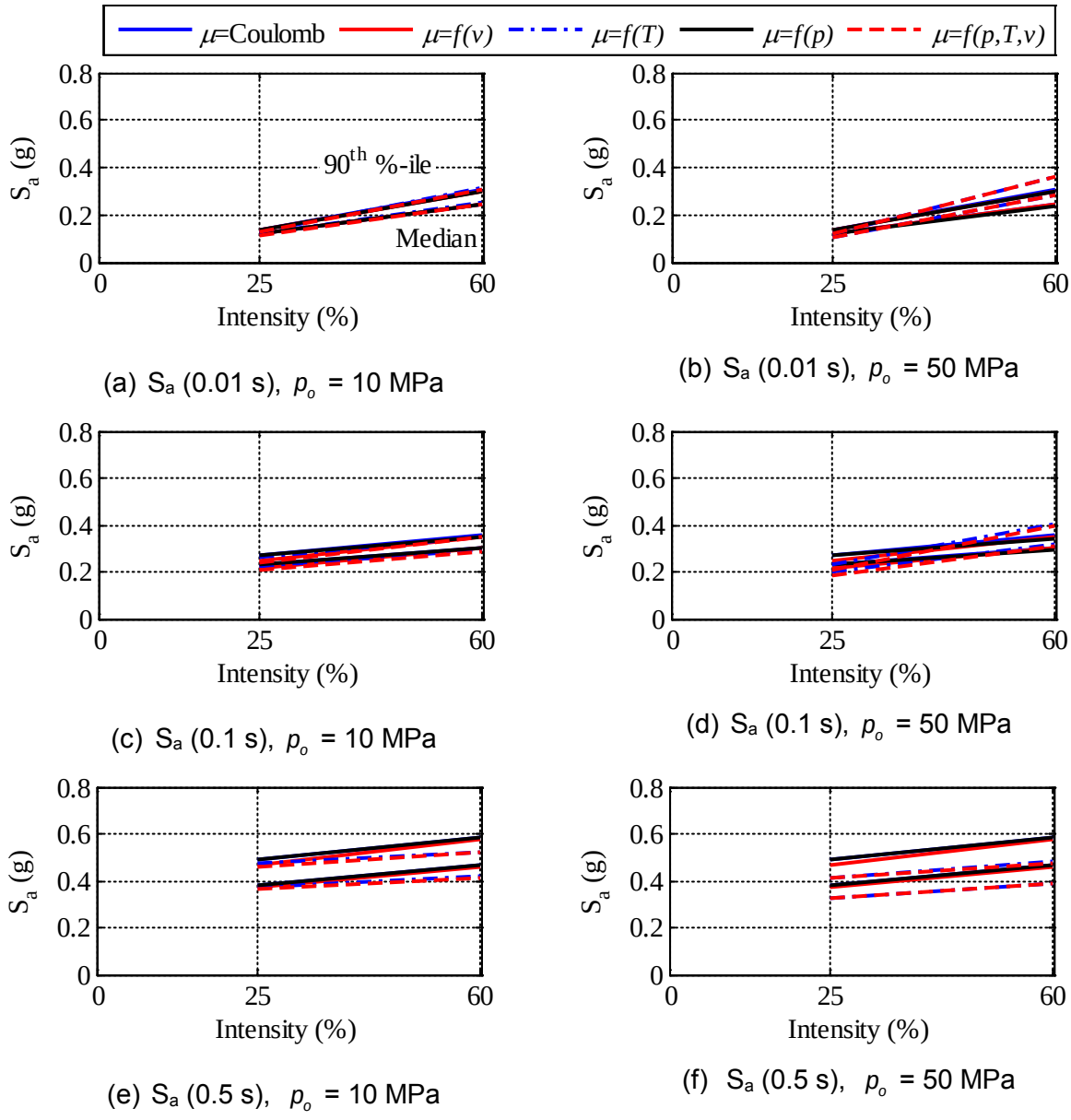

Figure 7-44 Five Percent Damped 50th and 90th Percentile Peak Floor Spectral Ordinates at Periods of 0.01 s, 0.1 s and 0.5 s, Corresponding to the Absolute Acceleration Response of the Slider in the Y Direction of an FP Bearing with a Sliding Period of 1.5 s, Reference Axial Pressures of 10 MPa and 50 MPa, and Reference Coefficient of Friction of 0.09, Subjected to the 30 Ground Motions Amplitude Scaled to Different Intensities

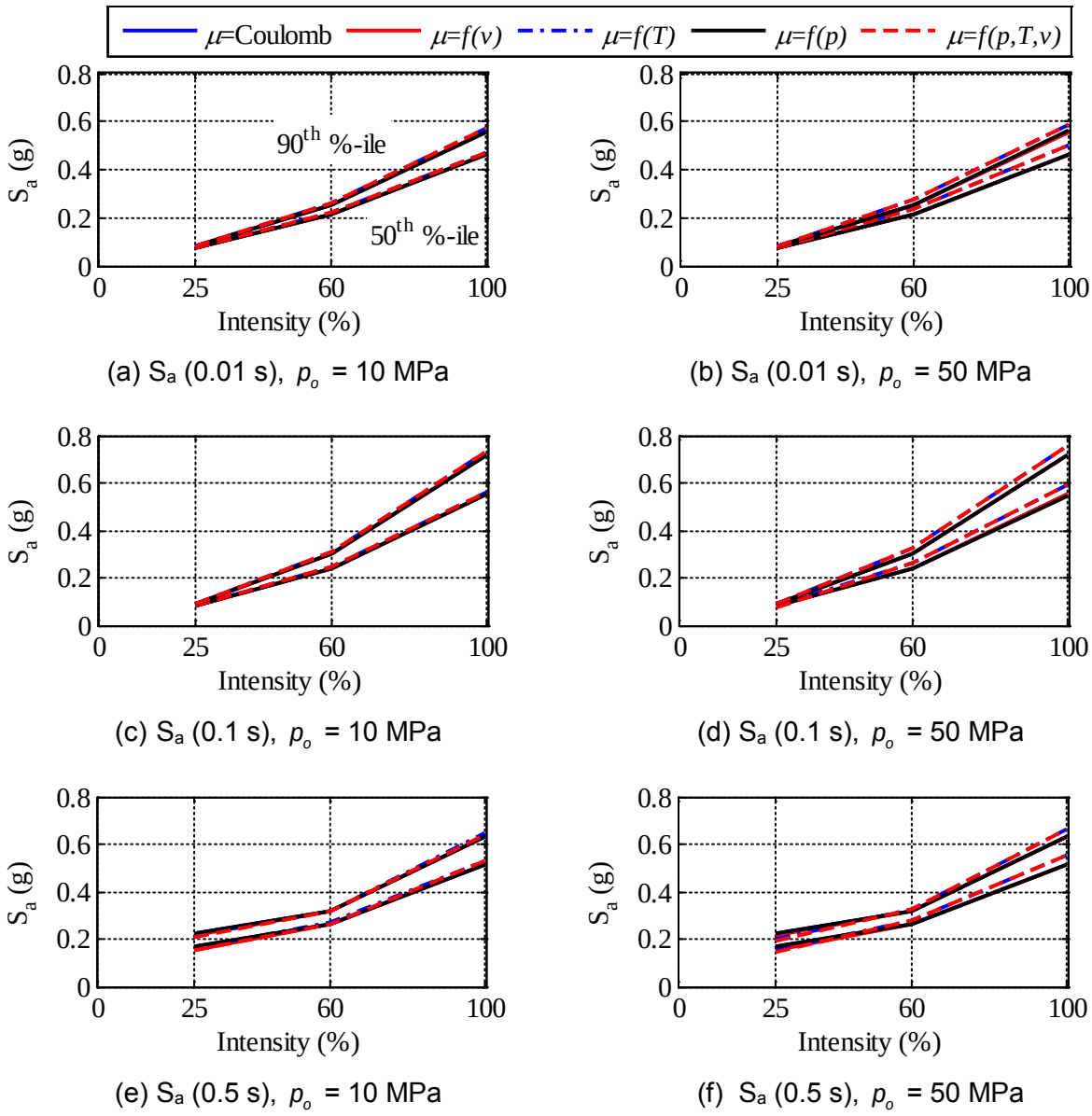

Figure 7-45 Five Percent Damped 50th and 90th Percentile Peak Floor Spectral Ordinates at Periods of 0.01 s, 0.1 s and 0.5 s, Corresponding to the Absolute Acceleration Response of the Slider in the X Direction of an FP Bearing with a Sliding Period of 2 s, Reference Axial Pressures of 10 MPa and 50 MPa, and Reference Coefficient of Friction of 0.03, Subjected to the 30 Ground Motions Amplitude Scaled to Different Intensities

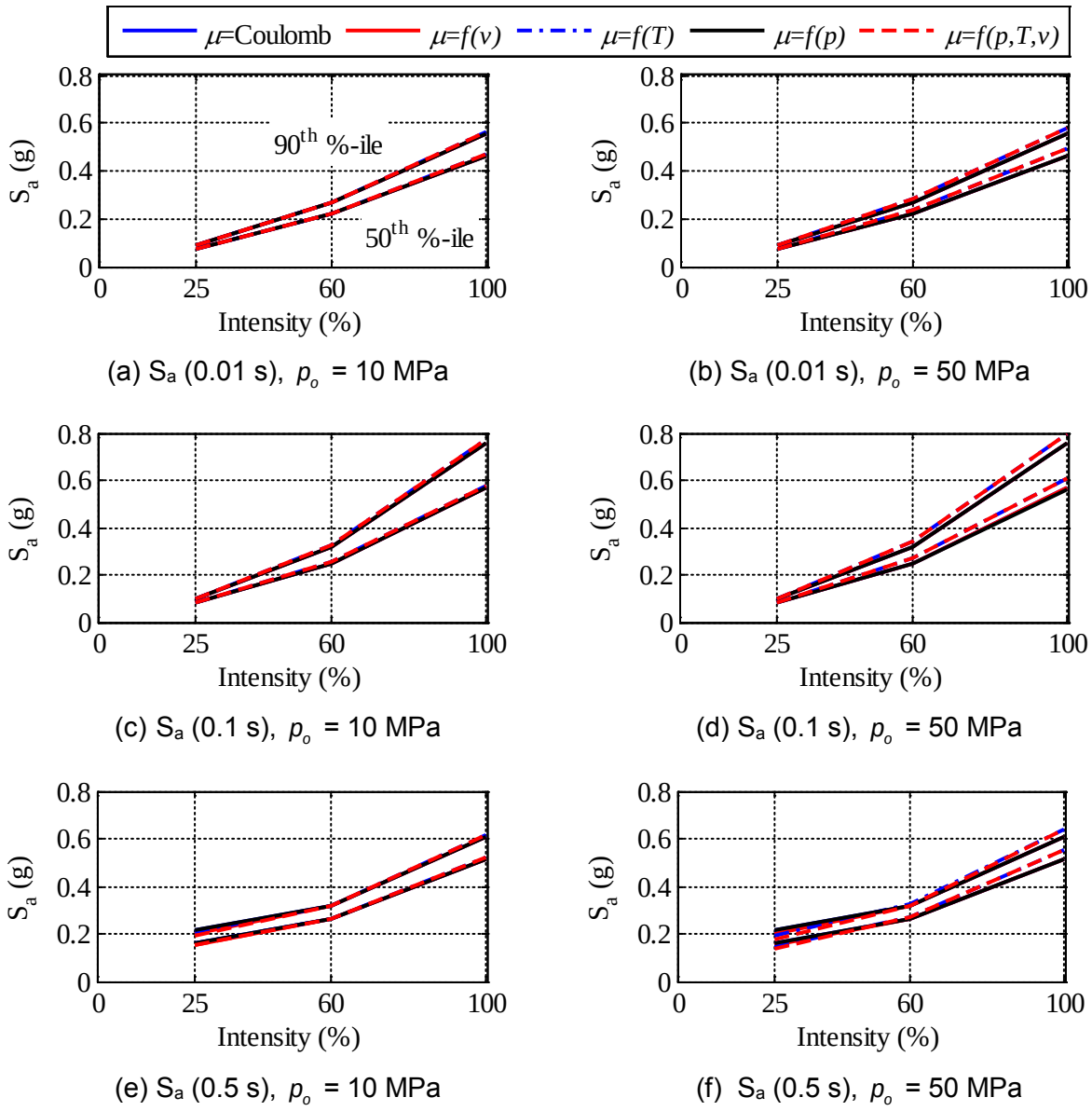

Figure 7-46 Five Percent Damped 50th and 90th Percentile Peak Floor Spectral Ordinates at Periods of 0.01 s, 0.1 s and 0.5 s, Corresponding to the Absolute Acceleration Response of the Slider in the Y Direction of an FP Bearing with a Sliding Period of 2 s, Reference Axial Pressures of 10 MPa and 50 MPa, and Reference Coefficient of Friction of 0.03, Subjected to the 30 Ground Motions Amplitude Scaled to Different Intensities

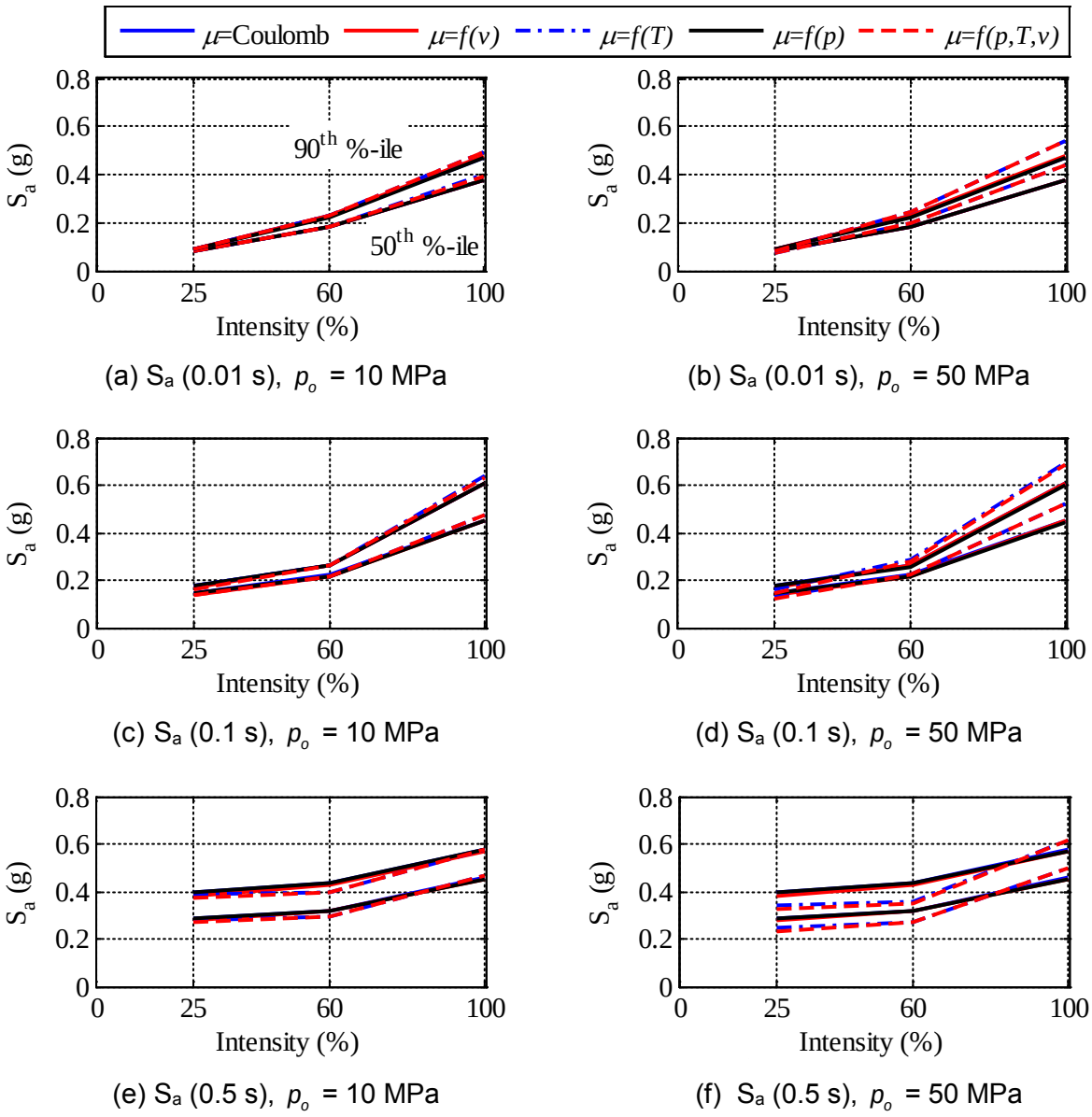

Figure 7-47 Five Percent Damped 50th and 90th Percentile Peak Floor Spectral Ordinates at Periods of 0.01 s, 0.1 s and 0.5 s, Corresponding to the Absolute Acceleration Response of the Slider in the X Direction of an FP Bearing with a Sliding Period of 2 s, Reference Axial Pressures of 10 MPa and 50 MPa, and Reference Coefficient of Friction of 0.06, Subjected to the 30 Ground Motions Amplitude Scaled to Different Intensities

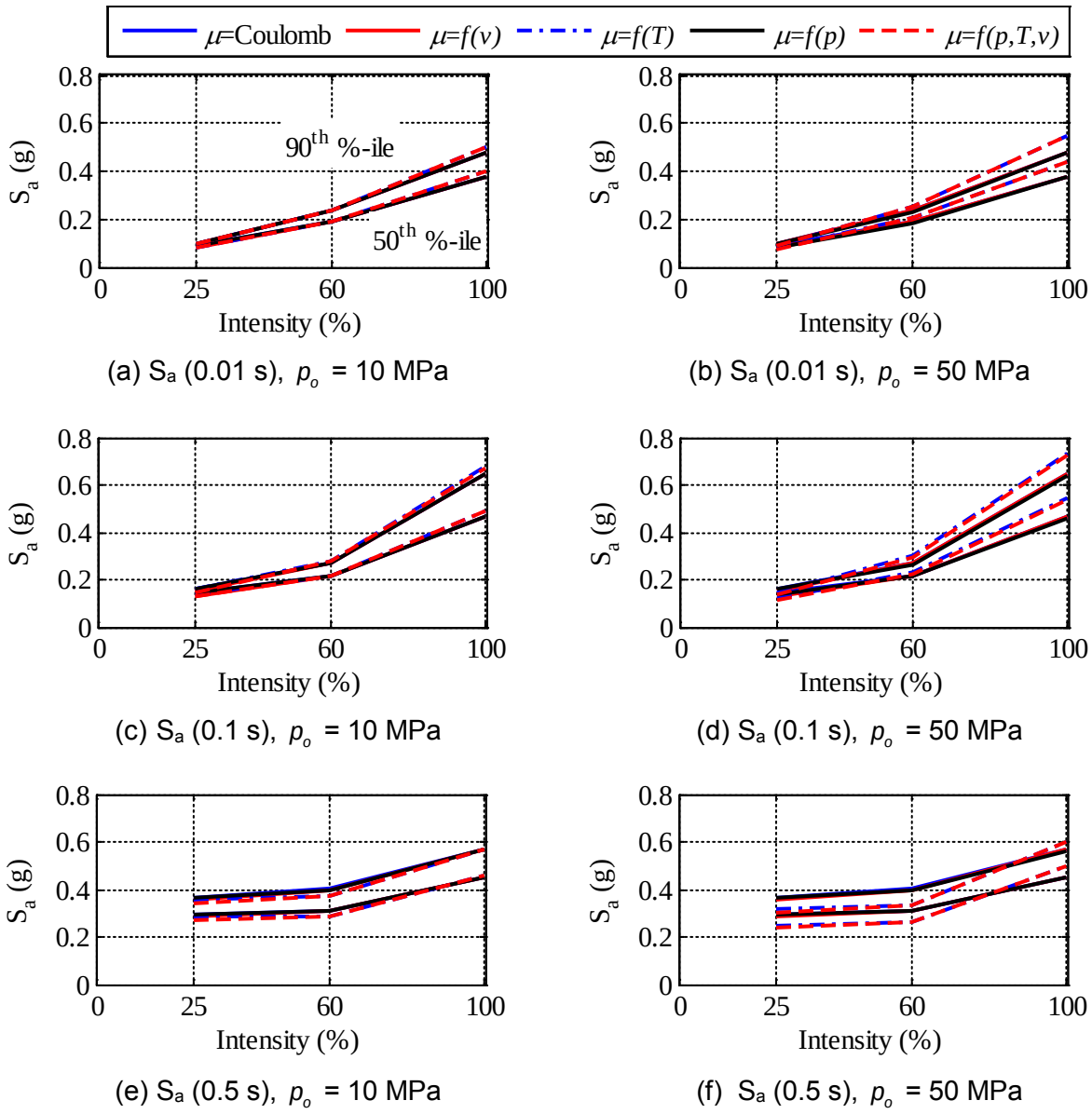

Figure 7-48 Five Percent Damped 50th and 90th Percentile Peak Floor Spectral Ordinates at Periods of 0.01 s, 0.1 s and 0.5 s, Corresponding to the Absolute Acceleration Response of the Slider in the Y Direction of an FP Bearing with a Sliding Period of 2 s, Reference Axial Pressures of 10 MPa and 50 MPa, and Reference Coefficient of Friction of 0.06, Subjected to the 30 Ground Motions Amplitude Scaled to Different Intensities

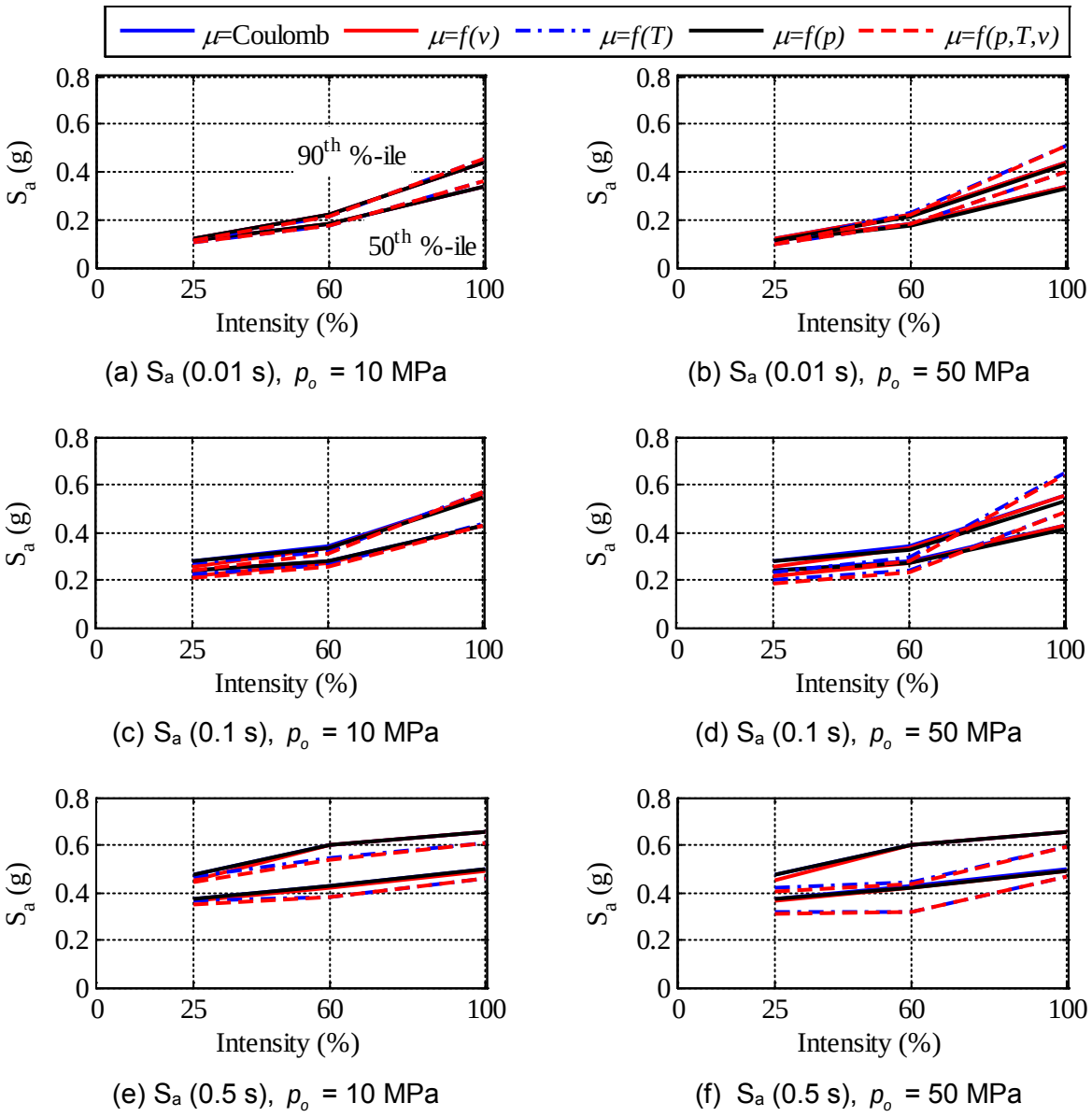

Figure 7-49 Five Percent Damped 50th and 90th Percentile Peak Floor Spectral Ordinates at Periods of 0.01 s, 0.1 s and 0.5 s, Corresponding to the Absolute Acceleration Response of the Slider in the X Direction of an FP Bearing with a Sliding Period of 2 s, Reference Axial Pressures of 10 MPa and 50 MPa, and Reference Coefficient of Friction of 0.09, Subjected to the 30 Ground Motions Amplitude Scaled to Different Intensities

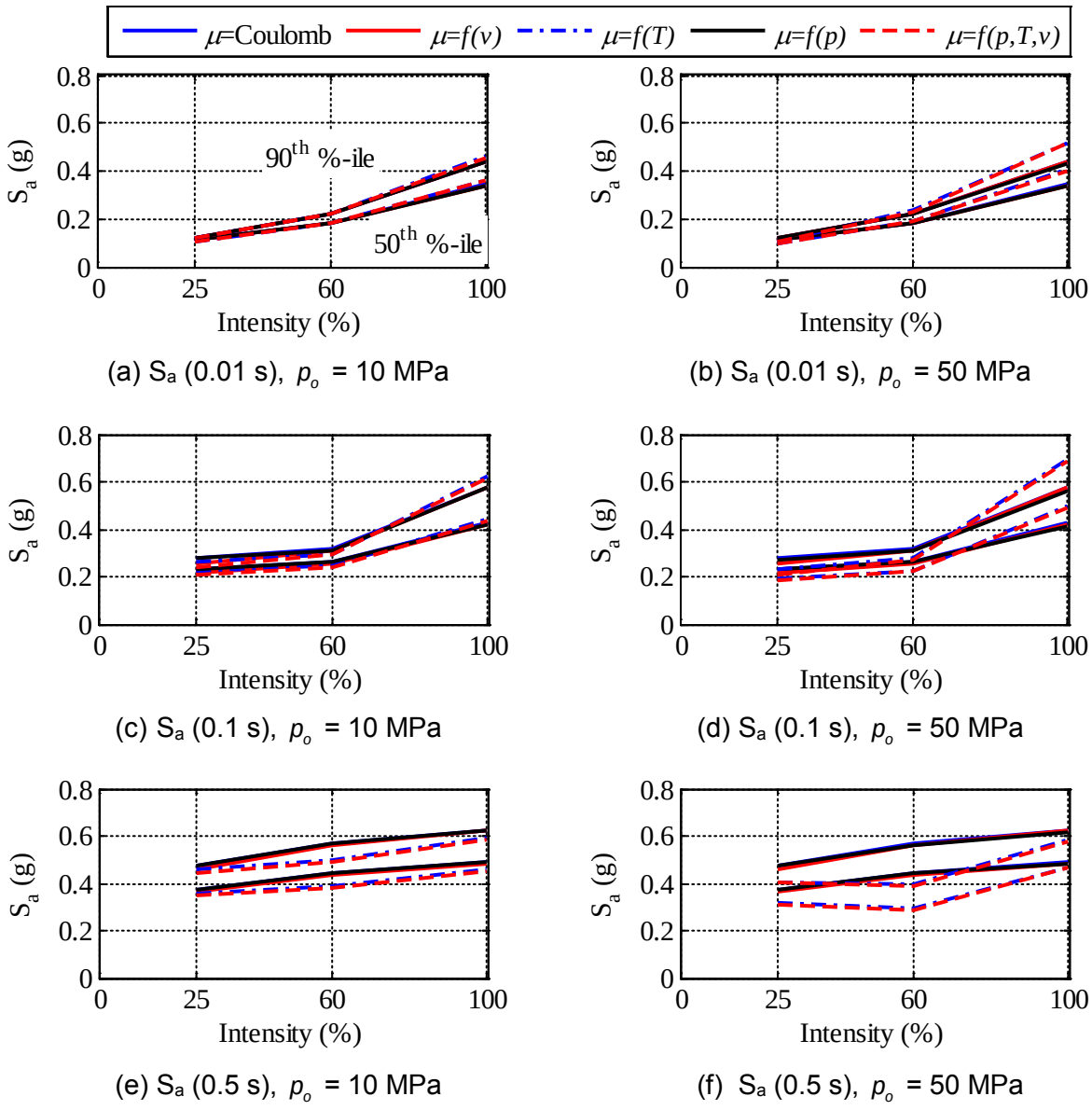

Figure 7-50 Five Percent Damped 50th and 90th Percentile Peak Floor Spectral Ordinates at Periods of 0.01 s, 0.1 s and 0.5 s, Corresponding to the Absolute Acceleration Response of the Slider in the Y Direction of an FP Bearing with a Sliding Period of 2 s, Reference Axial Pressures of 10 MPa and 50 MPa, and Reference Coefficient of Friction of 0.09, Subjected to the 30 Ground Motions Amplitude Scaled to Different Intensities

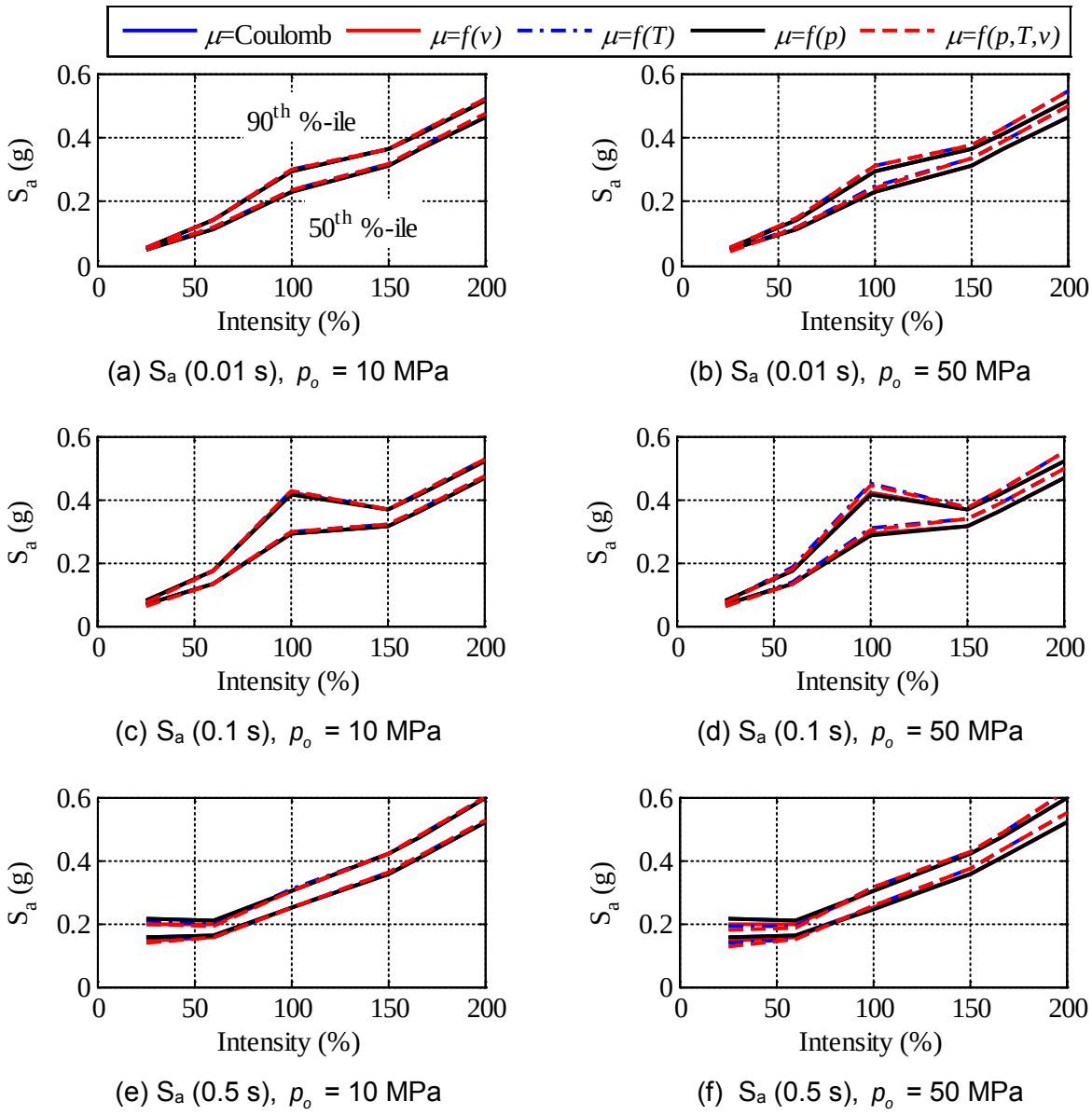

Figure 7-51 Five Percent Damped 50th and 90th Percentile Peak Floor Spectral Ordinates at Periods of 0.01 s, 0.1 s and 0.5 s, Corresponding to the Absolute Acceleration Response of the Slider in the X Direction of an FP Bearing with a Sliding Period of 3 s, Reference Axial Pressures of 10 MPa and 50 MPa, and Reference Coefficient of Friction of 0.03, Subjected to the 30 Ground Motions Amplitude Scaled to Different Intensities

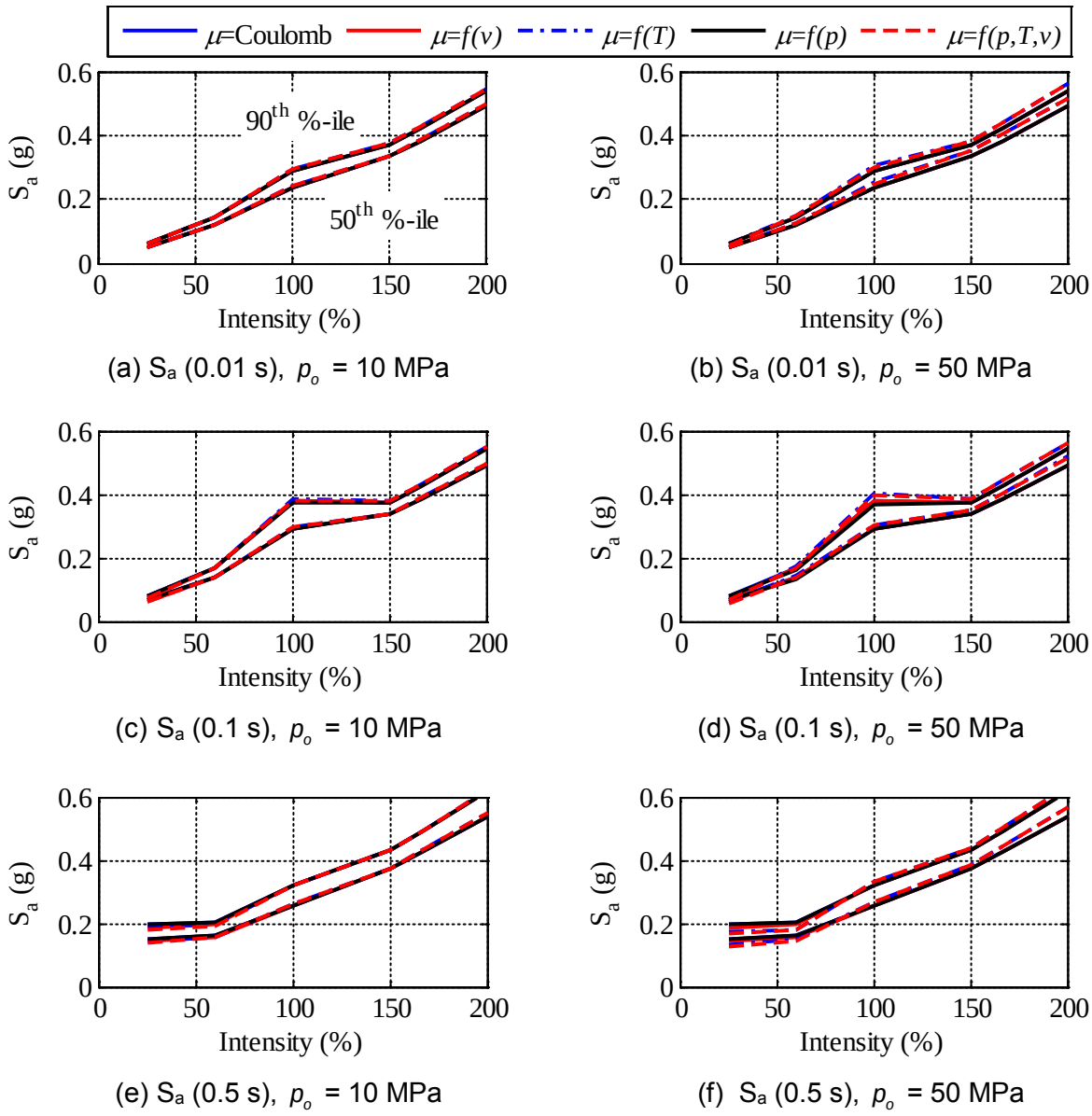

Figure 7-52 Five Percent Damped 50th and 90th Percentile Peak Floor Spectral Ordinates at Periods of 0.01 s, 0.1 s and 0.5 s, Corresponding to the Absolute Acceleration Response of the Slider in the Y Direction of an FP Bearing with a Sliding Period of 3 s, Reference Axial Pressures of 10 MPa and 50 MPa, and Reference Coefficient of Friction of 0.03, Subjected to the 30 Ground Motions Amplitude Scaled to Different Intensities

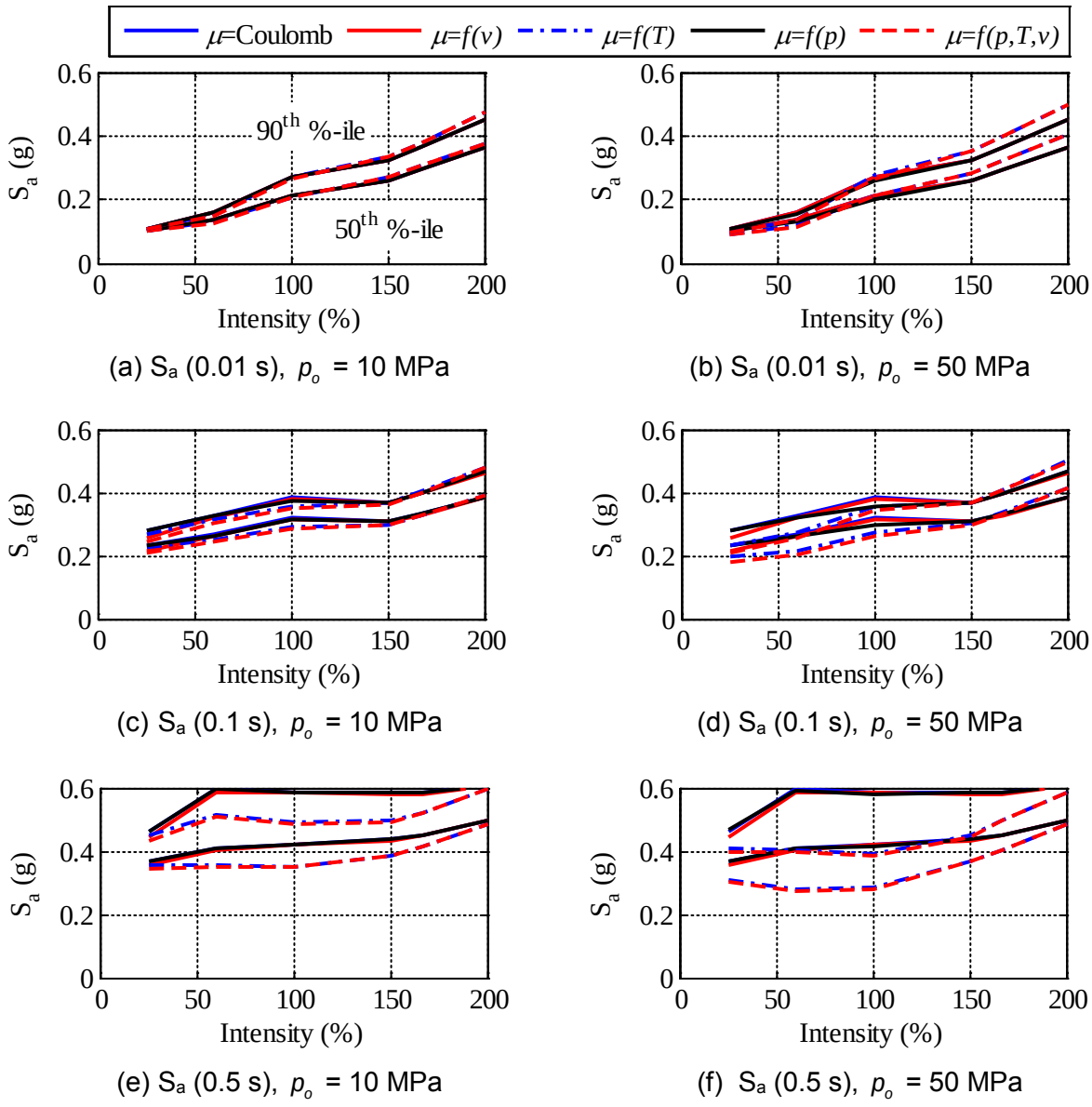

Figure 7-53 Five Percent Damped 50th and 90th Percentile Peak Floor Spectral Ordinates at Periods of 0.01 s, 0.1 s and 0.5 s, Corresponding to the Absolute Acceleration Response of the Slider in the X Direction of an FP Bearing with a Sliding Period of 3 s, Reference Axial Pressures of 10 MPa and 50 MPa, and Reference Coefficient of Friction of 0.09, Subjected to the 30 Ground Motions Amplitude Scaled to Different Intensities

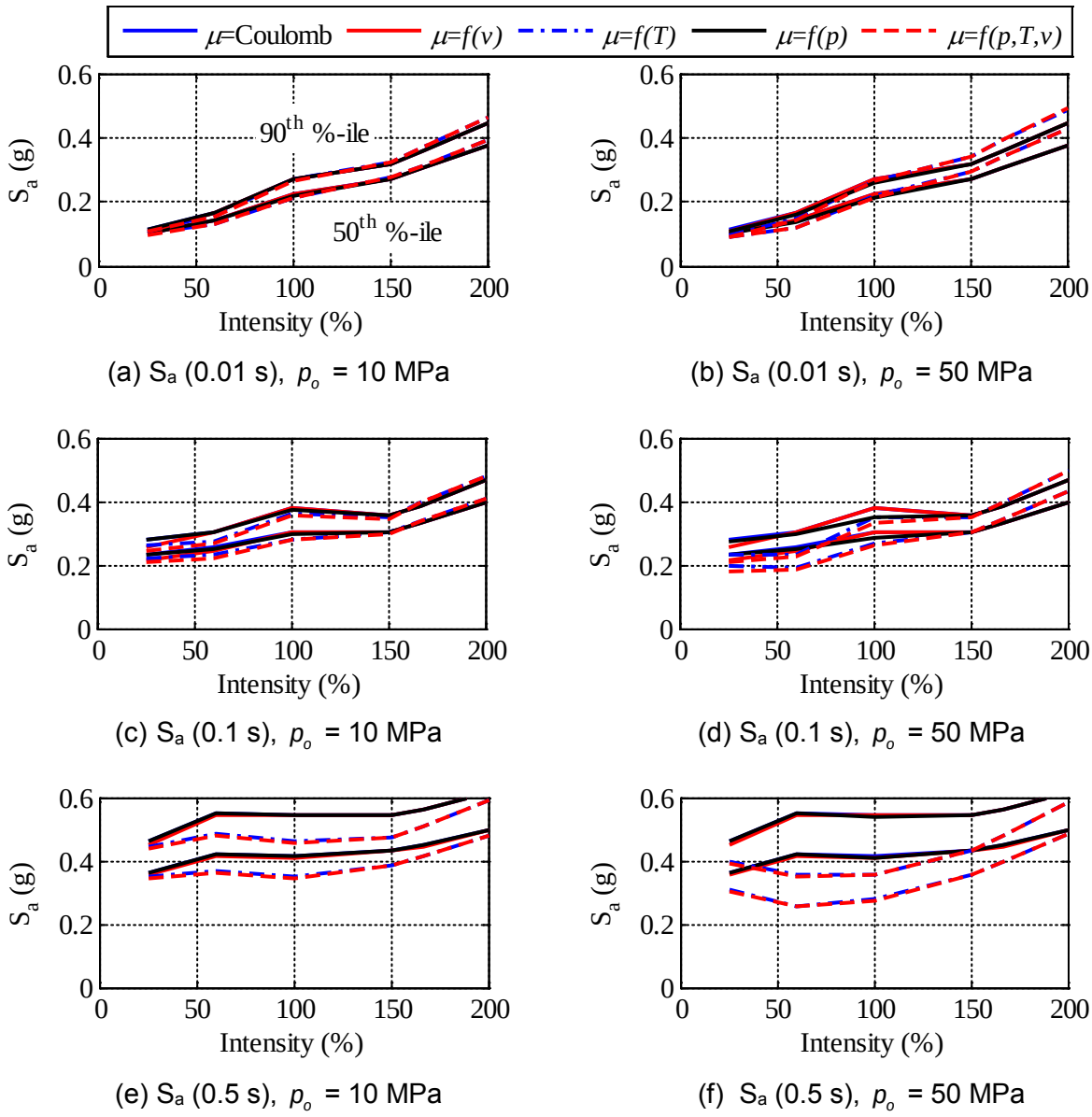

Figure 7-54 Five Percent Damped 50th and 90th Percentile Peak Floor Spectral Ordinates at Periods of 0.01 s, 0.1 s and 0.5 s, Corresponding to the Absolute Acceleration Response of the Slider in the Y Direction of an FP Bearing with a Sliding Period of 3 s, Reference Axial Pressures of 10 MPa and 50 MPa, and Reference Coefficient of Friction of 0.09, Subjected to the 30 Ground Motions Amplitude Scaled to Different Intensities

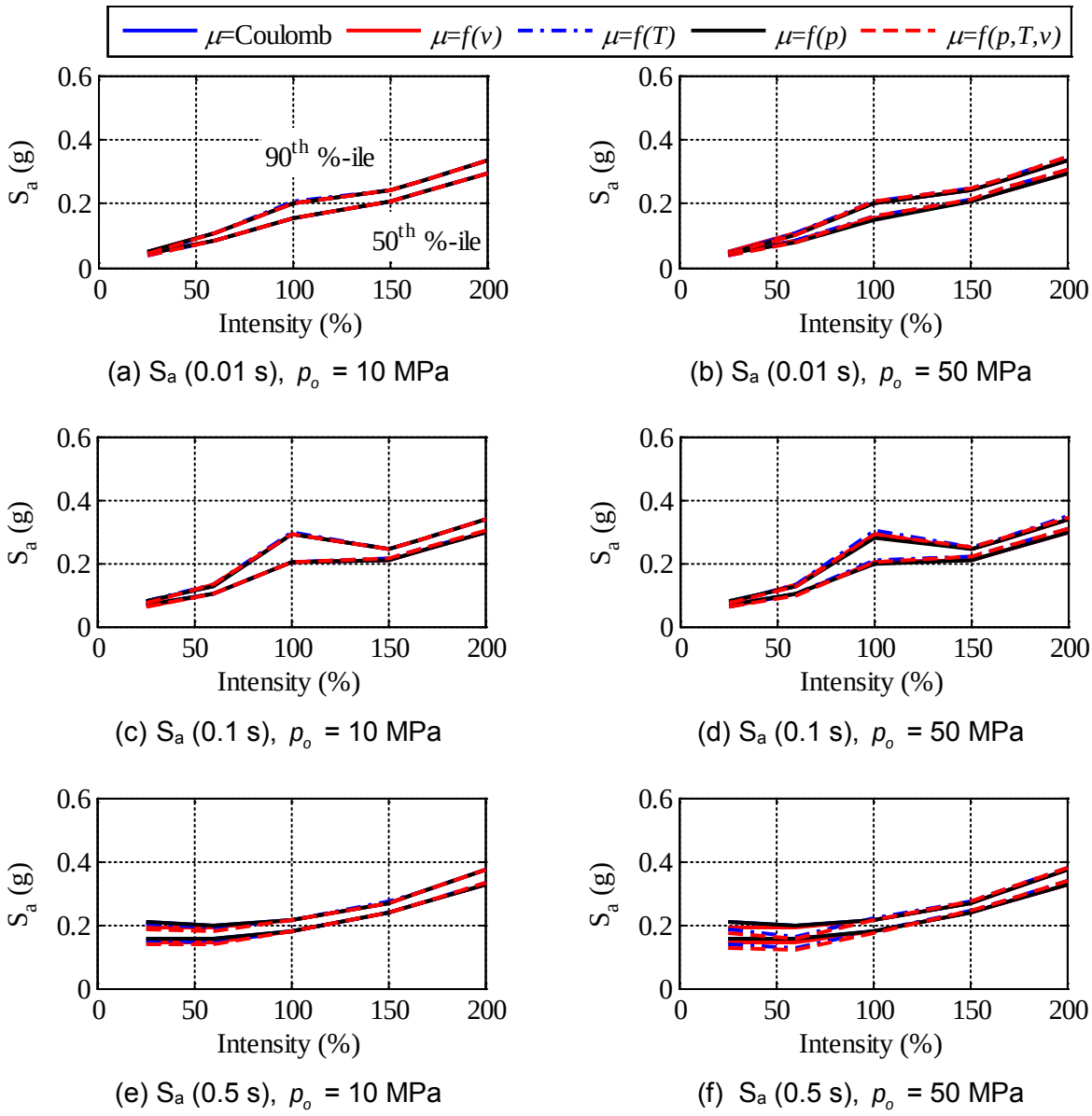

Figure 7-55 Five Percent Damped 50th and 90th Percentile Peak Floor Spectral Ordinates at Periods of 0.01 s, 0.1 s and 0.5 s, Corresponding to the Absolute Acceleration Response of the Slider in the X Direction of an FP Bearing with a Sliding Period of 4 s, Reference Axial Pressures of 10 MPa and 50 MPa, and Reference Coefficient of Friction of 0.03, Subjected to the 30 Ground Motions Amplitude Scaled to Different Intensities

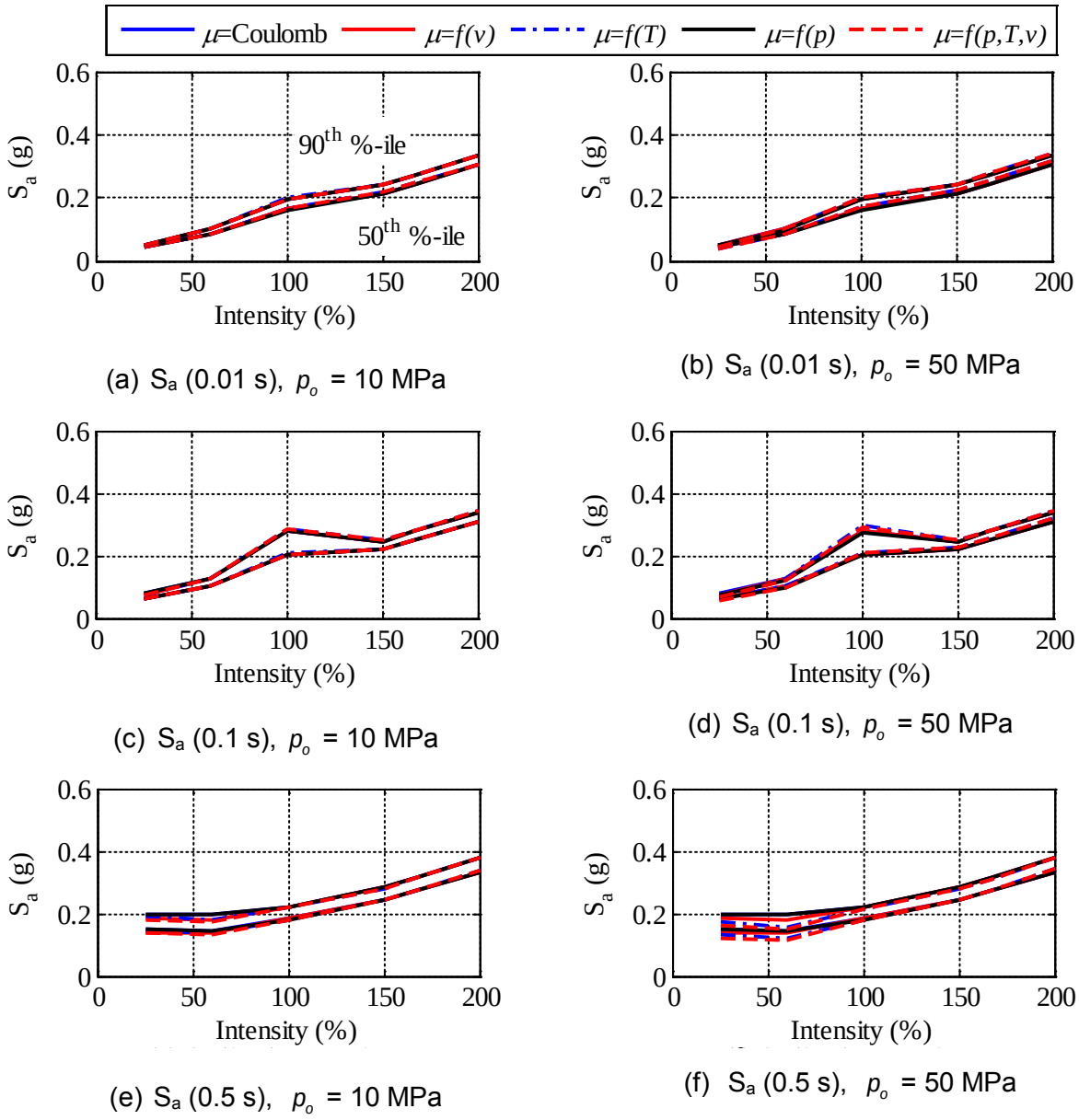

Figure 7-56 Five Percent Damped 50th and 90th Percentile Peak Floor Spectral Ordinates at Periods of 0.01 s, 0.1 s and 0.5 s, Corresponding to the Absolute Acceleration Response of the Slider in the Y Direction of an FP Bearing with a Sliding Period of 4 s, Reference Axial Pressures of 10 MPa and 50 MPa, and Reference Coefficient of Friction of 0.03, Subjected to the 30 Ground Motions Amplitude Scaled to Different Intensities

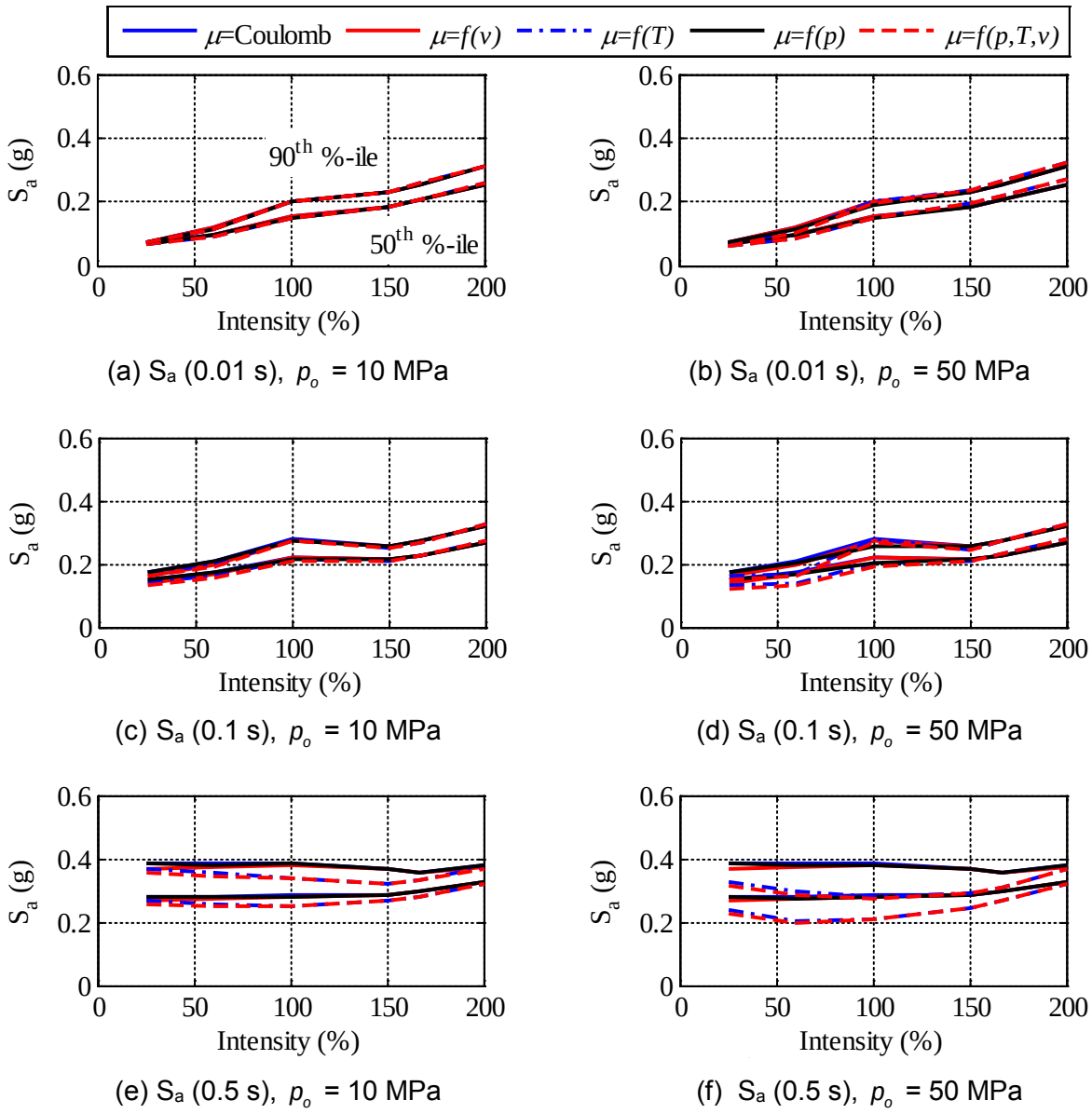

Figure 7-57 Five Percent Damped 50th and 90th Percentile Peak Floor Spectral Ordinates at Periods of 0.01 s, 0.1 s and 0.5 s, Corresponding to the Absolute Acceleration Response of the Slider in the X Direction of an FP Bearing with a Sliding Period of 4 s, Reference Axial Pressures of 10 MPa and 50 MPa, and Reference Coefficient of Friction of 0.06, Subjected to the 30 Ground Motions Amplitude Scaled to Different Intensities

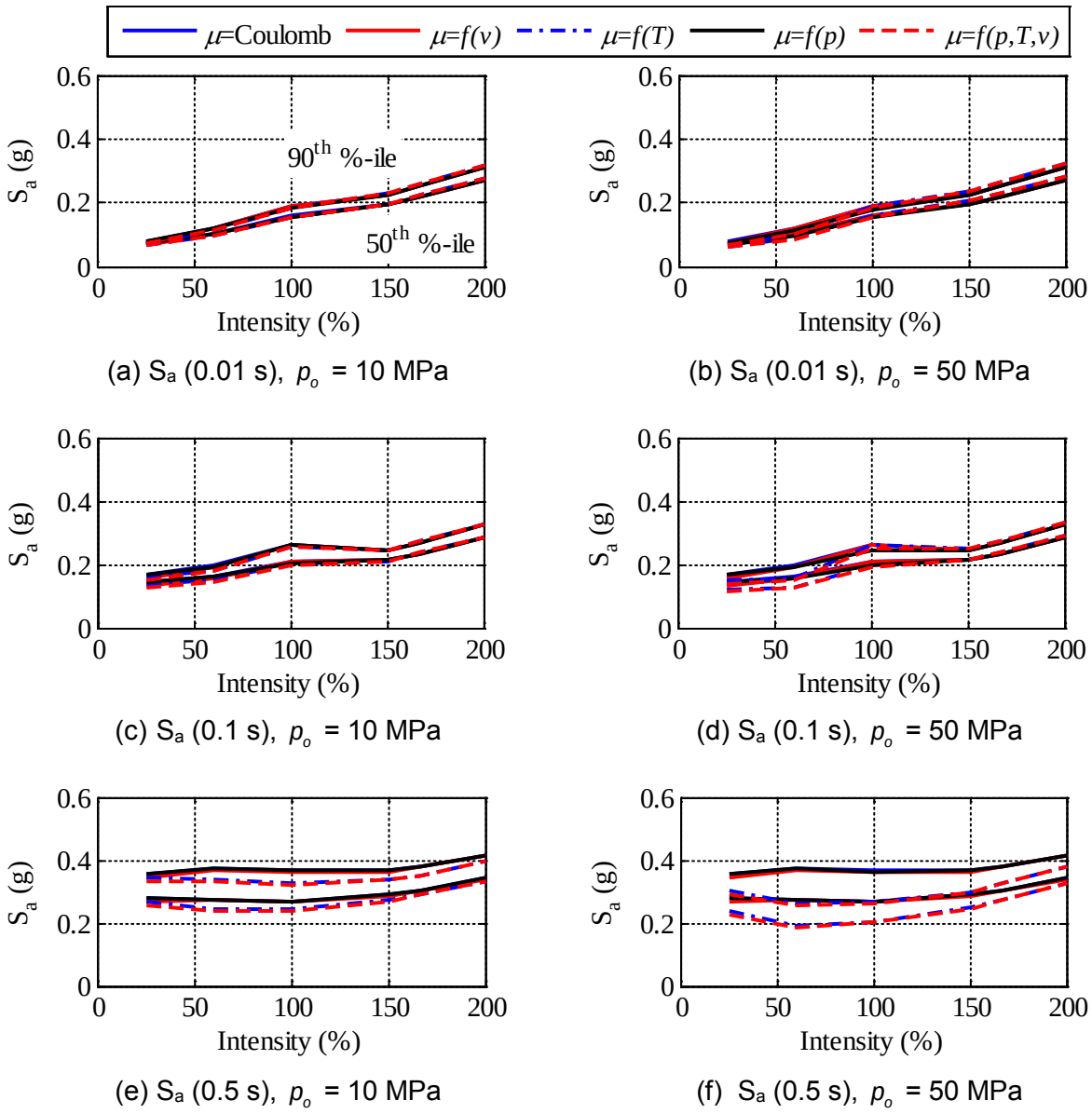

Figure 7-58 Five Percent Damped 50th and 90th Percentile Peak Floor Spectral Ordinates at Periods of 0.01 s, 0.1 s and 0.5 s, Corresponding to the Absolute Acceleration Response of the Slider in the Y Direction of an FP Bearing with a Sliding Period of 4 s, Reference Axial Pressures of 10 MPa and 50 MPa, and Reference Coefficient of Friction of 0.06, Subjected to the 30 Ground Motions Amplitude Scaled to Different Intensities

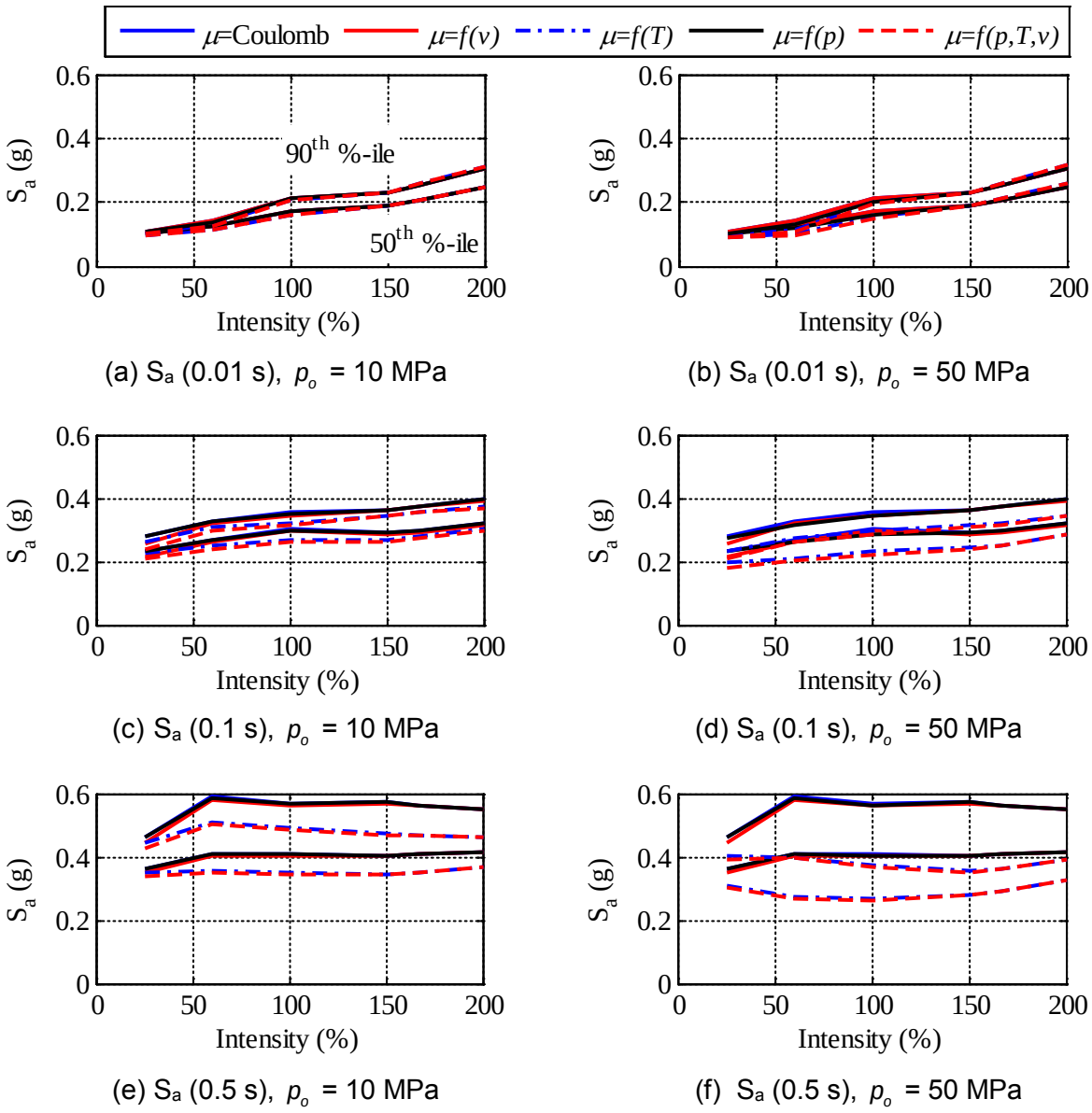

Figure 7-59 Five Percent Damped 50th and 90th Percentile Peak Floor Spectral Ordinates at Periods of 0.01 s, 0.1 s and 0.5 s, Corresponding to the Absolute Acceleration Response of the Slider in the X Direction of an FP Bearing with a Sliding Period of 4 s, Reference Axial Pressures of 10 MPa and 50 MPa, and Reference Coefficient of Friction of 0.09, Subjected to the 30 Ground Motions Amplitude Scaled to Different Intensities

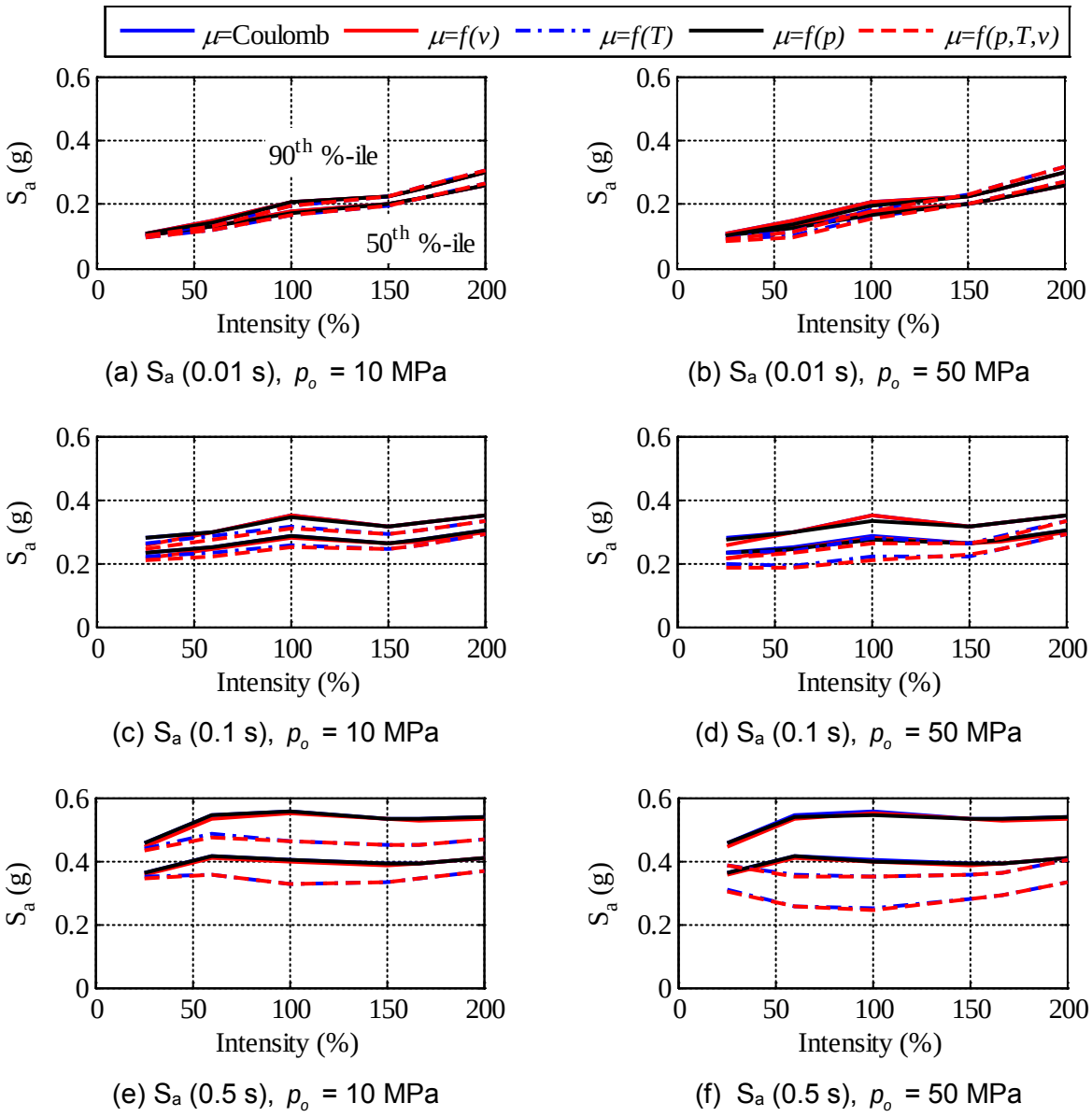

(a) S_a (0.01 s), p_o = 10 MPa

(b) S_a (0.01 s), p_o = 50 MPa

(c) S_a (0.1 s), p_o = 10 MPa

(d) S_a (0.1 s), p_o = 50 MPa

(e) S_a (0.5 s), p_o = 10 MPa

(f) S_a (0.5 s), p_o = 50 MPa

Figure 7-60 Five Percent Damped 50th and 90th Percentile Peak Floor Spectral Ordinates at Periods of 0.01 s, 0.1 s and 0.5 s, Corresponding to the Absolute Acceleration Response of the Slider in the Y Direction of an FP Bearing with a Sliding Period of 4 s, Reference Axial Pressures of 10 MPa and 50 MPa, and Reference Coefficient of Friction of 0.09, Subjected to the 30 Ground Motions Amplitude Scaled to Different Intensities

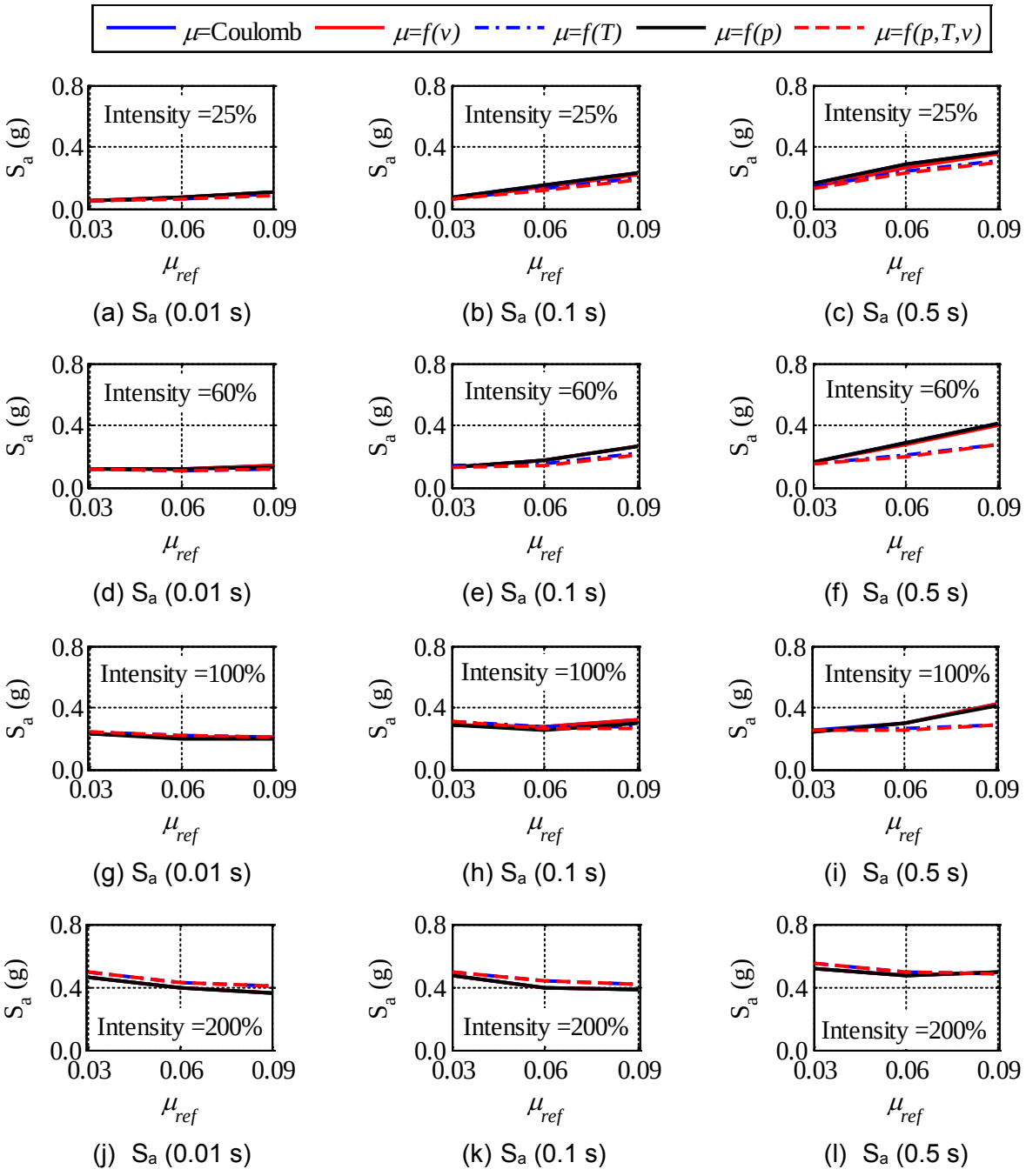

Figure 7-61 Five Percent Damped 50th Percentile Peak Floor Spectral Ordinates at Periods of 0.01 s, 0.1 s and 0.5 s, Corresponding to the Absolute Acceleration Response of the Slider in the X Direction of an FP Bearing with a Sliding Period of 3 s, Reference Axial Pressure of 50 MPa, and Reference Coefficients of Friction of 0.03, 0.06 and 0.09, Subjected to the 30 Ground Motions Amplitude Scaled to Different Intensities

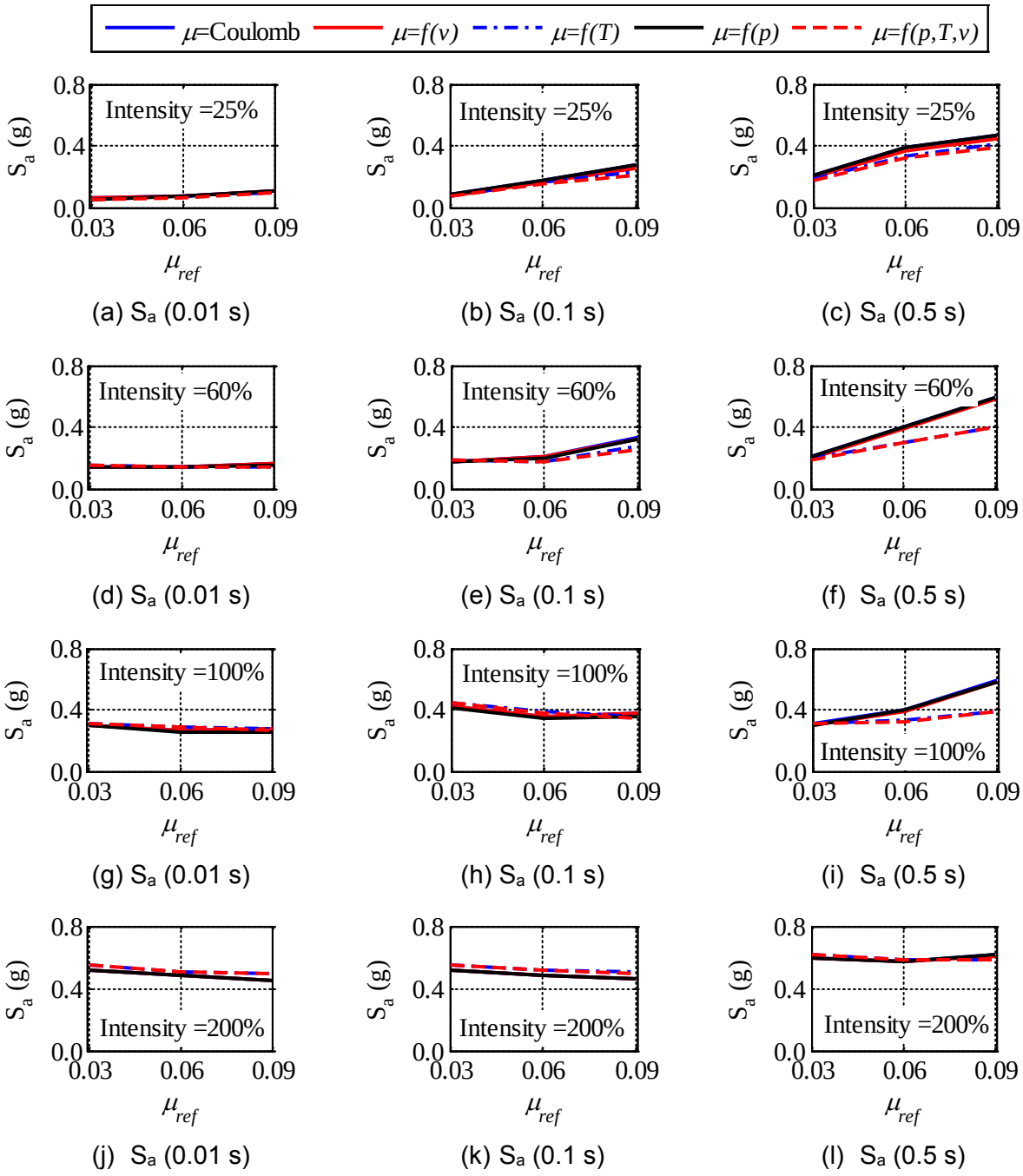

Figure 7-62 Five Percent Damped 90th Percentile Peak Floor Spectral Ordinates at Periods of 0.01 s, 0.1 s and 0.5 s, Corresponding to the Absolute Acceleration Response of the Slider in the X Direction of an FP Bearing with a Sliding Period of 3 s, Reference Axial Pressure of 50 MPa, and Reference Coefficients of Friction of 0.03, 0.06 and 0.09, Subjected to the 30 Ground Motions Amplitude Scaled to Different Intensities

8 RESPONSE OF A NUCLEAR POWER PLANT SEISMICALLY ISOLATED USING FRICTION PENDULUM™ BEARINGS

8.1 Introduction

This chapter presents results of response-history analyses performed using different models of a seismically isolated nuclear power plant (NPP). The results of the analysis are used to answer three practical questions: 1) How significantly does the choice of friction model affect horizontal displacement response?, 2) How significantly does the vertical component of ground motion affect the displacement response of an FP-isolation system, and 3) Can key response quantities be estimated with a macro model of the isolation system?

An NPP typically includes three major structures: auxiliary and shield building (ASB), containment steel structure (CIS) and steel containment vessel (SCV). The ASB considered herein is a 140,000-ton concrete structure with a footprint of 97 m $\times$ 60 m, and a total height of 89 m (Roche, 2013). The CIS weighs 41,000 tons with a total height of 33 m (Short *et al.*, 2007). The SCV weighs 3,700 tons and is ignored in this study due to its relatively small mass (see Short *et al.* (2007)).

The first model of the nuclear island is the ASB and CIS supported on a common isolation system comprising single Friction Pendulum™ (FP) bearings. The second model of the nuclear island involves a macro (single) FP isolator, similar to that used in Chapter 7. Friction at the sliding surface is described using all five models listed in Table 7-2. Two response quantities are studied: 1) isolation-system displacement, and 2) floor spectral ordinates at different locations in the CIS. The two nuclear island models are subjected to the ground motions consistent with seismic hazard at the two sites considered in Chapter 7: Diablo Canyon and Vogtle. Model 1 is subjected to the two horizontal and/or vertical components of ground motions. Model 2 is subjected only to the two horizontal components of ground motions.

The geometric properties of the ASB and the CIS considered in this study are presented in Section 8.2. The ASB and CIS models are described in Section 8.3. Two models of the seismically isolated nuclear island are presented in Section 8.4 and these are subjected to the ground motions of Section 8.5. Results of response-history analyses performed using the models of Section 8.4 subjected to ground motions of Section 8.5 are presented in Section 8.6.

8.2 Geometric Properties of the Nuclear Power Plant

This section presents the geometric properties of the ASB and CIS.

8.2.1 Auxiliary and Shield Building (ASB)

Figures 8-1 and 8-2 present plan and elevation views of the ASB, respectively. The dimensions of the ASB were provided by Roche (2013). The ASB is 97 m $\times$ 60 m in plan and its height is 89 m measured from the bottom of the basemat. The interior walls, floors and roof are 0.6 m (2 ft) thick. The exterior walls and the walls along the horizontal axes of symmetry are 0.9 m (3 ft) thick. The ASB is constructed of reinforced concrete with a density of 2400 kg/m^3, a characteristic concrete strength of 41 MPa and an elastic modulus of 30 GPa. The total mass of the ASB is 140,000 ton, with the 49,000 ton in the basemat, which is shown stippled in Figure 8-2.

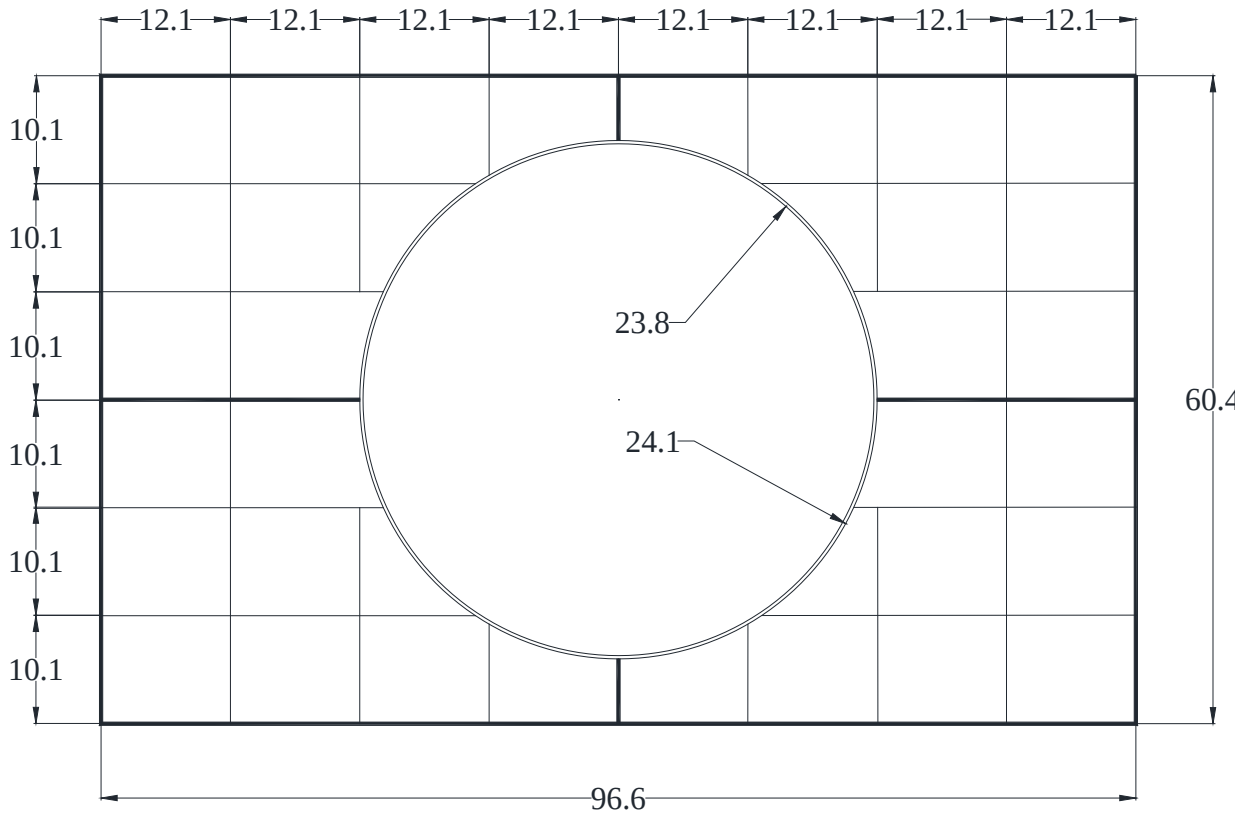

(a) Dimensions are in meters.
(b) Exterior walls and the walls along the two horizontal axes of symmetry are 0.9 m (3 ft) thick.
(c) Other walls are 0.6 m (2 ft) thick.
(d) The circle of radius 24.1 m (80 ft) indicates the 1.2 m (4 ft) thick cylindrical wall.
(e) The circle of radius 23.8 m (79 ft) indicates the 0.9 m (3 ft) thick hemispherical dome.

Figure 8-1 Plan View of Auxiliary and Shield Building (adapted from Roche (2013))

8.2.2 Containment Internal Structure (CIS)

The CIS considered herein comprises a vertical stick with masses lumped at different heights and at three outrigger nodes. Figure 8-3 is a schematic of the 33 m-tall CIS. The circles indicate the locations of concentrated masses. The total mass of CIS[41] is 41,000 ton. The CIS model used in this study is from Short *et al.* (2007).

8.3 Modeling ASB and CIS for Response-History Analysis

8.3.1 Introduction

This section summarizes the approach used to model the ASB for response-history analysis using OpenSees (PEER, 2014). The distribution of the mass to the walls, floors, roof, cylindrical wall and hemispherical dome, and of the lateral stiffness contributed by the walls, cylinder and dome is discussed. The mass associated with the nodes and the stiffness of the elements used in the OpenSees model are listed. The dynamic properties (e.g., natural period and

[41] The total mass of SCV considered by Short et al. (2007) is 3,700 ton, which is small compared to the masses of ASB (140,000 ton) and CIS (41,000 ton) considered in this study.

corresponding mode shape) of the ASB modeled in OpenSees are computed and compared with those obtained for the ASB modeled in LS-DYNA (LSTC, 2011), where the LS-DYNA model for the ASB was provided by Roche (2013).

The containment internal structure is modeled in OpenSees using the mass and stiffness data presented in Short *et al.* (2007).

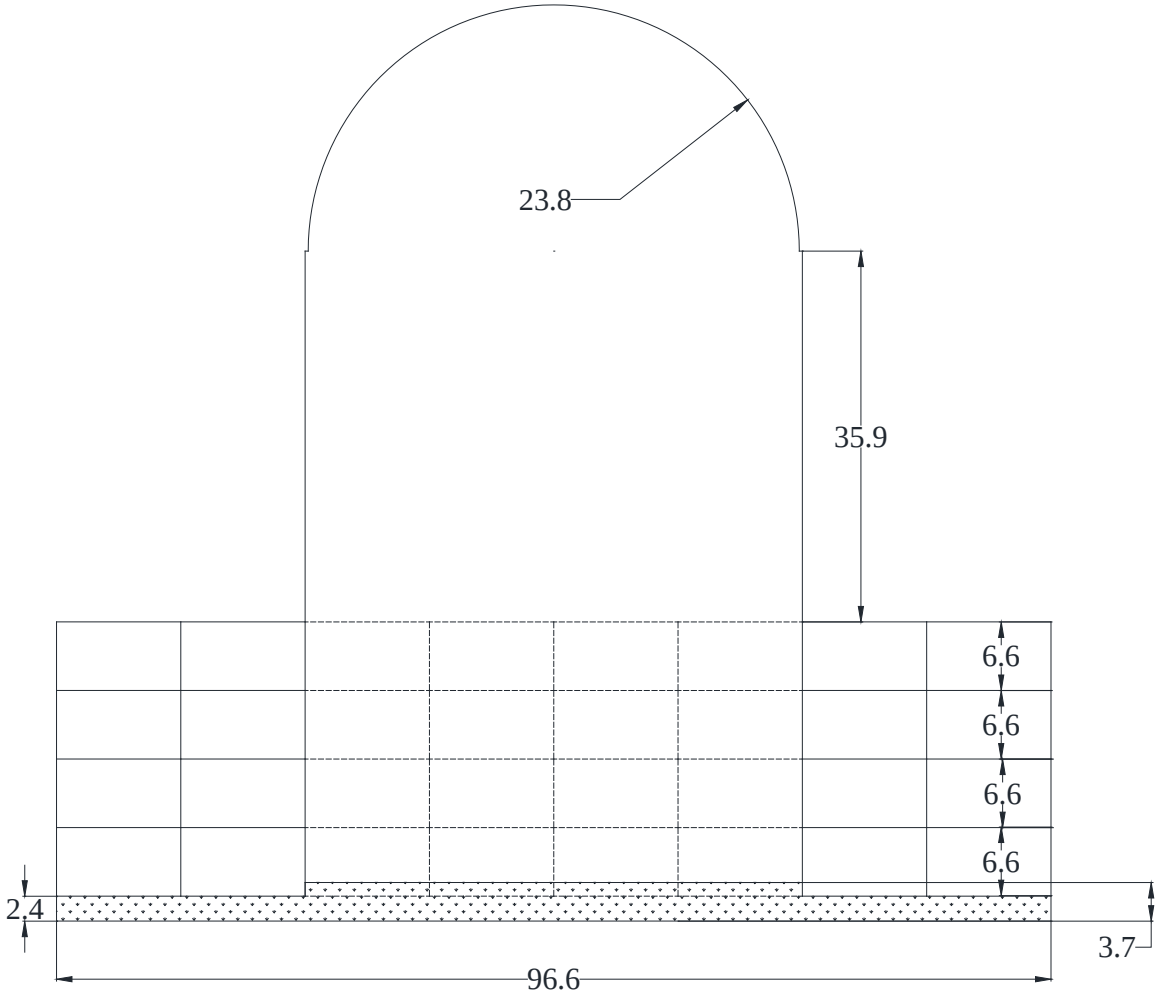

(a) Dimensions are in meters.
(b) Floors and roof are 0.6 m (2ft.) thick
(c) Thickness of cylindrical wall is 1.2m (4ft.)
(d) Thickness of hemispherical dome is 0.9 m (3ft.)

Figure 8-2 Elevation View of the Auxiliary and Shield Building (adapted from Roche (2013))

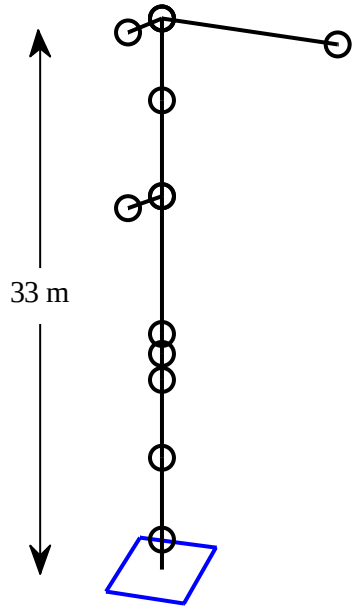

Figure 8-3 Containment Internal Structure (adapted from Short et al. (2007))

8.3.2 Auxiliary and Shield Building (ASB)

8.3.2.1 LS-DYNA Model

The nuclear power plant structure with plan and elevation views shown in Figures 8-1 and 8-2 was modeled in LS-DYNA LSTC, (2011) by Roche (2013). Figure 8-4 shows the model of the ASB. The concrete characteristic strength was 41.3 MPa and its elastic modulus was 30.4 GPa.

The natural periods for the first two modes of vibration of the ASB modeled using LS-DYNA are listed in Table 8-1. The first two mode shapes are shown in Figure 8-5.

8.3.2.2 OpenSees Model

8.3.2.2.1 Modeling of Mass

The auxiliary and shield building is divided into three segments to facilitate modeling in OpenSees. The three segments are shown in Figure 8-6. Segment 2 is the central portion of the ASB comprising the cylindrical wall and its dome, with plan dimensions of 48 m $\times$ 60 m. Segments 1 and 3 are symmetrically placed with respect to Segment 2; each has plan dimensions of 24 m $\times$ 60 m.

Segment 1 of the ASB comprises a 2.4 m-thick basemat and four floors (including the roof), each 0.6 m-thick. The total length of 0.9 m-thick external walls, 0.9 m-thick internal walls and 0.6 m-thick internal walls is 109 m, 24 m and 198 m, respectively. The story height is 6.6 m. Five elevations are considered in the segment, namely, 1.2 m, 9.1 m, 15.8 m, 22.6 m and 29.3 m, which represent the locations of the basemat and the floors. Masses are lumped at the floors and the basemat. The mass of each wall is split between the floors above and below. The mass at each level is listed in Table 8-2.

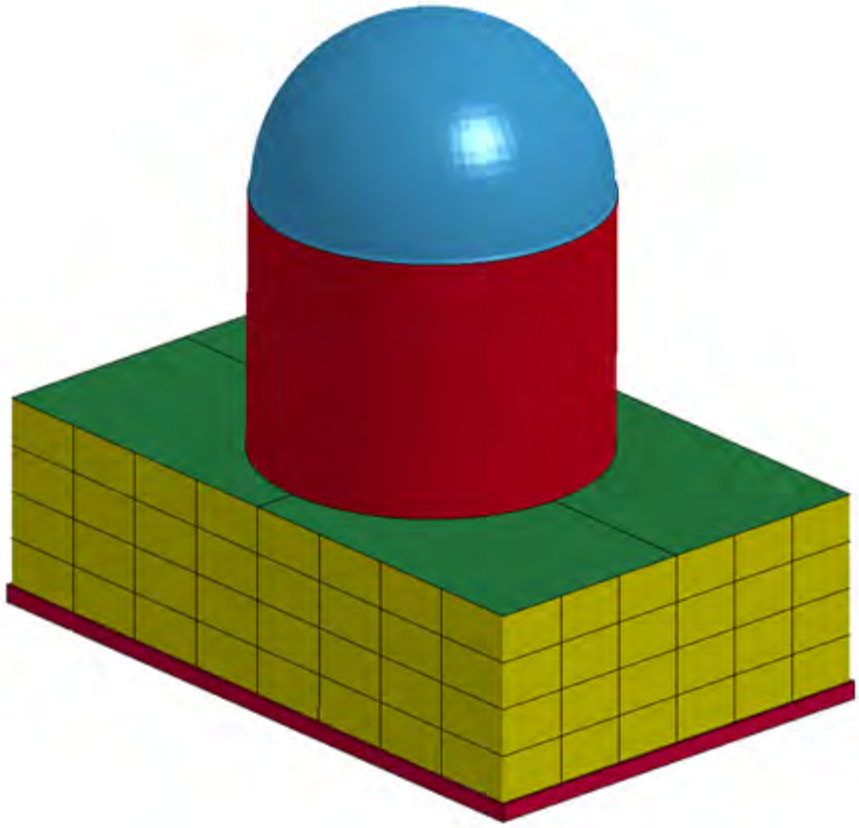

Figure 8-4 LS-DYNA Model of the ASB (adapted from Roche (2013))

Table 8-1 Natural Periods of the ASB

Mode	LS-DYNA	OpenSees
1	0.23 s	0.15 s
2	0.22 s	0.15 s

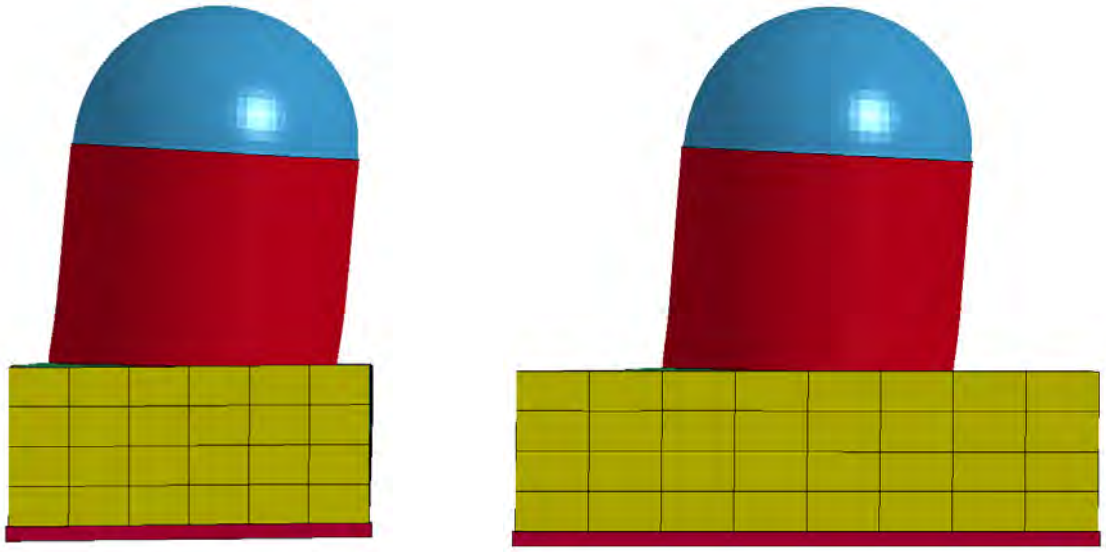

(a) First mode (b) Second mode

Figure 8-5 Mode Shapes of the ASB

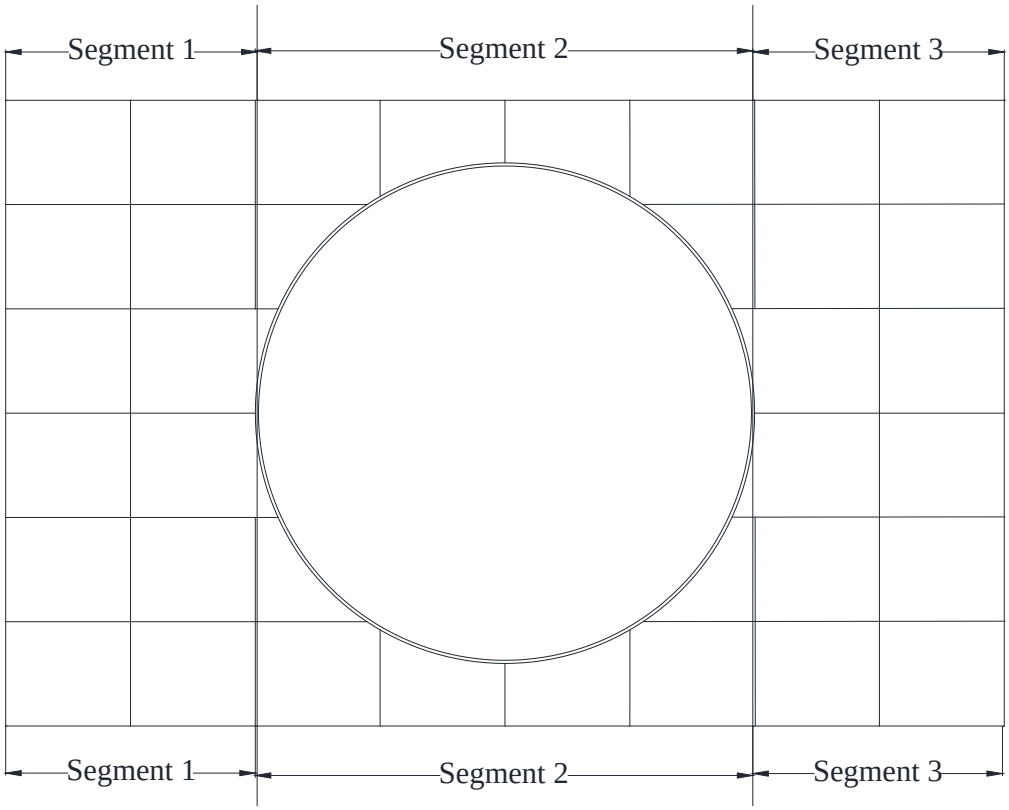

Figure 8-6 Segments of Auxiliary and Shield Building (ASB)

Segment 2 of the ASB comprises 1) a 1.2 m-thick cylindrical wall with a radius and a height of 24 m and 62 m, respectively, 2) a 0.9 m-thick hemisphere with a radius of 24 m, 3) 0.9 m-thick

exterior walls with a total length 97 m, 4) 0.9 m-thick interior walls with a total length of 12 m, 5) 0.6 m-thick interior walls with a total length of 89 m, 6) a 2.4 m-thick basemat with plan dimensions of 48 m $\times$ 60 m, 7) a 1.3 m-thick circular basemat on top of the rectangular basemat with a radius of 24 m, and 8) 0.6 m-thick floors at four levels (same as Segments 1 and 3) with a plan area of 1,100 m^2. In addition to the five elevations considered for Segments 1 and 3, four elevations, at heights of 41.5 m, 53.6 m, 65.8 m and 71.3 m measured from the bottom of the basemat, are considered for Segment 2. Mass is assigned to levels per the method adopted for Segments 1 and 3. The mass at the nine elevations of Segment 2 are listed in Table 8-2.

Table 8-2 Distribution of Mass in the ASB

Level	Height from bottom of basemat (m)	Mass (tonnes)		
		Segment 1	Segment 2	Segment 3
1	1.2	11,000	27,000	11,000
2	9.1	5,800	6,700	5,800
3	15.8	5,800	7,000	5,800
4	22.6	5,800	7,000	5,800
5	29.3	4,000	6,600	4,000
6	41.5	-	5,300	-
7	53.6	-	5,300	-
8	65.8	-	3,800	-
9	71.3	-	6,700	-
	Total	32,000	75,000	32,000

The mass associated with an elevation in a segment is then distributed across nodes that are equispaced in plan. For this study, the spacing between nodes is 6 m for all three segments of the ASB. Consequently, there are 187 nodes at each of the five elevations lower than 30 m, and 99 nodes at each of the four higher elevations: a total of 1331 nodes ($5 \times 187 + 4 \times 99$) for the ASB. Figure 8-7 presents the locations of the nodes in plan. Figure 8-8 presents the location of nodes in elevation.

A small value of mass moment of inertia is assigned about the three axes to all 1,331 nodes in the OpenSees model of the ASB to avoid numerical instability. The locations of nodes, and the masses and mass moments of inertia associated with the nodes are listed in Appendix I of Kumar et al. (2015b).

8.3.2.2.2 Modeling of Stiffness

The lateral stiffness of the ASB is modeled using discrete beam-column elements to speed the calculations. The ASB is assumed to be rigid in the vertical direction because its *true* dynamic response would not significantly affect the horizontal displacement response of the isolation systems and the assumption speeds calculations.

The lateral stiffness of the ASB is summarized in Table 8-3 by segment and story. The stiffness for each story-segment pair is distributed equally between the columns in that pair. The number of columns in a story-segment pair is equal to the number of nodes at a floor level in the segment (e.g., 44 vertical columns in the first segment of ASB between any two adjacent floors).

8.3.2.2.3 Implementation

A total of 1331 nodes are used to discretize the ASB. Rigid horizontal beams along the two principal horizontal directions connect the nodes. These beams are modeled using *elasticBeamColumn* element in OpenSees PEER, (2014). The connectivity of the horizontal beams is listed in Appendix I of Kumar et al. (2015b).

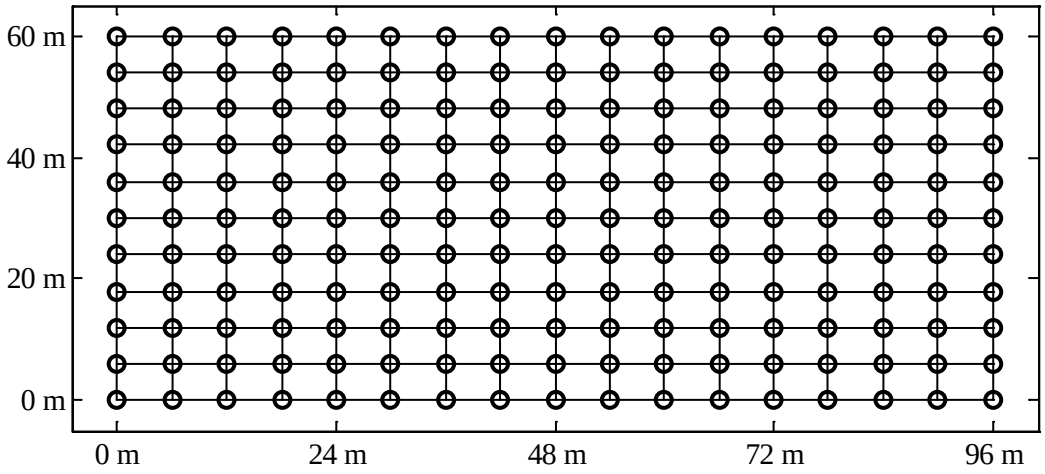

(a) Levels 1 through 5

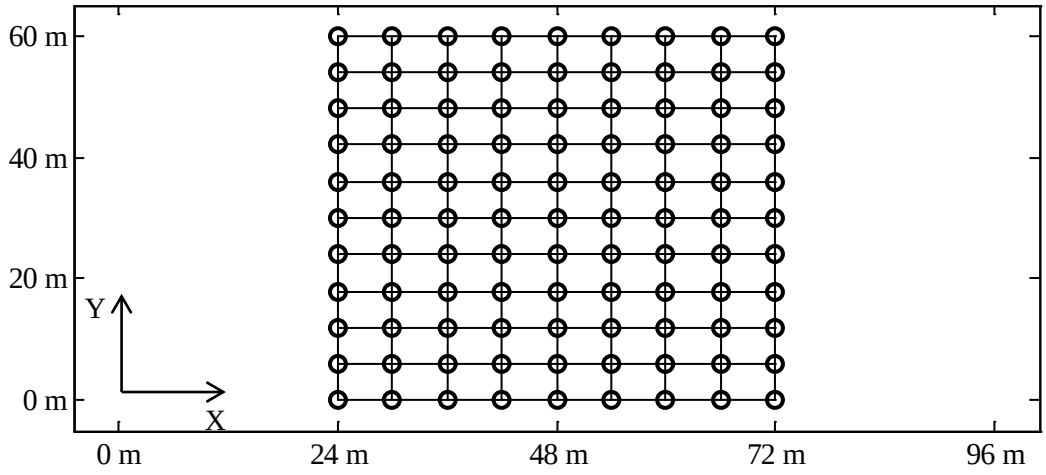

(b) Levels 6 through 9

Figure 8-7 Locations of Nodes (indicated by circles) in the ASB in Plan

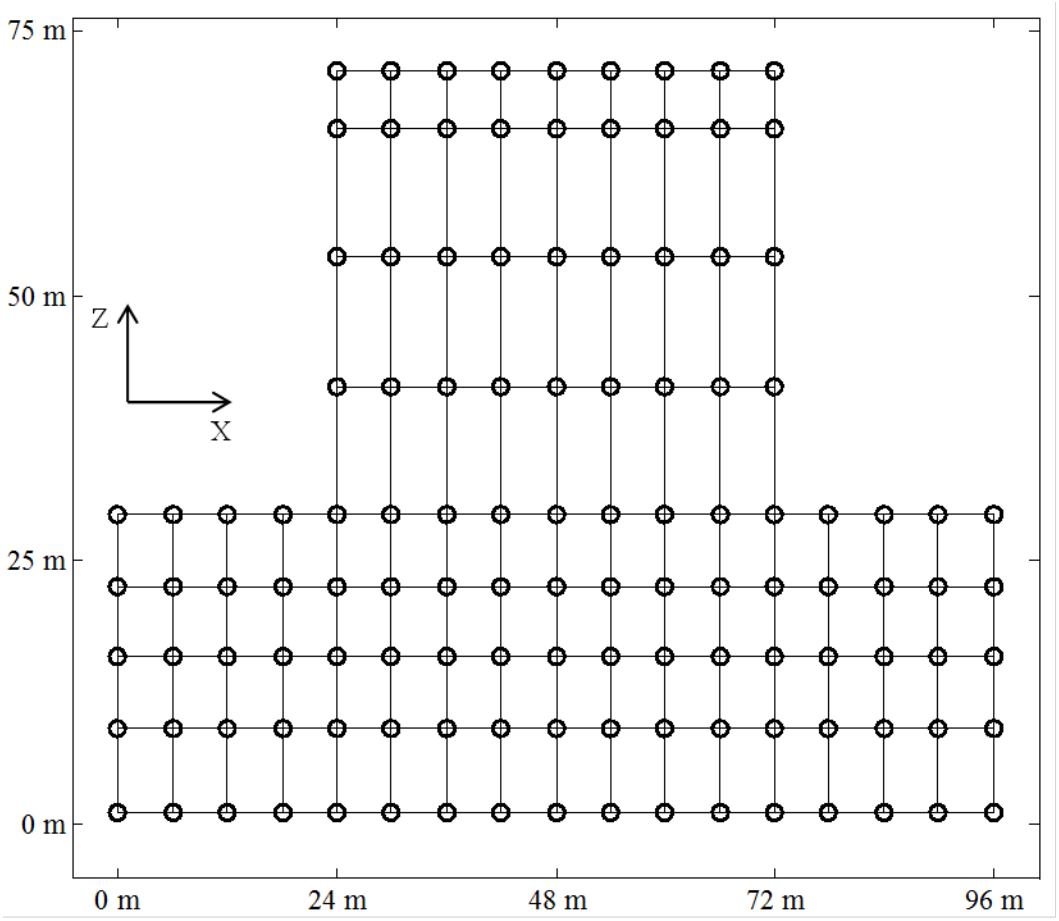

Figure 8-8 Locations of Nodes (indicated by circles) in the ASB in Elevation

Table 8-3 Segment and Story Distribution of Total Stiffness of the Auxiliary and Shield Building in the Two Orthogonal Horizontal Directions (X and Y)

Story	Elevation level (m)		Stiffness ($\times 10^{11}$ N/m)					
	Start	End	Segment 1		Segment 2		Segment 3	
			X	Y	X	Y	X	Y
1	1.2	9.1	2.4	1.8	6.3	5.5	2.4	1.8
2	9.1	15.8	2.4	1.8	5.5	4.7	2.4	1.8
3	15.8	22.6	2.4	1.8	5.5	4.7	2.4	1.8
4	22.6	29.3	2.4	1.8	5.5	4.7	2.4	1.8
5	29.3	41.5	-	-	1.0	1.0	-	-
6	41.5	53.6	-	-	1.0	1.0	-	-
7	53.6	65.8	-	-	1.0	1.0	-	-
8	65.8	71.3	-	-	2.2	2.2	-	-

The columns are modeled using the *elasticBeamColumn* element. The key user-defined input parameters for this element are: cross-sectional area, elastic modulus, shear modulus, and area moment of inertia about three orthogonal axes. The axial rigidity is achieved using a large cross-sectional area, which results in high shear stiffness. The lateral stiffness of each column

is defined in terms of flexural stiffness. The area moments of inertia in the two orthogonal horizontal directions are selected so that its total lateral stiffness is equal to its flexural stiffness. The node connectivity of the columns and their area moments of inertia about the two horizontal axes are listed in Appendix I of Kumar et al. (2015b).

8.3.2.2.4 Dynamic Properties

Table 8-1 lists the first two natural periods of the LS-DYNA and OpenSees models. The OpenSees mode shapes are plotted in Figure 8-9. The first translational mode is in the short direction (60 m, see Figure 8-1) of the ASB; the second translational mode is in the long direction. The natural periods compare sufficiently well for the purpose of the study, namely, to answer the three questions posed in Section 8.1. The OpenSees and LS-DYNA mode shapes are similar.

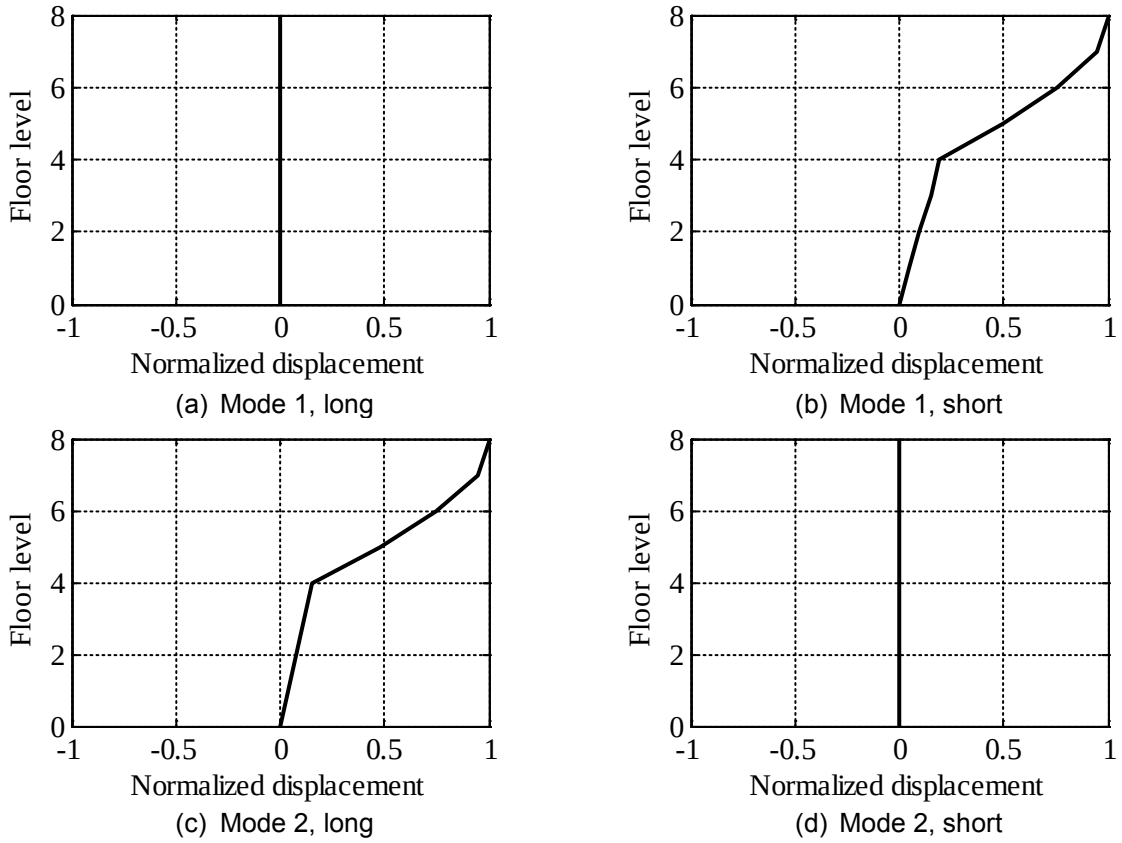

Figure 8-9 Mode Shapes Corresponding to the First Two Natural Periods of Vibration of the ASB

8.3.3 Containment Internal Structure (CIS)

The containment internal structure (CIS) is modeled in OpenSees as a vertical stick with three outrigger nodes (see Figure 8-3). This fixed-base CIS model is identical to that of Short *et al.* (2007). The coordinates of the nodes of the CIS model are listed in Table 8-4 and the masses lumped at the nodes are listed in Table 8-5. The directions X, Y and Z are shown in Figures 8-7 and 8-8. Node 109060 is at the center of the basemat in plan (see Figure 8-7 of this chapter and Appendix I of Kumar et al. (2015b)). Because the inertial effects of the vertical mass of the

CIS accumulate at this node, the vertical inertial forces are unrealistically high. The CIS model responds dynamically in the vertical and horizontal directions, but only the horizontal dynamic response is studied in this chapter.

Table 8-4 Location of Nodes in the CIS

Node	Coordinates (m)		
	X	Y	Z
109060	48.00	30.00	1.22
500	48.00	30.00	3.05
531	48.00	30.00	7.93
532	48.00	30.00	12.65
533	48.00	30.00	14.17
534	48.00	30.00	15.45
535	48.00	30.00	23.70
5351	44.95	26.95	23.70
536	48.00	30.00	29.41
537	48.00	30.00	29.41
538	48.00	30.00	34.29
5381	70.86	30.00	34.29
5382	44.95	26.95	34.29

The columns in the CIS are modeled using the *forceBeamColumn* element. The sections associated with the *forceBeamColumn* elements are *Elastic* and the properties of the section are listed in Table 8-6. The horizontal outriggers are modeled using the *rigidLink* element; the two nodes at the ends of the element are constrained to translate and rotate identically.

Table 8-5 Mass Associated with the Nodes in the CIS

Node	Mass in direction (in 100,000 kg)			Mass moment of inertia about axis (in 100,000 kg-m^2)		
	X	Y	Z	X	Y	Z
500	87	87	87	7701	7701	15402
531	135	135	135	19279	1859	21138
532	68	68	68	960	9219	10179
533	21	21	21	2508	2400	4908
534	47	47	47	4866	4327	9193
535	0	0	0	3825	3465	7290
5351	44	44	44	0	0	0
536	2	2	2	27	34	61
537	4	4	4	82	59	141
538	0	0	0	10	9	20
5381	0	0	0	0	0	0
5382	1	1	1	0	0	0

Table 8-6 Properties of Elements Connecting Nodes in the CIS

Element	Connecting nodes		Properties of elastic section					
	Start	End	Cross sectional area (m^2)	Area moment of inertia about axes (in 10,000 m^4)			Ratio of shear area to cross sectional area	
				X	Y	Z	X	Y
500	109060	500	1409.8	11.0	9.6	20.5	0.55	0.61
501	500	531	1409.8	10.7	9.6	20.3	0.55	0.61
502	531	532	625.4	3.9	2.9	6.8	0.44	0.44
503	532	533	738.0	5.8	5.1	11.0	0.50	0.56
504	533	534	479.4	4.0	2.5	6.5	0.52	0.59
505	534	535	158.4	0.7	0.5	1.2	0.24	0.36
506	535	536	30.3	0.0	0.0	0.0	0.21	0.04
507	535	537	45.0	0.0	0.0	0.0	0.13	0.19
508	537	538	15.2	0.0	0.0	0.0	0.10	0.18

The natural periods of the CIS associated with the motion in the horizontal directions are listed in Table 8-7. These periods compare well with the values reported in Short *et al.* (2007).

8.4 Description of the Seismically Isolated Models

Two models of a seismically isolated nuclear power plant are analyzed to compute isolation-system displacement and horizontal floor spectra for nodes at different locations in the CIS. Table 8-8 maps the computed response quantities to the models. Note that Model 2 is subjected to horizontal components of ground motion only.

Table 8-7 Natural Period of Containment Internal Structure

	Period (s)	
Mode	Present study	Short *et al.* (2007)
1	0.082	0.083
2	0.078	0.075
3	0.061	0.067
4	0.053	0.057
5	0.048	0.050
6	0.042	0.035

Two percent Rayleigh damping is assigned at periods of 0.05 s and 3 s (the sliding period for this study). The displacement at which sliding commences is set equal to 1 mm.

Table 8-8 Response Quantities Estimated Using the Two Models

Model	Description	Response quantity		
		Isolation-system displacement	Acceleration of basemat	Acceleration of nodes of CIS
1	Isolated ASB-CIS	✓	✓	✓
2	Macro model	✓	✓	×

8.4.1 Model 1: Seismically Isolated ASB and CIS

The ASB model comprises 187 nodes at the basemat level; the base of the CIS is represented by one node. One node is common to both the ASB and the CIS (109060). One hundred and eight seven single FP bearings are used to isolate the ASB and CIS. Each of the bottommost 187 nodes (height = 1.2 m; see Table 8-2 and Figure 8-7(a)) of the common basemat represents the slider of an FP bearing. One hundred and eighty seven additional nodes, each of which represents the sliding surface of an FP bearing, are introduced at the plan locations of the bottommost 187 nodes of the ASB. The nodes representing the sliding surface are restrained from translation and rotation; the nodes representing the slider are free to translate but restrained from rotation (a boundary condition enforced by the stiff basemat).

Gravity and inertial forces associated with the entire mass of the CIS are transferred at node 109060, which represents the slider of the FP bearing at the geometrical center of the basemat. The axial force on this bearing, and consequently the shear force and horizontal floor spectral ordinates, would be unrealistically high. The gravity force due to the CIS is therefore distributed equally among all 99 nodes of Segment 2 of the ASB (see Figure 8-6) representing sliders of FP bearings. The vertical inertial mass of the CIS is ignored in this study.

Model 1 is subjected to a) three components of ground motion, and b) two horizontal components of ground motions, to help answer the questions posed in Section 8.1.

8.4.1.1 Seismic Isolation System

The seismic isolation system comprises 187 single FP bearings with a sliding period of 3 s, reference coefficient of friction of 0.06, static axial pressure of 50 MPa and friction at the sliding surface defined using the five friction models of Table 7-2. The center-to-center distance between adjacent bearings is 6 m. The bearings are placed at the nodes shown in Figure 8-7(a). The static axial load on each FP bearing in Segments 1 and 3 (see Figure 8-6) is 7,100 kN (32,000 tons distributed between 44 bearings; see Table 8-2). The static axial load on the bearings in Segment 2 is 11,000 kN (75,000 tons from the ASB and 41,000 tons from the CIS, distributed between 99 bearings). The radius of the contact area for each of the 44 FP bearings in Segments 1 and 3 is 0.21 m, and 0.26 m for each of the 99 FP bearings in Segment 2.

8.4.2 Model 2: Macro Model (single FP bearing)

Model 2 is a macro-model of the NPP comprising a single FP bearing and a lumped mass to describe the superstructure. A sliding period of 3 s, reference coefficient of friction of 0.06, static axial pressure of 50 MPa and friction at the sliding surface defined using the five models

of Table 7-2 are considered. The static axial load on the bearing is the weighted average[42] of the static axial loads on the 187 FP bearings of Model 1: 9,200 kN. The radius of the contact area at the sliding surface is 0.24 m. The inertial masses associated with motion in the three translational directions are equal to the gravity load.

8.5 Ground Motions

A set of thirty three-component ground motions consistent with 10,000-year hazard at Diablo Canyon site is developed in Chapter 7. Sets of ground motions with four amplitude scale factors are considered in this chapter: 0.6, 1.0, 1.5 and 2.0, which approximately represent 100,000-year shaking at Vogtle, 10,000-year shaking at Diablo Canyon, 150% of 10,000-year shaking at Diablo Canyon, and 100,000-year shaking at Diablo Canyon, respectively (see Chapter 7).

8.6 Results

This section presents results of the response-history analyses performed on Models 1 and 2. Distributions of peak isolation-system displacement and floor spectral accelerations are presented and studied.

8.6.1 Distribution of Peak Displacements

Figure 8-10(a) presents the distributions of displacements of the center of the isolation system for Models 1 and 2, with friction at the sliding surface of FP bearings described using the Coulomb model, subjected to the set of 30 ground motions amplitude scaled by 0.6. Model 1 is subjected to ground motions with and without the vertical component. Expectedly, the distributions of the isolation-system displacements obtained using the two models are virtually identical with less than a 2 mm (5 mm) difference in the median (99th percentile) displacement. Including the vertical component of the ground motion in the response-history analysis of Model 1 alters the median (99th percentile) isolation system displacement estimate by 0.1 mm (1 mm).

Figures 8-10(b) through 8-10(e) present results for Model 1 and Model 2, with friction at the sliding surface described using the pressure-dependent, temperature-dependent, velocity-dependent, and *p*-*T*-*v* model, respectively. The distributions of the isolation-system displacement computed using the two nuclear island NPP models are virtually identical. Figures 8-11, 8-12 and 8-13 present results for ground motions amplitude scaled by 1.0, 1.5 and 2.0, respectively. The distributions of isolation-system displacement are similar, for a given intensity level and friction model. Including the vertical component of the ground motion in the response-history analysis of Model 1 does not change the distributions of horizontal displacement.

[42] The static axial force on each of the 44 FP bearings of the seismically isolated ASB-CIS (Section 8.4.1) in Segments 1 and 3 is 7,100 kN. The force on each of the 99 bearings in Segment 2 of this model is 11,000 kN.

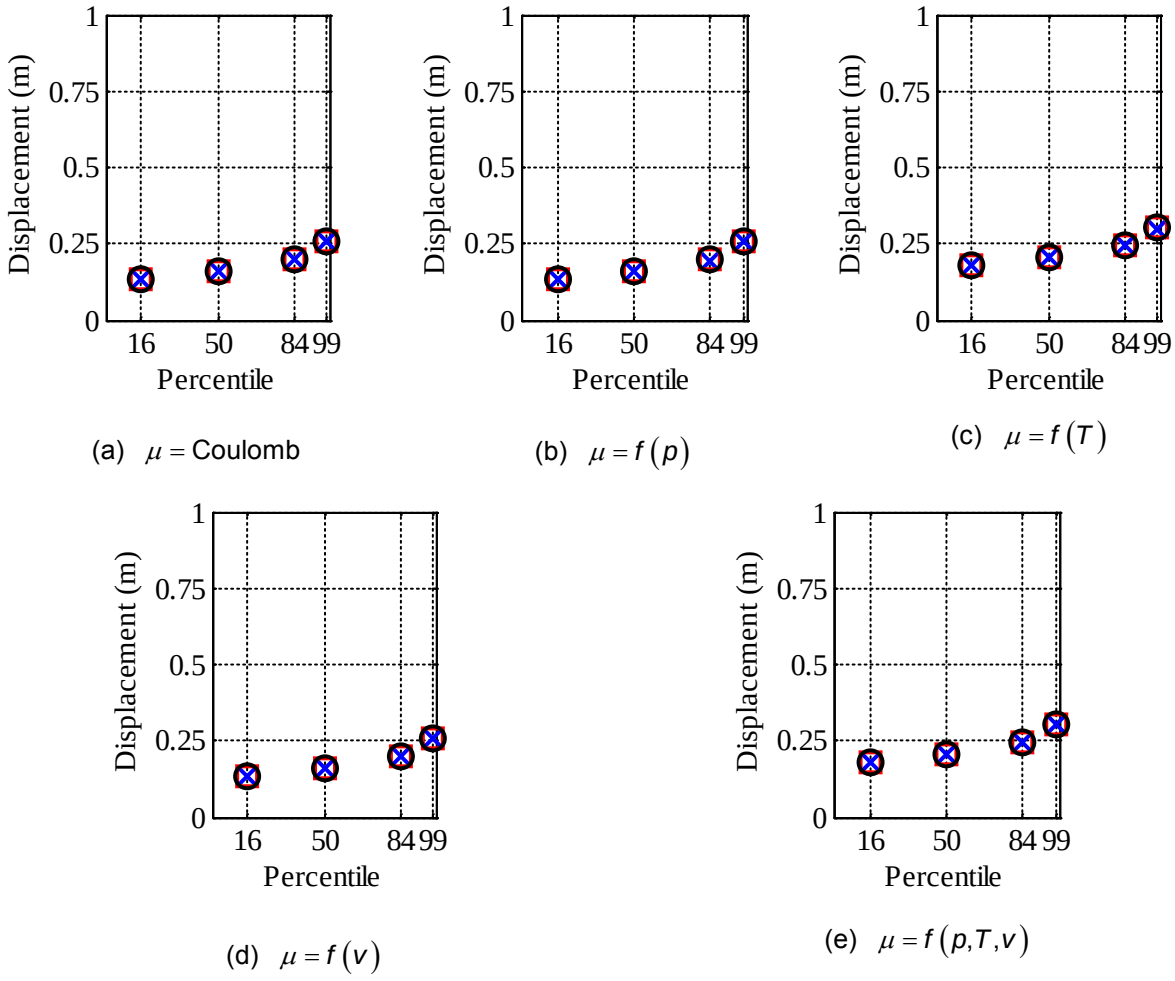

Figure 8-10 Distributions of Isolation-System Displacement for the Two Models Subjected to the Set of Ground Motions Amplitude Scaled by 0.6

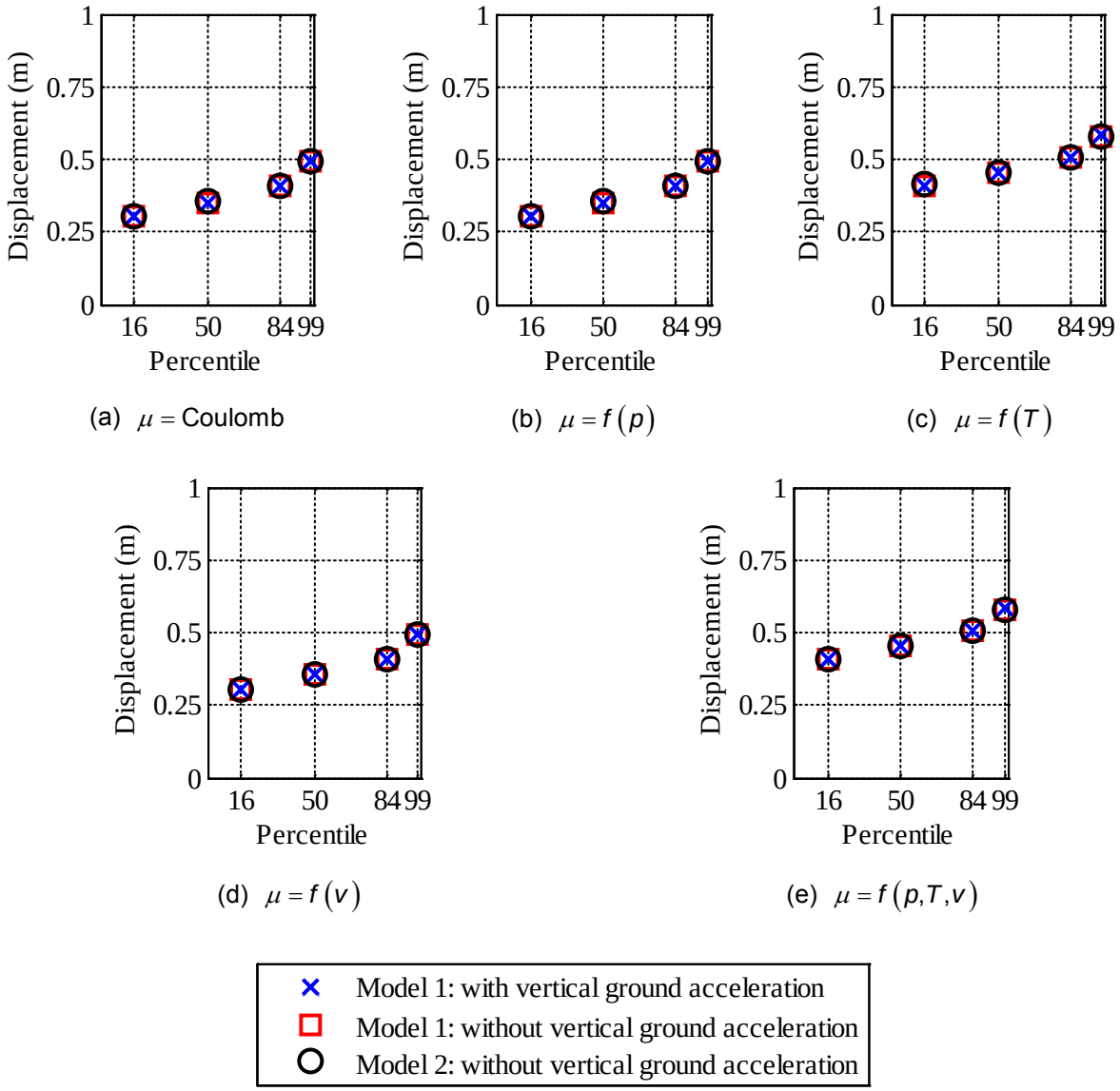

Figure 8-11 Distributions of Isolation-System Displacement for the Two Models Subjected to the Set of Ground Motions Amplitude Scaled by 1.0

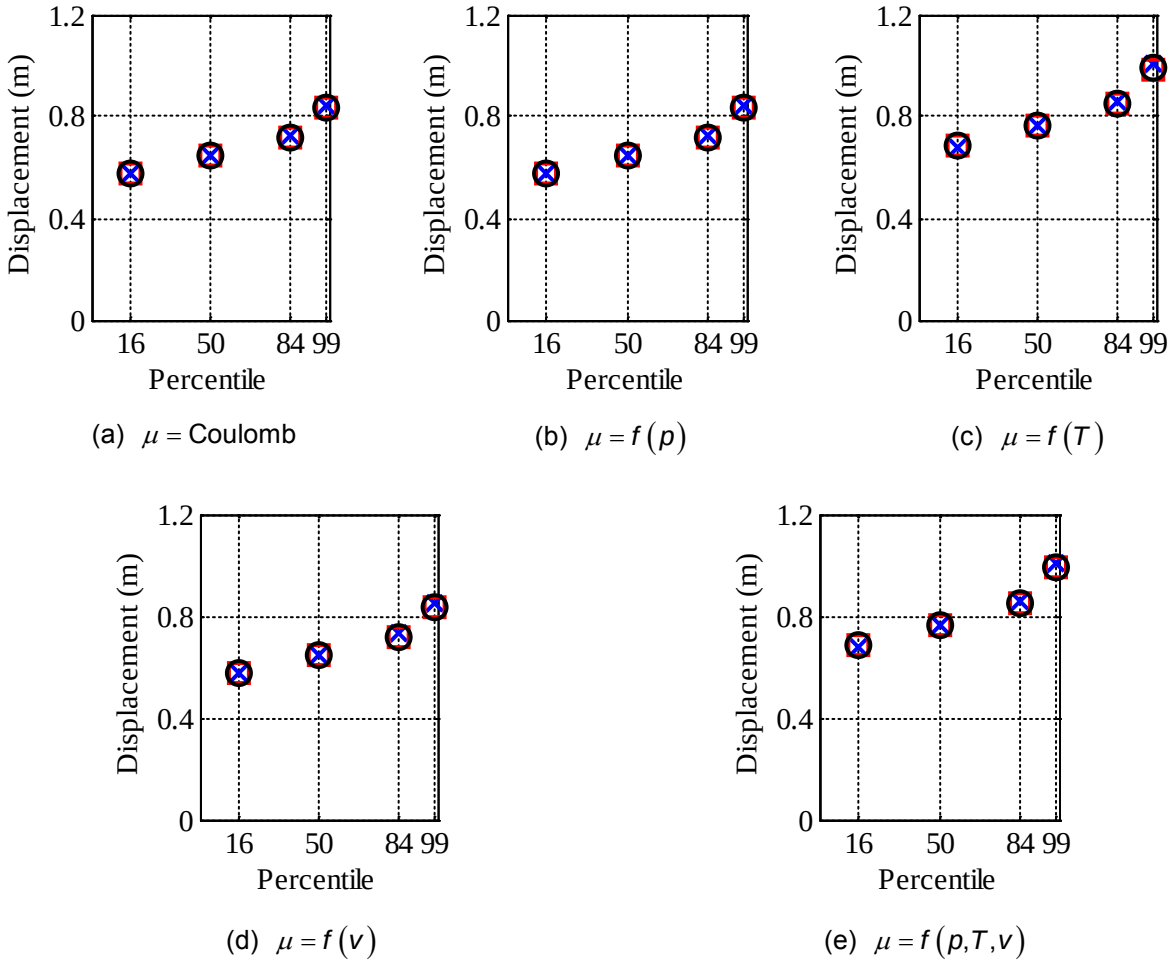

Figure 8-12 Distributions of Isolation-System Displacement for the Two Models Subjected to the Set of Ground Motions Amplitude Scaled by 1.5

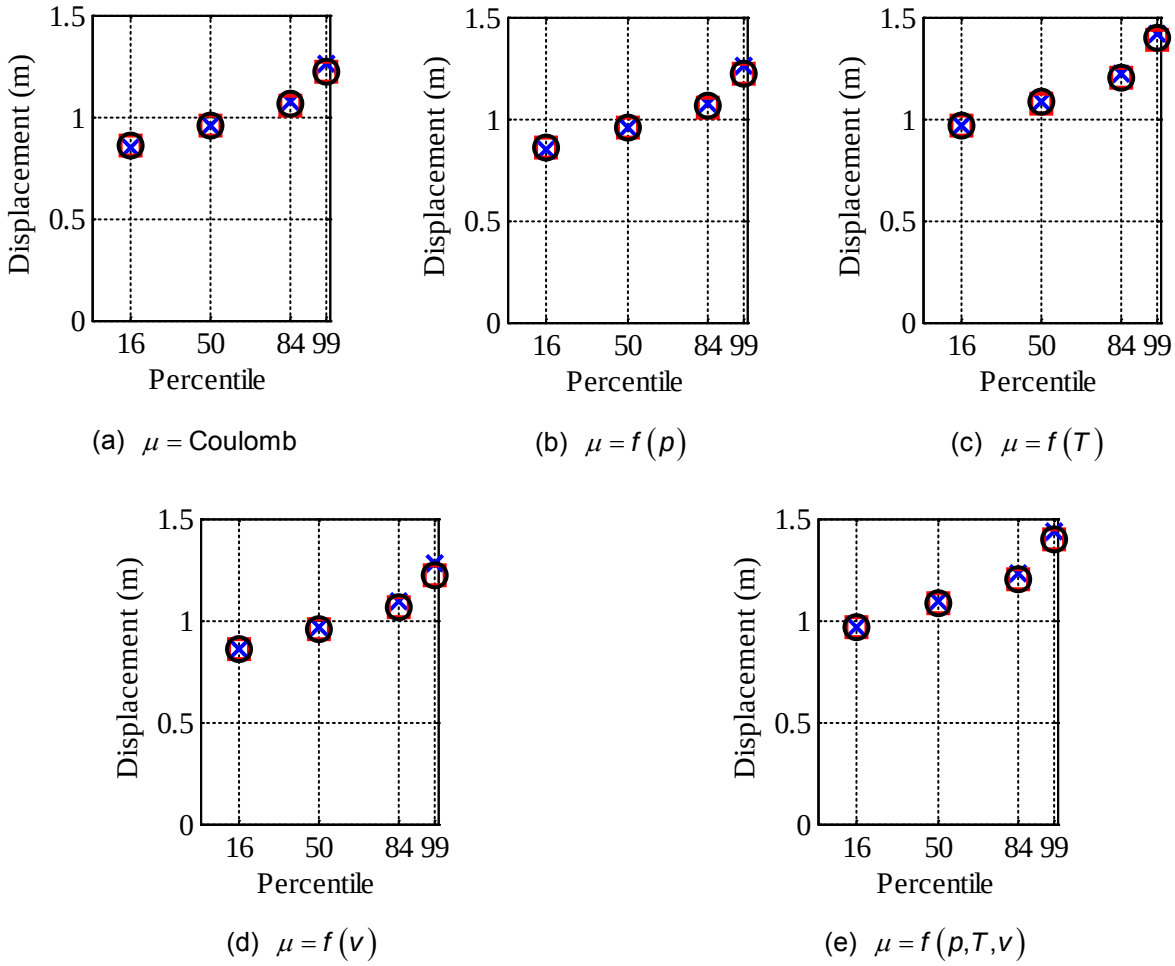

Figure 8-13 Distributions of Isolation-System Displacement for the Two Models Subjected to the Set of Ground Motions Amplitude Scaled by 2.0

8.6.1.1 Influence of Definition of Friction at the Sliding Surface

Large changes in the coefficient of friction are observed during the course of an analysis for bearings at different locations, when friction at the sliding surface is defined using the pressure-dependent model. Consider the seismically isolated ASB-CIS model (Model 1) with a reference coefficient of friction of 0.06 and friction at the sliding surface described using the pressure-dependent friction model subjected to the two horizontal and vertical components of ground motion 1 (GM1) with an amplitude scale factor of 1.0. The coefficient of friction at the sliding surface of the bearing at a corner of the isolation system varies between 0.046 and

0.082[43] during the course of shaking, and that at the center of the isolation system varies between 0.052 and 0.071. When the isolated ASB-CIS model is subjected only to the horizontal components of GM1, the coefficient varies between 0.051 and 0.069 for the bearing at the corner, and between 0.060 and 0.060 for the bearing at the center of the isolation system. These changes[44] in the coefficient of friction do not alter the distribution of isolation-system displacement[45] relative to that calculated ignoring the pressure-dependence of friction.

The calculated displacements are not materially affected by the velocity dependence of the coefficient of friction.

Inclusion of temperature dependency in the friction model significantly changes the estimate of isolation system displacement. The influence of heating on displacements, which is a function of shaking intensity, static axial pressure and reference coefficient of friction, is discussed in Chapter 7.

8.6.2 Floor Spectra

This section presents floor spectra at the nodes 109060 (basemat level), 532 (height of 13 m), 5351 (height of 24 m) and 5382 (height of 34 m) of the CIS (see Table 8-4) computed using the two NPP nuclear island models with friction at the sliding surface of the FP bearings defined using the five models of Table 7-2 subjected to the set of 30 ground motions amplitude scaled by 0.6, 1.0, 1.5 and 2.0.

Figure 8-14(a) presents the median floor spectrum in the X direction at node 109060 obtained using Model 1 with friction at the sliding surface of the FP bearings described using Coulomb model subjected to the two horizontal and vertical components of the 30 ground motions amplitude scaled by 0.6. The results for Model 1 subjected to the 30 sets of three-components ground motions are referred to as *benchmark* results in this section. Also plotted in the figure are the floor spectra for Models 1 and 2 subjected to only two horizontal components of the ground motions. The floor spectral ordinates at 0.01 s at node 109060 (basemat) indicate the peak floor acceleration and the shear force generated in the isolated superstructure. These ordinates are smaller than the *benchmark* results by 7% and 20% for the two models subjected to the horizontal components of the ground motions, respectively. These differences are 12% and 44% at 0.05 s, 3% and 18% at 0.1 s, and 1% and 3% at 1 s. Three components of motion are needed to generate horizontal floor spectra.

Figures 8-14(d) through 8-14(l) present the 50th, 90th and 99th percentile floor response spectra for the nodes 532, 5351 and 5382 of the CIS computed using Model 1. The general observations are similar to those for node 109060, namely, ignoring the vertical component of the ground is unconservative. The floor spectra for the velocity-dependent, temperature-dependent, pressure-dependent and *p-T-v* friction models are presented in Figures 8-15 through 8-18, respectively. Figures 8-19 through 8-23 present floor spectra in the X direction for the NPP nuclear island models with the five friction models subjected to the 30 ground motions

---

[43] As discussed in Chapter 3, the coefficient of friction increases with a decrease in axial pressure. The axial pressure on a bearing at a given location in the isolation system changes over the course of earthquake shaking due to the vertical component of ground motion and the response of the supported superstructure to the three components of ground motion.

[44] The average coefficient of friction for a bearing is 0.06 over the course of shaking, irrespective of the location.

[45] The median (99th percentile) displacements for Coulomb and pressure-dependent friction models differ by less than 0.5 mm.

amplitude scaled by 1.0. Figures 8-24 through 8-33 present the floor spectra for amplitude scale factors of 1.5 and 2.0. The spectral ordinates in the Y direction are similar to those in the X direction and are not reported here. The results presented in Figures 8-14 through 8-33 can be summarized as follows:

i. The horizontal spectral ordinates computed using Model 1 subjected to the two horizontal components of ground motions are considerably smaller than those obtained for the model subjected to three components of ground motions.

ii. The differences between the *benchmark* horizontal ordinates and those calculated for the two models subjected to only the two horizontal components of ground motions

   a. increase substantially with increase in shaking intensity at periods 0.01 s, 0.05 s and 0.1 s (see Figures 8-34 through 8-36).

   b. are small at 1 s irrespective of shaking intensity (see Figures 8-34 through 8-36).

   c. are greater at the higher percentiles.

   d. are generally greater for nodes at higher elevations inside containment.

iii. The choice of friction model does not considerably influence the floor spectral ordinates (see Figures 8-37 and 8-38).

The following recommendations are made for modeling, analysis and design of a nuclear power plant isolated with single concave FP bearings:

i. The friction model for the FP isolator must account for heating effects.

ii. Isolation-system horizontal displacement can be estimated for preliminary analysis and design using a macro model.

iii. A complete three-dimensional model will be required for final analysis and design to account for torsion and rocking, to accommodate soil-structure-interaction analysis, to compute member forces and generate floor spectra.

iv. Vertical ground motion must be included to generate floor spectra.

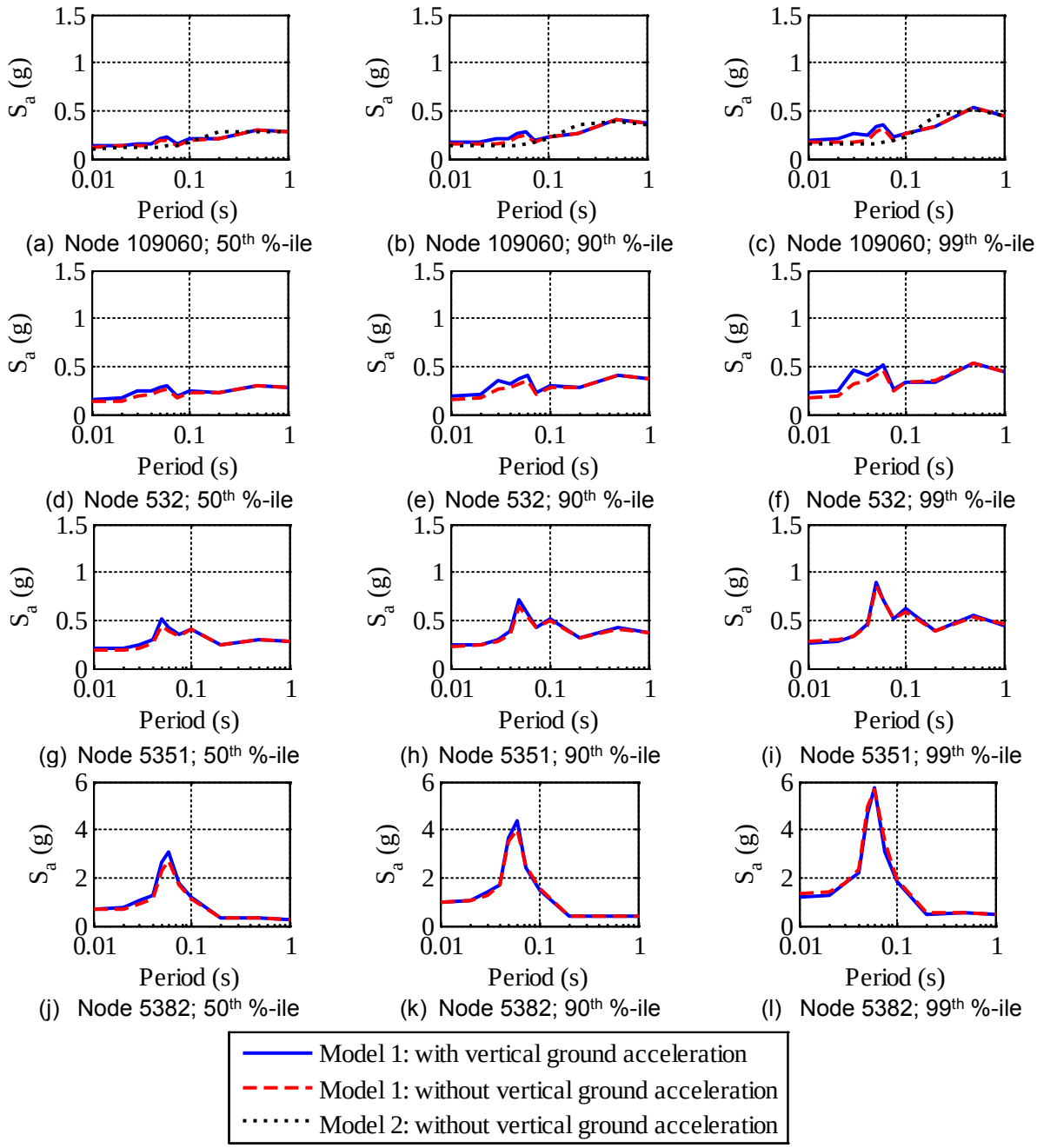

Figure 8-14 Floor Spectra in the X Direction at Different Nodes of the CIS Computed Using the Two Nuclear Island Models with Friction at the Sliding Surface Described Using the Coulomb Model Subjected to the Set of 30 Ground Motions Amplitude Scaled by 0.6

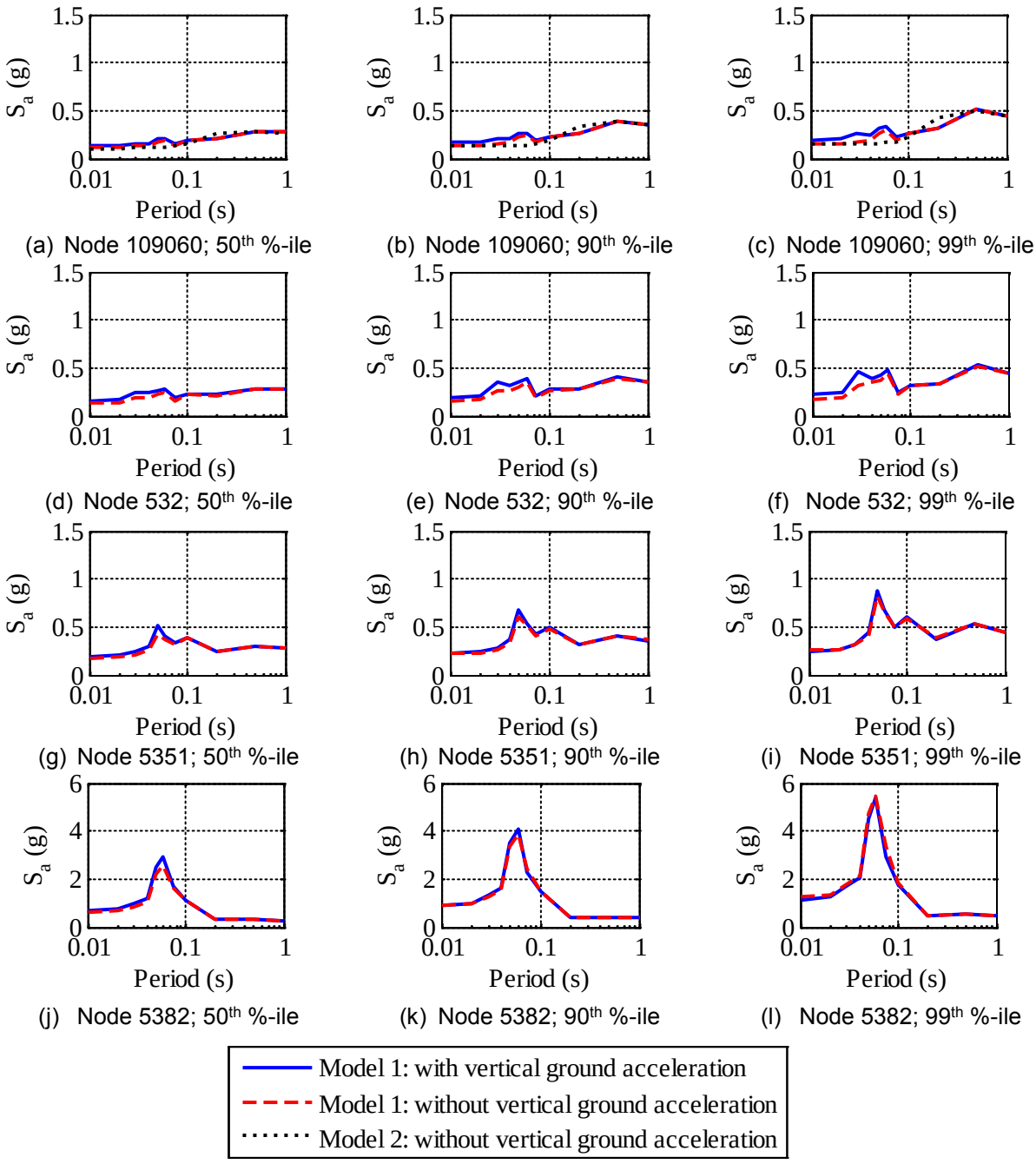

Figure 8-15 Floor Spectra in the X Direction at Different Nodes of the CIS Computed Using the Two Nuclear Island Models with Friction at the Sliding Surface Described Using the Velocity-Dependent Model Subjected to the Set of 30 Ground Motions Amplitude Scaled by 0.6

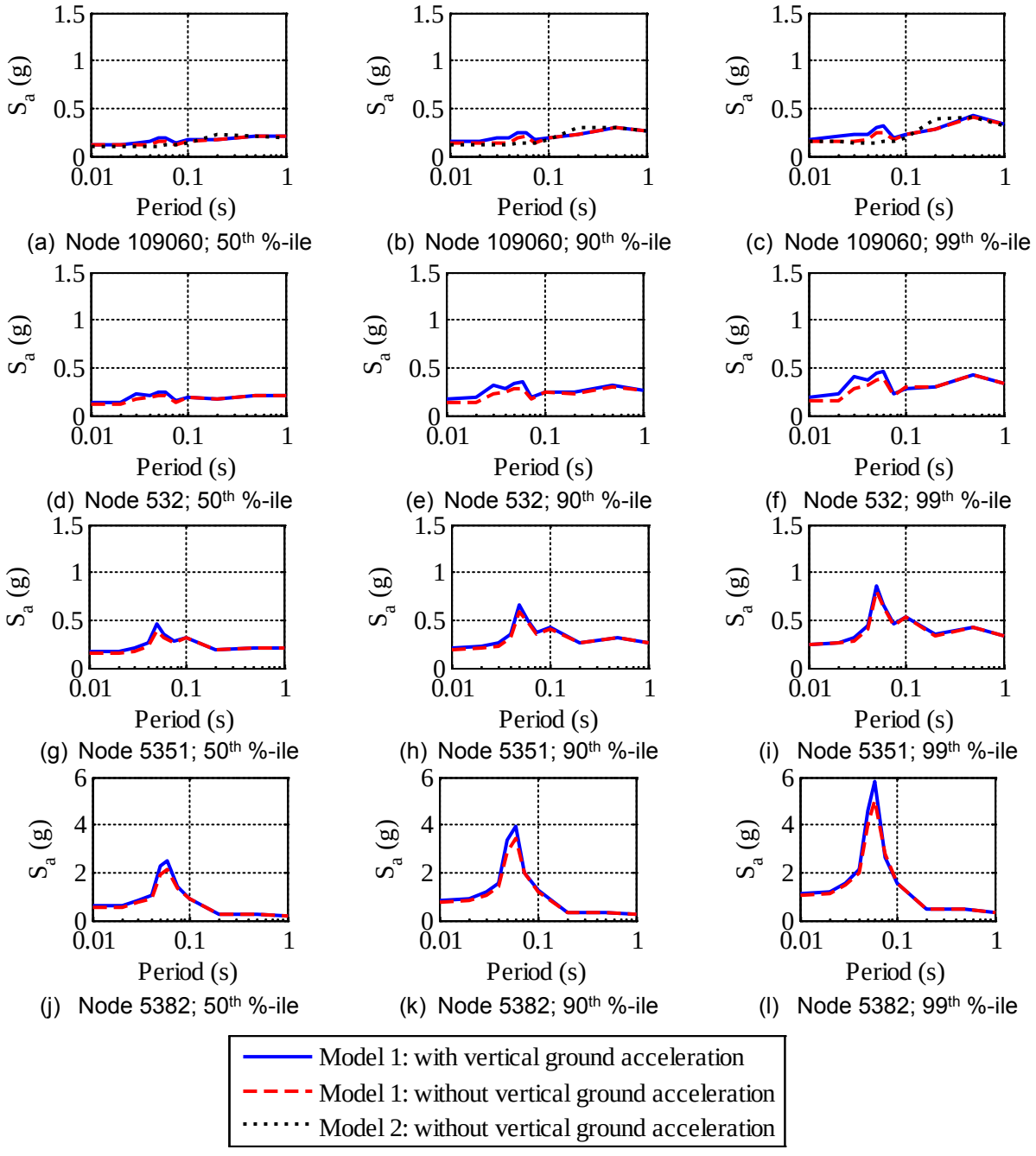

Figure 8-16 Floor Spectra in the X Direction at Different Nodes of the CIS Computed Using the Two Nuclear Island Models with Friction at the Sliding Surface Described Using the Temperature-Dependent Model Subjected to the Set of 30 Ground Motions Amplitude Scaled by 0.6

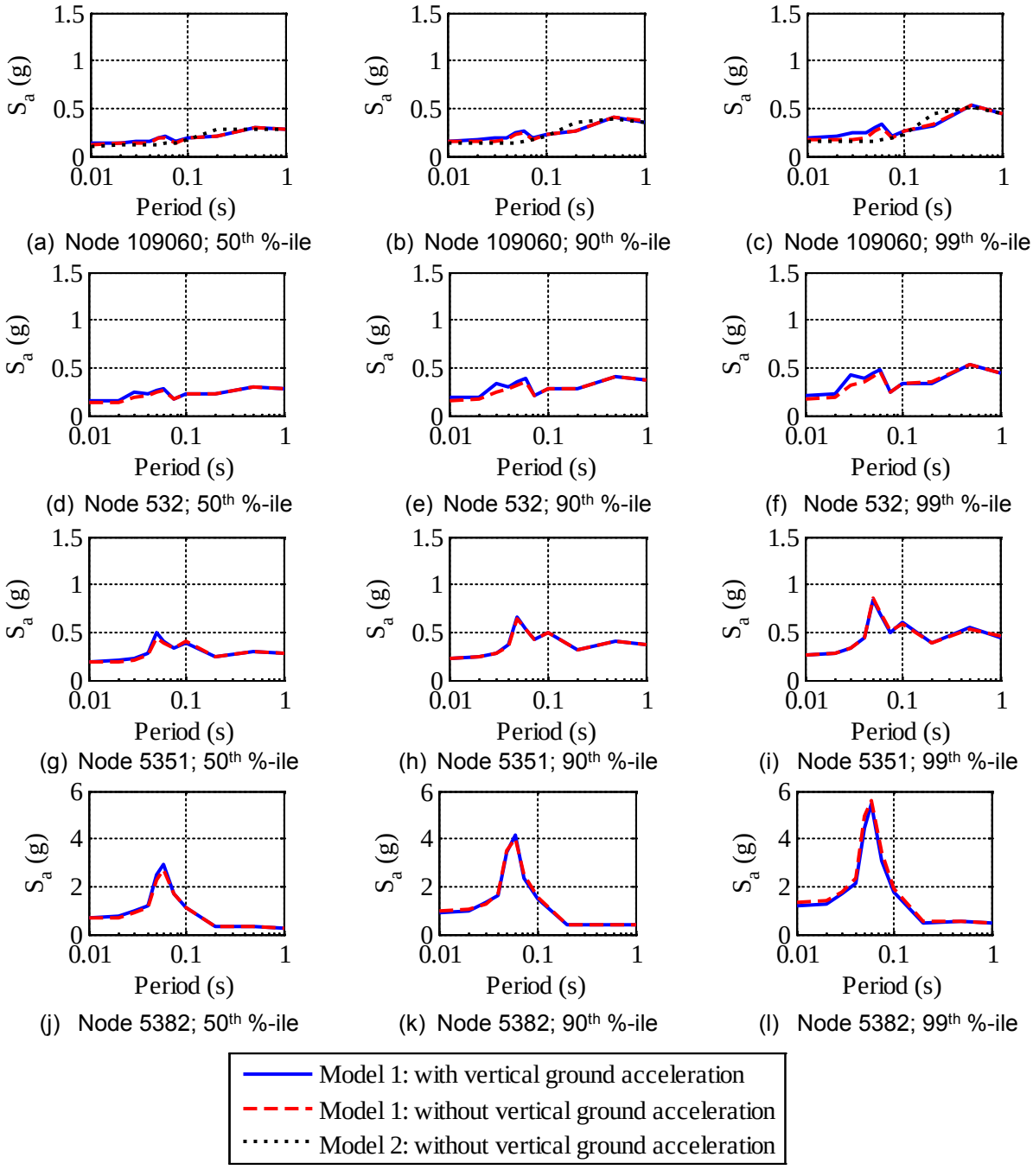

Figure 8-17 Floor Spectra in the X Direction at Different Nodes of the CIS Computed Using the Two Nuclear Island Models with Friction at the Sliding Surface Described Using the Pressure-Dependent Model Subjected to the Set of 30 Ground Motions with Amplitude Scaling Factor of 0.6

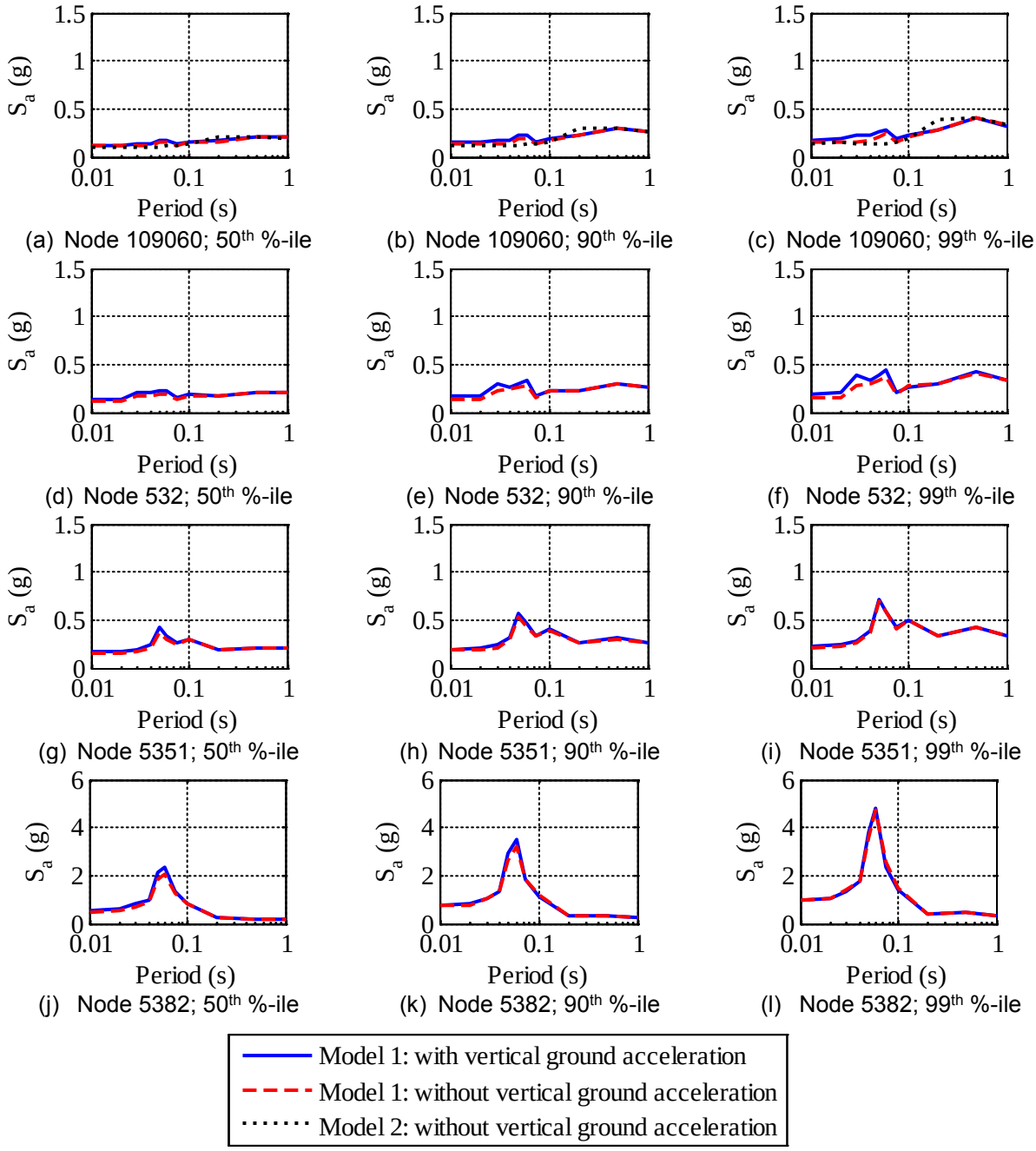

Figure 8-18 Floor Spectra in the X Direction at Different Nodes of the CIS Computed Using the Two Nuclear Island Models with Friction at the Sliding Surface Described Using the *p-T-v* Model Subjected to the Set of 30 Ground Motions with Amplitude Scaling Factor of 0.6

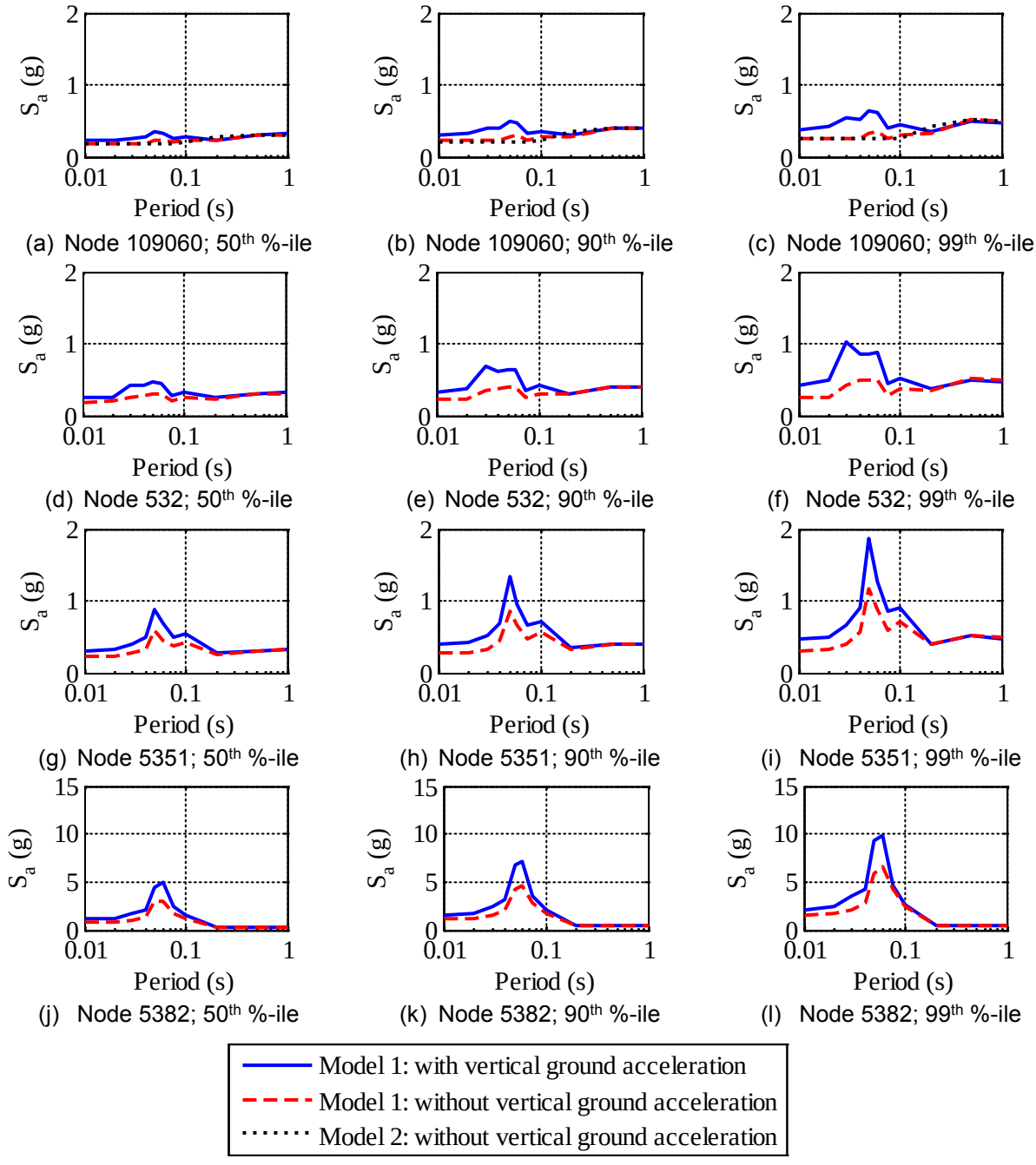

Figure 8-19 Floor Spectra in the X Direction at Different Nodes of the CIS Computed Using the Two Nuclear Island Models with Friction at the Sliding Surface Described Using the Coulomb Model Subjected to the Set of 30 Ground Motions Amplitude Scaled by 1.0

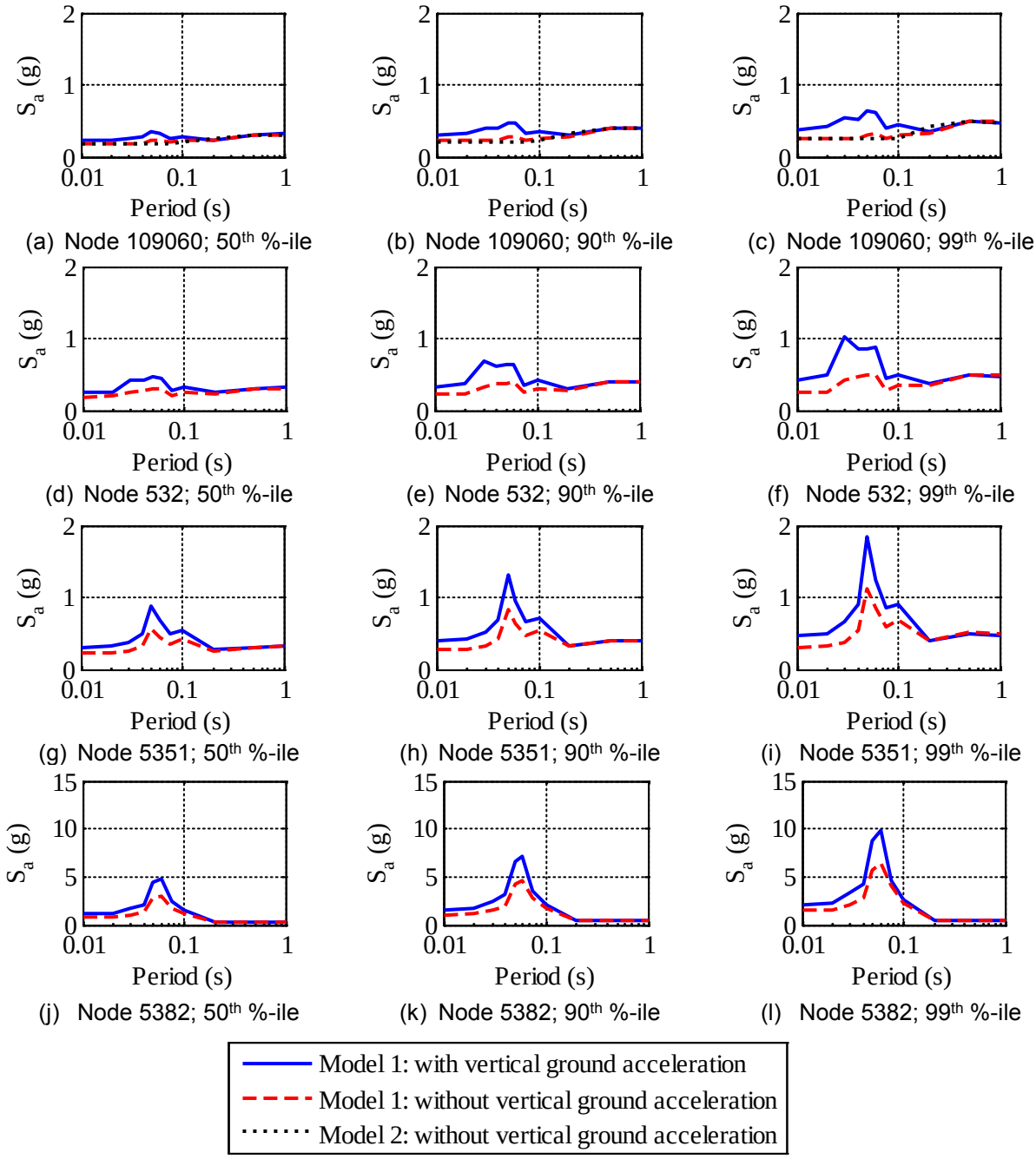

Figure 8-20 Floor Spectra in the X Direction at Different Nodes of the CIS Computed Using the Two Nuclear Island Models with Friction at the Sliding Surface Described Using the Velocity-Dependent Model Subjected to the Set of 30 Ground Motions Amplitude Scaled by 1.0

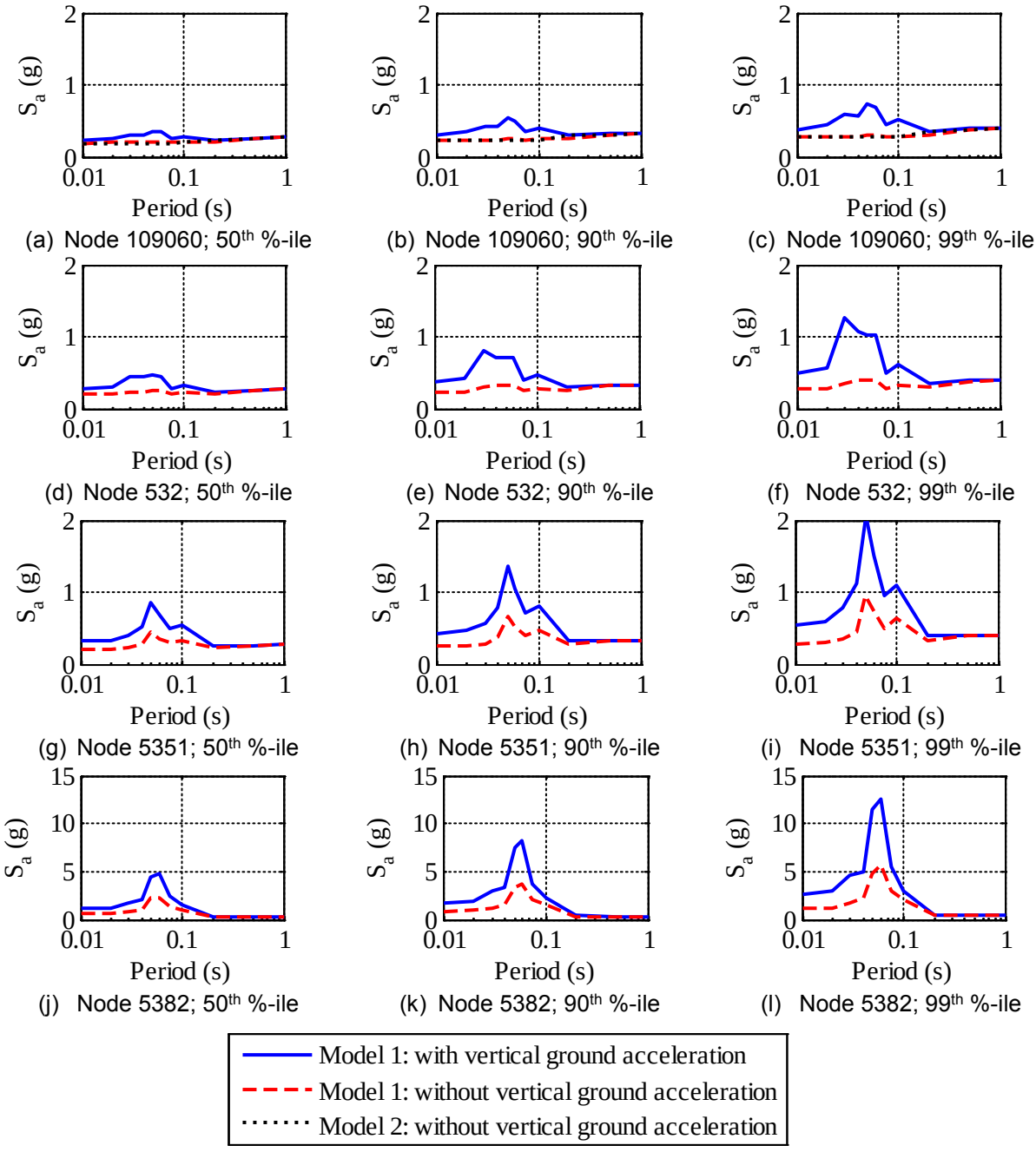

Figure 8-21 Floor Spectra in the X Direction at Different Nodes of the CIS Computed Using the Two Nuclear Island Models with Friction at the Sliding Surface Described Using the Temperature-Dependent Model Subjected to the Set of 30 Ground Motions Amplitude Scaled by 1.0

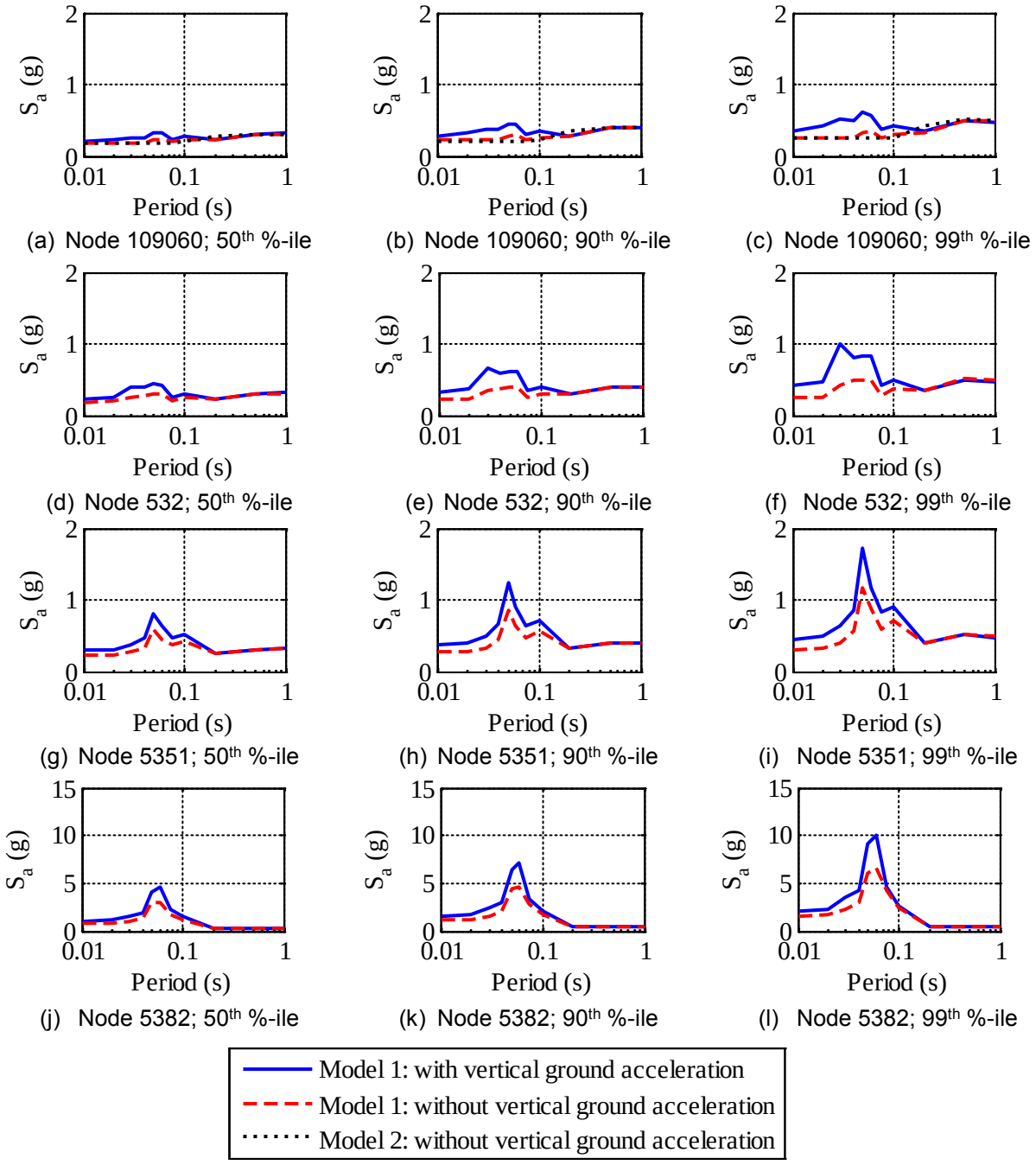

Figure 8-22 Floor Spectra in the X Direction at Different Nodes of the CIS Computed Using the Two Nuclear Island Models with Friction at the Sliding Surface Described Using the Pressure-Dependent Model Subjected to the Set of 30 Ground Motions Amplitude Scaled by 1.0

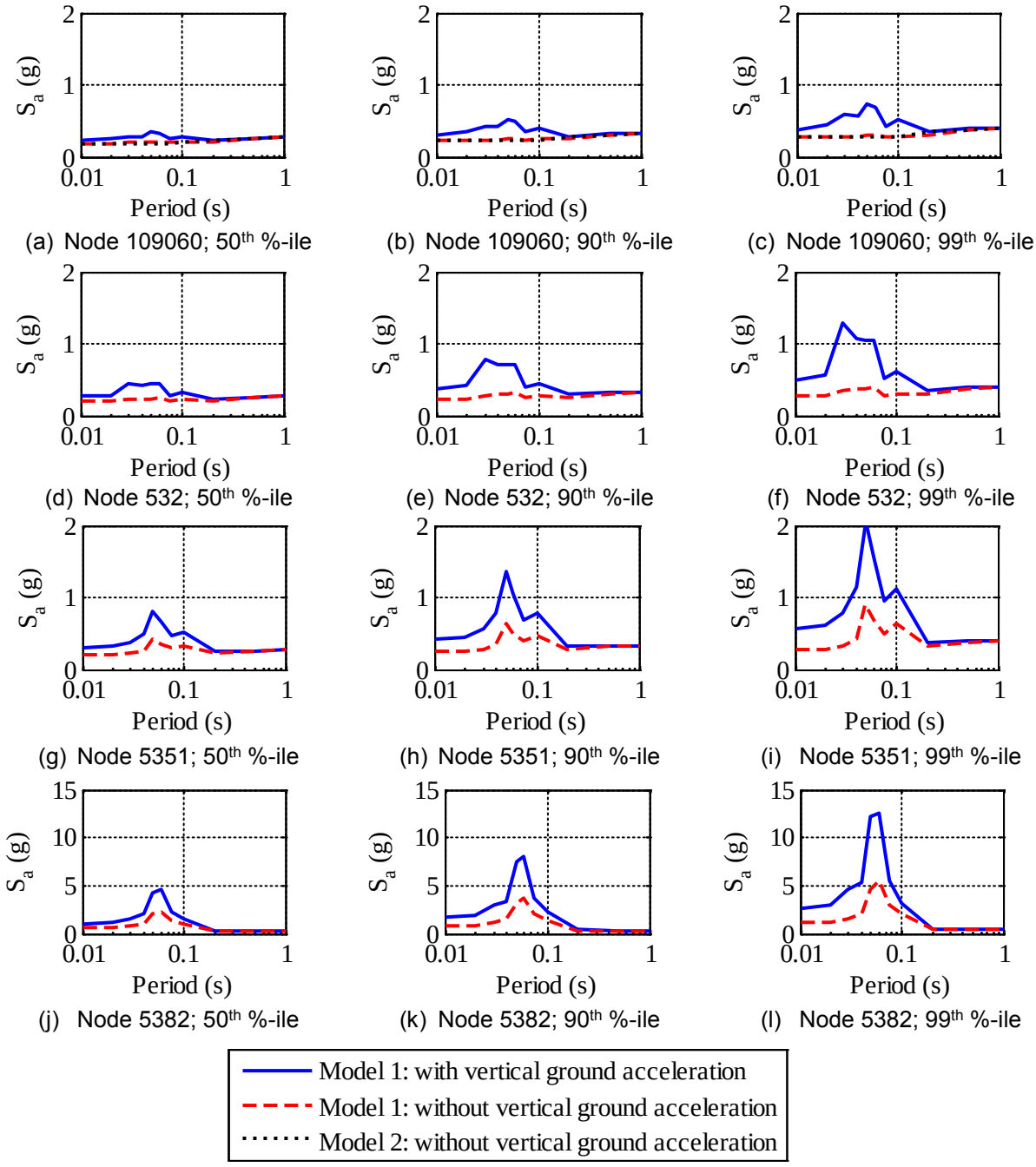

Figure 8-23 Floor Spectra in the X Direction at Different Nodes of the CIS Computed Using the Two Nuclear Island Models with Friction at the Sliding Surface Described Using the *p-T-v* Model Subjected to the Set of 30 Ground Motions Amplitude Scaled by 1.0

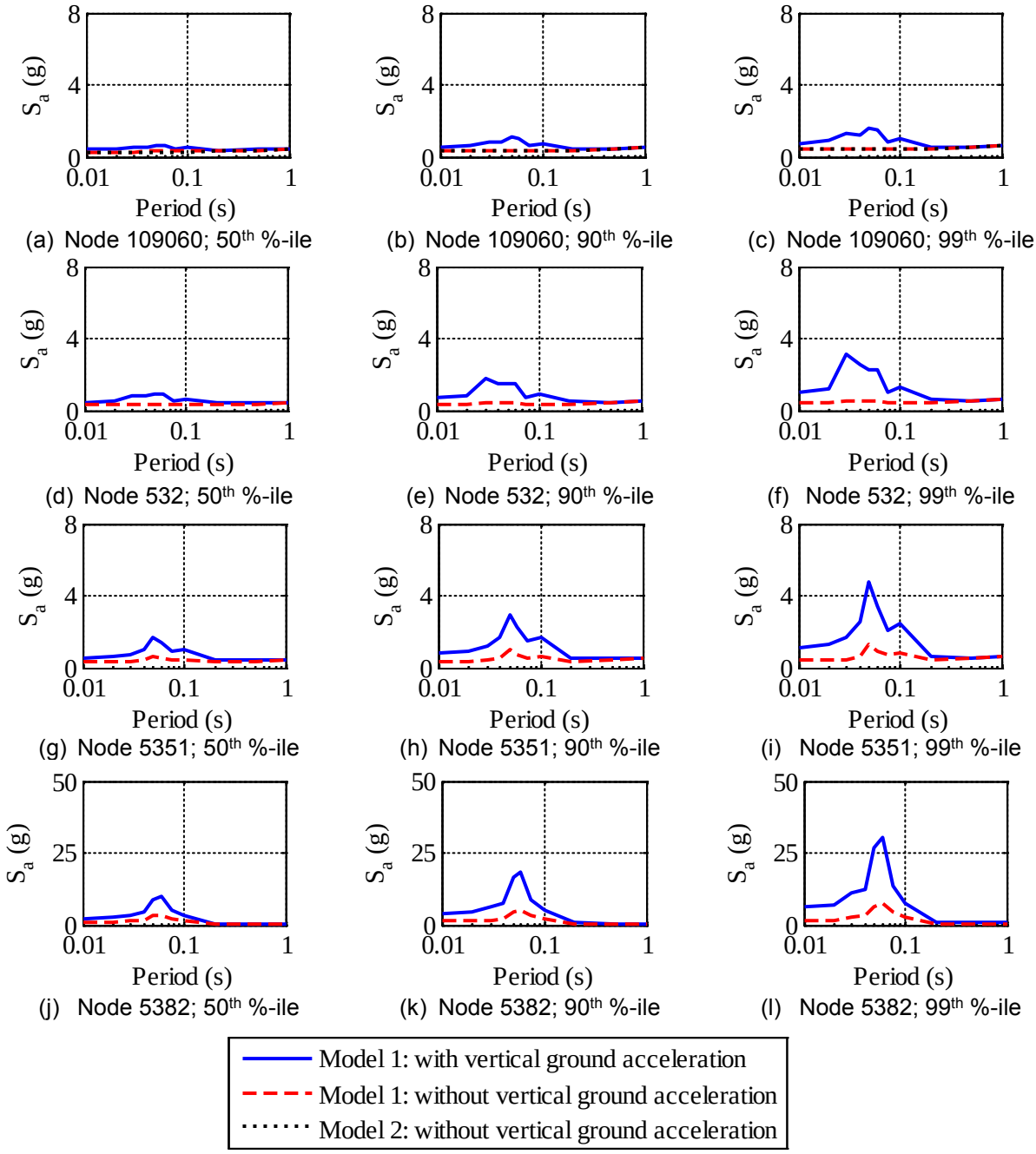

Figure 8-24 Floor Spectra in the X Direction at Different Nodes of the CIS Computed Using the Two Nuclear Island Models with Friction at the Sliding Surface Described Using the Coulomb Model Subjected to the Set of 30 Ground Motions Amplitude Scaled by 1.5

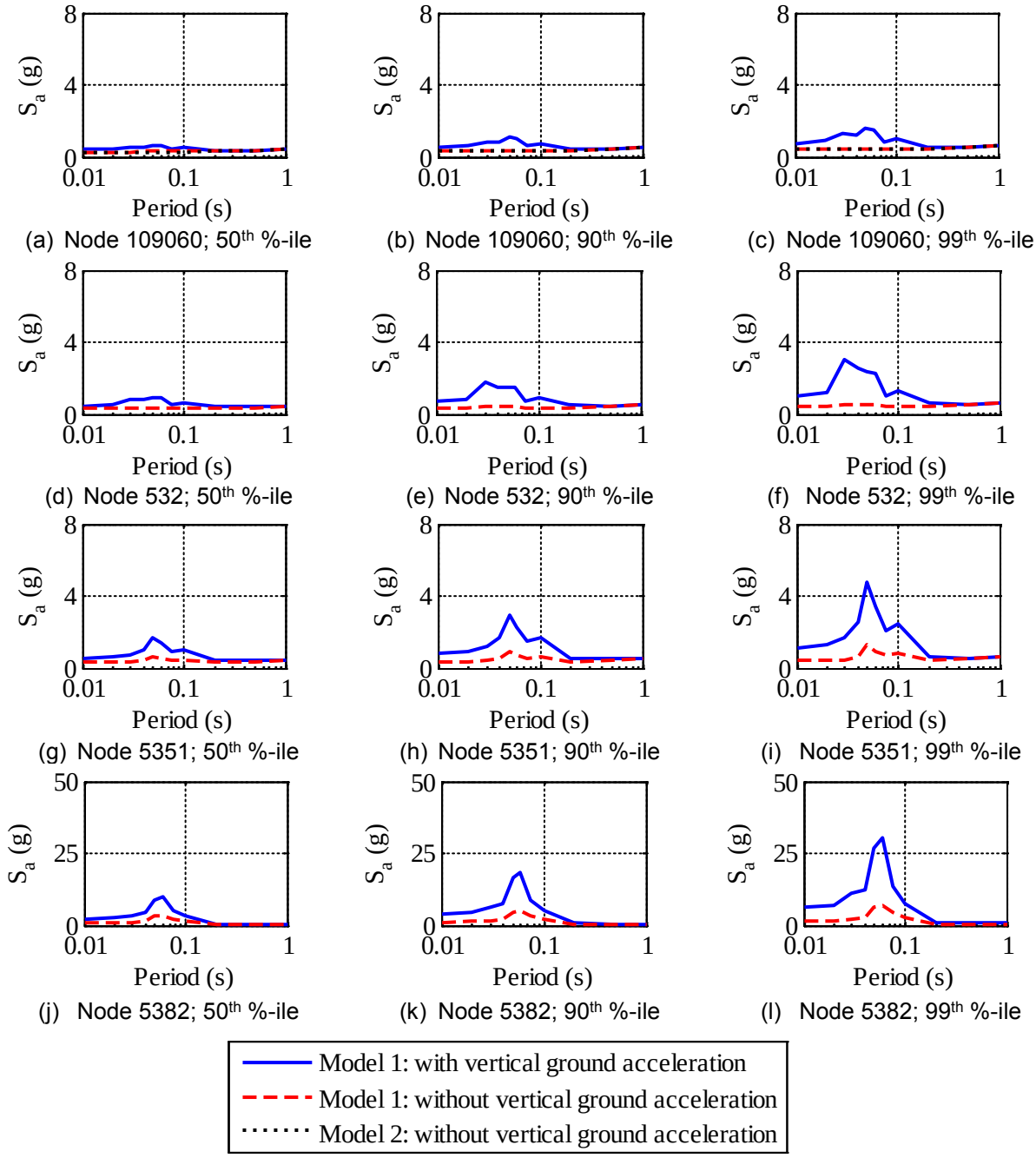

Figure 8-25 Floor Spectra in the X Direction at Different Nodes of the CIS Computed Using the Two Nuclear Island Models with Friction at the Sliding Surface Described Using the Velocity-Dependent Model Subjected to the Set of 30 Ground Motions Amplitude Scaled by 1.5

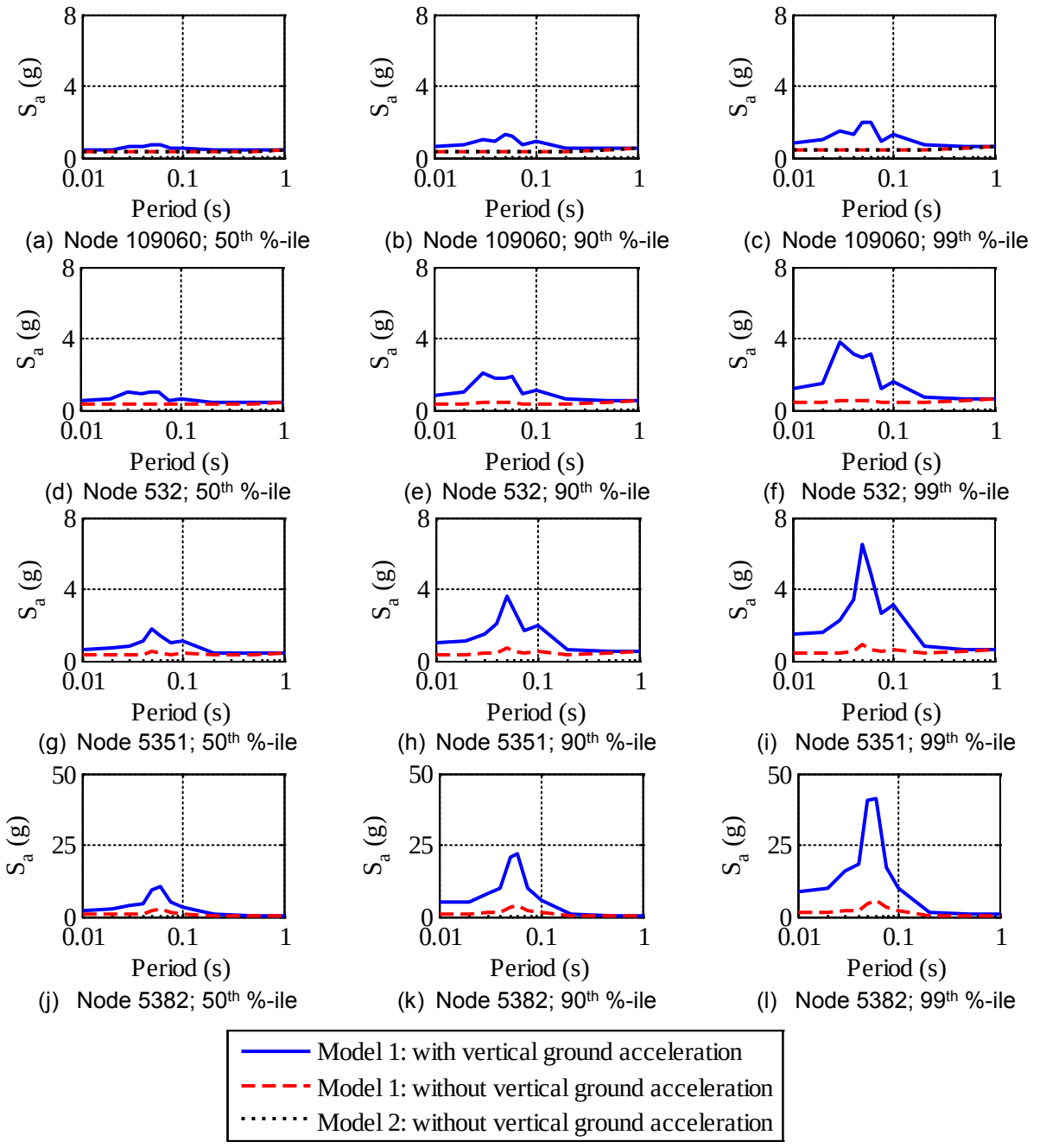

Figure 8-26 Floor Spectra in the X Direction at Different Nodes of the CIS Computed Using the Two Nuclear Island Models with Friction at the Sliding Surface Described Using the Temperature-Dependent Model Subjected to the Set of 30 Ground Motions Amplitude Scaled by 1.5

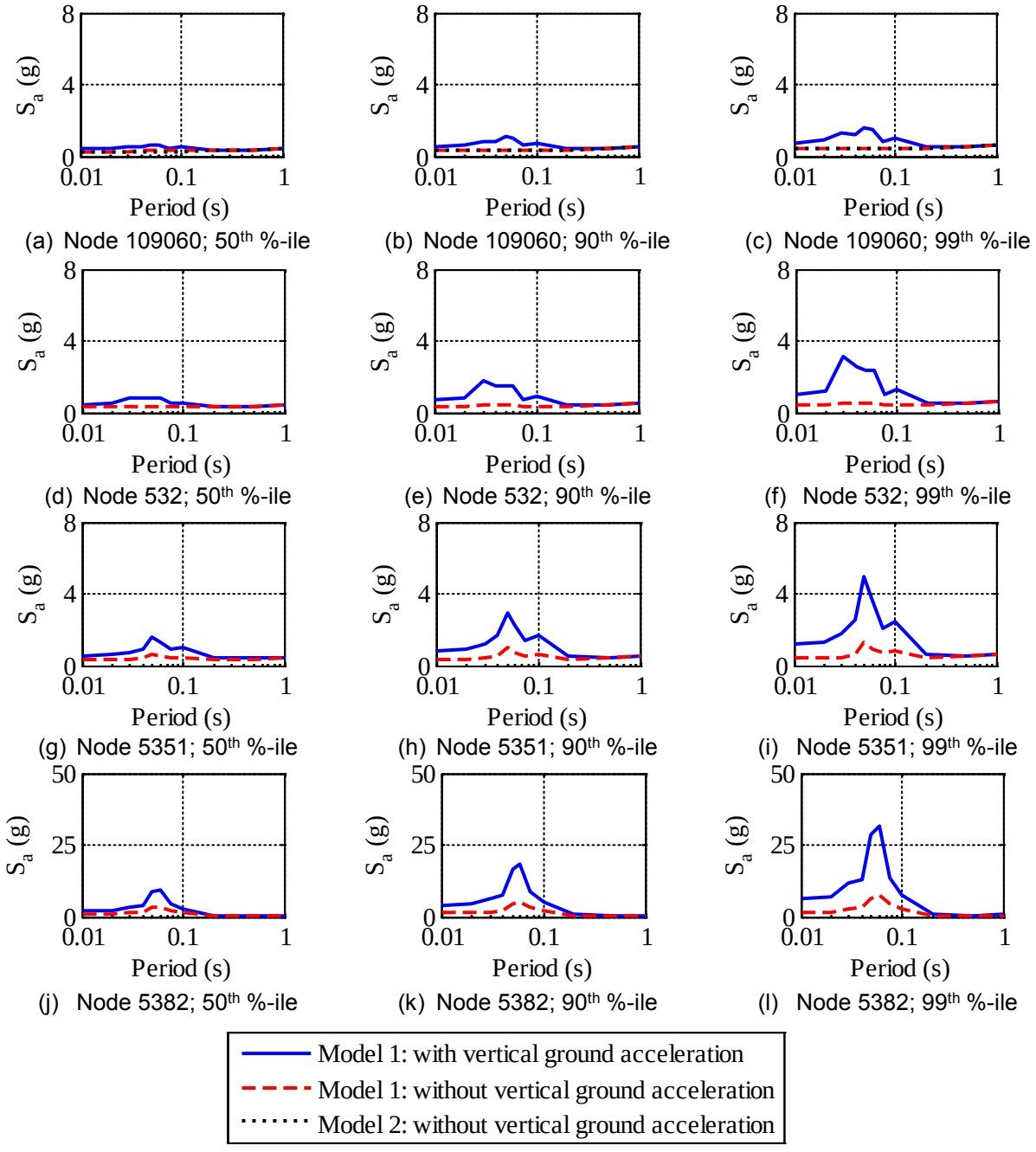

Figure 8-27 Floor Spectra in the X Direction at Different Nodes of the CIS Computed Using the Two Nuclear Island Models with Friction at the Sliding Surface Described Using the Pressure-Dependent Model Subjected to the Set of 30 Ground Motions Amplitude Scaled by 1.5

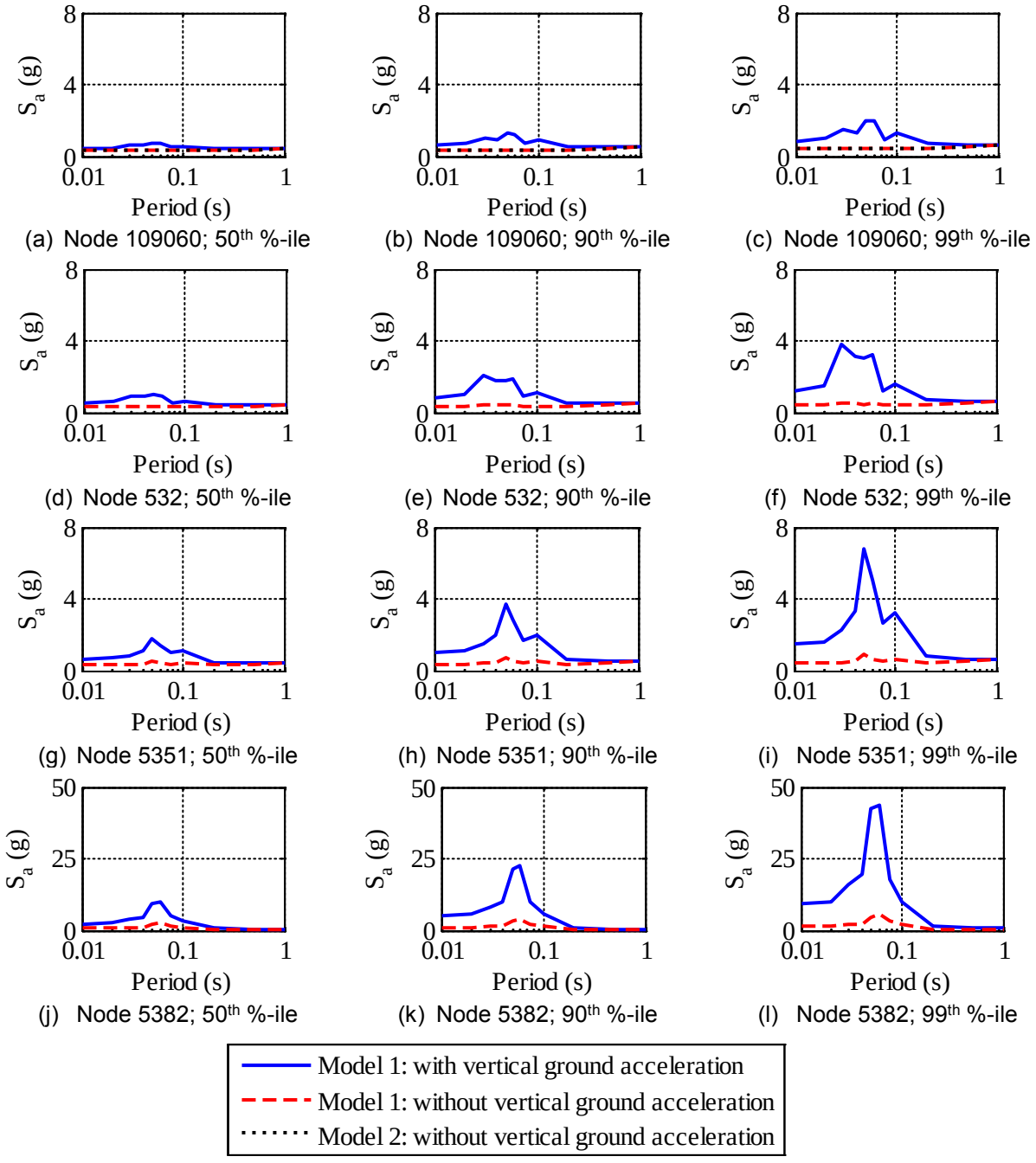

Figure 8-28 Floor Spectra in the X Direction at Different Nodes of the CIS Computed Using the Two Nuclear Island Models with Friction at the Sliding Surface Described Using the *p-T-v* Model Subjected to the Set of 30 Ground Motions Amplitude Scaled by 1.5

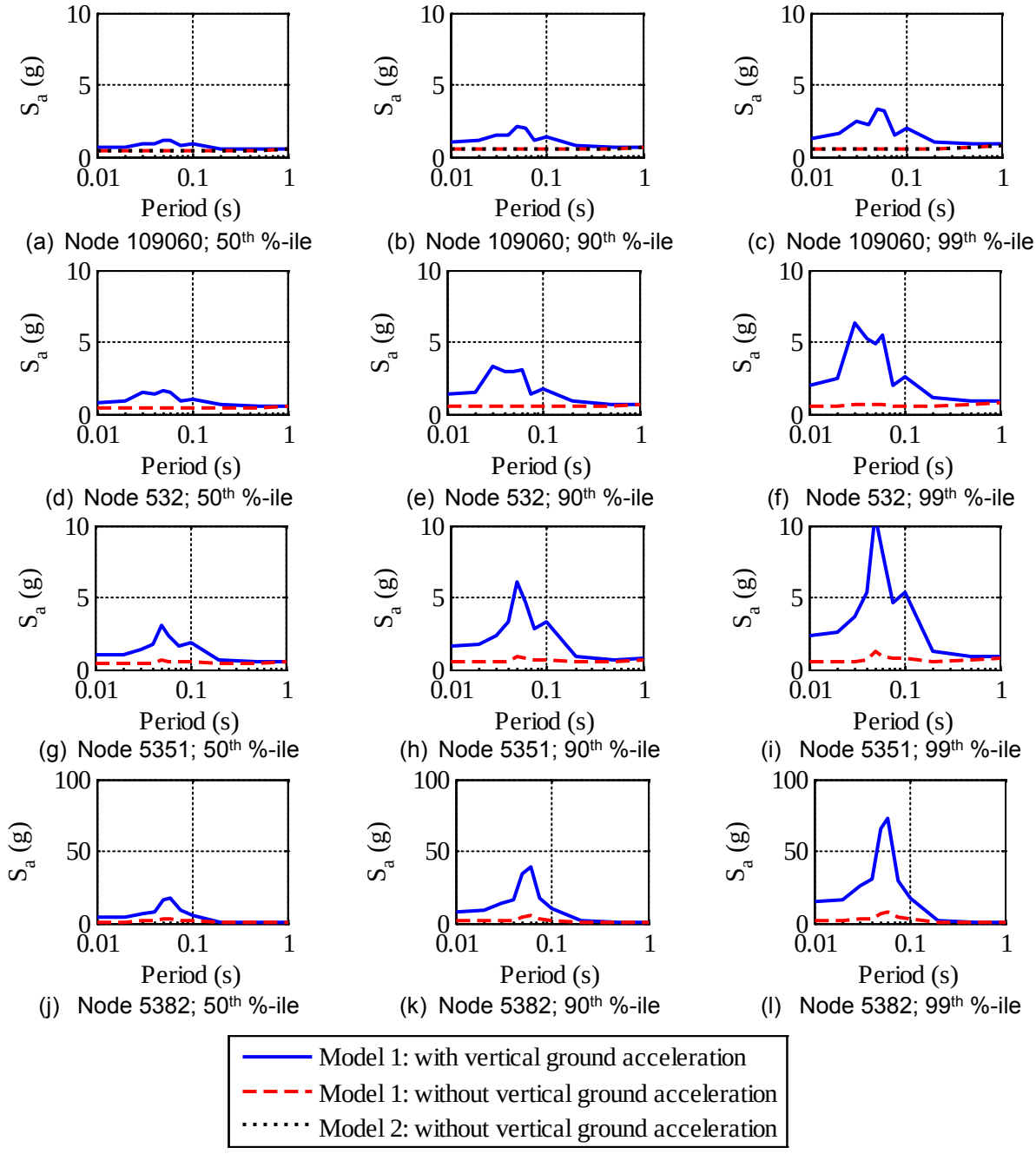

Figure 8-29 Floor Spectra in the X Direction at Different Nodes of the CIS Computed Using the Two Nuclear Island Models with Friction at the Sliding Surface Described Using the Coulomb Model Subjected to the Set of 30 Ground Motions Amplitude Scaled by 2.0

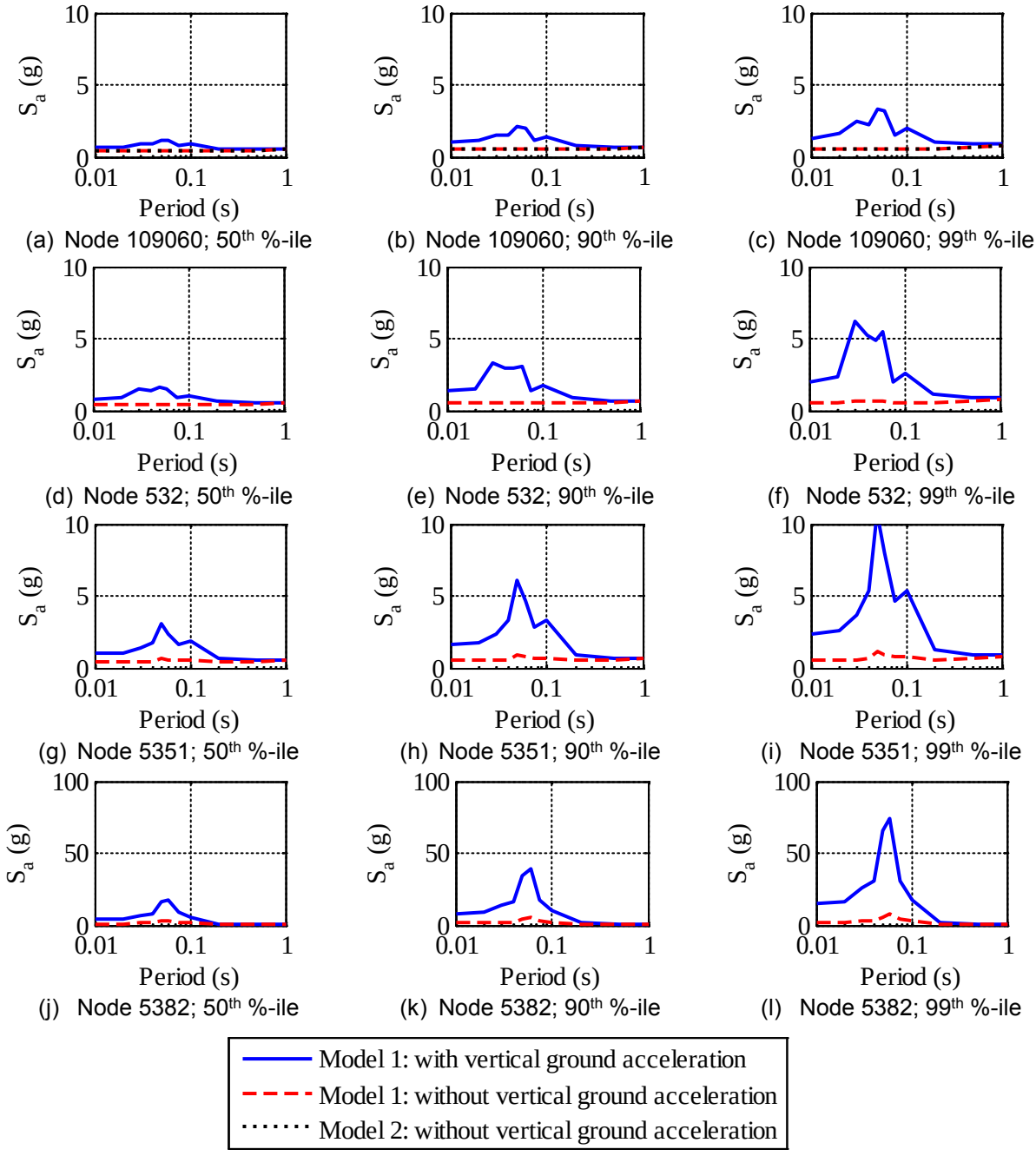

Figure 8-30 Floor Spectra in the X Direction at Different Nodes of the CIS Computed Using the Two Nuclear Island Models with Friction at the Sliding Surface Described Using the Velocity-Dependent Model Subjected to the Set of 30 Ground Motions Amplitude Scaled by 2.0

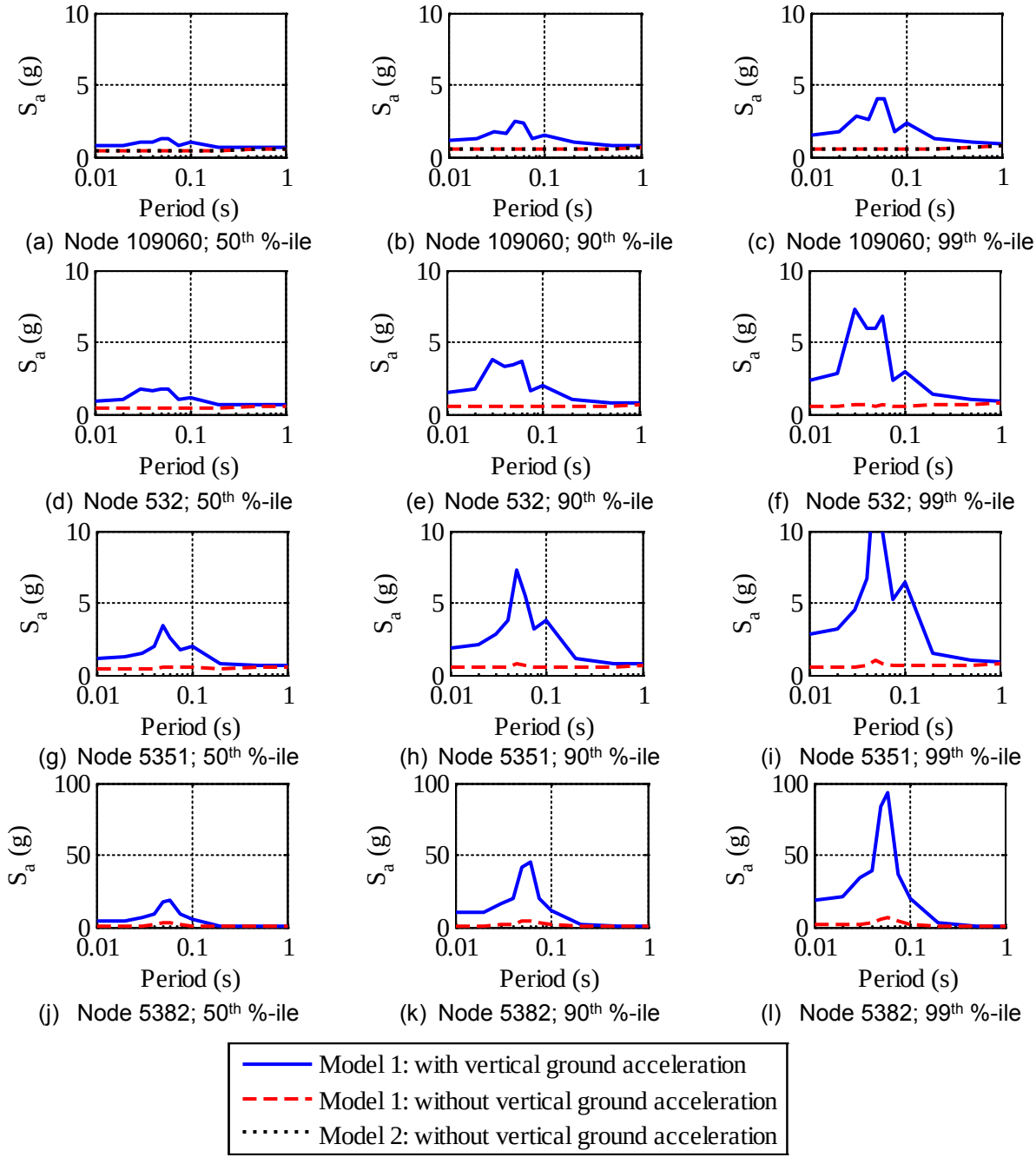

Figure 8-31 Floor Spectra in the X Direction at Different Nodes of the CIS Computed Using the Two Nuclear Island Models with Friction at the Sliding Surface Described Using the Temperature-Dependent Model Subjected to the Set of 30 Ground Motions Amplitude Scaled by 2.0

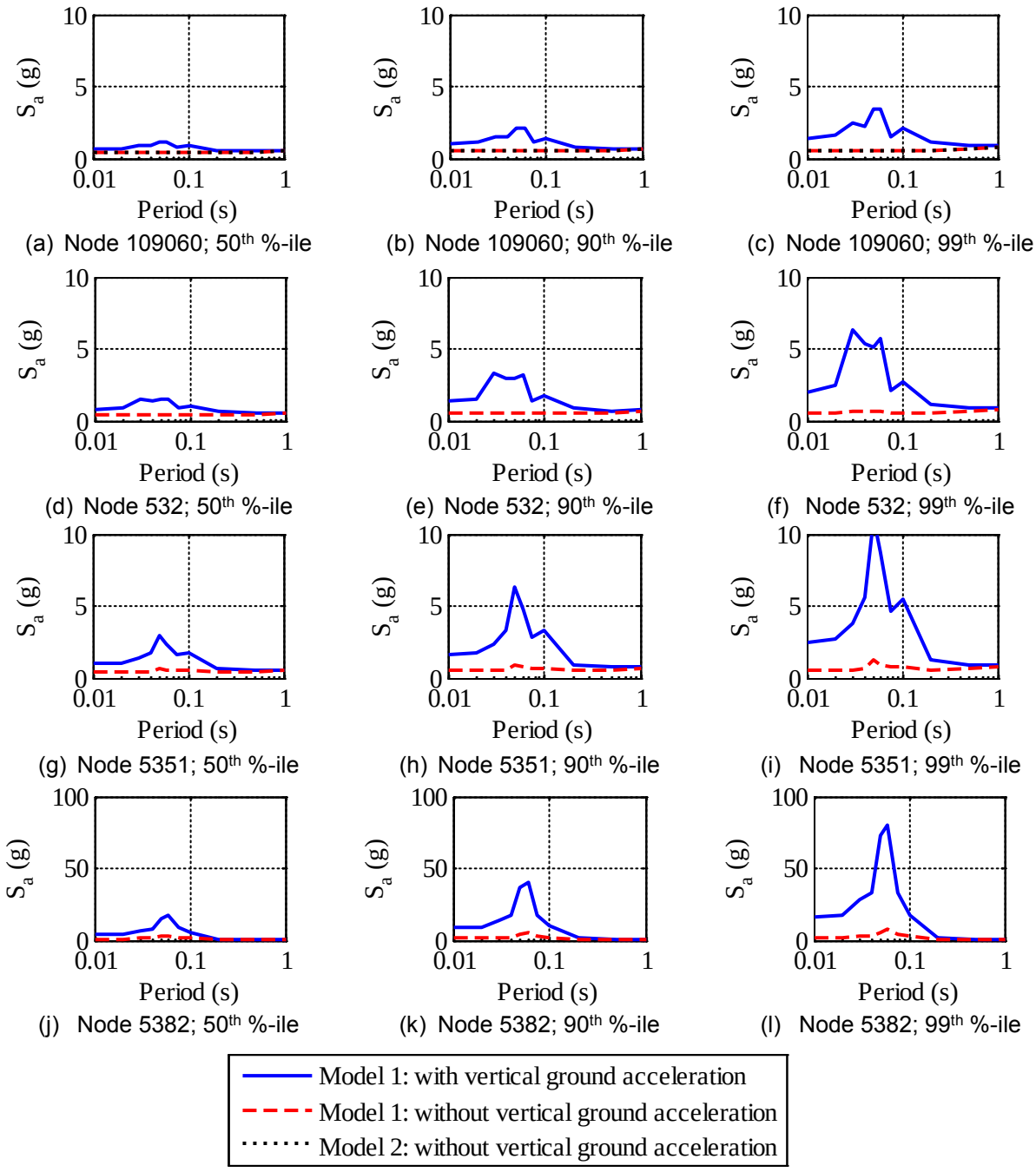

Figure 8-32 Floor Spectra in the X Direction at Different Nodes of the CIS Computed Using the Two Nuclear Island Models with Friction at the Sliding Surface Described Using the Pressure-Dependent Model Subjected to the Set of 30 Ground Motions Amplitude Scaled by 2.0

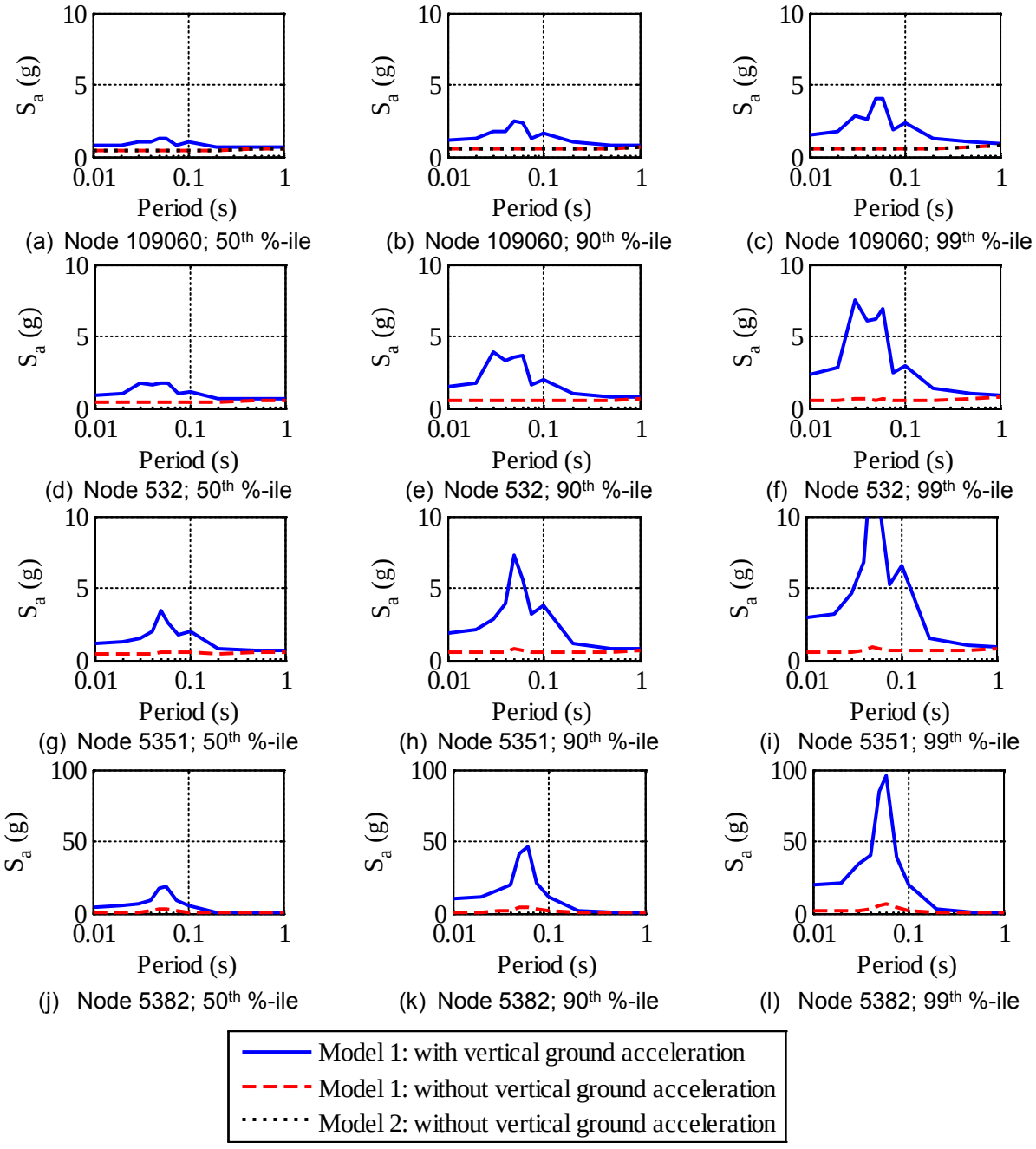

Figure 8-33 Floor Spectra in the X Direction at Different Nodes of the CIS Computed Using the Two Nuclear Island Models with Friction at the Sliding Surface Described Using the *p-T-v* Model Subjected to the Set of 30 Ground Motions Amplitude Scaled by 2.0

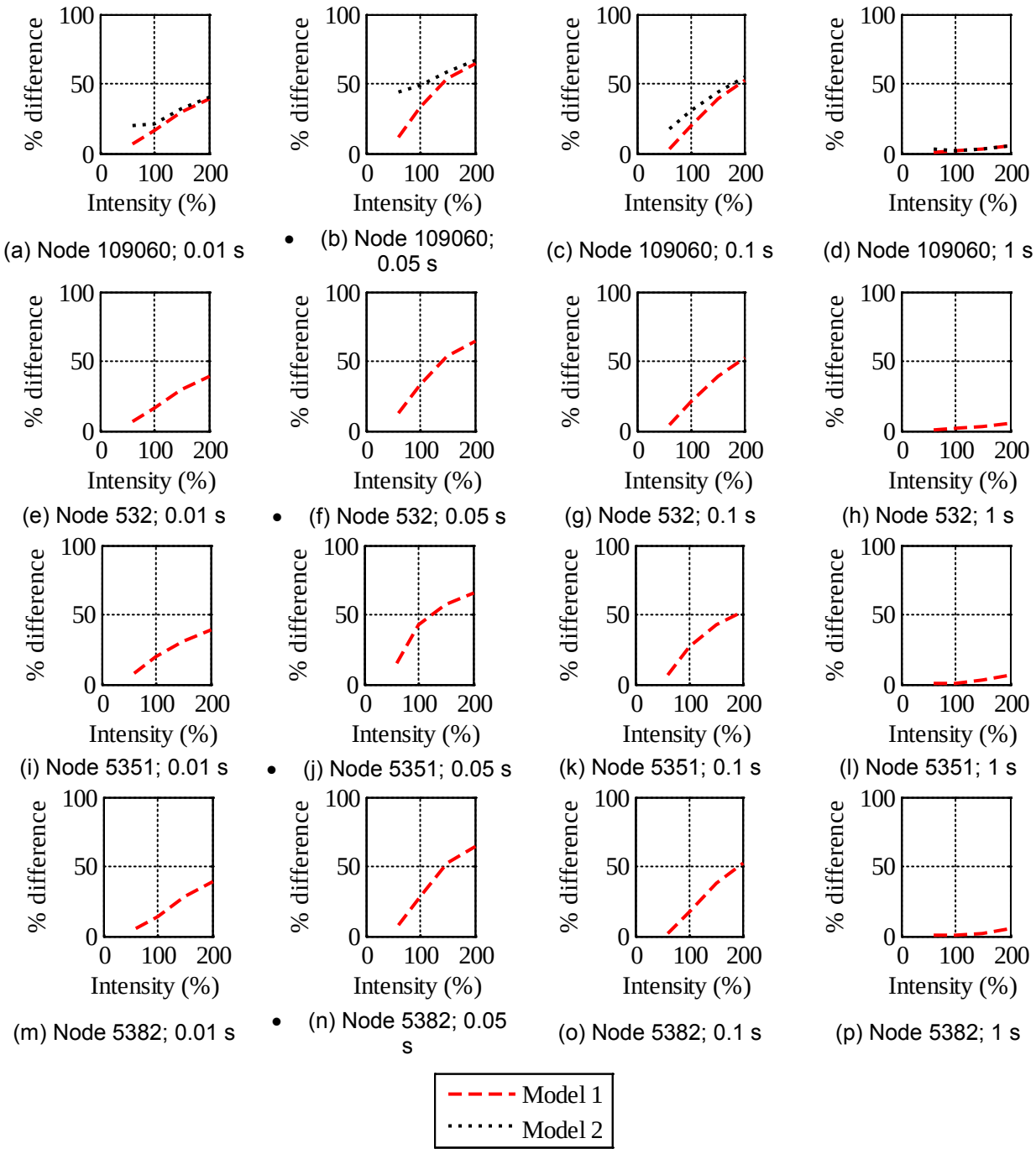

Figure 8-34 Percentage Difference Between the Median Floor Spectral Ordinates Computed Using the Two Nuclear Island Models Subjected to Two Horizontal Components of Ground Motions Relative to That Computed Using Model 1 Subjected to Three Components of the Ground Motion

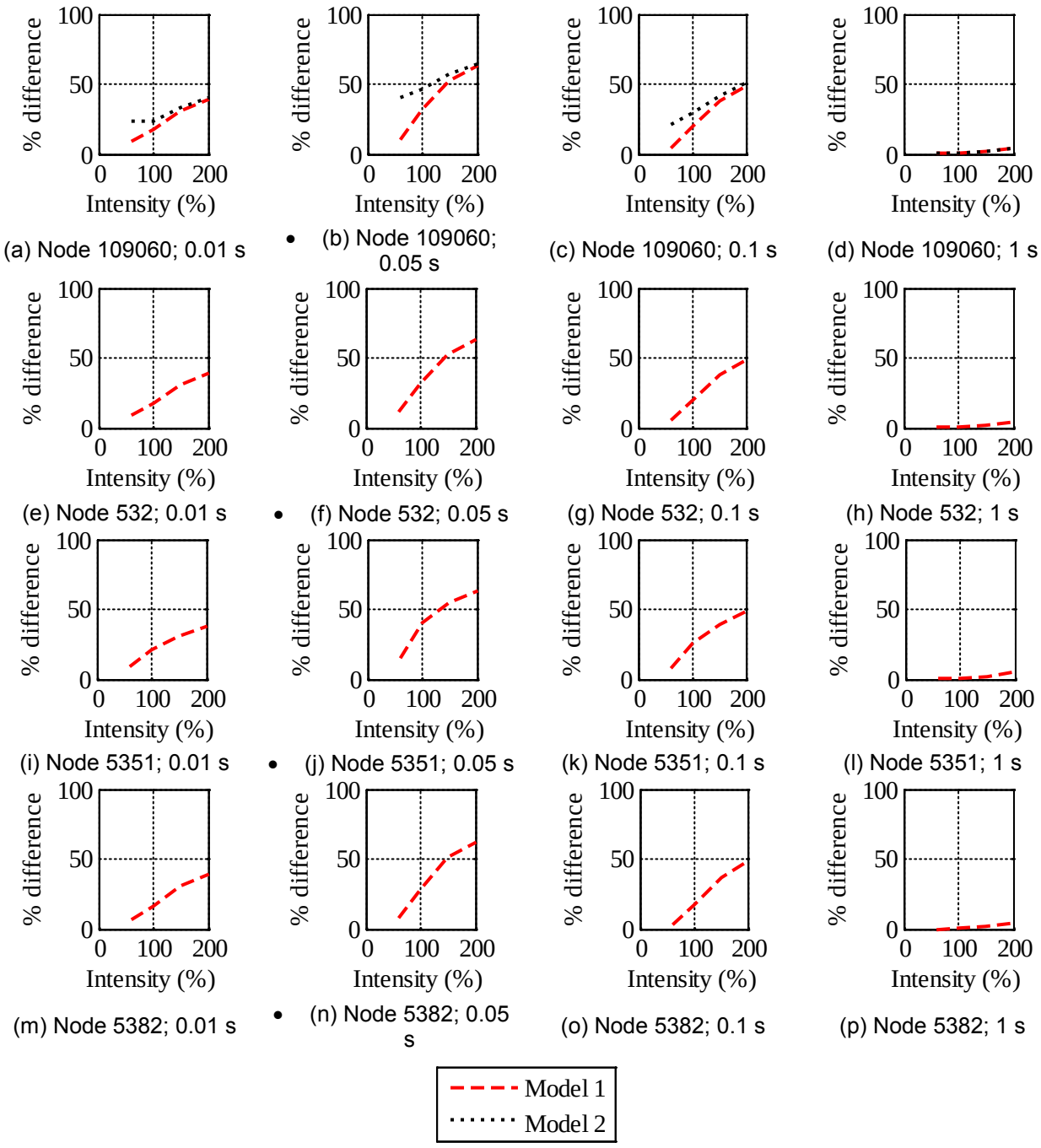

Figure 8-35 Percentage Difference Between the 90th Percentile Floor Spectral Ordinates Computed Using the Two Nuclear Island Models Subjected to Two Horizontal Components of Ground Motions Relative to That Computed Using Model 1 Subjected to Three Components of the Ground Motion

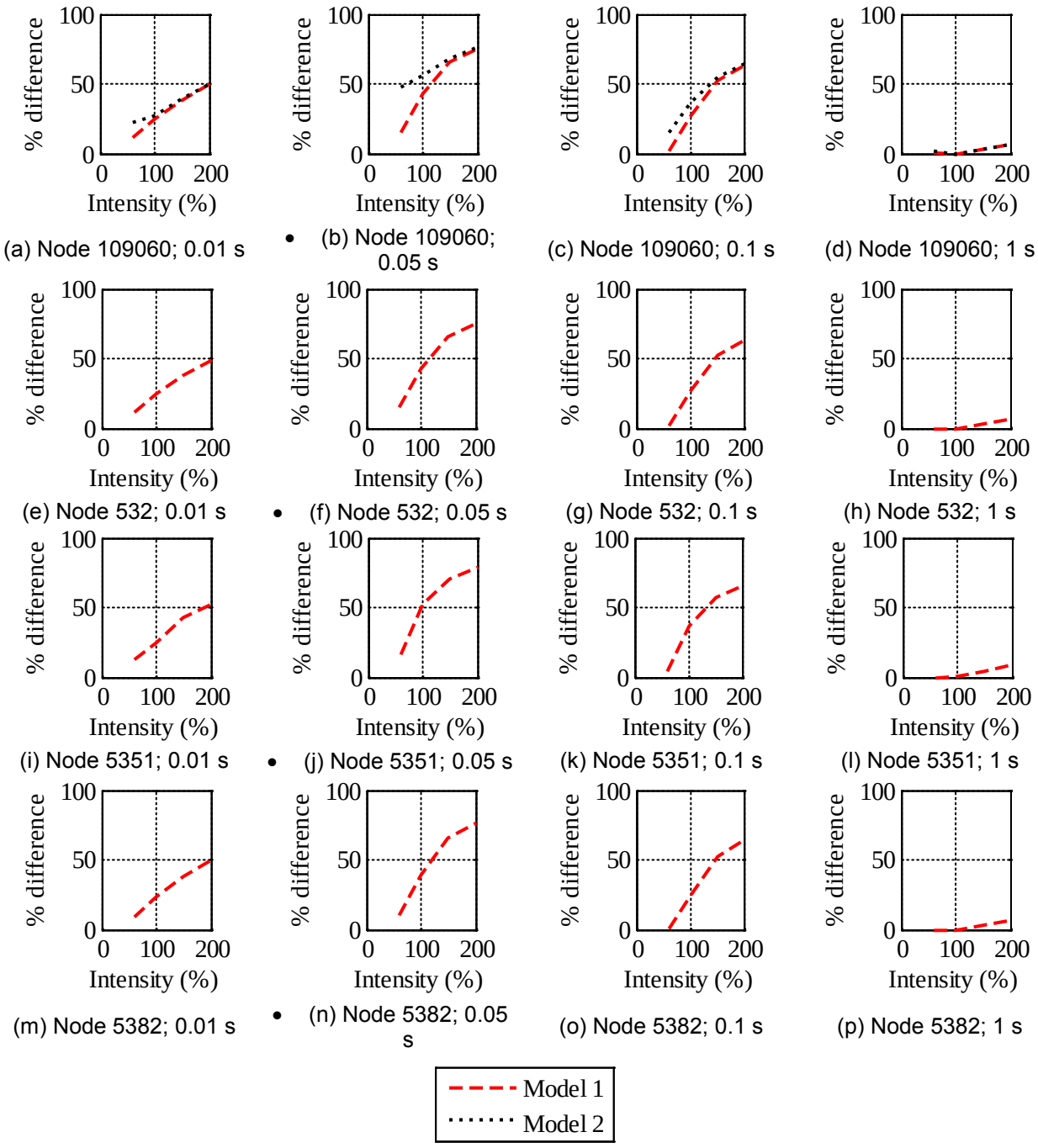

Figure 8-36 Percentage Difference Between the 99th Percentile Floor Spectral Ordinates Computed Using the Two Nuclear Island Models Subjected to Two Horizontal Components of Ground Motions Relative to That Computed Using Model 1 Subjected to Three Components of the Ground Motion

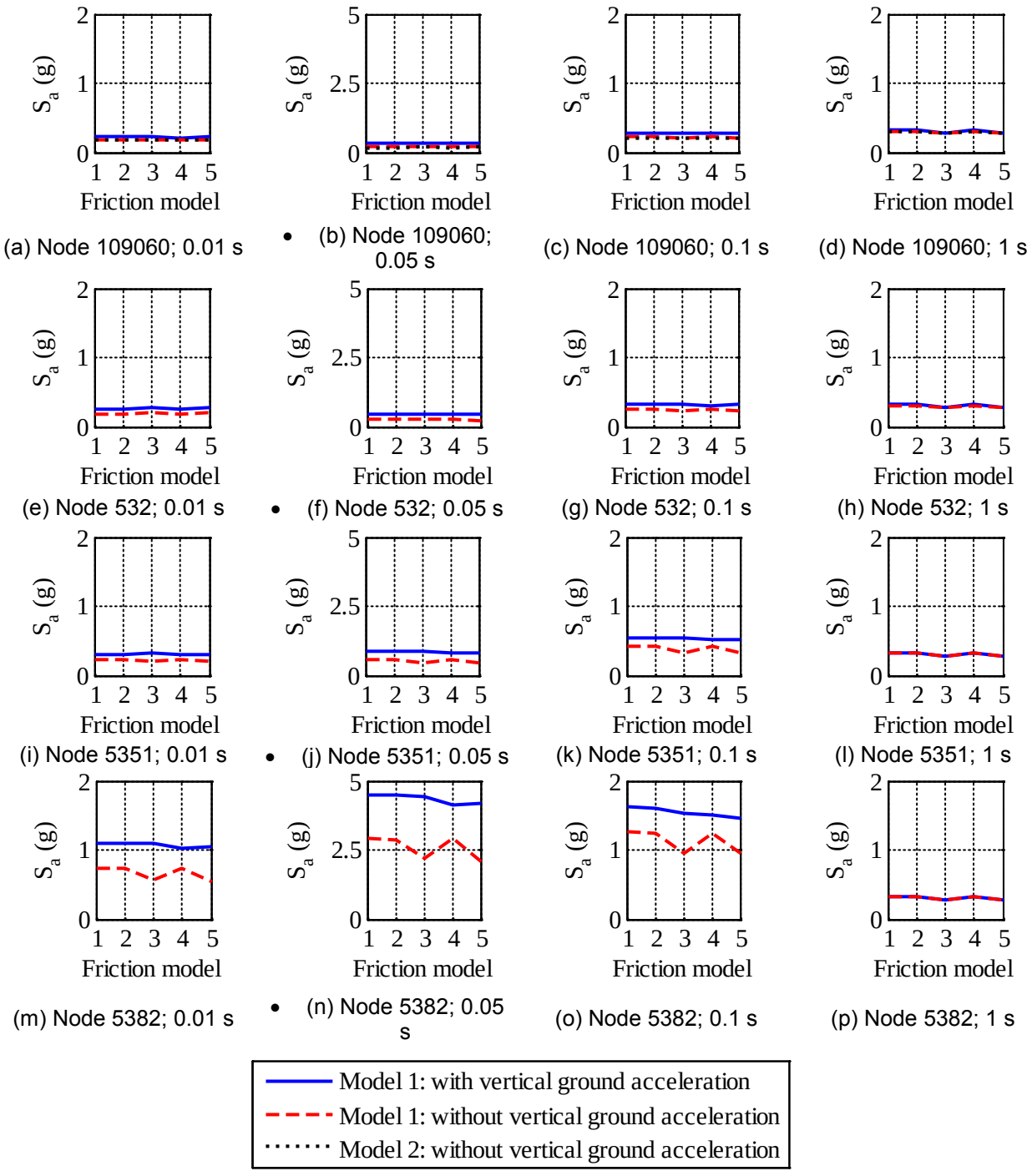

Figure 8-37 Median Spectral Accelerations in the X Direction for Four Nodes of the CIS Subjected to 30 Ground Motions Amplitude Scaled by 1.0; Friction Models 1 Through 5, Respectively, Denote Coulomb, Pressure-Dependent, Temperature-Dependent, Velocity-Dependent and *p-T-v* Models

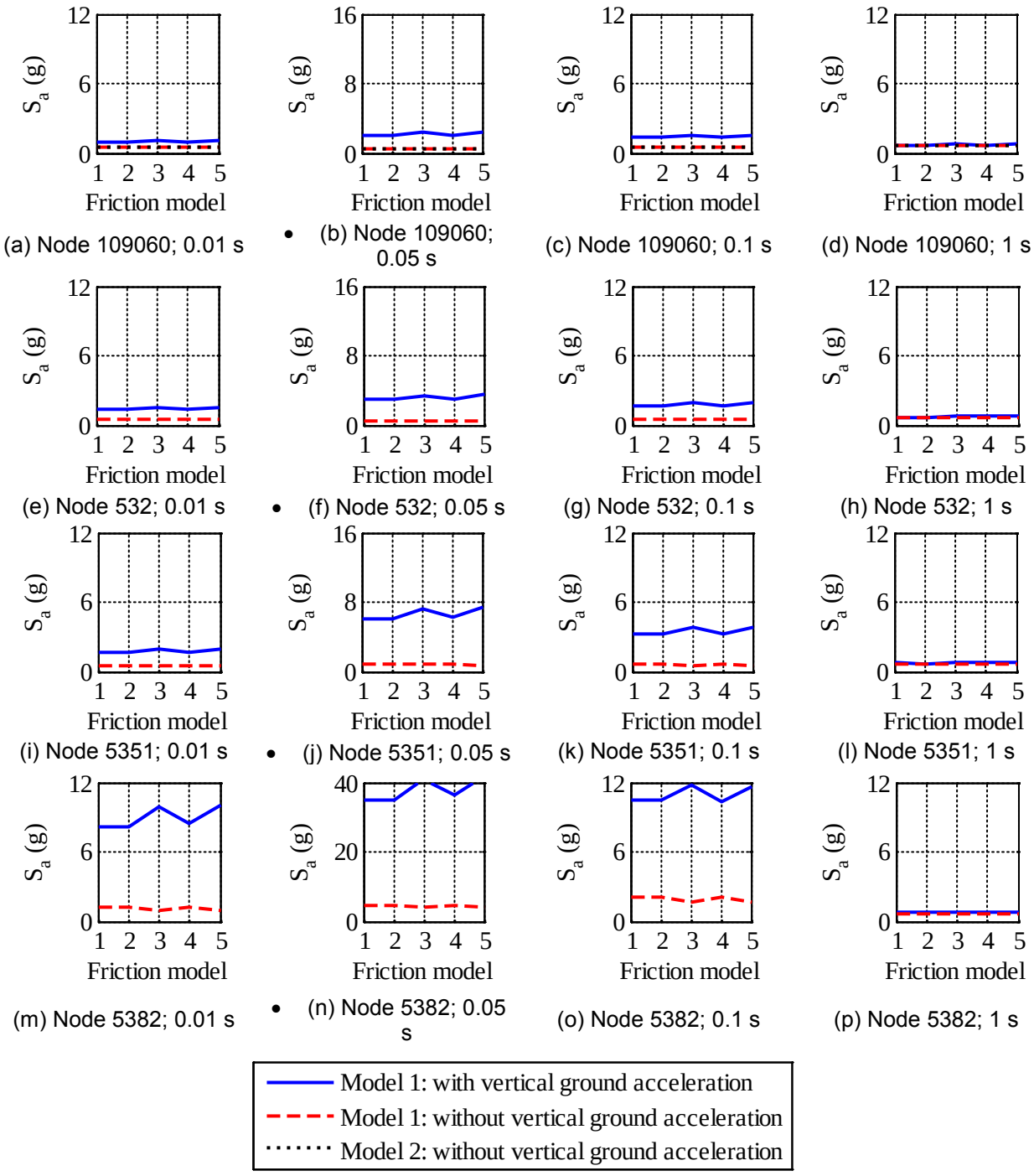

Figure 8-38 Spectral Accelerations at the 90th Percentile in the X Direction for Four Nodes of the CIS Subjected to 30 Ground Motions Amplitude Scaled by 2.0; Friction Models 1 Through 5, Respectively, Denote Coulomb, Pressure-Dependent, Temperature-Dependent, Velocity-Dependent and *p-T-v* Models

9 SUMMARY AND CONCLUSIONS

9.1 Introduction

In the United States, nuclear power plants (NPPs) are designed for severe internal and external natural and man-made hazards, including earthquakes. Severe earthquakes can challenge new and existing NPPs, with large forces expected in their internal structures, systems and components (SSCs) in design basis shaking. Base isolation is a viable strategy to seismically protect SSCs in NPPs, since it effectively filters a significant fraction of the high frequency, horizontal earthquake shaking, and it facilitates standardization of plant designs. Sliding isolators, here single concave Friction Pendulum™ (FP) bearings, are one type of hardware that could be used in the United States for safety-related nuclear structures, including nuclear power plants.

This report is composed of three key parts: 1) modeling of the coefficient of friction at the sliding surface of a single concave FP bearing, 2) characterization of seismic hazard for a seismically isolated nuclear power plants, and 3) results of response-history analyses performed using different models of FP isolated nuclear power plants.

9.2 Characterizing Friction in Sliding Isolation Bearings

9.2.1 Summary

Expressions to define the relationships between the coefficient of sliding friction and sliding velocity, axial pressure and temperature at the sliding surface are developed based in large part on past experiments. These expressions are coded into a new OpenSees element *FPBearingPTV*, which simulates the behavior of a single FP bearing. The assumptions involved in the modeling of the bearing are studied and the software is *verified* and *validated* using the procedure outlined in ASME (2006) and presented in Oberkampf and Roy (2010).

9.2.2 Conclusions

The key conclusions from the study on the characterization of the coefficient of friction are:

i. The assumption that the small-velocity coefficient of friction is half the high-velocity coefficient of friction does not affect the displacement response of a seismically isolated nuclear power plant, except for very low intensity shaking, which is of no practical importance.

ii. The temperature at the center of the sliding surface can be considered to represent the temperature of the sliding surface for the purpose of response-history analyses of the isolated structures.

iii. The infinite half-space assumption for the temperature calculations leads to reasonable predictions of the force-displacement response of FP bearings. Radiation losses are small and need not be considered in the temperature calculations.

iv. The new OpenSees element *FPBearingPTV* simulates the lateral force-displacement response of single FP bearings.

9.3 Representations of Seismic Hazard for Isolated Nuclear Power Plants

9.3.1 Summary

The seismic isolation NUREG/CR 7253 (Kammerer *et al.*, 2019) recommends that two levels of seismic hazard be considered for the analysis and design of seismically isolated NPPs in the United States: a ground motion response spectrum+ (GMRS+) and an beyond design basis (BDB) GMRS. The GMRS is defined as the product of a design factor and the uniform hazard response spectrum (UHRS) with a mean annual frequency of exceedance (MAFE) of 10^{-4} (return period of 10,000 years). The GMRS+ is the envelope of the GMRS and a regulator-specific minimum response spectrum (e.g., an appropriate spectral shape anchored to a peak ground acceleration of 0.1 g). The BDB GMRS is the UHRS at an MAFE of 10^{-5} (return period of 100,000 years) but can be no less than 1.67 times GMRS+.

The seismic isolation NUREG/CR recommends prototype isolators be tested at a horizontal displacement corresponding to the clearance between the isolated superstructure and the stop: the clearance to the stop (CS). The distance CS is determined by nonlinear response-history analysis and the NUREG/CR recommends it to be greater than the 99th (90th) percentile displacement for GMRS+ (BDB GMRS shaking). Distributions of peak isolation-system displacement (and thus the CS) can be substantially influenced by the definition of seismic hazard. Three alternate representations of seismic hazard are considered herein: UHRS, conditional mean spectrum (CMS) and conditional spectra (CS). The horizontal spectrum for each representation is a geometric mean spectrum of the two horizontal components. Sets of spectrally matched ground motions consistent with the 10,000-year and 100,000-year UHRS, CMS and CS are developed for the site of the Diablo Canyon Nuclear Generating Station, a site of high seismicity. An additional set of ground motions, UHRS with *maximum* and *minimum* components (UHRS-MaxMin), is generated for each return period, to recognize the difference in shaking along perpendicular horizontal axes that is observed in recorded ground motions. Single FP bearings with a range of geometrical and material properties are subjected to these four representations of ground shaking and the distributions of peak displacement are studied.

9.3.2 Conclusions

The following conclusions are drawn from the study on alternate representations of seismic hazard:

i. Distributions of peak displacement are significantly influenced by the choice of target spectrum. The choice of seed ground motions does not affect the distributions.

ii. The 90th percentile peak displacement for 100,000-year shaking is greater than the 99th percentile peak displacement for 10,000-year shaking, for a given target spectrum (or spectra), and dictates the required clearance to the stop.

iii. The UHRS-, CMS- and CS-displacements are comparable at the 90th percentile for the two levels of shaking. The 90th percentile UHRS-MaxMin displacements are substantially greater than those for the UHRS, CMS or CS, at the two levels of shaking. Seismic hazard for isolated nuclear power plants should be defined using a UHRS appropriately considering the differences between the two orthogonal horizontal components (i.e., UHRS-MaxMin motions).

iv. The choice of friction model has a considerable influence on the peak displacement of the isolation system, especially for sites of intense shaking and isolators with high contact pressures and high reference coefficient of friction. The temperature dependence of the coefficient of friction should be addressed in the calculation of the clearance to the stop: 90th percentile displacement for 100,000-year shaking.

9.4 Earthquake Risk for Seismically Isolated Nuclear Power Plants

9.4.1 Summary

The key performance goals for seismically isolated nuclear power plants, as outlined in the seismic isolation NUREG/CR 7253 (Kammerer *et al*., 2019), are: 1) the probability of the isolated superstructure striking the stop should be less than 10% for BDB GMRS shaking, 2) the probability of loss of axial load capacity of an individual isolator unit should be less than 10% at the 90th percentile BDB GMRS displacement, and 3) the probability of loss of function of the safety-related umbilical line should be less than 10% at the 90th percentile BDB GMRS displacement. The first goal is achieved by installing the stop (see Section 9.3.1) at a clear distance from the isolated superstructure at a displacement no less than the 90th percentile BDB GMRS displacement. The performance goal for individual isolators is achieved by prototype testing. The performance goal for the safety-related umbilical lines can be realized by a combination of analysis and testing. In this report, the mean annual frequencies of unacceptable performance of isolation systems (and umbilical lines) are calculated for eight sites of nuclear facilities across the United States, representing regions of low, moderate and high seismic hazard. The purpose of the calculations are two-fold, namely, 1) provide a roadmap for an applicant to calculate the earthquake risk associated with a seismic isolation system with a given horizontal displacement capacity, and 2) provide the US Nuclear Regulatory Commission (Chapter 6) and the US Department of Energy (Appendix F) with insight into the risk associated with a seismic isolation system, with and without a stop present.

Median fragility curves are developed for isolators tested at different displacements (e.g., 90th percentile displacement for BDB GMRS shaking in Chapter 6 and 90th percentile displacement for 150% DBE shaking in Appendix F) at different confidence levels (e.g., 90%). The stop is accounted for by truncating the fragility curve at the failure probability with which the isolators are tested (e.g., 10%). To enable the risk calculations, the hazard curves are defined in Chapter 6 as multiples of the GMRS (equal to the UHRS at an MAFE of 10^{-4}), which is taken as the average of the multiples of the GMRS ordinates at 1 s and 2 s. The fragility and hazard curves for the umbilical lines are identical to those for the individual isolators.

The earthquake risk associated with individual isolators is quantified in terms of annual frequency of unacceptable performance: providing a benchmark against which to compare risk reduction strategies. The risk associated with the isolation system is (very) conservatively set equal to the mean annual frequency of failure for individual isolators, noting that although isolator capacities are likely highly correlated if nuclear-industry quality assurance/quality control procedures are followed, isolator demands are likely weakly correlated. Three risk-reduction strategies are considered: 1) testing the prototype isolators with a greater confidence at a given displacement, 2) testing the isolators for a greater displacement and corresponding axial force at a given confidence level, and 3) providing a stop (which is recommended for USNRC-regulated isolated nuclear power plants). The annual frequency of unacceptable performance of individual bearings (loss of axial load capacity at the CS displacement) is calculated in Chapter 6 at eight sites of nuclear facility located across the United States. Companion calculations for Seismic Design Category 5 nuclear structures per ASCE 43-05

(ASCE, 2005) are presented in Appendix F. Median fragility curves are conservatively derived (overestimating risk) by setting the 90th percentile displacement for BDB GMRS shaking (or 150% DBE shaking in ASCE 43 space) equal to the median displacement for 110% BDB GMRS shaking (or 165% DBE shaking in ASCE 43 space).

9.4.2 Conclusions

The following conclusions are drawn on the subject of earthquake risk of seismically isolated nuclear power plants:

i. The mean annual frequency of unacceptable performance of individual isolators (and umbilical lines) tested in accordance with the recommendations of the seismic isolation NUREG/CR (i.e., 90% confidence at 90th percentile displacement for BDB GMRS shaking) ranges between 4.7×10^{-6} and 7.3×10^{-6} for a log standard deviation of 0.05: values substantially greater than a target goal of 1×10^{-6}. The risk is reduced in a meaningful manner if testing is performed to either the same displacement but higher confidence or the same confidence and greater displacement, but remains greater than 1×10^{-6}. The introduction of a stop at the 90th percentile displacement for BDB GMRS shaking achieves the goal of driving the risk below 1×10^{-6}. If the confidence level is increased from 90% to 99%, the risk drops well below 1×10^{-7}.

ii. A stop is generally needed to reduce the annual frequency of unacceptable performance of a DoE-regulated SDC 5 isolated safety-related nuclear structure below the target goal of 1×10^{-5}.

iii. The ground motion response spectrum in NRC space and the design response spectrum in DOE space are calculated for design of nuclear power plants (and other SDC 5 structures) by multiplying the ordinates of a uniform hazard response spectrum at the specified hazard exceedance frequency by a design factor that is greater than or equal to 1.0. The factor can be set equal to 1.0 for design of a seismically isolated nuclear power plant if the earthquake risk is dominated by horizontal ground shaking and a stop is provided.

9.5 Response of Seismically Isolated Nuclear Power Plants

9.5.1 Summary

The response of a sample nuclear power plant isolated on single concave FP™ bearings is studied to understand what design decisions most affect behavior. Two sites are considered, namely, Diablo Canyon and Vogtle, sites of high and moderate seismicity, respectively. Alternate models of the sample power plant are considered. Friction Pendulum bearings with a range of sliding periods, reference coefficients of friction, and reference axial pressures are considered with friction at the sliding surface defined using models that account for the pressure-, temperature- and/or velocity-dependencies.

9.5.2 Conclusions

The following conclusions are drawn from the response-history analyses presented in Chapters 7 and 8 and are specific to the type of composite material used in the FP bearing:

i. Isolation-system horizontal displacement can be estimated for preliminary design using a macro model (single bearing) of the isolation system. Considering the vertical component of ground motion in the response-history analysis does not change the horizontal displacement response, which was first observed in the experiments of Mosqueda *et al.* (2004).

ii. The friction model used to compute isolation-system displacement should include the heating effects. Displacements may be significantly underestimated if the heating effects are ignored and if the reference axial pressure, reference coefficient of friction and/or shaking intensity are high.

iii. The friction model need not consider the velocity- and pressure-dependence of the coefficient of friction to compute isolation-system displacement.

iv. Floor spectra in isolated nuclear structures should be computed using a detailed 3D finite element model of the isolated superstructure. Vertical ground motion must be included to compute horizontal floor spectra. The choice of friction model does not significantly influence the floor spectral ordinates.

10 REFERENCES

[1] Aiken, I. D., Nims, D. K., Whittaker, A. S., and Kelly, J. M. (1993). "Testing of passive energy dissipation systems." *Earthquake Spectra*, 9(3), 335-370.

[2] Al-Hussaini, T. M., Zayas, V. A., and Constantinou, M. C. (1994). "Seismic isolation of multi-story frame structures using spherical sliding isolation systems." Report NCEER-94-0007, University at Buffalo, State University of New York, Buffalo, NY.

[3] Almazán, J. L., De La Llera, J. C., and Inaudi, J. A. (1998). "Modeling aspects of structures isolated with the frictional pendulum system." *Earthquake Engineering & Structural Dynamics*, 27(8), 845-867.

[4] American Concrete Institute (ACI). (2013a). "Code requirements for nuclear safety-related concrete structures and commentary." ACI Standard 349-13, Farmington Hills, MI.

[5] American Concrete Institute (ACI). (2013b). "Code for concrete containments. " ACI Standard 359-13, Farmington Hills, MI.

[6] American Institute of Steel Construction (AISC). (2012). "Specification for safety-related steel structures for nuclear facilities." ANSI/AISC N690-12, Chicago, IL.

[7] American Nuclear Society (ANS). (2010). "Categorization of nuclear facility structures, systems, and components for seismic design." ANSI/ANS-2.26-2004, La Grange Park, IL.

[8] American Society of Civil Engineers (ASCE). (2005). "Seismic design criteria for structures, systems and components in nuclear facilities." ASCE/SEI Standard 43-05, Reston, VA.

[9] American Society of Civil Engineers (ASCE). (2010). "Minimum design loads for buildings and other structures." ASCE/SEI Standard 7-10, Reston, VA.

[10] American Society of Civil Engineers (ASCE). (2017). "Seismic analysis of safety-related nuclear structures and commentary." ASCE/SEI Standard 4-16, Reston, VA.

[11] Arya, A. S. (1984). "Sliding concept for mitigation of earthquake disaster to masonry buildings." *Proceedings, Eighth World Conference on Earthquake Engineering*, San Francisco, CA.

[12] American Society of Mechanical Engineers (ASME). (2006). "Guide for verification and validation in computational solid mechanics." ASME Standard V&V 10-2006, New York, NY.

[13] Badillo-Almaraz, H., Whittaker, A. S., and Reinhorn, A. M. (2007). "Seismic fragility of suspended ceiling systems." *Earthquake Spectra*, 23(1), 21-40.

[14] Baker, J. W., and Cornell, C. A. (2006). "Spectral shape, epsilon and record selection." *Earthquake Engineering & Structural Dynamics*, 35(9), 1077-1095.

[15] Baker, J. W., and Jayaram, N. (2008). "Correlation of spectral acceleration values from NGA ground motion models." *Earthquake Spectra*, 24(1), 299-317.

[16] Bathe, K. J. (1996). "Finite element procedures." Prentice-Hall, NJ.

[17] Benjamin, J. R., and Cornell, C. A. (1970). "Probability, statistics, and decision for Civil engineers." McGraw-Hill, New York, NY.

[18] Beyer, K., and Bommer, J. J. (2006). "Relationships between median values and between aleatory variabilities for different definitions of the horizontal component of motion." *Bulletin of the Seismological Society of America*, 96(4A), 1512-1522.

[19] Boore, D. M., Watson-Lamprey, J., and Abrahamson, N. (2006). "Orientation-independent measures of ground motion." *Bulletin of the Seismological Society of America*, 96(4A), 1502-1511.

[20] Buckle, I. G. (1985). "New Zealand seismic base isolation concepts and their application to nuclear engineering." *Nuclear Engineering and Design*, 84(3), 313-326.

[21] Buckle, I. G., and Mayes, R. L. (1990). "Seismic isolation: history, application and performance-a world view." *Earthquake Spectra*, 6(2), 161-201.

[22] Burningham, C., Mosqueda, G., and Saavedra, R. R. (2007). "Comparison of seismic fragility of free standing equipment using current testing protocols and recorded building floor motions." *Proceedings, Earthquake Engineering Symposium for Young Researchers*, August 8-12, Seattle, WA.

[23] Campbell, K. W., and Bozorgnia, Y. (2008). "NGA ground motion model for the geometric mean horizontal component of PGA, PGV, PGD and 5% damped linear elastic response spectra for periods ranging from 0.01 to 10 s." *Earthquake Spectra*, 24(1), 139-171.

[24] Civil Engineering Research Foundation (CERF). (1998). "Evaluation findings for Earthquake Protection Systems, Inc. Friction Pendulum bearings.", Report HITEC 98-07#40370, Highway Innovative Technology Evaluation Center, Washington, D.C.

[25] Chang, K. C., Hwang, J. S., and Lee, G. C. (1990). "Analytical model for sliding behavior of Teflon-stainless steel interfaces." *Journal of Engineering Mechanics*, 116(12), 2749-2763.

[26] Chopra, A. (2007). "Dynamics of structure–Theory and applications to earthquake engineering." Pearson Education, Upper Saddle River, NJ.

[27] Christopoulos, C., and Filiatrault, A. (2006). "Principles of passive supplemental damping and seismic isolation." IUSS Press, Pavia, Italy.

[28] Chung, J., and Hulbert, G. M. (1993). "A time-integration algorithm for structural dynamics with improved numerical dissipation: the generalized-α method." *ASME Journal of Applied Mechanics*, 60, 371-375.

[29] Cizelj, L., and Simonovski, I. (2011). "Fatigue relevance of stratified flows in pipes: A parametric study." *Nuclear Engineering and Design*, 241(4), 1191-1195.

[30] Clark, P. W., Aiken, I. D., Nakashima, M., Miyazaki, M., and Midorikawa, M. (1999). "The 1995 Kobe (Hyogo-ken Nanbu) earthquake as a trigger for implementing new seismic design technologies in Japan." *Lessons Learned Over Time, Learning From Earthquakes Series*, Vol. III, Earthquake Engineering Research Institute, CA.

[31] Clark, P. W., Higashino, M., and Kelly, J. M. (1996). "Performance of seismically isolated structures in the January 17, 1994 Northridge earthquake." *Proceedings, Sixth U.S.-Japan Workshop on the Improvement of Building Structural Design and Construction Practices in the United States and Japan*, Victoria, B.C., Canada.

[32] Clarke, C. S. J., Buchanan, R., Efthymiou, M., and Shaw, C. (2005). "Structural platform solution for seismic arctic environments--Sakhalin II offshore facilities." *Proceedings, Offshore Technology Conference*, Houston, TX.

[33] Constantinou, M. C., and Symans, M. D. (1992). "Experimental and analytical investigation of seismic response of structures with supplemental fluid viscous dampers." Report NCEER-92-0032, University at Buffalo, State University of New York, Buffalo, NY.

[34] Constantinou, M. C., Kalpakidis, I., Filiatrault, A., and Lay, R. A. E. (2011). "LRFD-based analysis and design procedures for bridge bearings and seismic isolators." Report MCEER-11-0004, University at Buffalo, State University of New York, Buffalo, NY.

[35] Constantinou, M. C., Tsopelas, P., Kasalanati, A., and Wolff, E. D. (1999). "Property modification factors for seismic isolation bearings." Report MCEER-99-0012, University at Buffalo, State University of New York, Buffalo, NY.

[36] Constantinou, M. C., Tsopelas, P., Kim, Y.-S., and Okamoto, S. (1993). "NCEER-Taisei Corporation research program on sliding seismic isolation systems for bridges: Experimental and analytical study of a Friction Pendulum System (FPS)." Report NCEER-93-0020, University at Buffalo, State University of New York, Buffalo, NY.

[37] Constantinou, M. C., Whittaker, A. S., Kalpakidis, Y., Fenz, D. M., and Warn, G. P. (2007). "Performance of seismic isolation hardware under service and seismic loading." Report MCEER-07-0012, University at Buffalo, State University of New York, Buffalo, NY.

[38] Computers and Structures Incorporated (CSI). (2013). SAP2000 (Version 15.2.1) [Computer Program], Berkeley, CA.

[39] Dao, N. D., Ryan, K. L., Sato, E., and Sasaki, T. (2013). "Predicting the displacement of triple pendulum™ bearings in a full-scale shaking experiment using a three-dimensional element." *Earthquake Engineering & Structural Dynamics*, 42(11), 1677-1695.

[40] Dassault Systemes (DS). (2013). ABAQUS/CAE 6.10-EF2 (Version 6.10-EF2) [Computer program], Waltham, MA.

[41] Drozdov, Y. N., Nadein, V. A., and Puchkov, V. N. (2007). "The effect of earthquake parameters on the tribological characteristics of friction pendulum bearings (seismic isolators)." *Journal of Machinery Manufacture and Reliability*, 36(2), 143-152.

[42] Drozdov, Y. N., Nadein, V. A., and Puchkov, V. N. (2010). "Seismic isolators for petroleum and gas platforms of the “Sakhalin-2” project." *Journal of Machinery Manufacture and Reliability*, 39(6), 591-604.

[43] Earthquake Protection Systems (EPS). (2011). "Earthquake protection systems", <http://www.earthquakeprotection.com/index.html>. (May 18, 2012).

[44] Federal Emergency Management Agency (FEMA). (2012). "Seismic performance assessment of buildings, Volume 1: methodology." FEMA P-58-1, Washington, D.C.

[45] Fenz, D. M., and Constantinou, M. C. (2006). "Behaviour of the double concave Friction Pendulum bearing." *Earthquake Engineering & Structural Dynamics*, 35(11), 1403-1424.

[46] Fenz, D. M., and Constantinou, M. C. (2008a). "Modeling Triple Friction Pendulum bearings for response-history analysis." *Earthquake Spectra*, 24(4), 1011.

[47] Fenz, D. M., and Constantinou, M. C. (2008b). "Mechanical behavior of multi-spherical sliding bearings." Report MCEER-08-0007, University at Buffalo, State University of New York, Buffalo, NY.

[48] Fenz, D. M., Seed, R., Slatnick, S., Stewart, H. R., and Constantinou, M. C. (2011). "Development of performance-based testing specifications for the Arkutun-Dagi Friction Pendulum bearings." *Proceedings, Arctic Technology Conference*, February 7-9, Houston, TX.

[49] Filiatrault, A., Kuan, S., and Tremblay, R. (2004). "Shake table testing of bookcase – partition wall systems." *Canadian Journal of Civil Engineering*, 31(4), 664-676.

[50] Grandis, S. D., Forni, M., Bruyn, D. D., and Cardini, S. (2011). "Seismic isolation of Gen IV lead-cooled reactors." *Transactions, 21st International Conference on Structural Mechanics in Reactor Technology (SMiRT21)*, November 6-11, New Delhi, India.

[51] Gülerce, Z., and Abrahamson, N. A. (2011). "Site-specific design spectra for vertical ground motion." *Earthquake Spectra*, 27(4), 1023-1047.

[52] Hancock, J., Watson-Lamprey, J., Abrahamson, N., Bommer, J., Markatis, A., McCoy, E., and Mendis, R. (2006). "An improved method of matching response spectra of recorded earthquake ground motion using wavelets." *Journal of Earthquake Engineering*, 10 (Special Issue 1), 67-89.

[53] Hilber, H. M., Hughes, T. J., and Taylor, R. L. (1977). "Improved numerical dissipation for time integration algorithms in structural dynamics." *Earthquake Engineering & Structural Dynamics*, 5(3), 283-292.

[54] Huang, Y.-N. (2008). "Performance assessment of conventional and base-isolated nuclear power plants for earthquake and blast loadings." PhD dissertation, University at Buffalo, State University of New York, Buffalo, NY.

[55] Huang, Y.-N., Whittaker, A. S., and Luco, N. (2010). "Seismic performance assessment of base-isolated safety-related nuclear structures." *Earthquake Engineering & Structural Dynamics*, 39(13), 1421-1442.

[56] Huang, Y.-N., Whittaker, A. S., Constantinou, M. C., and Malushte, S. (2007). "Seismic demands on secondary systems in base-isolated nuclear power plants." *Earthquake Engineering & Structural Dynamics*, 36(12), 1741-1761.

[57] Huang, Y.-N., Whittaker, A. S., Kennedy, R. P., and Mayes, R. L. (2013). "Response of base-isolated nuclear structures for design and beyond-design basis earthquake shaking." *Earthquake Engineering & Structural Dynamics*, 42(3), 339-356.

[58] Huang, Y.-N., Whittaker, A. S., Kennedy, R. P., and Mayes, R. L. (2009). "Assessment of base-isolated nuclear structures for design and beyond-design basis earthquake shaking." Report MCEER-09-0008, University at Buffalo, State University of New York, Buffalo, NY.

[59] Inagaki, Y., Kunitomi, K., Futakawa, M., Ikuo, I., and Kaji, Y. (2004). "R&D on high temperature components." *Nuclear Engineering and Design*, 233(1–3), 211-223.

[60] Incropera, F. P., and Dewitt, D. P. (1985). "Introduction to heat transfer." John Wiley & Sons, New York, NY.

[61] Izumi, M. (1988). "State-of-the art report: Base isolation and passive seismic response control." *Proceedings, Ninth World Conference on Earthquake Engineering*, August 2-9, 1988, Tokyo, Japan.

[62] Jarque, C. M., and Bera, A. K. (1987). "A test for normality of observations and regression residuals." *International Statistical Review / Revue Internationale de Statistique*, 55(2), 163-172.

[63] Jayaram, N., Lin, T., and Baker, J. W. (2011). "A computationally efficient ground-motion selection algorithm for matching a target response spectrum mean and variance." *Earthquake Spectra*, 27(3), 797-815.

[64] Kadak, A. C. B., Ronald G.; Driscoll, Michael J.; Yip, Sidney; Wilson, David Gordon; No, Hee Cheon; Wang, Jing; MacLean, Heather; Galen, Tamara; Wang, Chunyun; Lebenhaft, Julian; Zhai, Tieliang; Petti, David A.; Terry, William K.; Gougar, Hans D.; Ougouag, Abderrafi M.; Oh, Chang H.; Moore, Richard L.; Miller, Gregory K.; Maki, John T.; Smolik, Galen R.; Varacalle, Dominic J. (2000). "Modular pebble bed reactor." Report INEEL/EXT-2000-01034, Center for Advanced Nuclear Energy Systems, Massachusetts Institute of Technology, Cambridge, MA.

[65] Kammerer, A. M., Whittaker, A. S., and Constantinou, M. C. (2019). "Technical considerations for seismic isolation of nuclear facilities." Report NUREG/CR 7253, United States Nuclear Regulatory Commission, Washington, D.C.

[66] Kat, C.-J., and Els, P. S. (2012). "Validation metric based on relative error." *Mathematical and Computer Modelling of Dynamical Systems*, 18(5), 487-520.

[67] Kelly, J. M. (1986). "Aseismic base isolation: review and bibliography." *Soil Dynamics and Earthquake Engineering*, 5(4), 202-216.

[68] Kelly, J. M. (1993). "The implementation of base isolation in the United States." *Proceedings, 6th Symposium on Seismic, Shock, and Vibration Isolation, ASME Pressure Vessel and Piping Conference*, Denver, CO.

[69] Kelly, J. (2004). "Seismic isolation." Chapter II in *Earthquake engineering: From engineering seismology to performance-based engineering* eds. Y. Bozorgnia, and V. V. Bertero, CRC Press.

[70] Kelly, J. M., Skinner, R. I., and Heine, A. J. (1972). "Mechanisms of energy absorption in special devices for use in earthquake resistant structures." *Bulletin of the New Zealand Society for Earthquake Engineering*, 5(3), 63-88.

[71] Kumar, M., Whittaker, A. S., and Constantinou, M. C. (2014). "An advanced numerical model of elastomeric seismic isolation bearings." *Earthquake Engineering & Structural Dynamics*, 43(13), 1955-1974.

[72] Kumar, M., Whittaker, A. S., and Constantinou, M. C. (2015a). "Characterizing friction in sliding isolation bearings." *Earthquake Engineering & Structural Dynamics*, 44(9), 1409-1425.

[73] Kumar, M., Whittaker, A. S., and Constantinou, M. C. (2015b). "Seismic isolation of nuclear power plants using sliding bearings." Report MCEER-15-0006, University at Buffalo, State University of New York, Buffalo, NY.

[74] Kumar, M., Whittaker, A. S., Kennedy, R. P., Johnson, J. J., and Kammerer, A. M. (2017a). "Seismic probabilistic risk assessment for seismically isolated safety-related nuclear facilities." *Nuclear Engineering and Design*, 313, 386-400.

[75] Kumar, M., Whittaker, A. S., and and Constantinou, M. C. (2017b). "Extreme earthquake response of nuclear power plants isolated using sliding bearings." *Nuclear Engineering and Design*, 316, 9-25.

[76] Kumar, M., Whittaker, A. S., and Constantinou, M. C. (2019). "Seismic isolation of nuclear power plants using elastomeric bearings." Report NUREG/CR-7255, United States Nuclear Regulatory Commission, Washington, D.C.

[77] Kumar, M., and Whittaker, A. S. (2017). "Effect of seismic hazard definition on isolation-system displacements in nuclear power plants." *Engineering Structures*, 148, 424-435.

[78] Lilliefors, H. W. (1969). "On the Kolmogorov-Smirnov test for the exponential distribution with mean unknown." *Journal of the American Statistical Association*, 64(325), 387-389.

[79] Lomiento, G., Bonessio, N., and Benzoni, G. (2013). "Friction model for sliding bearings under seismic excitation." *Journal of Earthquake Engineering*, 17(8), 1162-1191.

[80] Livermore Software Technology Corporation (LSTC). (2011). LS-DYNA (Version 5.1.1) [Computer program], Livermore, CA.

[81] Makris, N., and Deoskar, H. S. (1996). "Prediction of observed response of base-isolated structure." *Journal of Structural Engineering*, 122(5), 485-493.

[82] Martelli, A., Clemente, P., Saitta, F., and Forni, M. (2012). "Recent worldwide application of seismic isolation and energy dissipation to steel and other materials structures and conditions for their correct use." *Behavior of Steel Structures in Seismic Areas*, *Stessa 2012*, eds. F. Mazzolani, and R. Herrera, Taylor & Francis Group, London, UK.

[83] McGuire, R. K. (2004). "Seismic hazard and risk analysis." Monograph MNO-10, Earthquake Engineering Research Institute, Oakland, CA.

[84] Mokha, A. S., Amin, N., Constantinou, M. C., and Zayas, V. (1996). "Seismic isolation retrofit of large historic building." *Journal of Structural Engineering*, 122(3), 298-308.

[85] Mokha, A., Constantinou, M. C., and Reinhorn, A. M. (1988). "Teflon bearings in aseismic base isolation: Experimental studies and mathematical modeling." Report NCEER-88-0038, University at Buffalo, State University of New York, Buffalo, NY.

[86] Morita, K., and Takayama, M. (2008). "Performance of seismic isolated buildings due to 2005 Fukuoka earthquake in Japan." *Proceedings, Fourteenth World Conference on Earthquake Engineering*, Beijing, China.

[87] Mosqueda, G., Whittaker, A. S., and Fenves, G. L. (2004). "Characterization and modeling of Friction Pendulum bearings subjected to multiple components of excitation." *Journal of Structural Engineering*, 130(3), 433-442.

[88] Naeim, F., and Kelly, J. M. (1999). "Design of seismic isolated structures: From theory to practice." John Wiley & Sons, New York, NY.

[89] Nagarajaiah, S., and Sun, X. (2001). "Base-isolated FCC building: impact response in Northridge earthquake." *Journal of Structural Engineering*, 127(9), 1063-1075.

[90] Nakashima, M., and Chulisp, P. (2003). "A partial view of Japanese post-Kobe seismic design and construction practices." *Earthquake Engineering and Engineering Seismology*, 4(1), 3-13.

[91] National Institute of Standards and Technology (NIST) (2011). "Selecting and scaling earthquake ground motions for performing response-history analyses." NIST GCR 11-917-15, Gaithersburg, MD.

[92] Nazin, V. V. (1978). "Buildings on gravitational seismoisolation system in Sevastopol." *Proceedings, VI Symposium on Earthquake Engineering*, Vol. I, Roorkee, India.

[93] Oberkampf, W. L., and Barone, M. F. (2006). "Measures of agreement between computation and experiment: Validation metrics." *Journal of Computational Physics*, 217(1), 5-36.

[94] Oberkampf, W. L., and Roy, C. J. (2010). "Verification and validation in scientific computing." Cambridge University Press, UK.

[95] Pall, A. S., and Marsh, C. (1982). "Response of friction damped braced frames." *Journal of the Structural Division,* 108(ST6), 1313-1323.

[96] Pacific Earthquake Engineering Research Center (PEER). (2014). Open System for Earthquake Engineering Simulation (Version 2.4.3) [Computer program], Berkeley, CA.

[97] Ray, T. (2013). "Modeling of multi-dimensional inelastic and nonlinear elastic structural systems." PhD dissertation, University at Buffalo, State University of New York, Buffalo, NY.

[98] Robinson, W. H. (1982). "Lead-rubber hysteretic bearings suitable for protecting structures during earthquakes." *Earthquake Engineering & Structural Dynamics*, 10(4), 593-604.

[99] Roche, R. (2013). "Nuclear power plant testbeds for seismic isolation." Personal Communication to A. Whittaker.

[100] Roy, C. J., McWherter-Payne, M. A., and Oberkampf, W. L. (2003). "Verification and validation for laminar hypersonic flowfields, part 1: verification." *AIAA Journal*, 41(10), 1934-1943.

[101] Sarin, H., Kokkolaras, M., Hulbert, G., Papalambros, P., Barbat, S., and Yang, R. J. (2010). "Comparing time histories for validation of simulation models: Error measures and metrics." *Journal of Dynamic Systems, Measurement, and Control*, 132(6), 061401.

[102] Sarkisian, M., Lee, P., Hu, L., Doo, C., Zayas, V., Constantinou, M., and Bachman, R. (2012). "Property verification of Triple Pendulum™ seismic isolation bearings." *Proceedings: 20th Analysis & Computational Specialty Conference, Structures Congress 2012*, March 29-31, Chicago, IL.

[103] Sarlis, A. A., and Constantinou, M. C. (2013). "Model of Triple Friction Pendulum bearing for general geometric and frictional parameters and for uplift conditions." Report MCEER-13-0010, University at Buffalo, State University of New York, Buffalo, NY.

[104] Schulz, T. L. (2006). "Westinghouse AP1000 advanced passive plant." *Nuclear Engineering and Design*, 236(14–16), 1547-1557.

[105] Schwer, L. E. (2007). "Validation metrics for response histories: perspectives and case studies." *Engineering with Computers*, 23(4), 295-309.

[106] Short, S., Hardy, G., Merz, K., and Johnson, J. (2007). "Program on technology innovation: validation of CLASSI and SASSI codes to treat seismic wave incoherence in soil-structure interaction (SSI) analysis of nuclear power plant structures." Report 1015111, Electric Power Research Institute, Palo Alto, CA.

[107] Simo, J. C., and Hughes, T. J. (1998). "Computational inelasticity." Springer, New York, NY.

[108] Sivaselvan, M. V., and Reinhorn, A. M. (2004). "Nonlinear structural analysis towards collapse simulation: a dynamical systems approach." Report MCEER-2004-05, University at Buffalo, State University of New York, Buffalo, NY.

[109] Skinner, R. I., Robinson, W. H., and McVerry, G. H. (1991). "Seismic isolation in New Zealand." *Nuclear Engineering and Design*, 127(3), 281-289.

[110] Syed, M. B., Patisson, L., Curtido, M., Slee, B., and Diaz, S. (2014). "The challenging requirements of the ITER anti seismic bearings." *Nuclear Engineering and Design*, 269(0), 212-216.

[111] Tajirian, F. F., Kelly, J. M., and Aiken, I. D. (1990). "Seismic isolation for advanced nuclear power stations." *Earthquake Spectra*, 6(2), 371-401.

[112] Tassios, T. P. (2009). "Seismic engineering contributions and trends to face future 1755 event." *The 1755 Lisbon Earthquake: Revisited*, Ed. A. Ansal, Springer.

[113] Trifunac, M. D., and Brady, A. G. (1975). "A study on the duration of strong earthquake ground motion." *Bulletin of the Seismological Society of America*, 65(3), 581-626.

[114] Tsai, C. S. (1997). "Finite element formulations for Friction Pendulum seismic isolation bearings." *International Journal for Numerical Methods in Engineering*, 40(1), 29-49.

[115] Tsopelas, P., Okamoto, S., Constantinou, M. C., Ozaki, D., and Fujii, S. (1994a). "NCEER-Taisei Corporation research program on sliding seismic isolation systems for bridges: Experimental & analytical study of systems consisting of sliding bearings, rubber restoring force devices and fluid dampers." Report NCEER-94-0002, University at Buffalo, State University of New York, Buffalo, NY.

[116] Tsopelas, P. C., Constantinou, M. C., and Reinhorn, A. M. (1994b). "3D-BASIS-ME: Computer program for nonlinear dynamic analysis of seismically isolated single and multiple structures and liquid storage tanks." Report NCEER-94-0010, University at Buffalo, State University of New York, Buffalo, NY.

[117] United States Atomic Energy Commission (USAEC). (1973). "Design response spectra for seismic design of nuclear power plants." Regulatory Guide 1.60, Washington, D.C.

[118] United States Department of Energy (DOE). (1994). "Natural phenomena hazards design and evaluation criteria for Department of Energy facilities." DOE-STD-1020-94, Washington, D.C.

[119] United States Nuclear Regulatory Commission (USNRC). (2007a). "A performance-based approach to define the site-specific earthquake ground motion." Regulatory Guide 1.208, Washington, D.C.

[120] United States Nuclear Regulatory Commission (USNRC). (2007b). "Standard review plan for the review of safety analysis reports for nuclear power plants." NUREG-0800, Washington, D.C.

[121] United States Nuclear Regulatory Commission (USNRC). (2014). "Design response spectra for seismic design of nuclear power plants." Regulatory Guide 1.60, Washington, D.C.

[122] United States Nuclear Regulatory Commission (USNRC). (2012). "Nuclear reactors", <http://www.nrc.gov/reading-rm/doc-collections/nuregs/staff/sr1350/v23/sr1350v23-sec-3.pdf>. (June 4, 2012).

[123] United States Nuclear Regulatory Commission (USNRC). (2013). "Information digest." Report NUREG-1350, Washington D.C.

[124] Wolff, E. (1999). "Frictional heating in sliding bearings and an experimental study of high friction materials." MS thesis, University at Buffalo, State University of New York, Buffalo, NY.

[125] Wolff, E. (2003). "Experimental study of seismic isolation systems with emphasis on secondary system response and verification of accuracy of dynamic response history analysis methods." PhD dissertation, University at Buffalo, State University of New York, Buffalo, NY.

[126] Wright, F. L. (1977). "An autobiography: Frank Llyod Wright." Horizon Press, New York, NY.

[127] Zayas, V. A., Low, S. S., and Mahin, S. A. (1987). "The FPS earthquake resisting system experimental report." Report UCB/EERC-87/01, Earthquake Engineering Research Center, Berkeley, CA.

[128] Zayas, V. A., Low, S., Mokha, A. S., and Imbsen, R. A. (2001). "Seismic isolation of Benicia-Martinez Bridge." *Proceedings, Structures Congress 2001*, American Society of Civil Engineers, May 21-23, Washington, D.C.

[129] Zekioglu, A., Huseyin, D., and Erkus, B. (2009). "Performance-based seismic design of a large seismically isolated structure: Istanbul Sabiha Gokcen International Airport Terminal Building." *Proceedings, Structural Engineers Association of California 2009 Convention*, September, San Diego, CA.

APPENDIX A
GROUND MOTIONS USED IN THE VERIFICATION STUDIES

A.1 Description of Ground Motion Records

This section presents details on the ground motions used in the analyses presented in chapters 3 and 4, and Appendix B. These chapters deal with verification of assumptions in modeling Friction Pendulum™ (FP) bearings. Thirty ground motions scaled to match a geomean spectrum with a mean annual frequency of exceedance of 10^{-4} for the site of the nuclear power plant at Diablo Canyon in California were considered. These motions are expected to impose significant displacement demand on isolators, considering the proximity of the site to San Andreas and Hosgri faults. The procedure for selection and scaling the ground motions is described in Huang *et al.* (2009). Figure A-1 shows the response spectra of the spectrally matched ground motions in the three orthogonal directions. Figure A-2 shows the duration of strong shaking for the thirty ground motions estimated using the approach suggested by Trifunac and Brady (1975). The duration of strong shaking is the greater of the values computed in the two horizontal directions. Of the thirty ground motions considered, the minimum duration of strong shaking is for ground motion number 20 (=6.6 s) and the maximum duration is for ground motion number 29 (=28.2 s).

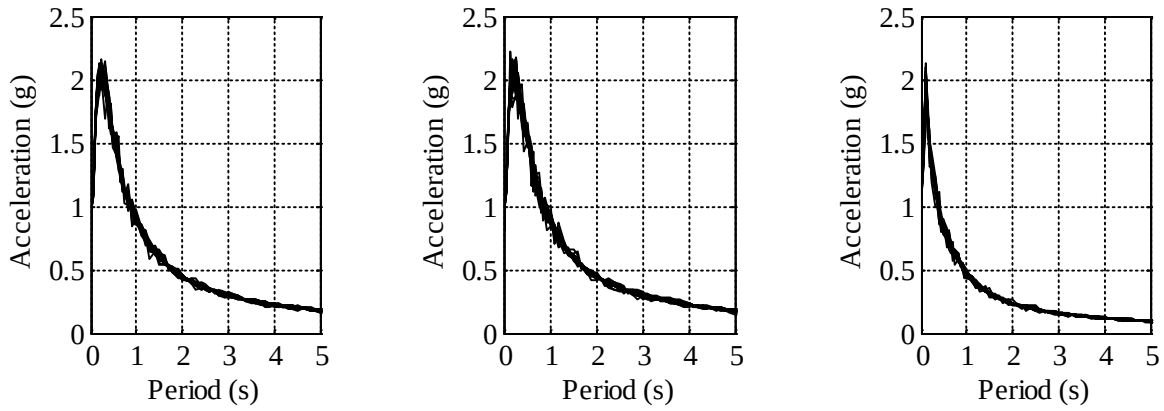

(a) X direction (H) (b) Y direction (H) (c) Z direction (V)

Figure A-1 Response Spectral of the Ground Motions for Diablo Canyon Nuclear Generating Station

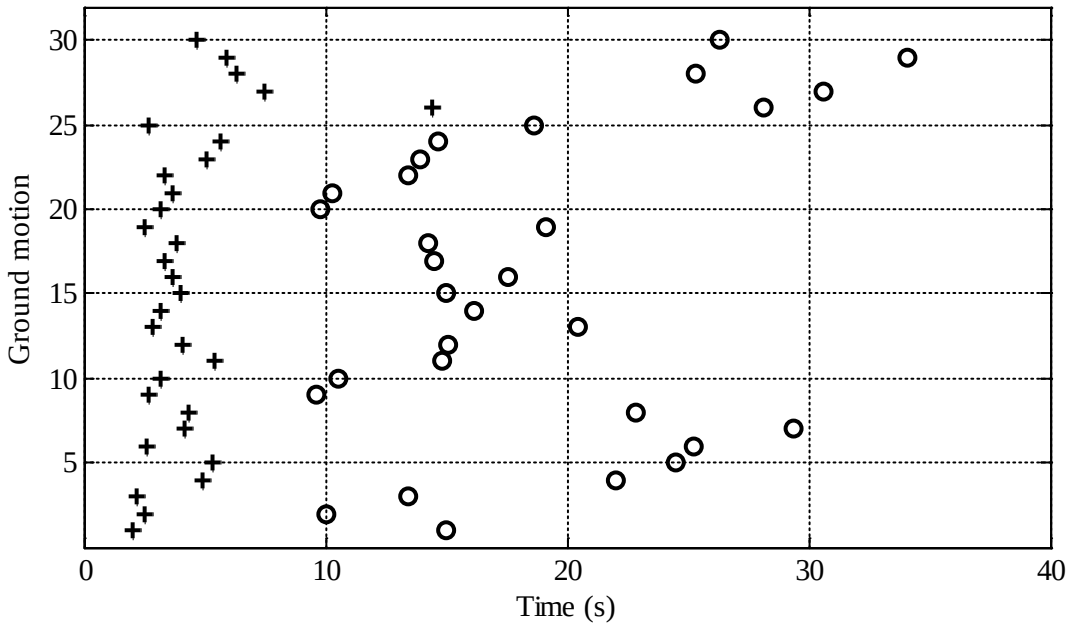

Figure A-2 Duration of Shaking for the Ground Motions, + = Beginning, O = End

APPENDIX B
EFFECT OF AN ASSUMPTION RELATED TO THE DEPENDENCE OF THE COEFFICIENT OF FRICTION ON THE VELOCITY OF SLIDING

B.1 Introduction

The relationship between the coefficient of sliding friction of a single concave Friction Pendulum™ (FP) bearing and the velocity of sliding at the interface is given in terms of the coefficients of friction at very small and very high velocities, and a rate parameter. The coefficient of friction at a high velocity is a function of axial pressure, while the coefficient does not vary significantly with change in the axial pressure on the bearing when measured at a small velocity (see Chapter 3). To decouple the influence of velocity and axial pressure on the coefficient of friction, an assumption is made that the coefficient of friction at a very small velocity also depends on the axial pressure and is half that at a very high velocity for all values of axial pressure. This appendix examines the effect of the assumption on the maximum displacement demand and the maximum absolute acceleration response and the maximum temperature at the sliding interface of an FP bearing subjected to earthquake ground motions of different intensities.

B.2 Analysis Scheme

A single FP bearing is considered for the analysis. The sliding period for the bearing is 3 s and the coefficient of friction measured at a reference axial pressure on the bearing p_o and at a high sliding velocity is 0.06. The radius of the area of contact is 200 mm. Two values of p_o, 10 MPa and 50 MPa, are considered, and masses associated with the slider are 128,000 kg and 640,000 kg, respectively. Thirty ground motions compatible with the geometric mean spectrum for the Diablo Canyon nuclear power generating site corresponding to a return period of 10,000 years (see Huang *et al.* (2009)) are considered. The details on the ground motions are given in the Appendix A. The ground motions are amplitude scaled to 100%, 50%, 25% and 5% of their original intensities.

Analyses were performed for two cases. Case 1 considers that the coefficient of friction at a small velocity $\left(\mu_{\min}\right)$ remains constant as the axial pressure on the bearing changes. The coefficient of friction at a small velocity is fixed at one half that measured at a high velocity with the bearing subjected to a reference axial pressure of p_o. The variation in the coefficient of sliding friction $\left(\mu(v)\right)$ with sliding velocity (v) is defined by the following equation

$$\mu(v) = \mu_{\max} \times \left(1 - \left(1 - \frac{\mu_{\min}}{\mu_{\max}}\right) e^{-av}\right) \qquad \textbf{(B-1)}$$

where $\mu_{\max}$ is the coefficient of sliding friction measure at a very high velocity, a is the rate parameter which defines the rate of transition between $\mu_{\min}$ and $\mu_{\max}$. Case 2 assumes that

the coefficient of friction at a very small velocity of sliding is half that measured at a high velocity at all values of axial pressure. With this assumption the above equation becomes

$$\mu(v) = \mu_{\max} \times \left(1 - 0.5e^{-av}\right) \quad \textbf{(B-2)}$$

The variation in $\mu_{\max}$ with axial pressure (p) is given by the following equation.

$$\mu_{\max} = \mu_{p=p_o} \times 0.7^{0.02(p-p_o)} \quad \textbf{(B-3)}$$

where $\mu_{p=p_o}$ is the coefficient of friction at a reference axial pressure of p_o measured at a high velocity of sliding. Pressure is measured in MPa units. Case 1 represents the "exact" coupled relationship between coefficient of friction, sliding velocity and axial pressure, whereas Case 2 represents an "approximate" relationship between the three quantities. The effect of temperature on the coefficient of sliding friction is ignored for the two cases.Panel (a) of Figure B-1 shows the variation in $\mu_{\min}$ and $\mu_{\max}$ with axial pressure for Case 1, with p_o set equal to 10 MPa. Panel (b) presents the curves for a p_o of 50 MPa. Panels (c) and (d) present the variation in $\mu_{\min}$ and $\mu_{\max}$ with axial pressure for Case 2, with p_o set equal to 10 MPa and 50 MPa, respectively.

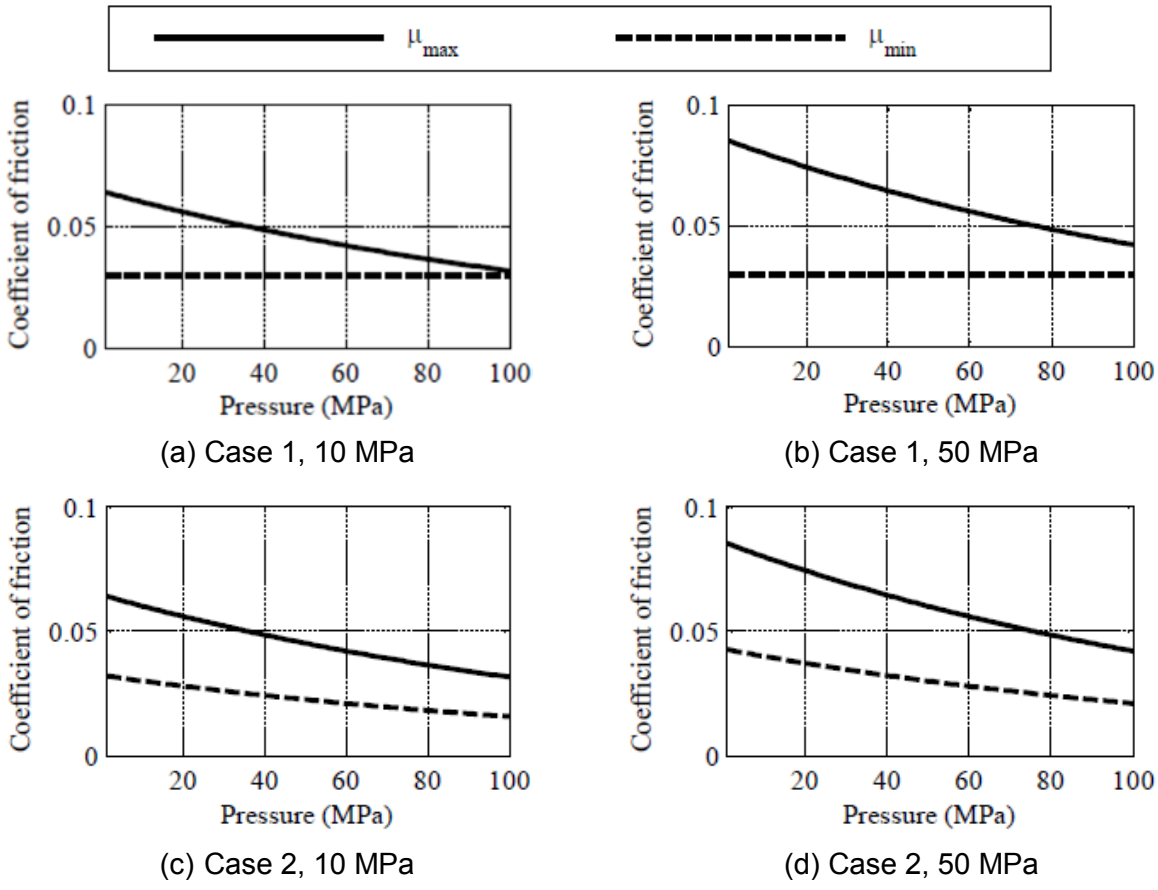

(a) Case 1, 10 MPa

(b) Case 1, 50 MPa

(c) Case 2, 10 MPa

(d) Case 2, 50 MPa

Figure B-1 "Exact" (Case 1) and "Approximate" (Case 2) Relationships Between Coefficient of Friction and Axial Pressure on Friction Pendulum™ Bearings

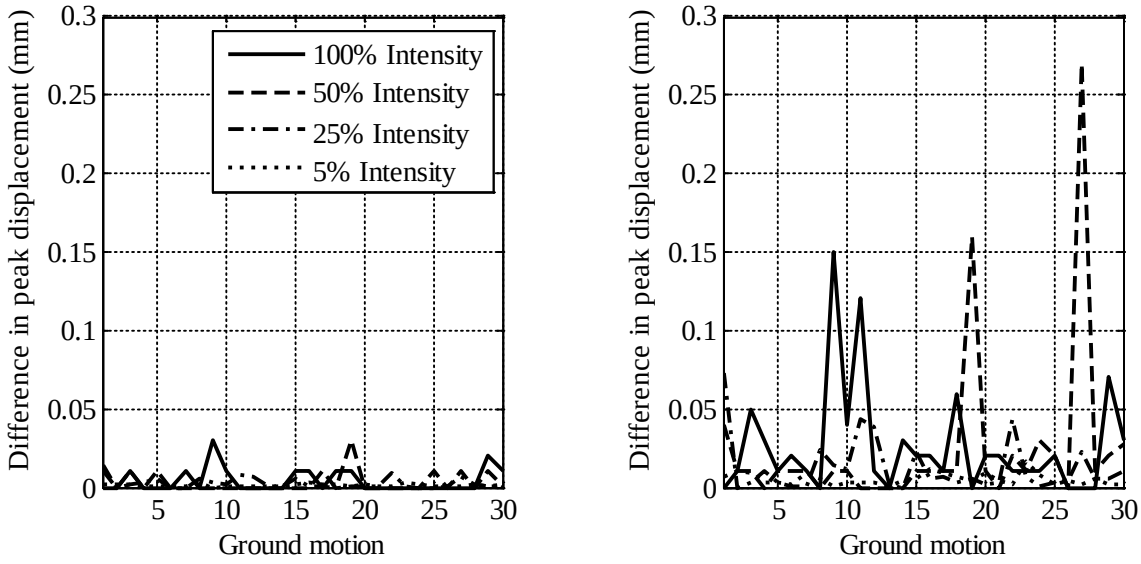

Figure B-2 Difference in the Peak Displacement for the FP Bearing with Sliding Period of 3 s Obtained Using "Exact" (Case 1) and "Approximate" (Case 2) Relationships Between Coefficient of Friction, Sliding Velocity and Axial Pressure

B.3 Results

Figure B-2 presents the differences in the maximum displacement of the FP bearing, when the friction at the sliding surface is defined using "exact" (Case 1) and "approximate" (Case 2) models. The value of p_o is set at 10 MPa for panel (a) and 50 MPa for panel (b). The maximum difference is smaller than 0.3 mm for all combinations of ground motions, shaking intensities and p_o. The peak displacement of the bearing with either 10 MPa or 50 MPa of static axial pressure subjected to the 30 ground motions scaled to 100% of their original intensities ranges between 260 mm and 690 mm. The analyses were also run for the FP bearing with the sliding period of 2 s. The maximum difference in the peak displacements due to the choice of the friction model across all combinations of static axial pressure, intensity level and ground motions is less than 0.15 mm, whereas the peak displacement of the bearing ranges between 310 mm and 570 mm, when the bearing is subjected to the 30 ground motions scaled to their original intensities irrespective of the level of axial pressure on the bearing. Hence, the choice of the "exact" or "approximate" relation between coefficient of sliding friction, axial pressure and sliding velocity does not considerably affect the maximum displacement response.

Figure B-3 presents the difference in peak acceleration response in a horizontal direction for the two approaches of defining the coefficient of friction for the bearing with the sliding period of 3 s. The maximum difference among all combinations of ground motions, intensities and p_o is less than 0.00015 g, which is very small compared to the peak acceleration of the original ground motions of about 1 g.

B.4 Summary

Two methods to define the coupled influence of axial pressure and sliding velocity on the coefficient of sliding friction are considered. In the "exact" method the high-velocity coefficient of friction is expressed as a function of axial pressure, whereas the small-velocity coefficient of friction remains fixed. It is assumed in the "approximate" method that the small-velocity coefficient of friction is half the high-velocity coefficient of friction at all levels of axial pressure. An FP bearing with a sliding period of isolation of 3 s and coefficient of friction at a reference axial pressure of 0.06 was subjected to ground motions scaled to different intensities. The results show that for all combinations of p_o, ground motion and intensity levels, the difference in the maximum displacement response of bearing is smaller than 0.3 mm, and that in the maximum absolute acceleration response is smaller than 0.00015 g, when the two methods to define the coefficient of friction are considered.

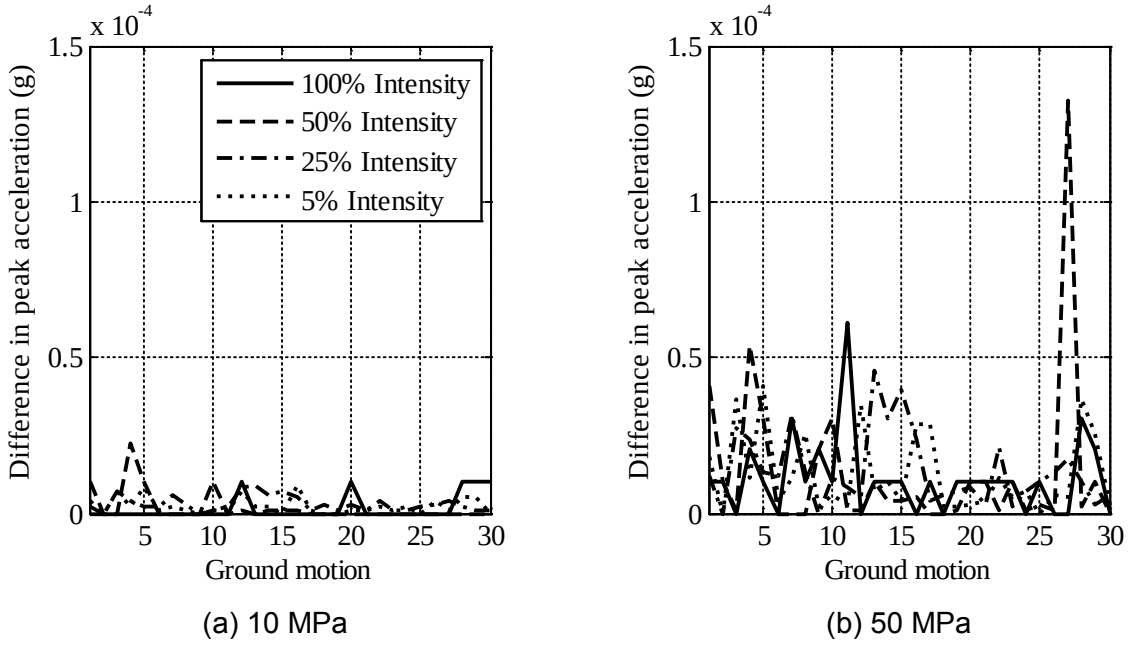

Figure B-3 Difference in the Peak Acceleration Response of the FP Bearing with a Sliding Period of 3 s in a Horizontal Direction Obtained Using "Exact" (Case 1) and "Approximate" (Case 2) Relationships Between Coefficient of Friction, Sliding Velocity and Axial Pressure

APPENDIX C
ACCELERATION OF THE SLIDER OF A FRICTION PENDULUM BEARING IN THE VERTICAL DIRECTION

C.1 Introduction

The motion of the slider across the sliding surface of a Friction Pendulum™ (FP) bearing is coupled in the vertical and horizontal directions. The total acceleration of the slider in the vertical direction at a given instant in time is the sum of the vertical ground acceleration and the vertical acceleration of the slider due to its motion relative to the sliding surface. The relative contributions to the total acceleration of the slider in the vertical direction are studied in this appendix.

C.2 Modeling and Analysis Scheme

FP bearings with a sliding period of oscillation 2 s, 3 s and 4 s, a reference coefficient of friction 0.06 and a reference pressure (= static axial pressure) of 50 MPa were subjected to the 30 ground motions of Appendix A. Friction on the sliding surface was described by the Coulomb model. The radius of the area of contact at the sliding surface was 200 mm. The entire mass associated with the static axial load was considered to be active in the three orthogonal directions. Mass proportional damping of 2% of critical was assigned to the system with the proportionality constant updated at every step of analysis based on the instantaneous fundamental frequency of the system.

C.3 Vertical Acceleration of the Slider

There are two components of the vertical acceleration of the slider of an FP bearing, namely, 1) the acceleration due to relative motion at the sliding surface, and 2) the ground acceleration; see Figure C-1. This section presents a method to estimate the acceleration of the slider relative to the sliding surface.

An estimate of the vertical displacement of the slider relative to its position at the beginning of the motion, $v_{\text{relative},t}$, at the time t is obtained using the following expression.

$$v_{\text{relative},t} = R - \sqrt{\left(R^2 - u_{\text{horizontal},t}^2\right)} \qquad \textbf{(C-1)}$$

where $u_{\text{horizontal},t}$ is the horizontal displacement of the slider relative to the center of sliding surface at time t and R is the radius of curvature of the sliding surface. The velocity in the vertical direction, $\dot{v}_{\text{relative},t}$, at time t is calculated as the change in vertical displacement of the slider in time interval Δt.

$$\dot{v}_{\text{relative},t} = \frac{v_{\text{relative},t} - v_{\text{relative},t-\Delta t}}{\Delta t} \qquad \textbf{(C-2)}$$

where all parameters were defined previously. The acceleration of the slider relative to the sliding surface, $\ddot{v}_{\text{relative},t}$, at time t is calculated similarly:

$$\ddot{v}_{\text{relative},t} = \frac{\dot{v}_{\text{relative},t} - \dot{v}_{\text{relative},t-\Delta t}}{\Delta t} \qquad \textbf{(C-3)}$$

where all parameters were defined previously. The total acceleration history of the slider is obtained by summing the relative acceleration and ground acceleration histories.

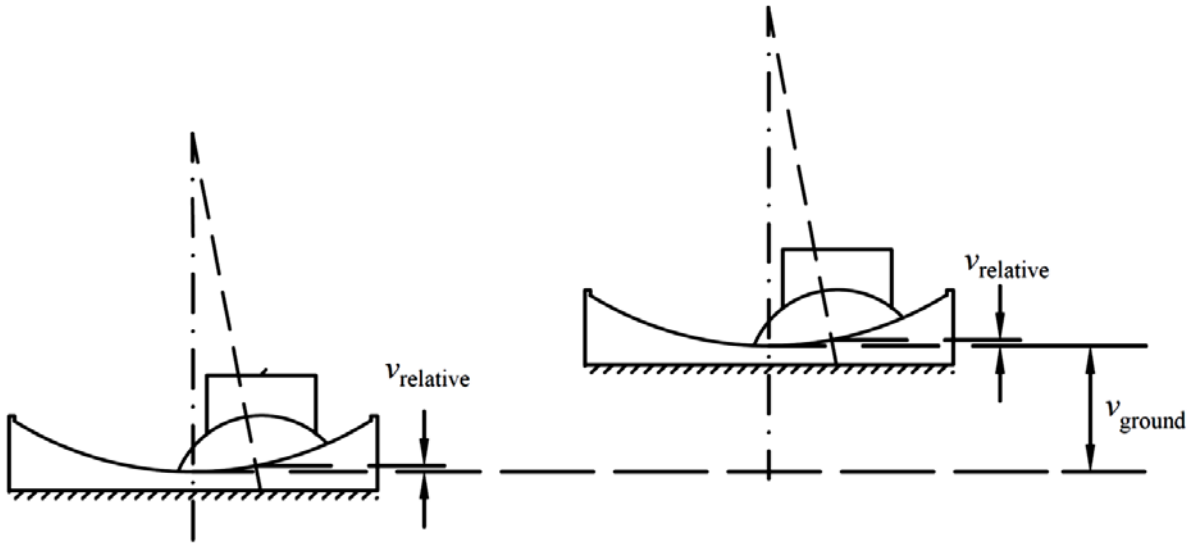

(a) Translation of slider relative to sliding surface, v_{relative}

(b) Ground translation, v_{ground}, and v_{relative}

Figure C-1 Vertical Translation of the Slider of an FP Bearing

C.4 Effect on Total Vertical Acceleration Histories

Figure C-2(a) presents the maximum and minimum values of the vertical ground acceleration (VGA) histories and the vertical total acceleration (VTA) histories of the slider of the 2 s FP bearing subjected to the 30 sets of ground motions. Also plotted in the panel are values for the vertical acceleration history of the slider relative (VRA) to the sliding surface. Panels (b) and (c) present information for 3 s and 4 s bearings, respectively.

The peak values of VRA decrease for bearings with longer sliding periods. The greatest absolute value of the peak VRA (= 6.5 m/s^2 or 0.7 g) is observed for the 2 s bearing subjected to ground motion number 1 (GM1). Although this value of VRA is comparable to the corresponding peak VGA of 6.8 m/s^2, the peak VTA (= 7.0 m/s^2) is not significantly affected by the relative acceleration of the slider because the peaks do not occur simultaneously. Figure C-3 presents the ground, relative and total acceleration histories for the 2 s bearing and GM1, for which the peak values occur at 3.39 s, 3.825 s and 3.77 s, respectively.

The vertical relative acceleration (VRA) influences VTA significantly for some values of sliding period and some ground motions. For example, for the 2 s bearing, the peak values of VGA and VTA are 7.0 m/s^2 and 9.2 m/s^2, respectively, when the bearing is subjected to GM21, and

6.7 m/s^2 and 9.8 m/s^2, respectively, when the bearing is subjected to GM26. The peak VTA for the two cases is greater by 30% and 50%, respectively, than the corresponding peak VGA. However, averaged across all ground motions, the percentage difference is relatively small: 7% for the 2 s bearing, 4% for the 3 s bearing, and 2% for the 4 s bearing.

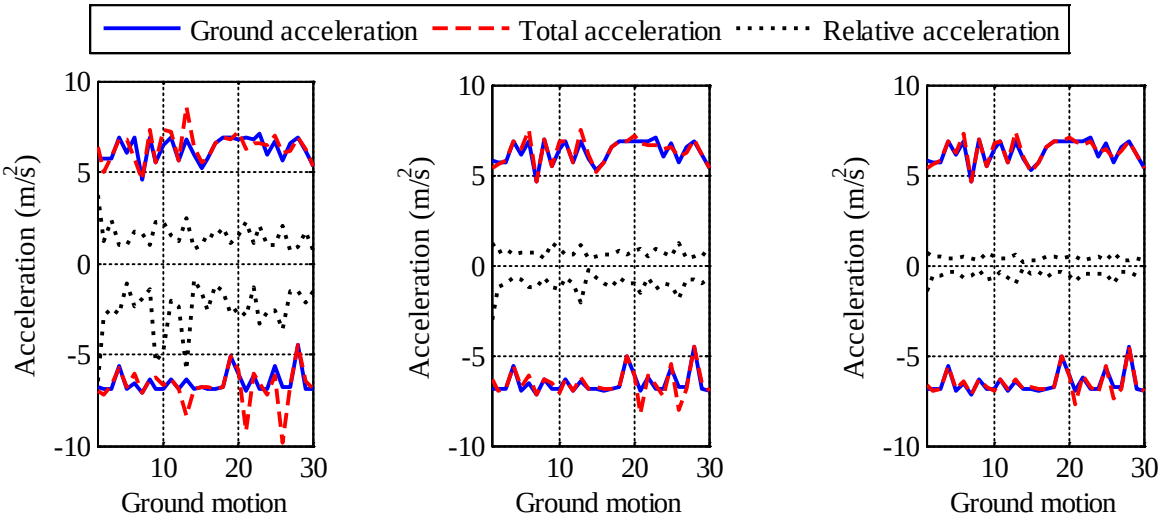

(a) Sliding period = 2 s (b) Sliding period = 3 s (c) Sliding period = 4 s

Figure C-2 Maximum and Minimum Values of the Vertical Components of the Ground Acceleration Histories, Total Acceleration Histories of the Slider, and Acceleration Histories of the Slider Relative to the Sliding Surface

Figure C-4 plots the data of Figure C-2 computed using three time steps, namely, 0.001 s, 0.002 s, and 0.005 s. The choice of time step has no influence on the results, for the values considered.

C.5 Effect on Vertical Floor Spectra

The maximum value of VRA was observed for the 2 s bearing subjected to GM1. The peak VTA was most influenced by VRA for the 2 s bearing subjected to GM21 and GM26, as noted previously. The vertical relative acceleration most influenced the peak VTA for the 3 s and 4 s bearings subjected to GM21 and GM26. Figure C- presents response spectra for VGA, VRA and VTA for GM1, GM21 and GM26, and sliding periods of 2 s, 3 s and 4 s. The floor spectral ordinates for VTA are comparable to those for VGA, indicating that the vertical motion of slider relative to the sliding surface does not significantly influence the floor spectral ordinates in the vertical direction.

C.6 Summary

Friction Pendulum™ (FP) bearings with sliding periods of 2 s, 3 s and 4 s, a Coulomb-type coefficient of friction of 0.06, and a static axial pressure of 50 MPa were subjected to the 30 ground motions of Appendix A. The peak values of vertical ground acceleration, vertical acceleration of the slider relative to the sliding surface and total vertical acceleration of the slider were computed. The acceleration of the slider relative to the sliding surface does not significantly influence the total peak acceleration of the slider or vertical response spectral ordinates, especially for sliding periods of 3 s and longer.

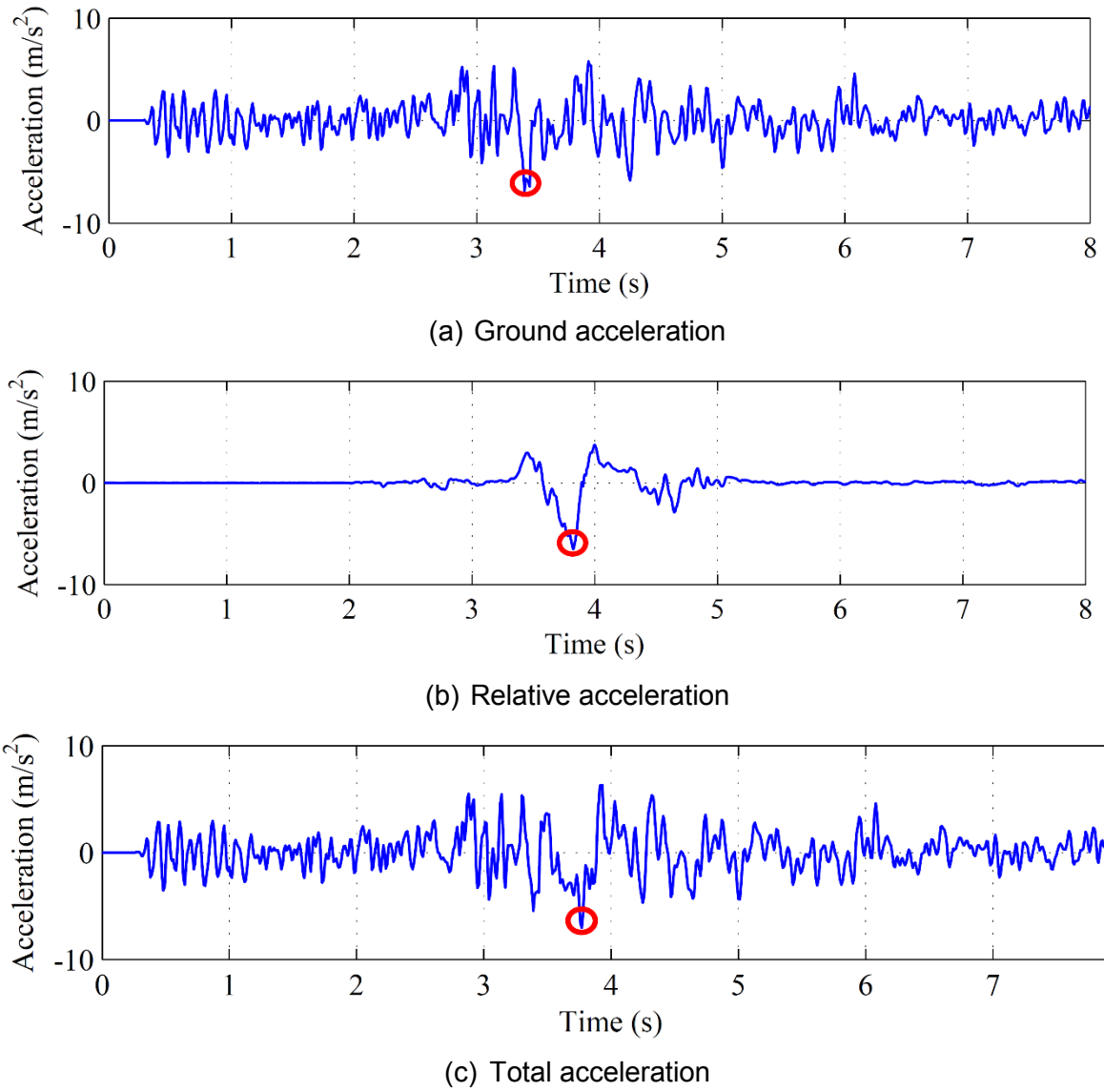

Figure C-3 Histories of Vertical Ground Acceleration, Acceleration of the Slider Relative to the Sliding Surface and the Total Acceleration of the Slider of the FP Bearing with a Sliding Period of 2 s Subjected to GM1

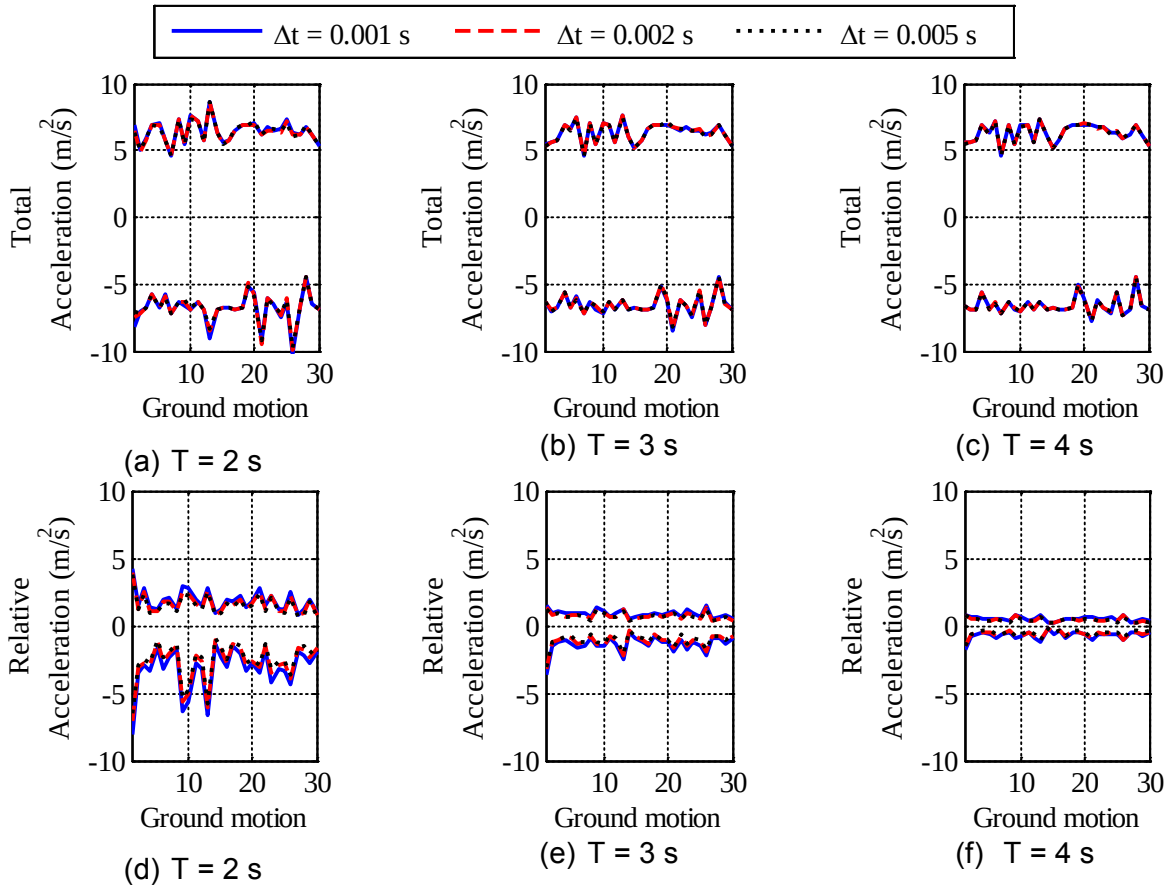

Figure C-4 Influence of Analysis Time Step on Peak Accelerations

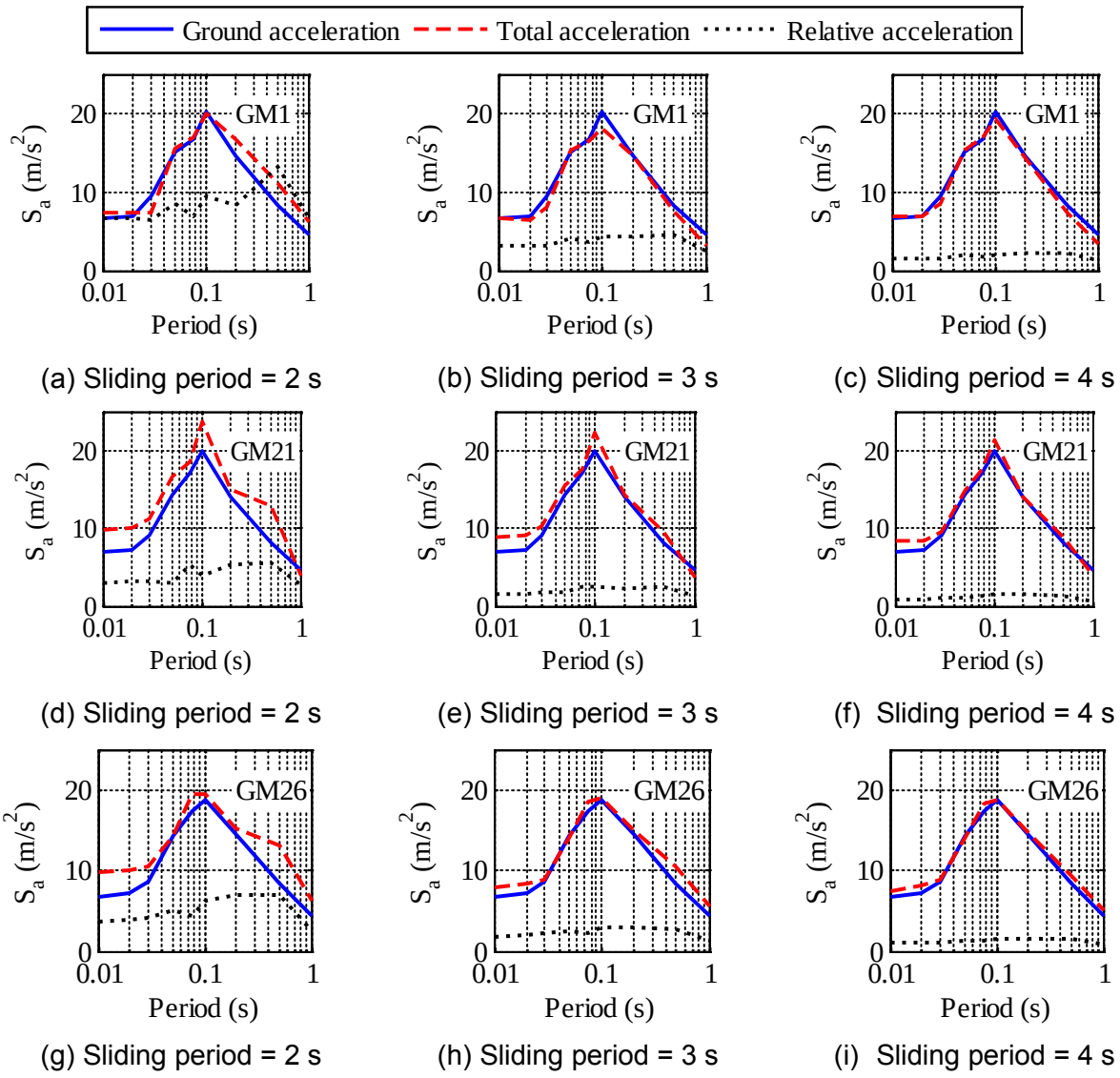

Figure C-5 Response Spectra for the Vertical Components of Ground Acceleration Histories, Total Acceleration Histories of the Slider, and Acceleration Histories of the Slider Relative to the Sliding Surface

APPENDIX D
RELATIVE VERTICAL DISPLACEMENTS IN FRICTION PENDULUM™ SEISMIC ISOLATION SYSTEMS

D.1 Introduction

A Friction Pendulum™ (FP) bearing undergoes vertical and horizontal displacement during earthquake shaking due to the curvature of the sliding surface. The vertical displacement is a function of the translation and rotation in the isolation system, and the location of the bearing in the isolation system. The relative vertical displacement between adjacent FP bearings will produce internal forces in the supported superstructure. Unlike elastomeric bearings that shorten when displaced laterally, the overall height of the FP bearing increases with horizontal displacement.

This appendix presents a study on the vertical displacements in isolation systems comprised of uniformly spaced FP bearings. A procedure to compute the displacement in individual bearings of an isolation system subjected to translation and rotation is presented. Two isolation systems with different geometric properties are subjected to differing levels of translational and rotational displacements. Vertical displacements in individual bearings are reported.

D.2 Procedure to Compute Change in Elevation of a Bearing

An isolation system with FP bearings installed in a square pattern is considered for this study. Panel (a) of Figure D-1 shows the undeformed isolation system. Panels (b) and (c) present the isolation system after translation and rotation, respectively. This section describes the procedure to compute the increase in height of the bearings in the isolation system subjected to combined translation and rotation.

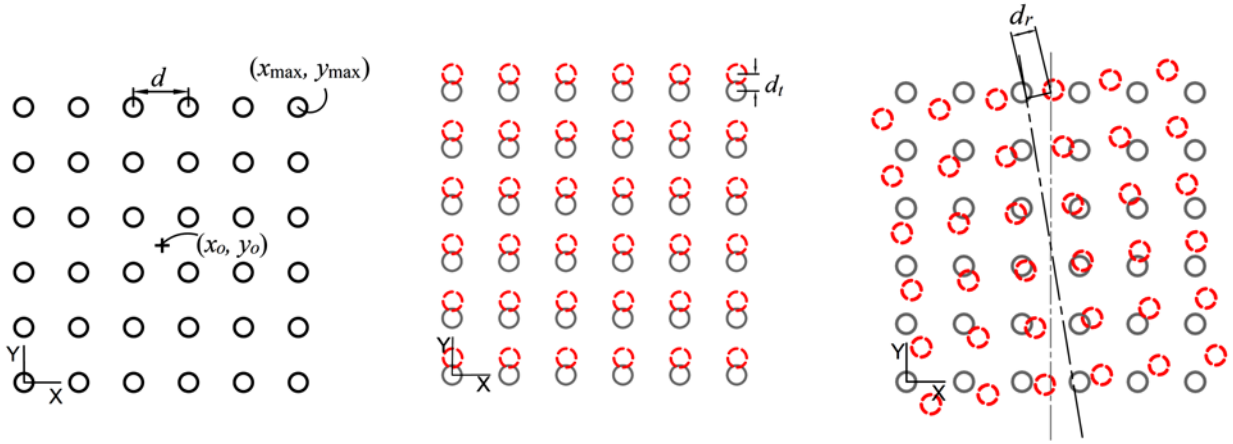

(a) Undeformed (b) After translation (c) After rotation

Figure D-1 Schematic of the Seismic Isolation System in Different Configurations

The angle of rotation, θ_{rot}, corresponding to a perimeter displacement, d_r, (panel (c) of Figure D-1) in the isolation system can be given by

$$\theta_{rot} = \tan^{-1}\left(\frac{|d_r|}{y_{\max} - y_o}\right) \approx \frac{|d_r|}{y_{\max} - y_o} \qquad \textbf{(D-1)}$$

where $|d_r|$ is the magnitude of d_r, y_o is the Y coordinate of the geometrical center of the undeformed isolation system and $y_{\max}$ is the Y coordinate of the center of bearings in the farthest row of the undeformed system (see panel (a) of Figure D-1). Assume r_{orient} is the distance between the center of the sliding surface of a bearing with coordinates (x,y) and the geometrical center of the isolation system with coordinates (x_o,y_o). The angle, θ_{orient}, between the line joining the center of the sliding surface of an FP bearing to the geometrical center of isolation system and the Y axis is

$$\theta_{orient} = \tan^{-1}\left|\frac{x - x_o}{y - y_o}\right| \qquad \textbf{(D-2)}$$

Following rotation of the isolation system, the relative horizontal displacement between the slider and the sliding surface of the bearing is the product of r_{orient} and θ_{rot}. The resulting changes in the X and Y coordinates (Δx_{rot} and Δy_{rot}) of the slider are given by the following expressions:

$$\Delta x_{rot} = -sign(y - y_o)(r_{orient} \times \theta_{rot})\cos(\theta_{orient}) \qquad \textbf{(D-3)}$$

$$\Delta y_{rot} = sign(x - x_o)(r_{orient} \times \theta_{rot})\sin(\theta_{orient}) \qquad \textbf{(D-4)}$$

where $sign(a) = 1$ if $a > 0$ and $sign(a) = -1$ if $a < 0$. All other parameters are defined previously.

If Δx_{trans} and Δy_{trans} are the change in the X and Y coordinates, respectively, of the slider of the bearing due to translation, then the new coordinate of the center of the slider of the bearing (x_{new},y_{new}) is given by

$$x_{new} = x + \Delta x_{trans} + \Delta x_{rot} \qquad \textbf{(D-5)}$$

$$y_{new} = y + \Delta y_{trans} + \Delta y_{rot} \qquad \textbf{(D-6)}$$

The next step is to compute the rise (or increase in height) at the center of the slider, Δz, of an FP bearing with sliding period, T, and radius of curvature, R. If the coordinates of center of its sliding surface are (x,y) and that of the center of its slider are (x_{new},y_{new}), then Δz is given by

$$\Delta z = R - \sqrt{R^2 - (x_{new} - x)^2 - (y_{new} - y)^2} \qquad \textbf{(D-7)}$$

where the radius of curvature R is related to the sliding period T by

$$R = \frac{T^2}{4\pi^2} g \qquad \textbf{(D-8)}$$

where g is the acceleration due to gravity.

D.3 Analysis Results

This section describes the geometrical properties of isolation systems and individual bearings, the translation and rotation imposed on the isolation systems, and results of the analysis. The closest distance d between two bearings (see Figure D-1(a)) is 6 m. Each row and column of the system has a total of 17 bearings, for a total of 289 bearings in an area of 96 m $\times$ 96 m, measured center to center of the bearings at the corners of the isolation system. Two values of sliding period are considered: 2 s and 4 s. Table D-1 lists the translations and rotations imposed on the isolation system, and points to results, presented in terms of increase in height, by figure number. The magnitudes of imposed translations and rotations are selected so that the peak displacement of an individual bearing of the system is greater than $0.2R$, which is a widely accepted limit on the displacement capacity of an FP bearing (see Constantinou *et al.* (2011)). Substantial amount of rotations are considered $\left(d_r = 0.5 d_t\right)$, despite the fact that this type of isolation system does not experience significant rotational motion during earthquake-induced shaking because the centers of gravity and lateral stiffness tend to coincide.

Table D-1 Translation and Rotation Imposed on Isolation Systems

Case	Isolation System	Sliding period (s)	Radius of curvature (m)	Translation (m)		Rotation	Results
				X	Y		
1	1	2	1	0	0.200	d_r = 0.000 m	Figure D-3
2	1	2	1	0	0.000	d_r = 0.100 m	Figure D-4
3	1	2	1	0	0.200	d_r = 0.100 m	Figure D-5
4	2	4	4	0	0.600	d_r = 0.000 m	Figure D-6
5	2	4	4	0	0.000	d_r = 0.300 m	Figure D-7
6	2	4	4	0	0.600	d_r = 0.300 m	Figure D-8

The height of all bearings in an isolation system rises by the same amount when only translation is imposed. For the system with 2 s isolators subjected to a translation of 0.200 m (Case 1, see Figure D-2), the increase in height is 0.020 m. The increase is 0.046 m for the 4 s isolator subjected to a translation of 0.600 m (Case 4, see Figure D-5).

Figure D-3 shows the increase in the height of the bearings in the 2 s isolation system subjected to a rotation described by d_r = 0.100 m (Case 2). There is no increase in height at the geometrical center of the system. The bearings at the corners of the 96 m $\times$ 96 m isolation system increase in height by 0.010 m. The maximum relative change in height between adjacent bearings is observed at the corners of the isolation system. The maximum gradient between two adjacent bearings is 0.002 m over a horizontal distance of 8.500 m or 1/4250. Figure D-6 shows the results for 4 s isolation system subjected to rotation described by d_r = 0.300 m (Case 5). The maximum gradient between two adjacent bearings is 6 mm over a

distance of 8.500 m or 1/1416. For all the cases considered, the maximum increase in height is 0.116 m (Case 6) and the maximum gradient between two adjacent bearings is 1/667.

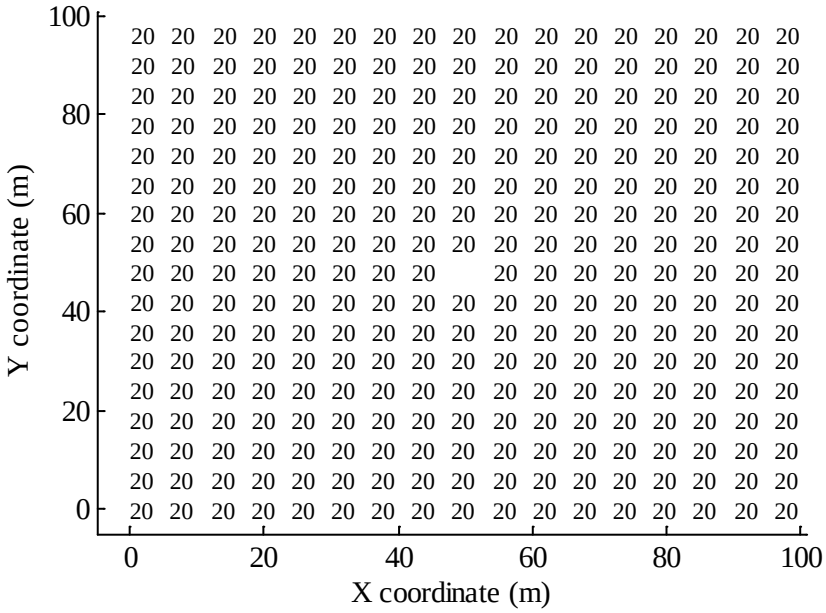

Figure D-2 Elevation in Bearings (mm) of the Isolation System Comprising FP Bearings with a Sliding Period of 2 s Subjected to a Translation of 0.200 m (Case 1)

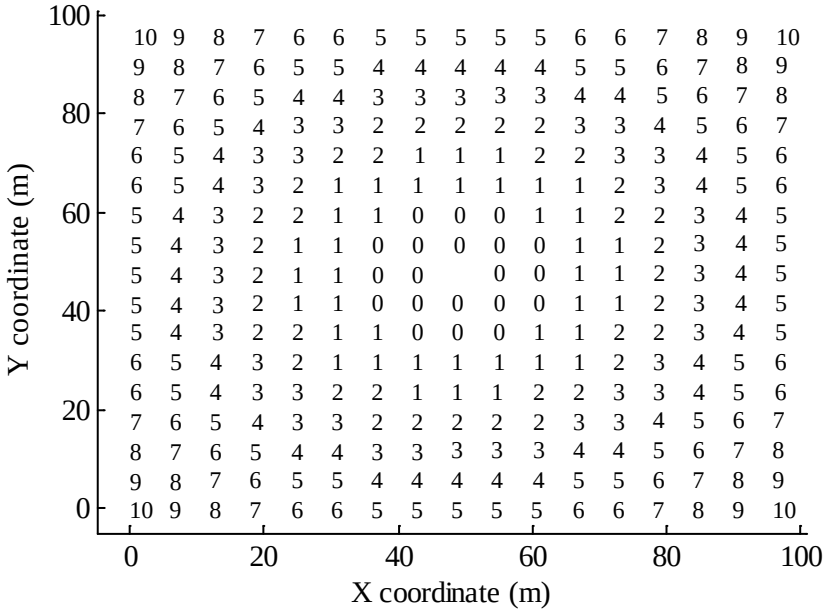

Figure D-3 Elevation in Bearings (mm) of the Isolation System Comprising FP Bearings with a Sliding Period of 2 s Subjected to a Rotation of 0.100 m (Case 2)

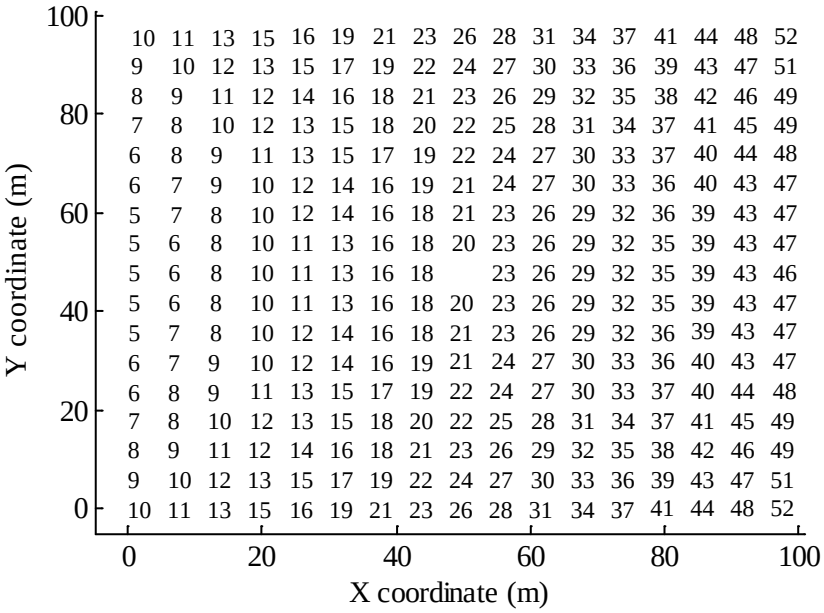

Figure D-4 Elevation in Bearings (mm) of the Isolation System Comprising FP Bearings with a Sliding Period of 2 s Subjected to a Translation of 0.200 m and a Rotation of 0.100 m (Case 3)

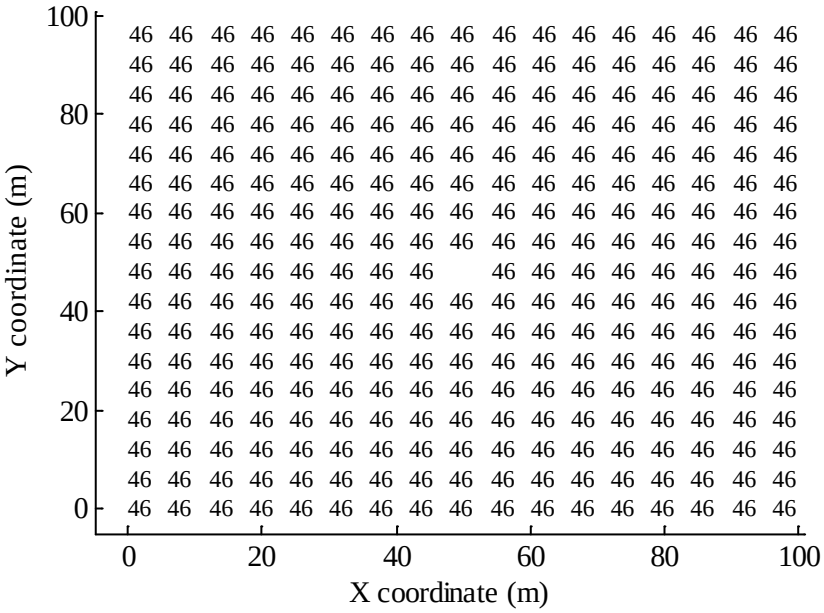

Figure D-5 Elevation in Bearings (mm) of the Isolation System Comprising FP Bearings with a Sliding Period of 4 s Subjected to a Translation of 0.600 m (Case 4)

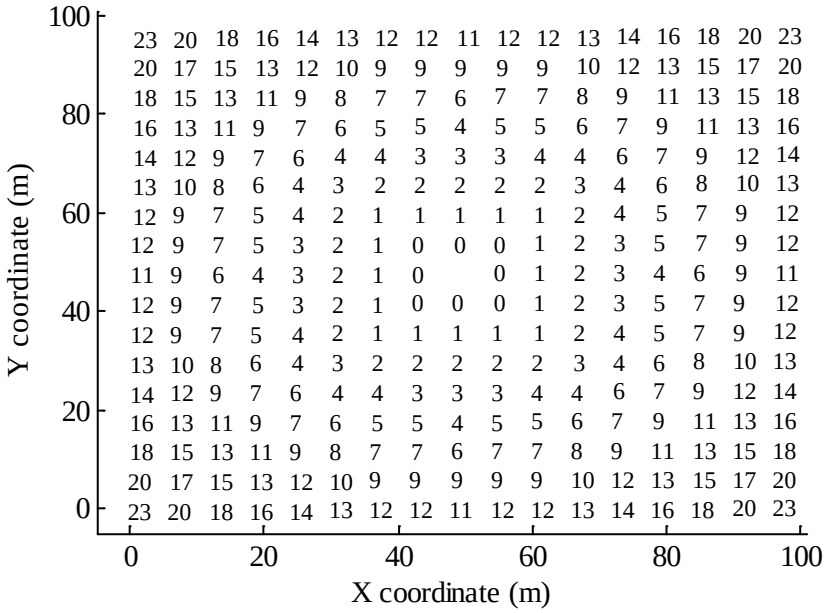

Figure D-6 Elevation in Bearings (mm) of the Isolation System Comprising FP Bearings with a Sliding Period of 4 s Subjected to a Rotation of 0.300 m (Case 5)

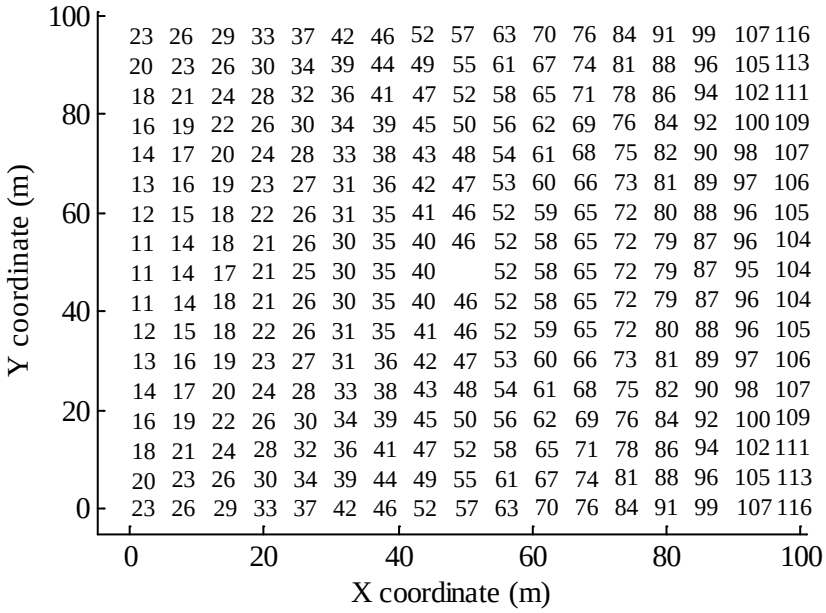

Figure D-7 Elevation in Bearings (mm) of the Isolation System Comprising FP Bearings with a Sliding Period of 4 s Subjected to a Translation of 0.600 m and a Rotation of 0.300 m (Case 6)

D.4 Summary

Seismic isolation bearings change in height when they are displaced laterally: elastomeric bearings shorten and the FP bearings rise. Basemats and diaphragms installed atop isolation systems could be structurally challenged if the relative change in height between adjacent bearings is significant.

Single concave FP isolation systems with plan dimensions of 96 m $\times$ 96 m and a 6 m spacing between the bearings (on center) were subjected to combinations of translation and torsion, noting that torsional response of FP isolation systems is generally small because the lateral stiffness of an FP isolator is a function of the supported mass. Friction Pendulum isolators are often sized such that the maximum lateral displacement, due to any combination of system translation and rotation, is less than $0.2R$, where R is the radius of curvature of the sliding surface. Effectively, this limits the displacement capacity of a 2 s isolation system to 0.200 m and a 4 s isolation system to 0.800 m.

For this study, the maximum lateral displacement imposed on the 2 (4) s isolation system was 0.300 (0.900) m: values greater than $0.2R$. The maximum increase in height in all of the isolators and displaced configurations considered was 0.116 m, the maximum relative difference in height between adjacent bearings was 0.009 m, and the maximum vertical gradient was 1/667. Given that the relative vertical displacement and gradient would be experienced in only beyond design basis shaking, and their small magnitudes, basemat or diaphragm design need not consider the relative change in height of the adjacent FP bearings.

APPENDIX E
SEED GROUND MOTIONS FOR RESPONSE-HISTORY ANALYSIS

E.1 Introduction

Three representations of seismic hazard at the site of Diablo Canyon Nuclear Generating Station (DCNGS) are considered in Chapter 5: uniform hazard spectrum (UHRS), conditional mean spectrum (CMS), and conditional spectra (CS). This appendix presents the lists of seed ground motions that were spectrally matched to the three representations of the 10,000-year seismic hazard at the DCNGS site. The seed motions are downloaded from the Pacific Earthquake Engineering Research (PEER) Center, Next Generation Attenuation (NGA) database from the webpage http://peer.berkeley.edu/peer_ground_motion_database (accessed on June 15, 2014).

E.2 Lists of Seed Motions

Table E-1 lists the 30 seeds scaled to the UHRS. Table E-2 lists the 30 seed motions spectrally matched to the CMS with conditioning periods of 2 s, 3 s and 4 s. Table E-3 (E-4, E-5) lists the set of 30 seed ground motions spectrally matched to the set of 30 CS with a conditioning period of 2 s (3 s, 4 s).

Table E-1 Set of Seed Motions to Be Scaled to a Uniform Hazard Spectrum Representing the Seismic Hazard at Diablo Canyon for a Return Period of 10,000 Years

Sl No	NGA Number	Event	Year	Magnitude	Epicentral Distance (km)
1	72	San Fernando	1971	6.6	24
2	77	San Fernando	1971	6.6	12
3	80	San Fernando	1971	6.6	39
4	143	Tabas	1978	7.4	55
5	284	Irpinia	1980	6.9	33
6	285	Irpinia	1980	6.9	23
7	286	Irpinia	1980	6.9	23
8	292	Irpinia	1980	6.9	30
9	763	Loma Prieta	1989	6.9	29
10	765	Loma Prieta	1989	6.9	29
11	2704	Chi-Chi	1999	6.2	30
12	810	Loma Prieta	1989	6.9	16
13	828	Cape Mendocino	1992	7.0	5
14	957	Northridge	1994	6.7	64
15	989	Northridge	1994	6.7	15
16	994	Northridge	1994	6.7	25
17	1011	Northridge	1994	6.7	19
18	1012	Northridge	1994	6.7	14
19	1021	Northridge	1994	6.7	50
20	1050	Northridge	1994	6.7	20
21	1051	Northridge	1994	6.7	20
22	1078	Northridge	1994	6.7	15
23	1091	Northridge	1994	6.7	38
24	1161	Kocaeli	1999	7.5	47
25	1165	Kocaeli	1999	7.5	5
26	1485	Chi-Chi	1999	7.6	78
27	1107	Kobe	1995	6.9	24
28	1509	Chi-Chi	1999	7.6	19
29	1633	Manjil	1990	7.4	40
30	3548	Loma Prieta	1989	6.9	20

Table E-2 Set of Seed Motions to Be Scaled to Conditional Mean Spectra Representing the Seismic Hazard at Diablo Canyon for a Return Period of 10,000 Years

Sl No	NGA Number	Event	Year	Magnitude	Epicentral Distance (km)
1	1051	Northridge	1994	6.7	20
2	1508	Chi-Chi	1999	7.6	21
3	68	San Fernando	1971	6.6	39
4	1511	Chi-Chi	1999	7.6	16
5	180	Imperial Valley	1979	6.5	28
6	1115	Kobe	1995	6.9	42
7	3282	Chi-Chi	1999	6.3	71
8	2704	Chi-Chi	1999	6.2	30
9	187	Imperial Valley	1979	6.5	49
10	184	Imperial Valley	1979	6.5	27
11	1118	Kobe	1995	6.9	39
12	3269	Chi-Chi	1999	6.3	57
13	2457	Chi-Chi	1999	6.2	26
14	879	Landers	1992	7.3	44
15	285	Irpinia	1980	6.9	23
16	159	Imperial Valley	1979	6.5	3
17	1510	Chi-Chi	1999	7.6	21
18	737	Loma Prieta	1989	6.9	40
19	1107	Kobe	1995	6.9	24
20	1633	Manjil	1990	7.4	40
21	1528	Chi-Chi	1999	7.6	45
22	1144	Gulf of Aqaba	1995	7.2	93
23	802	Loma Prieta	1989	6.9	27
24	169	Imperial Valley	1979	6.5	34
25	3512	Chi-Chi	1999	6.3	56
26	183	Imperial Valley	1979	6.5	28
27	1244	Chi-Chi	1999	7.6	32
28	3286	Chi-Chi	1999	6.3	101
29	3264	Chi-Chi	1999	6.3	108
30	292	Irpinia	1980	6.9	30

Table E-3 Set 1 of Seed Motions Scaled to 30 Conditional Spectra Representing the Seismic Hazard at Diablo Canyon for a Return Period of 10,000 Years

Sl No	NGA Number	Event	Year	Magnitude	Epicentral Distance (km)	Scaled to conditional spectrum number
1	1202	Chi-Chi	1999	7.6	44	1
2	1051	Northridge	1994	6.7	20	2
3	1787	Hector Mine	1999	7.1	27	3
4	884	Landers	1992	7.3	42	4
5	180	Imperial Valley	1979	6.5	28	5
6	1115	Kobe	1995	6.9	42	6
7	3282	Chi-Chi	1999	6.3	71	7
8	1762	Hector Mine	1999	7.1	48	8
9	187	Imperial Valley	1979	6.5	49	9
10	6	Imperial Valley	1940	7.0	13	10
11	1118	Kobe	1995	6.9	39	11
12	3269	Chi-Chi	1999	6.3	57	12
13	2457	Chi-Chi	1999	6.2	26	13
14	755	Loma Prieta	1989	6.9	31	14
15	285	Irpinia	1980	6.9	23	15
16	1209	Chi-Chi	1999	7.6	55	16
17	1078	Northridge	1994	6.7	15	17
18	737	Loma Prieta	1989	6.9	40	18
19	1503	Chi-Chi	1999	7.6	27	19
20	2458	Chi-Chi	1999	6.2	34	20
21	1528	Chi-Chi	1999	7.6	45	21
22	806	Loma Prieta	1989	6.9	42	22
23	802	Loma Prieta	1989	6.9	27	23
24	169	Imperial Valley	1979	6.5	34	24
25	3512	Chi-Chi	1999	6.3	56	25
26	183	Imperial Valley	1979	6.5	28	26
27	143	Tabas	1978	7.3	55	27
28	3286	Chi-Chi	1999	6.3	101	28
29	3264	Chi-Chi	1999	6.3	108	29
30	292	Trinidad	1980	7.2	77	30

Table E-4 Set 2 of Seed Motions Scaled to 30 Conditional Spectra Representing the Seismic Hazard at Diablo Canyon for a Return Period of 10,000 Years

Sl No	NGA Number	Event	Year	Magnitude	Epicentral Distance (km)	Scaled to conditional spectrum number
1	1009	Northridge	1994	6.7	20	1
2	881	Landers	1992	7.3	21	2
3	179	Imperial Valley	1979	6.5	27	3
4	68	San Fernando	1971	6.6	39	4
5	1511	Chi-Chi	1999	7.6	16	5
6	173	Imperial Valley	1979	6.5	26	6
7	1611	Duzce	1999	7.1	13	7
8	2899	Chi-Chi	1999	6.2	45	8
9	1107	Kobe	1995	6.9	24	9
10	1100	Kobe	1995	6.9	47	10
11	1540	Chi-Chi	1999	7.6	38	11
12	1488	Chi-Chi	1999	7.6	43	12
13	184	Imperial Valley	1979	6.5	27	13
14	1508	Chi-Chi	1999	7.6	21	14
15	3319	Chi-Chi	1999	6.3	97	15
16	879	Landers	1992	7.3	44	16
17	1633	Manjil	1990	7.4	40	17
18	1144	Gulf of Aqaba	1995	7.2	93	18
19	3271	Chi-Chi	1999	6.3	80	19
20	159	Imperial Valley	1979	6.5	3	20
21	170	Imperial Valley	1979	6.5	29	21
22	754	Loma Prieta	1989	6.9	31	22
23	1545	Chi-Chi	1999	7.6	26	23
24	1509	Chi-Chi	1999	7.6	19	24
25	174	Imperial Valley	1979	6.5	29	25
26	1111	Kobe	1995	6.9	9	26
27	1077	Northridge	1994	6.7	22	27
28	800	Loma Prieta	1989	6.9	46	28
29	1084	Northridge	1994	6.7	13	29
30	1183	Chi-Chi	1999	7.6	69	30

Table E-5 Set 3 of Seed Motions Scaled to 30 Conditional Spectra Representing the Seismic Hazard at Diablo Canyon for a Return Period of 10,000 Years

Sl No	NGA Number	Event	Year	Magnitude	Epicentral Distance (km)	Scaled to conditional spectrum number
1	1201	Chi-Chi	1999	7.6	46	1
2	2705	Chi-Chi	1999	6.2	35	2
3	1013	Northridge	1994	6.7	12	3
4	3317	Chi-Chi	1999	6.3	50	4
5	3302	Chi-Chi	1999	6.3	84	5
6	3275	Chi-Chi	1999	6.3	62	6
7	2752	Chi-Chi	1999	6.2	28	7
8	527	N. Palm Springs	1986	6.1	6	8
9	2655	Chi-Chi	1999	6.2	24	9
10	1487	Chi-Chi	1999	7.6	86	10
11	2495	Chi-Chi	1999	6.2	29	11
12	2897	Chi-Chi	1999	6.2	43	12
13	1085	Northridge	1994	6.7	14	13
14	1330	Chi-Chi	1999	7.6	137	14
15	885	Landers	1992	7.3	122	15
16	1460	Chi-Chi	1999	7.6	167	16
17	985	Northridge	1994	6.7	28	17
18	1636	Manjil	1990	7.4	84	18
19	2462	Chi-Chi	1999	6.2	39	19
20	1110	Kobe	1995	6.9	52	20
21	1161	Kocaeli	1999	7.5	47	21
22	826	Cape Mendocino	1992	7.0	53	22
23	1521	Chi-Chi	1999	7.6	7	23
24	3281	Chi-Chi	1999	6.3	71	24
25	882	Landers	1992	7.3	32	25
26	2884	Chi-Chi	1999	6.2	48	26
27	185	Imperial Valley	1979	6.5	20	27
28	2699	Chi-Chi	1999	6.2	28	28
29	3272	Chi-Chi	1999	6.3	89	29
30	549	Chalfant Valley	1986	6.2	20	30

APPENDIX F
RISK CALCULATIONS FOR SEISMICALLY ISOLATED SDC 5 NUCLEAR STRUCTURES DESIGNED PER ASCE STANDARD 4

F.1 Introduction

The annual frequencies of unacceptable performance of isolation systems designed and tested per the recommendations of the seismic isolation NUREG/ CR 7253 (Kammerer *et al.*, 2019) are calculated and presented in Chapter 6 for eight sites of nuclear facilities across the United States. This appendix presents companion calculations for isolation systems analyzed and tested per Chapter 12 of ASCE/SEI Standard 4-16 (ASCE, 2017) for a Seismic Design Category 5 safety-related nuclear structure.

F.2 Annual Frequency of Unacceptable Performance of an Isolation System

F.2.1 ASCE Standard 4 for Isolated Nuclear Structures

The US Department of Energy (DoE) uses ASCE Standard 4 and ASCE/SEI Standard 43-05 (ASCE, 2005) for seismic analysis and design of safety-related nuclear structures, which include nuclear power plants. Department of Energy-regulated nuclear power plants fall into Seismic Design Category (SDC) 5, which specifies the hazard exceedance frequency for the design earthquake ($=1\times10^{-4}$) and the target performance goal (1×10^{-5}).

Section 1.3 of ASCE 43-05 writes that the target performance can be achieved by satisfying two criteria, namely, 1) Less than about a 1% probability of unacceptable performance for the design basis earthquake (DBE) ground motion, and 2) Less than about a 10% probability of unacceptable performance for a ground motion equal to 150% of the DBE ground motion. In ASCE 43-05, the DBE ground motion is defined in terms of a design response spectrum with ordinates equal to the product of the uniform hazard response spectrum (UHRS) at the specified mean annual frequency of exceedance and a design factor. For a nuclear power plant, the UHRS is specified at a mean annual frequency of exceedance of 1×10^{-4}.

Chapter 12 of ASCE 4-16 provides guidance on the analysis and design of isolation systems, and requirements for testing isolators. The target performance goal of 1×10^{-5} for a seismically isolated SDC 5 safety-related nuclear structure is achieved using the two criteria listed above, where unacceptable performance of the isolation system is conservatively measured in terms of insufficient capacity of individual isolators, identical to Chapter 6. Herein, the design factor is assumed to be 1.0, which is confirmed through risk calculations.

The following sections present fragility curves and the calculation of annual frequency of unacceptable performance based on isolators being designed and tested per the provisions of Chapter 12 of ASCE 4-16, namely, there be 90+% confidence that the isolators can support axial loads at a horizontal displacement equal to the clearance to the stop, CS, where CS is no less than the 90th percentile horizontal displacement for 150% DBE shaking. The risk calculations are repeated for isolators tested with 90+% confidence at 90th percentile horizontal displacement for 200% DBE shaking. Similar to Chapter 6 (and confirmed in Chapter 7), the *median* fragility curves are developed assuming that the 90th percentile displacement for 150% (200%) DBE shaking is equal to the median displacement at 1.1 times 150% (200%) DBE shaking. The hazard curves plotted in Figure 6-7 are used for the risk calculations.

F.2.2 Isolators Tested at 90th Percentile Displacement for 150+% DBE Shaking

Figure F-1 presents fragility curves for isolators tested with 90% confidence at median displacement for 165% DBE shaking (or 90th percentile displacement for 150% DBE shaking) with no stop. Figure F-2 presents the disaggregation of risk for log standard deviation, β, equal to 0.01 at Diablo Canyon and North Anna. Figures F-3 and F-4 present fragility curves for isolators tested at median displacement for 165% DBE shaking with 95% and 99% confidence, respectively. Figure F-5 presents fragility curves for isolators tested with 90% confidence at median displacement for 187.5% DBE shaking. The annual frequencies of unacceptable performance for isolators with fragility curves of Figures F-1, F-3, F-4 and F-5 are listed in Tables F-1, F-2, F-3 and F-4, respectively. A small reduction in risk is achieved if the confidence level on isolator performance is increased from 90% to 99% (see Tables F-1 and F-3). The meaningful reduction in risk is achieved at 90% confidence if the isolators are tested (and perform acceptably) at the median displacement for 187.5% DBE shaking (compare the risk numbers in Tables F-1 and F-4). The annual frequencies of unacceptable performance reported in Tables F-1 through F-4 are greater than 1×10^{-5} for all bar one combinations considered here: a stop is most likely needed in isolated SDC 5 nuclear structures to achieve the target performance goal.

The above calculations were performed assuming no stop was present. The fragility curves of Figures F-1, F-3, F-4 and F-5 are truncated at the specified level of confidence to acknowledge the presence of a stop at the given median displacement in Figures F-6, F-7, F-8 and F-9, respectively. The annual frequencies of unacceptable performance for the stop-enabled fragility curves of Figures F-6 through F-9 are listed in Tables F-5 through F-8, respectively. All of the listed frequencies are considerably smaller than 1×10^{-5} for all combinations of site, confidence, test displacement and log standard deviation. A value of the design factor equal to 1.0 is appropriate for seismically isolated SDC 5 nuclear structures, provided the effects of vertical shaking do not control the design. A substantial reduction in risk is achieved if the confidence on isolator performance is increased from 90% to 99% (see Tables F-5 and F-7).

Chapter 6 identified the ratio of 5% damped spectral demand of 100,000- to 10,000-year earthquake shaking for periods of 1 s and 2 s and eight sites of nuclear facilities in the United States. The ratio is smaller in regions of high seismic hazard (e.g., = 2 for Diablo Canyon at 2 s, see Table 6-3) than low seismic hazard (e.g., = 3.1 for North Anna at 2 s, see Table 6-3). The seismic isolation NUREG requires bearings to be tested at the 90th percentile displacement for 100,000-year shaking (and not a constant fraction of DBE shaking). The variation in risk across the eight sites, assuming no stop is present, is relatively small: 4.7×10^{-6} for Diablo Canyon to 7.3×10^{-6} for North Anna (see Table 6-7, $\beta = 0.05$). The greatest difference in risk is by a factor of 1.5, which increases to 2.5 when the beyond design basis earthquake is presented as a contact fraction (=1.5) of design basis earthquake shaking: 14.7×10^{-6} for Diablo Canyon to 34.8×10^{-6} for North Anna (see Table F-1, $\beta = 0.05$).

F.2.3 Isolators Tested at 90th Percentile Displacement for 200% DBE Shaking

The 2 s seismic demand at the site of Diablo Canyon is greater by more than a factor of 2 than the demand at the other sites considered in this report, with the exception of Los Alamos: see Table 6-3. Isolators with capacity just sufficient for Diablo Canyon would have excess capacity at all other sites, leading to the question, “By how much is risk reduced if the beyond design basis shaking is assumed to be 2.0 times design basis shaking?”. This question is addressed below.

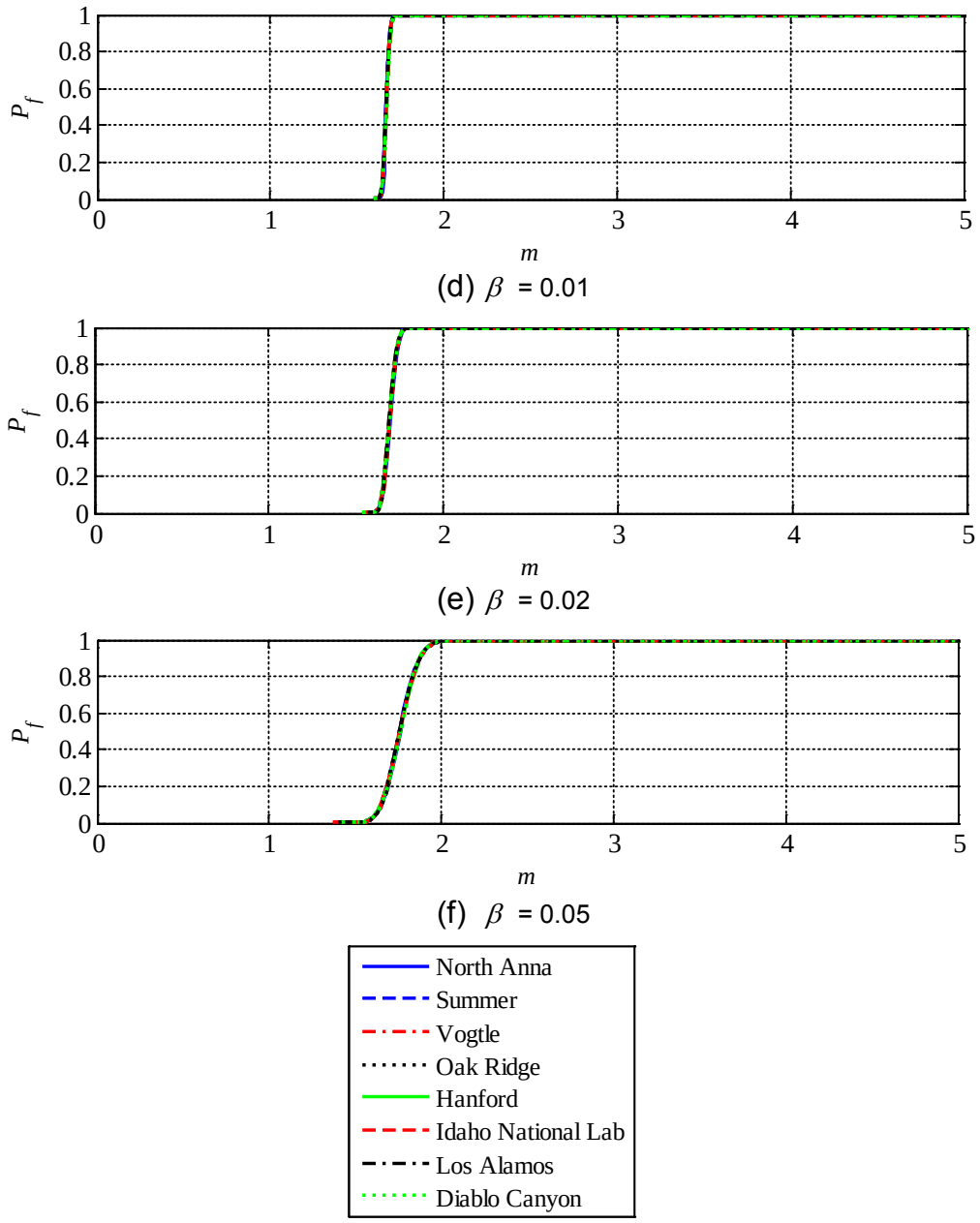

Figure F-1 Probability of Unacceptable Performance, P_f, of Individual Isolator Units for 90% Confidence at the Median Displacement for 165% DBE Shaking Plotted Against Multiples, *m*, of UHRS Shaking with MAFE of 10^{-4}, Without a Stop

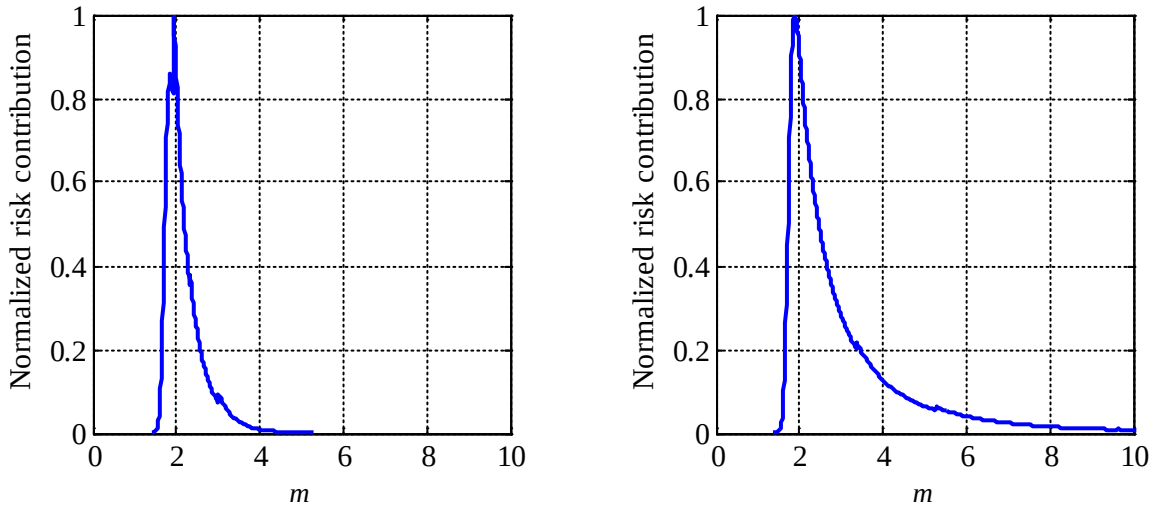

(c) Diablo Canyon (d) North Anna

Figure F-2 Disaggregation of Risk Corresponding to Figure F-1(a) for Two Sites

The fragility curves and risk disaggregation plots of Figures F-1, F-2, F-3, F-4, F-6, F-7 and F-8 are re-generated for isolators tested with 90%, 95% and 99% confidence at median displacement for 220% (= 1.1 times 200%: converting 90th percentile displacements to median displacements, as described previously) DBE shaking, and are plotted in Figures F-10 through F-16, respectively. The corresponding annual frequencies of unacceptable performance are listed in Tables F- through F-14, respectively. The frequencies are greater than 1×10^{-5} for five of the eight sites if a stop is not provided and considerably less than 1×10^{-5} for all eight sites if a stop is provided. (The risk numbers in the last column of Tables F-9 through F-11 are similar to those in the corresponding column of Tables 6-7 through 6-9, because 2.0 times DBE shaking for Diablo Canyon is approximately equal to shaking with a mean annual frequency of exceedance of 1×10^{-5}: the seismic isolation NUREG recommended definition of beyond design basis shaking.)

The increase in shaking intensity from 150% DBE to 200% DBE for the purpose of establishing displacements for testing isolators leads to a significant reduction in risk, with the greatest reductions for the sites of highest seismic hazard (e.g., Diablo Canyon, a factor of between 3.5 and 4) and the smallest reductions for the sites of lowest seismic hazard (e.g., North Anna, a factor of approximately 1.7). The significant difference in the slope on the seismic hazard curves for sites of low and high seismicity is the reason why the risk reductions are not uniform for a consistent increase in the shaking intensity from 150% DBE to 200% DBE. However, the annual frequency of unacceptable performance is greater than the target performance goal of 1×10^{-5} for five of the eight sites. A stop would still be needed for these five sites if 200% DBE shaking rather than 150% DBE shaking is used to define beyond design basis shaking. There is no practical risk-based benefit to increasing the shaking intensity used to define beyond design basis shaking.

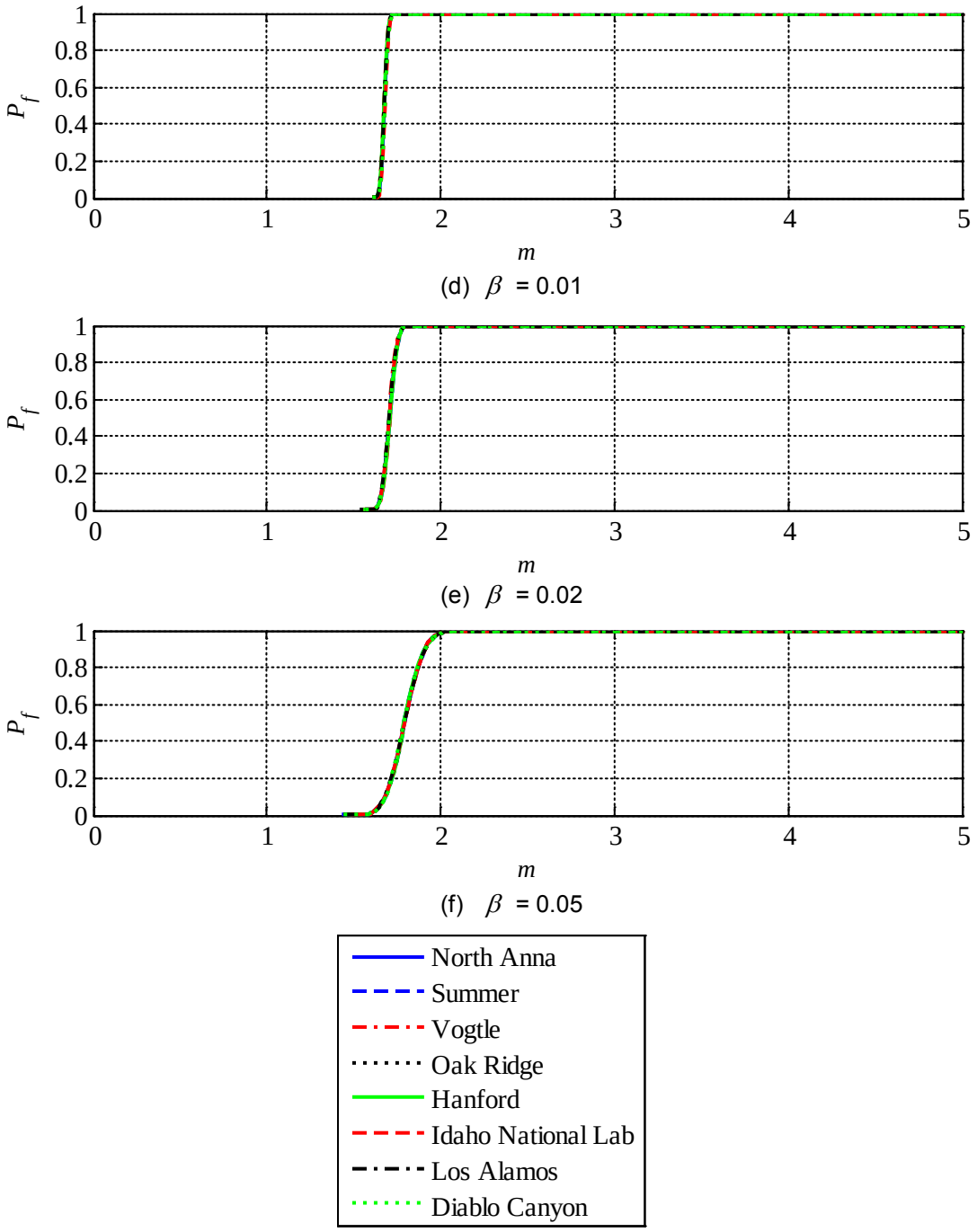

Figure F-3 Probability of Unacceptable Performance, P_f, of Individual Isolator Units for 95% Confidence at the Median Displacement for 165% DBE Shaking Plotted Against Multiples, *m*, of UHRS Shaking with MAFE of 10^{-4}, Without a Stop

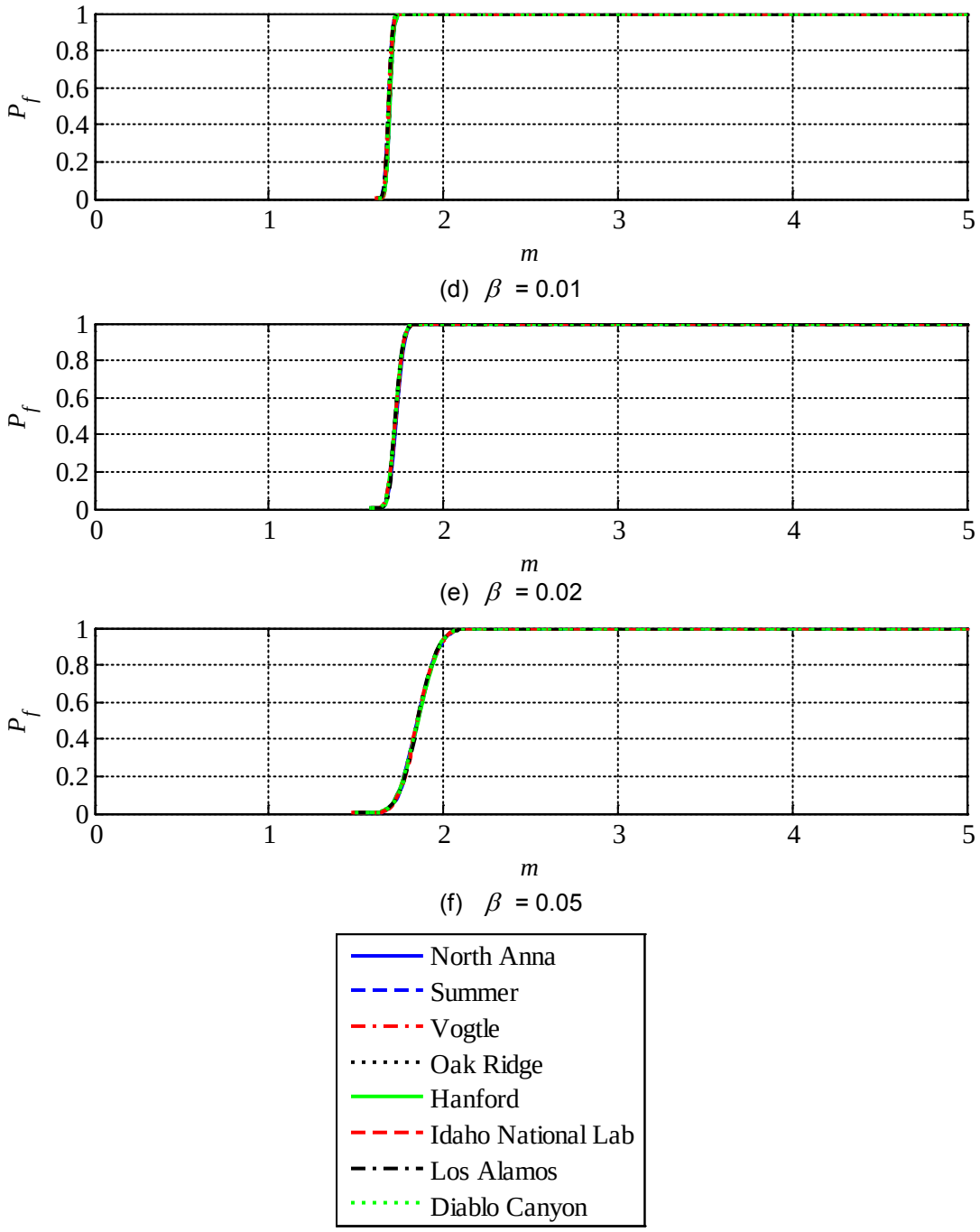

Figure F-4 **Probability of Unacceptable Performance, P_f, of Individual Isolator Units for 99% Confidence at the Median Displacement for 165% DBE Shaking Plotted Against Multiples, *m*, of UHRS Shaking with MAFE of 10^{-4}, Without a Stop**

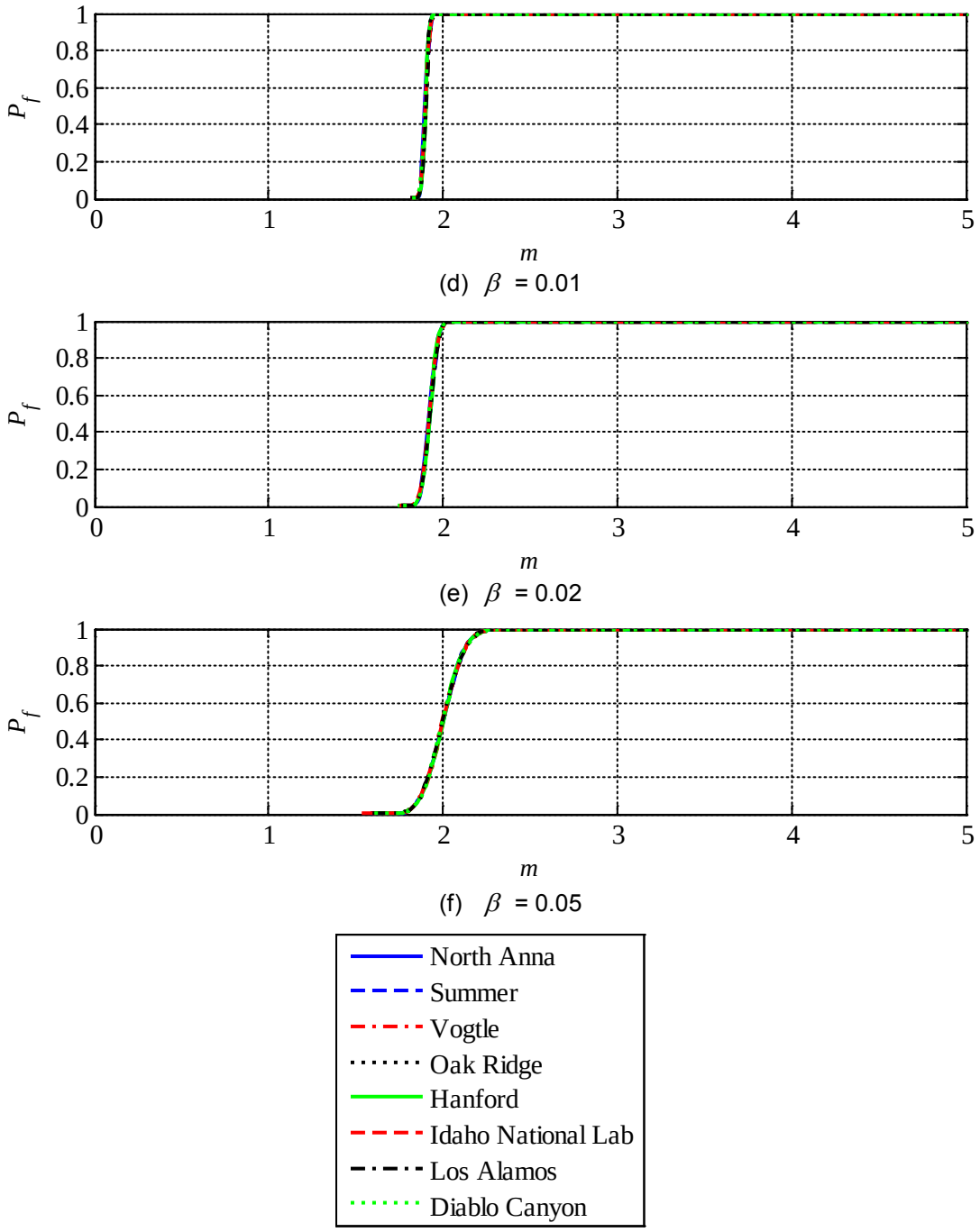

Figure F-5 **Probability of Unacceptable Performance, P_f, of Individual Isolator Units for 90% Confidence at the Median Displacement for 187.5% DBE Shaking Plotted Against Multiples, *m*, of UHRS Shaking with MAFE of 10^{-4}, Without a Stop**

Table F-1 Annual Frequency of Unacceptable Performance ($\times 10^{-6}$) of Individual Isolator Units Tested with 90% Confidence at the Median Displacement for 165% DBE Shaking, Without a Stop

	Site							
	North Anna	Summer	Vogtle	Oak Ridge	Hanford	Idaho	Los Alamos	Diablo Canyon
$\beta = 0.01$	38.2	28.4	26.2	33.8	21.0	17.9	38.6	17.6
$\beta = 0.02$	37.2	27.6	25.2	32.9	20.1	17.2	37.4	16.8
$\beta = 0.05$	34.8	25.2	22.8	30.5	17.9	15.2	34.3	14.7

Table F-2 Annual Frequency of Unacceptable Performance ($\times 10^{-6}$) of Individual Isolator Units Tested with 95% Confidence at the Median Displacement for 165% DBE Shaking, Without a Stop

	Site							
	North Anna	Summer	Vogtle	Oak Ridge	Hanford	Idaho	Los Alamos	Diablo Canyon
$\beta = 0.01$	37.7	28.2	25.9	33.5	20.7	17.7	38.3	17.4
$\beta = 0.02$	36.6	27.2	24.8	32.4	19.6	16.8	36.9	16.3
$\beta = 0.05$	33.5	24.2	21.7	29.4	16.8	14.2	33.0	13.7

Table F-3 Annual Frequency of Unacceptable Performance ($\times 10^{-6}$) of Individual Isolator Units Tested with 99% Confidence at the Median Displacement for 165% DBE Shaking, Without a Stop

	Site							
	North Anna	Summer	Vogtle	Oak Ridge	Hanford	Idaho	Los Alamos	Diablo Canyon
$\beta = 0.01$	37.3	27.7	25.4	33.1	20.2	17.2	37.7	16.8
$\beta = 0.02$	35.8	26.2	23.8	31.5	18.6	16.0	35.6	15.4
$\beta = 0.05$	31.4	22.0	19.8	27.2	15.0	12.6	30.3	12.0

Table F-4 Annual Frequency of Unacceptable Performance ($\times 10^{-6}$) of Individual Isolator Units Tested with 90% Confidence at the Median Displacement for 187.5% DBE Shaking, Without a Stop

	Site							
	North Anna	Summer	Vogtle	Oak Ridge	Hanford	Idaho	Los Alamos	Diablo Canyon
$\beta = 0.01$	29.8	20.5	18.3	25.6	13.6	11.4	28.5	10.7
$\beta = 0.02$	29.1	19.9	17.7	25.0	13.0	10.9	27.5	10.2
$\beta = 0.05$	27.2	18.1	16.1	23.1	11.5	9.6	25.3	8.7

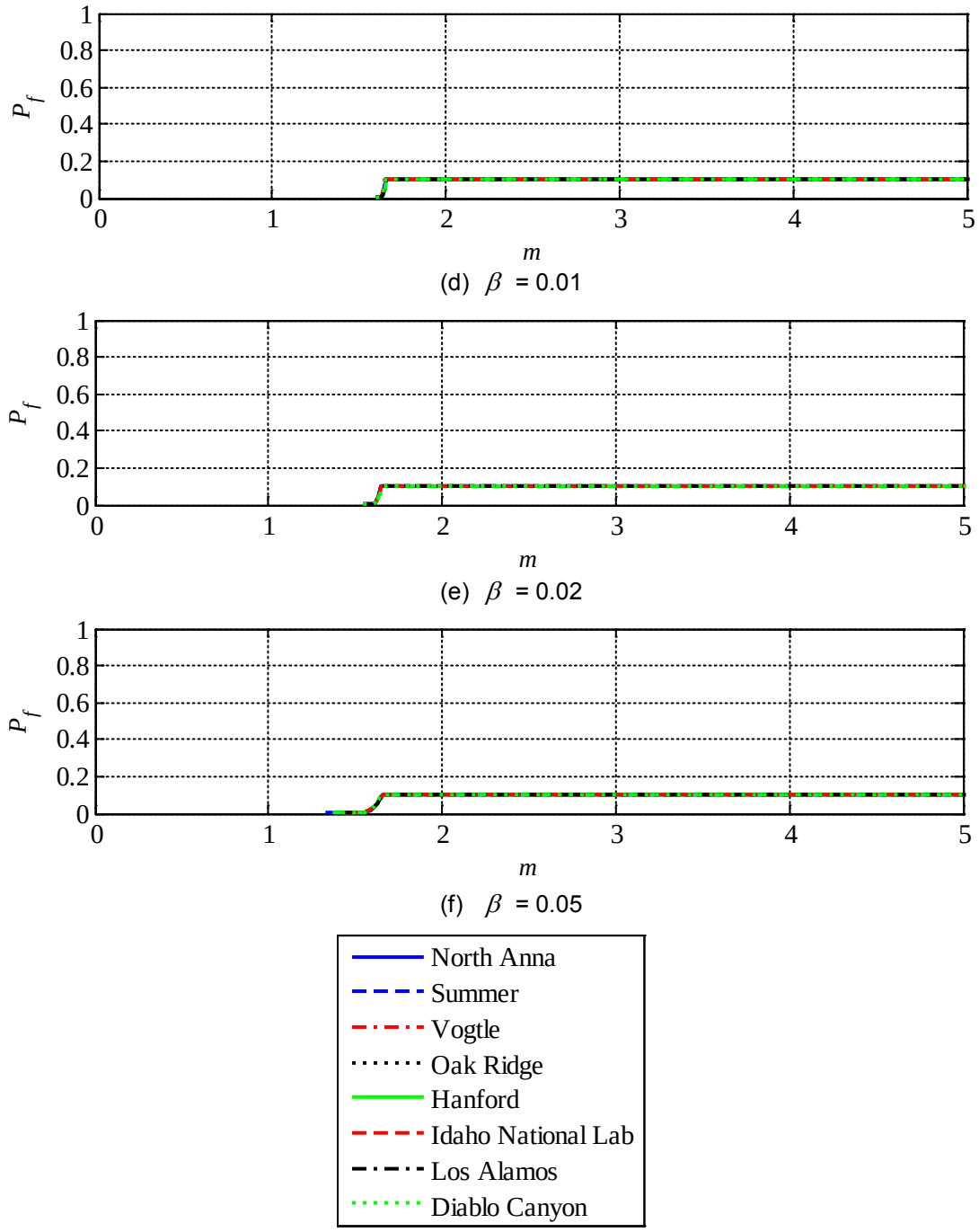

Figure F-6 **Probability of Unacceptable Performance, P_f, of Individual Isolator Units for 90% Confidence at the Median Displacement for 165% DBE Shaking Plotted Against Multiples, *m*, of UHRS Shaking with MAFE of 10^{-4}, with a Stop at Median Displacement for 165% DBE Shaking**

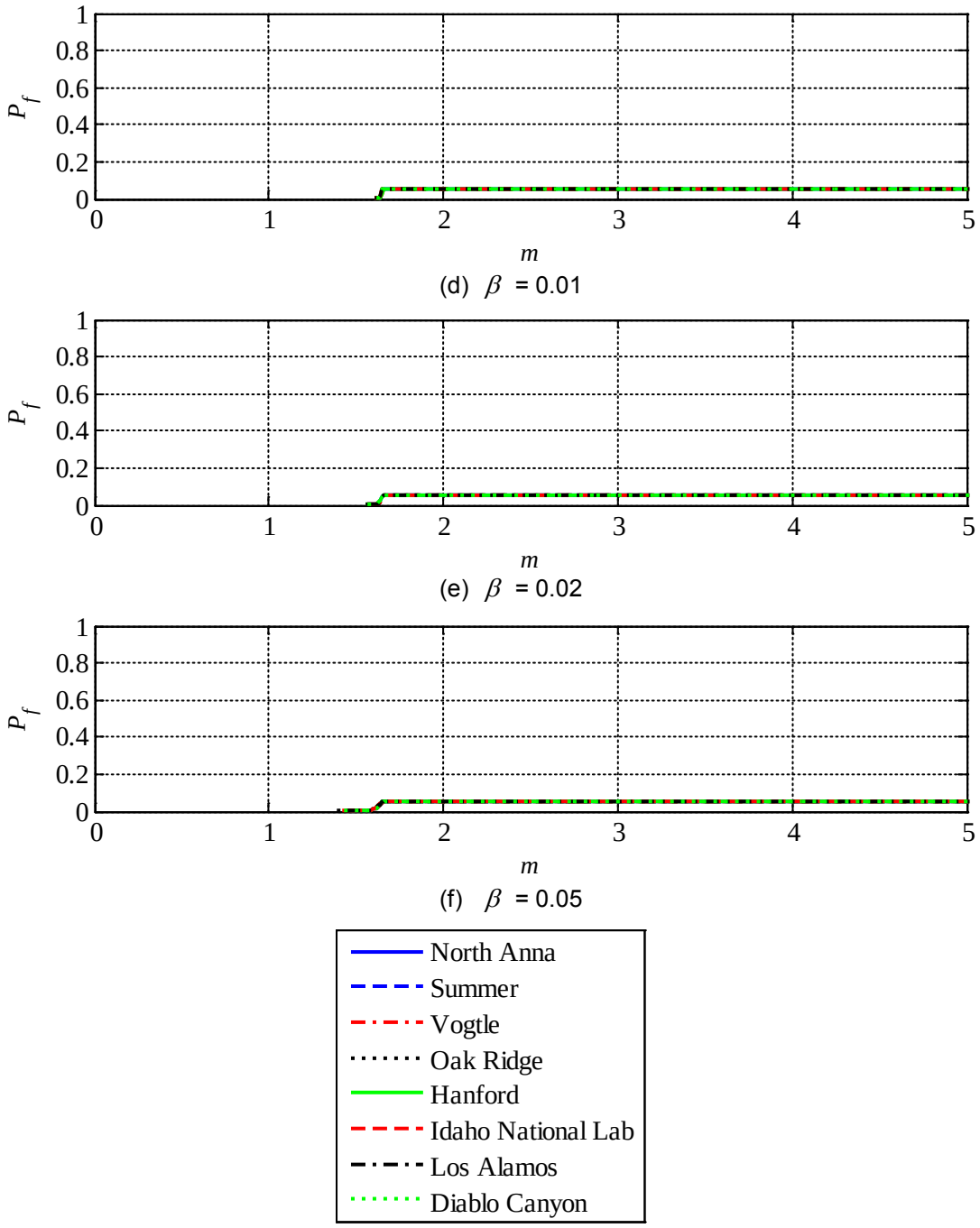

Figure F-7 **Probability of Unacceptable Performance, P_f, of Individual Isolator Units for 95% Confidence at the Median Displacement for 165% DBE Shaking Plotted Against Multiples, m, of UHRS Shaking with MAFE of 10^{-4}, with a Stop at Median Displacement for 165% DBE Shaking**

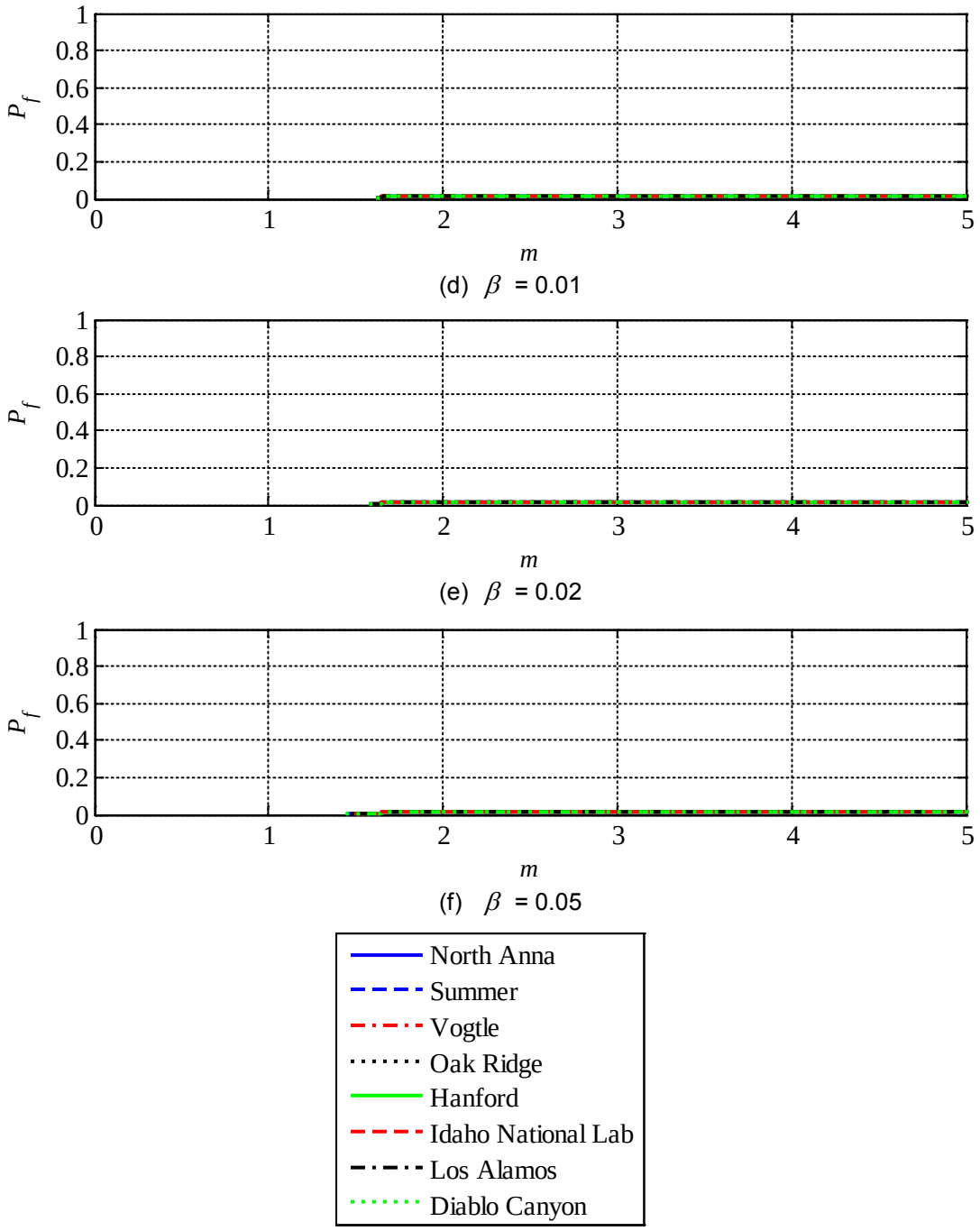

Figure F-8 Probability of Unacceptable Performance, P_f, of Individual Isolator Units for 99% Confidence at the Median Displacement for 165% GMRS Shaking Plotted Against Multiples, m, of UHRS Shaking with MAFE of 10^{-4}, with a Stop at Median Displacement for 165% DBE Shaking

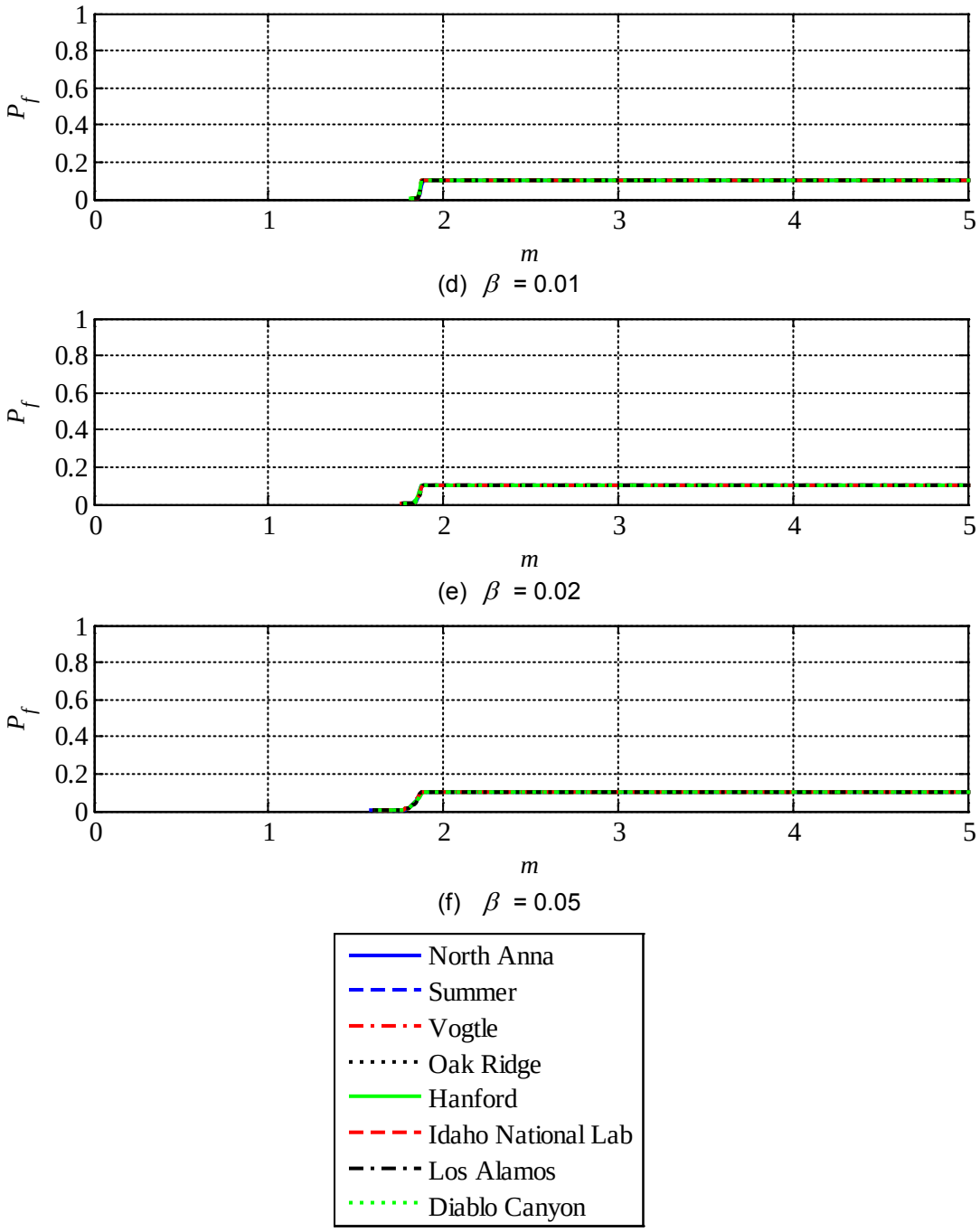

Figure F-9 **Probability of Unacceptable Performance, P_f, of Individual Isolator Units for 90% Confidence at the Median Displacement for 187.5% DBE Shaking Plotted Against Multiples, *m*, of UHRS Shaking with MAFE of 10^{-4}, with a Stop at Median Displacement for 187.5% DBE Shaking**

Table F-5 Annual Frequency of Unacceptable Performance ($\times 10^{-6}$) of Individual Isolator Units Tested with 90% Confidence at the Median Displacement for 165% DBE Shaking, with a Stop at Median Displacement for 165% DBE Shaking

	Site							
	North Anna	Summer	Vogtle	Oak Ridge	Hanford	Idaho	Los Alamos	Diablo Canyon
$\beta = 0.01$	3.9	3.0	2.7	3.5	2.2	1.9	4.0	1.9
$\beta = 0.02$	4.0	3.0	2.8	3.6	2.3	1.9	4.1	1.9
$\beta = 0.05$	4.1	3.1	2.9	3.7	2.4	2.1	4.2	2.0

Table F-6 Annual Frequency of Unacceptable Performance ($\times 10^{-6}$) of Individual Isolator Units Tested with 95% Confidence at the Median Displacement for 165% DBE Shaking, with a Stop at Median Displacement for 165% DBE Shaking

	Site							
	North Anna	Summer	Vogtle	Oak Ridge	Hanford	Idaho	Los Alamos	Diablo Canyon
$\beta = 0.01$	2.0	1.5	1.4	1.8	1.1	1.0	2.0	0.9
$\beta = 0.02$	2.0	1.5	1.4	1.8	1.1	1.0	2.0	0.9
$\beta = 0.05$	2.0	1.6	1.4	1.8	1.2	1.0	2.1	1.0

Table F-7 Annual Frequency of Unacceptable Performance ($\times 10^{-6}$) of Individual Isolator Units Tested with 99% Confidence at the Median Displacement for 165% DBE Shaking, with a Stop at Median Displacement for 165% DBE Shaking

	Site							
	North Anna	Summer	Vogtle	Oak Ridge	Hanford	Idaho	Los Alamos	Diablo Canyon
$\beta = 0.01$	0.4	0.3	0.3	0.4	0.2	0.2	0.4	0.2
$\beta = 0.02$	0.4	0.3	0.3	0.4	0.2	0.2	0.4	0.2
$\beta = 0.05$	0.4	0.3	0.3	0.4	0.2	0.2	0.4	0.2

Table F-8 Annual Frequency of Unacceptable Performance ($\times 10^{-6}$) of Individual Isolator Units Tested with 90% Confidence at the Median Displacement for 187.5% DBE Shaking, with a Stop at Median Displacement for 187.5% DBE Shaking

	Site							
	North Anna	Summer	Vogtle	Oak Ridge	Hanford	Idaho	Los Alamos	Diablo Canyon
$\beta = 0.01$	3.1	2.2	1.9	2.7	1.4	1.2	3.0	1.2
$\beta = 0.02$	3.1	2.2	1.9	2.7	1.5	1.2	3.0	1.2
$\beta = 0.05$	3.2	2.3	2.0	2.8	1.5	1.3	3.1	1.2

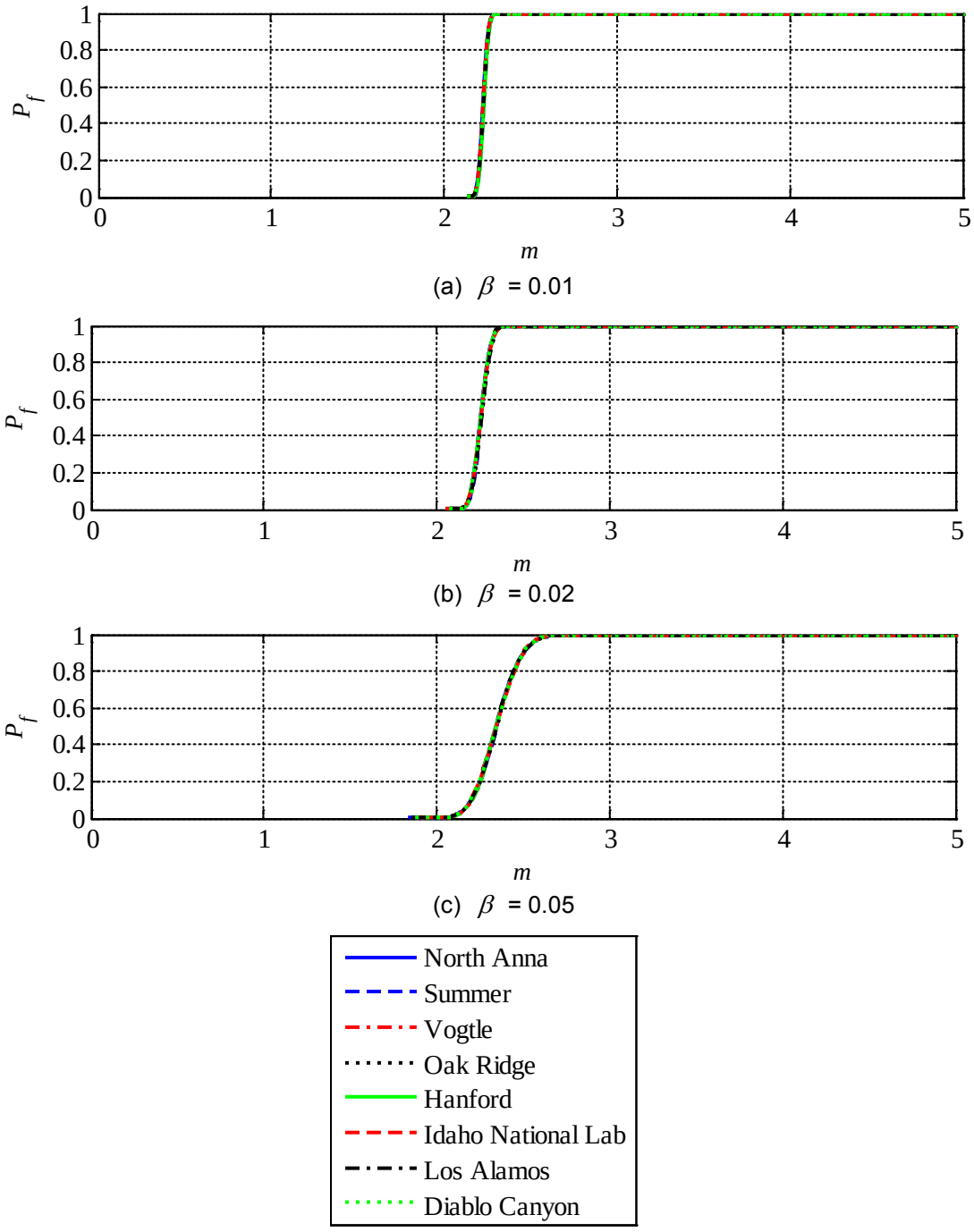

Figure F-10 Probability of Unacceptable Performance, P_f, of Individual Isolator Units for 90% Confidence at the Median Displacement for 220% DBE Shaking Plotted Against Multiples, *m*, of UHRS Shaking with MAFE of 10^{-4}, Without a Stop

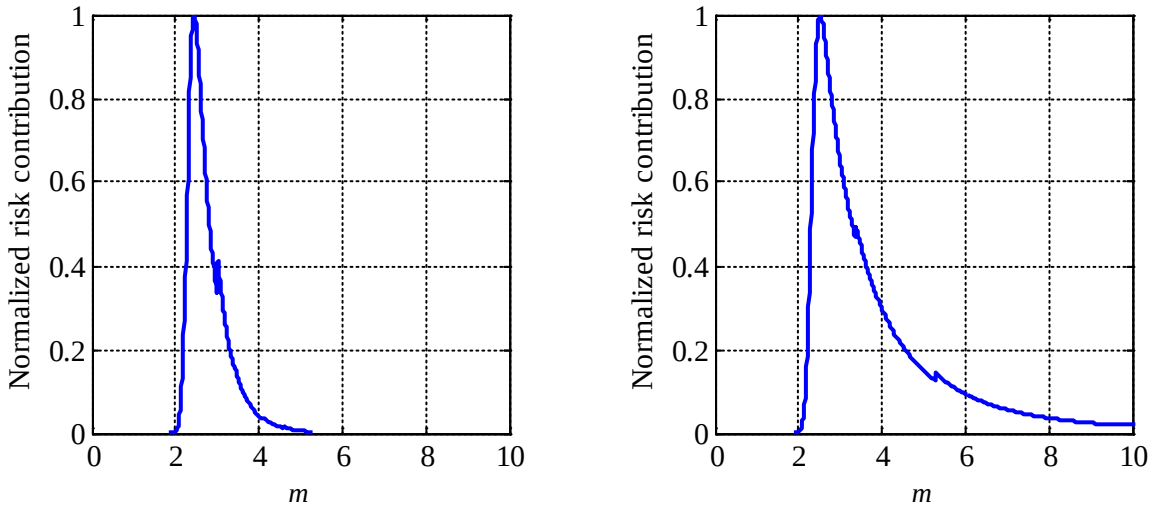

(a) Diablo Canyon (b) North Anna

Figure F-11 Disaggregation of Risk Corresponding to Figure F-10(a) for Two Sites

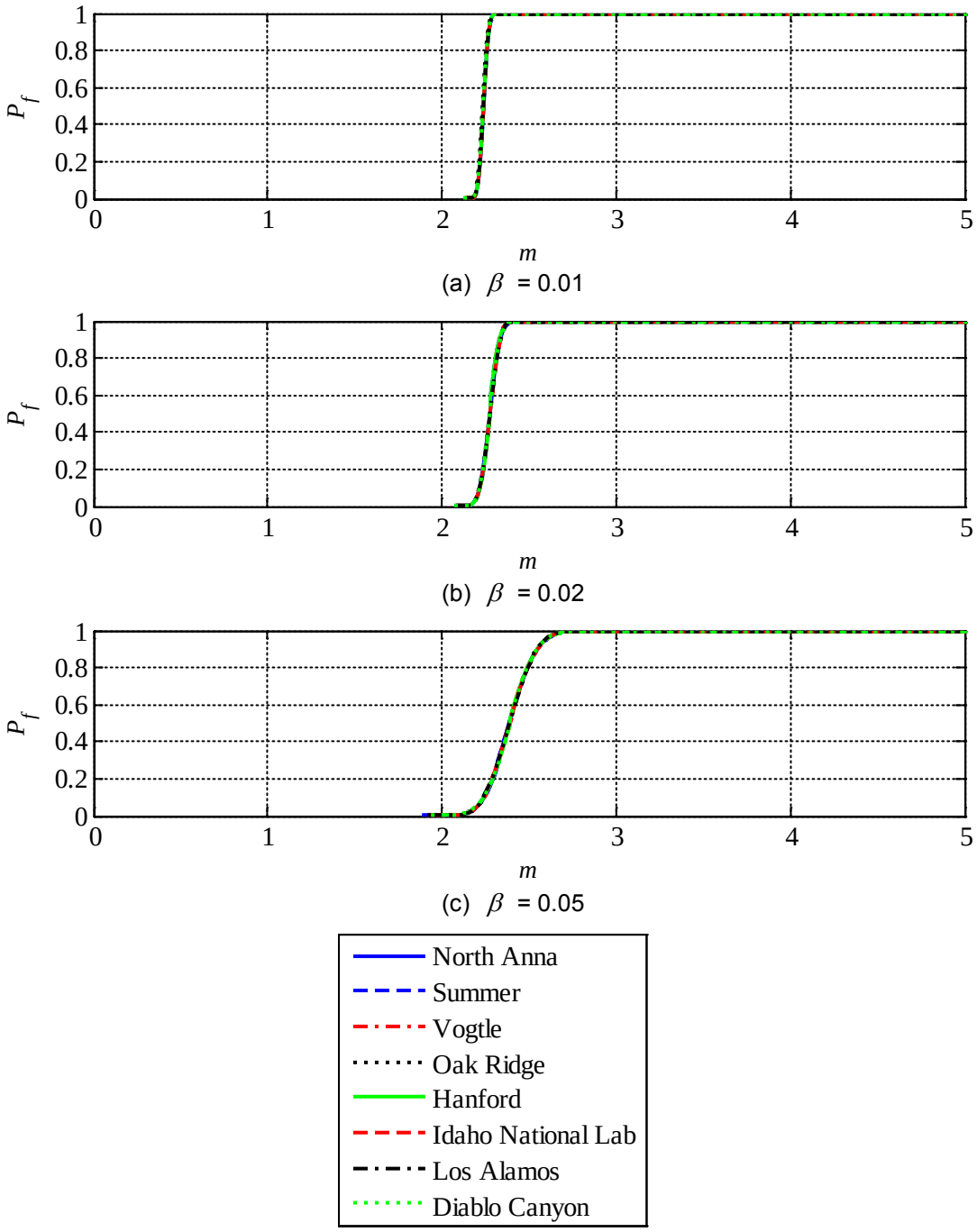

Figure F-12 Probability of Unacceptable Performance, P_f, of Individual Isolator Units for 95% Confidence at the Median Displacement for 220% DBE Shaking Plotted Against Multiples, *m*, of UHRS Shaking with MAFE of 10^{-4}, Without a Stop

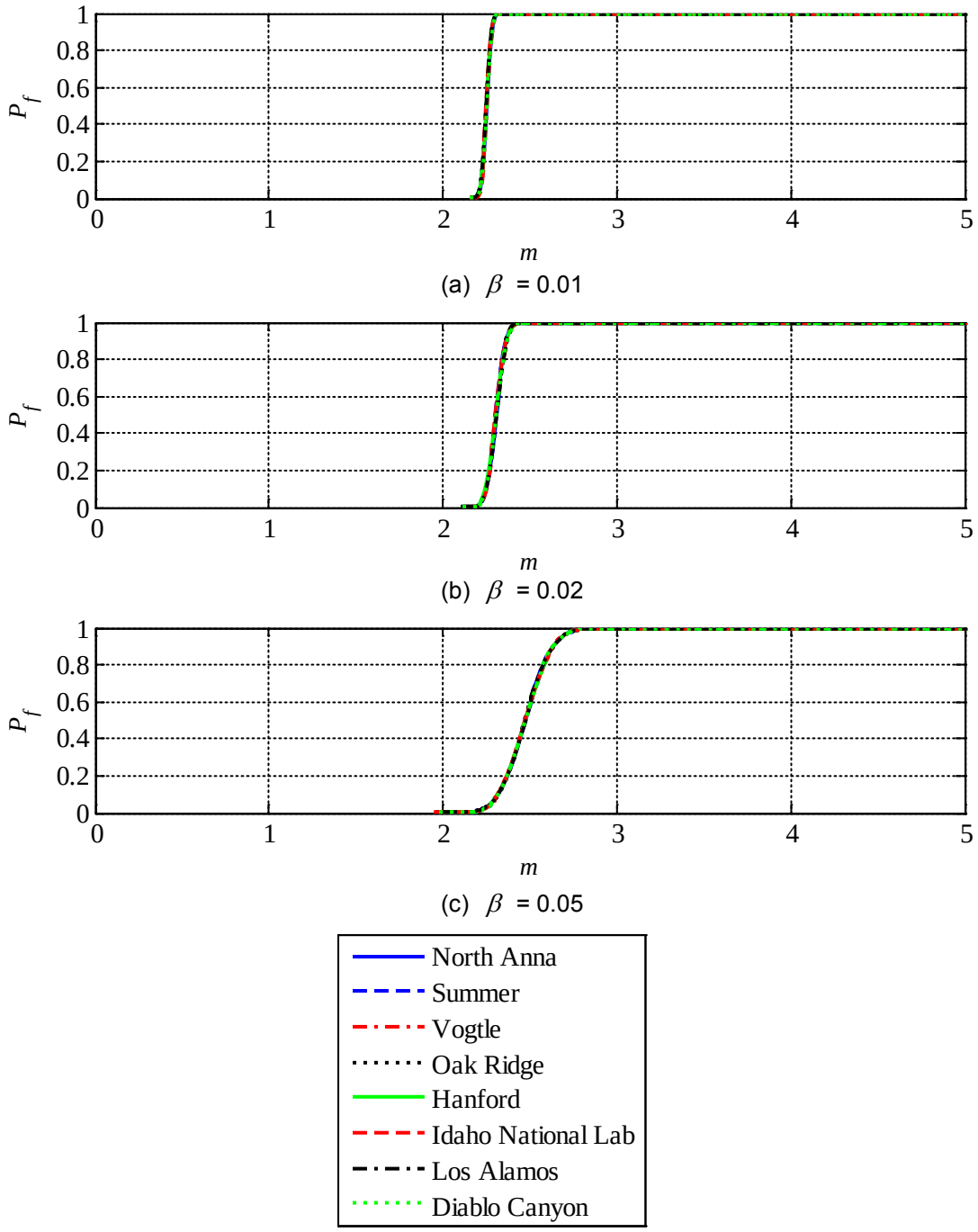

Figure F-13 Probability of Unacceptable Performance, P_f, of Individual Isolator Units for 99% Confidence at the Median Displacement for 220% DBE Shaking Plotted Against Multiples, *m*, of UHRS Shaking with MAFE of 10^{-4}, Without a Stop

Table F-9 Annual Frequency of Unacceptable Performance ($\times 10^{-6}$) of Individual Isolator Units Tested with 90% Confidence at the Median Displacement for 220% DBE Shaking, Without a Stop

	Site							
	North Anna	Summer	Vogtle	Oak Ridge	Hanford	Idaho	Los Alamos	Diablo Canyon
$\beta = 0.01$	22.0	13.7	11.8	18.1	7.5	6.1	19.4	5.0
$\beta = 0.02$	21.5	13.3	11.4	17.6	7.1	5.8	18.8	4.7
$\beta = 0.05$	20.1	12.1	10.2	16.3	6.2	5.0	17.3	4.0

Table F-10 Annual Frequency of Unacceptable Performance ($\times 10^{-6}$) of Individual Isolator Units Tested with 95% Confidence at the Median Displacement for 220% DBE Shaking, Without a Stop

	Site							
	North Anna	Summer	Vogtle	Oak Ridge	Hanford	Idaho	Los Alamos	Diablo Canyon
$\beta = 0.01$	21.9	13.5	11.7	18.0	7.4	6.0	19.2	4.9
$\beta = 0.02$	21.2	13.0	11.1	17.3	6.9	5.6	18.5	4.5
$\beta = 0.05$	19.4	11.5	9.7	15.7	5.8	4.7	16.5	3.6

Table F-11 Annual Frequency of Unacceptable Performance ($\times 10^{-6}$) of Individual Isolator Units Tested with 99% Confidence at the Median Displacement for 220% DBE Shaking, Without a Stop

	Site							
	North Anna	Summer	Vogtle	Oak Ridge	Hanford	Idaho	Los Alamos	Diablo Canyon
$\beta = 0.01$	21.6	13.3	11.4	17.7	7.2	5.8	18.9	4.7
$\beta = 0.02$	20.7	12.5	10.7	16.9	6.5	5.3	17.9	4.2
$\beta = 0.05$	18.2	10.5	8.8	14.5	5.0	4.1	15.2	3.0

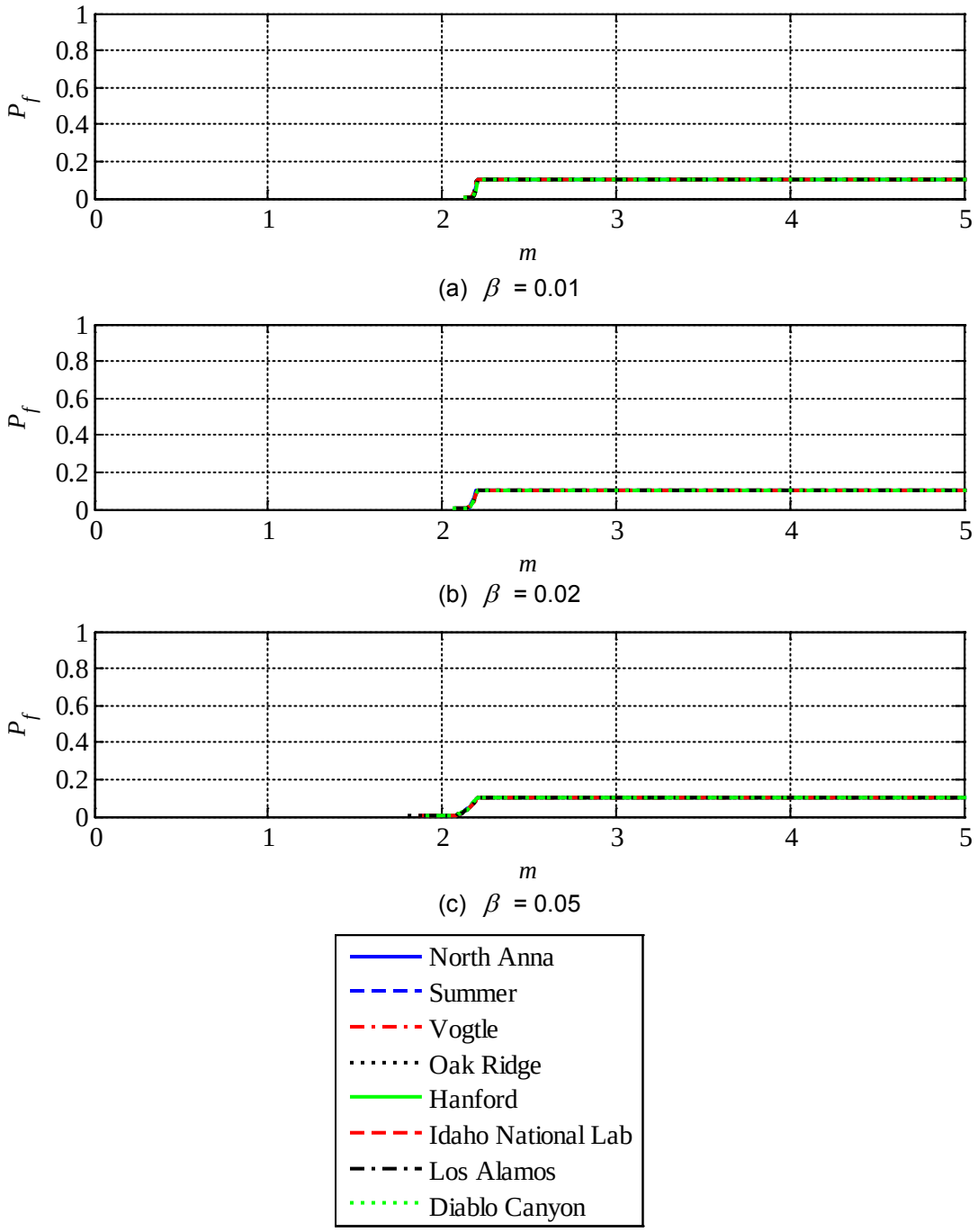

Figure F-14 Probability of Unacceptable Performance, P_f, of Individual Isolator Units for 90% Confidence at the Median Displacement for 220% DBE Shaking Plotted Against Multiples, *m*, of UHRS Shaking with MAFE of 10^{-4}, with a Stop at the Median Displacement for 220% DBE Shaking

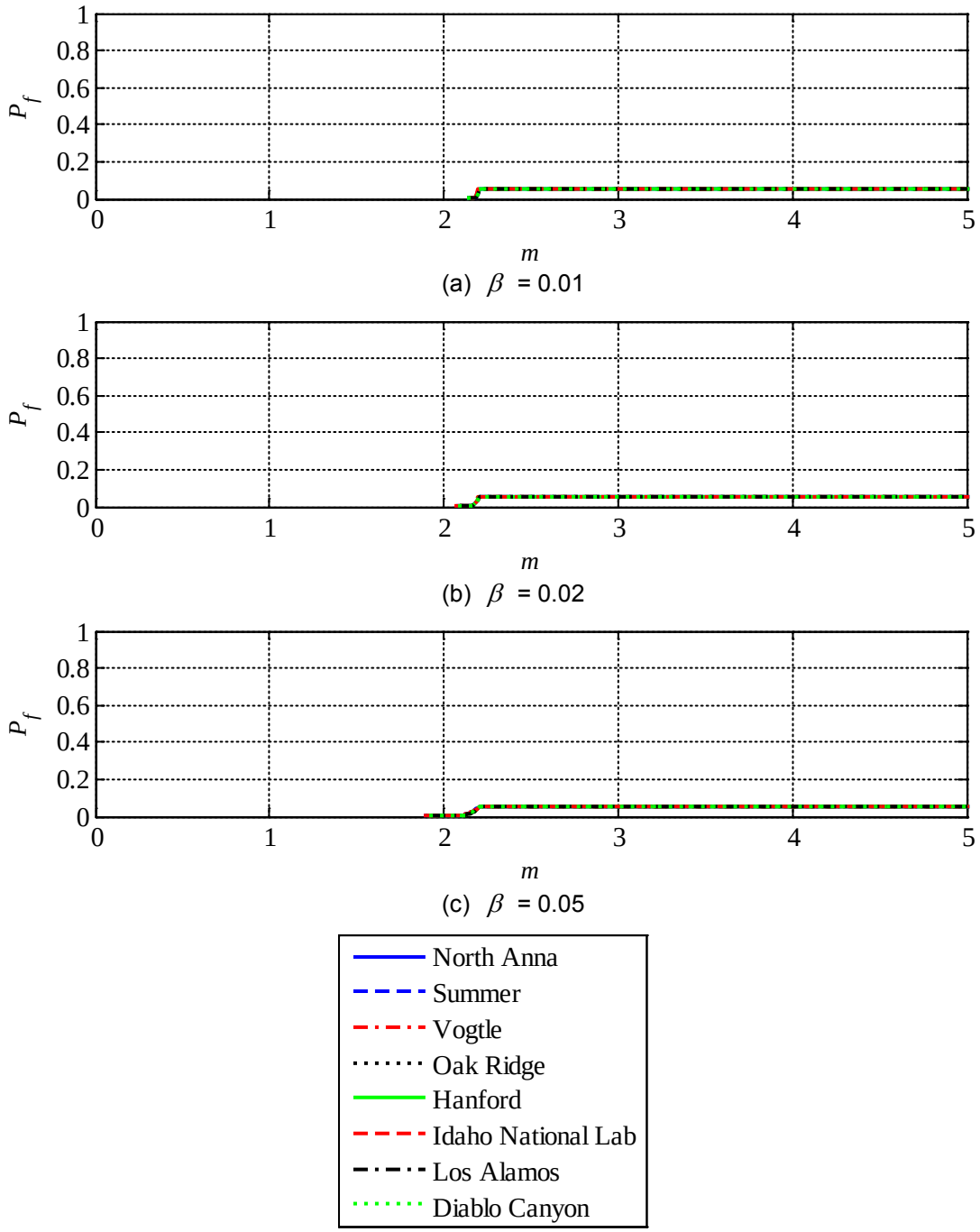

Figure F-15 Probability of Unacceptable Performance, P_f, of Individual Isolator Units for 95% Confidence at the Median Displacement for 220% DBE Shaking Plotted Against Multiples, *m*, of UHRS Shaking with MAFE of 10^{-4}, with a Stop at the Median Displacement for 220% DBE Shaking

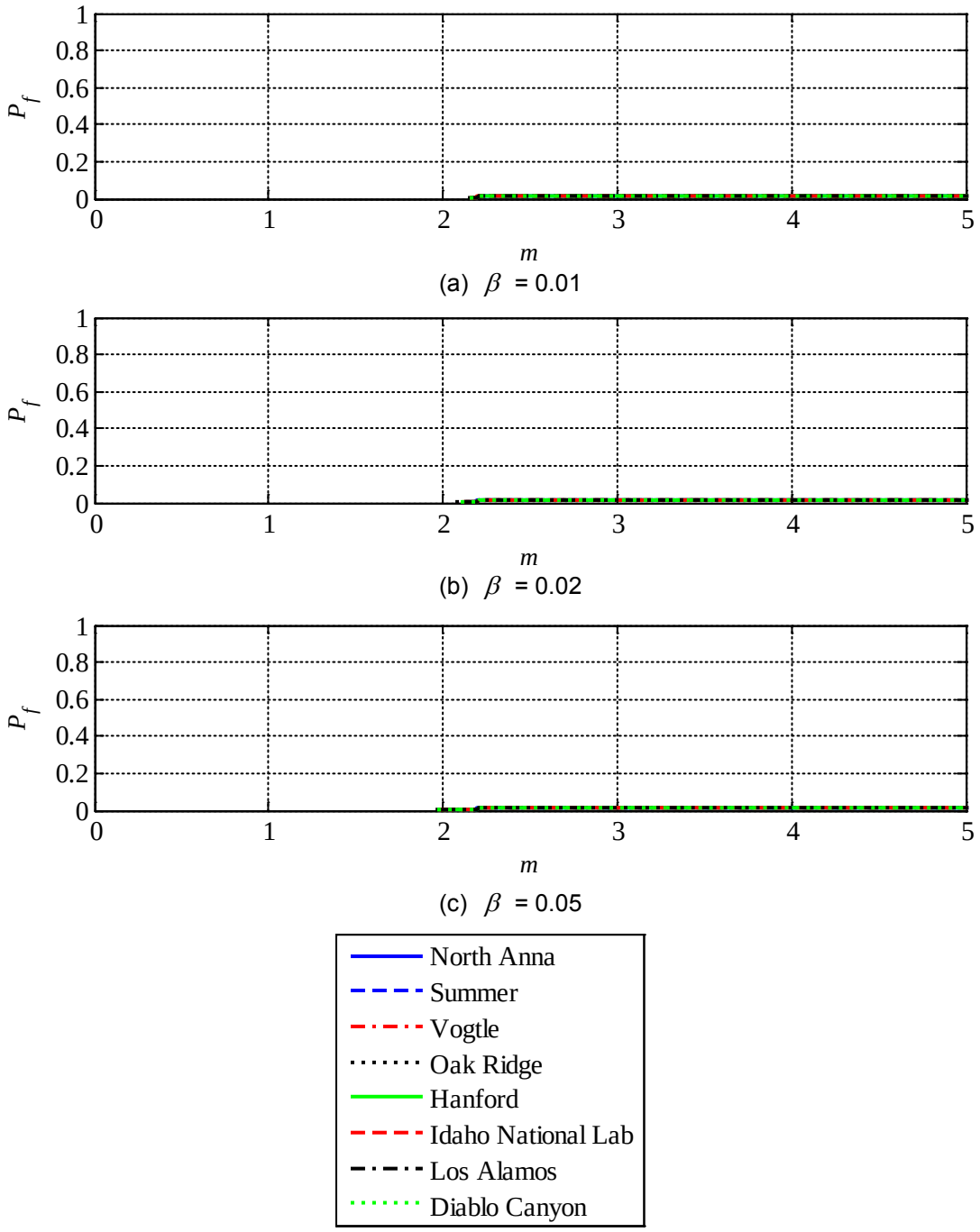

Figure F-16 Probability of Unacceptable Performance, P_f, of Individual Isolator Units for 99% Confidence at the Median Displacement for 220% DBE Shaking Plotted Against Multiples, m, of UHRS Shaking with MAFE of 10^{-4}, with a Stop at the Median Displacement for 220% DBE Shaking

Table F-12 Annual Frequency of Unacceptable Performance ($\times 10^{-6}$) of Individual Isolator Units Tested with 90% Confidence at the Median Displacement for 220% DBE Shaking, with a Stop at the Median Displacement for 220% DBE Shaking

	Site							
	North Anna	Summer	Vogtle	Oak Ridge	Hanford	Idaho	Los Alamos	Diablo Canyon
$\beta = 0.01$	2.3	1.4	1.2	1.9	0.8	0.6	2.0	0.5
$\beta = 0.02$	2.3	1.4	1.3	1.9	0.8	0.7	2.0	0.6
$\beta = 0.05$	2.4	1.5	1.3	2.0	0.9	0.7	2.1	0.6

Table F-13 Annual Frequency of Unacceptable Performance ($\times 10^{-6}$) of Individual Isolator Units Tested with 95% Confidence at the Median Displacement for 220% DBE Shaking, with a Stop at the Median Displacement for 220% DBE Shaking

	Site							
	North Anna	Summer	Vogtle	Oak Ridge	Hanford	Idaho	Los Alamos	Diablo Canyon
$\beta = 0.01$	1.1	0.7	0.6	0.9	0.4	0.3	1.0	0.3
$\beta = 0.02$	1.1	0.7	0.6	0.9	0.4	0.3	1.0	0.3
$\beta = 0.05$	1.2	0.7	0.6	1.0	0.4	0.4	1.1	0.3

Table F-14 Annual Frequency of Unacceptable Performance ($\times 10^{-6}$) of Individual Isolator Units Tested with 99% Confidence at the Median Displacement for 220% DBE Shaking, with a Stop at the Median Displacement for 220% DBE Shaking

	Site							
	North Anna	Summer	Vogtle	Oak Ridge	Hanford	Idaho	Los Alamos	Diablo Canyon
$\beta = 0.01$	0.2	0.1	0.1	0.2	0.1	0.1	0.2	0.1
$\beta = 0.02$	0.2	0.1	0.1	0.2	0.1	0.1	0.2	0.1
$\beta = 0.05$	0.2	0.1	0.1	0.2	0.1	0.1	0.2	0.1

APPENDIX G
SCALING GROUND MOTIONS FOR RESPONSE-HISTORY ANALYSIS

G.1 Introduction

Ground motions for three sites of nuclear facilities in the United States, namely, Diablo Canyon, Vogtle and North Anna, representing 10,000-year and 100,000-year shaking are used to perform the analyses presented in Chapters 6, 7 and 8. These ground motions are developed by either spectral matching or amplitude scaling. The appropriateness of amplitude scaling ground motions to represent seismic hazard at different sites and return periods is discussed here.

G.2 Response Spectral Shapes for Different Sites and Shaking Levels

The NIST report GCR 11-917-15, "Selecting and scaling earthquake ground motions for performing response-history analysis" (NIST, 2011) presents the state-of-knowledge and state-of-practice on generating sets of ground motions for response-history analysis of buildings (and nuclear power plants). The NIST report includes detailed discussions of probabilistic seismic hazard analysis; near-field effects, which is important for the Diablo Canyon site; and spectral matching of ground motions. Herein, one set of seed motions is selected for scaling to match or be consistent with response spectra at different sites. This decision is questionable for different return periods and different sites and should be justified.

In this report, ground motions are scaled to be consistent with spectral demands at three sites of nuclear facilities in the United States. The ground motions are used in Chapters 6, 7 and 8 to qualitatively understand a) the annual frequency of unacceptable performance of isolated nuclear structures designed in accordance with the recommendations of the seismic isolation NUREG (Kammerer *et al.*, 2019), b) the importance of pressure, velocity, and temperature on the coefficient of sliding friction of Friction Pendulum™ bearings, and c) the displacement response of sample isolated nuclear power plants located at Diablo Canyon and Vogtle. Site class B per ASCE 7-10 (ASCE, 2010) is assumed for each location to enable the reader to compare the risks at different sites and to provide insight into the impact of hazard-curve slope on the calculated risk.

Consider Figure G-1 that plots normalized uniform hazard response spectra for three of the sites of Figure 6-2: Diablo Canyon, Vogtle and North Anna. The latitude and longitude for the three sites are

- Diablo Canyon: latitude 35.2116 N, longitude 120.8556 W
- Vogtle: latitude 33.1433 N, longitude 81.7606 W
- North Anna: latitude 38.0606 N, longitude 77.7894 W

Two return periods are considered: 10,000 and 100,000 years. The three sites represent regions of high, moderate and low seismicity, and Western United States, Central United States and Eastern United States, respectively. The acceleration response spectra were generated from data available at the USGS website http://geohazards.usgs.gov/hazardtool/application.php (accessed on December 30, 2014) and normalized to 1.0 g at a period of 1.5 s. Of the three sites, only Diablo Canyon would possibly be associated with site class B for site-specific calculations.

In the period range between 1.0 s and 2.0 s, which is important for calculating isolation-system displacements, the spectral shapes are sufficiently similar to justify the use at all three sites and two return periods of one set of seed ground motions scaled to be consistent with 10,000-year shaking at Diablo Canyon. If floor spectral demands were the primary focus of the response-history analysis, attention would have to be paid to spectral demands in the period range from 0.02 s to 0.50 s, and alternate scaling procedures would have to be adopted.

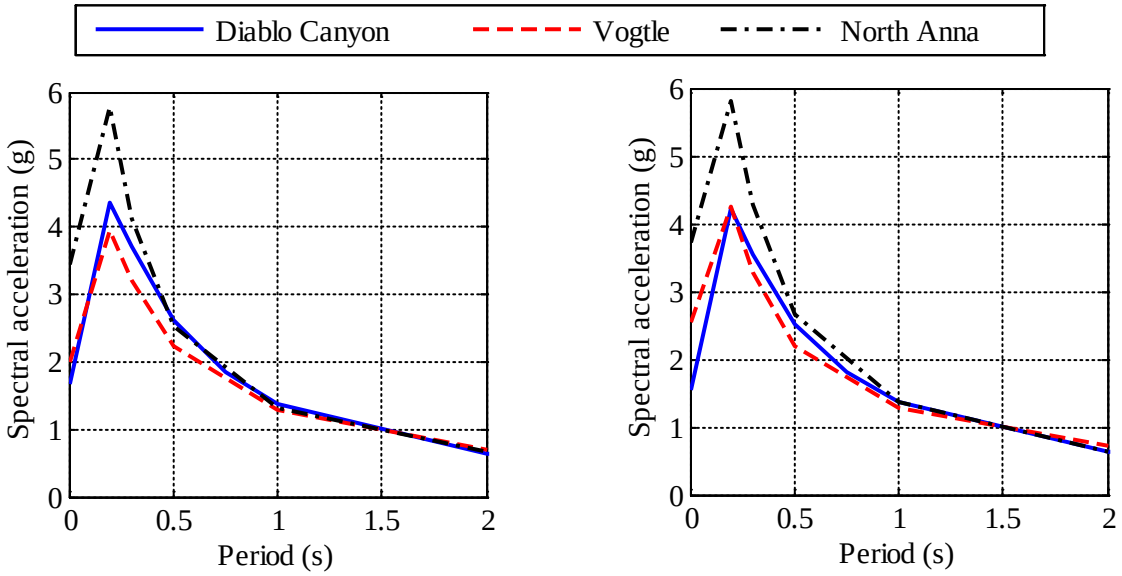

(a) 10,000-year shaking (b) 100,000-year shaking

Figure G-1 Normalized 5% Damped Uniform Hazard Response Spectra

Using 1.5 seconds as an anchor point, the factors of Table G-1 can be used to scale the 10,000-year ground motions at Diablo Canyon to other sites and return periods. A factor is not provided for 10,000 years and North Anna because risk computations in Chapter 6 are not required for this return period.

Table G-1 Ground Motion Amplitude Scale Factors

Site	Return period (years)	Scale factor
Diablo Canyon	10,000	1.00
	100,000	2.00
Vogtle	10,000	0.25
	100,000	0.60
North Anna	100,000	0.50

APPENDIX H
PROBABILITY DISTRIBUTIONS OF RESPONSES IN ISOLATED STRUCTURES

H.1 Introduction

Chapter 7 reports the results of response-history analyses performed on Friction Pendulum™ (FP) bearings with a range of geometrical and material properties, and static axial pressures. Three-component sets of thirty ground motions consistent with fractions of the seismic hazard at the site of a nuclear power plant in the United States were used for the analyses. The responses to each set of ground motions, namely, peak isolator displacements, peak temperature at the sliding surface, and floor spectral ordinates were assumed to distribute lognormally. This assumption is verified in this appendix.

H.2 Analysis Scheme

Single FP bearings with sliding periods of 1.5 s, 2 s, 3 s and 4 s, reference coefficients of friction of 0.03, 0.06 and 0.09, and reference axial pressures of 10 MPa and 50 MPa, were subjected to the sets of 30 ground motions consistent with 10,000-year return period seismic hazard (design basis earthquake, DBE) at Diablo Canyon. See Chapter 7 for details. The ground motions were amplitude scaled to six intensities: 25%, 60%, 100%, 150%, 167% and 200% DBE. Five models that consider the dependencies of the instantaneous values of axial pressure, sliding velocity and temperature at the sliding surface, on the coefficient of sliding friction were used to define friction at the sliding surface. Response-history analyses for some combinations of sliding period, reference coefficient of friction and shaking intensity could not be completed because of high displacements, for which converged solutions could not be obtained. These combinations are identified in Chapter 7.

H.3 Tests to Determine Normality

Three tests to determine the normality of a data set are considered: Lilliefors, Chi-square and Jarque-Bera. The test statistics for the data set are compared with corresponding values for a normally distributed data set. The statistics are briefly discussed below.

The statistic, LT, used in the Lilliefors test (Lilliefors, 1969) is the maximum absolute difference between the empirical cumulative distribution function, O_{CDF}, of the data and the cumulative distribution function, E_{CDF}, for a normal distribution with the same mean and variance:

$$LT = \max\left|O_{CDF} - E_{CDF}\right| \qquad \textbf{(H-1)}$$

where all terms were defined previously.

The Chi-square test (e.g., Benjamin and Cornell (1970)) is performed by grouping the data into bins and comparing the observed and expected counts in the bins. The test statistic, χ^2, is given by

$$\chi^2 = \sum_{j=1}^{n_{bin}} \frac{\left(O_j - E_j\right)^2}{E_j} \qquad \textbf{(H-2)}$$

where O_j and E_j are observed and expected counts in the bins, respectively, and n_{bin} is number of bins.

The test statistic, JB, for the Jarque-Bera test for normality of a data set (Jarque and Bera, 1987) is given by

$$JB = \frac{n_{JB}}{6}\left(s_{JB}^2 + \frac{\left(k_{JB} - 3\right)^2}{4}\right) \qquad \textbf{(H-3)}$$

where n_{JB} is number of data points in the sample, s_{JB} is the sample skewness given by

$$s_{JB} = \frac{\mu_3^2}{\mu_2^3} \qquad \textbf{(H-4)}$$

and k_{JB} is sample kurtosis given by

$$k_{JB} = \frac{\mu_4}{\mu_2^2} \qquad \textbf{(H-5)}$$

where $\mu_i \ \left(i = 2, 3, 4\right)$ is given by

$$\mu_i = \frac{1}{n}\sum_{j=1}^{n}\left(v_j - \bar{v}\right)^i \qquad \textbf{(H-6)}$$

where v_j is the j^{th} data point in the sample of size n_{JB} and $\bar{v}$ is the average of the sample.

The three tests are performed on the log of the response quantities (e.g., peak displacement) at 5% significance level[46,47] to determine if the sets of data distribute lognormally.

---

[46] A significance level of 5% means that there is a less than 5% probability of the distribution not being normal if the test indicates that the distribution is normal. A detailed discussion on the topic can be found in Benjamin and Cornell (1970).

[47] A significance level of 5% is used traditionally. A test conducted at a smaller significance level is more likely to lead to the conclusion that the data is lognormally distributed.

H.4 Results

Figure H-1(a) presents the cumulative distribution of the 30 values of peak displacements of the FP bearing with a sliding period of 3 s, a reference coefficient of friction of 0.03, friction at sliding surface defined using Model 1 (Coulomb model) of Table 6-1, and a reference axial pressure of 50 MPa, subjected to the 30 ground motions of 100% amplitude. Also plotted in the panel is the lognormal fit to the data. Figures H-1(b), H-1(c), H-1(d) and H-1(e) present results for the other four friction models of Table 6-1. The five sets of data distribute lognormally per the three tests of Section H.3, with the exception of the data of Figures H-1(c) and H-1(e) that do not distribute lognormally per the Lilliefors test at 5% significance level.

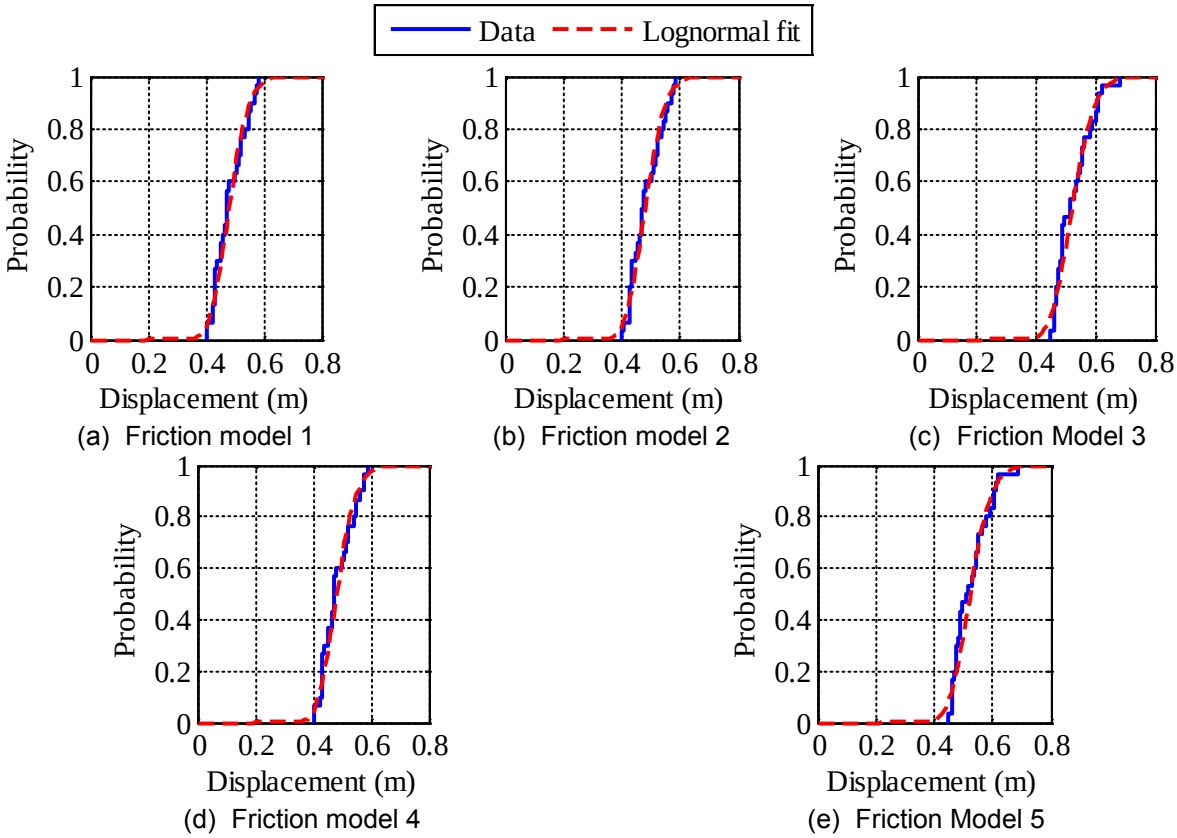

Figure H-1 Empirical Cumulative Distribution of the 30 Values of Peak Displacement and the Lognormal Fits

Figure H-2(a) presents the outputs of Lilliefors test performed on the 550 sets of 30 values of the log of peak displacements of FP bearings with different geometries, liners and loadings. A total of 513 (93%) of the 550 sets of data distribute lognormally per this test. Figures H-2(b) and H-2(c) present the results for Chi-square and Jarque-Bera tests, respectively. The sets of 30 peak displacements distribute lognormally for 100% and 94% of the 550 combinations, respectively.

Figure H-3 presents the cumulative distributions for the five sets of 30 values of peak temperatures at the sliding surface of the FP bearing considered in Figure H-1. All five sets of data distribute lognormally per the three tests. Figure H-4 presents the results of the three tests for all the 550 combinations. The 30 values of temperatures distribute lognormally for 80% to 90% of the combinations

Figure H-5 presents the cumulative distribution for the 30 values of spectral acceleration at 0.05 s corresponding to the absolute horizontal acceleration response of the slider of the FP bearing considered in Figures H-1 and H-3. All five sets of 30 values distribute lognormally per the three tests. Figure H-6 presents the results of the normality tests on the log of the spectral ordinates at nine periods (= 0.01 s, 0.02 s, 0.03 s, 0.05 s, 0.075 s, 0.1 s, 0.2 s, 0.5 s and 1 s) corresponding to the absolute acceleration of the slider in the vertical and two horizontal directions for all 550 combinations of Figure H-2 (and Figure H-4). The 30 values of spectral ordinates distribute lognormally for 90% to 95% of the 14850 cases ($3 \times 9 \times 550$).

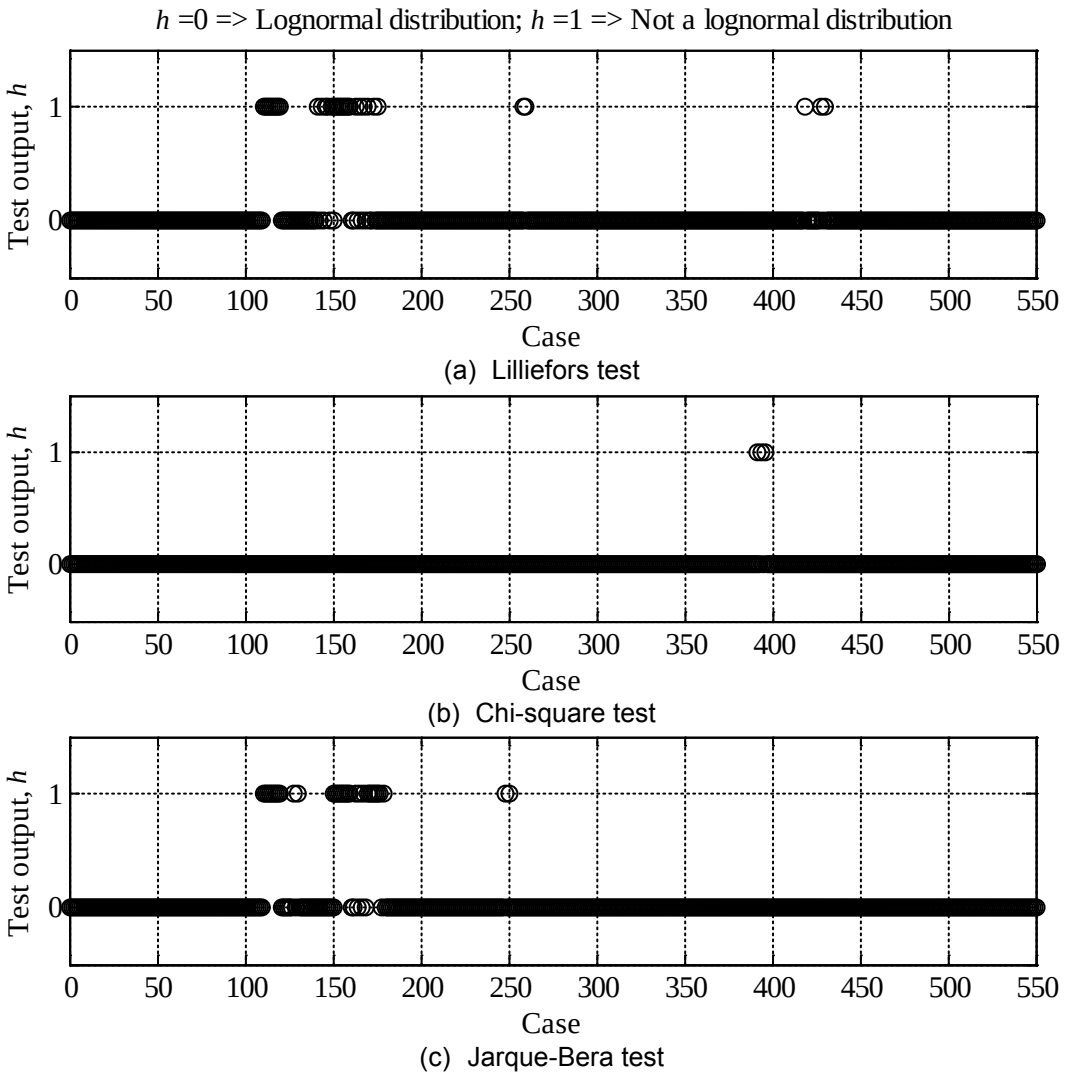

Figure H-2 Results of Normality Tests Performed on the Sets of the Logs of the 30 Values of Peak Displacements of FP Bearings

H.5 Summary

The distributions of the response quantities (e.g., peak temperature at sliding surface) of FP bearings with a range of geometrical and material properties, and static axial loads, subjected to ground motions consistent with different fractions of seismic hazards at the site of the Diablo Canyon nuclear power plant are studied. The Lilliefors, Chi-square and Jarque-Bera tests for normality are used to determine if the log of the response quantities distribute normally. The peak isolator displacements, peak temperatures at the sliding surface, and floor spectral accelerations distribute lognormally in at least 90%, 80% and 90% of the cases, respectively, according to the three tests performed at the 5% significance level. Therefore, the distributions can be assumed to be lognormal for all combinations of natural period, reference coefficient of friction, friction model, reference axial pressure and sets of ground motions.

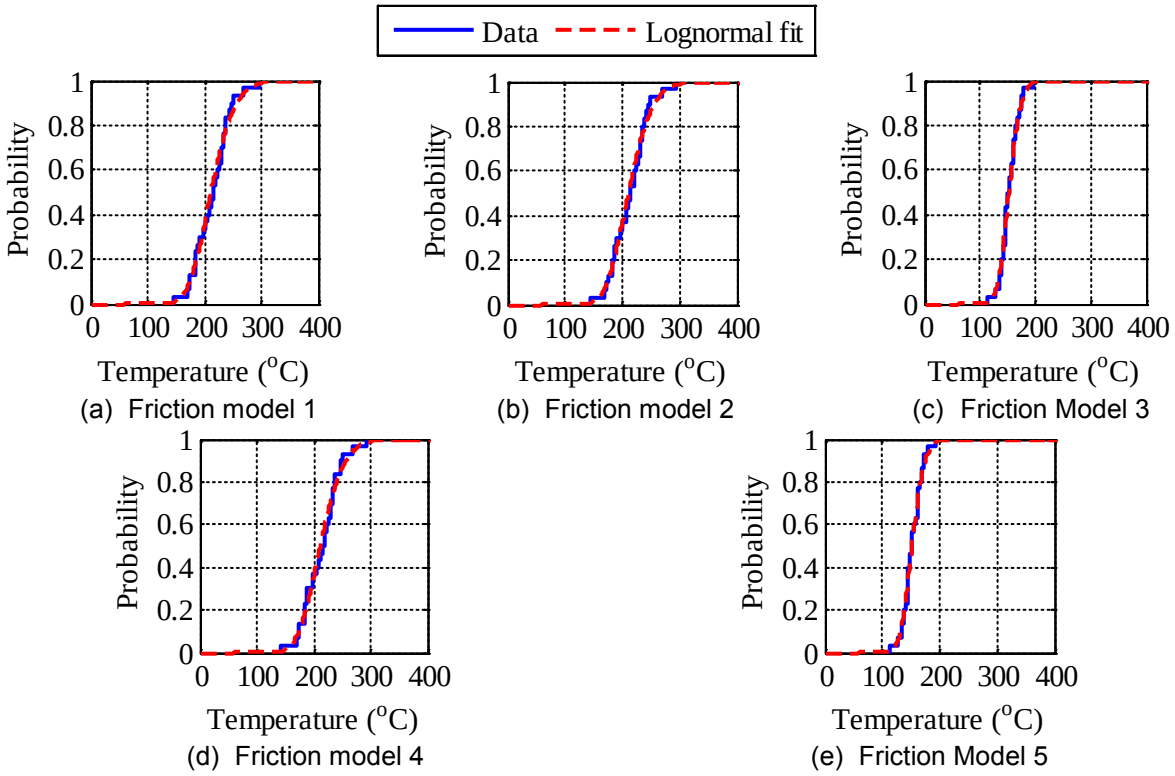

Figure H-3 Empirical Cumulative Distribution of the 30 Values of Peak Temperature and the Lognormal Fits

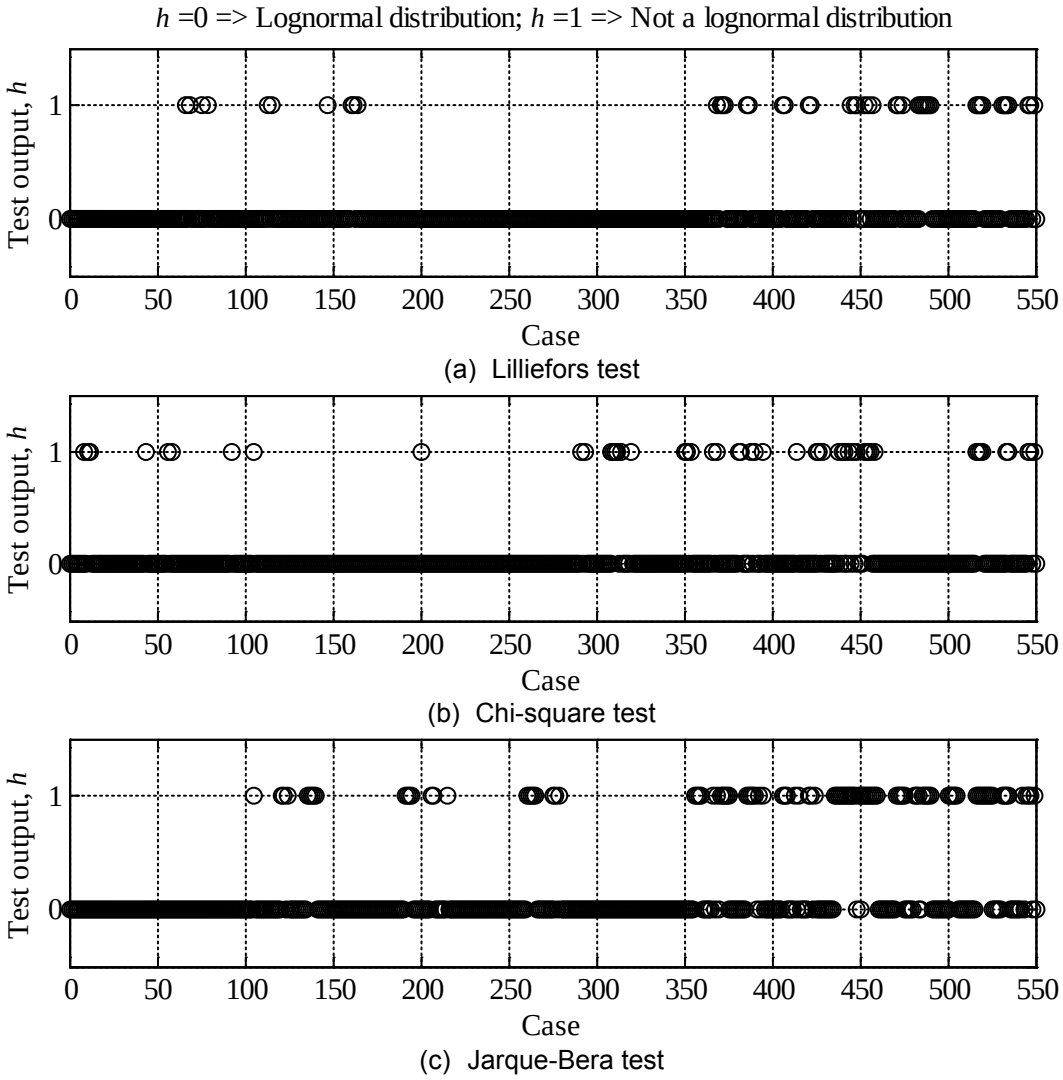

Figure H-4 Results of Normality Tests Performed on the Sets of the Logs of the 30 Values of Peak Temperature at the Sliding Surface of FP Bearings

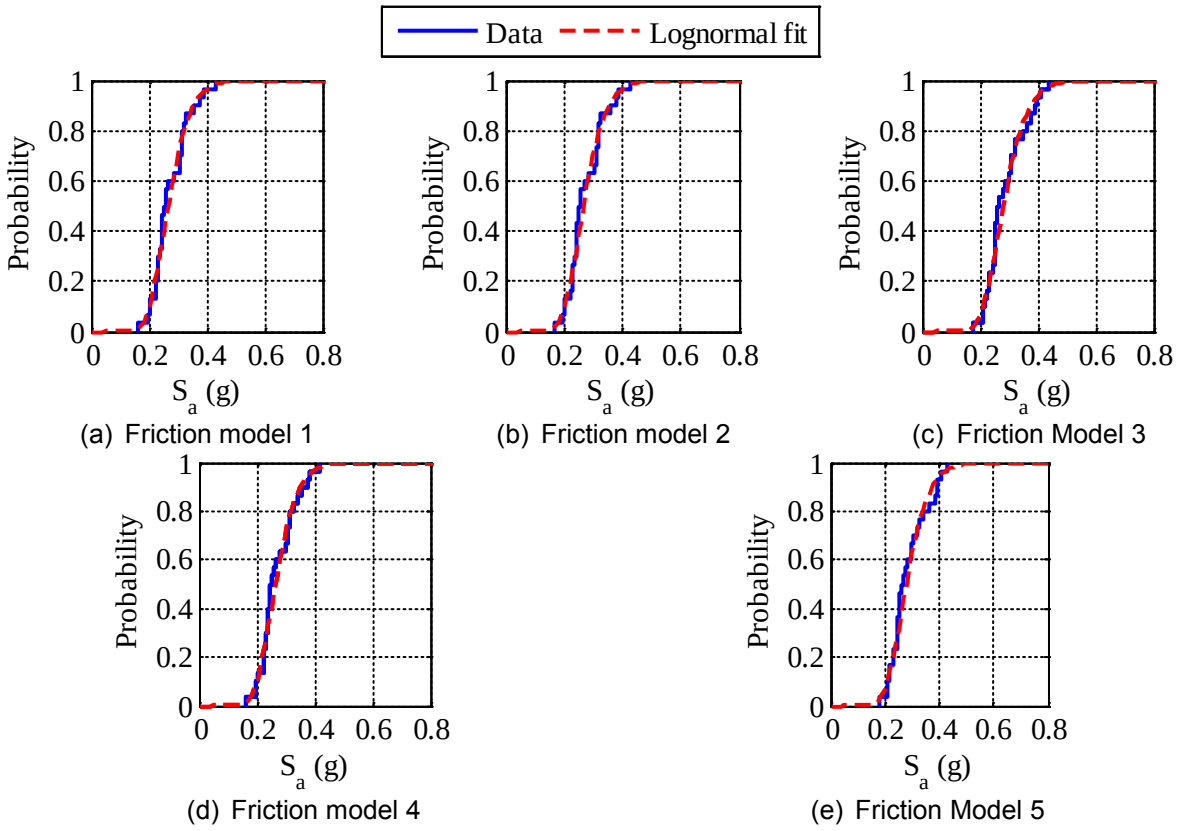

Figure H-5 Empirical Cumulative Distribution of the 30 Values of Floor Spectral Acceleration and the Lognormal Fits

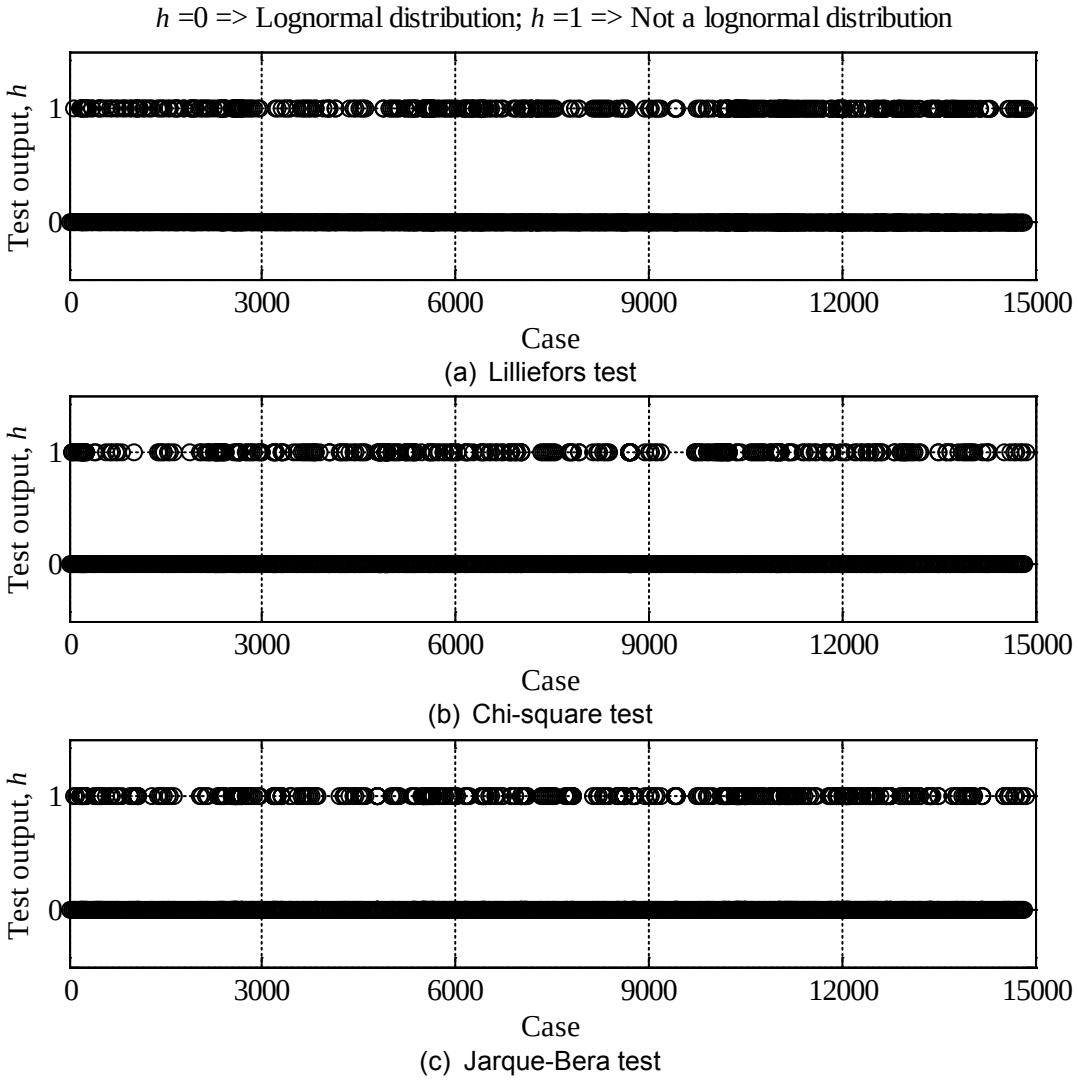

Figure H-6 Results of Normality Tests Performed on the Sets of the Logs of the 30 Values of Floor Spectral Acceleration

NRC FORM 335
(12-2010)
NRCMD 3.7

U.S. NUCLEAR REGULATORY COMMISSION

BIBLIOGRAPHIC DATA SHEET

(See instructions on the reverse)

1. REPORT NUMBER
(Assigned by NRC, Add Vol., Supp., Rev., and Addendum Numbers, if any.)

NUREG/CR-7254

2. TITLE AND SUBTITLE

Seismic Isolation of Nuclear Power Plants Using Sliding Bearings

3. DATE REPORT PUBLISHED

MONTH	YEAR
May	**2019**

4. FIN OR GRANT NUMBER

5. AUTHOR(S)

M. Kumar[1], A. Whittaker[2], M. Constantinou[2]

6. TYPE OF REPORT

Technical

7. PERIOD COVERED (Inclusive Dates)

8. PERFORMING ORGANIZATION - NAME AND ADDRESS (If NRC, provide Division, Office or Region, U. S. Nuclear Regulatory Commission, and mailing address; if contractor, provide name and mailing address.)

[1]IIT Gandhinagar; formerly graduate student, University at Buffalo, State University of New York, 212 Ketter Hall, Buffalo, NY 14260
[2]MCEER, University at Buffalo, State University of New York, 212 Ketter Hall, Buffalo, NY 14260

9. SPONSORING ORGANIZATION - NAME AND ADDRESS (If NRC, type "Same as above", if contractor, provide NRC Division, Office or Region, U. S. Nuclear Regulatory Commission, and mailing address.)

U.S. Nuclear Regulatory Commission
Office of Nuclear Regulatory Research
Washington, DC 20555

10. SUPPLEMENTARY NOTES

11. ABSTRACT (200 words or less)

This report presents a study on the seismic isolation of nuclear power plant (NPP) structures, with a focus on single concave sliding bearings. The key goals of the study were to 1) characterize the coefficient of friction at the sliding surface, 2) determine the influence of the definition of the coefficient of friction and alternate representations of seismic hazard on the response of isolated NPP structures, and 3) quantify the seismic vulnerability of isolated NPP structures. Consideration of heating effects may substantially influence the response of an isolated NPP. The uniform hazard response spectrum should be used to define seismic hazard for analysis of isolated NPPs with explicit consideration of the difference in amplitude of the orthogonal horizontal components of ground shaking. A stop must be provided to ensure that failure of the isolation system is not a key contributor to the seismic core damage frequency. Seismic risk can be reduced by designing and testing isolators for displacements greater than those expected in beyond design basis shaking.

12. KEY WORDS/DESCRIPTORS (List words or phrases that will assist researchers in locating the report.)

seismic isolation, nuclear power plant, sliding bearing, coefficient of friction, temperature dependence of friction, pressure dependence of friction, velocity dependence of friction, seismic hazard definition, seismic risk calculation

13. AVAILABILITY STATEMENT

unlimited

14. SECURITY CLASSIFICATION

(This Page)
unclassified

(This Report)
unclassified

15. NUMBER OF PAGES

16. PRICE

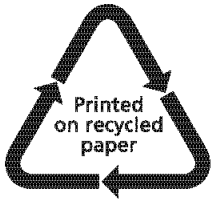

Federal Recycling Program

UNITED STATES
NUCLEAR REGULATORY COMMISSION
WASHINGTON, DC 20555-0001

OFFICIAL BUSINESS